polymers

Special Issue Reprint

Exploration and Innovation in Sustainable Rubber Performance

Edited by
Pilar Bernal-Ortega, Anke Blume and Rafał Anyszka

mdpi.com/journal/polymers

MDPI

Exploration and Innovation in Sustainable Rubber Performance

Exploration and Innovation in Sustainable Rubber Performance

Guest Editors

Pilar Bernal-Ortega
Anke Blume
Rafał Anyszka

MDPI

Basel • Beijing • Wuhan • Barcelona • Belgrade • Novi Sad • Cluj • Manchester

Guest Editors

Pilar Bernal-Ortega
Department of Mechanics of Solids, Surfaces & Systems (MS3)
University of Twente
Enschede
The Netherlands

Anke Blume
Department of Mechanics of Solids, Surfaces & Systems (MS3)
University of Twente
Enschede
The Netherlands

Rafał Anyszka
Department of Mechanics of Solids, Surfaces & Systems (MS3)
University of Twente
Enschede
The Netherlands

Editorial Office

MDPI AG
Grosspeteranlage 5
4052 Basel, Switzerland

This is a reprint of the Special Issue, published open access by the journal *Polymers* (ISSN 2073-4360), freely accessible at: https://www.mdpi.com/journal/polymers/special_issues/G98K4FU9G3.

For citation purposes, cite each article independently as indicated on the article page online and as indicated below:

Lastname, A.A.; Lastname, B.B. Article Title. *Journal Name* **Year**, *Volume Number*, Page Range.

ISBN 978-3-7258-7573-3 (Hbk)
ISBN 978-3-7258-7574-0 (PDF)
https://doi.org/10.3390/books978-3-7258-7574-0

Contents

About the Editors

Pilar Bernal-Ortega

Pilar Bernal-Ortega earned her degree in Chemical Engineering from the Polytechnic University of Valencia (UPV), Spain. She went on to complete a master's program in High Specialization in Plastics and Rubber at the International University Menéndez Pelayo (UIMP), also in Spain. In 2016, she was awarded a government grant to pursue a PhD in rubber technology with the Elastomers Group at the Institute of Polymer Science and Technology (ICTP), Spain. She successfully defended her PhD thesis, titled "Sulfur-Modified Carbon Nanotubes for the Development of Rubber Tire Tread Compounds," on March 13, 2020. In December 2019, Pilar joined the Elastomer Technology & Engineering Group as a postdoctoral researcher, contributing to a collaborative project with the tire manufacturer Bridgestone. Since December 2022, she has been serving as an Assistant Professor within the same group.

Anke Blume

Anke Blume was born on April 6, 1969, in Hanover, Germany. She studied chemistry at the Leibniz University Hanover from October 1988 to July 1993. She first worked in depth with rubber during her master's thesis. Consequently, she carried out her PhD thesis at the "German Institute for Rubber Technology" (DIK), which she completed in mid-November 1995. She continued her work at the DIK as a post-doc for nine months. In 1996, she joined the Degussa company in Cologne, Germany (now named "Evonik Industries"), where she was in charge of the development of silica and silanes for rubber applications, as well as the management of Evonik's intellectual property regarding the use of silica and silanes in rubber applications. She became the head of the Elastomer Technology and Engineering department of the University of Twente on October 1, 2013, in addition to her work at Evonik. In April 2021, she decided to fully dedicate her work to the university. This allows her to follow her passion for teaching and rubber, to further explore its mysteries, and to inspire young people to engage with this ascinating material.

Rafał Anyszka

Rafał Anyszka got his Ph.D. in 2014 at the Lodz University of Technology, designing ceramifiable elastomer composites for fire protection systems. Afterward, he was involved in the development of sulfur-derived polymers and sulfur concretes. In 2017, he started Postdoc projects at the University of Twente, designing molecular Velcro systems for silica-rubber coupling and surface-functionalized nano-silica for high-voltage DC polypropylene insulation composites. In 2025, he finished an EU-funded MSCA Global Fellowship project focused on designing rubber for the Mars environment. Recently, his focus shifted to more interdisciplinary areas between rubber technology and socioeconomic studies. Currently, he is coordinating the establishment of the first ECIU association – ECIU Rubber Network.

Preface

Elastomers represent a fundamental element of modern materials engineering and are indispensable across a wide spectrum of industrial and consumer applications. From tires and hoses to seals, vibration dampers, and flexible mechanical components, rubber-based materials provide a unique combination of elasticity, durability, resilience, and chemical resistance. These properties have made elastomers essential to transportation, infrastructure, manufacturing, and everyday products. However, the increasing global demand for rubber materials has also intensified concerns regarding their environmental impact, resource consumption, and end-of-life management.

In recent years, the elastomer and rubber industries have increasingly focused on improving the sustainability of rubber products while maintaining their performance characteristics. Achieving this balance represents a significant scientific and technological challenge. Traditional rubber systems rely heavily on petroleum-derived components, energy-intensive processing methods, and crosslinked networks that are difficult to recycle. Consequently, developing more sustainable elastomer technologies requires a comprehensive approach that addresses material sourcing, product durability, processing efficiency, and waste management.

Several complementary strategies have emerged to reduce the environmental impact of elastomeric materials. One important approach focuses on improving the intrinsic performance of rubber compounds. By enhancing mechanical strength, wear resistance, fatigue behavior, and aging stability, elastomer products can achieve longer service lifetimes. Extended durability directly translates into reduced material consumption and lower waste generation over time, contributing significantly to sustainability goals.

Another promising direction involves the increasing use of naturally sourced or bio-based materials. Researchers and industry professionals are actively exploring renewable fillers, bio-derived polymers, and sustainable additives that can partially or fully replace conventional fossil-based ingredients. These developments aim to reduce reliance on non-renewable resources while maintaining compatibility with established processing technologies and performance requirements.

Equally important is the advancement of technologies that improve the recyclability and circularity of rubber products. Because traditional vulcanized elastomers form permanent crosslinked networks, recycling remains a complex challenge. Innovations in devulcanization, reprocessing methods, and dynamic crosslinking systems are creating new opportunities to recover value from rubber waste and reintegrate it into new products.

This Special Issue brings together contributions from researchers working at the forefront of elastomer science and technology. The collected papers present new systems and material concepts designed to enhance rubber performance, introduce advanced functionalities, improve recyclability, and expand the use of bio-based resources. Collectively, these studies provide valuable insights into emerging strategies that can guide the development of more sustainable elastomeric materials.

We hope that the research presented in this issue will stimulate further innovation and collaboration within the elastomer community and contribute to the broader objective of designing rubber materials that meet both performance and sustainability requirements for future applications.

Pilar Bernal-Ortega, Anke Blume, and Rafał Anyszka
Guest Editors

polymers

MDPI

Editorial

Closing Editorial to the Special Issue "Exploration and Innovation in Sustainable Rubber Performance"

Pilar Bernal-Ortega *, Anke Blume and Rafal Anyszka

Elastomer Technology & Engineering, Department of Mechanics of Solids, Surfaces & Systems (MS3), Faculty of Engineering Technology, University of Twente, Drienerlolaan 5, 7522 NB Enschede, The Netherlands; a.blume@utwente.nl (A.B.); r.p.anyszka@utwente.nl (R.A.)
* Correspondence: p.bernal@utwente.nl

It is with great pleasure that we present the collection of articles published in this Special Issue of MDPI's *Polymers*, dedicated to "Exploration and Innovation in Sustainable Rubber Performance". When we began this Special Issue, our goal was to gather innovative research addressing the ways in which rubber materials can be transformed to be more sustainable, whether that be through bio-based raw ingredients, improved recyclability, enhanced performance for extended durability, or novel strategies that reduce environmental footprints.

We are thrilled by the outcome: this issue features a diverse set of studies covering fundamental research, applied materials science, and engineering solutions. The contributions include investigations into recycled or bio-based fillers, novel processing methods, innovative elastomer formulations, studies on aging and durability, analyses of environmental impact, and explorations of material performance under real-world conditions. Together, they provide a complete overview of the current state of the art of the sustainability of rubber, reflecting both academic and industrial interests.

Through these works, this Special Issue addresses several key topics regarding sustainability within the rubber field and achieves the following results:

- Demonstrates viable pathways for integrating bio-based or recycled materials into elastomer matrices without compromising essential properties.
- Improves our understanding of structure–property relationships in sustainable rubber compounds, enabling the effective design of durable, high-performance materials.
- Highlights recycling, waste reduction, and life-cycle considerations for rubber products, contributing to circular economy approaches.
- Encourages innovation in filler, compounding, and processing techniques and collaborations across academia and industry.

We would like to extend our sincere gratitude to all authors, reviewers, and colleagues involved in the peer review and editorial process. Their dedication and scientific rigor have made this Special Issue possible. We also thank the Editorial Office of *Polymers* for their support and guidance throughout this process.

Finally, we hope that this collection will serve as a useful resource for researchers and industries aiming to push the boundaries of sustainable elastomer development. We encourage readers to explore the full set of papers and to build upon their findings, whether towards improved recycling processes, greener materials, or novel applications. We look forward to seeing how the insights gathered here will inspire future work and contribute to a more sustainable rubber industry.

Conflicts of Interest: The authors declare no conflict of interest.

https://doi.org/10.3390/polym18050576

polymers

MDPI

Article

Synergistic Effects of Nitrosamine-Safe Accelerators for Enhanced Natural Rubber Latex Balloon in Sulfur Conventional Vulcanizing System

Thanakan Chang-In, Ekasit Anancharoenwong and Sunisa Suchat *

Faculty of Science and Industrial Technology, Prince of Songkla University, Surat Thani Campus, Surat Thani 84000, Thailand
* Correspondence: author: sunisa.su@psu.ac.th

Abstract

The vulcanization of natural rubber latex (NRL) relies on accelerators to achieve effective crosslinking by a sulfur conventional vulcanizing system and desirable properties such as tensile strength and elasticity. This study investigates the synergistic effects of carcinogenic nitrosamine-safe accelerators to develop a high-performance and safe NRL vulcanization system. A synergistic combination of 0.36 phr Zinc dibutyldithiocarbamate (ZBEC), 0.36 phr Tetrabenzylthiuram disulfide (TBzTD), and a trace amount of Zinc diethyldithiocarbamate (ZDEC), 0.03 phr, demonstrated optimal performance, yielding superior tensile strength (22.13 MPa), elongation at break (1153%), and thermal stability (Tmax 384.15 °C). Notably, this formulation exhibited below the detectable level limits of hazardous nitrosamines (*N*-nitrosodimethylamine (NDMA) and *N*-nitrosodibutylamine (NDBA)). The synergistic nitrosamine-safe accelerator system offers a promising strategy for producing environmentally responsible and consumer-safe NRL products with enhanced mechanical and thermal properties.

Keywords: natural rubber latex; nitrosamine-safe; synergistic accelerator system; mechanical properties

1. Introduction

The global balloon production volume is valued at around USD 1.85 billion in 2024, with growth expected to reach USD 3.38 billion by 2033, securing a significant market size and a consistent production volume increase across the world [1,2]. However, the production volume of natural rubber balloons is a small percentage of the total natural rubber production, as the global production of natural rubber in 2024 amounted to 28.8 million tons. Rubber balloons are thin gauge rubber products produced from natural rubber latex (NRL) compounds [3]. NRL balloons have superior elasticity, being capable of stretching to seven to eight times their original length while maintaining resilience: a quality not reached by synthetics. This exceptional performance has established rubber balloons as one of the most affordable and universally popular toys across all demographic segments [4]. Beyond children's entertainment, these versatile products serve multiple functions including celebratory decorations, retail environment enhancement, target practice activities, and festive displays, contributing to their sustained market growth.

However, this seemingly innocuous product harbors a concerning health risk: natural latex can break down to form nitrosamines, a group of known carcinogens detected in

various latex products (rubber nipples and gloves) [5,6]. This discovery has prompted the development of methods for extraction and concentration of volatile nitrosamine from latex balloons, highlighting an urgent need to address safety concerns in this growing industry without compromising the product's widespread appeal and accessibility.

Most toxicological assessments of nitrosamines focus on their carcinogenic and mutagenic properties. Nitrosatable substances can be converted into carcinogenic nitrosamines through reactions with nitrosating agents such as nitrite and nitrogen oxides [7]. Endogenous formation of *N*-nitroso compounds occurs via nitrosation (by nitrite derived from nitrate) of ureas, guanidine, amides, amino acids, and (primary, secondary and aromatic) amines [8]. Of the over 300 different nitrosamines, RIVM (2003) [9] identified *N*-nitrosodimethylamine (NDMA) and *N*-nitrosodibutylamine (NDBA) as being the most prevalent ones, being detected in 96% and 61% of samples, respectively. Both are classified by IARC and the EU as category 2 carcinogens [10]. NDMA, with the generic chemical structure R_2N-N=O, is the most frequently detected carcinogenic nitrosamine, another form of nitrosamines, although it is of a less dangerous class (BAuA). The European Union has established specific limits for nitrosamines and nitrosatable substances in natural rubber balloons according to European standard EN71-12 [11,12]. The Federal Republic of Germany has proposed limits for nitrosamines and nitrosatable substances in balloons, which are 50 μg/kg and 1000 μg/kg, respectively. Traditionally, nitrosamines and nitrosatable substances are analyzed using thermal energy analyzers (TEA), but due to the limited availability of this expensive equipment type, an improved analysis method using the more widely available gas chromatography–mass spectrometry (GC-MS) technique has been developed based on the EN 12868:2017 standard [13–15].

Natural rubber latex balloons can release carcinogenic nitrosamines when certain vulcanization accelerators (carbamates such as zinc diethyldithiocarbamate; ZDEC) are used during balloon production [16]. These substances pose health risks when released during balloon inflation or mouthing, with children being particularly vulnerable. Research by Smith and Norris (2003) [17] identified hazardous exposure levels when children mouth balloons with high nitrosamine content. The primary problematic accelerators are ZDEC, which shows mutagenic activity in bacterial tests, and tetramethyl thiuram disulfide (TMTD), which is a suspected carcinogen: an avoidable threat [18]. Fortunately, safe alternatives exist, namely zinc n-butylbenzothiazole-2-sulfenamide (ZBEC) and tetrabenzylthiuram disulfide (TBzTD) [19]. These alternatives contain low nitrosatable substances, effectively eliminating nitrosamine formation while maintaining product quality. The rubber industry has the knowledge and the technology to produce safer balloon products by transitioning to these alternative accelerators, making this health risk entirely preventable.

This study aimed to comprehensively investigate the performance characteristics of a nitrosamine-safe binary accelerator system comprising TBzTD and ZBEC in the sulfur vulcanization of an NRL balloon. To evaluate the cure characteristics, the swelling index for dipping processability and chemical control were tested for NRL compounds containing various ratios of ZBEC and TBzTD accelerators. The mechanical properties (modulus, elongation at break and tensile strength) of vulcanizates before and after aging, FTIR of the functional groups and the crosslinks formed when prepared with different combinations of the TBzTD/ZBEC accelerator system were determined. The potential synergistic effects that occur when progressively replacing ZDEC with combinations of TBzTD and ZBEC accelerators were assessed. The synergistic nitrosamine-safe accelerator systems are essential to ensure that rubber products (such as balloons), achieve the required mechanical properties while fully complying with stringent safety standards concerning nitrosamine content.

https://doi.org/10.3390/polym18040438

2. Experimental

This research was divided into five steps, beginning with optimizing the formulation to be devoid of nitrosamine-producing substances, as follows.

2.1. Materials

(1) Materials in NRL films

The centrifuged concentrated latex (Hevea brasiliensis), as a high-ammonia latex (HA) with 60% dry rubber content (DRC), was supplied by Muang Mai Guthrie Public Company Limited, Thailand. The NRL compound formulations for balloon rubber products (Tables 1 and 2) were purchased from Thanodom Technology Co., Ltd., Bangkok, Thailand. Cellulose nanocrystals (CNC) were obtained as a white powder from rubber seed shells. The average molecular weight was 14,700 g/mol, with particle lengths ranging from 100 to 300 nm and diameters of 20 nm. A 5% CNC dispersion was prepared at a low filler loading of 2 phr.

Table 1. The compound formulations of NRL used in the present study.

Ingredient in Formulation	Content (phr [a])					Function
	1	2	3	4	5	
60% HA-NR latex	100	100	100	100	100	Backbone (main component)
10% Potassium hydroxide	1.0	1.0	1.0	1.0	1.0	Stabilizers 1
10% Potassium oleate	1.0	1.0	1.0	1.0	1.0	Stabilizers 2
50% Sulfur	1.5	1.5	1.5	1.5	1.5	Vulcanizing Agent
50% ZnO	1.5	1.5	1.5	1.5	1.5	Activator
5% CNC	2.0	2.0	2.0	2.0	2.0	Filler
50% Wingstay L	1.5	1.5	1.5	1.5	1.5	Polyphenol Antioxidant
50% Accelerators [b]	0.75	0.75	0.75	0.75	0.75	Accelerators

Note: [a] Parts per hundred rubber (phr) and [b] 50% accelerators in Table 2.

Table 2. The accelerator content in NRL compound formulations.

Formula No. #	Accelerator Type	Content (phr)			
		TBzTD	ZBEC	ZDEC	Total
1	ZDEC	0.75	-	-	0.75
2	ZBEC	-	0.75	-	0.75
3	TBzTD	-	-	0.75	0.75
4	ZBEC/TBzTD	0.375	0.375	-	0.75
5	ZBEC/TBzTD	0.36	0.36	0.03	0.75

2.2. Preparation of NRL Films

The NRL balloon compound formulation combinations of the TBzTD/ZBEC accelerator system were optimized to reduce the tested generation of nitrosamines. Specifically, concentrated latex was used with various types and volumes of accelerators, such as TBzTD, ZDEC, and ZBEC (singly), as well as combinations like TBzTD/ZBEC (binary) and TBzTD/ZBEC/ZDEC (ternary) in NRL. These choices were made to prevent carcinogenic nitrosamine formation. The NRL compound was prepared as a liquid mixture with additives, and mixed in a blender at 2 rpm for 20 min at room temperature. The final mixture was degassed to remove the entrapped air and then poured into glass molds, with eventual film thickness control by the total solid content. The films were cured at 80 °C

for 24 h to evaporate water and achieve uniform films. The dried films were peeled off the molds and stored for characterization. By adjusting the types and amounts of accelerators and controlling parameters such as 62% total solid content and a 103% swelling index, the synergistic activities in sulfur vulcanization of NRL films formulations were assessed, emphasizing safety and mechanical properties. A diagram of the experimental design is shown in Figure 1.

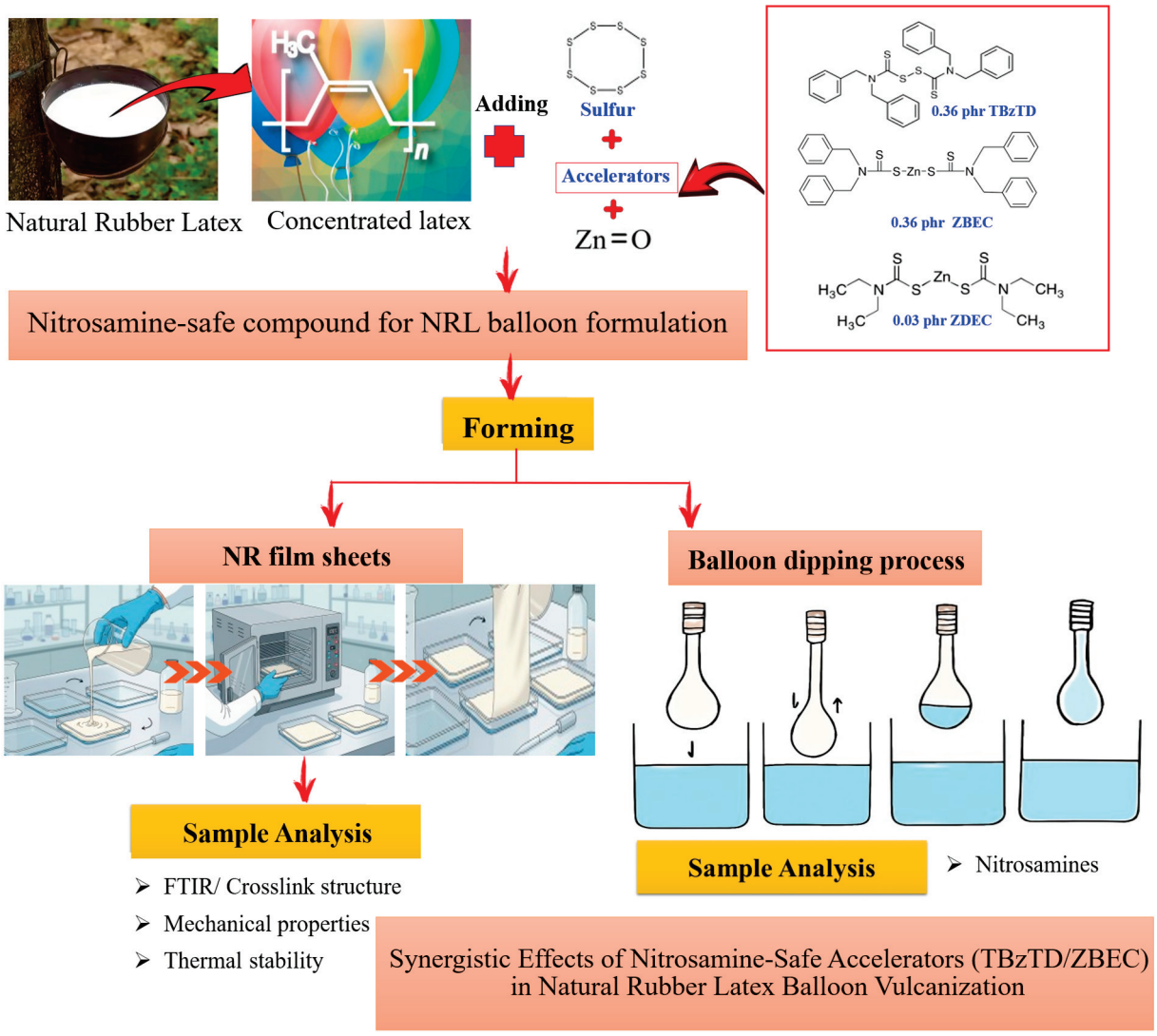

Figure 1. Experimental scheme to test synergistic activities in sulfur vulcanization of NRL balloon products.

2.3. NRL Balloon

The NRL balloon dipping process used a balloon mold, clean and dry, soaked in 10% calcium chloride coagulant and slightly dried at 45 °C, and then dipped in the NRL compound. The soaking time was 18 s, and to reuse the mold, it was washed with hot water at 70 °C for 10 min to remove coagulant or residues. The vulcanization dries the balloon in an oven at 100 °C for 1 h to complete the vulcanization process. Samples were removed from the oven and allowed to cool to room temperature. Talcum powder was applied to the balloon surface to prevent sticking.

The finished balloons were carefully removed from the mold, and samples without flaws or damage were kept for the nitrosamine test using GC-TEA, following the standard procedure based on EN 12868:2017 [20].

2.4. Characterization and Properties

2.4.1. The Swelling Test

The development of the NRL compound formula from concentrated latex involved varying the types and amounts of accelerator agents. In a sulfur vulcanized system, a stabilizer, activators, and an antioxidant were added to the NRL, and the mixture was matured until a swelling index of 103% was reached, indicating partial crosslinking via sulfur bridges. The compound was then poured onto a 2 mm thick layer on a glass plate, dried at 120 °C for 30 min, and finally cured by heating. The swelling test followed ISO 124, using 3.0 cm circular samples. The diameter was measured carefully at three points and the average was recorded, after which the specimens were immersed in toluene at 23 ± 2 °C for 3 h. The swelling (%) was calculated from the change in diameter caused by immersion, and the average is reported. The percentage swelling was computed as follows.

$$\% \text{ Swelling} = [(B - A)/A] \times 100 \quad (1)$$

where A is the initial diameter of the specimen before immersion in toluene, and B is the diameter of the specimen after immersion in toluene for 3 h.

For reliable results, this test was run in triplicates and the mean value was recorded, along with test conditions and sample identification.

2.4.2. FTIR Analysis

Fourier transform infrared spectroscopy (FTIR) was employed in transmission mode to analyze the structure, using a Spectrum Two FT-IR spectrometer equipped with a DTGS detector, manufactured by PerkinElmer, Inc., Waltham, MA, USA. Thin rubber sheets with smooth surfaces were analyzed in transmission mode, utilizing the attenuated total reflectance (ATR) accessory for solid-state sampling. FTIR spectra were recorded across the broad wavenumber range from 4000 to 400 cm^{-1} at a resolution of 4 cm^{-1}.

2.4.3. Mechanical Properties

The mechanical properties of the NRL film samples are reported as averages of five replicates. Tensile properties were measured, determining the modulus, strength and elongation at break, following the ASTM D 412 standard using a Tinius Olsen 10ST tensile testing machine (Honey Crock Lane, UK). Dumbbell Type C specimens were tested at a speed of 500 mm/min with a 5 kN load cell.

2.4.4. Thermal Stability

(1) Accelerated aging was conducted following ISO 188, where samples were subjected to thermal aging at 70 °C for 168 h. After aging, tensile strength, elongation at break, and modulus were tested.
(2) Thermogravimetric analysis (TGA) was performed using a TGA-SDTA 851 analyzer (Mettler Toledo, Zurich, Switzerland). Samples were heated from 30 °C to 600 °C under nitrogen atmosphere, then from 600 °C to 900 °C under oxygen atmosphere, both at a 10 °C/min heating rate.

2.4.5. Nitrosamines and Nitrosatable Substances

Nitrosamine testing of the balloon latex compound was done using a Gas Chromatography–Thermal Energy Analyzer (GC-TEA) at TÜV Rheinland Hong Kong Ltd., Tsuen Wan, Hong Kong. Nitrite migration from the samples was assessed following the European standard procedure, based on EN 12868:2017 [20]. This method determines nitrosamines by first extracting them into artificial saliva at 40 °C to simulate migration. Nitrosamines require an acidification step for conversion

https://doi.org/10.3390/polym18040438

prior to extraction and concentration. The prepared extracts are quantified using GC-TEA, due to its high specificity for nitroso compounds. The reported results are compared to standard limits (migratable nitrosamines, 0.05 mg/kg, and migratable nitrosatable substances, 1.0 mg/kg). The twelve target *N*-nitrosamines identified are *N*-nitrosodimethylamine (NDMA), *N*-nitrosodiethylamine (NDEA), *N*-nitrosodipropylamine (NDPA), *N*-nitrosodibutylamine (NDBA), *N*-nitrosodiisobutylamine (NDiBA), *N*-nitrosoethylphenylamine (NEPhA), *N*-nitrosopiperidine (NPIP), *N*-nitrosopyrrolidine (NPYR), *N*-nitrosomorpholine (NMOR), *N*-nitrosomethylphenylamine (NMPhA), *N*-nitrosodiisononylamine (NDiNA), and *N*-nitrosodibenzylamine (NDBzA).

3. Results and Discussion

3.1. Characterization and Properties

3.1.1. The Swelling Test

Figure 2 shows the results that are indicative of the crosslinking efficiency of individual accelerators (all tested) over time, with the swelling in all cases decreasing with the curing time, confirming continuous crosslink formation. The nitrosamine-safe alternatives, TBzTD/ZBEC/ZDEC, led to the fastest reduction in swelling, achieving the target crosslinking within 7 days. So, the curing time required to reach the 103% swelling index was reduced from 10 days (ZDEC and ZBEC) to 7 days. TBzTD and ZBEC binary and TBzTD alone were also effective, promoting sufficient crosslinking to reach the standard threshold (103% swelling) within 9 days.

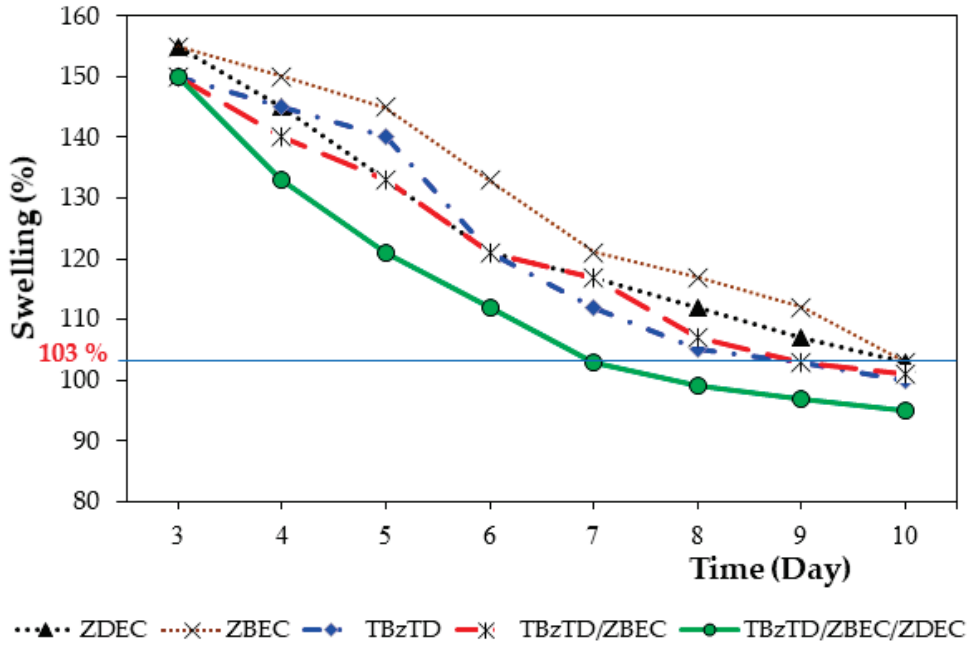

Figure 2. Swelling results are indicative of crosslink bond formation of compound rubbers with different accelerators.

Obtaining this 103% swelling index confirms the effectiveness of TBzTD/ZBEC/ZDEC as accelerators to reduce the curing time while maintaining the required crosslink density for product quality.

3.1.2. FTIR Analysis of Accelerator Types in Sulfur Vulcanization of NRL Films

The consulted expert sources focused on the formation and mitigation of nitrosamines in natural rubber latex balloons. One primary source details research into substituting problematic vulcanization accelerators like ZDEC with safer alternatives such as ZBEC

and TBzTD to eliminate the carcinogenic nitrosamine content while maintaining necessary mechanical properties like tensile strength and elasticity. The chemical and mechanical properties of the vulcanizate formed using a nitrosamine-free combination of 0.03 phr ZDEC with TBzTD/ZBEC 0.36/0.36 phr are compared to the properties of a vulcanizate with ZDEC in a neat recipe.

The experiment compared the use of two and three accelerators with the use of a single accelerator, specifically from ZBEC, TBzTD, and ZDEC. The NRL formulation uses a blend of two (TBzTD and ZBEC) or three types of accelerators with ZDEC added to enhance the accelerator system between TBzTD and ZBEC. The combinations of accelerators significantly improved the vulcanization efficiency, thermal stability, and mechanical properties, demonstrating the importance of synergistic accelerator selection for optimizing natural rubber balloons.

Characterization by Fourier transform infrared spectroscopy

The NRL formulation characterization in Figure 3 shows the Fourier transform infrared (FTIR) analysis that informs us of the functional groups and the crosslinks formed.

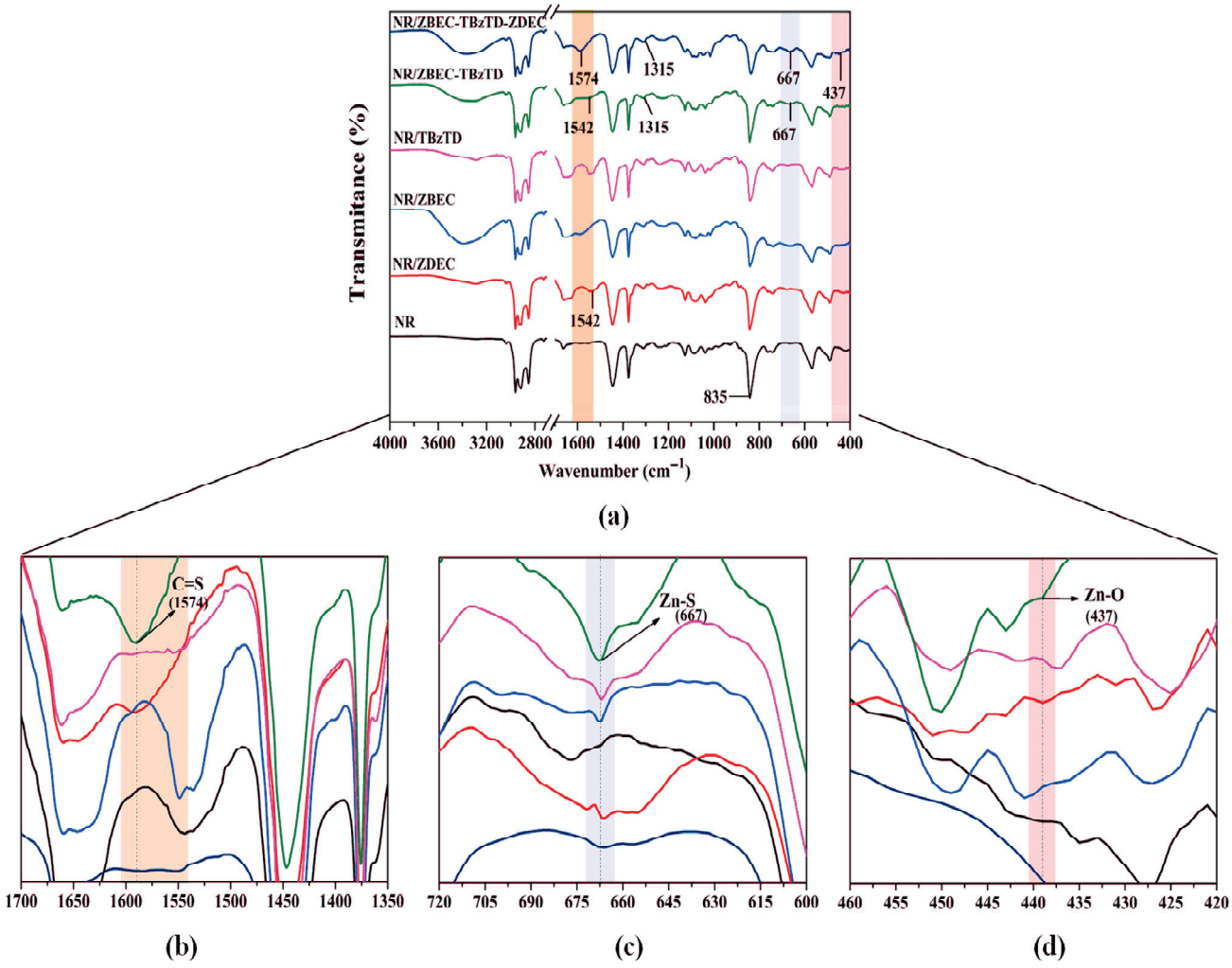

Figure 3. The FTIR spectra of NRL film formulations with different accelerators. (**a**) the FTIR spectra of the NRL; (**b**) the C=S band; (**c**) a cross-linking; (**d**) Zn–O bonding.

Figure 3a presents the FTIR spectra of the NRL formulations, demonstrating that the mixed-accelerator system (ZBEC/TBzTD/ZDEC) produces stronger C=S, C–S, Zn–S, and Zn–O peaks than single-accelerator systems. Around 1315 cm^{-1}, distinct C–S peaks indicate enhanced crosslink density, especially in formulations incorporating multiple

accelerators [21]. In Figure 3b, in the 1574 cm^{-1} region, the appearance and growth of the C=S band [22,23], together with its larger integrated area, confirms additional reactions of the accelerator with vulcanizing agents, leading to modified sulfur-containing structures. The distinct peak near 667 cm^{-1} confirms the formation of Zn–S bonds in Figure 3c, a key cross-linking of rubber chains in the sulfur vulcanization process [24]. In Figure 3d, the band at approximately 437 cm^{-1} evidences Zn–O bonding [25].

The spectral evidence confirms that the synergistic accelerator system (ZBEC/TBzTD/ZDEC) in NRL facilitates more efficient sulfur crosslinking and the formation of complex Zn–S, Zn–O, and C=S bonding networks. This enhanced crosslink density strengthens the mechanical performance and thermal resistance, outperforming single or dual accelerator systems (Table 3). Importantly, the formulation achieves these improvements without any or at a low generation of nitrosamine compounds.

Table 3. Mechanical properties of NRL formulation for balloons prepared with alternative accelerators.

Type of Accelerator	Mechanical Properties				
	Tensile Strength (MPa)	Elongation at Break (%)	100% Modulus (MPa)	200% Modulus (MPa)	300% Modulus (MPa)
Before aging					
ZBEC	18.74 ± 0.90	1079.31 ± 83	0.54 ± 0.01	0.81 ± 0.01	1.08 ± 0.03
TBzTD	19.57 ± 1.47	1136.74 ± 71	0.46 ± 0.01	0.65 ± 0.08	0.83 ± 0.03
ZDEC	21.36 ± 1.10	1040.86 ± 60	0.55 ± 0.07	0.88 ± 0.12	1.20 ± 0.14
ZBEC/TBzTD	17.91 ± 0.75	1115.82 ± 55	0.50 ± 0.13	0.67 ± 0.05	0.84 ± 0.10
ZBEC/TBzTD/ZDEC	22.13 ± 1.81	1152.90 ± 78	0.69 ± 0.02	0.95 ± 0.04	1.30 ± 0.07
After aging					
ZBEC	12.10 ± 2.11	626.50 ± 34	1.06 ± 0.01	1.81 ± 0.02	3.30 ± 0.02
TBzTD	13.25 ± 1.72	736.85 ± 26	1.24 ± 0.07	2.39 ± 0.12	3.21 ± 0.15
ZDEC	15.50 ± 0.89	851.9 ± 35	1.53 ± 0.02	2.00 ± 0.01	4.59 ± 0.10
ZBEC/TBzTD	13.85 ± 0.70	785.98 ± 15	0.95 ± 0.03	1.17 ± 0.03	3.50 ± 0.04
ZBEC/TBzTD/ZDEC	14.23 ± 1.81	892.91 ± 8	1.69 ± 0.02	2.48 ± 0.04	4.04 ± 0.07

3.1.3. Comparative Analysis of Mechanical Properties

The mechanical properties before and after accelerated aging in Table 3 indicate that changing the accelerator system greatly impacts the mechanical properties of natural rubber latex balloons. Formulations using single accelerators such as ZBEC, TBzTD or ZDEC provide moderate tensile strength and elongation at break, while binary combinations offer only limited improvements.

Notably, the ternary blend of 0.36 phr ZBEC/0.36 phr TBzTD/0.03 phr ZDEC, even with a minimal amount of ZDEC, achieved the highest tensile strength (22.13 ± 1.81 MPa) and elongation at break (~1153%) before aging, indicating a highly tough and well-developed crosslink network. The tensile strength of the optimized balloon compound remains within the internal specification range provided by the B.K. Latex Product Co., Ltd., with typical values around 25.792 MPa, elongation at break of approximately 1067%, and a 300% modulus of 1.569 MPa. In practice, the property that mainly influences whether a balloon is difficult to inflate is the 300% modulus, which should be relatively low to avoid excessive stiffness, while a sufficiently high tensile strength is still desirable to prevent rupture during inflation and use. This superior performance demonstrates a synergistic effect, where the combination of these three accelerators leads to more efficient vulcanization and greater reinforcement of the polymer structure. The ternary blend also resulted in the highest moduli at all elongation levels before aging, which is associated with increased initial stiffness and higher crosslink density in the rubber matrix. The thermal stability for natural rubber balloons, as described in standards such as TIS 685, BgVV, 2002 [26], and EN 71-12:2016 [12], is not defined by explicit numerical limits for thermal degradation,

but instead is evaluated indirectly through compliance with mechanical and physical tests after heat aging. Thermal stability is necessary so that the balloons continue to meet the required mechanical safety criteria (e.g., flexibility, absence of brittleness, and retention of tensile performance within acceptable range) following the specified heat-aging conditions, to ensure that the produce remains mechanically reliable throughout storage and use. After accelerated aging, the tensile strength and elongation when using the ternary system implies improved thermal resistance compared to single or binary accelerator systems. Each type of accelerator or combination thereof influences both the mechanical and thermal properties, with the three-accelerator system consistently yielding the best results. Overall, the synergistic accelerator system of ZBEC, TBzTD and ZDEC provides a high-performance, strong, and stable NRL balloon product, surpassing formulations with only one or two accelerators. The benefits impact both the mechanical properties and service life.

3.1.4. Thermal Stability of Sulfur Vulcanization

Figure 4 illustrates the thermal stability of NRL vulcanizates prepared with different accelerator systems, as evaluated by TGA and derivative thermogravimetry (DTG).

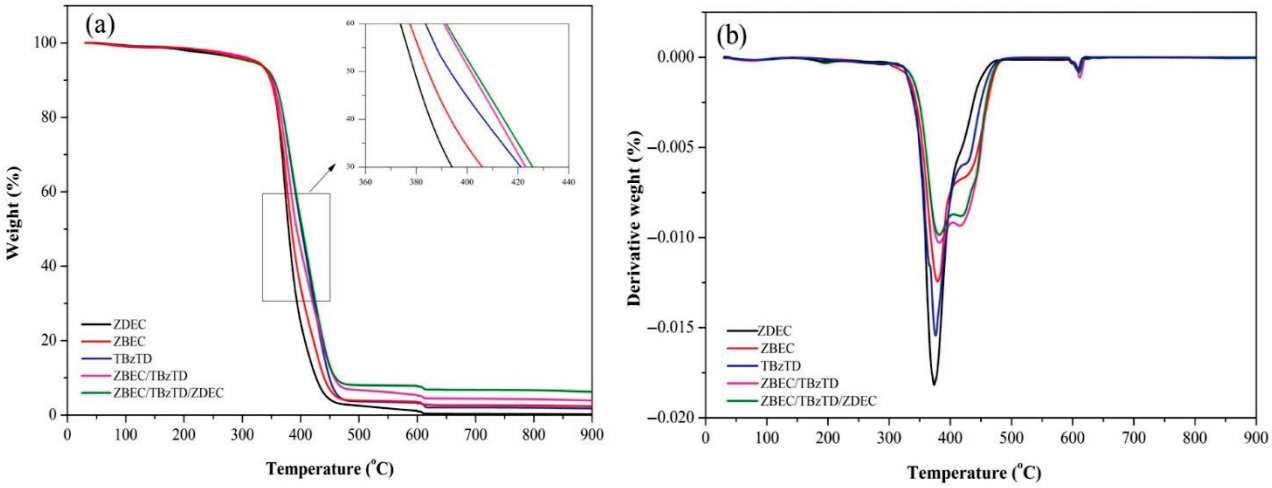

Figure 4. TGA (**a**) and DTG (**b**) graphs showing weight losses with the alternative types of accelerators in NRL formulation for balloons by sulfur vulcanization.

From Table 4, TGA curves in Figure 4a, and DTG in Figure 4b, it is found that all formulations exhibit a similar single-step degradation, with rapid weight loss between 180 and 320 °C being associated with the decomposition of the rubber backbone. The ZBEC/TBzTD/ZDEC formulation provides the greatest thermal stability, as evidenced by its highest T_{onset} (357.75 °C), T_{max} (384.15 °C), and final decomposition temperature (403.04 °C), together with the largest residual mass of 7.66%, indicating the presence of thermally stable species (e.g., ZnS, ZnO) within the measurement range. The DTG curves (Figure 4b) show the rate of that mass change and display a distinct shoulder at 400–500 °C arising from additional degradation of the crosslinked network and residue, confirming that the combined accelerator system enhances both the onset and completion temperatures of degradation compared with the other formulations.

https://doi.org/10.3390/polym18040438

Table 4. Thermal stability analysis of NRL film formulations with alternative accelerators for sulfur vulcanization.

Rubber Sample Type	T_{onset} * (°C)	T_{max} ** (°C)	Final Decomposition Temperature (FDT)	Final Residue (%)
ZBEC	356.01	374.78	379.79	0.38
TBzTD	356.13	378.01	391.14	4.47
ZDEC	358.05	376.47	384.47	2.63
ZBEC/TBzTD	342.16	382.62	400.56	2.05
ZBEC/TBzTD/ZDEC	357.75	384.15	403.04	7.66

Note: * T_{onset} is the decomposition onset temperature, T_{max} ** is the temperature at the maximum decomposition rate.

This balance between enhanced thermal stability and sulfur crosslinking makes the novel formulations suitable for applications requiring both mechanical performance and heat resistance [27–29]. These results confirm an accelerator synergistic effect in NRL compound sulfur vulcanizates, with increased thermal stability while maintaining adequate sulfur crosslinking for NRL balloon applications.

From the resulting increases in the mechanical strength, elasticity, and modulus of the NR compound, the synergistic accelerator system (ZBEC/TBzTD/ZDEC) in sulfur vulcanization is confirmed.

Figure 5 illustrates the interactions and cross-linking process between natural rubber latex (NRL), sulfur, zinc oxide, and cellulose nanocrystals, enhancing the entanglement and interfacial network within the rubber matrix. The CNC not only improves the dispersion of zinc oxide but also participates in the formation of ionic Zn–O–CNC crosslinks, which further connect to rubber chains via sulfur bridges. This leads to a robust NRL–S_8–Zn–O–CNC network, increasing the number of crosslink points and entanglement between rubber and filler.

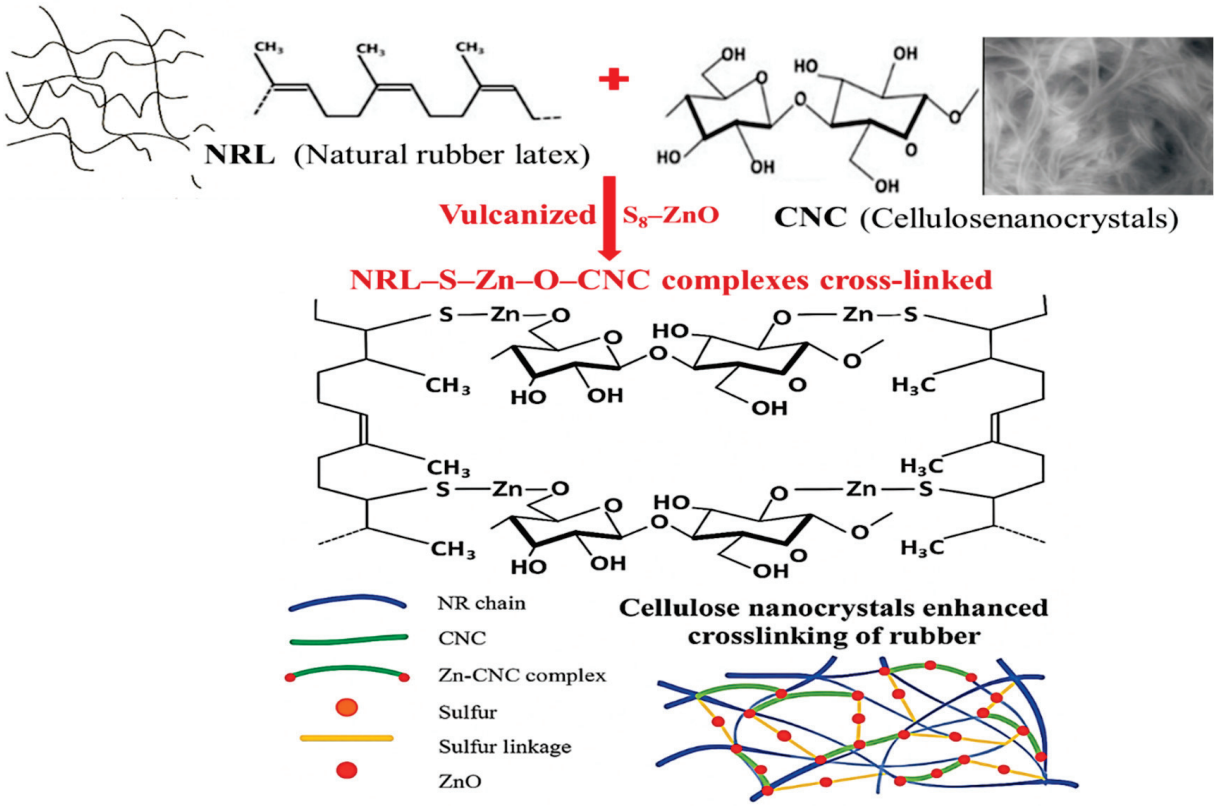

Figure 5. The formation of sulfur crosslinks in NRL–S_8–Zn–O–CNC complexes.

The curing mechanism indeed involves the CNC. The role of CNC is now exposed by reports that cellulose-based fillers can participate in zinc-containing curing domains and influence vulcanization behavior, which supports the plausibility of interactions between CNC surface groups, ZnO, and the sulfur–accelerator system. Regarding the proposed coupling of cellulose to the polymer via a Zn–S bridge, this structure is hypothetical and consistent with the generally accepted view that the active Zn complexes form at, or in association with, ZnO-containing domains. Additionally, we note that (i) Zn–accelerator–sulfur complexes generated at the ZnO surface can migrate into the rubber matrix, (ii) hydroxyl and modified functional groups on CNC can coordinate or interact with zinc species, and (iii) such interactions may contribute to a combined filler–curing network, rather than a single, unique structure. The proposed structures are one plausible realization among several possibilities, supported indirectly by the curing behavior and mechanical property trends, rather than by direct structural evidence. For related details and discussion, we refer to the works of Low et al. (2021) [30], Blanchard et al. (2020) [31], and Suchat et al. (2024, 2025) [13,32].

3.1.5. Nitrosamine Testing

The results of nitrosamine testing in the NRL formulation for balloons (Table 5), using GC-TEA according to EN 12868:2017, confirm that the synergistic activities of the novel combinations 0.03 phr ZDEC; 0.36 phr TBzTD/0.36 phr ZBEC and TBzTD, ZBEC, ZDEC, TBzTD/ZBEC, could be effective accelerator systems to replace the unsafe ZDEC neat for the sulfur vulcanization of NRL balloons.

Table 5. Test of migratable nitrosamines in NRL formulations for balloons.

Test Parameter	1-ZDEC		2-ZBEC		3-TBzTD		4-ZBEC + TBzTD		5-ZBEC + TBzTD + ZDEC	
	Nitrosamines (mg/kg)	Nitrosatable Substances (mg/kg)	Nitrosamines (mg/kg)	Nitrosatable Substances (mg/kg)	Nitrosamines (mg/kg)	Nitrosatable Substances (mg/kg)	Nitrosamines (mg/kg)	Nitrosatable Substances (mg/kg)	Nitrosamines (mg/kg)	Nitrosatable Substances (mg/kg)
1. NDMA	0.130	0.861	nd	nd	0.028	0.495	0.030	0.480	0.034	0.565
2. NDEA	0.100	0.405	nd	nd	nd	0.372	nd	0.250	0.006	0.329
3. NDPA	nd	nd	nd	nd	nd	nd	nd	nd	nd	nd
4. NDiBA	nd	nd	nd	nd	nd	nd	nd	nd	nd	nd
5. NDBA	nd	nd	0.045	0.300	nd	0.040	0.010	0.220	0.004	0.060
6. NPIP	nd	nd	nd	nd	nd	nd	nd	nd	nd	nd
7. NPYR	nd	nd	nd	nd	nd	nd	nd	nd	nd	nd
8. NMOR	nd	nd	nd	nd	nd	nd	nd	nd	nd	nd
9. NEPhA	nd	nd	nd	nd	nd	nd	nd	nd	nd	nd
10. NMPhA	nd	nd	nd	nd	nd	nd	nd	nd	nd	nd
11. NDiNA	nd	nd	nd	nd	nd	nd	nd	nd	nd	nd
12. NDBzA	nd	nd	nd	nd	0.015	0.076	0.004	0.035	0.004	0.040
Total	0.230	1.266	0.045	0.300	0.043	0.983	0.044	0.985	0.048	0.994
	Fail	Fail	pass *	pass **	pass *	pass **	pass *	pass **	pass *	pass **

Note: nd, not detected or lower than the reporting limit (* migratable nitrosamines, 0.05 mg/kg, and ** migratable nitrosatable substances 1.0 mg/kg). Requirements according to results of nitrosamine testing in the NRL formulation for balloons, using GC-TEA according to EN 12868:2017.

Table 5 indicates that migratable levels of nitrosamines were found: in particular, the detected levels of *N*-nitrosodimethylamine (NDMA) and *N*-nitrosodiethylamine (NDEA) were 0.13 and 0.10 mg/kg, respectively, in the NRL formulation for balloons using zinc diethyldithiocarbamate (ZDEC). The nitrosamine is a compound formed from the precursor diethylamine, which results from the decomposition of the accelerator ZDEC during the vulcanization. ZDEC is classified as a highly effective "super-accelerator" for NR latex but is also considered "unsafe" and is one of the "primary problematic accelerators" because it can form carcinogenic nitrosamines. The sources include diagrams showing the reaction mechanism in Figure 6. NDEA substance is classified by the International Agency for Research on Cancer (IARC) as a Group 2A carcinogen ("probably carcinogenic to humans") and is considered a very potent carcinogen [26].

https://doi.org/10.3390/polym18040438

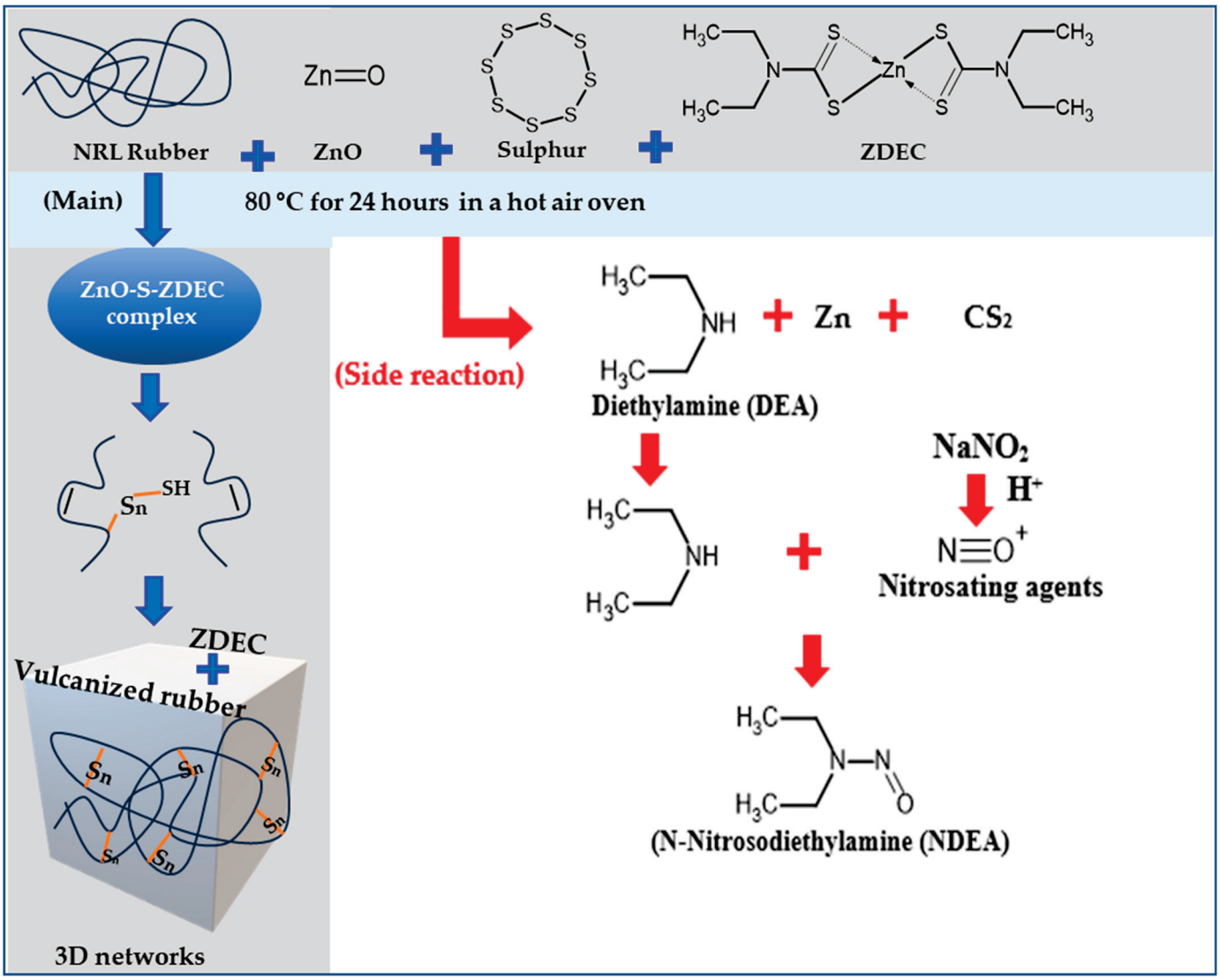

Figure 6. Diagram illustrating the reaction mechanisms that lead to the formation of nitrosodiethylamine in NRL formulation for balloons with ZDEC accelerator.

Figure 6 illustrates the mechanisms of NDEA formation from ZDEC that involve three steps: (1) decomposition of ZDEC during vulcanization, releasing diethylamine, a secondary amine; (2) nitrosation reaction where diethylamine reacts with nitrosating agents such as nitrites or nitrogen oxides, which may be present during the manufacturing process or in the environment; and (3) formation of NDEA, a nitrosamine classified as a carcinogen. The inductive and resonance effects of the amine group, along with steric factors, influence the formation of zinc–accelerator complexes.

The meaning of the red side-reaction arrow is to indicate that the chemical reaction leading to the release of *N*-nitrosodiethylamine (NDEA) does not occur in the developed formulation. The nitrosation pathway is suppressed by the novel accelerator system. The absence of NDEA formation has been verified through expert chemical review and confirmed by analytical testing, which showed non-detectable (nd) levels below the reporting limit. Regarding the mechanism, a conventional accelerator complex such as ZDEC can release NDEA because it decomposes during the heating for vulcanization, producing secondary amines (specifically diethylamine). These secondary amines then combine with nitrosating agents (such as nitrogen oxides (NOx) from the atmosphere or sodium nitrite ($NaNO_2$) used in processing) to form the carcinogenic *N*-Nitrosodiethylamine (NDEA).

https://doi.org/10.3390/polym18040438

The diagram aims to demonstrate that while conventional rubber compounds are prone to nitrosamine formation, the developed "nitrosamine-safe" formulation (using tetrabenzylthiuram disulfide (TBzTD) and zinc n-butylbenzothiazole-2-sulfenamide (ZBEC) as a big group) employs chemical structures that do not form secondary amines. This substitution effectively prevents the generation of regulated nitrosamines while maintaining the required mechanical properties for balloon production. While having chemical plausibility and consistency with established mechanistic understanding, the proposed reaction pathways remain indirectly supported by the works of Low et al. (2021) [30], Blanchard et al. (2020) [31] and Suchat et al. (2025) [32].

For safety reasons, we recommend choosing safer alternative accelerators, such as ZBEC and TBzTD, to replace ZDEC in the production of NRL products, especially those that come into contact with humans, such as balloons. The focus on the alternative accelerator compounds fulfilling the requirement of releasing no carcinogenic nitrosamines ensures that these alternative systems meet both the safety criterion of non-detectable carcinogenic nitrosamines and the required performance for balloon production, thereby strengthening the central message and focus of this study.

The use of multiple accelerants, whether two or three, compared to a single accelerant like TBzTD, still maintains the nitrosamines values below the latex balloon standard limits, as shown in Table 5 and Figures 7 and 8. The tables and figures corroborate that the novel formulations are safe for balloons made from natural rubber latex (NRL) [32,33].

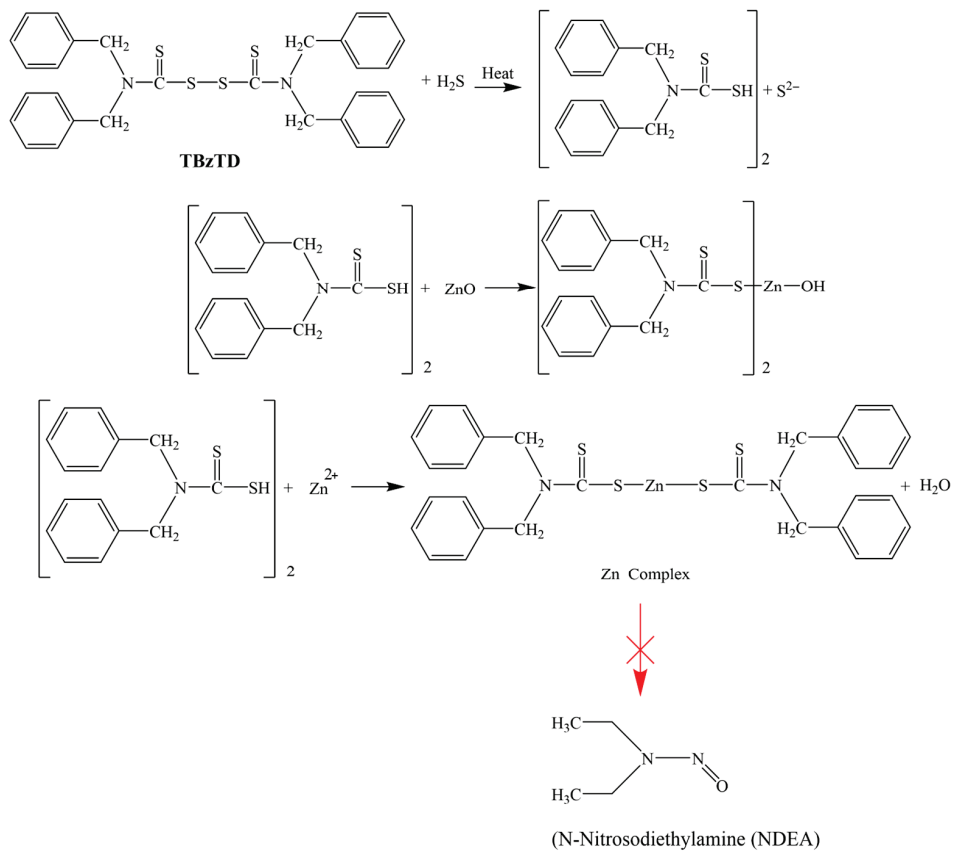

Figure 7. Diagram of the reaction mechanisms in the nitrosamine-free NRL formulation with TBzTD.

Tetrabenzyl thiuram disulfide (TBzTD), with the chemical formula C30H28S4N2 and a molecular weight of 542.78, undergoes a reaction, shown in Figure 7. The induction of the amine group, along with steric factors, influences the formation of zinc–accelerator complexes. Nonetheless, as shown in Table 5, *N*-nitrosodibenzylamine (NDBzA) is slightly produced, but this is safe and not a carcinogenic nitrosamine.

https://doi.org/10.3390/polym18040438

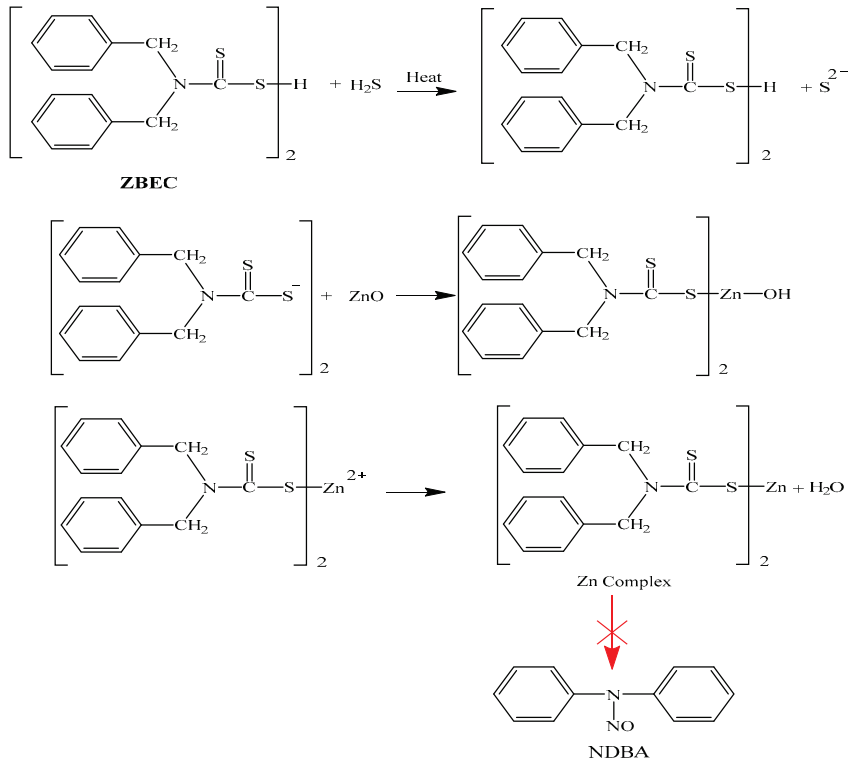

Figure 8. The reaction mechanisms in the nitrosamine-free NRL formulation for balloons with ZBEC.

Based on the data in Table 5 and Figure 8, when Zinc dibutyldithiocarbamate (ZBEC) is used in an NRL formulation for balloons, NDMA and NDEA are not detected (reporting limit 0.01 mg/kg). The inductive effect of the amine group, along with the steric factors, plays a significant role in influencing the formation of zinc complexes and accelerators during vulcanization. These factors affect how compounds interact and bond, thereby impacting the vulcanization. Comparative testing of NRL compounds showed clearly that the ZBEC accelerator contributed to sulfur vulcanization, and if a nitrosation reaction occurs, the resulting nitrosamine will be NDBA (nitrosodibutylamine) at a low concentration, which is safe and not a carcinogenic nitrosamine (Table 5).

It is also noteworthy that even though ZBEC could theoretically form NDBA, the test results shown in Table 4 have some NDBA, which is safe and not carcinogenic [19]. Using a ZBEC accelerator is an effective method for avoiding the formation of NDMA and NDEA in products, which is a key reason for its selection in formulations requiring safety by not carrying carcinogenic nitrosamines.

According to Table 5, the investigation of a novel synergistic accelerator system comprising a little bit of ZDEC (0.03 phr) with the combination of TBzTD (0.36 phr), and ZBEC (0.36 phr), suggests that this combination could be an effective and safer alternative to the unregulated ZDEC for the sulfur vulcanization of NRL balloons.

The formula of TBzTD/ZBEC and ZDEC in the NRL compound for balloons, incorporating the accelerators that complied with established nitrosamine and nitrosatable substances safety standards, appears to be suitable as a safer alternative to conventional accelerators. The bulky phenyl substituents exert steric hindrances that decrease the alkalinity of the amine. This reduction in alkalinity enhances the stability of the zinc–accelerator complex, which in turn suppresses the release of the reactive intermediates that are responsible for nitrosamine generation, thereby effectively reducing nitrosamine formation.

While TBzTD or ZBEC was specifically developed as a safer alternative to traditional, problematic accelerators like ZDEC, it cannot be considered completely safe. Here, the

balloon formulation was designed to have an effective accelerator system to replace the use of unsafe ZDEC neat.

Using a combination of TBzTD and ZBEC accelerators, supplemented with a very small amount (0.03 phr) of ZDEC, is a highly effective strategy for natural rubber latex balloon formulations. This approach achieves two critical goals.

(1) Enhanced product properties. Through a synergistic effect, it produces balloons with significantly higher tensile strength and thermal stability compared to other accelerator systems.

(2) High safety level. By relying on primarily safe accelerators and minimizing the precursor for harmful nitrosamines, it yields a final product with lower levels than the standard limits, thereby meeting the strict safety standards for rubber products that may be used by children.

The reaction mechanisms in nitrosamine-free NRL formulation for balloons with a synergistic accelerator combination of TBzTD and ZBEC are shown in Figure 9. The nitrosamine testing for the NRL balloon compounds that used the three alternative accelerator combinations, TBzTD/ZBEC/ZDEC, was done using GC-TEA according to EN 12868:2017 [15] and BgVV (2002) [26]. It confirmed that the total migration values of the nitrosamine and the nitrosatable substances were below the standard balloon limits (0.05 mg/kg for nitrosamines and 1.0 mg/kg for nitrosatable substances). Based on discussions with balloon manufacturers, exporters, and experts in this field, the proposed approach is considered acceptable, ensuring no exposure to carcinogenic nitrosamines for humans.

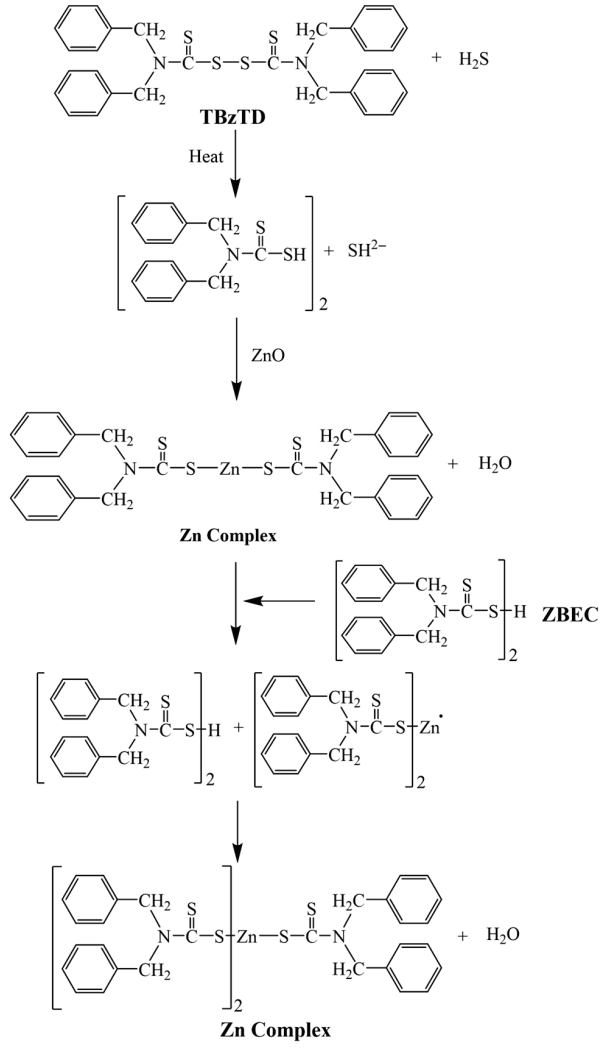

Figure 9. Reaction mechanisms in NRL formulation for balloons, based on a nitrosamine-free TBzTD/ZBEC combination.

4. Conclusions

This study developed a sulfur-vulcanized NRL compound formulation for balloon products, exceeding the required mechanical properties while controlling the carcinogenic nitrosamine content for compliance with the stringent safety standards. In experiments, the types and amounts of accelerators were manipulated, while controlling for the 103% swelling index and 62% total solid content targets. It was found that the synergistic accelerator system of TBzTD (0.36 phr) and ZBEC (0.36 phr), with a little bit of ZDEC (0.03 phr) gave significantly improved mechanical performance without detectable carcinogenic nitrosamines, outperforming formulations using a combination of TBzTD and ZBEC or each accelerator alone. Mechanical testing revealed the highest tensile strength (22.1 $\pm$ 1.8 MPa), elongation (1153 $\pm$ 78%), and 300% modulus (1.30 $\pm$ 0.07 MPa), complying with balloon product standards. The thermal stability was confirmed by its good mechanical properties after accelerated aging, and by thermogravimetric analysis, which showed a maximum decomposition temperature of 384.15 °C. Overall, the synergistic use accelerators enhanced the vulcanization efficiency, thermal stability, and mechanical properties, highlighting the critical role of accelerator synergy in optimizing natural rubber balloon performance, with safety standards concerning carcinogenic nitrosamine content.

Author Contributions: Conceptualization, S.S.; Methodology, T.C.-I. and E.A.; Validation, T.C.-I., E.A. and S.S.; Formal analysis, T.C.-I. and E.A.; Investigation, S.S.; Resources, T.C.-I.; Data curation, T.C.-I. and S.S.; Writing—original draft, S.S.; Writing—review & editing, S.S.; Visualization, E.A. and S.S.; Supervision, S.S.; Project administration, S.S.; Funding acquisition, S.S. All authors have read and agreed to the published version of the manuscript.

Funding: This research was supported by the National Science, Research and Innovation Fund (NSRF) and Prince of Songkla University, SIT6701127a, SIT6801101S and B.K. Latex Product Co., Ltd.

Institutional Review Board Statement: Not applicable.

Data Availability Statement: The original contributions presented in this study are included in the article. Further inquiries can be directed to the corresponding author.

Acknowledgments: We are grateful to Saranyoo Klaiklay and Seppo Karrila for their valuable assistance in improving the chemical reaction schemes and language of the draft manuscript.

Conflicts of Interest: The authors declare that this study received funding from B.K. Latex Product Co., Ltd. The funder was not involved in the study design, collection, analysis, interpretation of data, the writing of this article or the decision to submit it for publication.

References

1. Fortune Business Insights. *Xenon Market Size, Share & COVID-19 Impact Analysis, by Type (N3, N4. 5, and N5), by Application (Imaging & Lighting, Satellite, Electronics & Semiconductors, Medical and Others), and Regional Forcast, 2022–2029*; Fortune Business Insights: Pune, India, 2023.
2. Fortune Business Insights. Virtual Reality in Education Market Size, Share & Industry Analysis, by Component (Hardware, Software, and Content), by Application (K-12, Higher Education, and Vocational Training), and Regional Forecast, 2024–2032; Market Research Report. 2024. Available online: https://www.fortunebusinessinsights.com/industry (accessed on 29 January 2026).
3. Kędzia, J.R.; Sitko, A.M.; Haponiuk, J.T.; Lipka, J.K. Natural rubber latex-origin, specification and application. In *Application and Characterization of Rubber Materials*; IntechOpen: London, UK, 2022.
4. Stephens, H.L.; Bhowmick, A.K. *Handbook of Elastomers*; Dekker: New York, NY, USA, 2001.
5. Brunnemann, K.D.; Hoffmann, D. Analytical studies on tobacco-specific *N*-nitrosamines in tobacco and tobacco smoke. *Crit. Rev. Toxicol.* **1991**, *21*, 235–240. [CrossRef]
6. Biaudet, H.; Mouillet, L.; Debry, G. Migration of nitrosamines from condoms to physiological secretions. *Bull. Environ. Contam. Toxicol.* **1997**, *59*, 847–853. [CrossRef]
7. Farren, N.J.; Ramírez, N.; Lee, J.D.; Finessi, E.; Lewis, A.C.; Hamilton, J.F. Estimated exposure risks from carcinogenic nitrosamines in urban airborne particulate matter. *Environ. Sci. Technol.* **2015**, *49*, 9648–9656. [CrossRef]

8. Rao, T. *Genotoxicology of N-Nitroso Compounds*; Springer Science & Business Media: Berlin/Heidelberg, Germany, 2013.
9. van Bruggen, M.; van Putten, E.M.; Janssen, P.C.J.M. RIVM 2003. N-Nitrosamines in Balloons: Assessment of the Health Risk for Children. In *RIVM Report 609300002/2007 Nitrosamines Released from Rubber Crumb*; p. 17. Available online: https://www.rivm.nl/bibliotheek/rapporten/609300002.html (accessed on 29 January 2026).
10. World Health Organization. *Guidelines for Drinking-Water Quality: Incorporating the First and Second Addenda*; World Health Organization: Geneva, Switzerland, 2022.
11. Hwang, J.B.; Lee, J.E.; Kim, E.; Eom, K.Y.; Kim, H.-A.; Lee, S. Analysis of *N*-nitrosamines and *N*-nitrosatable substances from baby bottle rubber teats by liquid chromatography tandem mass spectrometry. *Food Addit. Contam. Part A* **2023**, *40*, 518–527. [CrossRef]
12. *EN 71-12:2016*; Safety of Toys—Part 12: N-Nitrosamines and N-Nitrosatable Substances. European Standard: Brussels, Belgium, 2016.
13. Suchat, S.; Boonrasri, S. Advancement of an environmentally friendly and innovative sustainable rubber wrap film with superior sealing properties. *Polymers* **2024**, *16*, 1499. [CrossRef]
14. Park, J.-e.; Seo, J.-e.; Lee, J.-y.; Kwon, H. Distribution of seven *N*-nitrosamines in food. *Toxicol. Res.* **2015**, *31*, 279–288. [CrossRef]
15. *EN 12868:2017*; Child Use and Care Articles—Method for Determining the Release of N-Nitrosamines and N-Nitrosatable Substances from Elastomer or Rubber Teats and Soothers. European Standard: Brussels, Belgium, 2017.
16. Fajen, J.; Carson, G.; Rounbehler, D.; Fan, T.; Vita, R.; Goff, U.; Wolf, M.; Edwards, G.; Fine, D.; Reinhold, V. *N*-nitrosamines in the rubber and tire industry. *Science* **1979**, *205*, 1262–1264. [CrossRef]
17. Smith, S.A.; Norris, B. Reducing the Risk of Choking Hazards: Mouthing Behaviour of Children Aged 1 Month to 5 Years. *Inj. Control. Saf. Promot.* **2003**, *10*, 145–154. [CrossRef] [PubMed]
18. Kędzia, J.; Haponiuk, J.; Formela, K. Natural Rubber Latex Wastes from Balloon Production as Valuable Source of Raw Material: Processing, Physico-Mechanical Properties, and Structure. *J. Compos. Sci.* **2024**, *8*, 365. [CrossRef]
19. Virdi, R.; Grover, B.; Ghuman, K. "Nitrosamine safe" thiuram disulfide. *Rubber Chem. Technol.* **2019**, *92*, 90–109. [CrossRef]
20. Park, S.J.; Jeong, M.J.; Park, S.R.; Choi, J.C.; Choi, H.; Kim, M. Release of *N*-nitrosamines and *N*-nitrosatable substances from baby bottle teats and rubber kitchen tools in Korea. *Food Sci. Biotechnol.* **2018**, *27*, 1519–1524. [CrossRef]
21. Murakami, L.M.S.; Azevedo, J.B.; Diniz, M.F.; Silva, L.M.; Dutra, R.d.C.L. Characterization of additives in NR formulations by TLC-IR (UATR). *Polímeros* **2018**, *28*, 205–214. [CrossRef]
22. Sujarit, J.; Phutdhawong, W. Synthesis of Zinc Diethyldithiocarbamate (ZDEC) and Structure Characterization using Decoupling ^{1}H NMR. In Proceedings of the Congress on Science and Technology of Thailand, Golden Jubilee Convention Hall, Khon Kean University (Thailand), Khon Kaen, Thailand, 20–22 October 2003.
23. Thajudin, N.N.; Shuib, R. Room temperature self-healing natural rubber based on ionic supramolecular network. *AIP Conf. Proc.* **2020**, *2267*, 020023. [CrossRef]
24. Liu, L.-N.; Dai, J.-G.; Zhao, T.-J.; Guo, S.-Y.; Hou, D.-S.; Zhang, P.; Shang, J.; Wang, S.; Han, S. A novel Zn (ii) dithiocarbamate/ZnS nanocomposite for highly efficient Cr^{6+} removal from aqueous solutions. *RSC Adv.* **2017**, *7*, 35075–35085. [CrossRef]
25. Sivakumar, P.; Thyagarajan, K.; Kumar, A. Investigations on physical properties of Zn ferrite nanoparticles using sol-gel auto combustion technique. *Dig. J. Nanomater. Bios.* **2018**, *13*, 1117–1122.
26. BgVV. Risk Assessment of N-Nitrosamines in Balloons. Federal Institute of Health Protection of Consumers and Veterinary Medicine, Expert Opinion. 11 April 2002. Available online: http://www.bgvv.de (accessed on 29 January 2026).
27. de Lima, D.R.; da Rocha, E.B.D.; de Sousa, A.M.F.; da Costa, A.C.A.; Furtado, C.R.G. Effect of vulcanization systems on the properties of natural rubber latex films. *Polym. Bull.* **2021**, *78*, 3943–3957. [CrossRef]
28. Larpkasemsek, A.; Raksaksri, L.; Chuayjuljit, S.; Chaiwutthinan, P.; Boonmahitthisud, A. Effects of sulfur vulcanization system on cure characteristics, physical properties and thermal aging of epoxidized natural rubber. *J. Met. Mater. Miner.* **2019**.
29. Boonkerd, K.; Deeprasertkul, C.; Boonsomwong, K. Effect of sulfur to accelerator ratio on crosslink structure, reversion, and strength in natural rubber. *Rubber Chem. Technol.* **2016**, *89*, 450–464. [CrossRef]
30. Low, D.Y.S.; Supramaniam, J.; Soottitantawat, A.; Charinpanitkul, T.; Tanthapanichakoon, W.; Tan, K.W.; Tang, S.Y. Recent developments in nanocellulose-reinforced rubber matrix composites: A review. *Polymers* **2021**, *13*, 550. [CrossRef]
31. Blanchard, R.; Ogunsona, E.O.; Hojabr, S.; Berry, R.; Mekonnen, T.H. Synergistic cross-linking and reinforcing enhancement of rubber latex with cellulose nanocrystals for glove applications. *ACS Appl. Polym. Mater.* **2020**, *2*, 887–898. [CrossRef]
32. Suchat, S.; Praksong, K.; Muangprathub, J.; Srisawat, T.; Abdullah, N.H.; Boonrasri, S. Agricultural performance of biomaterials mulch based on nitrosamine-free natural rubber. *Green Mater.* **2025**, *13*, 183–195. [CrossRef]
33. Suchat, S.; Boonrasri, S. Advancement of an Eco-Friendly and Innovative Sustainable Rubber Wrap Film Exhibiting Superior Sealing Properties. *Res. Sq.* **2024**. [CrossRef]

polymers

MDPI

Article

Alternative Natural Rubber Cross-Linking Utilizing a Disulfide-Containing Bismaleimide

Anureet Kaur [1], Maria Tucker [1], Keizo Akutagawa [1], Biqiong Chen [2] and James J. C. Busfield [1,*]

[1] School of Engineering and Materials Science, Queen Mary University of London, London E1 4NS, UK; k.akutagawa@qmul.ac.uk (K.A.)
[2] Department of Chemistry, University of Liverpool, Crown Street, Liverpool L69 7ZD, UK; biqiong.chen@liverpool.ac.uk
* Correspondence: j.busfield@qmul.ac.uk

Abstract

This study explores a disulfide-selective cross-linking strategy for natural rubber (NR) to formulate elastomeric materials with engineering-relevant mechanical properties. A disulfide-containing bismaleimide (BIS) cross-linker was synthesized from cystamine and maleic anhydride and compounded with NR. Three formulations were prepared: control (no inhibitor), $CuCl_2$-based, and copper(II) methacrylate (CuMA) based compounds, with BIS concentrations ranging from 3.55 to 8.88 phr. Rheological and mechanical testing revealed that $CuCl_2$ formulations suffered from molecular degradation, poor thermal stability, and mechanical brittleness due to oxidative reactions in the absence of antioxidants. In contrast, CuMA-based compounds exhibited intermediate molecular weights prior to curing, stable thermal behavior, and improved mechanical properties, including enhanced torque and tensile strength, indicating effective cross-linking and partial recyclability. The control formulations also performed reasonably well but did not match the mechanical strength of conventional sulfur-vulcanized NR. The results demonstrate that metal coordination, particularly with CuMA, can modulate disulfide metathesis kinetics and offer a pathway to thermally triggered network rearrangement. Overall, CuMA emerges as a promising candidate for developing high-performance, recyclable rubber materials, while $CuCl_2$ requires further stabilization strategies. This work establishes a baseline for future recyclability studies and advances the design of dynamic covalent networks in elastomers.

Keywords: bismaleimide; natural rubber; cross-linking; disulfide

1. Introduction

Conventional sulfur vulcanization (CV) yields robust three-dimensional polysulfide cross-linked networks that provide the mechanical performance required by engineering elastomers but render the resulting materials essentially unrecyclable [1]. Efforts to recover value from vulcanized rubber have therefore focused on devulcanization and other recycling routes, yet selective and efficient reclaiming of cross-linked networks remains an as yet unfulfilled challenge for the rubber industry [2,3]. One promising route to reconcile durable performance with recyclability is the introduction of dynamic covalent linkages into the cross-link network. Disulfide bonds (S–S) are known to behave as dynamic covalent bonds, which have been reported to undergo a free radical disulfide metathesis reaction following a radical-mediated [2 + 1] mechanism, consisting of cleavage of the disulfide bond and its subsequent reforming [4], that can occur spontaneously [5] or be

thermally initiated [6]. The latter category is particularly useful for the development of recyclable elastomers, as the exchange reaction necessary to rearrange the cross-linked network can be triggered only under specific conditions, retaining elastomeric behavior in a wide range of service conditions. The lability of S–S bonds relative to typical carbon–carbon single or carbon–carbon double bonds underpins their utility for this purpose [7]. Controlling the temperature, and therefore the timing, of disulfide metathesis is critical: facile exchange at ambient temperature compromises dimensional and mechanical stability, whereas an exchange that is triggerable only at processing temperatures enables reprocessing without loss of in-service performance. Recent work demonstrates that metal coordination, for example via copper(II) methacrylate (CuMA) or $CuCl_2$, can be used to modulate disulfide metathesis kinetics and thus tune the rearrangement temperature window in sulfur-based vulcanizates, as the activation temperature is reached, the copper(II)-based complex catalysis can enable cross-over reactions between disulfide and polysulfides [8,9]. Notably, we have previously reported that optimizing a sulfur-based cure package with CuMA promotes a reversible disulfide/polysulfide network that can be recovered by thermal processing, thereby enabling recyclable sulfur-cured natural rubber formulations [1]. Motivated by these developments, the present study aimed to implement a different cross-linking architecture in an elastomer matrix by selectively introducing disulfide-only cross-links and evaluating the mechanical performance of the resulting pristine materials. The introduction of disulfide cross-links can only be achieved by either adjusting the sulfur/accelerator (S/A) ratio to >1 in a sulfur-based vulcanization—hence using the CV system, favoring the formation of polysulfide cross-links over monosulfides—or by introducing small organic molecules that contain disulfide functional groups. However, in CV-cured compounds that are characterized by a large number of polysulfides, once an S-S bond is cleaved and thiyl radicals are formed, they would statistically be keener to react with the NR chains, slowly shifting the cross-linked network to a semi-efficient system (SEV, where $S/A \approx 1$ and 50% of the cross-links are polysulfides) or efficient system (EV, where $S/A \ll 1$ and 80% of the cross-links are monosulfides) [10,11]. An example of disulfide-containing small organic molecules that can be used to cross-link natural rubber is disulfide-containing bismaleimides. These have been reported in the literature as capable of introducing self-healable and reprocessable properties in elastomers. Kitagawa et al. synthesized Jaffamine-derived polymers using bis(2-maleimidoethyl) disulfide and 4-aminophenyl disulfide as cross-linkers, achieving self-healing efficiencies higher than 90% after reprocessing at 180 °C [12]. Sim et al. cross-linked poly(furfuryl methacrylate) (PFMA) brushes with a disulfide-containing bismaleimide via the Diels–Alder (DA) reaction at 70 °C, where these could be decross-linked at 110 °C via the retro-Diels–Alder (rDA) reaction, and the S–S bond could be cleaved upon thermal or photo stimulus and regenerated through oxidative stimulus, offering another reversible decross-linking/cross-linking pathway for cross-linked PFMA brushes [13]. Usually, the rubber backbone is first grafted with maleic anhydride, which is then reacted with furfurylamine, and then, through DA, the bismaleimide molecule is introduced as a cross-linker [14]. More generally, bismaleimides to be introduced in polymers as cross-linkers require a furan functional group to react through the DA pathway [14–16]. However, grafting of maleic anhydride has been reported in the literature via application of shearing action in internal mixers and heat [17,18]. Following a similar approach, this work reports the cross-linking of NR with disulfide-containing bismaleimide via mixing in a micro compounder, followed by compression molding.

This work reports the pre-synthesis of a disulfide-containing bismaleimide (BIS) cross-linker, starting from desalination of cystamine dihydrochloride with subsequent reaction of the resulting cystamine with maleic anhydride, followed by compounding with NR,

as shown in Figure 1. Three formulations were prepared: (i) control compounds without inhibitors, (ii) $CuCl_2$ compounds, and (iii) CuMA compounds. Copper(II) complexes act as catalysts; however, rather than lowering the activation energy, they increase the activation energy threshold to enable disulfide metathesis. Therefore, in this work, copper(II) compounds are referred to as inhibitors. In all three formulations, BIS concentration varied from 3.55 to 8.88 phr. Rheological cure behavior and standard mechanical tests were used to define cure parameters and to establish baseline tensile/elastic properties of the pristine compounds. This paper, therefore, (i) describes the design and processing of a disulfide-selective cross-linking strategy to form the intended dynamic and controlled cross-linked network, and (ii) reports the mechanical performance of the pristine materials as a baseline for any future recyclability studies. The results establish whether the selective introduction of disulfide cross-links and the incorporation of metal coordination agents can produce materials with engineering-relevant mechanical properties while offering a route to thermally trigger network rearrangement under controlled conditions. No additional accelerators or antioxidants were included in the formulations, as the primary objective of this study is to isolate and evaluate the specific influence of copper(II) compounds on disulfide-based cross-linking. Introducing accelerators or antioxidants could have introduced competing effects, such as altering cure rates or suppressing oxidative pathways, which would confound interpretation of the copper-mediated inhibition mechanism. By excluding these additives, we ensured that the observed changes in rheological and mechanical behavior could be attributed solely to the presence and coordination chemistry of the copper(II) species.

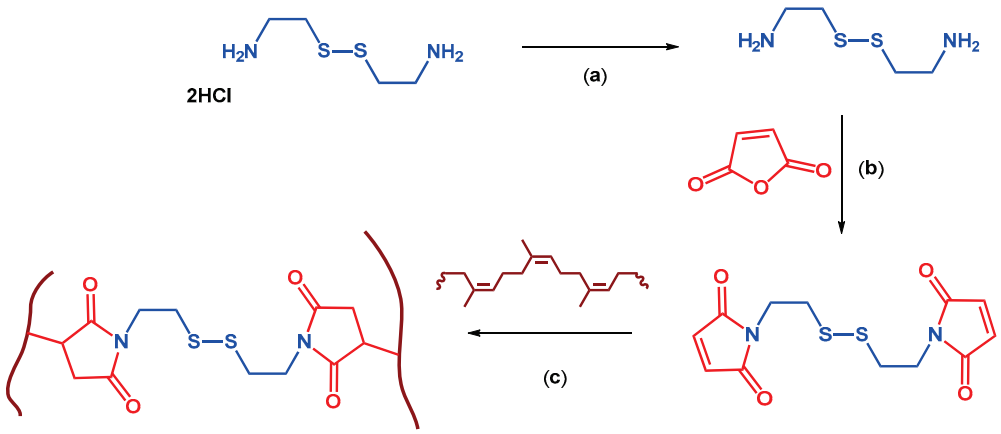

Figure 1. Schematic representation of rubber preparation. Conditions: (**a**) cystamine dihydrochloride, deionized water, NaOH, 12 h, room temperature; (**b**) 1. maleic anhydride, cystamine, toluene, 1 h, 30 °C, 2. hexamethyldisilazane, $ZnBr_2$, 12 h, 85 °C; (**c**) 1,1′-(disulfanediylbis(ethane-2,1-diyl))bis(1H-pyrrole-2,5-dione), NR, mixing in the micro compounder, followed by curing with hot press for the time required to reach 90% of maximum torque, t_{90}, at 180 °C.

2. Materials and Methods

2.1. Materials

Natural rubber (NR, SMR CV60 grade) was purchased from the Tun Abdul Razak Research Centre (Hertford, UK). Maleic anhydride (Man, purity ≥ 98%, technical grade) was purchased from VWR International (Leicestershire, UK). Copper(II) chloride ($CuCl_2$; purity ≥ 98%), hydrochloric acid (HCl; 37%, ACS reagent), hexamethyldisilazane (purity 99%), Chloroform-d ($CDCl_3$; 99.8 atom % D), methanol (purity ≥ 99.8%, ACS reagent), and dichloromethane (purity ≥ 99.9%, ACS reagent) were purchased from Sigma-Aldrich Co Ltd. (Dorset, UK). Cystamine dihydrochloride (Cys; purity 97%), sodium hydroxide (purity 98%), copper(II) methacrylate (CuMA, technical grade), zinc bromide (purity 98%, anhydrous), sodium hydrogen carbonate (purity 99%), and anhydrous sodium sulfate

(purity 99%) were purchased from Fisher Scientific (Loughborough, UK). Toluene (purity $\geq$ 99.9%, HPLC grade) and tetrahydrofuran (THF; purity $\geq$ 99.9%, inhibitor free, HPLC grade) were purchased from Honeywell International Inc. (Bracknell, UK).

In the present work, different rubber formulations with and without Cu(II) inhibitors were tested in different conditions, before and after curing and recycling. The terminology adopted to refer to the formulations and blends in specific conditions is as follows:

- NR/BIS-X: formulations without inhibitors, acting as control formulations, with X referring to phr of Bismaleimide introduced; generally called Control formulations;
- NR/BIS-X/CuMA: formulations with CuMA as inhibitor, with X referring to phr of Bismaleimide introduced; CuMA is equimolar to Bismaleimide;
- NR/BIS-X/$CuCl_2$: formulations with $CuCl_2$ as inhibitor, with X referring to phr of Bismaleimide introduced; $CuCl_2$ is equimolar to Bismaleimide;
- Compound: something that has been mixed, but not cured;
- Cured compound: new cured compound;
- Recycled compound: recycled cured compound.

2.2. Preparation of Cystamine

Sodium hydroxide (10.65 g, 266.430 mmol) was dissolved in 25 mL of deionized water and was added dropwise to an aqueous solution of cystamine dihydrochloride (30 g, 133.215 mmol, in 25 mL of deionized water), in an ice bath. The resulting solution was stirred for 1 h at room temperature. The obtained solution was transferred into a separatory funnel, and dichloromethane was added (20 mL $\times$ 4). The organic phase was dried over anhydrous sodium sulfate and filtered before drying under vacuum in a rotatory evaporator to obtain cystamine as a pale-yellow oily liquid (yield 29.9%). The resulting product was characterized by ^{1}H and ^{13}C NMR spectroscopy with Bruker Advance III 400 MHz. ^{1}H NMR ($CDCl_3$, 400 MHz): chemical shift δ = 1.21, 2.61, 2.85 ppm. ^{13}C DEPTQ135 NMR ($CDCl_3$, 100 MHz): chemical shift δ = 40.56, 42.51 ppm.

2.3. Synthesis of Bismaleimide Cross-Linker

A suspension of maleic anhydride (0.6641 g, 6.77 mmol) and cystamine (0.6846 g, 3.39 mmol) was prepared in 80 mL of toluene and stirred at 30 °C for 1 h. Subsequently, zinc bromide (1.524 g, 6.77 mmol) and hexamethyldisilazane (1.093 g, 6.77 mmol), dissolved in 15 mL of toluene, were added to the reaction mixture. The resulting suspension was heated to 85 °C and refluxed for 2 h. Reaction progress was monitored by thin-layer chromatography (TLC) using silica gel F254 plates on aluminum sheets and a dichloromethane:methanol (9:1) eluent system (product retention factor = 0.0678), and the reaction was considered complete once the reactant stains disappeared. Upon completion, the mixture was cooled to room temperature and quenched with 50 mL of 1 M hydrochloric acid. The organic layer was separated, and the aqueous layer was extracted twice with 50 mL portions of ethyl acetate. The combined organic extracts were washed with a saturated aqueous solution of sodium hydrogen carbonate and brine, then dried over anhydrous sodium sulfate. The solution was filtered and concentrated under reduced pressure using a rotary evaporator. The crude product was purified by crystallization, and the concentrated solution was placed in a refrigerator overnight. The resulting crystals were collected by filtration, washed with cold methanol, and dried under reduced pressure for 2 h. The resulting Bismaleimide (BIS) product, 1,1′-(disulfanediylbis(ethane-2,1-diyl))bis(1H-pyrrole-2,5-dione) (yield 48%), was characterized by ^{1}H and ^{13}C NMR spectroscopy. ^{1}H NMR ($CDCl_3$, 400 MHz): δ = 2.95, 3.88, 6.74 ppm. ^{13}C DEPTQ135 NMR ($CDCl_3$, 100 MHz): δ = 35.92, 36.81, 134.05 ppm.

2.4. Compound Preparation and Curing

NR/BIS, NR/BIS/CuMA, and NR/BIS/$CuCl_2$ formulations are reported in Table 1. Compounds were prepared in an Xplore MC15 HT Micro Compounder. Mixing was performed at 100 °C, 100 rpm speed, and a maximum torque of 35 Nm. NR, the previously synthesized BIS cross-linker, and the copper inhibitor were added together and mixed for 3 min. The compounds were then molded in a manual hot press at 180 °C, applying a constant pressure of about 12 MPa, for a curing time equal to t_{90} determined using Monsanto Moving Die Rheometer (MDR) 2000 with the lower die moving at 1.66 Hz, which was different for each formulation, as reported in Table 1.

Table 1. NR/BIS, NR/BIS/CuMA, and NR/BIS/$CuCl_2$ formulations and curing time.

Formulation	NR/phr	BIS/phr	CuMA/phr	$CuCl_2$/phr	t_{90}/min
NR/BIS-3.55	100	3.55			42
NR/BIS-3.55/CuMA	100	3.55	2.38		42
NR/BIS-3.55/$CuCl_2$	100	3.55		1.37	49
NR/BIS-5.33	100	5.33			43
NR/BIS-5.33/CuMA	100	5.33	3.58		44
NR/BIS-5.33/$CuCl_2$	100	5.33		2.06	45
NR/BIS-7.10	100	7.10			46
NR/BIS-7.10/CuMA	100	7.10	4.77		45
NR/BIS-7.10/$CuCl_2$	100	7.10		2.74	43
NR/BIS-8.88	100	8.88			46
NR/BIS-8.88/CuMA	100	8.88	5.96		45
NR/BIS-8.88/$CuCl_2$	100	8.88		3.43	44

2.5. Gel Permeation Chromatography

The number average molecular weight ($\overline{M}_n$), the weight average molecular weight ($\overline{M}_w$), and the dispersity ($Đ$) of NR and each compound prior to vulcanization were determined by performing Gel Permeation Chromatography (GPC) using Agilent Technologies 1260 Infinity GPC/SEC system equipped with a refractive index (RI) detector. Calibration was carried out using polystyrene standards ($\overline{M}_w$ range from 162 g/mol to 6,570,000 g/mol) from Agilent Technologies, Inc. (Santa Clara, CA, USA). Samples were prepared at least 48 h prior to the analysis by dissolving approximately 10 mg of sample in 5 mL of THF. The solutions were then filtered through a 0.2 μm PTFE syringe filter and transferred into GPC vials. Each run was performed by injecting 100 μL into the columns, kept at a constant temperature of 25 °C.

2.6. Dynamic Differential Scanning Calorimetry (DSC)

Dynamic DSC was conducted to determine the glass transition temperature, T_g, of all uncured compounds and cured compounds. Both analyses were carried out using a TA Instruments DSC25. All samples were placed in Tzero Aluminium Hermetic pans, and the normalized heat flow was measured. The thermal behavior of the uncured samples was investigated by conducting heat–cool–heat experiments. This is shown as follows: (1) first heating ramp from 20 °C to 200 °C at a rate of 5 °C/min; (2) second cool ramp from 200 °C to 20 °C at a rate of 5 °C/min; (3) third heat ramp from 20 °C to 200 °C at a rate of 5 °C/min. For the cured samples the heat–cool–heat experiments were carried as follows: (1) first heating ramp from −90 °C to 250 °C at a rate of 5 °C/min; (2) second cool ramp from 250 °C to −90 °C at a rate of 5 °C/min; (3) third heat ramp from −90 °C to 250 °C at a rate of 5 °C/min. The T_g of the cured samples was calculated by evaluating the minimum point of the first derivative of the normalized heat flow plot.

2.7. Mechanical Characterization

Tensile testing until failure was carried out on cured compounds. Dumbbell shape samples were cut out using an ISO-37-4 [19] die cutter 24 h after curing was completed. Testing was carried out using an Instron 5967 machine equipped with a 1 kN load cell and pneumatic side action grips, using a rate of 1 mm/s, which corresponds to an approximate strain rate of 0.1/s. The width and the thickness were measured prior to the start of the test, while the initial length, L_0, was measured after gripping the sample, ensuring the width of the sample remained constant in the gauge length. Uniaxial stress and strain were calculated using the following Equations (1) and (2):

$$\sigma = \frac{F}{A_0} \tag{1}$$

$$\varepsilon = \frac{\Delta L}{L_0} \tag{2}$$

where σ is the engineering stress, F is the measured force, A_0 is the initial unstrained cross-sectional area, ε is the strain, and ΔL is the measured elongation.

2.8. Density

Density measurements were carried out using a Micromeritics AccuPyc II 1345 gas-displacement pycnometer (Micromeritics Instrument Corporation, Norcross, GA, USA) using the following settings: number of purges 10, purge fill pressure 134.45 kPa, number of cycles 10, cycle fill pressure 134.45 kPa, equilibration rate 3.45 kPa min^{-1}, and chamber size 1 cm^3.

3. Results and Discussion

During the mixing stage, rubber compounds may undergo molecular degradation due to mechanical and thermal stresses. Specifically, excessive mastication in the micro compounder can reduce $\overline{M}_n$ and $\overline{M}_w$, while elevated temperatures may promote premature chemical interactions among formulation components. Disulfide metathesis reactions are particularly favored under these conditions, potentially leading to exchange reactions prior to curing. Figure 2a,b presents the $\overline{M}_n$ and $\overline{M}_w$ values respectively following a 3 min mixing period. The control formulation exhibits $\overline{M}_n$ and $\overline{M}_w$ values comparable to raw NR, with NR/BIS-8.88 showing lower $\overline{M}_w$ (500,000 g/mol) than NR (700,000 g/mol), while $\overline{M}_n$ remains in the range of 180,000–240,000 g/mol. In contrast, the $CuCl_2$ formulation displays significantly reduced $\overline{M}_n$ and $\overline{M}_w$ (10,000–20,000 g/mol and 100,000–150,000 g/mol, respectively), indicating poor compatibility with NR and suggesting substantial chain scission during processing. CuMA samples show intermediate $\overline{M}_n$ and $\overline{M}_w$ values (100,000–110,000 g/mol and 300,000–310,000 g/mol), which remain suitable for further processing. Additionally reported in Figure 2c, $Đ$ values for NR, Control, and CuMA formulations range between 3 and 5, indicating relatively uniform chain lengths.

However, $CuCl_2$ formulations exhibit much broader $Đ$ values between 11 and 23, further supporting the hypothesis of polymer degradation and incompatibility in the absence of antioxidants. Overall, the molecular weights of CuMA and $CuCl_2$ compounds are lower than those of NR and Control compounds, primarily due to the mixing conditions of 100 °C at 100 rpm, and an additional 3 min mixing step required for incorporating the copper(II) inhibitors, which was not performed for the control formulation. DSC analysis was performed to determine the thermal behavior and curing characteristics of the uncured and cured rubber formulations. Dynamic DSC thermograms of uncured Control samples are reported in Figure 3a. Two distinct peaks are revealed: peak A between 115 °C and 120 °C,

corresponding to the recrystallization of bismaleimide, and peak B (140–150 °C), associated with the reaction between NR and the cross-linker. As the cross-linker concentration increased from 3.55 to 8.88 phr, peak B shifted to higher temperatures, indicating delayed reaction onset. A curing temperature range of 170–190 °C was selected to accommodate all concentrations. DSC thermograms of CuMA samples reported in Figure 3b exhibited similar dual-peak behavior, with peak A representing bismaleimide crystallization, and peak B indicating NR-cross-linker interaction. The optimal curing temperature was again determined to be 170–190 °C. In contrast, $CuCl_2$ samples reported in Figure 3c showed irregular thermograms with no distinct peaks, suggesting degradation and incompatibility with NR. The absence of antioxidants likely led to oxidative degradation, producing hydrochloric acid and chlorine gas through complex redox reactions. Cured samples were also analyzed via DSC. Control formulations reported in Figure 4a displayed a single peak in the first heating cycle, possibly due to residual cross-linker reactions or bismaleimide copolymerization, as in the second heating cycle, no peak appears in the same region. CuMA samples in Figure 4b showed minor peaks, indicating further cross-linker activity. $CuCl_2$ samples in Figure 4c lacked distinct thermal transitions, reinforcing the conclusion of degradation. Glass transition temperatures, T_g, for all formulations were consistent with unfilled NR (~−65 °C), as reported in Figure 4d. Rheological measurements were employed to assess and confirm the curing behavior and network formation of the rubber compounds at 180 °C. As reported in Figure 5, NR, lacking curatives, exhibited a baseline torque of 1.5 dNm due to physical entanglements rather than chemical cross-links. As shown in Figure 5a, increasing the concentration of cross-linkers in the Control samples led to higher torque values from 3 to 6 dNm. NR/BIS-7.10 demonstrated optimal performance, with torque values nearly matching those of NR/BIS-8.88, suggesting efficient cross-link formation. CuMA formulations reported in Figure 5b exhibited a consistent increase in torque with cross-linker concentration going from 4 to 6.5 dNm. NR/BIS-8.88/CuMA showed the highest torque values, indicating robust and stable cross-link networks. $CuCl_2$ formulations reported in Figure 5c also showed increasing torque with higher cross-linker concentrations, going from 2 to 6 dNm. However, inconsistencies were observed, such as lower torque in NR/BIS-5.33/$CuCl_2$ compared with NR/BIS-3.55/$CuCl_2$, suggesting degradation. These results suggest that CuMA formulations are promising candidates for achieving high mechanical performance, while $CuCl_2$ formulations suffer from degradation and poor network stability. All formulations exhibit short or negligible scorch times, which could potentially hinder mold flow. However, full mold filling was achieved because the compounds were processed under controlled conditions that maintained sufficient mobility before significant network formation occurred. The marching cure behavior of these systems ensures that cross-linking progresses gradually rather than instantaneously; initial viscosity remains low enough for the material to flow and completely fill the mold before torque rises substantially. This dynamic curing characteristic is typical of disulfide-based systems, where bond exchange occurs progressively rather than locking the network immediately. Density measurements, presented in Figure 5d, were conducted to assess the structural integrity and packing efficiency within the rubber matrix. Among the formulations, $CuCl_2$ samples exhibited the highest density values between 0.98 and 1.00 g/mol, which suggests significant degradation. In contrast, CuMA formulations reported the lowest density values between 0.87 and 0.92 g/mol. This reduction may be attributed to the bulkier nature of the CuMA inhibitor, which could hinder tight packing and reduce the overall material density. Control samples reported higher density values compared with unfilled NR ($0.91 \pm 9.1 \times 10^{-4}$ g/mL), suggesting minimal structural disruption and effective cross-linking. Tensile testing was conducted on the cured rubber compounds to evaluate their mechanical performance, as shown in Figure 6. Due to extensive degradation

during hot pressing, the $CuCl_2$ samples produced were too brittle to grip for tensile testing, highlighting their poor thermal and chemical stability in the absence of antioxidants. In contrast, the Control formulations reported in Figure 6a demonstrated a clear trend of increasing tensile strength with higher cross-linker concentrations. The maximum tensile stress recorded for Control NR/BIS-8.88 was 7.5 MPa, with a corresponding tensile strain of 11.5. Similarly, CuMA samples in Figure 6b exhibited comparable mechanical behavior, reaching a maximum tensile stress for NR/BIS-8.88/CuMA of 8.4 MPa and tensile strain of 11.1. The tensile strength is directly correlated with the density of cross-links formed during curing. Both Control and CuMA samples showed promising results, although they remain significantly below the tensile strength of conventionally sulfur-vulcanized unfilled NR, which typically reaches ~16 MPa [1]. This reduction in strength suggests that while bismaleimide-based cross-linking is effective, further optimization is required to match commercial compounds. To explore the recyclability of the materials, recycled samples were evaluated using rheology as a preliminary indicator of network retention, as torque values can provide insight into the extent of cross-link rearrangement and degradation upon reprocessing. As reported in Figure 7a, the recycled torque values of the Control samples ranged from 2 to 6 dNm. All samples showed reduced torque values compared with the respective pristine samples, suggesting partial retention of the cross-linked network and potential for limited recyclability. CuMA samples reported in Figure 7b showed better performance upon reprocessing, with torque values ranging from 2.5 to 4.5 dNm. NR/BIS-8.88/CuMA formulation retained the highest torque of 4.6 dNm, suggesting that the disulfide-based cross-links formed in this system are more resistant to breakdown and may allow for limited reprocessability. $CuCl_2$ samples reported in Figure 7c exhibited similar behavior, with reprocessed torque values ranging from 1 to 5.5 dNm.

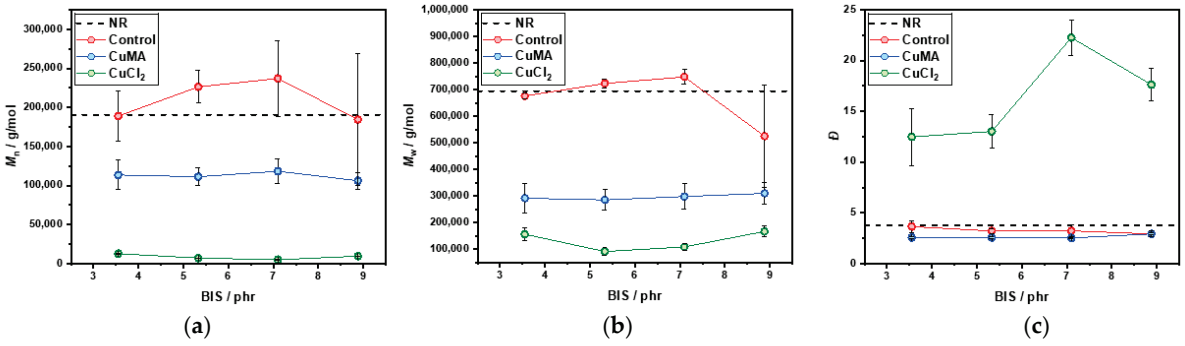

Figure 2. GPC analysis comparison between NR, Control, CuMA, and $CuCl_2$ formulations: (**a**) $\overline{M}_n$ results, (**b**) $\overline{M}_w$ results, (**c**) $Đ$ results.

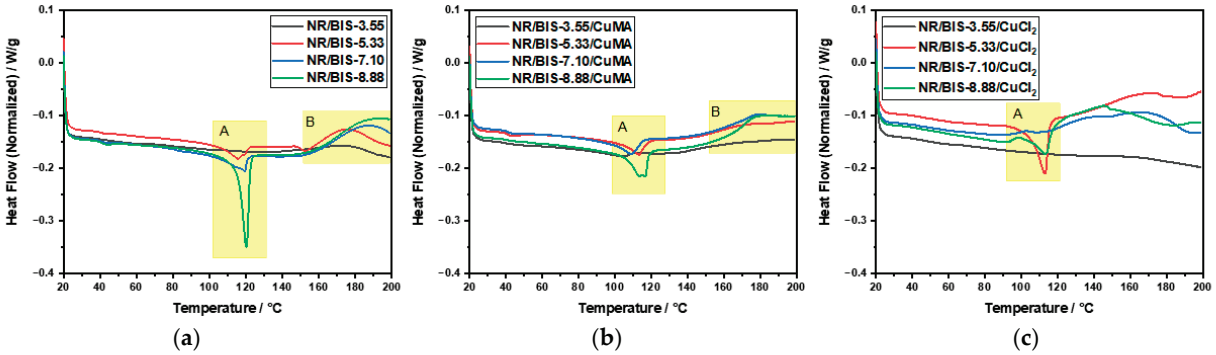

Figure 3. DSC analysis of uncured samples with peak A representing bismaleimide crystallization, and peak B indicating NR-cross-linker interaction: (**a**) Control, (**b**) CuMA, and (**c**) $CuCl_2$ formulations.

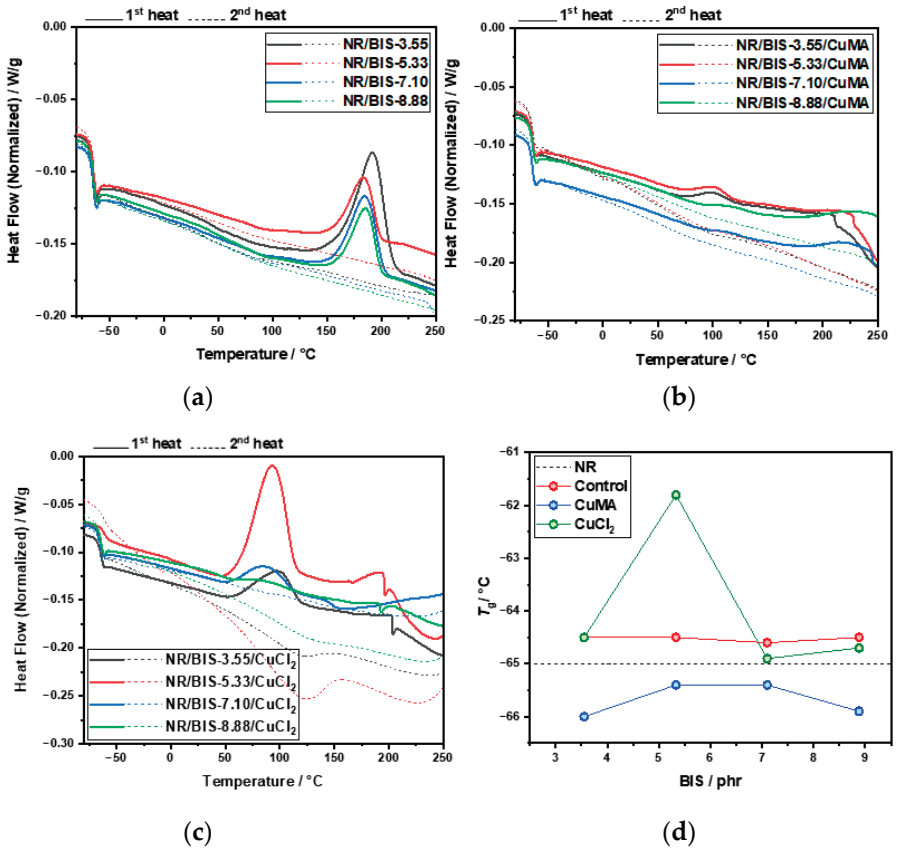

Figure 4. DSC analysis of cured samples: (**a**) Control, (**b**) CuMA, and (**c**) $CuCl_2$ formulations. (**d**) T_g of all samples.

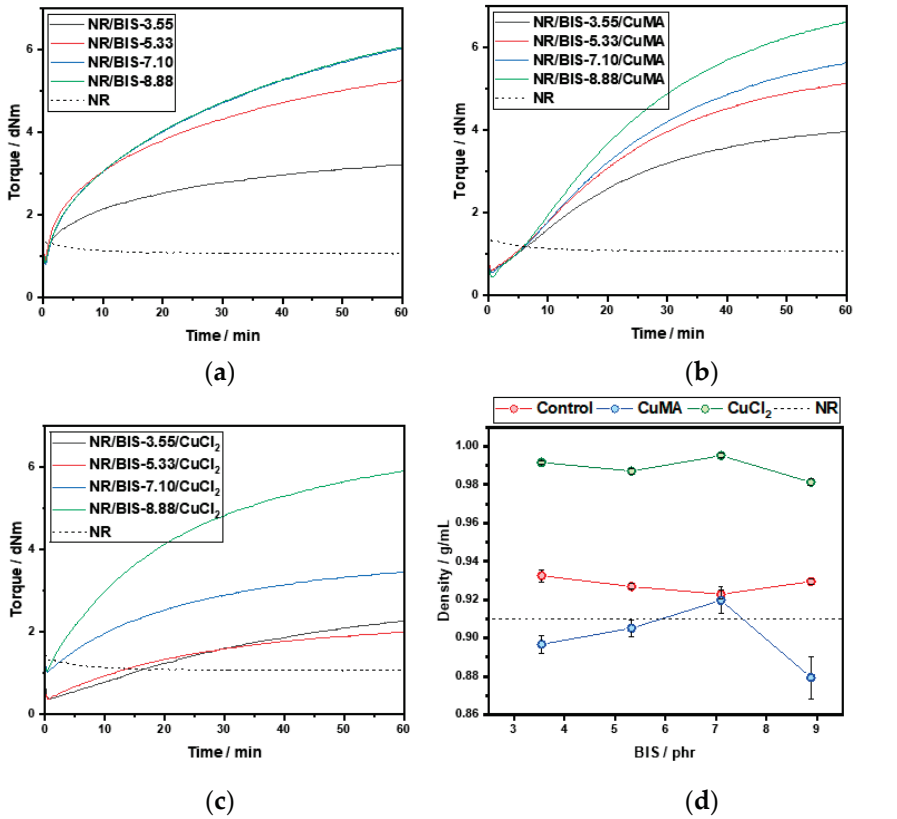

Figure 5. Rheology and density measurements. MDR analysis at 180 °C of (**a**) Control, (**b**) CuMA, and (**c**) $CuCl_2$ formulations. (**d**) Density vs. BIS concentration on the *x*-axis.

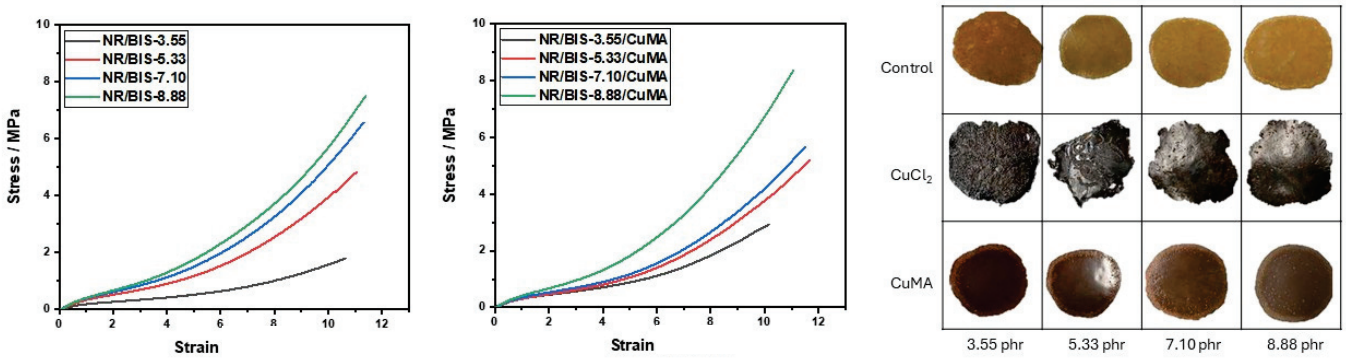

(**a**) (**b**) (**c**)

Figure 6. Tensile test analysis of (**a**) Control and (**b**) CuMA formulations. (**c**) Control, $CuCl_2$, and CuMA samples after vulcanization.

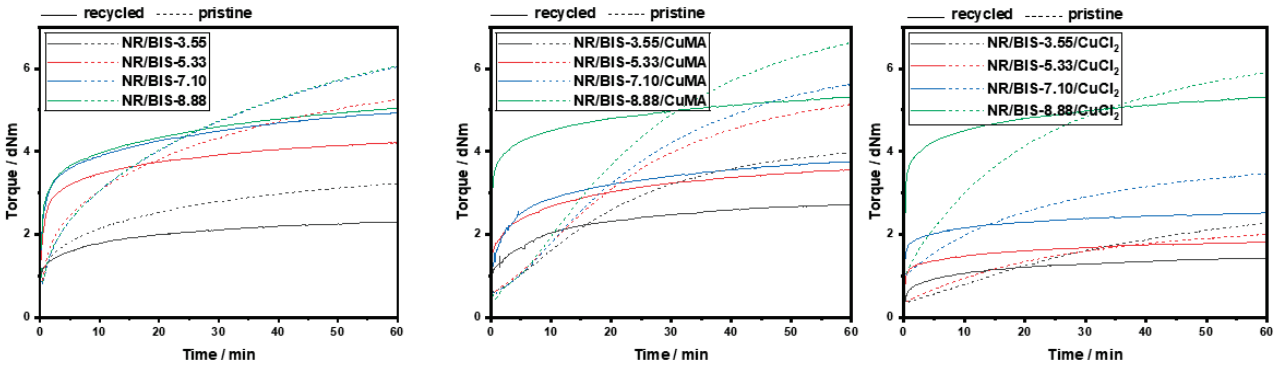

(**a**) (**b**) (**c**)

Figure 7. Rheology comparison between pristine and recycled samples: (**a**) Control, (**b**) CuMA, and (**c**) $CuCl_2$.

4. Conclusions

The study demonstrates that rubber formulations are highly sensitive to processing conditions and component compatibility. $CuCl_2$-based compounds exhibit significant main chain scission and degradation, poor thermal stability, and mechanical brittleness, largely due to oxidative reactions in the absence of antioxidants. In contrast, CuMA outperformed $CuCl_2$, likely because the methacrylate ligand provides a more stable coordination environment for copper(II) ions, thereby reducing their propensity to induce uncontrolled oxidation. As a result, CuMA formulations maintain intermediate molecular weights, stable thermal behavior, and promising mechanical properties, including enhanced torque and tensile strength, suggesting effective cross-linking and partial recyclability. Control formulations also perform well, though both CuMA and Control systems fall short of the mechanical strength observed in conventional sulfur-vulcanized NR. While recyclability testing was planned as a subsequent phase of the project, experimental progress ceased before those assessments could be completed. As such, recyclability data are not reported here. However, the observed molecular characteristics and mechanical resilience of CuMA formulations strongly support further investigation into their recyclability. Future studies could explore thermal reprocessing, chemical depolymerization, or mechanical recovery strategies to validate and optimize the recyclability of these materials. Overall, CuMA emerges as a viable alternative for high-performance, recyclable rubber materials, while $CuCl_2$ is unsuitable without further stabilization strategies.

Author Contributions: Conceptualization, A.K. and J.J.C.B.; methodology, A.K.; validation, A.K. and K.A.; formal analysis, A.K. and M.T.; investigation, A.K. and M.T.; resources, A.K. and J.J.C.B.; data curation, A.K. and M.T.; writing—original draft preparation, A.K. and M.T.; writing—review and editing, K.A., B.C., and J.J.C.B.; visualization, A.K. and M.T.; supervision, K.A., B.C., and J.J.C.B.; project administration, B.C. and J.J.C.B.; funding acquisition, B.C., and J.J.C.B. All authors have read and agreed to the published version of the manuscript.

Funding: This work was supported by the Engineering and Physical Sciences Research Council (EPSRC) grant EP/W018977/1.

Data Availability Statement: The original data presented in the study are openly available in the Queen Mary Research Online repository at https://qmro.qmul.ac.uk/xmlui/handle/123456789/114491 (accessed on 5 December 2025).

Conflicts of Interest: The authors declare no conflicts of interest.

References

1. Kaur, A.; Fefar, M.M.; Griggs, T.; Akutagawa, K.; Chen, B.; Busfield, J.J.C. Recyclable sulfur cured natural rubber with controlled disulfide metathesis. *Commun. Mater.* **2024**, *5*, 212. [CrossRef]
2. Markl, E.; Lackner, M. Devulcanization Technologies for Recycling of Tire-Derived Rubber: A Review. *Materials* **2020**, *13*, 1246. [CrossRef] [PubMed]
3. Coran, A.Y. Chemistry of the vulcanization and protection of elastomers: A review of the achievements. *J. Appl. Polym. Sci.* **2003**, *87*, 24–30. [CrossRef]
4. Nevejans, S.; Ballard, N.; Miranda, J.I.; Reck, B.; Asua, J.M. The underlying mechanisms for self-healing of poly(disulfide)s. *Phys. Chem. Chem. Phys.* **2016**, *18*, 27577–27583. [CrossRef] [PubMed]
5. Rekondo, A.; Martin, R.; Ruiz de Luzuriaga, A.; Cabañero, G.; Grande, H.J.; Odriozola, I. Catalyst-free room-temperature self-healing elastomers based on aromatic disulfide metathesis. *Mater. Horiz.* **2014**, *1*, 237–240. [CrossRef]
6. Kaur, A.; Gautrot, J.E.; Cavalli, G.; Watson, D.; Bickley, A.; Akutagawa, K.; Busfield, J.J.C. Novel Crosslinking System for Poly-Chloroprene Rubber to Enable Recyclability and Introduce Self-Healing. *Polymers* **2021**, *13*, 3347. [CrossRef] [PubMed]
7. Imbernon, L.; Oikonomou, E.K.; Norvez, S.; Leibler, L. Chemically crosslinked yet reprocessable epoxidized natural rubber via thermo-activated disulfide rearrangements. *Polym. Chem.* **2015**, *6*, 4271–4278. [CrossRef]
8. Xiang, H.P.; Qian, H.J.; Lu, Z.Y.; Rong, M.Z.; Zhang, M.Q. Crack healing and reclaiming of vulcanized rubber by triggering the rearrangement of inherent sulfur crosslinked networks. *Green Chem.* **2015**, *17*, 4315–4325. [CrossRef]
9. Xiang, H.P.; Rong, M.Z.; Zhang, M.Q. Self-healing, Reshaping, and Recycling of Vulcanized Chloroprene Rubber: A Case Study of Multitask Cyclic Utilization of Cross-linked Polymer. *ACS Sustain. Chem. Eng.* **2016**, *4*, 2715–2724. [CrossRef]
10. Kong, Y.; Chen, X.; Li, Z.; Li, G.; Huang, Y. Evolution of crosslinking structure in vulcanized natural rubber during thermal aging in the presence of a constant compressive stress. *Polym. Degrad. Stab.* **2023**, *217*, 110513. [CrossRef]
11. Wang, M.; Wang, R.; Chen, X.; Kong, Y.; Huang, Y.; Lv, Y.; Li, G. Effect of non-rubber components on the crosslinking structure and thermo-oxidative degradation of natural rubber. *Polym. Degrad. Stab.* **2022**, *196*, 109845. [CrossRef]
12. Kitagawa, S.; Ozawa, M.; Shibata, M. Self-healing and reprocessable bismaleimide-diamine thermosets containing disulfide linkages. *Polymer* **2023**, *278*, 126008. [CrossRef]
13. Sim, X.M.; Wang, C.-G.; Liu, X.; Goto, A. Multistimuli Responsive Reversible Cross-Linking–Decross-Linking of Concentrated Polymer Brushes. *ACS Appl. Mater. Interfaces* **2020**, *12*, 28711–28719. [CrossRef] [PubMed]
14. Polgar, L.M.; Cerpentier, R.R.J.; Vermeij, G.H.; Picchioni, F.; Duin, M.v. Influence of the chemical structure of cross-linking agents on properties of thermally reversible networks. *Pure Appl. Chem.* **2016**, *88*, 1103–1116. [CrossRef]
15. Gevrek, T.N.; Sanyal, A. Furan-containing polymeric Materials: Harnessing the Diels-Alder chemistry for biomedical applications. *Eur. Polym. J.* **2021**, *153*, 110514. [CrossRef]
16. Post, C.; van den Tempel, P.; Herrera Sánchez, P.; Maniar, D.; Bose, R.K.; Voet, V.S.D.; Folkersma, R.; Picchioni, F.; Loos, K. Thermoreversible Diels–Alder Cross-Linking of BHMF-Based Polyesters: Synthesis, Characterization and Rheology. *ACS Sustain. Chem. Eng.* **2025**, *13*, 3543–3553. [CrossRef] [PubMed]
17. Hayeemasae, N.; Sensem, Z.; Sahakaro, K.; Ismail, H. Maleated Natural Rubber/Halloysite Nanotubes Composites. *Processes* **2020**, *8*, 286. [CrossRef]

18. Ujianto, O.; Noviyanti, R.; Wijaya, R.; Ramadhoni, B. Effect of maleated natural rubber on tensile strength and compatibility of natural rubber/coconut coir composite. *IOP Conf. Ser. Mater. Sci. Eng.* **2017**, *223*, 012014. [CrossRef]
19. *ISO 37:2024(en)*; Rubber, Vulcanized or Thermoplastic—Determination of Tensile Stress-strain Properties. International Organization for Standardization: Geneva, Switzerland, 2024.

polymers

MDPI

Article

Analysis of Tyre Pyrolysis Oil as Potential Diesel Fuel Blend with Focus on Swelling Behaviour of Nitrile-Butadiene Rubber

Steffen Seitz [1,2,*], Tobias Förster [2] and Sebastian Eibl [2]

[1] Institute of Mechanics, Faculty of Aerospace Engineering, University of the Bundeswehr Munich, Werner-Heisenberg-Weg 39, 85579 Neubiberg, Germany
[2] Bundeswehr Research Institute for Materials, Fuels and Lubricants (WIWeB), Institutsweg 1, 85435 Erding, Germany; tobias1foerster@bundeswehr.org (T.F.); sebastianeibl@bundeswehr.org (S.E.)
* Correspondence: steffen.seitz@unibw.de

Abstract

This study examines the swelling behaviour of nitrile-butadiene rubber (NBR) when interacting with tyre pyrolysis oils (TPO), with a focus on the chemical composition of TPO and their interaction with rubber matrices. Initially, a comparative analysis with conventional diesel fuel (DF) was performed using advanced analytical techniques, including two-dimensional gas chromatography coupled to mass spectrometry (2D-GC/MS), infrared (IR) spectroscopy, and nuclear magnetic resonance (^{1}H-NMR) spectroscopy. The analysis revealed that TPO contains a significantly higher proportion of aromatic hydrocarbons than DF, along with unsaturated and oxygen-containing compounds not present in DF. Based on these compositional differences, blends of TPO and DF were formulated and evaluated for their suitability as liquid energy carriers according to the specifications of DF. In principle, blends with an addition of up to 5 vol% TPO in DF are technically suitable for use as fuel. Subsequently, the sorption behaviour of TPO, DF, and their blends in NBR was investigated. The swelling potential was determined based on mass, density, and volume, and the changes in the hardness and tensile strength of NBR were recorded. The results demonstrate that TPO induces pronounced swelling in NBR, as evidenced by a marked increase in mass uptake and volume expansion. A linear increase was observed between the degree of swelling and the increasing TPO content in the blends. Mechanical property assessments revealed a corresponding decrease in the hardness and tensile strength of NBR upon exposure to TPO, with the most severe effects associated with neat TPO. This work provides a comprehensive assessment of TPO as a potential blend component for DF. It highlights the need for careful consideration of material compatibility in practical applications.

Keywords: nitrile-butadiene rubber; tyre pyrolysis oil; chemical analysis; swelling behaviour; mechanical testing

1. Introduction

Around 3.4 million tons of tyre waste are generated across Europe every year. Processes for recycling tyres include combustion, which is predominantly used in the cement industry and material reuse, for which the plastic components have to be separated. Due to the complex composition of tyres, the challenge is to achieve complete separation of the components. The composition of tyres varies depending on their application. According to manufacturers, tyres typically consist of 41% rubbers, 30% fillers, 15% steel and textiles,

6% plasticizers, 6% vulcanization reagents, and 2% antioxidants [1]. The pyrolysis process is making the complete recycling of used tyres increasingly important. Textiles and steel can be separated from the rubber and recycled to produce new tyres. During pyrolysis, polymer chains in the tyre granulate are depolymerized under inert conditions to produce gas, oil, and coke residues [2–4]. The quantity of pyrolysis products depends on the type of tyres used and the process parameters [5–7]. T. Williams has evaluated various reactor types that were tested to preferably gain tyre pyrolysis oil (TPO) [8]. Pyrolysis gas is mostly used as an energy source and the solid residue can be reprocessed as recycled carbon black in tyres [3,9].

The individual pyrolysis mechanisms have been described by several authors for the elastomer types of natural rubber (NR), styrene-butadiene rubber (SBR) and butadiene rubber (BR) [10–15]. Due to the complexity of the tyre composition, further studies were carried out for corresponding elastomer mixtures [16–20]. In general, the polymer chains undergo depolymerization, disproportionation reactions or β-cleavages and are pyrolyzed into smaller molecules such as monomers, dimers, and oligomers. For example, NR predominantly forms isoprene and dipentene and BR produces butadiene, vinyl cyclohexene, and dipentene [10,15,21]. Diels–Alder reactions, addition reactions, cyclisation, aromatisation, and intramolecular hydrogen transfer convert the primary products into benzene, indene, and naphthalene with alkyl and alkenyl substituents [11,15,19]. SBR pyrolyzes mainly to styrene and methyl styrene and reacts via Diels–Alder reaction to alkylbenzenes or diaromatics like biphenyl, and with the BR and NR products to alkyl naphthalenes [12–14,16]. The oil component can be used as a fuel [22,23]. TPO is regarded as a possible blend for diesel fuel (DF) due to its similar composition [24]. Pyrolysis thus contributes to more sustainable tyre recycling and the conservation of fossil resources.

When TPO is used as a liquid energy carrier in civil or military transport vehicles, it is necessary to ensure operational availability and that TPO is compatible with the system. Compatibility with the elastomers must hence be analyzed. The resistance of sealing materials depends on the chemical composition of the liquid medium [25,26]. It is, therefore, crucial to determine the chemical composition of TPO when estimating its diffusion behaviour. This can be observed through swelling, extraction of additives, and changes in the mechanical properties of the elastomer [27–29]. Nitrile-butadiene rubber (NBR) is an elastomer widely utilized in the automotive and aerospace industries for applications such as seals, hoses, and tank linings. Its utilization is primarily attributed to its excellent resistance to non-polar liquids, including fuels, as well as its favourable mechanical and ageing properties [30]. With an increasing acrylonitrile content in the polymer, the polarity of the NBR increases, leading to better resistance to non-polar liquids [31,32].

This study aims to investigate the potential use of TPO as a replacement or blend for DF and to understand TPO's diffusion behaviour in the established sealing material NBR. On the one hand, the focus is on comparing the chemical composition of DF and TPO and determining the characteristic properties of TPO-DF blends according to DIN EN590 [33]. On the other hand, the work presents compatibility tests of the liquids with NBR with different acrylonitrile content to estimate its swelling potential and resulting influence on mechanical properties. In addition, the temperature dependence of the diffusion process of neat TPO and DF is investigated. The results contribute to an understanding of the sorption behaviour of TPO in contact with NBR and promote its potential use as a liquid energy source.

2. Materials

Polymer Service Merseburg (Merseburg, Germany) produced sulphur cross-linked nitrile-butadiene rubber (NBR) samples with an acrylonitrile content of 18 wt%, 28 wt%,

and 39 wt% in the NB-copolymer. In this study, these are abbreviated as NBR18, NBR28, and NBR39. The exact formulations are shown in Table 1. The NBR samples contained additives, including DPHP and 6-PPD, which served as plasticizers and antioxidants. The cross-linking of the elastomer required zinc oxide, stearic acid, and sulphur, while N-Cyclohexyl-2-benzothiazolylsulfenamide (CBS) and Tetramethyl thiuram monosulfide (TMTM-80) acted as accelerators for the vulcanisation process. S2 Tension rods were punched out of the NBR sheets [34]. These were split to a thickness of 1 mm using a band knife splitting machine NAF470 from Fortuna GmbH (Weil der Stadt, Germany).

Table 1. Formulation of the three NBR elastomers with the specification in parts-per-hundred rubber (phr).

Ingredient	**Concentration/phr**		
Acrylonitrile content/wt%	18	28	39
Perbunan 1846	100		
Perbunan 2846		100	
Perbunan 3946			100
Carbon black (Typ N550)		60	
Di(2-propylheptyl) phthalate (DPHP)		20	
N-(4-Methylpentan-2-yl)-N-phenylbenzene-1,4-diamine (6-PPD)		2	
Zinc oxide		5	
Stearic acid		1	
Sulphur		2	
N-Cyclohexyl-2-benzothiazolylsulfenamide (CBS)		1.5	
Tetramethyl thiuram monosulfide (TMTM-80)		0.5	

To produce tyre pyrolysis oil (TPO), Pyrum Innovations AG from Dillingen/Saar (Germany) provided thermolysis oil from a mixture of truck, car, and bicycle tyres. The TPO was vacuum filtered for further use. Blends with the pyrolysis oil were created using a commercially available diesel fuel (DF) according to DIN EN 590. The mixing ratio was 1 vol%, 5 vol%, and 10 vol% of TPO in DF, abbreviated as DF99TPO1, DF95TPO5, and DF90TPO10.

3. Experiment

3.1. Analysis of Fuels

The liquids were tested using the A-test according to DIN EN 590 (2022-05) for DF [33]. The individual test methods and the standards used are shown in Table 2. In addition, the total acid number (TAN) was determined according to ASTM D664 [35]. A potentiometric titration with potassium hydroxide (KOH) was used for this determination. TAN represents the mass of KOH, in milligrams, required to neutralize one gram of the sample. Using the concentration (c) of the KOH solution, the sample mass (m_s), and the titration volumes of the blank (V_B) and the sample (V_S), the TAN can be calculated according to Equation (1).

$$\mathrm{TAN} = \frac{56.1 \times c(V_S - V_B)}{m_S} \quad (1)$$

The iodine value is calculated in accordance with DIN EN ISO 3961 [36]. In this method, iodine chloride reacts with carbon–carbon double bonds, followed by the addition of potassium iodide to release iodine, which is subsequently titrated with sodium thiosulfate. The resulting iodine number is obtained from Equation (2), which relates the concentration

of the sodium thiosulfate solution (c), the titration volume of the blank (V_B) and for the samples (V_S), and the mass of fuel sample (m_s).

$$\text{Iodine value} = \frac{12.69 \times c(V_B - V_S)}{m_S} \quad (2)$$

Table 2. Selected parameters from DIN EN 590 with standards used.

Parameter	Norm
Viscosity Density	ASTM D7042-21a [37]
Polyaromatic content	DIN EN 12916 [38]
Flash point	DIN EN ISO 2719 [39]
HFRR [1]-test	DIN EN ISO 12156-1 [40]
CFPP [2]	DIN EN 116 [41]
Cupper corrosion	DIN EN ISO 2160 [42]
Oxidation stability	DIN EN 16091 [43]
Water content	DIN 51777-2 [44]
Carbon residue	DIN EN ISO 10370 [45]
Ash	DIN EN ISO 6245 [46]
Sulphur content	DIN EN ISO 20884 [47]
Distillation process	DIN EN ISO 3405 [48]

[1] HFRR (high frequency reciprocating rig); [2] CFPP (cold filter plugging point).

Two-dimensional gas chromatography coupled to mass spectrometry (2D-GC/MS) analyses were performed with a Shimadzu GC-2010 Plus gas chromatograph equipped with a ZOEX ZX1 modulator and a Shimadzu GCMS-QP2010 Ultra mass spectrometer operated in electron ionization mode. The column combination used was a 30 m Restek Txi-1ms (0.25 mm; 0.25 µm film) with 3 m SGE Analytical Science BPX 50 (0.15 mm; 0.15 µm film). Measurements were performed in 1:10 split mode with helium as a carrier gas and a modulation time of 8 s. The oven temperature was maintained at 50 °C for 3 min, before heating to 320 °C at a constant heating rate of 5 °C min^{-1}, where it was held for 2 min.

In addition, 10 mL TPO was added to a HyperSep silica stationary solid phase extraction (SPE) column from Thermo Scientific and washed with 20 mL heptane and 10 mL acetone. The polar acetone fraction was analyzed by GC/MS using an HP5 column at 50 °C for 2 min and a 10 °C min^{-1} heated to 300 °C and held for 2 min.

^{1}H-Nuclear magnetic resonance (^{1}H-NMR) analyses were performed with a Spinsolve 80 Carbon from Magritek in Powerscan mode at 80 MHz and analyzed with MestReNova software. Octamethyl silane was added to TPO as reference.

Fourier transform infrared (FTIR) spectra were recorded with a Bruker Tensor 27 spectrometer, which was equipped with a 50 µm zinc selenid cuvette at a spectral resolution of 4 cm^{-1}. The spectra were averaged over 32 scans in a wavenumber range between 4000 cm^{-1} and 500 cm^{-1}. The spectra were baseline corrected and normalized to the band intensity at 2725 cm^{-1}.

3.2. Sorption Experiments

For preparation, the volatile components such as plasticizer DPHP and antioxidant 6-PPD were extracted from the NBR samples in a Soxhlet apparatus for 16 h with acetone. For the sorption tests, the NBR samples were stored in the liquids for 0.5 h, 1 h, 7 h, 24 h, 72 h, and 168 h. The NBR28 and NBR39 samples were additionally stored for 672 h and 2016 h and NBR39 for 4032 h. Additionally NBR18 were kept in TPO and DF at 50 °C and

80 °C. The relative mass change Δm_{grav} was calculated using Equation (3), where m_t is the mass after a certain storage time, and m_0 is the initial mass.

$$\Delta m_{grav} = \frac{(m_t - m_o)}{m_0} * 100\,\text{wt\%} \tag{3}$$

Using Fick's second diffusion law and the solution for one-dimensional diffusion, Equation (4) can be derived [49]. This Equation uses a sorption curve to determine the specific relative mass changes. The mean diffusion coefficient D can be determined by calculating the mass after specific time intervals m_t, the thickness of the NBR samples h (1 mm), the equilibrium mass m_∞ of the samples and the number of iteration steps n.

$$\frac{\Delta m_t}{\Delta m_\infty} = 1 - \frac{8}{\pi^2}\sum_{n=0}^{\infty}\left(\frac{1}{(2n+1)^2} exp\left(\frac{-(2n+1)^2\pi^2 Dt}{h^2}\right)\right) \tag{4}$$

After storage, the samples were immersed in 40/60 gasoline to remove any fuel adhering to the outside and blotted with a paper towel. To determine the density, the samples were weighed in water using the VF 4601 kit from Satorius (Göttingen, Germany) and calculated according to Archimedes' principle using Equation (5). The volume change in the NBR sample can be determined using Equation (6) with mass and density.

$$\rho_{NBR} = \frac{m_{NBR,Air} * \rho_{Water}}{m_{NBR,Air} - m_{NBR,Water}} \tag{5}$$

$$\Delta V = \frac{(V_t - V_o)}{V_0} * 100\,\text{vol\%} \tag{6}$$

A Bareiss® digi test II testing machine (Oberdischingen, Germany) was used to determine the micro-Shore-A hardness of the NBR according to DIN ISO 48-4:2021-02 [50]. Tensile tests according to DIN 53504 were carried out to determine the elongation at break and tensile strength using a Zwick A universal testing machine from ZwickRoell GmbH (Ulm, Germany) with a 500 N load cell and optical extensometer with an elongation rate of 0.167 s^{-1} [34].

4. Results

4.1. Comparison of the Chemical Composition of DF and TPO

4.1.1. GC/MS Analysis

Figure 1 presents the two-dimensional gas chromatogram (2D-GC/MS) of DF (Figure 1A) and TPO (Figure 1B). For a semi-quantitative analysis, the areas of the individual peaks from the 2D GC-MS chromatogram were integrated and assigned to a substance class based on the mass spectra. The results of this classification are summarized in Table 3. In region 1 TPO shows a homologous series of alkanes ranging from C_8 to C_{34}, along with the corresponding mono- and diunsaturated alkenes. In contrast, DF contains a broader range of alkanes (C_6 to C_{36}) with higher degree of structural variability in the branches and higher relative signal intensity (74 area%) compared to TPO (8 area%). Region 2 of the chromatogram reveals cyclic alkanes with methyl and ethyl substituents in DF (9 area%), whereas TPO (7 area%) is characterized by an intense peak of substituted cyclohexene (1-methyl-4-(1-methylethyl)-cyclohexene). Toluene is detectable in TPO at low retention time. Monoaromatic hydrocarbons are detected in region 3 for both DF and TPO. They consist of mono-, di-, tri-, or tetra-substituted methyl- or ethylbenzenes. Prominent examples include 1,3-diemehtylbenzene, 1-ethyl-2-methylbenzene, mesitylene, 1-methyl-4-(1-methylethyl)-benzene as well as with linear and/or branched C_3- to C_8-alkylbenzenes

such as pentylbenzene. Similar substituents as in the aromatics are identified in region 4 for the various indenes (e.g., 1-methyl-1H-inden; 1,2,3-trimethylindene).

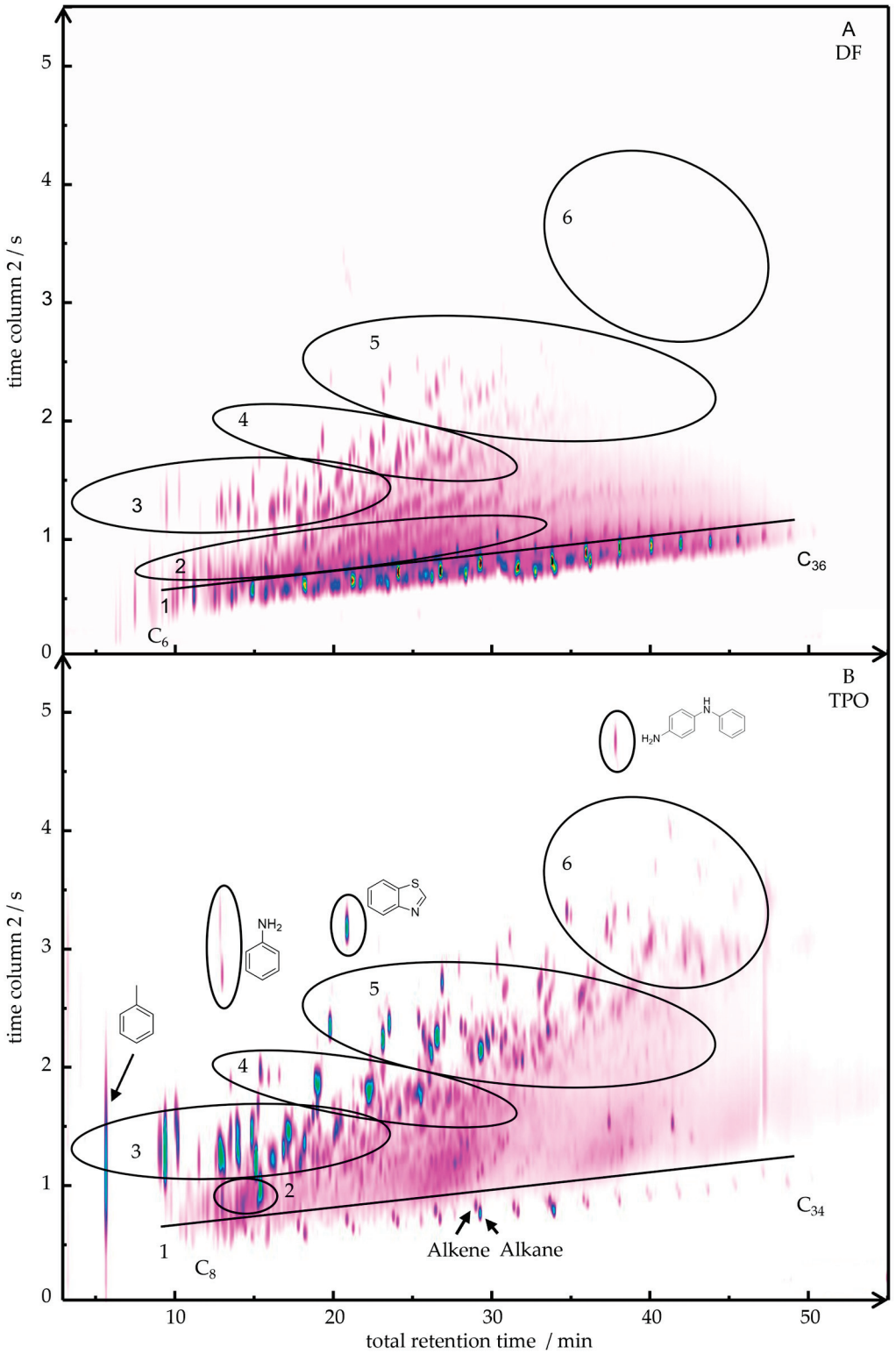

Figure 1. 2D-chromatograms of DF (**A**) and TPO (**B**) with marked areas of substance classes: 1 Alkanes and Alkenes; 2 Cyclic alkanes and alkenes, 3 Monoaromatics, 4 Indenes, 5 Diaromatics, 6 Polyaromatics.

Table 3. Intensity percentage in area% of the substance classes for DF and TPO.

Range	Substance Class	Intensity Percentage Area%	
		DF	TPO
1	Alkanes/Alkenes	74	8
2	Cycloalkanes	9	7
3	Aromatics	11	40
4	Indenes	4	12
5	Diaromatics	2	22
6	Polyaromatics	-	5
	Others *	≤1	6

* nitrogen-, oxygen-, and sulphur-containing compounds.

Naphthalenes substituted with mono-, di-, or trimethyl groups (e.g., 1-methylnaphthalene, 1,6-dimethylnaphthalene, 2,3,6-trimethylnaphthalene) and dihydronaphthalene (e.g., 1,2-dihydro-6-methylnaphthalene) can be seen in region 5. In addition, other diaromatic hydrocarbons including, e.g., biphenyl, fluorene, and chamazulene are detected in TPO. The most notable contrast in region 3 to 5 lies in the markedly higher peak intensity of the aromatic compounds in TPO. Polyaromatic hydrocarbons (PAHs) such as anthracene, pyrene, and retene, which are only present in TPO (5 area%), can be seen in range 6. Furthermore, TPO contains nitrogen-, oxygen-, and sulphur-containing compounds (6 area%) with the most intense occurrences of aniline, benzothiazole, and N-phenyl-1,4-benzenediamine, as illustrated in Figure 1.

The polar substances in the TPO were enriched by SPE and analyzed by GC/MS. Nitrogen-containing substances were detected, such as amines, with cyclic and linear hydrocarbons, and anilines, such as diphenyl diamines. Various oxygen-containing substances, such as phenol or stearic acid, palmitic acid, and myristic acid, could be detected in the TPO. The presence of heteroatoms can result from the additives used during tyre manufacturing. These include, for example, vulcanization agents (such as thiazoles, organic peroxides, nitro compounds), antioxidants (amines, phenols), plasticizers (aromatic esters), or processing aids (such as mineral oils and peptizers) [51]. In addition, during tyre usage, oxygen can diffuse into the material, initiating ageing processes such as oxidation. As a result, oxygen-containing compounds may form during pyrolysis [52].

In summary, significant differences in the chemical composition of TPO and DF were detected. DF showed a higher content and variability of linear and branched alkanes and cycloalkanes. TPO indicated linear alkanes and branched alkenes, and the corresponding content of monoaromatic and diaromatic compounds was much higher. Additionally, TPO showed PAHs and nitrogen-, oxygen- and sulphur-containing compounds, which were not detected in DF.

4.1.2. ^{1}H-NMR-Spetroscopy

Figure 2 presents the ^{1}H-NMR spectra of TPO and DF. The application of this technique facilitates the comparison of functional group distributions in complex liquid mixtures through the quantification of hydrogen environments. The majority of hydrogen atoms in DF and TPO are associated with aliphatic hydrocarbon chains with 91% for DF and 56% for TPO (0.5–3.3 ppm) [53–56]. These signals can be further separated and attributed to CH_3– (0.5–1 ppm), CH_2– (1–1.5 ppm) and CH–groups (1.5–2.0 ppm). Hydrogen in carbon chains adjacent to aromatic rings, like α-methyl carbons, appears between 2.0 ppm and 3.3 ppm and comprises 6% in DF and 21% in TPO [53,57]. A minor signal in TPO between 3.3 ppm and 4.5 ppm indicates a small amount (1%) of hydroxyl groups [54]. TPO also exhibits a signal (4.5 ppm and 6.5 ppm), representing hydrogen atoms bound to

unsaturated hydrocarbons or phenolic structures, with a relative intensity of 6% [54,57]. Hydrogen atoms directly attached to monoaromatic rings can be located in the range of 6.5–7.25 ppm, with 3% in DF and more prominently with 13% in TPO. Signals between 7.25 ppm and 9.0 ppm, corresponding to polyaromatic structures, are observed in TPO (3%), as described by Rodríguez et al. [58,59]. The results differ from the 2D-GC/MS analysis, which detected polyaromatic compounds for TPO and Diaromatics for DF.

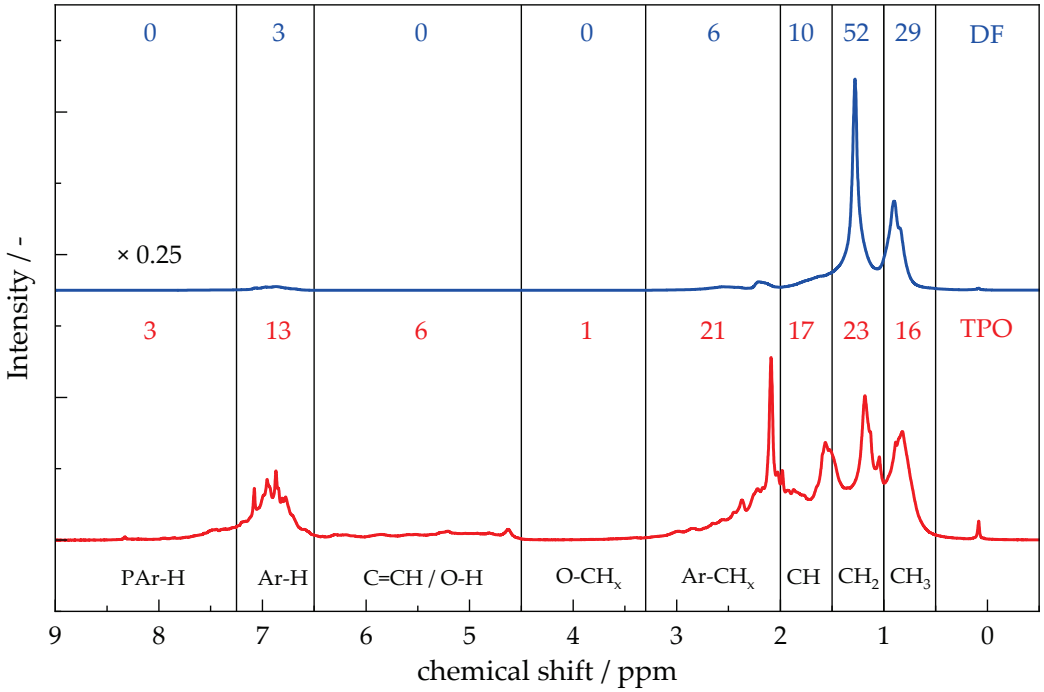

Figure 2. ^{1}H-NMR spectra of TPO an DF with the corresponding percent of hydrogen atoms in the defined areas. 0.5–1 ppm "CH_3 aliphatic"; 1–1.5 ppm "CH_2 aliphatic; 1.5–2 ppm, "CH aliphatic"; 2.0–3.3 ppm "aliphatic bonded to aromatic; 3.3–4.5 ppm "aliphatic bonded to oxygen"; 4.5–6.5 ppm "olefins and hydroxyl"; 6.5–7.25 ppm "monoaromatic"; 7.25–9 ppm "polyaromatic".

TPO exhibits a lower proportion of hydrogen in aliphatic carbon chains compared to DF, but a higher proportion of hydrogen atoms directly bound to aromatic rings. The proportion of carbon chains bound to an aromatic ring is also significantly higher in TPO. The presence of polyaromatic and unsaturated structures in TPO, which are absent in DF, highlights the considerable differences in molecular composition between the two substances. In summary, the results correspond to the 2D-GC/MS results.

4.1.3. ATR-FTIR-Spectroscopy

Figure 3 presents the ATR-FTIR spectra of TPO and DF. For both fluids the C-H valence vibrations of alkanes are observed between 3000 cm^{-1} and approx. 2700 cm^{-1}, and the corresponding deformation vibrations for CH_2 and CH_3 are at 1460 cm^{-1} and 1385 cm^{-1}, respectively [60,61]. A mixture of iso-alkanes can be assigned in TPO and DF at 1169 cm^{-1}, 1154 cm^{-1} and the in-plane bending at 960 cm^{-1} and 906 cm^{-1} [60–63]. DF shows n-alkanes with a band at 722 cm^{-1} [60–63]. TPO indicates a high intensity of tert-butyl groups with absorption bands at 1244 cm^{-1} and 1206 cm^{-1}, which are weakly expressed in DF [61,62]. A high intensity of cyclohexene in TPO can be characterized by a band at 890 cm^{-1} and aligns with the presence of 1-methyl-4-(1-methylethyl)-cyclohexene detected in 2D-GC/MS analysis. Aromatic compounds can be identified in TPO and DF with valence and deformation vibrations at 3020 cm^{-1} and 1605 cm^{-1} [60,61]. Mono-aromatics such as alkyl benzenes can be assigned to the bands at 700 cm^{-1} and 740 cm^{-1}.

Di- and tri-substituted aromatics can be assigned to 770 cm^{-1}, 806 cm^{-1}, and 815 cm^{-1} [63]. Di-aromatics can be identified by the intermediate bands at 780 cm^{-1}. The ring vibration of the aromatics in TPO can be associated with the two split bands at 1515 cm^{-1} and 1494 cm^{-1} [61,62]. The intensity of the aromatics bands, especially of di- and triaromatics, is considerably higher for TPO than for DF, indicating a higher concentration of the aromatic compounds, agreeing with the 2D-GC/MS and ^{1}H-NMR results. Alkenes are also detected in the TPO spectrum, as indicated by C–H stretching at 3095 cm^{-1} and C=C stretching at 1640 cm^{-1} [61,62], whereas these features are absent in DF. These suggest that there are considerably less unsaturated compounds in DF than in TPO. These results confirm the findings from the 2D-GC/MS chromatograms and ^{1}H-NMR-spectra. In addition, various oxygen-containing functional groups are evident in the TPO spectra. Carboxylic acids are indicated by a broad O-H band at 3395 cm^{-1} and a raised background down to 2800 cm^{-1}. The presence of carboxylic acids can be confirmed by the C-O region between 990 cm^{-1} and 1120 cm^{-1} and the characteristic C=O band (1710 cm^{-1}). However, these bands can also originate from other compounds like ethers, alcohols, carboxylic acids, carboxylate, and ketones [61,62,64]. In summary, the ATR-FTIR spectra clearly demonstrate that TPO contains significantly higher concentrations of aromatic and unsaturated compounds, as well as oxygenated species, which are largely absent in DF. These spectral differences underscore the distinct chemical compositions of the two substances.

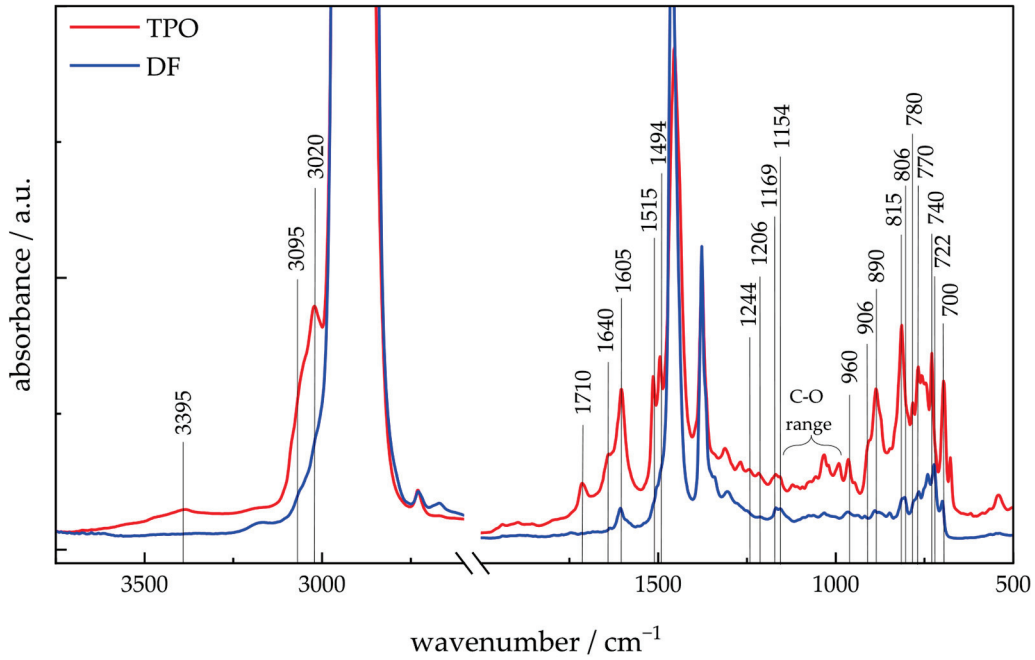

Figure 3. FTIR spectra of TPO and DF with indication of important bands.

4.1.4. Further Chemical Analysis

The total acid number (TAN) (see Table 4) corresponds to the amount of potassium hydroxide (KOH) required to neutralize the acids present in one gram of fuel. DF exhibits an acid number of 0 mg g^{-1}, indicating the absence of detectable acid compounds. With addition of TPO in DF, the TAN rises to 0.05 mg g^{-1} for DF99TPO1, 0.14 mg g^{-1} for DF95TPO5, 0.23 mg g^{-1} for DF90TPO10, and reaches a maximum of 2.08 mg g^{-1} for neat TPO. These findings corroborate the assumption derived especially from FTIR-spectroscopy, that acidic compounds are present in TPO. The iodine value serves as an indicator of the concentration of unsaturated compounds in olefines in a sample. The iodine value is calculated in accordance with DIN EN ISO 3961. The results show that the highest

iodine value of 93 g 100 g^{-1} is observed for neat TPO, indicating a significant presence of unsaturated hydrocarbons. DF contains only a minimal fraction of unsaturated compounds, with an iodine value of 2.9 g 100 g^{-1}. This value increases slightly with the addition of TPO: 3.1 g 100 g^{-1} for DF99TPO1, 3.7 g 100 g^{-1} for DF95TPO5, and 14 g 100 g^{-1} for DF90TPO10. These findings are consistent with the results obtained from ^{1}H-NMR and FTIR-spectroscopy, confirming the presence of olefinic compounds in TPO. The aromatic content of TPO was quantified using High-Performance Liquid Chromatography (HPLC), according to DIN EN 12916. For this analysis, blends of DF and TPO were prepared. Based on linear regression (R^2 = 0.9989) of the data presented for DF, DF99TPO1, DF95TPO5, and DF90TPO10 in Table 4, the total aromatic content of TPO was determined to be ~60 vol%. This result corroborates the findings of the current analyses and agrees with previously published studies reporting a high aromatic content in TPO [7,16,17,65,66].

Table 4. Total acid number, iodine value, and aromatic content of DF, DF99TPO1, DF95TPO5, DF90TPO10, and TPO.

Characteristic	Units	DF	DF99TPO1	DF95TPO5	DF90TPO10	TPO
Total acid number	mg g^{-1}	0	0.05	0.14	0.23	2.08
Iodine value	g 100 g^{-1}	2.9	3.1	3.7	14	93
Aromatic content	wt%	24.1	24.4	26.0	27.7	~60 *

* with linear extrapolation (R^2 = 0.9989) of the data of DF and DF-TPO blends.

In summary, the chemical composition of TPO differs from that of DF. TPO has a significantly higher proportion of aromatic and polyaromatic hydrocarbons. In addition, olefinic compounds as well as oxygen- and nitrogen-containing compounds, were identified in TPO compared to DF.

4.2. Characteristics of TPO and DF-TPO-Blends

To assess the suitability of TPO as a blend component in DF, the key values according to DIN EN 590-2022 for DF, TPO, and the blends are determined. The results of the analysis and the corresponding specific target ranges are summarized in Table 5. With a distillation start at 36 °C, TPO shows a remarkably low initial boiling temperature for fuels fractions. This is plausible, as the pyrolysis process can result in molecules with low boiling points and vapour pressure. In comparison, usually DF has a distillation range from 150 °C to 390 °C, with the DF used in this study showing a distillation start at 171 C.

On this basis, TPO is expected to also have a low flash point. The addition of 10 vol% TPO to DF results in a linear drop of the flash point to 53.1 °C below the specified limit of 55 C. As the TPO content increases, the start of distillation shifts to lower temperatures, reaching 157 °C at 10 vol% TPO. However, over the course of distillation, a divergence in temperature progression becomes apparent. 50 vol% distillate volume is reached at 273 °C for DF and at 275 °C for DF90TPO10. This trend, which other authors have also described, is that DF-TPO blends require a higher temperature than neat DF to distil the same volume percent, and this trend persists until the end of the distillation [67]. The end of the distillation is recorded at 390 °C at a distillate volume of 92 vol% for TPO exceeding the result for DF at 358 °C. This indicates that TPO contains higher-boiling components, compared to DF. DF-TPO blends adhere to the target values for DF at 90 vol% and at 95 vol%.

Table 5. Characteristics of DF, DF99TPO1, DF95TPO5, DF90TPO10, and TPO according to DIN EN 590-2022.

Characteristic	Unit	Target	DF	DF99TPO1	DF95TPO5	DF90TPO10	TPO
Density	kg m^{-3}	822.0–845.0	833.3	834.2	838.1	843.1	917.1
Viscosity	mm^2 s^{-1}	2.000–4.500	2.840	2.836	2.830	2.826	1.985
Polyaromatic content	wt%	≤8.0	2.9	3.0	3.8	4.7	21.8 *
Flash point	°C	>55	65.5	64.0	58.0	53.1	-
HFRR [1]-Test	µm	≤460	420.5	359.5	222.5	209.5	175.5
CFPP [2]	°C	≤−20	−25	−25	−13	−14	-
Cu corrosion	extent	1	1a	1a	1a	1a	1a
Oxidation stability	min	≥60	85	196	183	93	22
Water content	mg kg^{-1}	≤200	37	30	60	40	2054
Coke residue	wt%	≤0.30	0.02	0.14	0.75	1.39	2.53
Ash	wt%	≤0.010	<0.001	0.001	0.001	0.001	-
Sulphur content	mg kg^{-1}	≤10.0	7.3	134	648	1292	11,600 (1.16%)
Distillation curve							
Start	vol%		171.3	177.9	165.3	157.0	36.0
10% *v*/*v*			210.7	208.0	203.8	200.4	124.0
50% *v*/*v*			273.2	275.1	274.3	274.8	226.0
90% *v*/*v*		≤360	334.5	336.2	338.1	342.2	387.0
95% *v*/*v*		≤360	349.4	349.9	353.1	358.8	-
End			358.6	356.9	357.9	363.4	390.1

[1] HFRR (high frequency reciprocating rig); [2] CFPP (cold filter plugging point), * with linear Extrapolation (R^2 = 0.9989) of the data of DF and DF-TPO blends.

A solid, slightly porous residue remains in the distillation flask, which is also reflected in the carbon residue measurements. At 2.53 wt%, TPO has a higher value of coke residues compared with 0.02 wt% in DF, a consequence attributed to the polyaromatic content of 21.8 wt% in TPO. Whereas DF show a significantly lower content of 2.9 wt%, the blends show a linear increase to 4.7 wt% at 10 vol% TPO. The CFPP, which evaluates fuel filterability at low temperatures weather conditions, is also affected by the polyaromatic content. At low temperatures, polyaromatics tend to precipitate, causing an increase in the CFPP with higher TPO content. The density and viscosity of the fuels are strongly affected by their aromatic and polyaromatic composition. Since polyaromatic compounds possess higher densities than aliphatic species, an increased aromatic content results in a higher overall fuel density. TPO, characterized by a higher polyaromatic fraction, therefore exhibits a higher density and a lower viscosity compared to DF. Upon blending TPO with DF, the density of the blends increases proportionally with the TPO content, following an approximately linear correlation with TPO content. Overall, these results reveal the interdependence of characteristic values on the aromatic content. An increase in the polyaromatic content might not only affect the emission of hazardous substances and particles, posing challenges for modern engine and exhaust technologies, but also promote the formation of residues due to agglomeration during thermal processing [68,69].

Oxidation stability was evaluated by measuring the time required for the consumption of 1 bar of hydrogen after applying an initial pressure of 10 bar H_2 to the fuel sample. Hydrogen reacts with unsaturated compounds present in the fuel, and the rate of consumption is proportional to their concentration. Thus, the higher the content of unsaturated compounds, the faster the pressure drops by 1 bar [70]. Due to the elevated concentration of unsaturated compounds formed during the pyrolysis process, TPO exhibits a low oxidation stability of 22 min, which is considerably lower than that of DF and the DF-TPO blends. The water content in TPO was determined to be 2053 mg kg^{-1}, which significantly exceeds

the values measured in DF and the DF-TPO blends. This elevated level is likely influenced by the presence of unsaturated compounds and free alkalis in TPO, which may interfere with standard water quantification methods [71].

According to current EU regulations, DF may contain no more than 10 ppm sulphur to limit the formation of sulphur oxides and sulfuric acid, which contribute to environmental pollution, catalyst degradation, and engine corrosion [72]. No visible corrosion was observed in the copper strip test for any fuel blend. The DF used in this study complied with specifications at 7.3 mg kg^{-1} sulphur. In contrast, TPO contained 1.16 wt% sulphur, far exceeding regulatory limits. Consequently, sulphur levels in DF–TPO blends increase linearly with TPO content. The high sulphur content in TPO is attributed to vulcanized rubber in tyres, which contains sulphur-based compounds [73,74]. Fuel lubricity was assessed using the High-Frequency Reciprocating Rig (HFRR), where lower wear scar diameters indicate better lubrication. DF and its blends showed relatively high wear values, while TPO exhibited superior lubricity, likely due to its elevated sulphur content, as sulphur compounds enhance lubricating properties.

In summary, the applicability of TPO and its blends with DF according to DIN EN 590 can be considered limited. The addition of 5 vol% TPO to DF results in parameters such as sulphur content, carbon residue, and CFPP exceeding the specified limits. At 10 vol% TPO, the flash point also falls outside the acceptable range, while oxidation stability and density approach the threshold values. Due to the significant changes observed with increasing TPO content, the quality of the base DF is of particular importance and should be determined in advance to assess the feasible blending ratio of TPO. Several parameters exhibit mathematical dependencies, allowing for the determination of the precise dosage that can be applied.

4.3. Swelling Behaviour of NBR and Its Influence on Mechanical Properties

4.3.1. Mass and Volume Change in NBR After the Sorption

Figure 4 presents the relative mass and volume changes in NBR18 (Figure 4A,D), NBR28 (Figure 4B,E), and NBR39 (Figure 4C,F), along with the corresponding sorption curves based on Equation (4), following storage in DF, TPO, and various DF-TPO blends. The mass changes are plotted as a function of the square root of time. The equilibrium mass uptake and the diffusion coefficients derived from these experiments are summarized in Table 6. For NBR39, equilibrium was not reached in DF or the DF-TPO blends within the experimental timeframe. As a result, no sorption curves and diffusion coefficient according to Equation (4) were calculated for these. All calculated sorption curves show an initial linear increase, fulfilling the requirement for applying Fick's second diffusion law. The equilibrium mass uptake is lowest for DF across all elastomers, with values of 26 wt% for NBR18, 14 wt% for NBR28, and 6 wt% for NBR39. In contrast, TPO exposure results in the highest mass uptakes: 153 wt% (NBR18), 106 wt% (NBR28), and 74 wt% (NBR39), respectively. Identical trends can be observed for the relative volume changes in the NBR samples compared to the relative mass changes. With a volume increase of 199 vol% due to TPO, NBR18 exhibits an almost threefold expansion of the sample. NBR28 and NBR39 also exhibit a significant increase in volume with 134 vol% and 91 vol%, respectively, which underlines the pronounced influence of TPO on material behaviour.

To investigate the relationship between mass and volume of the NBR sample stored in TPO-DF blends, the relative mass change was plotted as a function of the relative volume change (see Figure 5). The data for pure TPO were excluded from the analysis, as their values are significantly higher than those of the blends, which would obscure a clear representation of the results. For NBR18, the blends exhibit a linear correlation between mass and volume changes. In contrast, NBR28 (for DF) and NBR39 (for DF and the blends)

show a delayed volume expansion at the beginning of sorption, which is evident from the stage observed in the mass–volume relationship. With increasing TPO content, this delayed expansion diminishes. This behaviour can be attributed to the initially small mass uptake, during which the free volume of the NBR is filled before the material begins to swell. The addition of TPO leads to a more pronounced mass increase, thereby reducing this effect.

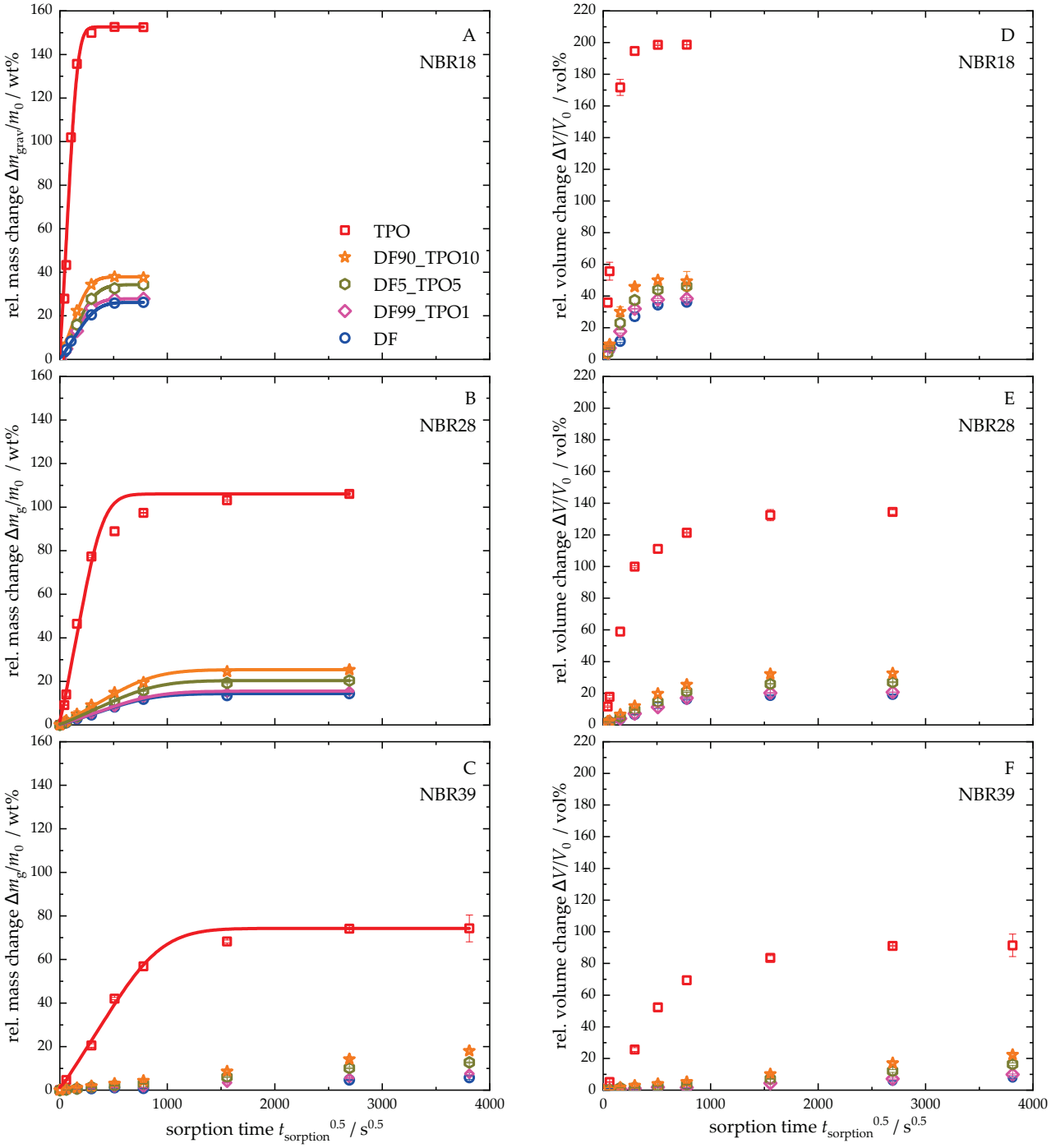

Figure 4. Relative mass and volume changes in NBR18 (**A**,**D**), NBR28 (**B**,**E**), and NBR39 (**C**,**F**) in DF, TPO and the mixtures with the ratios DF99TPO1, DF95TPO5, and DF90TPO10. The continuous lines show the calculated fit according to Equation (4). For NBR39 (**C**), the sorption curve could only be calculated for TPO, as these were in mass equilibrium.

Table 6. Determined diffusion coefficients D and the relative equilibrium mass increases m_∞ of NBR18, NBR28, and NBR39 after storage in DF, TPO, and the mixtures.

Fuel	NBR18		NBR28		NBR39	
	m_∞ wt%	$D \times 10^{-6}$ mm^2 s^{-1}	m_∞ wt%	$D \times 10^{-6}$ mm^2 s^{-1}	m_∞ wt%	$D \times 10^{-6}$ mm^2 s^{-1}
DF	26	1.6	14	0.21	-	-
DF99TPO1	28	1.8	16	0.23	-	-
DF95TPO5	34	2.8	20	0.23	-	-
DF90TPO10	38	4.3	25	0.24	-	-
TPO	153	11.8	106	1.2	74	0.21

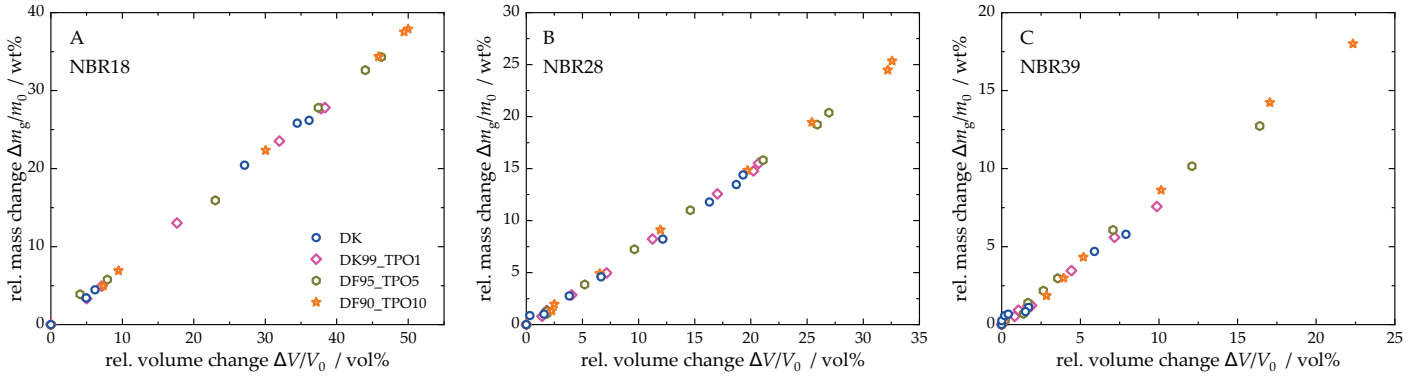

Figure 5. Relative mass change versus relative volume change in NBR18 (**A**), NBR28 (**B**), and NBR39 (**C**) for DF and TPO-DF blends.

The diffusion coefficients follow the same trend as the equilibrium mass uptakes. For DF, the values are 1.6 × 10^{-6} mm^2 s^{-1} (NBR18) and 0.21 × 10^{-6} mm^2 s^{-1} (NBR28). For TPO results the diffusion coefficients of 11.8 × 10^{-6} mm^2 s^{-1} (NBR18), 1.2 × 10^{-6} mm^2 s^{-1} (NBR28), and 0.21 × 10^{-6} mm^2 s^{-1} (NBR39). For the DF-TPO blends, the equilibrium mass uptake and the diffusion coefficients for the elastomers increase with rising TPO content. This relationship is clearly visible when plotting the equilibrium mass uptake and the mean diffusion coefficients against the TPO volume fraction in DF, as shown in Figure 6, where a linear correlation is observed.

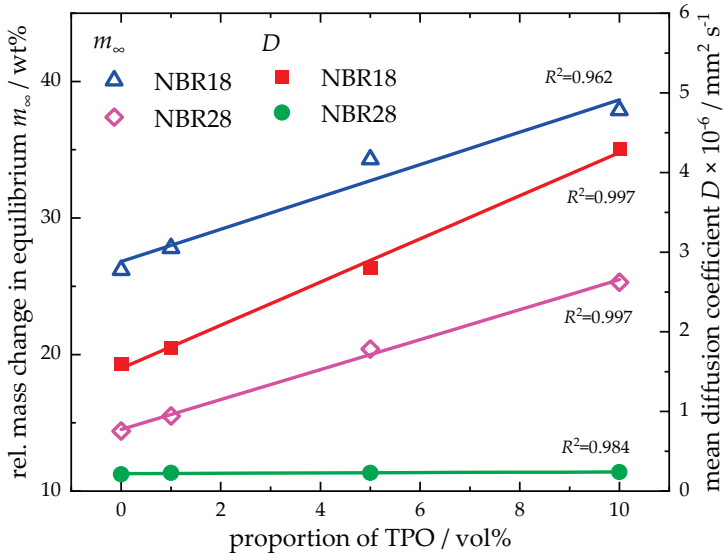

Figure 6. Relative equilibrium mass change and determined diffusion coefficients as a function of the volume fraction of TPO in DF. Linear fits with coefficient of determination (R^2) are also given.

The unusually high mass uptake observed for TPO can be attributed to its elevated aromatic content [25,75]. In addition to dispersion interactions, aromatic compounds in TPO also undergo π–π interactions with the acrylonitrile groups of the polymer matrix, which favours the sorption of these molecular classes [26]. Due to its higher acrylonitrile content, NBR39 exhibits stronger intramolecular interactions within the polymer chains, resulting in reduced free volume in the matrix. Consequently, NBR39 absorbs less fuel compared to NBR18 and NBR28. However, its greater affinity for the aromatic and polar compounds present in TPO results in a steeper initial slope in the sorption curves for NBR39, which means that equilibrium is reached faster when comparing TPO with DF. Additionally, low-molecular-weight aromatic compounds exhibit planar structures and less steric hindrance, which facilitates their diffusion into the polymer matrix more readily than larger, branched aliphatic molecules [25]. Since TPO contains polar compounds such as acids, enhanced swelling is expected due to the behaviour observed for fatty acid esters and alcohols in biodiesel [76–78]. These interactions reduce the intermolecular forces between the polymer chains, thereby increasing the matrix's free volume and enlarging the effective surface area in contact with the liquid medium [79]. Consequently, the material's surface tension can be affected, which reduces the resistance to sorption and facilitates further diffusion of TPO into the elastomeric network.

In summary, the pronounced and rapid diffusion of TPO into NBR, regardless of its high acrylonitrile content, typically selected for resistance to non-polar fuels, indicates that its use as a fuel in neat form is not recommended. However, depending on the blend ratio and the specific NBR formulation, the DF-TPO blends show mass uptakes and diffusion coefficients comparable to neat DF, suggesting that application in the form of blends appears possible.

4.3.2. Temperature Dependence of the Diffusion Process of DF and TPO

In Figure 7, the sorption curves of neat TPO and DF at 20 °C, 50 °C, and 80 °C are plotted against the square root of time. For NBR18, the equilibrium mass uptake increases with temperature in DF, while it remains nearly constant for TPO. The diffusion coefficients, calculated using Equation (4), show a temperature-dependent increase for both fluids. In the case of DF, the diffusion coefficient rises by a factor of approximately 21 from 0.73×10^{-6} mm^2 s^{-1} at 20 °C to 15.3×10^{-6} mm^2 s^{-1} at 80 °C. For TPO, the diffusion coefficient increases by a factor of about six, from 3.43×10^{-6} mm^2 s^{-1} to 21.8×10^{-6} mm^2 s^{-1}. The results are summarized in Table 7. It is well established that the diffusion of liquid media into elastomers increases with temperature. In a study by Blivernitz [26], the temperature dependence of model substances in NBR with 18 wt% acrylonitrile revealed that the equilibrium mass uptake of aliphatic compounds increases significantly with temperature, whereas aromatic compounds show either no change or only a slight increase. Consequently, the higher aliphatic content in DF results in a more pronounced temperature dependence. For DF-TPO blends, this implies that increasing the TPO content, thus raising the aromatic proportion, leads to a reduced temperature dependence of sorption behaviour.

The temperature-dependent diffusion coefficients can be used to determine the activation energy for diffusion according to Arrhenius (Equation (7)) [80]. In the Arrhenius plot (see Figure 8) the slopes (E_A/R) of the linear regressions result in activation energies of 48 kJ mol^{-1} for DF and 29 kJ mol^{-1} for TPO.

$$D = D_0 \exp\left(-\frac{E_A}{RT}\right) \rightarrow \ln(D) = \ln(D_0) - \frac{E_A}{R}\,\frac{1}{T} \tag{7}$$

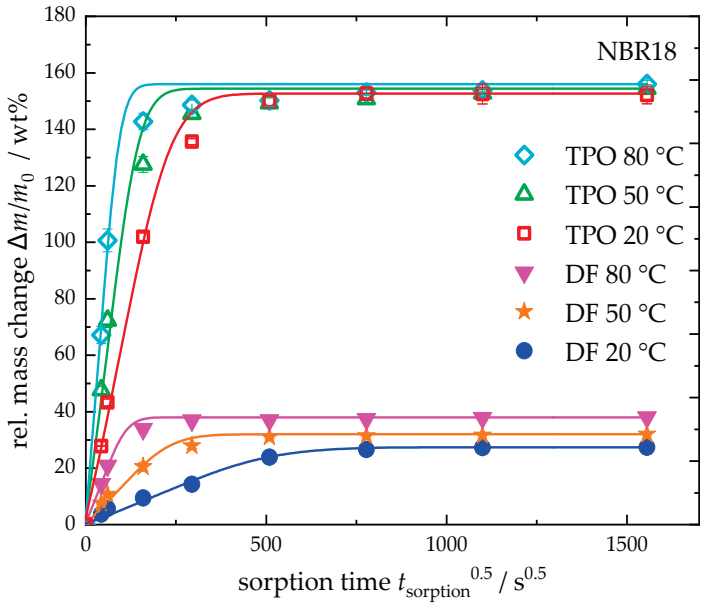

Figure 7. Relative mass change and sorption curves (Equation (4)) of NBR18 in neat DF and TPO at 20 °C, 50 °C and 80 °C.

Table 7. Mass change at equilibrium and determined diffusion coefficients of NBR18 in DF and TPO at 20 °C, 50 °C and 80 °C.

Sorption Temperature °C	DF		TPO	
	m_∞	$D \times 10^{-6}$	m_∞	$D \times 10^{-6}$
	wt%	mm^2 s^{-1}	wt%	mm^2 s^{-1}
20	27	0.73	153	3.43
50	32	3.36	154	8.83
80	38	15.3	156	21.8

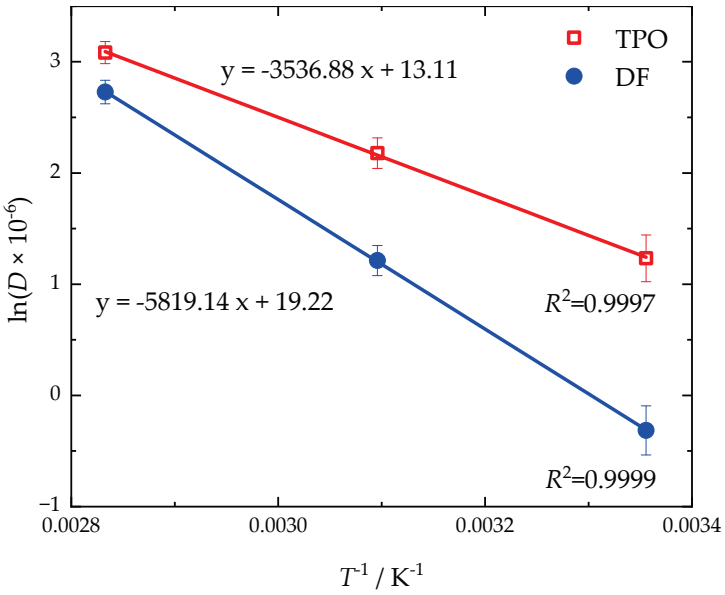

Figure 8. Arrhenius plot for the sorption of neat DF and TPO in NBR18. The coefficients of determination (R^2) for the linear regression are also given.

These results confirm the assumption that DF's diffusion rate is more temperature-dependent than TPO. However, no statement can be made about the equilibrium absorption. It can be assumed that the diffusion properties of blends of TPO and DF are less dependent on temperature than neat DF. Applications of blends at elevated temperatures should therefore not show any deterioration of swelling behaviour with NBR.

In summary, a rise in temperature results in a faster rate of mass increase and higher total mass uptake. This observation is more evident in DF, demonstrating its stronger temperature dependence relative to TPO.

4.3.3. Change in the Mechanical and Physical Properties of the NBR

Figure 9 illustrates the density and Shore A hardness of NBR18 (Figure 9A,D), NBR28 (Figure 9B,E), and NBR39 (Figure 9C,F) as a function of the square root of time. Both parameters decrease with increasing sorption time. The trend in density and hardness for NBR results from the mass uptake of TPO, as shown in Figure 4. During diffusion, both DF and TPO reduce the density of NBR, since the pristine material (ρ_{NBR18} = 1.19 g cm^{-3}; ρ_{NBR28} = 1.21 g cm^{-3}; ρ_{NBR39} = 1.23 g cm^{-3}) has a higher density than TPO, ρ_{TPO} = 0.917 g cm^{-3}, and DF, ρ_{DF} = 0.833 g cm^{-3}. The decrease in hardness is attributable to the plasticizing effect of the absorbed fluids, which are stored between the polymer chains, weakening intermolecular interactions and thereby reducing the counterforce of the material. Blends containing up to 10 vol% TPO exhibit slightly lower density and hardness values compared to neat DF, indicating a measurable influence of TPO. As the acrylonitrile content increases, the reduction in equilibrium density and hardness upon exposure to DF, TPO, and their blends becomes less pronounced, following the order: NBR18 > NBR28 > NBR39. Figure 10 shows the equilibrium density and hardness values plotted against the TPO volume fraction in DF. The results indicate that, with increasing acrylonitrile content, the influence of the material to changes in density and hardness due to TPO in DF becomes more pronounced. The initial increase in density and hardness observed for NBR39 in Figure 9 is attributed to the slower diffusion of DF and the blends. In this case, the free volume within the polymer is filled before swelling occurs, which temporarily restricts chain mobility and leads to an increase in the mechanical counterforce of the material. Furthermore, it is observed that NBR28 and NBR39 reach equilibrium in hardness after approximately three days, which is earlier than the mass uptake shown in Figure 4. This discrepancy is explained by the fact that hardness measurements primarily reflect changes at the surface, where the medium penetrates first, while full diffusion into the sample core occurs later in accordance with Fick's second law of diffusion.

Figure 11 presents the development of tensile strength at break (Figure 11A–C) and elongation at break (Figure 11D–F) for NBR18 (Figure 11A,D), NBR28 (Figure 11B,E), and NBR39 (Figure 11C,F) as a function of the square root of time. For all elastomers, a decrease in both mechanical parameters is observed with increasing sorption time. The influence of TPO on the sorption behaviour is particularly pronounced, as its higher and more rapid mass uptake accelerates and intensifies the decrease in tensile strength and elongation at break compared to DF. NBR18 in TPO exhibits the strongest decline in mechanical properties, with tensile strength decreasing from 13.5 MPa to 4 MPa and elongation at break from 413% to 137%. In contrast, storage in DF and the blends results in significantly lower reductions. As the acrylonitrile content increases, the extent of mechanical characteristics decreases. NBR28 shows a decline from 15.4 MPa and 345% to 6 MPa and 161% while NBR39 decreases from 15.9 MPa and 390% to 8 MPa and 210% over three months ($t^{0.5}$ = 2016 s$^{0.5}$). For NBR28, a smaller reduction is observed, though the measurement scatter increases. In NBR39, a more pronounced reduction in tensile strength is evident even with 5 vol% and 10 vol% TPO in DF, with values decreasing to 15.3 MPa

(DF) and 12.6 MPa (DF90TPO10). After six months of storage ($t^{0.5}$ = 3810 $s^{0.5}$), elongation at break for DF and its blends shows significant variation, ranging from 320% to 350%. The observed decrease in mechanical properties is directly related to the uptake of the liquid media. As previously described, sorption weakens the intermolecular interactions within the elastomer, facilitating chain mobility and thereby reducing strength under mechanical stress. The higher the mass uptake, the more severe the deterioration of mechanical integrity [81]. The particularly strong decrease caused by TPO can be predominantly attributed to its high aromatic content. This is explained by the specific interaction of aromatic compounds with the polar nitrile groups in the polymer, which disrupts the internal structure of the material.

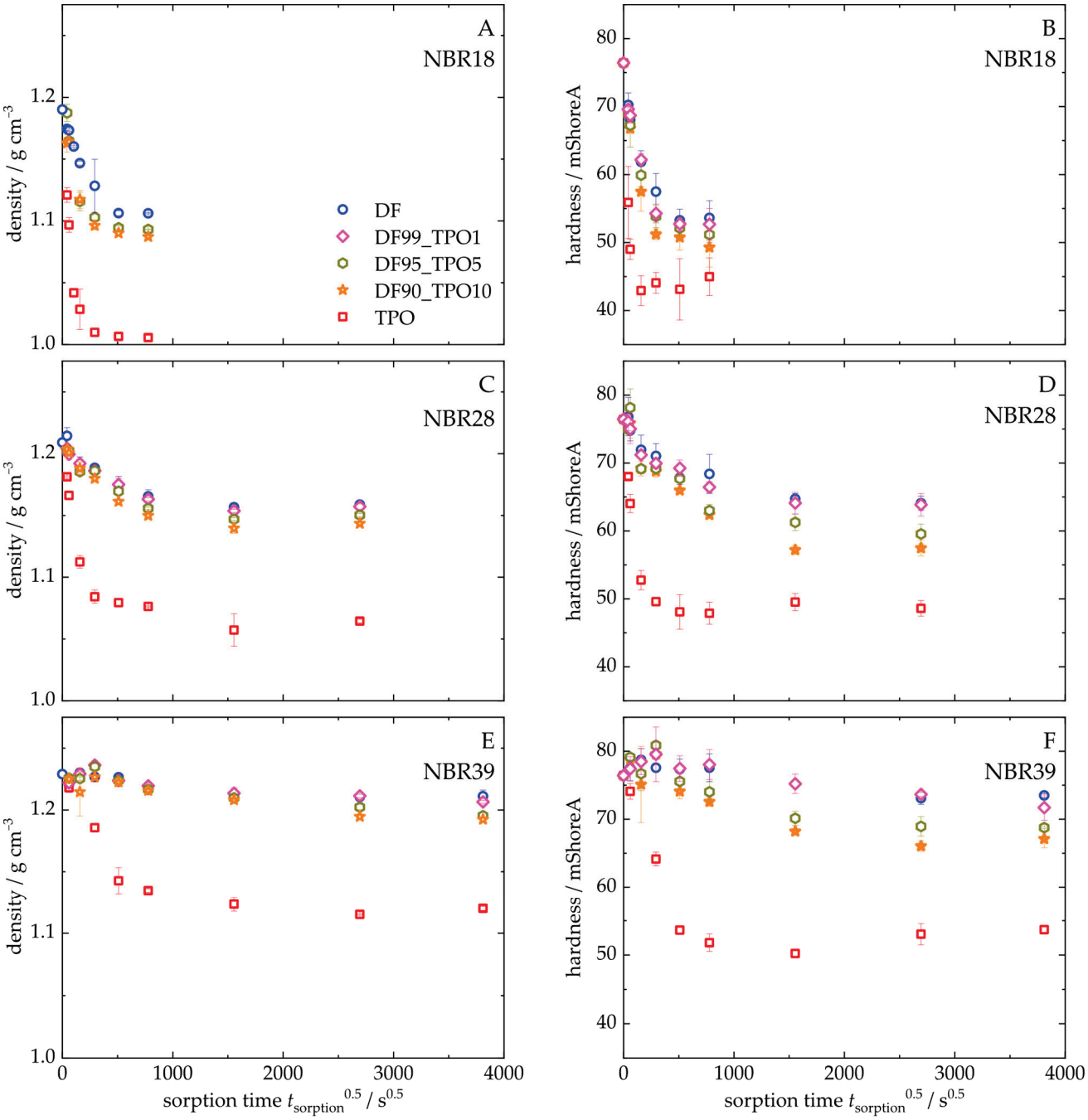

Figure 9. Density (**A**–**C**) and hardness (**D**–**F**) over sorption time of NBR18 (**A**,**D**), NBR28 (**B**,**E**), and NBR39 (**C**,**F**) after storage in DF, TPO, and the DF-TPO mixtures.

In summary, none of the examined NBR types is suitable for long-term contact with neat TPO due to the pronounced loss in mechanical performance. However, blends with low TPO content show a decrease in mechanical characteristics comparable to neat DF, suggesting their potential suitability for application as a fuel.

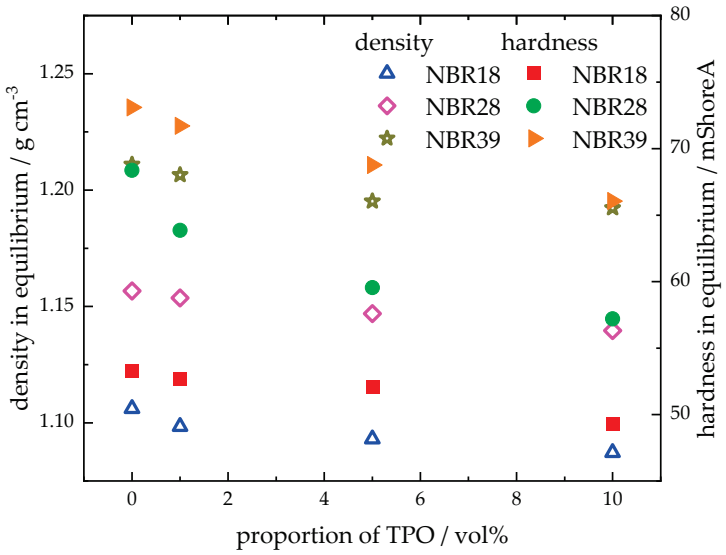

Figure 10. Density and hardness in equilibrium as a function of the volume fraction of TPO in DF.

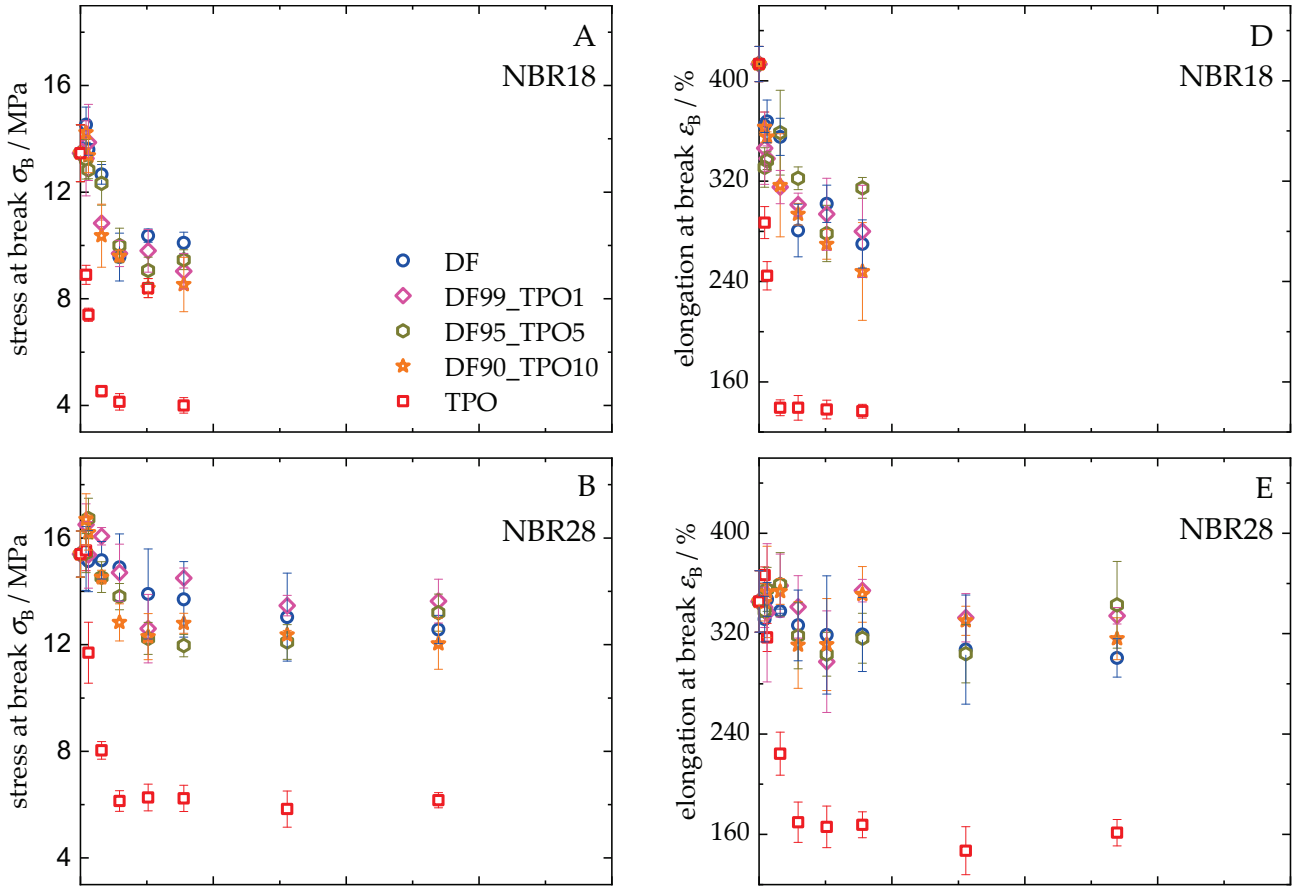

Figure 11. *Cont.*

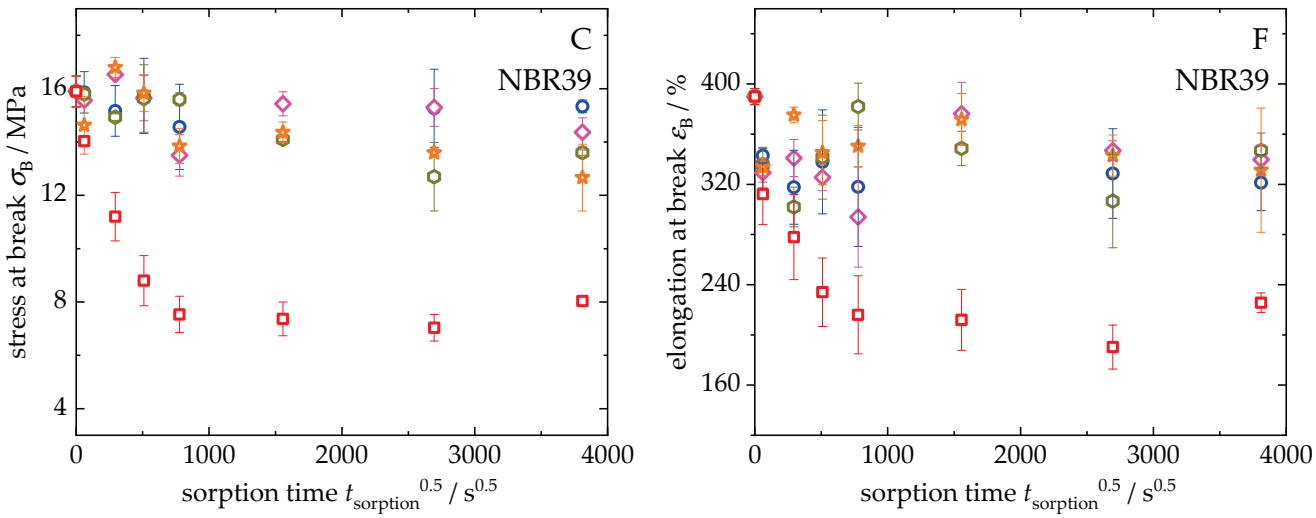

Figure 11. Stress (**A**–**C**) and elongation at break (**D**–**F**) over sorption time of NBR18 (**A**,**D**), NBR28 (**B**,**E**), and NBR39 (**C**,**F**) after storage in DF, TPO, and DF-TPO blends.

5. Conclusions

In this study, tyre pyrolysis oil (TPO) was analyzed, and the characteristic properties of its blends with diesel fuel (DF) were determined. The sorption behaviour of these blends and the resulting changes in the mechanical properties of nitrile-butadiene rubber (NBR) were investigated. The objective of the study was to understand the TPO diffusion behaviour in elastomeric materials and to evaluate the feasibility of TPO as a fuel component.

Through detailed analysis using 2D-GC/MS, complementary analytical techniques such as infrared and NMR spectroscopy become more informative, allowing for the acquisition of more precise data. This combination of analytical methods enables a comprehensive and detailed understanding of the chemical composition. Chemical analysis revealed several notable differences between the composition of TPO and DF. Compared to DF, TPO contains the following:

- Higher monoaromatic and polyaromatic contents. This property makes TPO a potential blending component for aromatic-free synthetic fuels.
- Higher sulphur content. Desulfurization is required to reduce the sulphur concentration to within the target range. Alternatively, due to its high sulphur content and correspondingly low value in the high frequency reciprocating rig test, TPO could be considered as a blend component for lubricating oils.
- Higher proportions of olefinic compounds. Hydrogenation is necessary to saturate olefins and improve oxidation stability, thereby expanding the possible applications of both neat TPO and its blends with other fuels and oils.
- Larger amounts of low- and high-boiling components. Distillation of TPO to separate these fractions could produce a cut similar to DF, potentially lowering the polyaromatic content, as these are typically found in the high-boiling fraction, and raising the flash point by removing low-boiling compounds.

Without further chemical processing, the use of TPO in its raw form may present challenges. When blended at 1 vol% and 5 vol% with DF, most characteristic parameters remain within the target ranges specified by DIN EN 590, with the exception of sulphur content. However, under specific circumstances, such as emergencies or fuel shortages, use could be permitted according to StVZO § 70(4).

TPO exhibits strong affinity towards NBR, leading to rapid and substantial mass uptake and increasing volume during sorption. This pronounced swelling significantly

reduces mechanical stability properties such as hardness, tensile strength, and elongation at break, thereby permanently affecting the viscoelastic behaviour of the elastomer. With increasing nitrile content, TPO uptake decreases, but equilibrium mass uptake is reached markedly faster for TPO than for DF. Increasing TPO content in DF results in proportionally higher absorption and diffusion coefficients, with a linear relationship observed between these parameters and the TPO volume fraction. Blends containing 1 vol% and 5 vol% TPO show no critical deviations in mass uptake, volume expansion, or mechanical properties compared to neat DF.

Further research is required to elucidate the interactions between individual TPO components and NBR. Analytical methods could be used to monitor the sorption of individual compounds, as unsaturated components or acids in TPO may react chemically with NBR, potentially altering its molecular structure and thus permanently impairing its mechanical performance.

Author Contributions: Conceptualization, S.S.; methodology, S.S.; validation, S.S.; writing—original draft preparation, S.S.; writing—review and editing, T.F. and S.E.; visualization, S.S.; supervision, S.S.; funding acquisition, T.F. and S.E. All authors have read and agreed to the published version of the manuscript.

Funding: We acknowledge financial support by Universität der Bundeswehr München.

Institutional Review Board Statement: Not applicable.

Data Availability Statement: The original contributions presented in this study are included in the article. Further inquiries can be directed to the corresponding author(s).

Acknowledgments: The authors want to thank Kathrin Hufschmid for her experimental support. The authors would also like to thank Pyrum Innovations AG for providing the tyre pyrolysis oil.

Conflicts of Interest: The authors declare no conflicts of interest.

Abbreviations

The following abbreviations are used in this manuscript:

DF	Disel fuel
TPO	Tyre pyrolysis oil
NBR	Nitrile-butadiene rubber
NR	natural rubber
SBR	Styrene-butadiene rubber
BR	Butadiene rubber
phr	Parts-per-hundred rubber
DPHP	Di(2-propylheptyl)phthalate
6-PPD	N-(4-Methylpentan-2-yl)-N-phenylbenzene-1,4-diamine
TAN	Total acid number
HFRR	High frequency reciprocating rig
CFPP	cold filter plugging point
2D-GC/MS	Two-dimensional gas chromatography coupled to mass spectrometry
SPE	Solid phase extraction
GC/MS	Gas chromatography coupled to mass spectrometry
^{1}H-NMR	1H-Nuclear magnetic resonance
FTIR	Fourier transform infrared
HPLC	High-Performance Liquid Chromatography
PAHs	Polyaromatic hydrocarbons
KOH	Potassium hydroxide

References

1. Continental Reifen Deutschland GmbH. Reifengrundlagen. Available online: https://www.continental-reifen.de/tire-knowledge/tire-mixture/ (accessed on 19 August 2025).
2. Conesa, J.A.; Martín-Gullón, I.; Font, R.; Jauhiainen, J. Complete Study of the Pyrolysis and Gasification of Scrap Tires in a Pilot Plant Reactor. *Environ. Sci. Technol.* **2004**, *38*, 3189–3194. [CrossRef] [PubMed]
3. Roy, C.; Chaala, A.; Darmstadt, H. The Vacuum Pyrolysis of Used Tires End-Uses for Oil and Carbon Black Products. *J. Anal. Appl. Pyrolysis* **1999**, *51*, 201–221. [CrossRef]
4. Dai, X.; Yin, X.; Wu, C.; Zhang, W.; Chen, Y. Pyrolysis of Waste Tires in a Circulating Fluidized-Bed Reactor. *Energy* **2001**, *26*, 385–399. [CrossRef]
5. Uçar, S.; Karagöz, S.; Yanik, J.; Saglam, M.; Yuksel, M. Copyrolysis of Scrap Tires with Waste Lubricant Oil. *Fuel Process. Technol.* **2005**, *87*, 53–58. [CrossRef]
6. González, J.F.; Encinar, J.M.; Canito, J.L.; Rodríguez, J.J. Pyrolysis of Automobile Tyre Waste. Influence of Operating Variables and Kinetics Study. *J. Anal. Appl. Pyrolysis* **2001**, *58–59*, 667–683. [CrossRef]
7. De, I.; Rodriguez, M.; Laresgoiti, M.F.; Cabrero, M.A.; Torres, A.; Chomon, M.J.; Caballeró, B. Pyrolysis of Scrap Tyres. *Fuel Process. Technol.* **2001**, *72*, 9–22. [CrossRef]
8. Williams, P.T. Pyrolysis of Waste Tyres: A Review. *Waste Manag.* **2013**, *33*, 1714–1728. [CrossRef]
9. Okoye, C.O.; Jones, I.; Zhu, M.; Zhang, Z.; Zhang, D. Manufacturing of Carbon Black from Spent Tyre Pyrolysis Oil–A Literature Review. *J. Clean. Prod.* **2021**, *279*, 123336. [CrossRef]
10. Groves, S.A.; Lehrle, R.S.; Blazso, M.; Szckely, T. Natural Rubber Pyrolysis: Study of Temperature and Thickness-Dependence Indicates Dimer Formation Mechanism. *J. Anal. Appl. Pyrolysis* **1991**, *19*, 301–309. [CrossRef]
11. Chen, F.; Qian, J. Studies on the Thermal Degradation of Polybutadiene. *Fuel Process. Technol.* **2000**, *67*, 53–60. [CrossRef]
12. Huang, J.; Li, X.; Meng, H.; Tong, H.; Cai, X.; Liu, J. Studies on Pyrolysis Mechanisms of Syndiotactic Polystyrene Using DFT Method. *Chem. Phys. Lett.* **2020**, *747*, 137334. [CrossRef]
13. Gardner, P.; Lehrle, R. Polystyrene Pyrolysis Mechanisms-as Deduced from the Dependence of Product Yields in Film Thickness. *Eur. Polym. J.* **1993**, *29*, 425–435. [CrossRef]
14. Liqiu, F.; Jin, J.; Zang, Z.; Zhang, Q.; Sun, X.; Deng, L.; Zhang, J. Mechanism of Remarkable Interference of Styrene-Butadiene to Gasoline Identification for Fire Debris Analysis Based on TG-IR-GC/MS. *J. Anal. Appl. Pyrolysis* **2025**, *186*, 106958. [CrossRef]
15. Chen, F.; Qian, J. Studies on the Thermal Degradation of Cis-1,4-Polyisoprene. *Fuel* **2002**, *81*, 2071–2077. [CrossRef]
16. Williams, P.; Taylor, D. Aromatization of Tyre Pyrolysis Oil to Yield Polycyclic Aromatic Hydrocarbons. *Fuel* **1993**, *72*, 1469–1474. [CrossRef]
17. Williams, P.T.; Besler, S. Pyrolysis-Thermogravimetric Analysis of Tyres and Tyre Components. *Fuel* **1995**, *14*, 1277–1283. [CrossRef]
18. Sainz-Diaz, C.I.; Kelly, D.R.; Avenell, C.S.; Griffiths, A.G. Pyrolysis of Furniture and Tire Wastes in a Flaming Pyrolyzer Minimizes Discharges to the Environment. *Energy Fuels* **1997**, *11*, 1061–1072. [CrossRef]
19. Williams, P.T.; Brindle, A.J. Aromatic Chemicals from the Catalytic Pyrolysis of Scrap Tyres. *J. Anal. Appl. Pyrolysis* **2003**, *67*, 143–164. [CrossRef]
20. Fairburn, J.A.; Behie, L.A.; Svrcek, W.Y. Ultrapyrolysis of N-Hexadecane in a Novel Micro-Reactor. *Fuel* **1990**, *69*, 1537–1545. [CrossRef]
21. Brazier, D.W.; Schwartz, N. The Effect of Heating Rate on the Thermal Degradation of Polybutadiene. *J. Appl. Polym. Sci.* **1978**, *22*, 113–124. [CrossRef]
22. Frigo, S.; Seggiani, M.; Puccini, M.; Vitolo, S. Liquid Fuel Production from Waste Tyre Pyrolysis and Its Utilisation in a Diesel Engine. *Fuel* **2014**, *116*, 399–408. [CrossRef]
23. Arya, S.; Sharma, A.; Rawat, M.; Agrawal, A. Tyre Pyrolysis Oil as an Alternative Fuel: A Review. *Mater. Today Proc.* **2020**, *28*, 2481–2484. [CrossRef]
24. Goyal, A.; Kumar, N. Some Experimental Studies on the Use of Tyre Pyrolysis Oil (TPO) in an Agricultural Diesel Engine. *SAE Tech. Pap.* **2019**, *1*, 796. [CrossRef]
25. Graham, J.L.; Striebich, R.C.; Myers, K.J.; Minus, D.K.; Harrison, W.E. Swelling of Nitrile Rubber by Selected Aromatics Blended in a Synthetic Jet Fuel. *Energy Fuels* **2006**, *20*, 759–765. [CrossRef]
26. Blivernitz, A. Untersuchung Der Verträglichkeit von Elastomeren. Ph.D. Thesis, Universität der Bundeswehr, Neubibierg, Germany, 2019.
27. Musil, B.; Demmel, B.; Lion, A.; Johlitz, M. A Contribution to the Chemomechanics of Elastomers Surrounded by Liquid Media: Continuum Mechanical Approach for Parameter Identification Using the Example of Sorption Experiments. *J. Rubber Res.* **2021**, *24*, 271–279. [CrossRef]
28. Gormley, R.J.; Link, D.D.; Baltrus, J.P.; Zandhuis, P.H. Interactions of Jet Fuels with Nitrile O-Rings: Petroleum-Derived versus Synthetic Fuels. *Energy Fuels* **2009**, *23*, 857–861. [CrossRef]

29. Lou, W.; Zhang, W.; Wang, H.; Jin, T.; Liu, X. Influence of Hydraulic Oil on Degradation Behavior of Nitrile Rubber O-Rings at Elevated Temperature. *Eng. Fail. Anal.* **2018**, *92*, 1–11. [CrossRef]
30. Röthemeyer, F. *Kautschuk Technologie*, 3rd ed.; Hanser: München, Germany, 2013; Volume 3.
31. Starmer, P. Swelling of Nitrile Rubber Vulcanizates-Part 3: Factors Affecting Maximum Swelling. *Elastomers Plast.* **1993**, *25*, 188–215. [CrossRef]
32. Lachat, V. Understanding Oil Resistance of Nitrile Rubber Group Interactions at Interfaces. Ph.D. Thesis, University of Akron, Akron, OH, USA, 2008.
33. *DIN EN 590*; Kraftstoffe–Dieselkraftstoff–Anforderungen Und Prüfverfahren. DIN Deutsches Institut für Normung e. V: Berlin, Germany, 2022.
34. *DIN 53504:2017-03*; Testing of Rubber-Determination of Tensile Strength at Break, Tensile Stress at Yield, Elongation at Break and Stress Values in a Tensile Test. DIN Deutsches Institut für Normung e. V: Berlin, Germany, 2017.
35. *D7042-21a*; ASTM International Standard Test Method for Dynamic Viscosity and Density of Liquids by Stabinger Viscometer (and the Calculation of Kinematic Viscosity). ASTM International: West Conshohocken, PA, USA, 2022.
36. *DIN EN 12916*; Mineralölerzeugnisse–Bestimmung von Aromatischen Kohlenwasserstoffgruppen in Mitteldestillaten–Hochleistungsflüssigkeitschromatographie-Verfahren Mit-Detektion. DIN Deutsches Institut für Normung e. V: Berlin, Germany, 2022.
37. *DIN EN ISO 2719*; Bestimmung Des Flammpunktes–Verfahren Nach Pensky-Martens Mit Geschlossenem Tiegel. DIN Deutsches Institut für Normung e. V: Berlin, Germany, 2021.
38. *DIN EN ISO 12156-1*; Dieselkraftstoff –Bestimmung Der Schmierfähigkeit Unter Verwendung Eines-Prüfgerätes (HFRR). DIN Deutsches Institut für Normung e. V: Berlin, Germany, 2019.
39. *DIN EN 116*; Dieselkraftstoffe Und Haushaltsheizöle–Bestimmung Des Temperaturgrenzwertes Der Filtrierbarkeit–Verfahren Mit Einem Stufenweise Arbeitenden Kühlbad. DIN Deutsches Institut für Normung e. V: Berlin, Germany, 2018.
40. *DIN EN ISO 2160*; Mineralölerzeugnisse Auf Kupfer-Kupferstreifenprüfung. DIN Deutsches Institut für Normung e.V: Berlin, Germany, 1999.
41. *DIN EN 16091*; Bestimmung Der Oxidationsstabilität Mit Beschleunigtem Und Kleiner Probenmenge. DIN Deutsches Institut für Normung e. V: Berlin, Germany, 2022.
42. *DIN 51777*; Mineralölerzeugnisse–Bestimmung Des Wassergehaltes Durch Titration Nach Karl Fischer. DIN Deutsches Institut für Normung e. V: Berlin, Germany, 2020.
43. *DIN EN ISO 10370*; Mineralölerzeugnisse–Bestimmung Des Koksrückstandes–Mikroverfahren. DIN Deutsches Institut für Normung e.V: Berlin, Germany, 2015.
44. *DIN EN ISO 6245*; Mineralölerzeugnisse Bestimmung Der Asche. DIN Deutsches Institut für Normung e. V: Berlin, Germany, 2003.
45. *DIN EN ISO 20884*; Mineralölerzeugnisse–Bestimmung Des Schwefelgehaltes in Kraftstoffen–Wellenlängendispersive Röntgenfluoreszenz-Spektrometrie. DIN Deutsches Institut für Normung e. V: Berlin, Germany, 2022.
46. *DIN EN ISO 3405*; Mineralölerzeugnisse Und Verwandte Produkte Mit Natürlichem Oder Ursprung–Bestimmung Des Destillationsverlaufes Bei Atmosphärendruck. DIN Deutsches Institut für Normung e. V: Berlin, Germany, 2019.
47. *D664−24*; ASTM International Test Method for Acid Number of Petroleum Products by Potentiometric Titration. ASTM International: West Conshohocken, PA, USA, 2024.
48. *DIN EN ISO 3961*; Tierische Und Pflanzliche Fette Und Öle–Bestimmung Der Iodzahl. DIN Deutsches Institut für Normung e. V: Berlin, Germany, 2025.
49. John, C. *The Mathematics of Diffusion*, 2nd ed.; Clarendon Press: Oxford, UK, 1975; ISBN 0198533446.
50. *DIN ISO 48-4*; Elastomere Oder Thermoplastische Elastomere-Bestimmung Der Härte-Teil 4: Eindringhärte Durch Durometer-Verfahren (Shore-Härte). DIN Deutsches Institut für Normung e. V: Berlin, Germany, 2021.
51. Wagner, S.; Hüffer, T.; Klöckner, P.; Wehrhahn, M.; Hofmann, T.; Reemtsma, T. Tire Wear Particles in the Aquatic Environment-A Review on Generation, Analysis, Occurrence, Fate and Effects. *Water Res.* **2018**, *139*, 83–100. [CrossRef]
52. Di Salvi, W.; de Santo, C.E.; Matsumoto, A.; Calhabeu, A.M.; Lopes, É.S.N.; Gabriel, L.P. Characterization of Thermal-Oxidative Aging Mechanism of Commercial Tires. *Eng. Fail. Anal.* **2023**, *154*, 107631. [CrossRef]
53. Uebe, J.; Kryzevicius, Z.; Majauskiene, R.; Dulevicius, M.; Kosychova, L.; Zukauskaite, A. Use of Polypropylene Pyrolysis Oil in Alternative Fuel Production. *Waste Manag. Res.* **2022**, *40*, 1220–1230. [CrossRef]
54. Islam, M.R.; Tushar, M.S.H.K.; Haniu, H. Production of Liquid Fuels and Chemicals from Pyrolysis of Bangladeshi Bicycle/Rickshaw Tire Wastes. *J. Anal. Appl. Pyrolysis* **2008**, *82*, 96–109. [CrossRef]
55. Gupta, P.L.; Dogra, P.V.; Kuchhal, R.K.; Kumar, P. Estimation of Average Structural Parameters of Petroleum Crudes and Coal-Derived Liquids by 13C and 1H n.m.r. *Fuel* **1985**, *65*, 515–519. [CrossRef]
56. Banar, M.; Akyildiz, V.; Özkan, A.; Çokaygil, Z.; Onay, Ö. Characterization of Pyrolytic Oil Obtained from Pyrolysis of TDF (Tire Derived Fuel). *Energy Convers. Manag.* **2012**, *62*, 22–30. [CrossRef]
57. Elbaz, A.M.; Gani, A.; Hourani, N.; Emwas, A.H.; Sarathy, S.M.; Roberts, W.L. TG/DTG, FT-ICR Mass Spectrometry, and NMR Spectroscopy Study of Heavy Fuel Oil. *Energy Fuels* **2015**, *29*, 7825–7835. [CrossRef]

58. Rodriguez, J.; Tierney, J.W.; Wender, I. Evaluation of a Delayed Coking Process by 1H and 13C n.m.r. Spectroscopy: 1. Material Balances. *Fuel* **1994**, *73*, 1863–1869. [CrossRef]
59. Rodriguez, J.; Tierney, J.W.; Wender, I. Evaluation of a Delayed Coking Process by 1H and 13C n.m.r. Spectroscopy: 2. Detailed Interpretation of Liquid n.m.r. Spectra. *Fuel* **1994**, *73*, 1870–1875. [CrossRef]
60. Hummel, O.; Scholl, F. *Atlas of Polymer and Plastics Analysis*; Carl Hanser: Munich, Germany, 1988; Volume 2.
61. Socrates, G. *Infrared and Raman Characteristic Group Frequencies*, 2nd ed.; John Wiley & Sons: Chichester, UK, 1994.
62. Lin-Vien, D.; Colthup, N.B.; Fatley, W.G.; Grasselli, J.G. *The Handbook of Infrared and Raman Caracteristic Frequencies of Organic Molecules*; Academic Press: Cambridge, MA, USA, 1991.
63. Scheuermann, S.S.; Forster, S.; Eibl, S. In-Depth Interpretation of Mid-Infrared Spectra of Various Synthetic Fuels for the Chemometric Prediction of Aviation Fuel Blend Properties. *Energy Fuels* **2017**, *31*, 2934–2943. [CrossRef]
64. Smith, B. The C=O Bond, Part III Carboxylic Acids. *Spectroscopy* **2018**, *33*, 14–20.
65. Cunliffe, A.M.; Williams, P.T. Composition of Oils Derived from the Batch Pyrolysis of Tyres. *J. Anal. Appl. Pyrolysis* **1998**, *44*, 131–152. [CrossRef]
66. Mastral, A.M.; Murillo, R.; Callén, M.S.; García, T.; Snape, C.E. Influence of Process Variables on Oils from Tire Pyrolysis and Hydropyrolysis in a Swept Fixed Bed Reactor. *Energy Fuels* **2000**, *14*, 739–744. [CrossRef]
67. Day, M.; Cooney, J.D.; Shen, Z. Pyrolysis of Automobile Shredder Residue: An Analysis of the Products of a Commercial Screw Kiln Process. *J. Anal. Appl. Pyrolysis* **1996**, *37*, 49–61. [CrossRef]
68. Totton, T.S.; Misquitta, A.J.; Kraft, M. A Quantitative Study of the Clustering of Polycyclic Aromatic Hydrocarbons at High Temperatures. *Phys. Chem. Chem. Phys.* **2012**, *14*, 4081–4094. [CrossRef]
69. Elvati, P.; Violi, A. Thermodynamics of Poly-Aromatic Hydrocarbon Clustering and the Effects of Substituted Aliphatic Chains. *Proc. Combust. Inst.* **2013**, *34*, 1837–1843. [CrossRef]
70. Pullen, J.; Saeed, K. An Overview of Biodiesel Oxidation Stability. *Renew. Sustain. Energy Rev.* **2012**, *16*, 5924–5950. [CrossRef]
71. Lopez, G.; Alvarez, J.; Amutio, M.; Mkhize, N.M.; Danon, B.; van der Gryp, P.; Görgens, J.F.; Bilbao, J.; Olazar, M. Waste Truck-Tyre Processing by Flash Pyrolysis in a Conical Spouted Bed Reactor. *Energy Convers. Manag.* **2017**, *142*, 523–532. [CrossRef]
72. Stockwell, W.R.; Calvert, J.G. The Mechanism of the HO-SO2 Reaction. *Atmos. Environ.* **1983**, *17*, 2231–2235. [CrossRef]
73. Serefentse, R.; Ruwona, W.; Danha, G.; Muzenda, E. A Review of the Desulphurization Methods Used for Pyrolysis Oil. *Procedia Manuf.* **2019**, *35*, 762–768. [CrossRef]
74. Williams, P.T.; Bottrill, R.P. Sulfur-Polycyclic Aromatic Hydrocarbons in Tyre Pyrolysis Oil. *Fuel* **1995**, *74*, 736–742. [CrossRef]
75. Blivernitz, A.; Förster, T.; Eibl, S. Simultaneous and Time Resolved Investigation of Diffusion Processes of Individual Model Fuel Components in Acrylonitrile-Butadiene-Rubber in the Light of Swelling Phenomena. *Polym. Test.* **2018**, *70*, 47–56. [CrossRef]
76. Haseeb, A.S.M.A.; Masjuki, H.H.; Siang, C.T.; Fazal, M.A. Compatibility of Elastomers in Palm Biodiesel. *Renew. Energy* **2010**, *35*, 2356–2361. [CrossRef]
77. Kass, M.; Theiss, T.; Janke, C.; Pawel, S.; Technology, J.C.-S. Compatibility of Elastomers with Test Fuels of Gasoline Blended with Ethanol. *Seal. Technol.* **2012**, *2012*, 7–12. [CrossRef]
78. Zhu, L.; Cheung, C.S.; Zhang, W.G.; Huang, Z. Compatibility of Different Biodiesel Composition with Acrylonitrile Butadiene Rubber (NBR). *Fuel* **2015**, *158*, 288–292. [CrossRef]
79. Lachat, V.; Varshney, V.; Dhinojwala, A.; Yeganeh, M.S. Molecular Origin of Solvent Resistance of Polyacrylonitrile. *Macromolecules* **2009**, *42*, 7103–7107. [CrossRef]
80. George, S.; Varughese, K.T.; Thomas, S. Molecular Transport of Aromatic Solvents in Isotactic Polypropylene/ Acrylonitrile-Co-Butadiene Rubber Blends. *Polymer* **2000**, *41*, 579–594. [CrossRef]
81. Chai, A.B.; Andriyana, A.; Verron, E.; Johan, M.R. Mechanical Characteristics of Swollen Elastomers under Cyclic Loading. *Mater. Des.* **2013**, *44*, 566–572. [CrossRef]

polymers

MDPI

Article

Application of Sawdust-Derived Activated Carbon as a Bio-Based Filler in Vulcanized Rubber Bushings

Enasty Pratiwi Wulandari [1], Popy Marlina [2], Nasruddin [3,*], Lanjar [3], Heryoki Yohanes [3], Wahju Eko Widodo [3], S. Joni Munarso [3], Astuti [3], Eko Bhakti Susetyo [3], Yenni Bakhtiar [3], Haixin Guo [4] and Wahyu Bahari Setianto [3]

[1] Mechanical Engineering Department, Tamansiswa University, Palembang 30126, Indonesia; enastypratiwi@gmail.com
[2] The Palembang Center for Standardization and Industrial Services (BSPJI), Palembang 30128, Indonesia; popymarlina16@gmail.com
[3] National Research and Innovation Agency (BRIN), KST B.J. Habibie, South Tangerang 15314, Indonesia; lanj001@brin.go.id (L.); hery009@brin.go.id (H.Y.); wahj003@brin.go.id (W.E.W.); sjon001@brin.go.id (S.J.M.); astu001@brin.go.id (A.); ekob002@brin.go.id (E.B.S.); yenn001@brin.go.id (Y.B.); wahy013@brin.go.id (W.B.S.)
[4] Agro-Environmental Protection Institute, Ministry of Agriculture and Rural Affairs, Tianjin 300191, China; haixin_g@126.com
* Correspondence: nasr006@brin.go.id

Abstract

This study investigated sawdust-derived activated carbon (SAC) as a sustainable reinforcing filler for vulcanized rubber bushings (VRBs). Two types SAC200 (75 μm, carbonized at 200 °C) and SAC400 (38 μm, carbonized at 400 °C) were chemically activated and incorporated into natural rubber (NR) at 25–55 phr loadings, while SAC free VRBs served as controls. Fourier transform infrared (FTIR) analysis revealed that SAC400 exhibited stronger hydroxyl and carbonyl functional groups, indicating higher surface reactivity compared with SAC200. The incorporation of SAC increased cross-linking density, thereby enhancing both curing behavior and mechanical performance. VRBs reinforced with SAC400 demonstrated higher maximum torque (up to 38.07 kg·cm), shorter scorch time (5 min 58 s), and reduced cure time (11 min 05 s) relative to SAC200 and the control. Mechanical properties improved markedly, with hardness and tensile strength rising from 45 Shore A and 5.52 MPa in the control to 70 Shore A and 13.40 MPa in SAC400. Although elongation at break decreased slightly, it remained within the acceptable range for dynamic applications. Swelling resistance also increased, reaching 101.76% at 25 °C and 106.61% at 100 °C. Overall, SAC400 consistently outperformed SAC200 and the control, highlighting its potential as a renewable, biomass-derived filler for high-performance rubber bushings and promising a sustainable alternative to conventional fillers in industrial applications.

Keywords: activated carbon; bio-based filler; mechanical properties; sawdust-derived activated carbon; vulcanized rubber bushings

1. Introduction

Natural rubber (NR) is an elastomeric biopolymer composed of cis-1,4-polyisoprene [1,2]. It is one of the most widely used elastomers, with global production reaching 13.77 million tons in 2021 [3]. NR is extensively applied across diverse sectors, including automotive components, medical devices, petrochemicals, mining, and other industrial applications [4]. The growing diversity of NR-based applications has stimulated the development of advanced compounding systems, which incorporate various additives such as accelerators, activators, plasticizers [5], antioxidants [6], vulcanizing agents, and reinforcing fillers. Among these,

reinforcing fillers play a pivotal role in enhancing the mechanical and dynamic performance of vulcanizates, including tensile strength, modulus, elongation at break, abrasion resistance, compression set, swelling resistance, and dimensional stability [7–9]. Nearly all commercial rubber vulcanizates utilize reinforcing fillers derived from petroleum-based carbon black (CB) [10,11]. Petroleum-derived CB is produced via incomplete combustion of hydrocarbons, where approximately two metric tons of petroleum feedstock are required to produce one metric ton of CB [12]. However, this reliance on petroleum-based CB imposes significant environmental burdens.

Among these, reinforcing fillers play a pivotal role in enhancing the mechanical and dynamic performance of vulcanizates, including tensile strength, modulus, elongation at break, abrasion resistance, compression set, swelling resistance, and dimensional stability [12–15]. In automotive applications, rubber bushings are essential for vibration isolation, enabling controlled movement between components while reducing noise and improving both comfort and safety [13–15]. To optimize these properties, conventional fillers such as CB are widely employed. Nevertheless, concerns regarding environmental impact and the depletion of fossil resources have driven interest in sustainable biomass-derived alternatives [16,17]. Bio-based fillers (bio-fillers) offer several advantages, including biodegradability, a lower environmental footprint, reduced density, and cost-effectiveness [18]. Their compatibility with rubber matrices further strengthens their potential for developing green composites [16].

The mechanical behavior of rubber bushings is strongly influenced by polymer type, filler loading, and compounding formulation [19]. Hence, the integration of bio-fillers into NR not only aligns with sustainable materials engineering but also provides promising mechanical reinforcement. Several bio-derived fillers have been investigated in NR systems. Cifriadi et al. [12] reported the utilization of cassava starch and tamarind wood, while Haslilywaty et al. [20] employed rice husk ash and tacca starch. Joshi et al. [21] demonstrated the reinforcing effects of banana fibers. These bio-fillers improved mechanical performance while also offering biodegradability [22]. Thomas et al. [23] highlighted the advantageous properties of cellulose-, chitin-, and starch-based fillers, which are cost-effective and environmentally friendly. Furthermore, Sowińska et al. and Suhu [24] reported improved thermal oxidation resistance and reinforcement using walnut shell powder and corn starch, respectively.

Activated carbon derived from lignocellulosic biomass, particularly sawdust, has recently emerged as a promising bio-filler due to its high surface area, porous structure, and abundant surface functionalities [25,26]. According to Negara et al., [27] sawdust-derived activated carbon exhibits mesoporous structures with an average pore diameter of 2.43 nm, a pore volume of 0.369 $cm^3\ g^{-1}$, and a specific surface area 409.7 $m^2\ g^{-1}$, enabling broad applicability. These properties facilitate both mechanical interlocking and physicochemical interactions with rubber matrices. Although its reinforcing potential is recognized, systematic studies remain limited on how processing parameters, particularly carbonization temperature and particle size affect its performance.

Rubber bushings operating under dynamic and cyclic loading conditions require high compressive strength, elasticity, and fatigue resistance [28]. While conventional fillers such as CB and silica provide excellent reinforcement [29,30], they often increase stiffness at the expense of elasticity. Consequently, bio-based fillers are sought as alternative reinforcements that can maintain mechanical performance while offering environmental benefits. Activated carbon from renewable precursors is an inexpensive and abundant alternative with the potential to generate added value [31].

Sawdust-derived activated carbon (SAC) typically exhibits high surface area, porosity, and functional group density, which promote strong interactions with polymer matrices.

For example, SAC has been reported to possess a hierarchical porous structure with micropores (0.55 nm) and mesopores (2.58 nm), resulting in a specific surface area of 621 m^2 g^{-1} and a pore volume of 0.35 cm^3 g^{-1} [32]. With such characteristics, SAC enhances interfacial interactions within rubber matrices. Previous studies synthesized SAC via chemical activation followed by carbonization 43. Chemically activated SAC exhibited favorable properties, including a BET surface area of ~1250 m^2 g^{-1}, a pore volume of 0.78 cm^3 g^{-1}, carbon content of ~93%, low ash content (7.36%), and an iodine number of 1161.3 mg g^{-1} [33]. Incorporation of SAC into rubber compounds at loadings up to 100 phr improved torque response and hardness.

Despite these advantages, most prior studies employed only a single SAC variant, limiting insights into how carbonization temperature and particle size govern reinforcement efficiency. Understanding these parameters is critical for tailoring filler morphology and functionality toward optimal performance in NR vulcanizates, particularly for high-demand automotive components such as bushings. This study aims to investigate the influence of carbonization temperature (200 °C and 400 °C) and particle size (75 μm and 38 μm) of SAC on the curing characteristics and mechanical properties of NR composites for automotive bushing applications. SAC200 and SAC400 were incorporated at various loadings and compared with an unfilled control. Fourier transform infrared spectroscopy (FTIR) was employed to explore surface chemistry variations, while vulcanization behavior (maximum torque, scorch time, and optimum cure time) and mechanical properties (tensile strength, elongation at break, hardness, and compression set) were systematically evaluated.

This work contributes to the development of environmentally friendly, high-performance rubber composites while supporting biomass waste valorization in advanced materials engineering. The incorporation of SAC into NR-based bushing compounds enhances interfacial polar interactions absent in conventional CB, resulting in superior reinforcement efficiency. Moreover, the findings emphasize that SAC surface chemistry plays a decisive role in determining the mechanical properties of rubber bushings.

Unlike previous studies, this study uses a single variant of activated carbon derived from sawdust. This study systematically explores the combined effects of carbonization temperature and particle size on the performance of reinforcing fillers in rubber vulcanizates. The novelty of this study lies in demonstrating how these processing parameters govern the drying behavior and mechanical response of rubber bushings under dynamic conditions. The results provide new insights into the tailoring of biomass-derived fillers for high-performance elastomer applications, while also promoting sustainable materials engineering through the utilization of sawdust waste.

2. Methods

2.1. Instrumentation

The preparation of the rubber compounds and vulcanized samples was conducted using the equipment listed in Table 1. Key instruments included a muffle furnace (Nabertherm GmbH) for sawdust carboniation, an XK-160 open two-roll mill for mastication and compounding, and a hydraulic hot press for vulcanization. Additional equipment included a digital balance for accurate weighing of materials and a Monsanto Moving Die Rheometer (MDR 2000, Alpha Technologies, Bellingham, WA, USA) for measuring vulcanization characteristics.

Table 1. Equipment specifications for the preparation of rubber compounds.

No	Equipment	Specifications
1	Muffle Furnace (Nabertherm GmbH, Lilienthal, Germany)	Max Temp: 1700 °C; Volume: 0.15 ft^3; Heating Elements: $MoSi_2$; Controller: Shimaden FP93
2	XK-160 Open Mill (Qingdao Ouli Machine Co., Ltd., Qingdao, China)	Roll Ø: 160 mm; Working length: 320 mm; Motor: 7.5 kW
3	Hydraulic Press (HTM10042T, Toyo Seiki Seisaku-sho, Ltd., Tokyo, Japan)	Pressure: 100 Ton; Platens: 2 levels; Temp: up to 300 °C
4	Digital Scale (Ohaus Corporation, Parsippany, NJ, USA)	Capacity: 5 kg; Resolution: 0.1 g; LCD display

2.2. Materials and Specifications

The materials utilized in this experiment are listed in Table 2.

Table 2. Materials used in the formulation of rubber composites.

No	Chemical Name	Source and Specifications
1	Natural Rubber (SIR-20)	PT. Prasidha Aneka Niaga Tbk, Indonesia; Compliant with SNI 1903:2017 (Ash: 0.25%, Dirt: 0.042%, Nitrogen: 0.24%, Volatile matter: 0.2%, PRI: 65%, Mooney viscosity: 70)
2	SAC200 (75 μm), SAC400 (38 μm)	Local supplier, Palembang, Indonesia
3	Zinc oxide (ZnO)	Shanghai, China; CAS No.: 1314-13-2; Purity: 99.7%
4	Stearic acid	Guangdong, China; CAS No.: 57-11-4; Purity: 99%
5	TMTD	Jiangsu, China; CAS No.: 137-26-8; Purity: 98%
6	CBS	Fujian, China; CAS No.: 95-33-2; Purity: 96%
7	TMQ	Hunan, China; CAS No.: 793-47-8; Purity: 99.9%
8	Paraffin oil (PO-60)	PT. Pertamina, Indonesia
9	6PPD	China; CAS No.: 793-24-8; Purity: 96%
10	PVI	Henan, China; CAS No.: 17796-82-6; Purity: 99%
11	Maleated Natural Rubber (MNR)	Local supplier
12	Phosphoric Acid (H_3PO_4)	Zhejiang, China; Purity: 85%
13	Sulfur	Tamil Nadu, India; CAS No.: 7704-34-9; Purity: 99.5%
14	Engine Oil 10W/40 4T	Local supplier, Indonesia

Note: All materials were procured from local Indonesian vendors.

2.3. Experimental Design

2.3.1. Preparation of Activated Charcoal

Sawdust was first washed with distilled water and oven-dried at 110 °C for 24 h. The carbonization process was conducted in a muffle furnace at 900 °C for 30 min to obtain raw charcoal, which was then ground and sieved to 200 mesh (75 μm) and 400 mesh (38 μm). The chemical activation process was initiated by soaking 5000 g of sieved charcoal in a 10% phosphoric acid (H_3PO_4) solution for 24 h at ambient temperature. Following impregnation, the samples were thoroughly rinsed with distilled water to remove residual acid. Subsequent carbonization was performed in a muffle furnace equipped with a gas circulation system utilizing hydrogen (H_2) and nitrogen (N_2), along with a hydrogen combustion safety unit. Two types of sawdust-derived activated charcoal were produced: SAC200—particle size of 75 μm, carbonized at 200 °C for 120 min; SAC400—particle size of 38 μm, carbonized at 400 °C for 120 min.

Post-carbonization, the activated charcoal was allowed to cool within the furnace for 24 h to prevent oxidation and then stored in airtight containers to maintain its integrity. The equipment utilized in this process is shown in Figure 1.

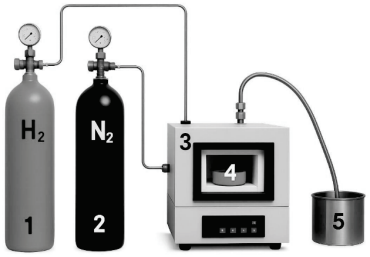

Figure 1. Schematic diagram of the carbonization equipment setup: (1) hydrogen gas cylinder, (2) nitrogen gas cylinder, (3) furnace, (4) carbonization reactor, and (5) nitrogen gas trap.

The quality parameters of the resulting activated charcoal were evaluated in accordance with SNI 06-3730-1995 standards (refer to Table 3) [34].

Table 3. Physicochemical characteristics of sawdust-based activated charcoal.

Parameter	Content
Water content	6.24%
Ash content	7.36%
Volatile matter	11.34%
Carbon	87.85%
Absorption of iodine	1161.34 mg/g

2.3.2. Rubber Compounding Procedure

Rubber compounding was conducted based on the formulation presented in Table 4 using a two-roll open mill. Natural rubber was first masticated for approximately 8 min until a plasticized state was achieved. The activator (ZnO) and co-activator (stearic acid) were then added and mixed for 3 min to ensure uniform dispersion. SAC was gradually incorporated and milled for 4 min until evenly distributed within the rubber matrix. Subsequently, the plasticizer, antioxidant, accelerator, scorch retarder, and coupling agent were sequentially introduced and mixed for 5 min to achieve a fully homogeneous compound. Finally, the vulcanizing agent (sulfur) was added and mixed for an additional 5 min until the compound reached complete uniformity.

Table 4. Formulations of natural rubber compounds with varying SAC particle sizes and loadings (phr).

Material	Formula (Per Hundred Rubber, phr)								
	1	**2**	**3**	**4**	**5**	**6**	**7**	**8**	**9**
SIR 20	100	100	100	100	100	100	100	100	100
ZnO	5	5	5	5	5	5	5	5	5
Stearic acid	1	1	1	1	1	1	1	1	1
6PPD	2	2	2	2	2	2	2	2	2
TMQ	1	1	1	1	1	1	1	1	1
SAC200	-	25	35	45	55	-	-	-	-
SAC400	-	-	-	-	-	25	35	45	55

Table 4. *Cont.*

Material	Formula (Per Hundred Rubber, phr)								
	1	**2**	**3**	**4**	**5**	**6**	**7**	**8**	**9**
Minarex oil	1	1	1	1	1	1	1	1	1
CBS	3	3	3	3	3	3	3	3	3
TMTD	2	2	2	2	2	2	2	2	2
MNR	1	1	1	1	1	1	1	1	1
Sulfur	2	2	2	2	2	2	2	2	2
PVI	0.5	0.5	0.5	0.5	0.5	0.5	0.5	0.5	0.5

2.3.3. Vulcanization

The rubber compounds were molded and vulcanized using a hydraulic hot press at 150 °C for 10 min under a pressure of 170 kgf/cm^2 to produce vulcanized rubber bushing (VRB) specimens.

2.4. Test Method

2.4.1. FTIR Spectroscopy

Fourier transform infrared (FTIR) spectroscopy was performed in this study using a Shimadzu IRTracer-100 spectrometer equipped with an Attenuated Total Reflectance (ATR) accessory to identify the surface functional groups present on the sawdust-derived activated carbon (SAC). Special attention was given to the detection of hydroxyl (–OH) and carbonyl (C=O) groups, which are known to promote interfacial interactions with elastomeric matrices and enhance filler–rubber compatibility. The presence of these oxygen-containing groups plays a crucial role in improving filler dispersion, interfacial adhesion, and overall reinforcement efficiency in rubber composites [35].

2.4.2. Curing Characteristics

Curing behavior was evaluated using a Moving Die Rheometer (MDR 2000) at 150 °C, following ISO 3417:2008 [36]. The parameters measured included minimum torque (Smin), maximum torque (Smax), scorch time (ts_2), and optimum cure time (t_{90}) [37,38]. The cure rate index (CRI) [39] was calculated using the following equation:

$$CRI = \frac{100}{tc_{90} - t_2} \times 100\% \quad (1)$$

2.4.3. Mechanical Testing Procedures

Mechanical properties were evaluated through standard test methods. Hardness was measured using a durometer in accordance with ASTM D2240-15 [40]. Tensile strength according to ASTM D395-18 (22 h at 100 °C) [40]. Swelling resistance was assessed following ASTM D471 [41] by immersing samples in engine oil at 100 °C for 72 h. The percentage swelling [42] was calculated using the following equation:

$$\% \, Swelling = \frac{W_2 - W_1}{W_1} \times 100\% \quad (2)$$

where W_1 is the mass of the specimen prior to immersion, and W_2 is the mass following immersion.

All mechanical tests were conducted in triplicate, and the results are presented as the mean ± standard deviation.

3. Results and Discussion

3.1. FTIR Analysis of Sawdust-Based Activated Carbon

The FTIR spectrum of sawdust-derived activated carbon (SAC) (Figure 2) revealed the presence of characteristic functional groups that contribute to the reinforcing capability of SAC in the natural rubber matrix. A broad absorption band centered at 3639–3138 cm^{-1} corresponds to O–H stretching vibrations from hydroxyl groups in phenolic, alcoholic, or adsorbed moisture species.

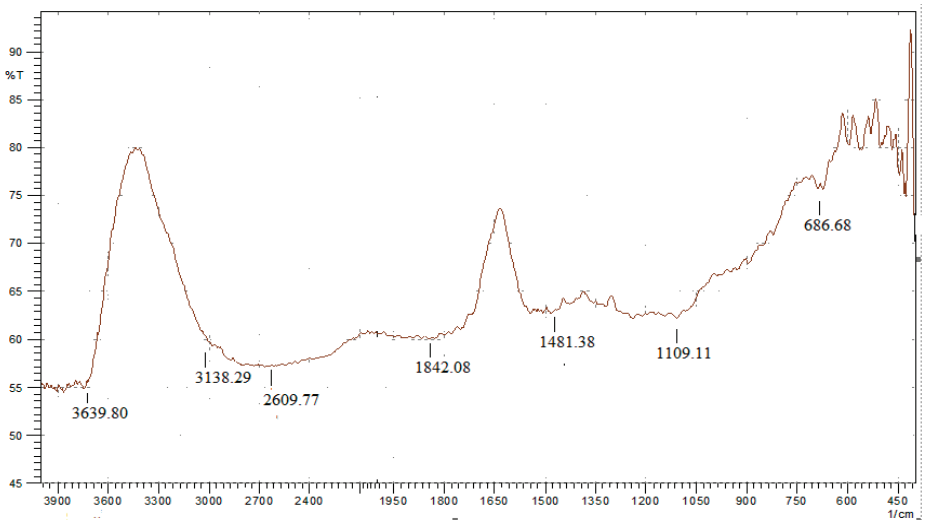

Figure 2. The FTIR spectrum of carbon black derived from sawdust indicates the presence of major functional groups.

These polar functionalities increase surface polarity, enabling hydrogen bonding and improved filler–rubber interactions. The bands observed at 2609.77 cm^{-1} and 1720–1842 cm^{-1} are assigned to C=O stretching vibrations, suggesting the presence of carbonyl groups from carboxylic acids, aldehydes, or ketones generated during oxidative activation. Such oxygenated groups are known to enhance interfacial reactivity and promote higher crosslinking density during vulcanization [36]. In addition, weak peaks near 2920 cm^{-1} (C–H stretching of $–CH_2/–CH_3$), 1481.38 cm^{-1} (C–H bending), and 1109.11 cm^{-1} (C–O stretching of secondary alcohols or ethers) further confirm the partial retention of lignocellulosic structures and the introduction of oxygen-based moieties. The fingerprint region (500–1100 cm^{-1}) also exhibits bands characteristic of alcohols, ethers, and esters, while the peak at 686.68 cm^{-1} corresponds to aromatic C=C stretching, indicating the presence of condensed aromatic structures derived from lignin carbonization [43]. While FTIR provides direct evidence of surface functional groups, the confirmation of elemental composition and chemical states requires complementary analysis. X-ray Photoelectron Spectroscopy (XPS) has been widely recommended in recent studies to quantify oxygen-containing groups (C–O, C=O, O–C=O) and to verify their chemical environment. For instance, XPS deconvolution of the C 1s region typically reveals sp^2-hybridized carbon (C=C), sp^3-hybridized carbon (C–C), and oxygenated species (C–O, C=O), in agreement with the oxygen functionalities detected by FTIR. The O 1s spectrum further distinguishes between hydroxyl, carbonyl, and carboxyl contributions. Therefore, the combination of FTIR and XPS provides a robust verification: FTIR identifies vibrational modes of functional groups, while XPS quantifies the atomic-level chemical states and confirms the abundance of oxygen functionalities that facilitate strong interfacial adhesion in SAC-filled rubber composites. The FTIR–XPS results in this study are in line with the report from Rosan et al. [44], Yang et al. [45], Marija Ilić et al. [46], where FTIR detects the characteristic vibra-

tions of oxygenated groups (C–O, C=O), while XPS quantifies the contribution of oxygen species through the deconvolution of C1s and O1s peaks. This consistency strengthens the evidence that the presence of oxygen groups plays an important role in enhancing interfacial interactions in activated carbon-based materials.

This dual characterization not only validates the surface chemistry of SAC but also underpins its reinforcing role in natural rubber compounds formulated in Table 4. The simultaneous presence of hydroxyl, carbonyl, ether, and aromatic structures contributes to improved filler dispersion, increased cross-link density during vulcanization, and enhanced mechanical performance of vulcanized rubber bushings compared to conventional carbon black. Such complementary evidence highlights SAC as a sustainable and multifunctional bio-based filler with clear advantages in polymer reinforcement applications [47,48].

3.2. Curing Characteristics of Natural Rubber Compounds

The curing characteristics of natural rubber (NR) compounds filled with SAC200 and SAC400 at various loadings (0–55 phr) were evaluated using rheometric parameters, including maximum torque (S_{max}), minimum torque (S_{min}), torque difference ($\Delta_S = S_{max} - S_{min}$), scorch time ($ts_2$), optimum cure time ($t_{90}$), and cure rate index (CRI) [49]. The results, summarized in Table 5, reveal significant variations in vulcanization behavior across formulations. The chemical functionality of SAC, particularly the presence of oxygen-containing groups like hydroxyl and carbonyl, which improve interactions with curing agents and the rubber matrix, is primarily responsible for these variations [50]. FTIR test results indicate the presence of dominant hydroxyl and carbonyl groups in SAC400. The presence of these groups affects the hardening characteristics of the rubber compound. With the presence of this group, the maximum torque (Smax) of SAC400 vulcanizate increased significantly from 3.451 N·m to 3.733 N·m when compared with SAC200 and the control.

Table 5. Curing characteristics of natural rubber composites filled with SAC200 and SAC400.

Sample	Loading (phr)	Curing Characteristic					
		S_{max} (N·m)	S_{min} (N·m)	$S_{max} - S_{min}$ (N·m)	Opt Cure Time (tc_{90}) (min; s)	Scorch Time (ts_2) (min; s)	CRI (s^{-1})
NR/CB Without filler	0	3.683	0.874	2.810	12:35	6:79	0.316
Without filler	0	3.451	0.796	2.655	15:59	8:45	0.230
SAC200 (75 μm)	25	3.037	0.610	2.427	15:29	8:02	0.223
	35	3.065	0.584	2.480	14:45	7:56	0.244
	45	3.143	0.512	2.631	13:57	7:25	0.255
	55	3.247	0.708	2.539	13:07	7:10	0.273
Without filler	0	3.451	0.796	2.655	15:59	8:45	0.230
SAC400 (38 μm)	25	3.241	0.775	2.466	14:57	7:47	0.233
	35	3.526	0.834	2.693	13:15	7:00	0.267
	45	3.722	0.847	2.874	12:28	6:46	0.292
	55	3.733	0.884	2.850	11:05	5:58	0.326

Note: Torque values originally expressed in kg·cm were converted to N·m using the conversion factor 1 kg·cm = 0.0980665 N·m. NR: natural rubber; phr: per hundred rubber; CB: carbon black; SAC: sawdust-activated carbon.

The difference in filler loading has a significant effect on cross-link formation. At a filler loading of 30 phr, the cross-link density increases and the torque delta (Δ_S) changes. This implies that the network structure and stiffness of the rubber have improved [51]. However, at filler loadings above 30 phr, Δ_S decreases and the ts_2 and t_{90} values increase. This phenomenon implies that excessive amounts of filler can cause the rubber chain to become unstable and the resulting cross-link system to become less uniform.

Among the measured parameters, maximum torque (S_{max}) rose significantly with increasing SAC content, particularly for SAC400. A S_{max} of 38.07 kg·cm was recorded by SAC400 at 55 phr, indicating increased stiffness and cross-link density. This was ascribed to enhanced filler–matrix adhesion, which was facilitated by the polar surface and numerous active sites of SAC400 [52–55]. Conversely, minimum torque (S_{min}), which reflects compound viscosity before curing, showed only minor variation with SAC loading. Yet, SAC400 showed a marked increase in Δ_S at higher loadings, peaking at 29.31 kg·cm at 45 phr, likely due to its finer particle size (38 μm), which enhances surface area and dispersion efficiency [56]. SAC400, with a surface area of 38 μm, has a higher density of polar functional groups (–OH, –COOH, –C=O). These groups act as catalytic sites that can interact with sulfur during vulcanization. These groups accelerate the cross-linking reaction. Furthermore, vulcanizates loaded with SAC400 exhibited a faster ts_2 time than SAC200, resulting in a faster cross-linking reaction.

Similar trends have been reported in previous studies, where activated carbon with abundant surface functionalities accelerated the drying kinetics and enhanced the rubber–filler interactions. Li et al. [57] showed that activated carbon with very high surface area had abundant oxygen functionalities, while Ma et al. [58] reported that Sakura-derived activated carbon exhibited significant –OH, –C=O, and –COOH groups. The results indicate that the bio-based activated carbon filler accelerated the drying time and improved the mechanical performance of natural rubber composites, consistent with the faster ts_2 observed in the SAC400-filled vulcanizate.

The SAC material used in this study possessed high porosity and carbon content (72.32%), contributing to better surface reactivity and adsorption capacity [59]. These properties enabled more efficient heat transfer and molecular mobility during vulcanization, leading to denser crosslinking and improved mechanical response. Consequently, both scorch time (ts_2) and optimum cure time (t_{90}) decreased with SAC400 loading, reaching their lowest values at 5 min 58 sec and 11 min 05 sec, respectively. Acceleration of the curing process, in line with previous findings that finer particles increase thermal conductivity and internal friction, thereby shortening the overall curing time [60]. A shorter t_{90} increases energy efficiency in processing [61,62], while a lower ts_2 improves the processability of the compound.

The cure rate index (CRI), representing vulcanization kinetics, was highest for SAC400 at 55 phr, confirming its superior curing performance [63]. SAC400's enhanced surface properties high surface area, porosity, and polarity are key contributors to this outcome, promoting faster heat distribution and chain mobility. As observed in Table 5, the trend of increasing Smax with SAC loading suggests a corresponding increase in cross-link density, likely driven by interactions between SAC hydroxyl groups and the NR matrix [64]. Meanwhile, S_{min} values fluctuated moderately, likely influenced by the balance between filler dispersion and matrix viscosity.

At equivalent loadings, SAC400 consistently outperformed SAC200 in terms of ts_2, t_{90}, and CRI, confirming its superior curing efficiency. Variations in cross-link density and internal heat generation largely governed the differences in curing behavior from filler–rubber friction [65]. Overall, NR compounds filled with 45–55 phr SAC400 exhibited the most favorable curing characteristics, high Smax, low ts_2, t_{90}, and elevated CRI values. These findings position SAC400 not only as a reinforcing filler but also as an active contributor to vulcanization kinetics. Its dual role underscores its potential as an efficient, bio-based alternative to conventional fillers, particularly for demanding applications such as automotive rubber bushings [66].

3.3. Mechanical Properties and Performance Analysis

3.3.1. Hardness

Hardness is a key mechanical parameter reflecting the resistance of a vulcanizate to surface deformation and is directly related to cross-linking density and filler–matrix interactions. In automotive rubber bushings (VRBs), which must maintain dimensional stability under repeated mechanical stress, hardness serves as a crucial performance metric. As shown in Figure 3 and Table 4, the addition of SAC to natural rubber compounds can significantly increase hardness.

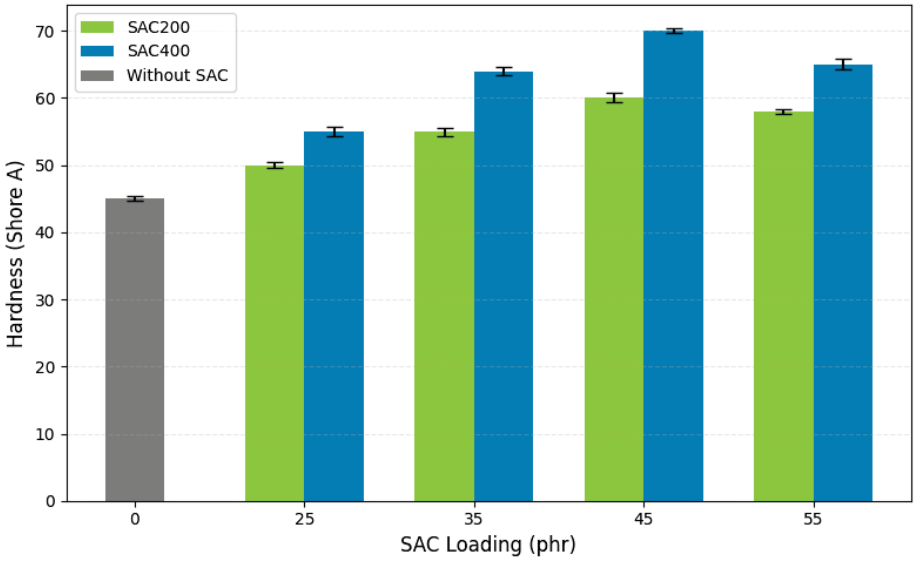

Figure 3. The effect of SAC type and loading on the Shore A hardness of vulcanized natural rubber bushings.

The unfilled control sample exhibited a baseline hardness of 45 Shore A. With increasing SAC loading, a progressive rise in hardness was observed. SAC400, carbonized at 400 °C and possessing a finer particle size (38 μm), consistently yielded higher hardness values than SAC200 (75 μm, 200 °C). At 55 phr, SAC400 reached 70 Shore A, fulfilling the industrial standard for VRB (70 ± 5 Shore A). Because SAC200 could only support 60 Shore A at the same loading, the reinforcement was less effective. Activated carbon with smaller particle size and richer surface functionality provides better reinforcement in the rubber matrix, resulting in higher hardness values compared to larger particle fillers.

The superior performance of SAC400 is attributed to its higher surface area and carbon purity, which promote effective filler dispersion and interfacial bonding. FTIR analysis (Figure 2) confirmed the presence of functional groups such as C=C and C=O, along with reduced –OH intensity in SAC400, indicating greater graphitization and hydrophobicity. The detection of sulfur-containing bonds (C–S, S–S) further indicates that SAC400 can participate in the vulcanization reaction, contribute to the formation of three-dimensional networks, and influence the VRB hardness value. The enhancement in hardness is closely related to increased crosslink density. The observed increase in hardness is primarily due to the presence of functional groups in SAC, as identified through FTIR analysis. These functional groups enhance interfacial interactions with the rubber matrix. Furthermore, cross-linking formed by sulfur, accelerated by accelerators and activators, increases the overall cross-linking density. This contributes to the increase in VRB hardness. These findings are consistent with previous findings on bio-based fillers [67]. The use of the ZnO stearic acid system, in combination with CBS and TMTD accelerators, supported efficient vulcanization and uniform crosslink distribution. However, hardness plateaued at loadings

above 45 phr, likely due to filler agglomeration, which may hinder matrix uniformity and restrict further reinforcement.

The presence of coupling agents during mixing reduces interfacial tension and improves filler–rubber adhesion [68]. In modified natural rubber (MNR), polar functional groups can interact favorably with SAC, while non-polar domains align with the rubber matrix. Larger SAC particles may limit chain mobility during deformation, resulting in greater localized indentation and decreased hardness [69]. Overall, SAC400-filled NR compounds at 45 and 55 phr met commercial hardness requirements, demonstrating the material's capability for application in high-performance automotive bushings (VRB). The combination of optimized morphology and surface chemistry supports SAC400 as a viable bio-derived alternative to conventional fillers in elastomeric systems.

3.3.2. Tensile Strength

Tensile strength is a fundamental parameter for assessing the mechanical performance of vulcanized rubber (VRB), especially in reinforced systems. It represents the material's ability to withstand stress under tensile loading before failure. Figure 4 presents the tensile strength of VRB filled with SAC200 and SAC400 across various loadings.

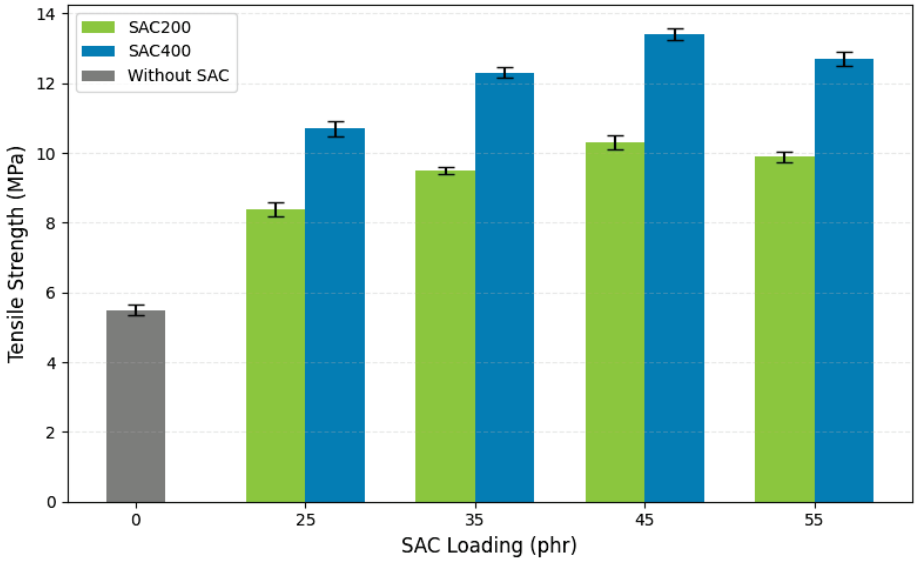

Figure 4. The effect of SAC type and loading on the tensile strength of vulcanized rubber bushings.

The unfilled compound exhibited a tensile strength of 5.52 MPa, establishing the baseline for comparison. As SAC content increased, tensile strength improved progressively, confirming SAC's reinforcing capability. The increased tensile strength is due to improved filler–matrix adhesion, interfacial stress transfer, and physical interlock, all of which are facilitated by SAC's porous structure and large surface area. These results are consistent with earlier studies on the enhancement of elastomeric properties by carbon fillers derived from biomass [70]. The existence of polar functional groups on the filler surface explains the higher tensile strength of VRB, particularly those reinforced with SAC400.

The polar groups actively encourage greater interfacial adhesion by forming hydrogen bonds and dipole–dipole interactions with the non-polar polyisoprene chains. Interfacial adhesion improves stress transfer effectiveness in the composite. Furthermore, the polar surface properties of SAC400 promote better dispersion into the NR matrix. The resulting interfacial adhesion interacts with ZnO, stearic acid, sulfur, and other additives to form tighter cross-links. This results in a significant increase in tensile strength.

Across all loadings, SAC400 outperformed SAC200. At 45 phr, SAC400 reached a peak tensile strength of 13.4 MPa, significantly higher than SAC200's 9.56 MPa at the same

loading, an increase of approximately 40%. This value exceeds the tensile strength range typically reported for carbon black-filled NR (11–13 MPa at 30 phr) [71,72], highlighting SAC400's competitive performance. The superior performance of SAC400 is attributed to its finer particle size (38 μm), higher carbonization temperature (400 °C), and higher surface area, which collectively enhance dispersion and interfacial bonding. At 55 phr, SAC400 maintained a high tensile strength of 12.51 MPa, surpassing the minimum industry requirement of 11 MPa for automotive VRB. In contrast, SAC200 exhibited a marked reduction at this loading, likely due to agglomeration and poor dispersion, common challenges in particulate-filled elastomer systems.

The reinforcing mechanism involves both physical and chemical interactions. Physically, SAC particles interact with rubber chains via van der Waals forces. Chemically, functional groups on the SAC surface (–OH, C=O) form bonds with the rubber matrix during vulcanization [72]. The presence of maleated natural rubber (MNR) as a coupling agent further enhances compatibility and stress distribution. SAC400's optimized morphology also contributes to a more uniform crosslink network, resulting in higher tensile strength [73]. These results support earlier findings on the importance of filler particle size, surface area, and dispersion in achieving mechanical reinforcement [74]. Overall, SAC400 demonstrated superior performance compared to SAC200, positioning it as a highly effective, sustainable filler for high-performance vulcanized rubber bushings.

3.3.3. Elongation at Break

Elongation at break is an important parameter that reflects the flexibility and toughness of VRB under tensile stress. This parameter indicates the extent to which a material can stretch before breaking. As shown in Figure 5, the unfilled control sample (0 phr SAC) exhibited an elongation at break of 530%, demonstrating unrestricted chain mobility in the absence of fillers. The SAC200 and SAC400 loadings on each VRB significantly affected these properties. The loading of SAC200 and SAC400 on each VRB significantly affected these properties, consistent with previous findings that the addition of bio- or carbon-based fillers limits chain mobility and reduces elongation at break due to stronger filler–rubber interactions. According to Azura et al. [71], elongation at break is influenced by filler load, where increasing filler load will reduce elongation at break.

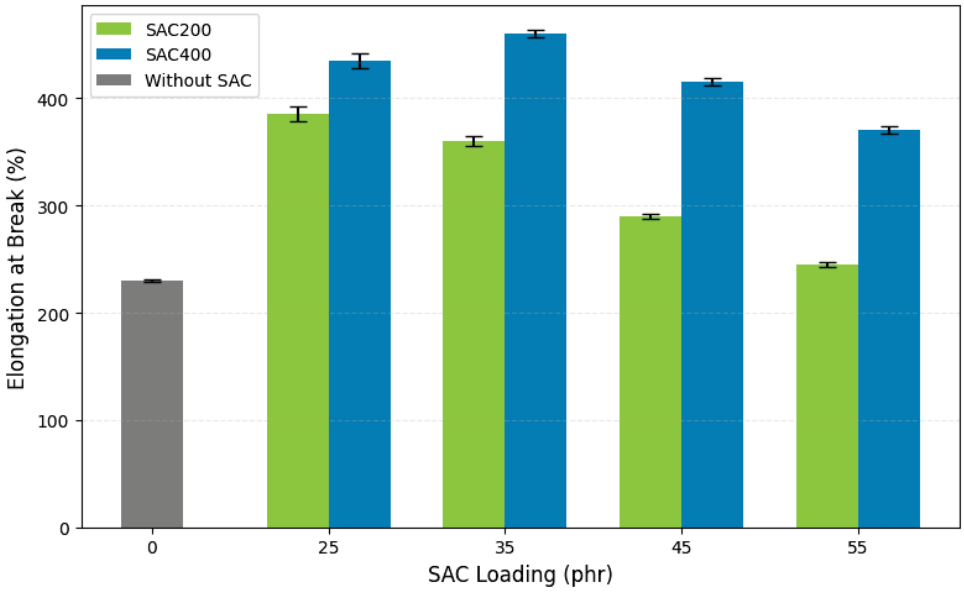

Figure 5. The effect of SAC type and loading on the elongation at break of vulcanized rubber bushings.

The gradual addition of SAC fillers reduced elongation due to restricted polymer chain mobility, as the rigid particles acted as physical crosslinking points. In SAC200-filled compounds, elongation values declined notably, especially at 35–55 phr, where values fell below the minimum industrial standard of 400%. This was attributed to poor dispersion, weak filler–rubber interfacial bonding, and filler agglomeration, which disrupted matrix homogeneity and increased stiffness.

At higher SAC content, the reduction in free volume further hindered chain flexibility. Excess filler led to saturation, preventing complete interaction between the SAC and the VRB. This condition compromises elasticity and promotes premature failure under tensile loading. In contrast, SAC400 demonstrated superior elongation-at-break performance. At 25 phr and 35 phr, elongation at break reached 435% and 460%, respectively, within the optimal range (400–500%) for VRB applications. However, further increasing the loading to 45 phr and 55 phr reduced elongation to 415% and 370%, respectively. This reduction was due to filler aggregation, which restricted chain extension and introduced stress concentration points.

The improved performance of SAC400 is largely due to its smaller particle size (38 μm) and higher carbonization temperature (400 °C), which results in greater surface area and porosity. These characteristics enhance stress distribution across the VRB, interfacial adhesion, and filler dispersion. SAC400's higher porosity resulting from thermal activation also allowed for tighter rubber filler contact and better stress transfer, as shown in similar studies using biomass-based carbon [54]. By comparison, SAC200 with a larger particle size (75 μm) led to uneven stress distribution, localized microvoids, and poor elongation results at higher loadings. These phenomena underline the importance of filler structure and dispersion quality in mechanical reinforcement [75].

The 35 phr SAC400 formulation represented the optimal filler level, where elongation at break peaked at 460%. Above this threshold, the performance declined below the 400% standard, reflecting the onset of filler overloading. Similar behavior was observed in carbon-filled composites post-thermal treatment, as reported [76]. Notably, SAC-filled VRB outperformed conventional carbon black systems, which typically exhibit maximum elongation between 350% and 400% at 20–30 phr [77]. In comparison, SAC400 reached 460% at 35 phr, demonstrating its superior reinforcement efficiency. This also highlights SAC400's viability as a sustainable alternative to petroleum-based fillers, combining mechanical reliability with environmental advantages, wide availability, and renewability. When considered together, the data confirm that SAC400 enhances both elasticity and toughness of VRB more effectively than SAC200, particularly at optimal loading. Its favorable elongation performance, alongside its bio-based origin, supports its use in the development of environmentally sustainable, high-performance rubber composites.

3.3.4. Compression Set

Compression set is an important parameter for evaluating the long-term dimensional stability and elastic recovery of rubber materials, especially in VRB applications. Compression set measures the ability of a rubber vulcanizate to return to its original shape after prolonged compression at elevated temperatures [78]. Lower VRB compression set values indicate superior elasticity, structural resistance, and the material's capacity to maintain mechanical integrity under thermal and compression loads [79]. Figure 6 presents the compression set values of VRB reinforced with various loadings of SAC200 and SAC400. All samples were aged at 100 °C for 72 h to simulate thermal degradation conditions. The control (unfilled) sample exhibited a compression set of 29.5%, typical of non-reinforced vulcanizates. In contrast, the addition of SAC fillers significantly reduced compression set values across all formulations, suggesting enhanced elastic recovery due to increased

crosslink density and stronger filler–matrix interactions. Figure 6 presents the improved VRB compression set values with various SAC200 and SAC400 loadings.

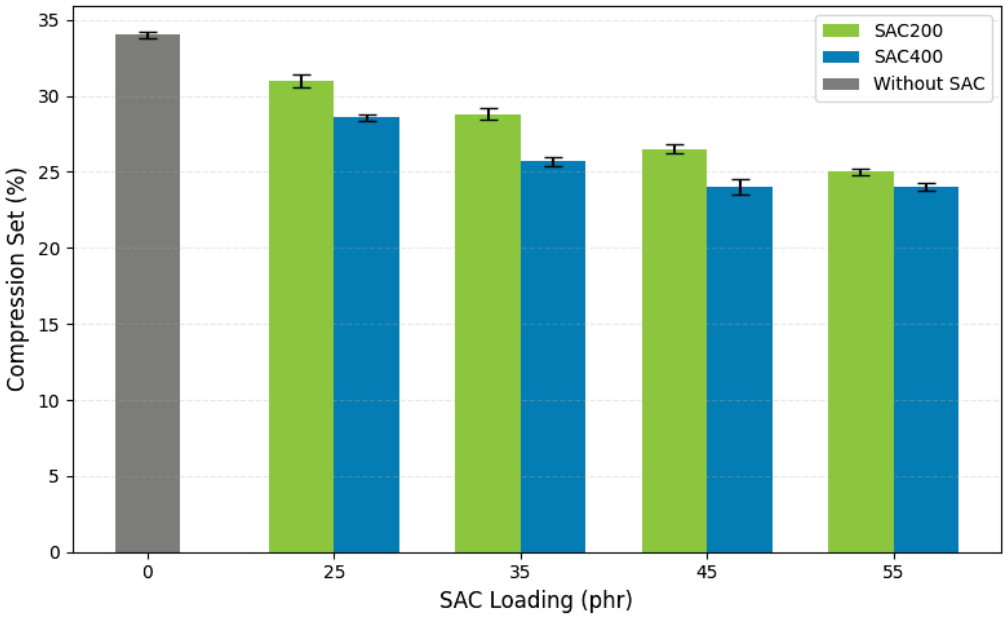

Figure 6. The effect of SAC type and loading on the compression set values of vulcanized rubber bushings.

For samples loaded with SAC200, the VRB compression set decreased from 24.2% at 10 phr to 20.3% at 30 phr, indicating improved dimensional stability. SAC400 consistently outperformed SAC200 at equivalent loads. At 30 phr, SAC400 achieved the lowest compression set value of 18.7%, representing a 36.6% reduction compared to the control. At 45 phr, SAC400 maintained a value around 24%, still lower than the SAC200 counterpart.

These improvements are attributed to SAC400's smaller particle size (38 μm), higher surface area, and more porous structure—resulting from carbonization at 400 °C, which facilitated better dispersion and stronger interfacial bonding with the rubber matrix [66,71]. The superior performance of SAC400 is further supported by its higher surface polarity and structural stability, which helped distribute applied pressure more evenly and restricted polymer chain relaxation [80]. This led to reduced permanent deformation and improved dimensional resilience. The enhanced filler–rubber bonding in SAC400 composites is due to greater contact area and a more favorable distribution of functional groups, consequences of its higher carbonization temperature and optimized microstructure.

A sharp decline in compression set was observed when filler loading exceeded 25 phr, suggesting the formation of a percolation network. This interconnected filler structure enhanced matrix reinforcement and minimized voids through increased physical contact and interfacial bonding [81]. Similar trends have been reported in elastomers filled with high-surface-area carbon materials, where enhanced stress transfer and limited chain mobility reduced permanent deformation [29]. These observations align with the study by Yan et al. [55], which demonstrated that finer carbon fillers significantly improve stress distribution and limit molecular relaxation. The 25 phr threshold appeared critical, beyond which compression set performance improved markedly [82]. Notably, SAC400-filled VRB in the 35–55 phr range showed compression set values between 24% and 30%, meeting the industrial requirement ($\leq$30%) for automotive and general-purpose bushing applications.

The excellent compression set resistance of SAC400 is also linked to its high porosity and functional surface chemistry, which promote physical entrapment of polymer chains and the formation of van der Waals and hydrogen bonds [83]. These interactions increase network compactness, reduce voids, and enhance the rubber's ability to recover from com-

pressive strain. The synergy between small particle size, high carbonization temperature, and broad surface functionality highlights the potential of SAC400 as a sustainable active filler alternative derived from biomass.

3.3.5. Swelling Behavior

Swelling behavior in VRB is primarily governed by free volume, crosslink density, and interfacial interactions between the rubber matrix and the swelling medium. The swelling rate, defined as the percentage of absorbed oil, reflects the extent of solvent diffusion within the polymer network [42]. In this study, swelling tests were conducted on VRB using oil immersion at two temperatures (25 °C and 100 °C), as shown in Figure 7.

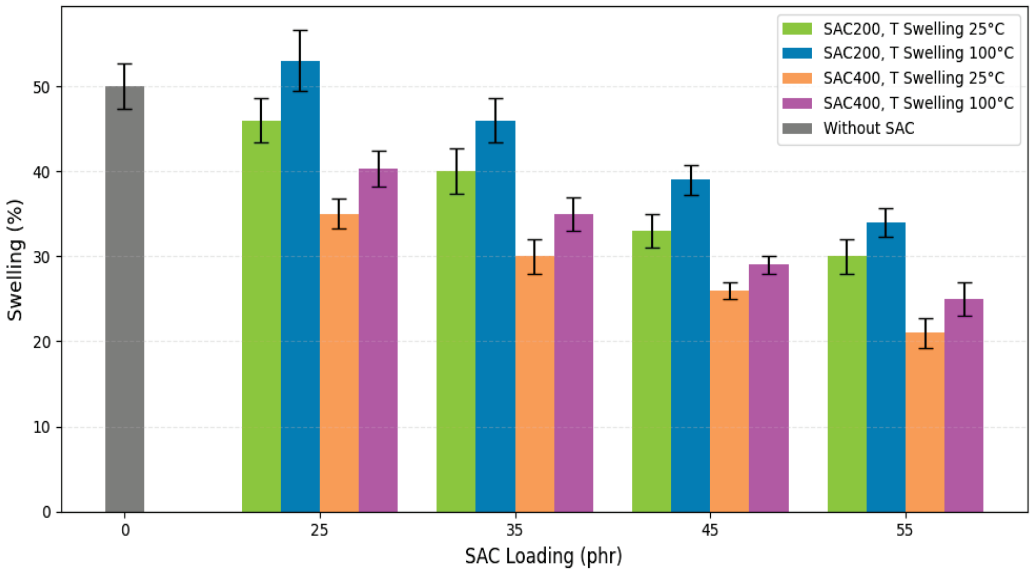

Figure 7. The effect of SAC type and loading on the oil swelling behavior of vulcanized rubber bushings.

The formulations are detailed in Table 4. At 25 phr filler loading, SAC200 and SAC400 exhibited the highest swelling ratios, indicating lower crosslink densities. SAC200 swelled up to 50% at 25 °C, while the unfilled compound showed ~55% swelling at 100 °C. This high swelling [84], is associated with insufficient crosslink formation, which permits solvent penetration and polymer chain expansion. Additionally, polar groups result in less swelling in non-polar solvents, which suggests improved network integrity and solvent resistance.

When the filler content increased to 55 phr, the swelling percentage of VRB decreased significantly. This phenomenon indicates increased cross-linking and improved compatibility of the filler with the rubber matrix due to the addition of SAC. VRB filled with SAC400 consistently showed lower swelling compared to SAC200. Furthermore, the denser three-dimensional network formed during vulcanization reduces solvent uptake by physically restricting chain mobility and void space. This effect is supported by FTIR results and aligns with previous findings that higher cross-linking density reduces matrix permeability and swelling [62]. Furthermore, the results of FTIR analysis showed that the presence of polar groups increased tissue integrity and solvent resistance by reducing the amount of swelling in non-polar solvents.

Swelling resistance was consistently lower at higher SAC loadings, particularly in the range of 35–55 phr for SAC400. These results emphasize the role of filler morphology and surface chemistry in limiting chain relaxation and solvent transport. This behavior is more pronounced at high temperatures (100 °C), where solvent diffusion is accelerated and mechanical integrity is reduced. Nevertheless, SAC-filled samples maintained better swelling

resistance compared to unfilled VRB. Furthermore, strong interfacial bonding through hydrogen bonding, van der Waals forces, and chemical linkages contributed to improved matrix cohesion and solvent exclusion, This was especially evident in SAC400 systems, which offered superior dimensional and chemical stability under thermal and chemical stress. In summary, VRB filled with SAC400 exhibited superior swelling resistance compared to SAC200. This was attributed to the finer structure of SAC400, higher surface reactivity, and better integration into the rubber matrix. These findings support the use of SAC400 as a reinforcing filler to enhance cross-linking and reduce solvent-induced degradation of VRB in vulcanized rubber systems.

4. Conclusions

(1) Sawdust-derived activated carbon (SAC) successfully incorporates oxygenated and aromatic functional groups, as confirmed by FTIR and XPS.
(2) The addition of SAC improves the hardening properties, tensile strength, modulus, hardness, and tear resistance of NR vulcanizates.
(3) SAC200 retains more oxygenated groups, enhancing interfacial interactions, while SAC400 increases stiffness due to the increase in aromatic domains.
(4) Compared with conventional carbon black and other biomass-derived fillers, SAC exhibits superior sustainability and reinforcement potential.

Author Contributions: E.P.W.: Conceptualization, Data curation, Methodology, Writing—original draft, Writing—review & editing. P.M.: Conceptualization, Funding acquisition, Project administration, Writing—original draft. N.: Conceptualization, Funding acquisition, Methodology, Writing—original draft, Writing—review & editing. L.: Resources, Writing—review & editing. H.Y.: Data curation, Validation, Writing—review & editing. W.E.W.: Formal analysis, Investigation, Visualization. S.J.M.: Formal analysis, Investigation, Supervision. A.: Data curation, Project administration, Validation. E.B.S.: Data curation, Formal analysis, Resources, Investigation. Y.B.: Formal analysis, Investigation, Visualization. H.G.: Formal analysis, Investigation, Writing—review & editing. W.B.S.: Conceptualization, Supervision, Writing—original draft, Writing—review & editing. All authors have read and agreed to the published version of the manuscript.

Funding: This research received funding and research facilitation from the Palembang Industrial Research and Standardization Center, Industrial Research and Development Agency, Ministry of Industry of the Republic of Indonesia.

Institutional Review Board Statement: This research does not involve humans and animals as research objects.

Data Availability Statement: The original contributions presented in this study are included in the article material. Further inquiries can be directed to the corresponding author.

Acknowledgments: The authors are deeply grateful to the Research Organization for Agriculture and Food, a part of the National Research and Innovation Agency of the Republic of Indonesia, for the invaluable support for this work. They also express sincere appreciation for the funding and facilitation of this research by the Palembang Center for Standardization and Industrial Services (BSPJI). Furthermore, the authors would like to acknowledge the technical assistance provided by the technicians at the Rubber Laboratory of the Palembang Industrial Research and Standardization Center.

Conflicts of Interest: The authors declare that they have no known competing financial 566 interests or personal relationships that could have appeared to influence the work re- 567 ported in this paper.

Abbreviations

The following abbreviations are used in this manuscript:

NR	Natural rubber
SAC	Sawdust-derived activated carbon
VRB	vulcanized rubber bushings
SAC200	Activated carbon derived from sawdust with a particle size of 75 μm, carbonized at a temperature of 200 °C
SAC400	Activated carbon derived from sawdust with a particle size of 38 μm, carbonized at a temperature of 400 °C
ZnO	Zinc Oxide
CBS	N-Cyclohexyl2-benzothiazole sulfenamide
TMTD	Tetramethyl thiuram disulfide
MNR	Maleated natural rubber
SIR-20	Standar Indonesia Rubber
TMQ	Polymerized 2,2,4-trimethyl-1,2-dihydroquinoline
6PPD	N-(1,3-dimethylbutyl)-N′-phenyl-p-phenylenediamine
PVI	Pre-Vulcanization Inhibitor
H_3PO_4	Phosphoric Acid
CB	Carbon black
H_2	Hydrogen
N_2	Nitrogen
FTIR	Fourier transform infrared
ATR	Attenuated Total Reflectance
MDR	Moving Die Rheometer
CRI	Cure rate index
ASTM	American Society for Testing and Material
W	Weight
Mpa	Megapascal
°C	Degrees Celsius
%	Percent
Mikrometer	μm
kgf	Kilogram-force
cm	Centimeters
μm	micrometer
phr	parts per hundred of rubber
ts_2	Scorch time
t_{90}	Cure time
S_{max}	Maximum torque
S_{min}	Minimum torque
Δ_S	Torque difference

References

1. Andler, R. Bacterial and enzymatic degradation of poly(cis-1,4-isoprene) rubber: Novel biotechnological applications. *Biotechnol. Adv.* **2020**, *44*, 107606. [CrossRef]
2. Whba, R.; Su'ait, M.S.; Whba, F.; Sahinbay, S.; Altin, S.; Ahmad, A. Intrinsic challenges and strategic approaches for enhancing the potential of natural rubber and its derivatives: A review. *Int. J. Biol. Macromol.* **2024**, *276*, 133796. [CrossRef]
3. Marrero Nunes, F.; Emmel Silva, A.L.; May, J.; da Silva Szarblewski, M.; Flemming, L.; Assmann, E.E.; Ribas Moraes, J.A.; Machado, Ê.L. Environmental impacts associated with the life cycle of natural rubbers: A review and scientometric analysis. *Ind. Crops Prod.* **2025**, *224*, 120350. [CrossRef]
4. Dunuwila, P.; Rodrigo, V.H.L.; Goto, N. Sustainability of natural rubber processing can be improved: A case study with crepe rubber manufacturing in Sri Lanka. *Resour. Conserv. Recycl.* **2018**, *133*, 417–427. [CrossRef]
5. Rahman, M.M.; Oßwald, K.; Reincke, K.; Langer, B. Influence of bio-based plasticizers on the properties of NBR materials. *Materials* **2020**, *13*, 2095. [CrossRef]

6. Zhao, W.; He, J.; Yu, P.; Jiang, X.; Zhang, L. Recent progress in the rubber antioxidants: A review. *Polym. Degrad. Stab.* **2023**, *207*, 110223. [CrossRef]
7. Yang, J.; Wang, F.; Liang, C.; Zhou, S.; Huang, J.; Zhao, G.; Liu, Y. Trans-1,4-poly(isoprene-co-butadiene) rubber enhances abrasion resistance in natural rubber and polybutadiene composites. *Polymer* **2025**, *316*, 127855. [CrossRef]
8. Sethulekshmi, A.S.; Saritha, A.; Joseph, K. A comprehensive review on the recent advancements in natural rubber nanocomposites. *Int. J. Biol. Macromol.* **2022**, *194*, 819–842. [CrossRef]
9. Lee, S.H.; Park, G.W.; Kim, H.J.; Chung, K.; Jang, K.S. Effects of Filler Functionalization on Filler-Embedded Natural Rubber/Ethylene-Propylene-Diene Monomer Composites. *Polymers* **2022**, *14*, 3502. [CrossRef]
10. Farida, E.; Bukit, N.; Ginting, E.M.; Bukit, B.F. The effect of carbon black composition in natural rubber compound. *Case Stud. Therm. Eng.* **2019**, *16*, 100566. [CrossRef]
11. Mekbuntoon, P.; Kongpet, S.; Kaeochana, W.; Luechar, P.; Thongbai, P.; Chingsungnoen, A.; Chinnarat, K.; Kaewnisai, S.; Harnchana, V. The Modification of Activated Carbon for the Performance Enhancement of a Natural-Rubber-Based Triboelectric Nanogenerator. *Polymers* **2023**, *15*, 4562. [CrossRef]
12. Cifriadi, A.; Sugita, P.; Wismogroho, A.S.; Kemala, T.; Nikmatin, S.; Widayatno, W.B.; Amal, M.I.; Jayadi; Firdharini, C.; Kinasih, N.A. Development and Characterization of Biomass-Based Biocarbon Fillers for Natural Rubber Composites. *Int. J. Technol.* **2025**, *16*, 982–992. [CrossRef]
13. Adduci, R.; Vermaut, M.; Perrelli, M.; Cosco, F.; Vanpaemel, S.; Naets, F.; Mundo, D. A review of bushing modelling approaches for MultiBody simulations. *Mech. Mach. Theory* **2024**, *191*, 105496. [CrossRef]
14. Guo, P.; Li, J.; Lin, Z.; Lin, J. Analysis and Optimization of Driveline Bushing for Lateral Ride Vibration under Shock Excitation. *Appl. Sci.* **2021**, *11*, 2647. [CrossRef]
15. Ambarev, K.; Taneva, S. A Comparative Study of Vibrations in Front Suspension Components Using Bushings Made from Different Materials. *Eng. Proc.* **2025**, *100*, 42. [CrossRef]
16. Dadkhah, M.; Messori, M. A comprehensive overview of conventional and bio-based fillers for rubber formulations sustainability. *Mater. Today Sustain.* **2024**, *27*, 100886. [CrossRef]
17. Mokhothu, T.H.; John, M.J. Bio-based fillers for environmentally friendly composites. *Handb. Compos. Renew. Mater.* **2017**, *1–8*, 243–270. [CrossRef]
18. Wang, L.; Li, Q.; Jin, H.; Wang, J.; Wang, N.; Zhou, X. Research progress of bio-filler and its application in asphalt materials: Review and discussion. *Clean Technol. Environ. Policy* **2025**. [CrossRef]
19. Kiran, M.D.; Govindaraju, H.K.; Jayaraju, T.; Kumar, N. Review-Effect of Fillers on Mechanical Properties of Polymer Matrix Composites. *Mater. Today Proc.* **2018**, *5*, 22421–22424. [CrossRef]
20. Haslilywaty, G.; Siti Fatma, A.K.; Roslim, R.; Mohibbah, M.; Jefri, J. Effect of bio fillers on mechanical properties of natural rubber latex films. *Key Eng. Mater.* **2019**, *797*, 249–254. [CrossRef]
21. Joshi, M.; Dwivedi, C.; Manjare, S. A renewable cellulose-rich biofiller material extracted from waste banana stem fibers for reinforcing natural rubber composites. *J. Mater. Sci.* **2024**, *59*, 519–534. [CrossRef]
22. Tong, H.S.; Kabeb, S.M.; Abd Hamid, H.; Zulkifli, F.H. A review of biodegradability of natural rubber products: Physicochemical, thermal and mechanical properties. *Int. J. Biol. Macromol.* **2025**, *318*, 144973. [CrossRef] [PubMed]
23. Thomas, S.K.; Parameswaranpillai, J.; Krishnasamy, S.; Begum, P.M.S.; Nandi, D.; Siengchin, S.; George, J.J.; Hameed, N.; Salim, N.V.; Sienkiewicz, N. A comprehensive review on cellulose, chitin, and starch as fillers in natural rubber biocomposites. *Carbohydr. Polym. Technol. Appl.* **2021**, *2*, 100095. [CrossRef]
24. Sahu, N. Walnut Shells ' Potential Use as Biofillers in Natural Rubber Composites. *Int. J. Polym. Sci. Eng.* **2024**, *10*, 1–5.
25. Kumar Mishra, R.; Singh, B.; Acharya, B. A comprehensive review on activated carbon from pyrolysis of lignocellulosic biomass: An application for energy and the environment. *Carbon Resour. Convers.* **2024**, *7*, 100228. [CrossRef]
26. Eguare, K.O.; Ekabafe, L.O.; Ayo, M.D. Comparative Study of Acetylated Sawdust Powder as Filler in Natural Rubber Compounding. *NIPES—J. Sci. Technol. Res.* **2020**, *2*, 78–84.
27. Negara, D.N.K.P.; Nindhia, T.G.T.; Kencanawati, C.I.P.K.; Suriadi, I.G.A.K.; Widiyarta, I.M.; Lokantara, I.P.; Budiarsa, I.N. The Effect of Carbonisation Heating Rates on the Properties of N-Doped Teak Sawdust Waste Activated Carbon. *J. Phys. Sci.* **2023**, *34*, 1–20. [CrossRef]
28. Wang, A.; Wang, H.; Ling, C.; Wang, T.; Li, F.; Yang, S.; Zhao, M. Fatigue life prediction of rubber suspension bushings based on virtual road load spectrum pulses. *Results Eng.* **2024**, *23*, 102693. [CrossRef]
29. Fan, Y.; Fowler, G.D.; Zhao, M. The past, present and future of carbon black as a rubber reinforcing filler—A review. *J. Clean. Prod.* **2020**, *247*, 119115. [CrossRef]
30. Calaf-Chica, J.; Cea-González, V.; García-Tárrago, M.J.; Gómez-Gil, F.J. Fractional viscoelastic models for the estimation of the frequency response of rubber bushings based on relaxation tests. *Results Eng.* **2023**, *20*, 101465. [CrossRef]
31. Ying, D.; Addimulam, S. Innovative Additives for Rubber: Improving Performance and Reducing Carbon Footprint. *Asia Pac. J. Energy Environ.* **2022**, *9*, 81–88. [CrossRef]

32. Mohamad Aini, N.A.; Othman, N.; Hussin, M.H.; Sahakaro, K.; Hayeemasae, N. Lignin as Alternative Reinforcing Filler in the Rubber Industry: A Review. *Front. Mater.* **2020**, *6*, 329. [CrossRef]
33. Oladimeji, T.E.; Odunoye, B.O.; Elehinafe, F.B.; Obanla, O.R.; Odunlami, O.A. Production of activated carbon from sawdust and its efficiency in the treatment of sewage water. *Heliyon* **2021**, *7*, e05960. [CrossRef]
34. Gong, Y.; Chen, X.; Wu, W. Application of fourier transform infrared (FTIR) spectroscopy in sample preparation: Material characterization and mechanism investigation. *Adv. Sample Prep.* **2024**, *11*, 100122. [CrossRef]
35. Nguyen, V.H.; Nguyen, D.T.; Nguyen, T.T.; Nguyen, H.P.T.; Khuat, H.B.; Nguyen, T.H.; Tran, V.K.; Woong Chang, S.; Nguyen-Tri, P.; Nguyen, D.D.; et al. Activated carbon with ultrahigh surface area derived from sawdust biowaste for the removal of rhodamine B in water. *Environ. Technol. Innov.* **2021**, *24*, 101811. [CrossRef]
36. Candau, N.; Fernández Navarrete, A.; Lara Casanova, G.; Utrera-Barrios, S.; Hernandez Santana, M.; Stoclet, G.; Maspoch, M.L. Control by the curing time of the strain induced crystallization and elastocaloric properties in natural rubber and natural/waste rubber blends. *Polymers* **2024**, *312*, 127628. [CrossRef]
37. Poyraz, B. Poly(ethylene-co-(acrylic acid)) and maleic anhydride effect on micro crystalline cellulose and lignin-filled EPDM automotive sealing profiles. *Int. J. Biol. Macromol.* **2025**, *297*, 139602. [CrossRef]
38. Liu, X.; Qi, R.; Liao, W.; Dai, B.; Liu, D.; Wang, Q. Shear-sensing characteristics and theoretical model analysis of multiwalled carbon nanotube/natural rubber composite. *Compos. Commun.* **2025**, *53*, 102215. [CrossRef]
39. Methods, S.T. D395-14: Standard Test Methods for Rubber Property—Compression Set 1. *Current* **2003**, *9*, 1–6. [CrossRef]
40. *ASTM D471-16a*; Standard Test Method for Rubber Property—Effect of Liquids. ASTM—Amereican Society for Testing and Materials: West Conshohocken, PA, USA, 2021; pp. 1–16.
41. Darko, C. The link between swelling ratios and physical properties of EPDM rubber compound having different oil amounts. *J. Polym. Res.* **2022**, *29*, 325. [CrossRef]
42. Joselin, J.; Benila, B.S.; Brintha, T.S.S.; Jeeva, S. Phytochemical profiling, FT-IR spectroscopy, and antioxidant evaluation of select Lamiaceae species. *Intell. Pharm.* **2025**, *3*, 111–117. [CrossRef]
43. Rosson, E.; Sgarbossa, P.; Mozzon, M.; Venturino, F.; Bogialli, S.; Glisenti, A.; Talon, A.; Moretti, E.; Carturan, S.M.; Tamburini, S.; et al. Novel correlations between spectroscopic and morphological properties of activated carbons from waste coffee grounds. *Processes* **2021**, *9*, 1637. [CrossRef]
44. Yang, S.Y.; Bai, B.C.; Kim, Y.R. Effective Surface Structure Changes and Characteristics of Activated Carbon with the Simple Introduction of Oxygen Functional Groups by Using Radiation Energy. *Surfaces* **2024**, *7*, 12–25. [CrossRef]
45. Ilić, M.; Haegel, F.H.; Lolić, A.; Nedić, Z.; Tosti, T.; Ignjatović, I.S.; Linden, A.; Jablonowski, N.D.; Hartmann, H. Surface Functional Groups and Degree of Carbonization of Selected Chars from Different Processes and Feedstock. *PLoS ONE* **2022**, *17*, e0277365. [CrossRef] [PubMed]
46. Nakamura, S.; Tsuji, Y.; Yoshizawa, K. Role of Hydrogen-Bonding and OH-πInteractions in the Adhesion of Epoxy Resin on Hydrophilic Surfaces. *ACS Omega* **2020**, *5*, 26211–26219. [CrossRef] [PubMed]
47. Saito, K.; Xu, T.; Ishikita, H. Correlation between C●O Stretching Vibrational Frequency and p KaShift of Carboxylic Acids. *J. Phys. Chem. B* **2022**, *126*, 4999–5006. [CrossRef]
48. Kingkohyao, N.; Boonsiri, T.; Johns, J.; Nip, R.L.; Nakaramontri, Y. Synergistic effect of zinc ions from tire waste and modified zinc oxide on mechanical, thermo-mechanical and antibacterial properties in epoxidized natural rubber composites. *Ind. Crops Prod.* **2025**, *225*, 120577. [CrossRef]
49. Qiu, C.; Jiang, L.; Gao, Y.; Sheng, L. Effects of oxygen-containing functional groups on carbon materials in supercapacitors: A review. *Mater. Des.* **2023**, *230*, 111952. [CrossRef]
50. Hiranobe, C.T.; Ribeiro, G.D.; Torres, G.B.; Dos Reis, E.A.P.; Cabrera, F.C.; Job, A.E.; Paim, L.L.; Dos Santos, R.J. Cross-linked density determination of natural rubber compounds by different analytical techniques. *Mater. Res.* **2021**, *24* (Suppl. S1), e20210041. [CrossRef]
51. Wang, Y.; Su, S.; Liu, H.; Wang, R.; Liao, L.; Peng, Z.; Li, J.; Wu, H.; He, D. Effect of Proteins on the Vulcanized Natural Rubber Crosslinking Network Structure and Mechanical Properties. *Polymer* **2024**, *16*, 2957. [CrossRef]
52. Yan, Z.; Zaoui, A.; Zaïri, F. Physical and mechanical properties of vulcanized and filled rubber at high strain rate. *Chin. J. Phys.* **2023**, *86*, 12–23. [CrossRef]
53. Naik, P.; Pradhan, S.; Sahoo, P.; Acharya, S.K. Effect of filler loading on mechanical properties of natural carbon black reinforced polymer composites. *Mater. Today Proc.* **2019**, *26*, 1892–1896. [CrossRef]
54. Aboughaly, M.; Babaei-Ghazvini, A.; Dhar, P.; Patel, R.; Acharya, B. Enhancing the Potential of Polymer Composites Using Biochar as a Filler: A Review. *Polymer* **2023**, *15*, 3981. [CrossRef] [PubMed]
55. Sivaselvi, K.; Varma, V.S.; Harikumar, A.; Jayaprakash, A.; Sankar, S.; Krishna, C.Y.; Gopal, K. Improving the mechanical properties of natural rubber composite with carbon black (N220) as filler. *Mater. Today Proc.* **2020**, *42*, 921–925. [CrossRef]
56. Li, G.; Iakunkov, A.; Boulanger, N.; Lazar, O.A.; Enachescu, M.; Grimm, A.; Talyzin, A.V. Activated carbons with extremely high surface area produced from cones, bark and wood using the same procedure. *RSC Adv.* **2023**, *13*, 14543–14553. [CrossRef]

57. Ma, F.; Ding, S.; Ren, H.; Liu, Y. Sakura-based activated carbon preparation and its performance in supercapacitor applications. *RSC Adv.* **2019**, *9*, 2474–2483. [CrossRef]
58. Alfatah, T.; Mistar, E.M.; Supardan, M.D. Porous structure and adsorptive properties of activated carbon derived from Bambusa vulgaris striata by two-stage KOH/NaOH mixture activation for Hg^{2+} removal. *J. Water Process Eng.* **2021**, *43*, 102294. [CrossRef]
59. Mumtaz, N.; Li, Y.; Artiaga, R.; Farooq, Z.; Mumtaz, A.; Guo, Q.; Nisa, F.U. Fillers and methods to improve the effective (out-plane) thermal conductivity of polymeric thermal interface materials—A review. *Heliyon* **2024**, *10*, e25381. [CrossRef]
60. Ren, X.; Barrera, C.S.; Tardiff, J.L.; Gil, A.; Cornish, K. Liquid guayule natural rubber, a renewable and crosslinkable processing aid in natural and synthetic rubber compounds. *J. Clean. Prod.* **2020**, *276*, 122933. [CrossRef]
61. Gobetti, A.; Cornacchia, G.; La Monica, M.; Zacco, A.; Depero, L.E.; Ramorino, G. Assessment of the influence of electric arc furnace slag as a non-conventional filler for Nitrile Butadiene Rubber. *Results Eng.* **2023**, *17*, 100987. [CrossRef]
62. Hu, Y.; Cai, Y.; Wei, J.; Yin, Z.; Fan, H. Design and preparation of novel silicon rubber with homogeneous crosslinking network and its application in high-performance SR/EPDM blend. *Eur. Polym. J.* **2023**, *198*, 112381. [CrossRef]
63. Kratina, O.; Pöschl, M.; Stoček, R. The effect of apparent density of sulfidic crosslink and their chemical nature on self-heat build-up in carbon black filled Natural Rubber under cyclic mechanical loading. *Polym. Degrad. Stab.* **2024**, *227*, 110871. [CrossRef]
64. Wu, J.; Chen, L.; Su, B.L.; Wang, Y.S. Evolution of Payne effect of silica-filled natural rubber in curing process. *J. Rubber Res.* **2019**, *22*, 127–132. [CrossRef]
65. Lubura, J.; Kočková, O.; Strachota, B.; Bera, O.; Pavlova, E.; Pavličević, J.; Ikonić, B.; Kojić, P.; Strachota, A. Natural Rubber Composites Using Hydrothermally Carbonized Hardwood Waste Biomass as a Partial Reinforcing Filler—Part II: Mechanical, Thermal and Ageing (Chemical) Properties. *Polymer* **2023**, *15*, 2397. [CrossRef]
66. Ajay, C.; Das Gupta, S.; Mukhopadhyay, R.; Chattopadhyay, D.; Das, M. Exploring crosslink density in rubber vulcanisates—A comprehensive analysis using a dynamic mechanical analyser and an insight into mechanical properties. *J. Rubber Res.* **2025**, *28*, 305–323. [CrossRef]
67. Wang, W.; Yu, X.; Lai, C.; Li, G.; Zhu, P.; Sun, R. Systematic study of the effect of silane coupling agent on the hydrothermal aging resistance of the underfill epoxy resin and silica interface via molecular dynamics simulation. *Appl. Surf. Sci.* **2025**, *688*, 162313. [CrossRef]
68. Wei, Y.; Jia, X.; Chen, Y.; Ji, J. Single step carbonating and activating fir sawdust to activated carbon by recyclable molten carbonates and steam. *Sci. Total Environ.* **2022**, *818*, 151778. [CrossRef]
69. Xiao, J.; Zhang, Z.; Luan, Y.; Wu, S.; Wu, Y. Influence of carbon black surface characteristics on CB-NR interfacial interaction: Molecular simulation and experimental study. *Compos. Part A Appl. Sci. Manuf.* **2024**, *182*, 108198. [CrossRef]
70. Azura, A.R.; Leow, S.L. Effect of carbon black loading on mechanical, conductivity and ageing properties of Natural Rubber composites. *Mater. Today Proc.* **2019**, *17*, 1056–1063. [CrossRef]
71. Głowacka, K.; Klemenc, J.; Nagode, M.; Łagoda, T. Fatigue lifetime of rubber composites—State-of-the-art. *Polym. Test.* **2025**, *143*, 108713. [CrossRef]
72. Sultana, S.; Munna, N.; Sakib, T.U.; Ahmed, N.; Akanda, M.R.; Saha, M.S.; Zaman, M.N. High performance activated carbon derived from sawdust: Preparation, characterizations, methyl orange removal and kinetics investigation. *Biomass Convers. Biorefinery* **2025**, *15*, 17295–17307. [CrossRef]
73. Samal, S. Effect of shape and size of filler particle on the aggregation and sedimentation behavior of the polymer composite. *Powder Technol.* **2020**, *366*, 43–51. [CrossRef]
74. Sittitanadol, I.O.; Srakeaw, N.L.O.; Somdee, P.; Chumsamrong, P.; Noyming, S.; Singsang, W.; Prasoetsopha, N. Utilizing Coconut Biochar as a Bio-reinforcing Agent in Natural Rubber Composites. *Starch/Staerke* **2024**, *77*, 2400168. [CrossRef]
75. Chen, Q.; Yang, K.; Feng, Y.; Liang, L.; Chi, M.; Zhang, Z.; Chen, X. Recent advances in thermal-conductive insulating polymer composites with various fillers. *Compos. Part A Appl. Sci. Manuf.* **2024**, *178*, 107998. [CrossRef]
76. Kartal, İ.; Karagöz, İ. Enhancing natural rubber properties: A comprehensive study on the synergistic effects of wood sawdust and carbon black as fillers in rubber composites. *Polym. Bull.* **2025**, *82*, 2091–2109. [CrossRef]
77. Amoke, A.; Tenebe, O.G.; Ayo, M.D. Comparison of Mechanical Properties of Natural Rubber Vulcanizates Filled with Hybrid Fillers (Carbon Black/Palm Kernel Shell and Palm Kernel Shell/Sandbox Seed Shell). *Int. J. Res. Innov. Appl. Sci.* **2021**, *6*, 2454–6194.
78. He, S.; Zhang, F.; Liu, S.; Cui, H.; Chen, S.; Peng, W.; Chen, G.; Liao, X.; Liao, L. Influence of sizes of rubber particles in latex on mechanical properties of natural rubber filled with carbon black. *Polymer* **2022**, *261*, 125393. [CrossRef]
79. Li, X.; Ding, Y.; Zhang, H.; He, T.; Hao, J.; Wu, J.; Wu, Y.; Bai, H. Pine sawdust derived ultra-high specific surface area activated carbon: Towards high-performance hydrogen storage and supercapacitors. *Int. J. Hydrogen Energy* **2024**, *84*, 623–633. [CrossRef]
80. Bernal-Ortega, P.; Bernal, M.M.; González-Jiménez, A.; Posadas, P.; Navarro, R.; Valentín, J.L. New insight into structure-property relationships of natural rubber and styrene-butadiene rubber nanocomposites filled with MWCNT. *Polymer* **2020**, *201*, 122604. [CrossRef]

81. Wang, Z.; Wang, S.; Yu, X.; Zhang, H.; Yan, S. Study on the Use of CTAB-Treated Illite as an Alternative Filler for Natural Rubber. *ACS Omega* **2021**, *6*, 19017–19025. [CrossRef]
82. Buaksuntear, K.; Panmanee, K.; Wongphul, K.; Lim-arun, P.; Jansinak, S.; Shah, D.U.; Smitthipong, W. Enhancing mechanical properties and stabilising the structure of epoxide natural rubber using non-covalent interactions: Metal–ligand coordination and hydrogen bonding. *Polymer* **2024**, *291*, 126626. [CrossRef]
83. Mensah, B.; Onwona-Agyeman, B.; Nsaful, F.; Aboagye, I.A.; Sowah, N.L.; Angnunavuri, P.N.; Apalangya, V.A. Vulcanization kinetics and reinforcement behaviour of natural rubber-carbon black composites: Addition of Shea-butter versus aromatic oil as plasticizers. *Heliyon* **2024**, *10*, e25592. [CrossRef]
84. Zedler, L.; Colom, X.; Cañavate, J.; Saeb, M.R.; Haponiuk, J.T.; Formela, K. Investigating the impact of curing system on structure-property relationship of natural rubber modified with brewery by-product and ground tire rubber. *Polymer* **2020**, *12*, 545. [CrossRef]

polymers

MDPI

Article

Reduction in Sulfur Diffusion in Recycled Ground Rubber-Containing Compounds to Improve Tensile Strength †

Stefan Frosch [1,*], Volker Herrmann [1], Fabian Grunert [2] and Anke Blume [2]

[1] Faculty of Plastics Engineering and Surveying, Technical University of Applied Sciences Würzburg-Schweinfurt, 97070 Würzburg, Germany
[2] Elastomer Technology and Engineering (ETE), University of Twente, 7522 NB Enschede, The Netherlands
* Correspondence: stefan.frosch@thws.de; Tel.: +49-931-3511-8522
† In memory of Irene Dürr.

Abstract

Recycling end-of-life rubber to compound components for new formulations is one of the most promising ways to reach the sustainability goals of the rubber industry. Today, devulcanization and pyrolysis are both methods to reuse crosslinked elastomers. A third recycling approach is to process end-of-life rubber into ground rubber (GR), which is then added to green compounds. However, free sulfur diffuses during mixing, storage and vulcanization from the matrix material into the GR particles. As a result, the crosslink density in the matrix is reduced, which deteriorates the in-rubber properties of GR-containing vulcanizates compared to those that do not contain GR. Therefore, GR particles are mainly used today for rubber parts with less demanding dynamic-mechanical requirements, which limits the use of the particles. This study presents an approach for reducing the sulfur diffusion from the matrix into the GR particles by prevulcanizing the green matrix material. This leads to GR-containing vulcanizates with significantly improved mechanical properties. This new approach shows that the quality of the recycled rubber product can be significantly increased by blocking the sulfur diffusion. Even though such prevulcanization is currently only feasible under laboratory conditions, it might also pave the way for finding solutions in a production scale for an effective incorporation of GR into new rubber compounds.

Keywords: rubber; ground rubber; rubber recycling; sulfur diffusion; prevulcanization; crosslink density

1. Introduction

In terms of sustainability and the circular economy, the rubber industry is seeking ways to reduce energy consumption and CO_2 emissions in the manufacturing of rubber products. Recycling plays a key role in achieving such a reduction. Efforts are being made to further process polymer material from end-of-life tires (ELTs) by pyrolysis [1,2], devulcanization [3,4] or refining into ground rubber (GR) [5,6] as an additive for new products. This recycled additive reduces the absolute need for virgin material of a new vulcanizate and thus contributes to the overall goal of the circular economy. In this study, the recycling method of GR is examined in more detail, and a solution is presented to improve the tensile properties of GR-containing compounds.

To date, shredding and grinding ELTs into small particles is common practice. The size of these particles ranges roughly from diameters from 20 to 40 mm ("chips"), to 1–20 mm

("granulate"), and down to 0–0.4 mm ("powder") [7]. In this study, GR is referred to as particles with diameters between 0.2 and 2 mm, as previous measurements [8] have shown.

The incorporation of GR particles into green rubber during compounding is an approach for recycling the polymer fraction of ELTs. However, the properties of GR-containing vulcanizates are deteriorated in comparison to those that do not contain the recycled material [9–16]. The main reason for this effect is the diffusion of sulfur from the surrounding green matrix into the GR particles [9,14,15,17–19]. This diffusion out of the uncured compound leads to a reduction of the sulfur concentration in the matrix and consequently to a reduction in crosslink density (CLD) within the matrix [19,20]. At the same time, the sulfur concentration increases in the GR particles, which leads to particles with a higher CLD [19,20]. This diffusion effect causes an inhomogeneous vulcanizate in terms of different local sulfur concentrations and thus different local viscoelastic properties [19]. The combination of stiff GR particles in a flexible matrix is therefore responsible for the deteriorated in-rubber behavior of the vulcanizate.

It could be shown in [19] that the concentration difference of free, i.e., not covalently bound soluble sulfur (cyclo-S_8) between the matrix and GR particles is the driving force of the curative diffusion, as the concentration of free cyclo-S_8 is high in the green matrix. In contrast, the concentration of free cyclo-S_8 is low in the GR particles because these are vulcanized, and thus the sulfur is covalently bound. When GR is incorporated into the green matrix compound, free cyclo-S_8 diffuses from the matrix into the GR particles to reestablish a concentration equilibrium of free cyclo-S_8 in both phases. The diffusion ends when both phases contain the same amount of free cyclo-S_8. However, the diffusion also ends with the start of the vulcanization process in both phases. This also explains why the sulfur diffusion from the matrix into the GR particles is even more pronounced when the scorch time of the GR is shorter than that of the surrounding matrix: with a short scorch time of the GR, the sulfur diffuses from the surrounding matrix into the GR until final vulcanization, as the sulfur is only bound in the matrix at a later stage. Thus, the concentration difference of free cyclo-S_8 between matrix and GR is maintained until the vulcanization also starts in the matrix, which significantly reduces sulfur diffusion.

Phadke et al. [15,18] developed an approach for counteracting the effects of sulfur diffusion. They achieved higher sulfur concentrations in the vulcanized matrix by increasing the amount of both the sulfur and the also mobile accelerator in the green matrix compound before crosslinking. Sulfur diffusion continues to occur, as described above. However, the increased sulfur content in the matrix led to a higher sulfur equilibrium between both the matrix and GR particles. As the matrix became supersaturated with sulfur, it continued to release it through diffusion. However, due to the overall high sulfur concentration, the matrix retained a sufficient amount of sulfur. A satisfactory CLD in the matrix thus was formed and the deterioration of in-rubber properties of the entire vulcanizate is less severe. Until today, this method is a good way to counteract the negative influence due to the incorporation of GR particles [6,19,21].

Therefore, this technique is a first step in reducing the detrimental effects of sulfur diffusion. Nevertheless, sulfur enrichment in the GR continues to reduce the homogeneity between matrix and GR particles with respect to e.g., CLD. Furthermore, the use of a sulfur supersaturated matrix has the disadvantage of allowing diffusion to proceed unimpeded. For example, GR particle solubility and crosslinking kinetics will alter if its compound formulation changes. Thus, for every variation in GR type and quantity, the sulfur concentration may need to be adjusted. Determining the ideal ratio between GR quantity and sulfur supersaturated matrix requires long and laborious preliminary testing [19].

To minimize the deterioration of the properties of GR-containing vulcanizates, it therefore seems more appropriate to prevent sulfur diffusion. Three approaches were

investigated in [19]. It could be shown that a sulfur donor system does not lead to reduced sulfur diffusion during vulcanization conditions. In contrast, the use of polymeric sulfur could significantly reduce the diffusion of sulfur during mixing and storage conditions. However, during the vulcanization process, the polymeric sulfur converts back into free cyclo-S_8 and thus leads to a diffusion behavior similar to that described above.

The third approach, however, showed promising results in reducing sulfur diffusion and thus increasing the in-rubber properties of GR-containing vulcanizates. It was shown that sulfur diffusion mainly occurs during mixing, storage and the scorch time of the curing process due to the elevated temperatures. At the same time, it was demonstrated that sulfur diffusion is mainly limited to the pure form of free cyclo-S_8. In contrast, sulfur species in combination with ZnO, stearic acid or accelerators are significantly less mobile in the elastomeric matrix. These species can be, e.g., ZnS or the active sulfurating agent complex that are formed during mixing and the scorch time of the crosslinking process [19].

For these reasons, the idea of prevulcanization of the matrix before the incorporation of GR particles was introduced. The current process thus enables the pure cyclo-S_8 to diffuse from the matrix into the GR particles during mixing, storage and vulcanization processes. In contrast, large proportions of the added free cyclo-S_8 are first converted into a less mobile sulfur species in the matrix during prevulcanization, as explained above. The reduced mobility of the sulfur-containing species is expected to lead to less sulfur diffusion from the matrix into the subsequently incorporated GR particles. This hypothesis of prevulcanization will be investigated in the following sections.

2. Materials and Methods

For the following investigations, the same experimental approach was used as already described in previous publications [19,20,22]. In total, the same compounds were produced five times together with the previous work cited and all vulcanization curves were compared with each other, so that in each case a very good match could be established and reproducibility was ensured.

2.1. Process Chain Overview

The entire process chain, from compounding to the finished test specimens, is illustrated in Figure 1. First, the natural rubber (NR, red) and styrene–butadiene rubber (SBR, blue) compounds are produced separately in mixing step 1. The vulcanization properties at 155 °C of both compounds are then determined in the rubber process analyzer (RPA). With this vulcanization information, the NR compound (red) is vulcanized to t_{95} and formed into 6 mm thick sheets (130 mm × 117 mm). The NR sheets are then converted into GR in a mill, as described in [8]. This material is thus defined as "NR-GR". Alternatively, the SBR compound (blue) is prevulcanized to the vulcanization time t_x with $x < 10$ in the available heating press to 6 mm thick sheets. This prevulcanization of the matrix compound is the only difference to the current state of the art in processing GR. To date, the GR is incorporated into a non-prevulcanized matrix. The material pairing of NR-GR in an SBR matrix was chosen because [19] showed that sulfur diffusion is pronounced in this material combination, since t_{95} of the NR-GR material is 4 times lower than that of the surrounding SBR matrix material.

In mixing step 2, the NR-GR is incorporated into the prevulcanized SBR matrix on a two-roll mill. The crosslinking characteristics of the new compound (red-and-blue-colored arrows) are then determined again in the RPA. With this information, rubber sheets with a thickness of 2 and 6 mm are vulcanized to t_{95}. These sheets are converted into test specimens for the following examinations.

The following sections describe the separate production steps and the equipment used in more detail.

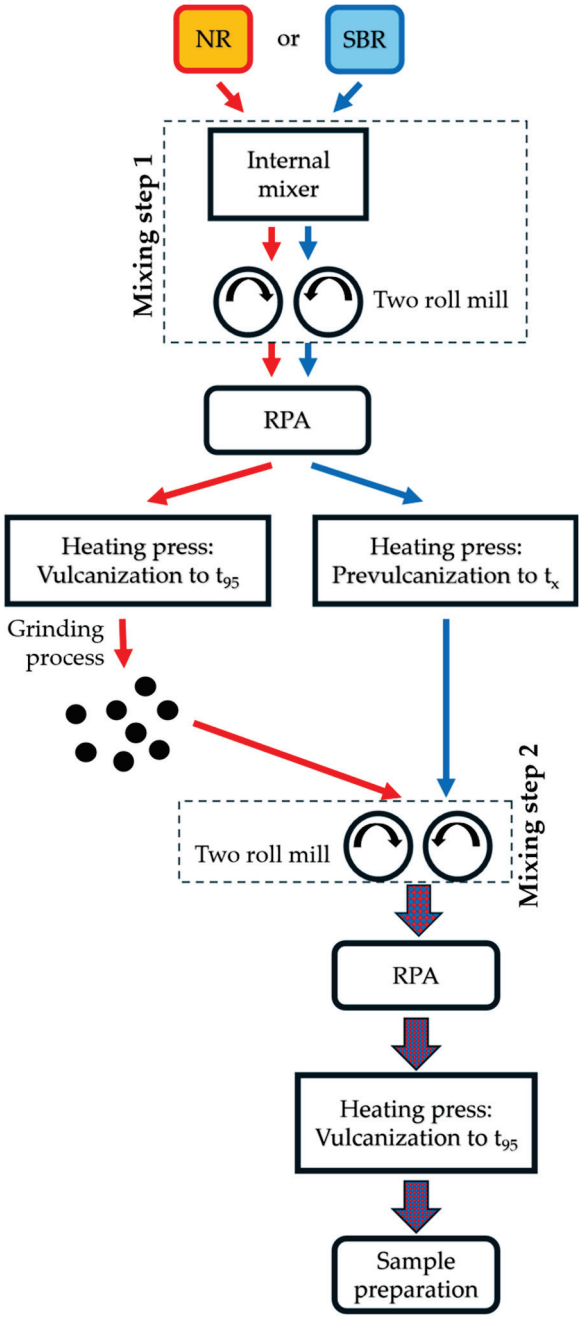

Figure 1. Process chain overview.

2.2. Compound Formulations and Mixing Conditions

This study investigates the diffusion behavior of soluble sulfur between the SBR matrix and the NR-GR material. The formulations, as well as the names and manufacturing companies of the individual compound components, are depicted in Table 1. The NR vulcanizate was manufactured to be subsequently converted into GR and then to be incorporated into compounds of SBR. In total, three SBR compounds were manufactured, each prevulcanized to different t_x. Details are explained in the following table.

Table 1. Compound formulations; all values are given in parts per hundred rubber (phr), adapted from [20].

	NR	SBR	Name	Company
NR	100	-	SIR 20	Weber & Schaer GmbH & Co. KG, Hamburg, Germany
E-SBR	-	100	Buna SE 1502 L	Arlanxeo Deutschland GmbH, Cologne, Germany
N330	50	50	Corax N330	Orion Engineered Carbons S.A., Eschborn, Germany
ZnO	5	5	Zinkoxid Rotsiegel	L. Brüggemann GmbH & Co. KG, Heilbronn, Germany
Stearic acid	3	3	Palmera B1804	KLK Emmerich GmbH, Emmerich am Rhein, Germany
Soluble sulfur	1.2	1.2	K46859483 542	Merck Chemicals GmbH, Darmstadt, Germany
CBS	1.2	1.2	Vulkacit CZ/EG-C	Lanxess Deutschland GmbH, Krefeld, Germany

The compound components described in Table 1 were mixed in mixing step 1 using an internal mixer (Werner & Pfleiderer, 1.5 l, PES3) and a laboratory mill (Schwabenthan 200 × 450). Mixing step 1 is a two-stage mixing process, divided into the preparation of the base and the final compounds. An overview of the mixing sequence and the key parameters of the base compounds can be found in Table 2. Prior to the compounding of the base compounds, 1 kg of the NR is masticated in the internal mixer for 20 min at 20 rpm and 25 °C.

Table 2. Production procedure of base compounds of mixing step 1 [19].

Time/Min	Processing Step of Base Compounds
0	Polymer
1	ZnO, stearic acid, carbon black
2.5	Cleaning step
4.5	Dump
	Weight check
	Sheeted off on laboratory mill (both rollers 20 rpm, gap 2.5 mm, 40 °C) for 1 min. Relaxation for 1 h.

Table 3 depicts manufacturing details of the final compounds of mixing step 1.

Table 3. Production procedure of final compounds of mixing step 1 [19].

Time/Min	Processing Step of Final Compounds
0	Base compound, sulfur, accelerator
3	Dump
	Weight check
	Sheeted off on laboratory mill (front roller 16 rpm, back roller 20 rpm gap 2.0 mm, 40 °C)
0	Final compound on laboratory mill
1	Cutting three times left and right, roll up and blend back at a gap of 1 mm
4	Gap: 2.5 mm, both rollers at 20 rpm, dump

The NR vulcanizate was then ground in a centrifugal mill (see Section 2.4). In contrast, the SBR compounds were prevulcanized to t_x and formed into 6 mm thick sheets with dimensions of 130 mm × 117 mm. Each sheet was then cut with common rubber scissors into four stripes to increase the processability on the two-roll mill in mixing step 2.

In the latter compounding process, 30 phr of NR-GR was incorporated on the two-roll mill into the prevulcanized SBR matrix (see mixing step 2 in Figure 1). This compound

is referred to as "SBR&NR-GR" in the remainder of this article. Table 4 describes the compound constituents of SBR&NR-GR in detail.

Table 4. Compound formulation for mixing step 2: addition of 30 phr NR-GR into a prevulcanized SBR-matrix; all values are given in phr.

	SBR&NR-GR	
E-SBR	100	Prevulcanized to t_x with x < 10; cut into 6 mm thick stripes
N330	50	
ZnO	5	
Stearic acid	3	
Soluble sulfur	1.2	
CBS	1.2	
NR-GR	30	

The procedure of incorporating 30 phr NR-GR into a prevulcanized SBR-matrix in mixing step 2 is displayed in Table 5.

Table 5. Production procedure for mixing step 2.

Time/Min	**Processing Step of SBR&NR-GR**
	Laboratory mill (both rollers 20 rpm, gap 6 mm, 40 °C)
0	Start feeding stripes of the prevulcanized SBR compound onto both rollers
5	All stripes are incorporated; reduction of gap to 2.5 mm
6	Friction: front roller at 16 rpm, back roller at 20 rpm
7	Reduction of gap to 2.0 mm
8	Friction: front roller to 20 rpm, back roller to 16 rpm
9	Cutting two times left and right
10	Adding 30 phr ground rubber
14	3 x roll up and blend back at gap of 1.0 mm
15	Both rollers at 20 rpm, gap of 2.0 mm, dump

2.3. Vulcanization Behavior

Subsequent to mixing steps 1 and 2, specimens were cut from the compound sheets with the SIS-VS punch press from TA Instruments (New Caste, Delaware, USA, former Scarabaeus) for the following investigations with the RPA. The latter is a SIS V50 from TA Instruments (former Scarabaeus) and was used to determine the curing behavior of all samples at 155 °C, with a frequency of 1.667 Hz and an oscillation angle amplitude of 0.50° within a measurement time of 60 min. Every compound was measured three times. The rheometer was equipped with the software SQS—RPA Monitor Version 6.15.

2.4. Mill

A centrifugal mill, ZM200, from the company Retsch (Haan, Germany), with a 12 tooth rotor and a sieve with a mesh size of 2 mm was used to grind the NR at a frequency of 18.000 rpm. To prepare the samples for this grinding process, the 6 mm thick sheets of NR were cut with common rubber scissors into approximately $6 \times 6 \times 6$ mm^3 cubes. Subsequently, these cubes were cooled below their glass transition temperature (Tg) using liquid nitrogen. Then, they were placed in portions of several 10 g into the mill. In the centrifugal mill, the vulcanizate cubes were further reduced to GR. The SBR material was not ground.

2.5. Heating Press

The heating press Polystat 200 T from Servitec (Wustermark, Germany) was used to prevulcanize the SBR matrix to t_x and to vulcanize both the NR and SBR&NR-GR to t_{95}. The heating press was equipped with two molds to produce both 2 and 6 mm thick sheets with dimensions of 130 mm × 117 mm.

2.6. Micro X-Ray Fluorescence Analysis

A micro X-ray fluorescence analysis (μ-XRF) was employed to investigate areas of 10 mm × 10 mm of the vulcanized 6 mm thick sheets. This technique is used to qualify and quantify chemical elements on (rubber) surfaces in an imaging manner [22–25]. For the investigations, an M4 Tornado from Bruker Nano Analytics (Berlin, Germany) was equipped with a rhodium tube that was set to 200 μA and 50 kV. The target material was rhodium, no filter was chosen. The diameter of the X-ray beam was set to 25 μm, identical to the resolution (distance between two measurement spots). Each spot was measured three times for 40 ms. The fluorescence radiation was detected with two silicon drift detectors. To enhance the sulfur signal by eliminating the argon present in the ambient air, the sample chamber was evacuated to an absolute pressure of 20 mbar for the analysis. This was necessary, since the fluorescence energies of both elements are similar [26]. The software Esprit M4 (version: 1.6.0.286) was used to qualify and quantify the local sulfur concentrations [19].

2.7. Tensile Tests

S2 tensile test specimens were cut out of the 2 mm thick vulcanized rubber sheets using a Zwick punch press 7103 (Ulm, Germany). These specimens were then investigated using a Zwick 1474 tensile testing machine (Ulm, Germany) based on DIN 53,504 with a crosshead speed of 50 mm min^{-1}. The software Doli Test & Motion, version 4.6.0.6, was used to process the data.

2.8. Measurement Errors

For all results, mean values were calculated, which are listed in the following chapter. These mean values are presented with their measurement error, calculated using the Student's t-test with a 95% confidence interval. This means that the mean values reported in this article, including their measurement errors, are valid with a 95% probability [27,28].

3. Results

The results of the different test methods are described in the following section.

3.1. Vulcanization Behavior

The crosslinking behavior is depicted in Figure 2. The elastic torque S' in dNm is plotted over the measurement time in min. The median curves for S'_{max} from three measurements of the NR and SBR1 (one of three investigated SBR compounds) are illustrated. The NR shows a relatively short scorch time, after which S' rises to a maximum value of 16.6 ± 0.2 dNm. In the following, S' decreases again, indicating that the material shows reversion. Compound SBR1, however, behaves differently: the material reaches a plateau with a value of 16.5 ± 0.4 dNm for S'; therefore, the maximum S' values of NR and SBR1 are at an identical level, taking the measurement error into account. Furthermore, the scorch time of SBR1 is significantly longer than that of NR, although identical concentrations of sulfur and accelerator were used in both compounds. This increased scorch time could be due to the retarding effect of the added ZnO in the SBR, as described in [29]. In this article, it was found that the postulated vulcanization process described by Morrison and

Porter [30] applies to NR. In contrast, it was found that for other polymers, such as high vinyl SBR, other ring opening and vulcanization reactions occur, and that ZnO can exhibit a retarding effect in these processes. For example, sulfur can accumulate in the ZnO crystal and can therefore not participate in vulcanization reactions [31].

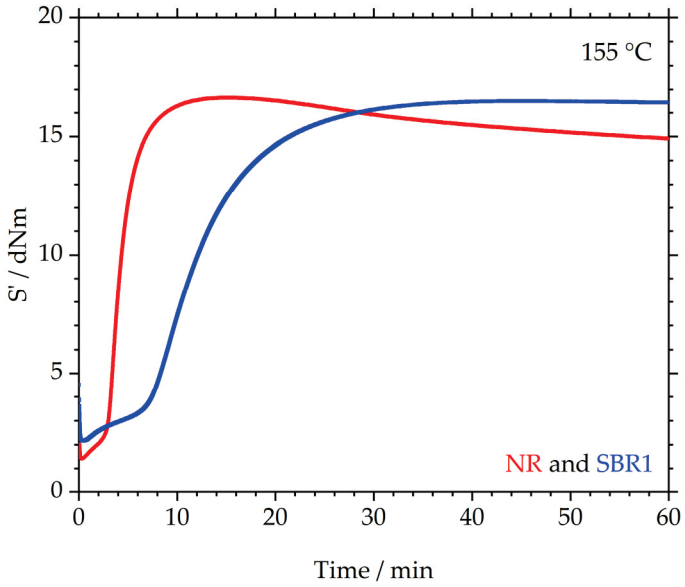

Figure 2. Crosslinking behavior of NR and SBR1: median curves (maximum of S') of three measurements each.

In Table 6, characteristic values of the RPA measurements of all analyzed samples are listed. Each compound was measured three times, with the mean values including errors for t_{10}, t_{50}, t_{95} and S'_{max} given in each case. It is evident that the NR compound cures significantly faster than the three compounds made of SBR (SBR1, SBR2 and SBR3).

Table 6. Crosslink characteristics of the investigated compounds.

Compound	t_{10}/min	t_{50}/min	t_{95}/min	S'_{max}/dNm
NR	3.0 ± 0.0	4.2 ± 0.2	8.5 ± 0.2	16.6 ± 0.2
SBR1	6.9 ± 0.6	11.7 ± 0.9	26.9 ± 3.0	16.5 ± 0.4
SBR2	7.2 ± 0.3	12.1 ± 0.5	29.2 ± 2.1	16.9 ± 0.3
SBR3	6.8 ± 0.3	11.4 ± 0.8	26.6 ± 2.9	17.1 ± 0.6
SBR_0min&NR-GR *	3.1 ± 0.1	8.6 ± 0.1	28.8 ± 1.3	11.3 ± 0.8
SBR1_2min&NR-GR	3.9 ± 0.1	8.7 ± 0.8	24.6 ± 3.7	12.0 ± 0.3
SBR2_4min&NR-GR	2.5 ± 0.1	6.3 ± 0.2	19.9 ± 0.6	12.0 ± 0.3
SBR3_6min&NR-GR	1.2 ± 0.0	4.0 ± 0.2	15.2 ± 1.6	11.6 ± 0.2

* Reference sample without prevulcanization but identical compound formulation; adapted from [12,32].

The three SBR compounds each have a t_{10} of approximately 7 min. Preliminary tests were carried out, which showed that GR could not be incorporated into t_{10} prevulcanized matrix compounds. This can be explained by the lack of viscous processing behavior of the compound because first crosslinking reactions initiated the transformation of the matrix into a vulcanizate. Accordingly, the prevulcanization time was shortened to enable the incorporation of the recycled material. Consequently, SBR1, SBR2 and SBR3 were prevulcanized to different t_x with $x < 10$. Prevulcanization times of 2, 4 and 6 min (t_2, t_5 and t_7 accordingly) were selected for SBR1, SBR2 and SBR3, before 30 phr of NR-GR was incorporated into each. The GR-containing and prevulcanized compounds are referred to as "SBR1_2min&NR-GR", "SBR2_4min&NR-GR" and "SBR3_6min&NR-GR".

Figure 3 depicts the median (S'_{max}) vulcanization curves of these three compounds. The S'-values of all three GR-containing samples settle on a plateau of approximately 12 dNm. These plateaus are approx. 4 dNm below that of SBR1, which was not prevulcanized, does not contain GR and serves as a reference here. Because the three prevulcanized specimens reach the same plateau, it appears that the degree of prevulcanization has no influence on the resulting S'_{max}. Thus, the 4 dNm difference between SBR1 and the three prevulcanized samples corresponds to the general influence of the GR. This influence is underlined by "SBR_0min&NR-GR", a sample with an identical formulation to the first three specimens. The difference from the other three samples is that the matrix was not prevulcanized before the incorporation of 30 phr of NR-GR. It is therefore a sample that represents the current manufacturing process in the rubber industry. The sample has already been examined in more detail in [12,19]; however, the results are illustrated here again because, together with those of the three prevulcanized specimens, they demonstrate the influence of prevulcanization. It is therefore evident that the reduction of S'_{max} is an effect of the addition of GR and not of prevulcanization (see also Table 6).

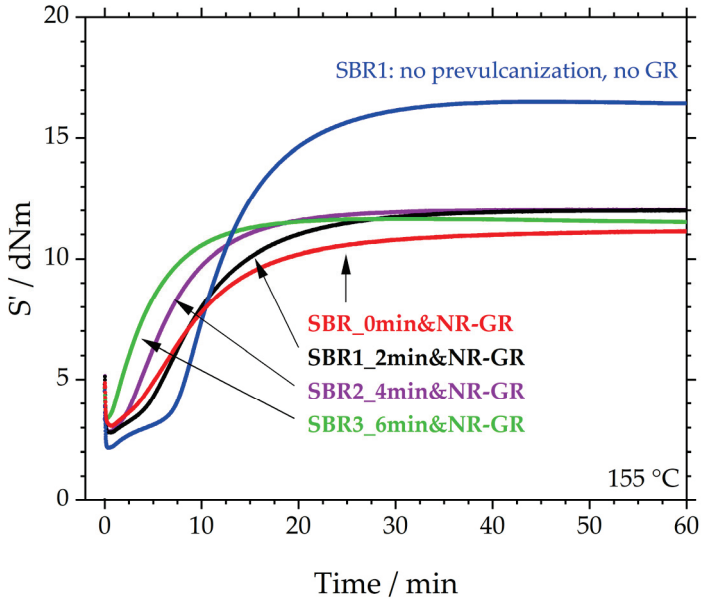

Figure 3. Crosslinking behavior of the prevulcanized and the 30 phr NR-GR-containing compounds SBR1_2min&NR-GR, SBR2_4min&NR-GR and SBR3_6min&NR-GR with the reference compounds SBR1 (compound that was not prevulcanized and does not contain GR) and SBR_0min&NR-GR (not prevulcanized but contains 30 phr NR-GR). Median curves (maximum of S') were derived from three measurements each.

In comparison, however, the scorch time decreases significantly with the degree of prevulcanization. The reactions of all three prevulcanized samples start earlier than the SBR1 reference. The scorch time is reduced with increasing prevulcanization: t_{10} decreases from 6.9 ± 0.6 min for SBR1, to 3.9 ± 0.1 min for SBR1_2min&NR-GR, 2.5 ± 0.1 min for SBR2_4min&NR-GR and 1.2 ± 0.0 min for SBR3_6min&NR-GR. This reduction in scorch time can be explained by the matrix material having already been prevulcanized, thereby initiating and interrupting scorch reactions. This scorch status is maintained during the incorporation of NR-GR and then continues at crosslinking temperatures.

The non-prevulcanized reference SBR_0min&NR-GR also exhibits a shorter scorch time compared to SBR1. This is consistent with the findings of Gibala and Hamed [14] and can be explained by the diffusion processes of accelerator fragments from the GR particles to the matrix material, speeding up vulcanization.

The comparison with SBR1 (blue) reveals that S'_{min} is higher for the other four samples. This is because each of them contains 30 phr of NR-GR, i.e., already crosslinked material, which increases the initial torque. It becomes apparent that the 6 min prevulcanized specimen (green) exhibits the highest initial torque. The possible reason for this could be that parts of the matrix had already crosslinked slightly, increasing S'_{min}.

The exact t_{10}, t_{50} and t_{95} can be found in Table 6 and in Figure 4. The latter shows t_{10}, t_{50} and t_{95} of the investigated samples from Figure 3 during the prevulcanization of the matrix material. It is evident that all three characteristic times decrease linearly as prevulcanization progresses. This reduction can be explained by the matrix material having already been prevulcanized, thereby both initiating and interrupting scorch reactions. Longer prevulcanization times of the matrix compound thus lead to shorter characteristic vulcanization times of the NR-GR-containing compounds.

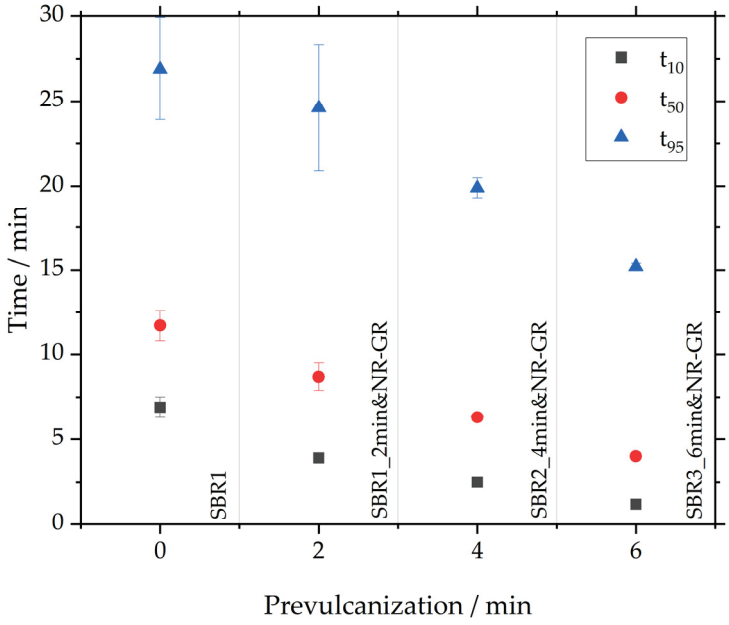

Figure 4. The influence of prevulcanization on t_{10}, t_{50} and t_{95}.

3.2. Micro X-Ray Fluorescence Analysis

Using µ-XRF, the local sulfur concentrations of the three samples with different degrees of prevulcanization SBR1_2min&NR-GR, SBR2_4min&NR-GR and SBR3_6min&NR-GR, as well as those of the non-prevulcanized reference SBR_0min&NR-GR, were determined, investigating areas of 10 mm × 10 mm. The results can be found in Figure 5.

The non-prevulcanized sample SBR_0min&NR-GR—top left in Figure 5—shows an inhomogeneous sulfur distribution because of the diffusion processes during the mixing, storage and crosslinking steps [19]. The GR particles can be identified by their green-to-red coloration. The local sulfur concentration is therefore approx. 1.8–3.5 wt%. Considering that the initial concentration according to the formulation was only 0.93 wt%, it can be concluded that the sulfur concentration in the GR particles is locally doubled to quadrupled. The reason for the sulfur enrichment is that the latter diffuses from the matrix into the GR particles due to the concentration differences in free sulfur between the matrix and GR [19]. This depletes the matrix of sulfur, which can be distinguished from the GR particles by its dark blue coloration. A sulfur concentration of approx. 0.4 wt% is achieved within the matrix, i.e., approximately halving the sulfur concentration according to the initial formulation (0.93 wt%). In [19], it is shown that the local viscoelastic properties also change with the local inhomogeneous sulfur distribution, whereby the in-rubber properties of the entire vulcanizate are deteriorated.

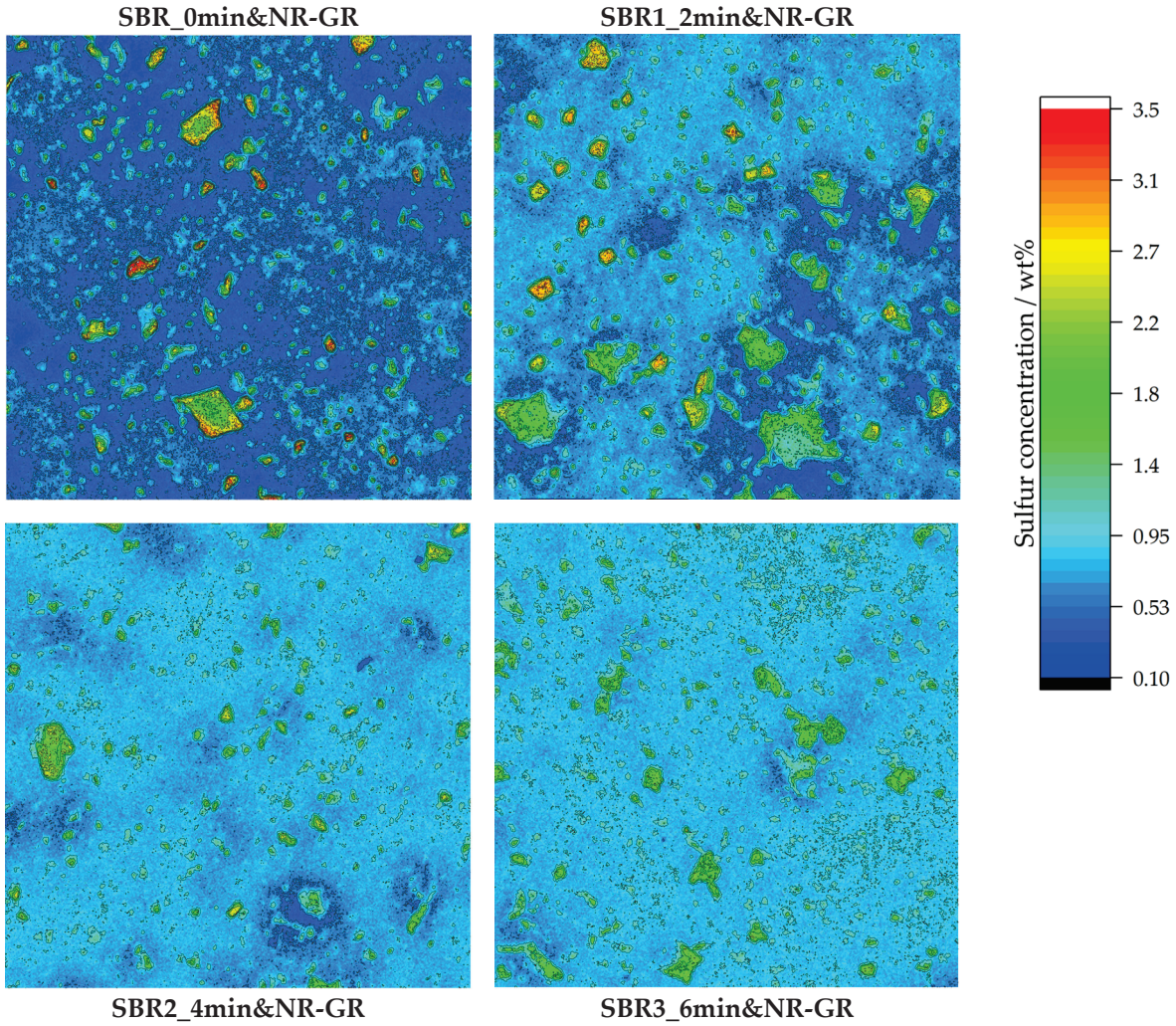

Figure 5. Local sulfur concentrations detected via μ-XRF on different vulcanizate surfaces with measurement areas of 10 mm × 10 mm for every specimen. The GR particles are identifiable by their higher sulfur concentration compared to the surrounding matrix. With increasing prevulcanization of the matrix material, the homogeneity of the sulfur distribution increases. Levels of matrix prevulcanization: 0, 2, 4 and 6 min (from top left to bottom right).

Sample SBR1_2min&NR-GR (top right in Figure 5) also shows an inhomogeneous local sulfur distribution. Higher sulfur concentrations are found in the GR particles compared to in the surrounding matrix. Compared to sample SBR_0min&NR-GR, however, it is evident that there are fewer red zones with sulfur concentrations of 3.5 wt% in the GR particles. At the same time, more GR particles are colored green, which indicates a local sulfur concentration of approx. 1.8 wt%. It is therefore clear that less sulfur accumulates in the GR particles if the matrix was prevulcanized for 2 min before incorporating the NR-GR. There are still regions in the matrix with a concentration of approximately 0.4 wt% because 2 min of prevulcanization could not fully stop the sulfur diffusion from the matrix into the GR. However, there are also areas in the matrix which, at around 0.9 wt%, are within the target range according to the compound formulation. It is therefore evident that a matrix prevulcanization of 2 min already restricts sulfur diffusion.

If the prevulcanization is extended to 4 min—bottom left in Figure 5—it reveals that sulfur diffusion is further restricted. Most GR particles are displayed in green, which corresponds to a local sulfur concentration of approx. 1.8 wt%, and thus a doubling of the initial concentration (0.93 wt%) and at the same time a halving in comparison to the concentrations of the non-prevulcanized sample (3.5 wt%). The extremely low-sulfur

zones in the matrix become steadily smaller. Most of the matrix has a sulfur content of approx. 0.75 wt%, which is closer to the target range (0.93 wt%) according to the compound formulation. Accordingly, sulfur diffusion seems to be further restricted with prolonged prevulcanization.

This trend continues with 6 min of prevulcanization (see bottom right in Figure 5). This specimen exhibits the most uniform sulfur homogeneity of all four analyzed samples. At the same time, an increased sulfur concentration is still determined in the GR particles. However, the difference from the concentration in the matrix is the lowest in this compound in comparison to all other compounds. An extension of the prevulcanization time therefore leads to a more homogeneous distribution of sulfur within the sample.

A summary of the µ-XRF investigations of the local sulfur concentration is depicted in Figure 6 in the form of distribution curves. The locally measured sulfur concentrations are plotted on the abscissa. According to the formulation, both compounds—i.e., NR and SBR—contain 0.93 wt% sulfur. This concentration is plotted on the abscissa as a dashed line. The distribution curve of the sulfur concentration was determined using the matrix material SBR, which has not yet been prevulcanized and does not yet contain NR-GR, shown here as an example (blue curve). The data originates from [19]. The most frequently detected sulfur concentration in SBR is 0.9 wt%, but there are also zones with lower and higher local concentrations of sulfur. The curve of sample SBR_0min&NR-GR (red curve, also originating from [19]) shifts towards lower sulfur concentrations. This means that the matrix has a significantly lower sulfur concentration due to diffusion processes.

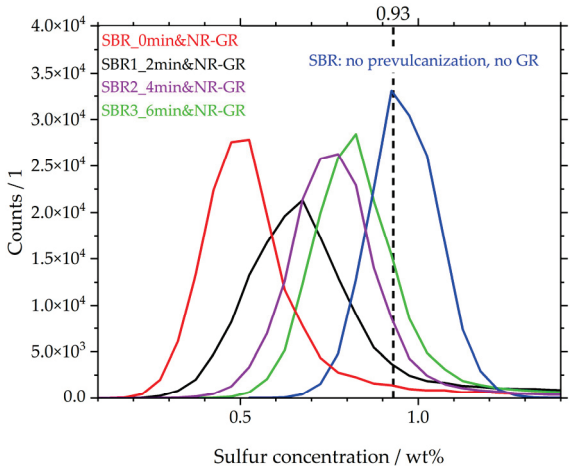

Figure 6. Distribution curves of local sulfur concentrations in the matrices of different vulcanizates.

However, if the matrix is prevulcanized for 2 min (black curve) before NR-GR is incorporated, the local sulfur concentration changes. The distribution curve shifts to higher concentrations compared to that for the non-prevulcanized sample (red). More sulfur remains in the matrix because of the reduced diffusion behavior of the sulfur species formed during prevulcanization. This behavior increases with longer prevulcanization times of 4 min (purple) and 6 min (green). Compared to the non-prevulcanized sample (red), with a maximum of approx. 0.45 wt%, the vulcanizate with a matrix prevulcanized for 6 min reaches a peak at 0.8 wt%. This behavior supports the hypothesis proposed by [19], that species formed during crosslinking—e.g., the active sulfurating agent postulated by Morrison and Porter [30]—are less mobile than the free sulfur initially present. It is thus evident that with increasing prevulcanization of the matrix, less free sulfur is able to diffuse into the GR particles. As a result, more sulfur remains in the matrix, and the distribution curves shift with increasing prevulcanization to the SBR-reference (blue). Even during the relatively short prevulcanization of 2 min, the content of the less mobile species

formed is so high that the distribution curve (black) differs significantly from that of the non-prevulcanized curve (red).

The distribution curves indicate that, apart from the matrix peak, there is no other peak representing the sulfur concentration in the GR particles. Instead, there are higher sulfur concentrations at moderate counts to the right of the matrix peaks. It therefore indicates that the sulfur concentration in the GR particles is less uniform and instead extends over a wide concentration range, e.g., from concentrations of approx. ≥1 wt% in the 2 min prevulcanized sample (black).

Compared to the SBR reference (blue), the matrices of the prevulcanized compounds are comparatively less sulfur-depleted, which leads to the expectation of increased mechanical properties compared to the non-prevulcanized specimen (red), for example. This is investigated in the following section.

3.3. Tensile Tests

To assess the influence of prevulcanization on mechanical properties, tensile tests were carried out.

In Figure 7 and Table 7, the sample SBR1 (blue) reaches a tensile strength of approx. 22.5 MPa at an elongation at break of 435%. For the same matrix material to which 30 phr NR-GR was added, and for which the matrix was not prevulcanized (SBR_0min&NR-GR, red), the tensile strength and elongation at break are significantly reduced. SBR_0min&NR-GR is again derived from [12,19] and serves as a reference to assess the influence of the prevulcanization.

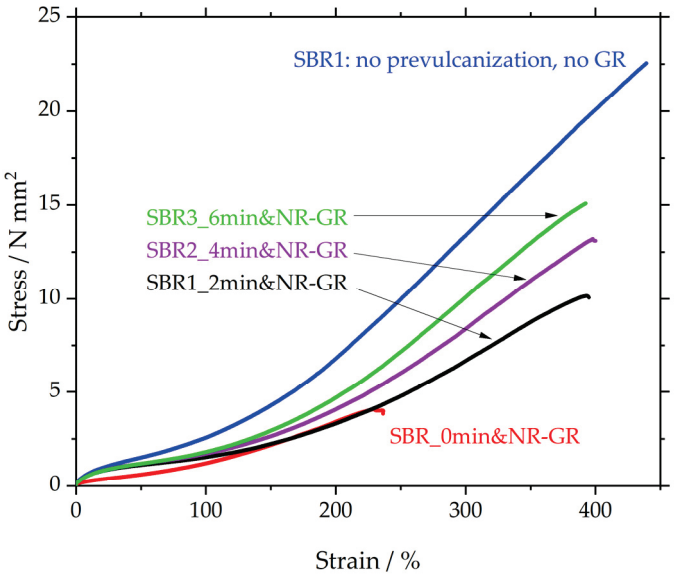

Figure 7. Stress strain curves of SBR1 and vulcanizates containing ground rubber with different degrees of prevulcanization.

Table 7. Summary of tensile properties of the investigated vulcanizates.

Specimen	Number of Valid Tests	Mean Stress /N mm² Incl. 95% Error	Mean Strain /% Incl. 95% Error
SBR1	12	21.8 ± 1.0	421 ± 13
SBR_0min&NR-GR	10	4.0 ± 0.3	232 ± 12
SBR1_2min&NR-GR	12	10.1 ± 0.8	379 ± 19
SBR2_4min&NR-GR	11	12.9 ± 0.8	395 ± 17
SBR3_6min&NR-GR	11	15.0 ± 0.5	372 ± 11

This influence of prevulcanization is demonstrated by the curves of SBR1_2min&NR-GR, SBR2_4min&NR-GR and SBR3_6min&NR-GR. The samples differ from SBR_0min&NR-GR (red) only in terms of the prevulcanization of the matrix for 2, 4 or 6 min, respectively. A 2 min prevulcanization already leads to a more than doubled tensile strength of 10 MPa compared to the red reference curve, exhibiting only 4.8 MPa. The elongation at break increases from 240% to almost 400%. This significant effect is the result of the prevulcanization step prior the incorporation of GR particles. Extending the prevulcanization time leads to a further increase in tensile strength with the same elongation at break. The significant increase in tensile strength and elongation at break can be explained by the higher sulfur concentration in the matrix and therefore an assumed higher CLD. The fact that the elongation at break for all three prevulcanized specimens remains identical at just under 400% could be due to the GR particles increasing the intrinsic elongation of the surrounding matrix. This leads to a local rise in strain in the vicinity of the particles, leading to failure of the entire specimen when this strain exceeds the elongation at break of the matrix material. The tensile tester, however, detected only one non-local strain value of the entire specimen, which is listed in Table 7 to be between 372 and 395%. This value might not be sensitive enough to distinguish differences between the different prevulcanized samples.

4. Discussion

The rubber industry is making efforts to drive towards a more circular economy to increase its sustainability. The recycling of rubber components such as end-of-life tires (ELTs) is an essential part of this procedure. Recycling rubber is challenging due to the covalent crosslinks between the polymer chains formed during the vulcanization process. These bonds define the viscoelastic properties of the vulcanizate. One recycling method involves grinding the ELTs into ground rubber (GR) particles. These particles can then be incorporated into green compounds to reduce the need for raw material. However, GR-containing compounds exhibit significantly deteriorated properties compared to those without GR. This is firstly because the GR particles perform as an inactive filler, increasing the intrinsic elongation of the matrix material in their vicinity. Secondly, free sulfur diffuses from the matrix into the GR particles during compounding, storage and vulcanization, resulting in matrix systems with lower and GR particles with higher crosslink density (CLD).

To improve the properties of GR-containing vulcanizates, the influence of matrix prevulcanization upon the diffusion behavior of sulfur was investigated in this article. It was found that the mobility of sulfur is significantly reduced when it forms different intermediates or species during the vulcanization process. Therefore, it was investigated whether the incorporation of GR particles into a prevulcanized matrix leads to less sulfur diffusion and thus increased tensile properties compared to a compound with the particles being incorporated into a non-prevulcanized matrix.

RPA measurements showed that prevulcanization reduces the scorch time of GR-containing compounds, because the heating phase continues the already started but interrupted vulcanization process during prevulcanization. An influence of the prevulcanization upon the maximum torque could not be detected.

It was demonstrated, by using micro X-ray fluorescence analysis (μ-XRF), that sulfur diffusion significantly decreases with the degree of prevulcanization. This indicates that the mobility of sulfur is reduced in prevulcanized matrix compounds in comparison to those that have not been prevulcanized. In contrast to the conventional production process without prevulcanization, the sulfur content in the matrix could almost be doubled, because less sulfur diffused out of the matrix into the GR particles.

The increased sulfur concentration in the matrix results in the formation of a higher CLD, which has a positive effect both on tensile strength and elongation at break. It was

thus possible to increase tensile strength from about 4 MPa to 15 MPa, improving the elongation at break at the same time from about 230% to almost 400%. Besides that, the elongation at break reaches a maximum, indicating the influence of the GR particles in form of an inactive filler.

Prevulcanization is a comparatively simple method on a laboratory scale because it does not need any additional machinery or changes of compound formulations besides the prevulcanization step itself. However, the prevulcanization will face challenges bringing it into industrial scale production because of higher resulting viscosities (compounding, energy consumption) and vulcanization processes (scorching). If the scorching behavior could be tailored with respect to torque rise over a relatively long time, the prevulcanization could be installed into the rubber production procedure. Therefore, prevulcanization might pave the way for effective incorporation of GR into new rubber compounds, even at production scale.

Author Contributions: Conceptualization, S.F., V.H., F.G. and A.B.; methodology, S.F.; software, S.F.; validation, S.F., V.H., F.G. and A.B.; formal analysis, S.F., V.H., F.G. and A.B.; investigation, S.F.; resources, S.F. and V.H.; data curation, S.F.; writing—original draft preparation, S.F.; writing—review and editing, S.F., V.H., F.G. and A.B.; visualization, S.F.; supervision, S.F.; project administration, S.F.; funding acquisition, S.F. and V.H. All authors have read and agreed to the published version of the manuscript.

Funding: This research was financially supported by DKG (German Rubber Society). In addition, it was supported by the publication fund of the Technical University of Applied Sciences Würzburg-Schweinfurt.

Data Availability Statement: Dataset available on request from the authors.

Acknowledgments: The authors would like to thank the companies L. Brüggemann GmbH & Co. KG, KLK Emmerich GmbH and Lanxess Deutschland GmbH for their material donations of ZnO, stearic acid and accelerator, respectively. The authors would also like to express their gratitude to Stefan Schneider for his help mixing the compounds.

Conflicts of Interest: The authors declare no conflicts of interest. The funders had no role in the design of this study; in the collection, analyses, or interpretation of data; in the writing of the manuscript; or in the decision to publish the results.

Abbreviations

The following abbreviations are used in this manuscript:

μ-XRF	Micro X-ray fluorescence analysis
CLD	Crosslink density
cyclo-S_8	Soluble sulfur
ELTs	End-of-life tires
GR	Ground rubber
RPA	Rubber process analyzer
S′	Elastic torque
S'_{max}	Maximum elastic torque
S'_{min}	Minimum elastic torque
t_{10}	Time to reach 10% of full vulcanization
t_{50}	Time to reach 50% of full vulcanization
t_{95}	Time to reach 95% of full vulcanization
Tg	Glass transition temperature
t_x	Time to reach x % of full vulcanization

References

1. Norris, C.J.; Cerdán, A.L.; Ter Haar, P. Understanding recovered Carbon Black. *Rubber Chem. Technol.* **2023**, *96*, 196–213. [CrossRef]
2. Anjum, A. Recovered Carbon Black from Waste Tire Pyrolysis: Characteristics, Performance, and Valorisation. Ph.D. Thesis, University of Twente, Enschede, The Netherlands, 2021.
3. van Hoek, J.W. Closing the Loop: Reuse of Devulcanized Rubber in New Tires. Ph.D. Thesis, University of Twente, Enschede, The Netherlands, 2022.
4. Dorigato, A.; Rigotti, D.; Fredi, G. Recent advances in the devulcanization technologies of industrially relevant sulfur-vulcanized elastomers. *Adv. Ind. Eng. Polym. Res.* **2022**, *6*, 288–309. [CrossRef]
5. Karger-Kocsis, J.; Mészáros, L.; Bárány, T. Ground tyre rubber (GTR) in thermoplastics, thermosets, and rubbers. *J. Mater. Sci.* **2013**, *48*, 1–38. [CrossRef]
6. Schüwer, N.; Clayfield, T.; Martineau, P.; Estudante Ventura, M.J.; Marshall, S.M.; Hofmann, S.; Ilisch, S.; Stratton, T. Eigenschaften S-SBR-basierter Vulkanisate mit recyceltem Gummimehl. *Gummi Fasern Kunststoffe* **2021**, *74*, 100–109.
7. KURZ Karkassenhandel. (18 August 2020). Available online: https://kurz-karkassenhandel.de/gummi-produkte/gummiprodukte-anfragen/ (accessed on 30 January 2024).
8. Herrmann, V.; Speyer, Y.; Leiber, J. Herstellung und Verarbeitung von sortenreinem Gummimehl im Labormaßstab. *Gummi Fasern Kunststoffe* **2017**, *70*, 240–247.
9. Kim, S.W.; Park, H.Y.; Lim, J.C.; Jeon, I.R.; Seo, K.H. Cure characteristics and physical properties of ground-rubber-filled natural rubber vulcanizates: Effects of the curing systems of the ground rubber and rubber matrix. *J. Appl. Polym. Sci.* **2007**, *105*, 2396–2406. [CrossRef]
10. Hrdlička, Z.; Brejcha, J.; Šubrt, J.; Vrtiška, D.; Malinová, L.; Čadek, D.; Kadeřábková, A. Ground tyre rubber produced via ambient, cryogenic, and waterjet milling: The influence of milling method and particle size on the properties of SBR/NR/BR compounds for agricultural tyre treads. *Plast. Rubber Compos.* **2022**, *51*, 497–506. [CrossRef]
11. Rodgers, B.; D'Cruz, B. Recycling of Rubber. In *Rubber Compounding—Chemistry and Applications*; Taylor & Francis Group: Boca Raton, FL, USA; London, UK; New York, NY, USA, 2016.
12. Herrmann, V.; Frosch, S.; Maslowski, T.; Werner, D. Einsatz von definiertem Gummimehl aus NR und SBR in unterschiedlichen Matrixwerkstoffen. *Gummi Fasern Kunststoffe* **2021**, *74*, 200–207.
13. Han, S.-C.; Han, M.-H. Fracture behavior of NR and SBR vulcanizates filled with ground rubber having uniform particle size. *J. Appl. Polym. Sci.* **2002**, *85*, 2491–2500. [CrossRef]
14. Gibala, D.; Hamed, G.R. Cure and Mechanical Behavior of Rubber Compounds Containing Ground Vulcanizates. Part I—Cure Behavior. *Rubber Chem. Technol.* **1994**, *67*, 636–648. [CrossRef]
15. Phadke, A.A.; Bhowmick, A.K.; De, S.K. Effect of cryoground rubber on properties of NR. *J. Appl. Polym. Sci.* **1986**, *32*, 4063–4074. [CrossRef]
16. Herrmann, V.; Schulz, A. Der Einfluss von Lkw-Reifenmehl als Additiv auf die Eigenschaften einer Lkw-Laufflächenmischung. *Gummi Fasern Kunststoffe GAK* **2016**, *69*, 698–705.
17. Kim, S.-W.; Hong, K.-H.; Seo, K.-H. Effects of ground rubber having different curing systems on the crosslink structures and physical properties of NR vulcanizates. *Mater. Res. Innov.* **2003**, *7*, 149–154. [CrossRef]
18. Phadke, A.A.; Chakraborty, S.K.; De, S.K. Cryoground Rubber-Natural Rubber Blends. *Rubber Chem. Technol.* **1984**, *57*, 19–33. [CrossRef]
19. Frosch, S. Diffusion Processes in Ground Rubber Containing Compounds. Ph.D. Thesis, University of Twente, Enschede, The Netherlands, 29 October 2024.
20. Frosch, S.; Herrmann, V.; Schülein, T.; Grunert, F.; Blume, A. Sulfur Diffusion Studies Imitating Recycled Ground-Rubber-Containing Compounds. *Polymers* **2024**, *16*, 3112. [CrossRef]
21. Herrmann, V.; Hanning, S.; Kreyenschmidt, M.; Wolff, A.; Ludwig, D.; Ludwig, J. Untersuchungen zur Diffusion des Schwefels in Rezyklat-Kautschukmischungen: Teil 2: Schwefeldiffusion in Mischungen mit Gummimehl. *Gummi Fasern Kunststoffe* **2018**, *71*, 340–349.
22. Frosch, S.; Herrmann, V.; Grunert, F.; Blume, A. Quantification of sulfur distribution on rubber surfaces by means of μ-X-ray fluorescence analysis. *Polym. Test.* **2023**, *128*, 108237. [CrossRef]
23. Haschke, M. *Laboratory Micro-X-Ray Fluorescence Spectroscopy: Instrumentation and Applications*; Springer: Cham, Switzerland, 2014; Volume 55.
24. Mellawati, J.; Sumarti, M.; Menry, Y.; Surtipanti, S.; Kump, P. Application of X-ray fluorescence spectrometry in multielement analysis of rubber samples. *Appl. Radiat. Isot.* **2001**, *54*, 881–885. [CrossRef] [PubMed]
25. Brouwer, P. *Theory of XRF: Getting Acquainted with the Principles*, 5th ed.; Malvern Panalytical: Almelo, The Netherlands, 2018.
26. Markowicz, A.A. X-Ray Physics. In *Handbook of X-Ray Spectrometry*, 2nd ed.; van Grieken, R.E., Markowicz, A.A., Eds.; Marcel Dekker: New York, NY, USA, 2002; Volume 29, pp. 1–94.

27. Ahsanullah, M.; Kibria, B.M.G.; Shakil, M. *Normal and Students t Distributions and Their Applications*; Atlantis Press: Paris, France, 2014.
28. Brell, C.; Brell, J.; Kirsch, S. (Eds.) Verteilungen. In *Statistik von Null auf Hundert: Mit Kochrezepten Schnell Zum Statistik-Grundwissen*; Springer: Berlin/Heidelberg, Germany, 2017; pp. 153–157. [CrossRef]
29. Blume, A.; van Elburg, F.; Grunert, F.; Talma, A. "Re-Think" Sulfur Curing. *Molecules* **2024**, *29*, 5198. [CrossRef]
30. Morrison, N.J.; Porter, M. Temperature Effects on the Stability of Intermediates and Crosslinks in Sulfur Vulcanization. *Rubber Chem. Technol.* **1984**, *57*, 63–85. [CrossRef]
31. Banerjee, P.; Jain, P.K. Mechanism of sulfidation of small zinc oxide nanoparticles. *RSC Adv.* **2018**, *8*, 34476–34482. [CrossRef] [PubMed]
32. Maslowski, T. Untersuchungen zum Einsatz von Nicht Sortenreinem Gummimehl in Kautschukmischungen: NR-Mehl in Einer SBR-Matrix. Bachelor's Thesis, University of Applied Sciences Würzburg-Schweinfurt, Würzburg, Germany, 2020.

polymers

MDPI

Article

The Importance of Feedstock and Process Control on the Composition of Recovered Carbon Black

Christopher Norris [1,*], Antonio Lopez-Cerdan [1], Peter Eaton [2], Richard Moon [3] and Mark Murfitt [1]

[1] Murfitts Industries, Station Road, Lakenheath, Suffolk IP27 9AD, UK; antonio.lopez-cerdan@murfittsindustries.com (A.L.-C.); mark@murfittsindustries.com (M.M.)
[2] The Bridge, Joseph Ruston Building, University of Lincoln, Edgewest Road, Lincoln, Lincolnshire LN6 7EL, UK; peaton@lincoln.ac.uk
[3] Materials Innovation, Avon Protection, Hampton Park West, Semington Road, Melksham, Wiltshire SN12 6NB, UK; richard.moon@avon-protection.com
* Correspondence: chris.norris@murfittsindustries.com; Tel.: +44-1842-860220

Abstract

Pyrolysis has emerged as a commercially viable material recovery process that supports circularity in the tyre industry. Here, it is demonstrated that a high degree of control can be imparted over the UK tyre waste stream and that statistically different feedstocks can be used to produce different grades of rCB based on their ash contents. The lower ash content rCB produced from truck tyres had superior in-rubber properties, closely matching those of the N550 reference. Silica, when not paired with a coupling agent, is known to be less reinforcing than CB, lowering the reinforcing behaviour of the high ash content rCB variant produced from car tyres. This justifiably places ash content within the classification and specification development discussion. However, a proximate analysis of UK waste tyres suggests that the typical rCB ash specifications of <20 wt% are unrealistic. Such limits would force producers to consider modifying process conditions to allow the deposition of carbonaceous residues to artificially dilute the ash content. This study investigates this process philosophy but conclusively demonstrates that carbonaceous residue is more detrimental to rCB performance than ash content. As such, carbonaceous residue content demands far more attention from the industry than it is currently afforded.

Keywords: rCB; pyrolysis; waste tyres; recycling; rubber; reinforcement; sustainability

1. Introduction

The UK generates approximately 50 million waste tyres, equivalent to 700,000 tonnes, each year. Since the EU ban on landfilling came into effect in 2003 (EC Directive 1999/31), most of these waste tyres have been utilised in civil engineering applications, sports and recreational surfaces and for energy recovery as fuel in cement kilns [1]. The emergence of policy drivers to combat climate change and to promote material circularity, such as the European Commission Green Deal [2], has increased pressure on the industry to recover materials from waste tyres. Now, all the major tyre brands have imposed stringent sustainability goals, with most targeting the construction of tyres from 100% sustainable materials by 2050. This necessitates a movement away from traditional mechanical recycling technologies to those that can chemically deconstruct waste tyres into reusable raw materials. Pyrolysis has emerged as the frontrunning commercially capable material recovery process to support circularity in the tyre industry. As well as offering recovered products with low

global warming potential and avoiding the consumption of fossil resources [3,4], properly controlled tyre pyrolysis comes with minimal emissions or residual waste [5].

Pyrolysis is defined as the thermal decomposition of organic materials in the absence of oxygen [6]. In the case of tyres, this involves cracking the long organic polymer chains into a hot gas phase, which consists of low-molecular-weight non-condensable gas and condensable tyre pyrolysis oil (TPO) fractions. The removal of organic matter leaves behind a solid mixture consisting of carbon black (CB), inorganic compounding ingredients and other pyrolysis residues, defined as 'raw recovered carbon black (rCB)' by ASTM committee D36 [7]. Assuming the raw rCB is of sufficient quality, it undergoes further milling and pelletising processes to alter its physical properties to meet the specification requirements of the end user [8]. This paper focusses on demonstrating how the properties of rCB are controlled by both feedstock selection and pyrolysis conditions.

The key to any material recovery process, including pyrolysis, is to produce consistent products that always meet the specification requirements of the end user. This poses a significant challenge to rCB producers, given that tyres are structurally complex articles comprising several different rubber components, including the tread, carcass and sidewall, alongside steel and textile reinforcements [9]. Each of the rubber components will typically contain one or more elastomers, reinforcing fillers such as CB and silica, plasticising agents, antidegradants, processing aides, curatives and other additives. It has been reported that more than one hundred ingredients can be added to the tyre, the precise nature of which depends on its specific use requirements [10,11]. To tackle the challenges associated with product consistency, it seems prudent to narrow the compositional variance of pyrolysis feedstocks by segregating the waste stream into structurally and compositionally similar tyres. However, it is acknowledged that manufacturer variability will persist even when segregating the waste stream by type. In the UK and the EU, the two main classes of tyres are passenger car and truck, accounting for approximately 70 wt% and 20 wt% of the total tyre waste stream, respectively. Passenger car tyres contain a higher synthetic rubber content and a greater utilisation of silica filler and textile reinforcements [12]. In contrast, truck tyres contain higher levels of steel, natural rubber and carbon black [13]. An additional benefit of feedstock selection is to narrow the aggregate size distribution of the resultant rCB, as passenger car and truck tyres contain different grades of CB. A broader aggregate size distribution has been linked to a reduced reinforcing potential for rCB [8,14].

The first aim of this study was to assess the ability to produce compositionally different pyrolysis feedstocks by segregating car and truck tyres from the UK waste stream, and, further, to assess the impact on the composition and reinforcing ability of the resultant rCB products. The major difference between the feedstocks is the higher silica content of the passenger car tyre, arising from the drive to enhance fuel efficiency following the introduction of labelling rules by the European Commission in 2012 [15]. Assuming a complete pyrolysis of the tyre rubber, the resultant solid rCB product is a mixture of CB, silica and other inorganic compounding ingredients. rCB produced from passenger car tyres is, therefore, expected to contain a higher silica (ash) content. The ash content of an rCB has been reported as an influential factor on rubber reinforcing potential [16–18], the dominant factor being that silica, when not paired with a coupling agent, is a less reinforcing filler than CB, with laboratory produced rCB samples demonstrated to decrease in reinforcing potential with increasing silica content [8]. It is also documented that silica interacts with zinc during compounding, leading to the removal of soluble zinc from its normal accelerator activating function, subsequently reducing crosslink density [19]. Based on these observations, it is understandable that tyre manufacturers have developed rCB specifications that stipulate a requirement for ash content to be $\leq$20 wt% [20]. However,

these observations are only relevant to 'clean', low-residue-content rCB produced from the complete pyrolysis of the rubber feedstock.

The goal of tyre pyrolysis is the complete conversion of all organic matter into TPO and non-condensable gas products, yielding an rCB free of pyrolysis residues. Process optimisation with this in mind has two major benefits:

1. By preventing the formation of pyrolysis residues, the surface of the recovered fillers is accessible in the elastomer phase, thus promoting reinforcing behaviour.
2. The biogenic carbon contained within the feedstock is recovered in the TPO and gas phases, where it adds value by reducing scope 1 emissions when using these materials directly, or after refinement as fuels.

rCB pyrolysis residues arise from two primary routes. Firstly, the incomplete removal of organic matter will leave oily residues on the surface of the rCB which, at high levels, have been conclusively linked to poor reinforcing properties [21]. Such residues pose little challenge to the industry, as they are easily identifiable by both the producer and end user using standard ASTM techniques, such as toluene discolouration (D1618) and thermogravimetric analysis (D8474) [22,23]. The second type of residue arises from polymer decomposition reactions that lead to the formation of additional fixed carbon, often referred to as carbonaceous residue [21,24,25]. Carbonaceous residue contents of >20 wt% have been reported and linked to a significantly reduced surface activity of rCB [8,26–30]. This residue is much harder to differentiate from the CB content of rCB, and so it often goes unnoticed. The net result of these pyrolysis residues is a reduction in ash content by the dilution effect, and this may be seen as an opportunity to meet the stringent ash content specifications applied in the rubber industry. The second aim of this study was to intentionally produce a high-carbonaceous-residue-content rCB from car tyres to explore an alternative strategy to meet ash specifications, and to assess the impact on morphological and in-rubber properties.

2. Materials and Methods

2.1. Tyre Granulate Preparation and Characterisation

Through careful selection of waste tyres, pyrolysis feedstocks were prepared from 100% car tyres or 100% truck tyres using Murfitts Industries commercial processing line at Lakenheath in the UK. The multi-stage process comprises shredding, granulation and separation steps to produce a $\leq$8 mm granulate with at least 99% steel and 98% fibre removal.

Proximate and ultimate analyses of twenty batches each of the car and truck feedstocks were completed. Proximate analysis followed the procedure outlined in ASTM D8474 [23], using a Perkin Elmer TGA4000 (Waltham, MA, USA) to yield volatile matter (VM), fixed carbon (FC) and ash contents.

2.2. rCB Materials Preparation

Pyrolysis trials were conducted using a two-stage continuous process comprising two in-sequence ETIA Technologies Spirajoule® (Lacroix-Saint-Ouen, France) reactors with an overall throughput capacity of 90 kg/h. The operating conditions of the first stage were designed to complete $\geq$90% of the pyrolysis, with the second stage operating at a higher temperature to remove the residual organic matter from the raw rCB. Although the full process conditions cannot be disclosed for proprietary reasons, a brief description of how the process was optimised to produce the different rCB materials for this study is provided below.

Two grades of rCB were produced from the different feedstocks using process conditions optimised to minimise the rCB yield. This means that the target yield was based on the FC + ash content from the feedstock proximate analysis, producing material that is as

free as possible from pyrolysis residues. The car tyre-derived rCB is referred to as Mi360+ and the truck tyre-derived grade as Mi360HP.

A further rCB material was produced from the car tyre feedstock but using very different process conditions to minimise the ash content. The different process conditions, including higher temperatures, were selected to promote the formation of carbonaceous residue on the rCB, thus diluting the inorganic components. This material is referred to as HCR (high carbonaceous residue).

All three materials were finalised in the same manner. The particle size was reduced to a target D97 of 10 ± 0.5 µm using a Hosokawa jet mill (Augsburg, Germany) before wet pelletising with a MARS Minerals (Mars, PA, USA) pin mixer and subsequent drying to produce pellets of <80 gf maximum hardness.

2.3. rCB Material Characterisation

A series of ASTM standardised techniques developed for carbon black and rCB were used to characterise the samples: this included BET surface area (D6556) [31], toluene discolouration (D1618) [22], bulk composition by TGA (D8474) [23], milled particle size distribution (WK87480) [32] and pellet hardness (D5230) [33].

To determine zinc and silicon contents, 250 mg of sample was digested on a hotplate with sulphuric and perchloric acids. When cold, they were transferred to plastic flasks where hydrofluoric acid was added to digest the silicon. Quantitative elemental analysis was performed using an Agilent 5800 (Agilent, CA, USA) inductively coupled plasma optical emission spectrometer (ICP-OES).

rCB morphology and inorganic distribution assessments were made using a Thermo Scientific F200i scanning (Waltham, MA, USA)/transmission electron microscope (S/TEM) fitted with a Bruker SDD XFlash 6.100 Energy Dispersive X-ray (EDX) detector (Berlin, Germany). The TEM was operated at 200 kV, and Velox software v3.19 used to acquire and process the elemental maps. Sample preparation involved a modified version of ASTM D3849 [34], as described by Grulke et al. [35].

2.4. In-Rubber Characterisation Protocol

The ASTM D3191 styrene butadiene rubber (SBR) formulation was used to evaluate the in-rubber behaviour of the rCB samples and an N550 reference [36]. A filler loading of 70 parts per hundred rubber (pphr) was used, as recommended in ASTM D8491 for rCB materials [37]. Compounds were produced using a 78 cc Haake Rheomix OS/3000 (Waltham, MA, USA) with Banbury style rotors set at 40 °C, with a rotor speed of 60 rpm.

Moving die rheometer (Alpha Technologies MDR2000, Akron, OH, USA) testing (to ASTM D5289) at 160 °C was used to assess the cure characteristics of each compound and to allow preparation of cured test sheets using a cure time to T90 + 5 min [38]. The cured rubber sheets were tested as follows:

- Tensile properties were determined using a Llyod LR5K (AMETEK, Bognor Regis, UK) following ASTM D412 [39].
- Shore A Hardness was determined using a Wallace H17A (Walace Instruments, Dorking, UK) in accordance with ASTM D2240 [40].
- Filler dispersion was assessed by examining surfaces cut with fresh razor blades at 250× magnification using a Hitachi TM3030 Scanning Electron Microscope (SEM) (Tokyo, Japan). Surface roughness plots and average surface roughness (Ra) values were generated using 3D-Image Viewer software v2.0 (Denshi Kougaku Kenkyusyo Co., Ltd., Tokyo, Japan).

- Strain sweeps were conducted using a Perkin-Elmer DM8000 (Waltham, MA, USA) configured in tension mode. During this step, 2 × 2 × 10 mm specimens were tested at 40 °C, 10 Hz and a double strain amplitude (DSA) range of ~0.04 to 4%.

3. Results and Discussion

3.1. Feedstock Characterisation

Estimates suggest that four million tons of waste tyres are generated globally every year [41]. Such statistics give the impression that this waste stream represents an almost infinite resource that can be misleading in relation to securing a consistent pyrolysis feedstock locally. Without doubt, compositionally consistent pyrolysis outputs necessitate a compositionally consistent feedstock. To emphasise this point, twenty batches of two compositionally different feedstocks, from 100% car or 100% truck tyres, were prepared, and their bulk compositional properties were determined through a proximate analysis. An example TGA weight loss profile is provided in Figure 1, showing the determination of volatile matter (VM), fixed carbon (FC) and ash contents, as adopted by Bowles and Fowler in their review of published rubber pyrolysis feedstocks [13]. Assuming pyrolysis is fully complete, the VM value derived from the TGA test should correlate with the hot gas yield of a pyrolysis process. Likewise, the sum of the FC and Ash values should offer a theoretical rCB yield, assuming that pyrolysis is complete and no process losses occur.

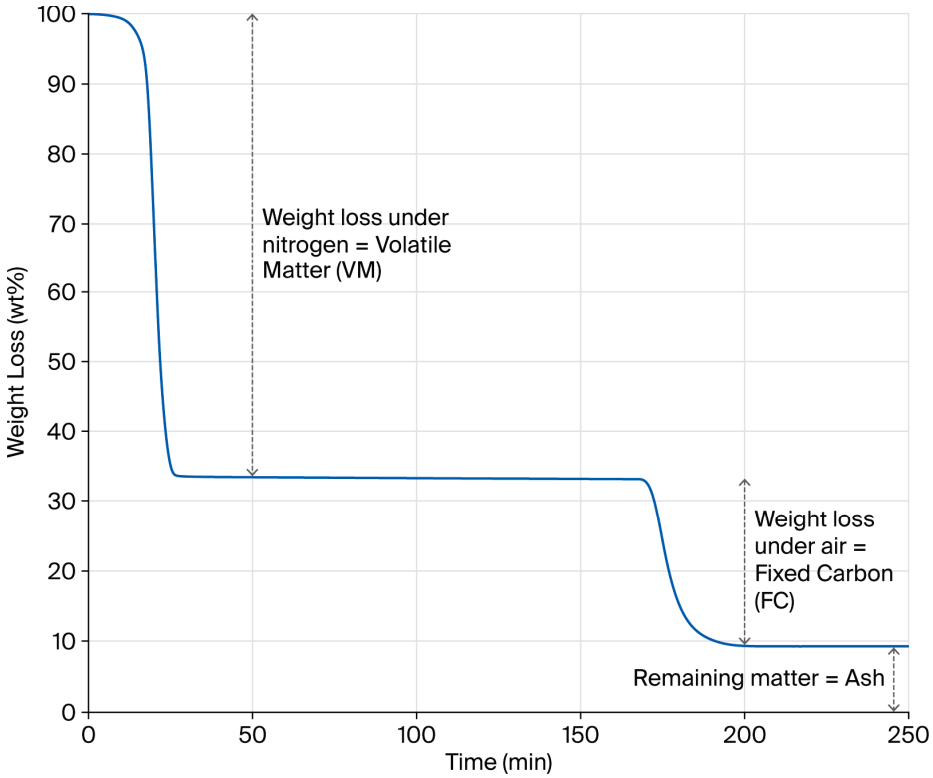

Figure 1. Example of rubber granulate TGA weight loss profile.

A summary of the bulk compositional properties of the two feedstocks is provided in Table 1, showing that the truck granulate contains a higher VM, higher FC and lower ash content. Two sample T-tests for each of the parameters yielded *p*-values of 0, confirming that the differences between the feedstocks are statistically significant. The narrow band of the 95% confidence intervals also demonstrates that it is possible to impart a high level of feedstock compositional control. Based on this data, the predicted pyrolysis rCB yields (FC + ash) are 35 wt% and 38 wt% when using truck and car granulate feedstocks,

respectively. This data provides a valuable reference point when optimising the process to limit rCB contamination from pyrolysis residues. The data can also be used to predict the ash content of the resultant rCB. It is worthy of note that, even with the lower-ash-content truck feedstock, the theoretical ash content of the rCB is marginally above the industry standard of <20 wt%. This alone questions the practicality of the current specifications, especially when considering that the higher-ash-content car tyre rubber represents the bulk of the waste stream.

Table 1. Mean proximate analysis values with 95% confidence intervals in brackets.

Parameter	Unit	Truck Granulate	Car Granulate
VM Content	wt%	64.7 (64.0→65.3)	62.5 (61.8→63.0)
FC Content	wt%	28.2 (27.6→28.8)	24.5 (23.4→25.7)
Ash Content	wt%	7.1 (6.5→7.8)	13.1 (12.1→14.0)
Theoretical rCB Yield (FC + Ash)	wt%	35.3	37.6
Theoretical rCB Ash Content	wt%	20.1	34.8

3.2. rCB Characterisation

The properties of the three different rCB materials are summarised in Table 2. The rCB yields of samples optimised for low residue content, Mi360HP (truck) and Mi360+ (car), were in good agreement with the theoretical yields derived from the proximate analysis of the feedstock. Compared to the Mi360+, the high carbonaceous residue (HCR) sample produced from the same feedstock had an elevated FC content, confirming that the changes in the pyrolysis process conditions had the intended effect of increasing the carbonaceous residue content. The difference in yield between the Mi360+ and HCR suggests that approximately 17 wt% of the feedstock was converted into carbonaceous residue for the latter. All samples had comparably low organic residue contents, as demonstrated by both the toluene extract transmittance and VM content values. This parameter can therefore be disregarded when considering the differences in rubber reinforcing behaviour between the samples. The VM fraction will contain a contribution from moisture and a small amount of residual organic matter.

Table 2. Summary of rCB sample properties.

Parameter	Unit	Truck rCB (Mi360HP)	Car rCB (Mi360+)	Car rCB HCR
Measured rCB Yield	wt%	36	38	55
Toluene Transmission	%	98	99	100
VM–TGA	wt%	1.3	1.7	1.8
FC–TGA	wt%	79.0	67.6	79.4
Ash–TGA	wt%	18.9	30.8	18.7
Si–ICP	wt%	3.7	9.1	7.0
SiO_2–Calculated *	wt%	7.9	19.5	15.0
Zn–ICP	wt%	5.0	3.5	2.5
ZnS–Calculated *	wt%	7.5	5.2	3.7
BET Surface Area–Raw rCB	m^2/g	79.3	82.7	44.7
BET Surface Area–rCB	m^2/g	89.9	85.8	75.0
Milled Particle Size, d97	µm	10.3	9.5	10.3
Average Pellet Hardness	gF	33	35	39

* ICP derived atomic mass data converted to molecular mass of associated chemical.

The measured ash contents of the Mi360 grades were slightly below that predicted from the feedstock analysis. However, a good agreement between theoretical and measured rCB yields would suggest that the residue content is very low. The discrepancy may arise from natural variability (i.e., only one sample measured compared to the average of twenty feedstock samples) and may also result from the different temperature profiles used for the TGA test and pyrolysis process. The key point is that the deposition of carbonaceous residues within the car tyre-derived HCR sample reduced the ash content in line with the truck tyre-derived Mi360HP. This provides the basis for assessing the relative effects of ash and carbonaceous residues on the reinforcing behaviour of the rCB materials.

One of the strategies adopted by rCB producers to meet ash content targets is to dilute the higher-ash-content car tyre feedstock with lower-ash-content truck tyres. Using the ash contents of the low-residue Mi360HP and Mi360+, predictions can be made on the necessary blend ratio to meet the <20 wt% ash content, as seen in Figure 2. The prediction assumes that, by blending the feedstock, the residue content of the rCB does not differ to those produced from the segregated waste streams. Based on this data, a feedstock blend containing no less than 91 wt% truck tyres would be necessary to meet the target and is by no means reflective of the relative abundance of this waste tyre category. Such ash content targets almost necessitate the need to form carbonaceous residue during pyrolysis.

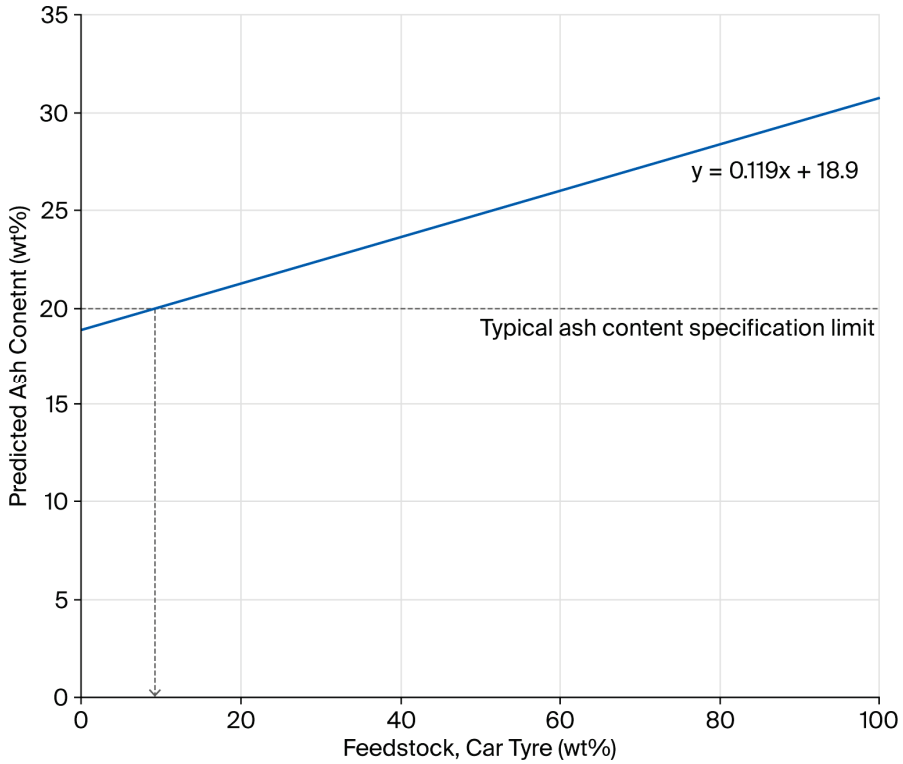

Figure 2. Relationship between rCB ash content and the percentage of car tyres used in a feedstock blend with truck tyres.

Of course, ash is a poor descriptor of the inorganic components contained within an rCB product. Most of the inorganic matter arises from the use of silica filler and zinc oxide additives [8,13,16–18,21], as confirmed by an ICP-OES analysis of acid digests. Car tyres contain a much higher loading of silica, but it is also apparent that silica has found use in truck tyres. The data also confirm that truck tyres contain a higher zinc loading compared to car tyres. The rCB materials will also contain low levels of other inorganic matter, such as iron and other trace metals originating from the feedstock, but these were not quantified as part of this study.

STEM/EDX mapping of the rCB samples was performed to better understand the distribution of these inorganic components. An example of an Mi360+ fused agglomerate is displayed in Figure 3, showing that the silica clusters are intimately entwined amongst the CB aggregates. Zinc was found to be in the form of zinc sulphide, appearing as discrete particles at the surface of the fillers, in agreement with other microscopy assessments of rCB [16,18]. As such, no evidence was identified to suggest that the zinc sulphide particles influenced agglomeration. The pyrolysis gas phase contains an abundance of hydrogen sulphide, with levels of up to 5.1 vol% reported [42,43]. It is highly likely that the simple reaction between zinc oxide and hydrogen sulphide yields the observed particles of zinc sulphide:

$$ZnO + H_2S \rightarrow ZnS + H_2O$$

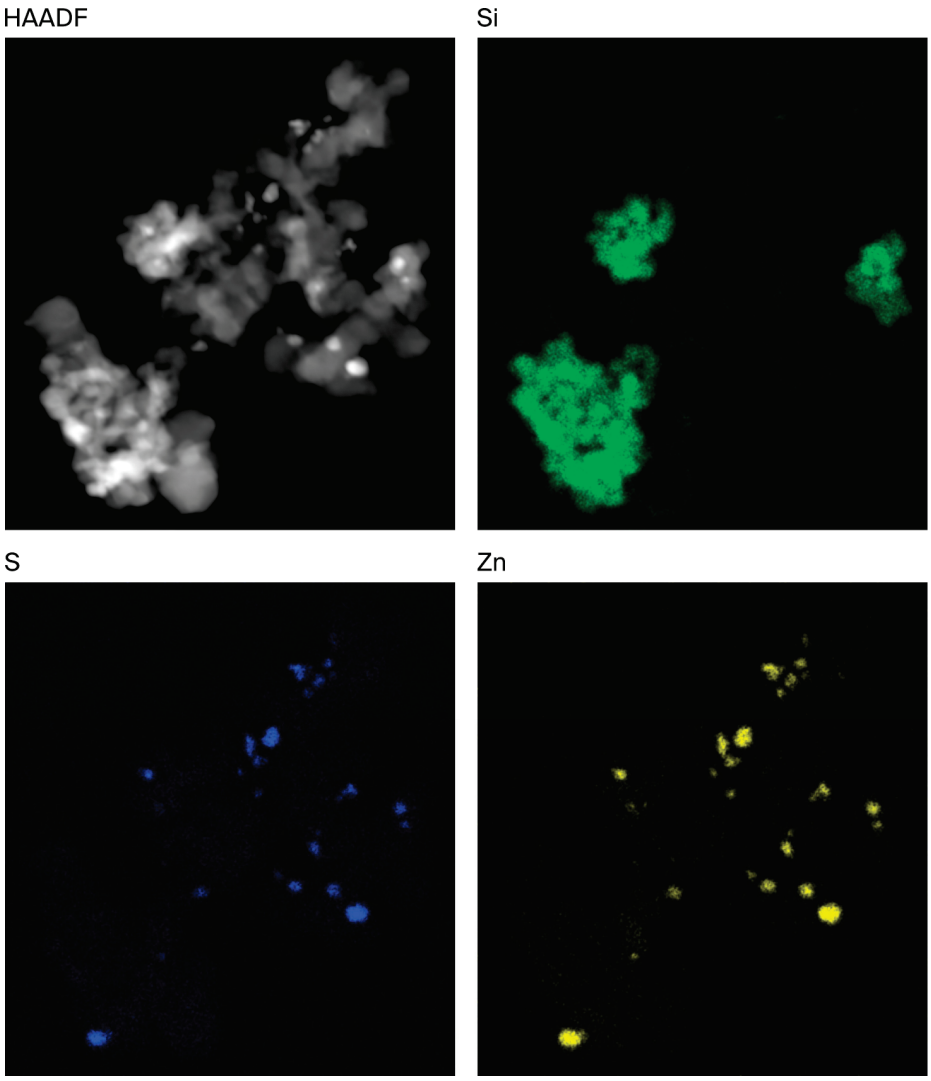

Figure 3. STEM HAADF (electron) image of rCB fused agglomerate alongside silicon, sulphur and zinc distribution maps.

The conversion of ZnO to ZnS may not be true for all pyrolysis processes, depending on the process conditions utilised.

The same observations were made for the Mi360HP, but with lower amounts of silica present.

The presence of carbonaceous residue within the HCR sample had a dramatic effect on morphology, with the aggregate nature much less apparent in many of the particles studied, as seen in Figure 4. This observation aligns with the BET measurements of the raw

rCBs (prior to milling and pelletising), with the HCR exhibiting 46% less surface area than the Mi360+ produced from the equivalent feedstock. As structure level and surface area are regarded as fundamental properties of rubber reinforcement [44–46], the HCR would be expected to exhibit an inferior reinforcing behaviour.

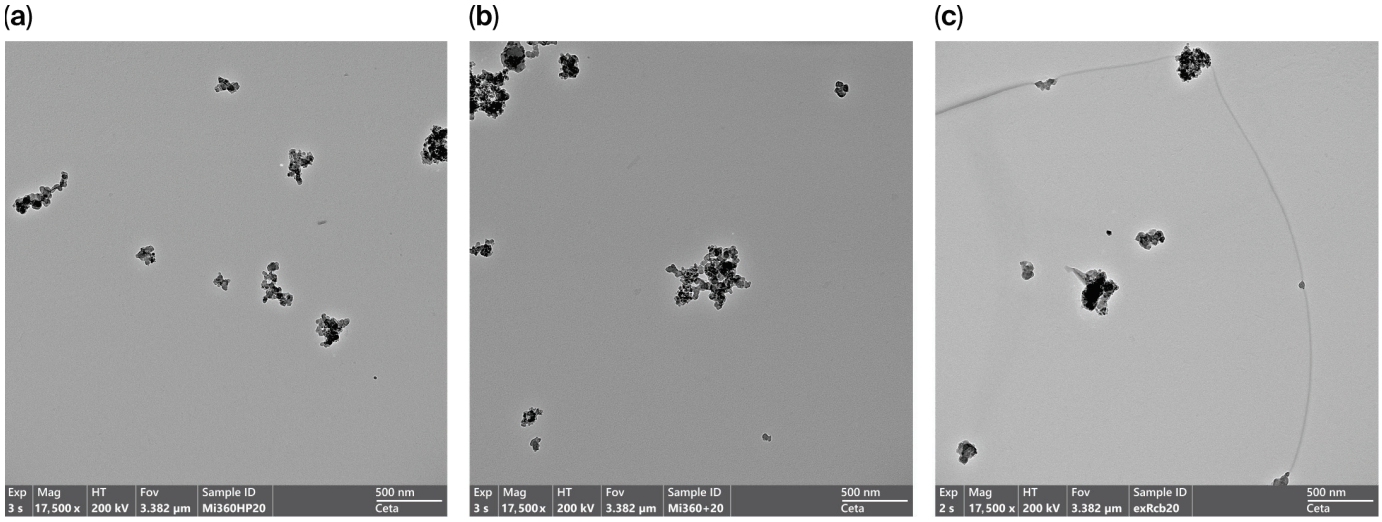

Figure 4. TEM images showing rCB morphology; (**a**) Mi360HP, (**b**) Mi360+ and (**c**) HCR.

The milled particle size target of d97 10 ± 0.5 µm was achieved for all samples. This parameter is directly related to dispersion [47], and so it is important that all were size-reduced to the same level to allow for a fair comparison of in-rubber properties. All samples were noted to exhibit an increased surface area post milling: Mi360HP by 13%, Mi360+ by 4% and HCR by 68%. These data suggest that the presence of carbonaceous residue is linked to a significant increase in milled surface area, closing the gap between the HCR and the Mi360 grades. Traditional carbon black colloidal tests have long been established as poor predictors of the in-rubber properties of rCB [8,21]. These observations further challenge the value of surface area in rCB specifications, especially when considering that the end-user cannot test the material in the pre-milled state.

Finally, all samples were successfully pelletised to industry standard levels to facilitate proper handling and rubber compounding behaviour.

3.3. In-Rubber Characterisation

The rCB materials were compounded into the SBR-based ASTM D3191 formulation to investigate the effects of the compositional differences on their in-rubber properties, as seen in Table 3. Comparing the properties of Mi360HP and Mi360+ offers insight into the effect of ash content, whilst the differences between the Mi360+ and HCR are wholly related to the carbonaceous residue content.

Surface roughness maps indicating the level of filler dispersion are shown in Figure 5. The dispersion of the Mi360 grades almost matched that of the N550. It should be noted that N550 is one of the easiest grades to disperse, with its low surface area and high structure level. Although milled to the same particle size, the HCR was found to be harder to disperse compared to the Mi360 grades. This would suggest that the Mi360 grades underwent a level of agglomerate breakdown during the mixing process. It is likely that the presence of carbonaceous residue on the HCR prevents effective de-agglomeration, leading to an inferior dispersion. The presence of larger agglomerates has been linked to poorer mechanical properties [14], as discussed below.

Table 3. Summary of in-rubber properties.

Parameter	Unit	N550	Truck rCB (Mi360HP)	Car rCB (Mi360+)	Car rCB HCR
Dispersion–Ra	µm	0.34	0.43	0.46	0.75
Shore A Hardness	°	80	78	76	70
M100%	MPa	8.38	8.51	5.08	4.74
M200%	MPa	17.92	17.39	11.72	10.72
Break Stress	MPa	21.6	21.3	17.1	13.6
Break Strain	%	252	247	296	303
E'_0	MPa	24.1	23.0	19.4	15.0
E'_∞	MPa	14.6	14.6	13.0	11.3
$\Delta E'$	MPa	9.5	8.4	6.4	3.8
Tan δ_{max}	-	0.19	0.18	0.17	0.16

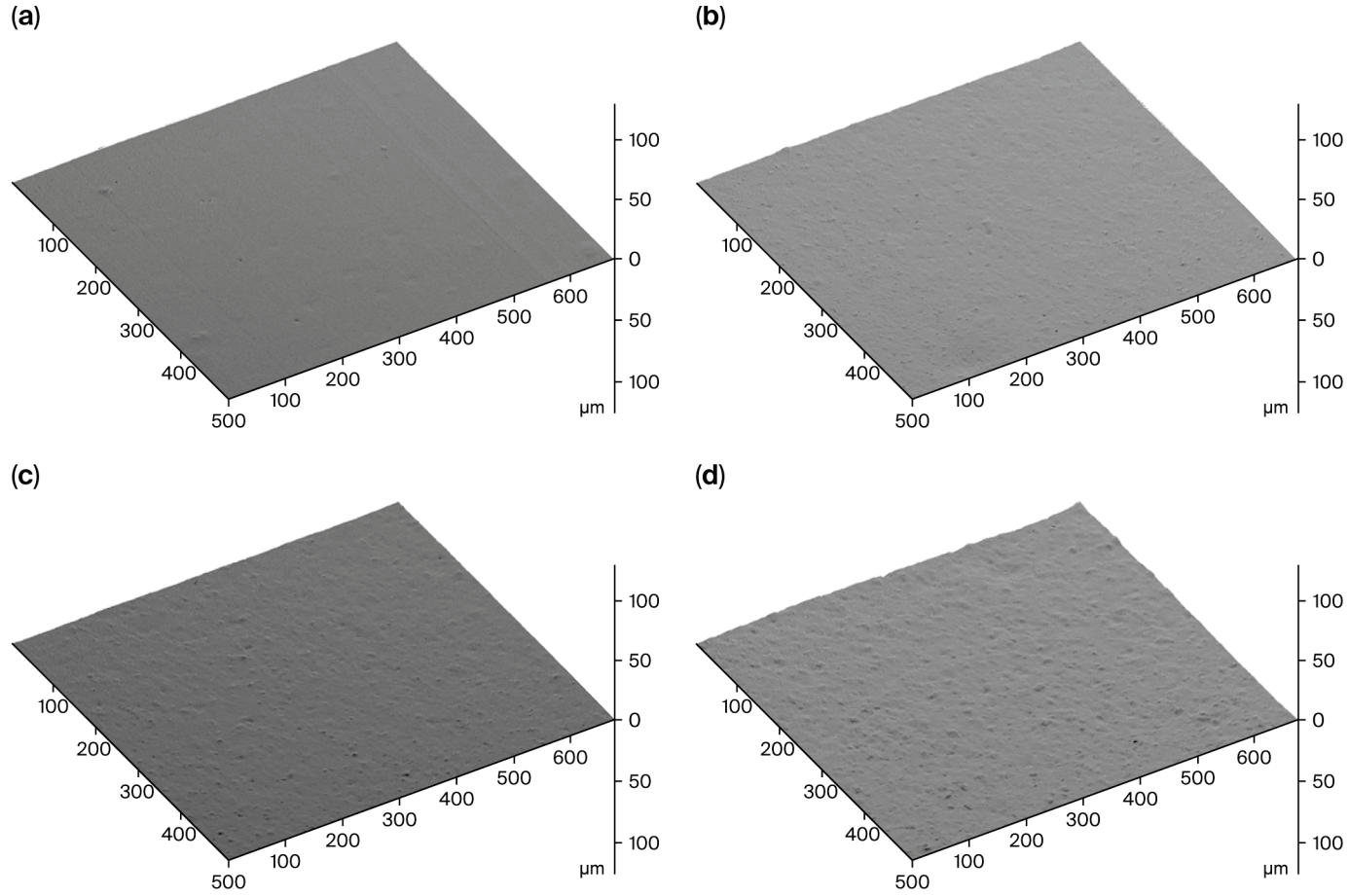

Figure 5. SEM Surface roughness maps of sectioned surfaces of model SBR compounds containing (**a**) N550, (**b**) Mi360HP, (**c**) Mi360+ and (**d**) HCR.

The mechanical properties of the Mi360HP were a good match to the N550 reference. The higher ash content Mi360+ had significantly reduced stiffness values. Most of the difference between the Mi360HP and the Mi360+ is attributable to the higher silica content of the latter. Silica, without a coupling agent, is known to be less reinforcing than carbon black [19]. In addition, silica can remove soluble zinc from its normal accelerator activating function, resulting in a reduced crosslink density [18]. Another factor is likely to be the different grades of CB recovered from the truck and car tyre feedstocks. Truck tyres utilise more N100 series in the tread sections and N300 series in the sidewalls to provide the necessary abrasion and stiffness characteristics. Car tyres tend to use N300 series in the

treads and N500 to N600 in the sidewalls. In short, the CB content of Mi360HP is expected to be more reinforcing than the CB content of Mi360+.

Although the ash content matched that of the Mi360HP, the deposition of carbonaceous residues in the HCR reduced the hardness and modulus values further compared to the Mi360+. This conclusively demonstrates that carbonaceous residues are more detrimental to reinforcing behaviour than ash. In particular, there is an apparent loss of filler–polymer interaction at higher tensile strains above approximately 200%, as seen in Figure 6. This aligns with the loss of structure identified during the TEM assessment and reports that the carbonaceous residue masks the surface activity of the original carbon black.

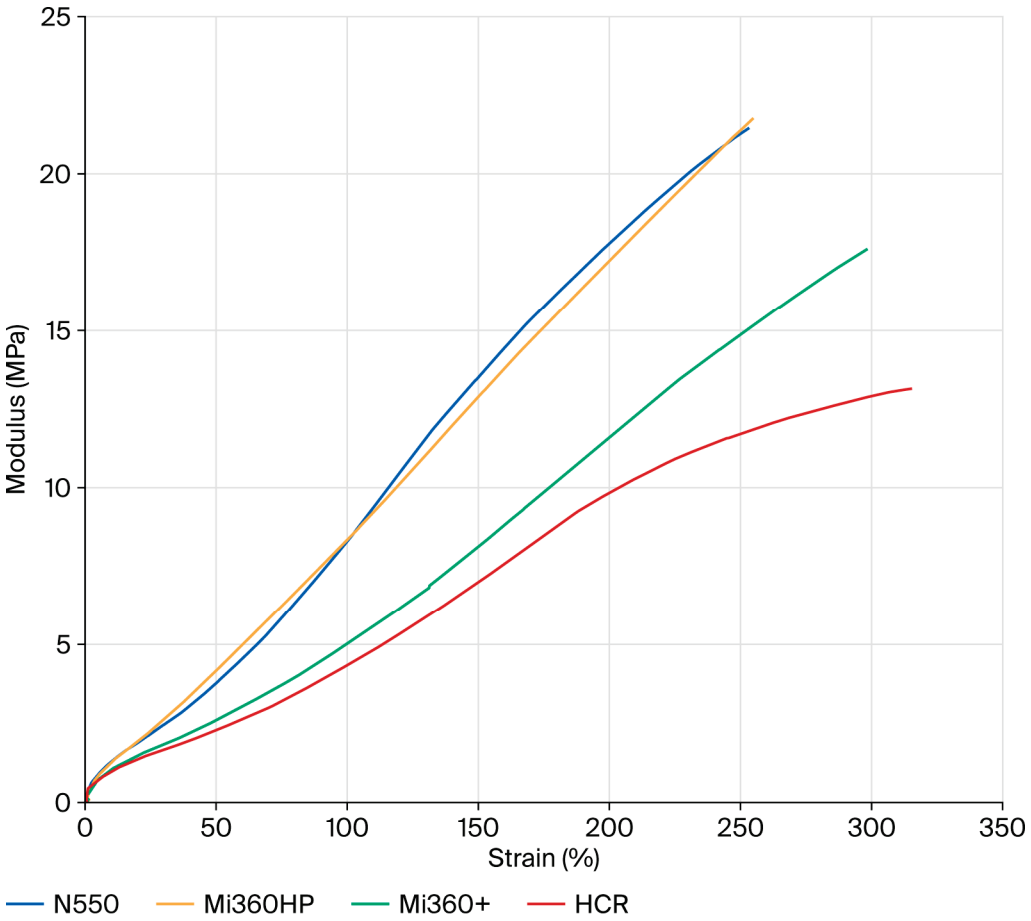

Figure 6. Tensile curves of the different rCB variants compared to N550 in the model SBR formulation.

Given that the ultimate goal of tyre pyrolysis is to provide raw materials back into the tyre industry, it was prudent to evaluate the dynamic properties of the rCB materials. Elastic modulus plots showing the non-linearity of compounds filled with N550 and different rCB materials are provided in Figure 7. At a low strain (E'_0), the dynamic stiffness contains the full contribution of the filler network. As the dynamic strain increases, the filler–filler interactions are gradually disrupted, leading to a plateau at E'_∞. This phenomenon is known as the Payne effect [48]. The difference between the low and high strain modulus ($\Delta E' = E'_0 - E'_\infty$) can therefore be used as a measure of the filler network. Assuming equal filler loadings and dispersion, the two key parameters that influence the level of filler–filler interaction are the surface area and surface chemistry. For standard grades of CB, $\Delta E'$ scales directly with surface area, as all exhibit the same surface chemistry. Given the higher surface area of the rCB materials, they would be expected to exhibit higher $\Delta E'$ values than N550 if their surface chemistry was the same. This is clearly not the case for the rCBs, with all exhibiting a lower filler networking efficiency, in line with previous studies that

attributed the networking reduction to the presence of carbonaceous residue masking the active sites of CB [8,21]. Considering the effect of ash, there is a general trend for reducing filler–filler interactions from N550→Mi360HP→Mi360+ as ash content increases. In some respects, the rCBs behave like a dual-filler system, with silica and zinc sulphide particles acting to disrupt the CB network. The clear effect of carbonaceous residue is seen when comparing the HCR to the Mi360+, with further reduced filler–filler interactions for the former. This will be a function of both the reduced surface area and surface activity of the HCR.

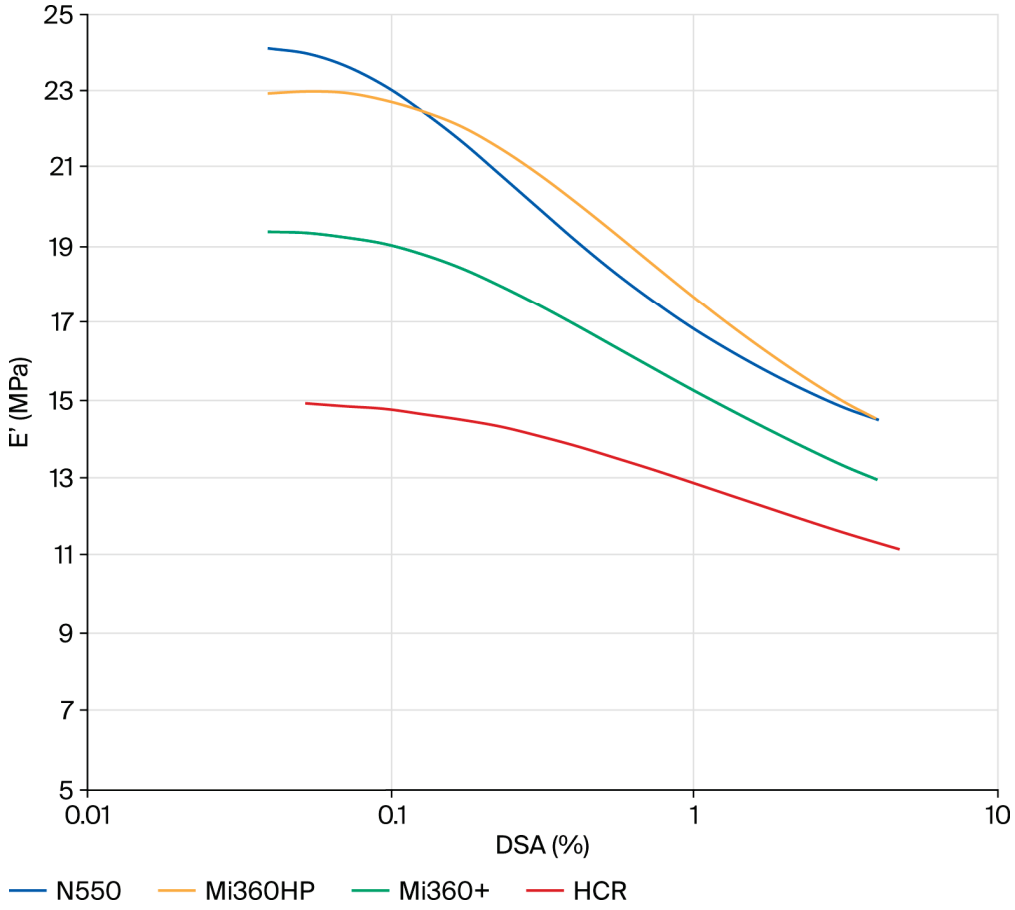

Figure 7. Strain dependency plots of the different rCB variants compared to N550 in the model SBR formulation.

At a high strain (E'_{∞}), the dynamic stiffness is a combination of gum modulus, hydrodynamic effects and filler–polymer interactions [48]. Considering the formulation and filler loadings were constant, E'_{∞} can be used as a measure of the filler–polymer interaction. In this case, the Mi360HP exhibits a similar level of filler–polymer interaction as the N550, in good agreement with the physical properties data. As the silica level increases for the Mi360+, the filler–polymer interaction lessens. A previous study has shown that the silica content of an rCB is amenable to silane coupling, offering a route to enhancing the polymer–filler interaction of residue-free rCB [49]. As for the other parameters, the effects of carbonaceous residue on reducing the polymer–filler interaction were pronounced.

4. Conclusions

This study demonstrates that it is possible to impart a high degree of control to prepare statistically different feedstocks to produce different grades of rCB. Furthermore, a detailed understanding of the feedstock composition can be used to predict both rCB yields and

rCB ash contents, offering useful tools in the optimisation of a pyrolysis process. The fixed carbon and ash content of a pyrolysis feedstock should correspond to the rCB yield, if free from organic and carbonaceous residues. This approach was used in the production of two grades of rCB, Mi360HP and Mi360+, produced from truck and car tyres, respectively. The primary difference between the two is their ash content, at 19% for the Mi360HP and 31% for the Mi360+. The term ash is a poor descriptor of the inorganic components of rCB, with TEM/EDX and ICP-OES analyses confirming the bulk to be silica filler clusters entangled with the CB aggregates, being more prevalent in the car tyre derived Mi360+. The other key inorganic component was zinc sulphide, found to reside as discrete particulates on the surface of the filler aggregates.

It has long been established that, for equivalent colloidal properties, rCB does not exhibit the same in-rubber behaviour as CB. Clearly, ash content, and to be more precise silica content, is a contributing factor. Silica, without a coupling agent, exhibits a lower polymer interaction compared with CB, manifesting as lower quai-static and dynamic modulus values for the Mi360+ when compared to the lower-silica-content Mi306HP. Ash content, therefore, performs an important role in the development of rCB specifications. However, the typical rCB ash content specifications of <20 wt% are unrealistic from UK waste tyres, especially when considering that the theoretical rCB ash contents from truck and car tyres were determined as 20 and 35 wt%, respectively. Furthermore, the Mi360HP was close to this limit (19 wt%), but still closely matched the tensile properties and filler–polymer interaction of the N550.

To demonstrate that ash is far from the only consideration regarding rCB reinforcing behaviour, a high carbonaceous residue (HCR) sample was prepared from car tyres to dilute the ash content to 19 wt%, i.e., within typical ash content specifications. This material ranked worse than the high-silica-content Mi360+ for all of the in-rubber properties, including dispersion, tensile and dynamic behaviour. TEM and colloidal assessments identified the carbonaceous residues as significantly reducing the surface area and structure of the rCB, both of which are fundamental to rubber reinforcement. Although ash content attracts a lot of attention, this study conclusively shows that carbonaceous residues are more detrimental to rCB performance.

Many have studied rCB ash reduction [16,17,50–52], but little attention has been given to controlling and limiting carbonaceous residues. This is likely linked to the availability of well-established test methods for the easy determination of ash content [23,53]; however, the same is not true for carbonaceous residues, which are difficult to differentiate from the CB content of an rCB. A fast and reliable method for carbonaceous residue determination would be extremely beneficial to the industry, offering the missing piece of the jigsaw in the classification and specification debate. Furthermore, the ability to silane-couple the silica component of a residue-free rCB provides an opportunity to benefit from the growing silica content of road tyres.

Author Contributions: Conceptualization, C.N. and M.M.; data curation, C.N., R.M. and P.E.; formal analysis, C.N., P.E. and R.M.; methodology, A.L.-C., P.E. and R.M.; project administration, C.N.; resources, C.N.; supervision, M.M.; writing—original draft, C.N.; writing—review and editing, C.N. All authors have read and agreed to the published version of the manuscript.

Funding: This research received no external funding.

Institutional Review Board Statement: Not applicable.

Data Availability Statement: The original contributions presented in this study are included in the article. Further inquiries can be directed to the corresponding author.

Acknowledgments: The authors would like to thank the Itochu Corporation of Japan for supporting this R&D activity.

Conflicts of Interest: Authors Christopher Norris, Antonio Lopez-Cerdan and Mark Murfitt were employed by the company Murfitts Industries. Author Richard Moon was employed by the company Avon Protection. The remaining author declares that the research was conducted in the absence of any commercial or financial relationships that could be construed as a potential conflict of interest.

Abbreviations

The following abbreviations are used in this manuscript:

rCB	Recovered carbon black
TPO	Tyre pyrolysis oil
CB	Carbon black
VM	Volatile matter
FC	Fixed carbon
HCR	High carbonaceous residue
BET	Brunauer–Emmett–Teller
TGA	Thermogravimetric analysis
ICP-OES	Inductively coupled plasma optical emission spectrometer
EDX	Energy dispersive X-ray
S/TEM	Scanning/transmission electron microscope
MDR	Moving die rheometer
SEM	Scanning Electron Microscope

References

1. Zerin, N.; Rasul, M.; Jahirul, M.; Sayem, A. End-of-life tyre conversion to energy: A review on pyrolysis and activated carbon production processes and their challenges. *Sci. Total Environ.* **2023**, *905*, 166981. [CrossRef]
2. European Commission. *The European Green Deal, COM(2019) 640 Final*; European Commission: Brussels, Belgium, 2019.
3. Banar, M. Life cycle assessment of waste tire pyrolysis. *Fresenius Environ. Bull.* **2015**, *24*, 1215.
4. Briones-Hidrovo, A.; Costa, S.M.; Maganinho, C.; Silva, C.M.; Rocha, J.; Dias, A.C.; Portugal, I.; Silva, C.M. Recovering carbon black from end-of-life tires: A consequential life cycle assessment. *Environ. Impact Assess. Rev.* **2025**, *115*, 108044. [CrossRef]
5. Zhang, Y.; Hwang, J.Y.; Peng, Z.; Andriese, M.; Li, B.; Huang, X.; Wang, X. Microwave Absorption Characteristics of Tire. In *Characterization of Minerals, Metals, and Materials*; Carpenter, J.S., Bai, C., Escobedo, J.P., Hwang, J.-Y., Ikhmayies, S., Li, B., Li, J., Monteiro, S.N., Peng, Z., Zhang, M., Eds.; Springer: Cham, Switzerland; Hoboken, NJ, USA, 2015; pp. 235–243.
6. Inamuddin; Asiri, A.M.; Kanchi, S. (Eds.) Green rubber composites. In *Green Sustainable Process for Chemical and Environmental Engineering and Science*; Elsevier: Amsterdam, The Netherlands, 2022; Chapter 14; pp. 273–312.
7. *ASTM D8178-20*; Standard Terminology Relating to Recovered Carbon Black (rCB). ASTM International: West Conshohocken, PA, USA, 2020.
8. Norris, C.J.; Lopez-Cerdan, A.; ter Haar, P. Understanding Recovered Carbon Black. *Rubber Chem. Technol.* **2023**, *96*, 196. [CrossRef]
9. Xiao, Z.; Pramanik, A.; Basak, A.; Prakash, C.; Shankar, S. Material recovery and recycling of waste tyres—A review. *Clean. Mater.* **2022**, *5*, 100115. [CrossRef]
10. Martínez, J.D.; Puy, N.; Murillo, R.; García, T.; Navarro, M.V.; Mastral, A.M. Waste tyre pyrolysis—A Review. *Renew. Sustain. Energy Rev.* **2013**, *23*, 179. [CrossRef]
11. Hoyer, S.; Kroll, L.; Sykutera, D. Technology comparison for the production of fine rubber powder from end of life tyres. *Procedia Manuf.* **2020**, *43*, 193. [CrossRef]
12. Valentini, F.; Pegoretti, A. End-of-life options of tyres. A review. *Adv. Ind. Eng. Polym. Res.* **2022**, *5*, 203. [CrossRef]
13. Bowles, A.J.; Fowler, G.D. Assessing the impacts of feedstock and process control on pyrolysis outputs for tyre recycling. *Resour. Conserv. Recycl.* **2022**, *182*, 106277. [CrossRef]
14. Paul, S.; Rahaman, M.; Ghosh, S.K.; Das, P.; Katheria, A.; Ghosh, T.; Das, N.C. Effects of tire-derived pyrolytic carbon black and pyrolytic heavy oil on the curing and mechanical properties of styrene-butadiene rubber composites. *Polym. Eng. Sci.* **2023**, *63*, 2942. [CrossRef]

15. European Union. Regulation (EU) 2020/740 of the European Parliament and of the Council of 25 May 2020 on the labelling of tyres with respect to fuel efficiency and other parameters, amending Regulation (EU) 2017/1369 and repealing Regulation (EC) No 1222/2009. *Off. J. Eur. Union* **2020**, *177*, 1–31.
16. Bowles, A.J.; Wilson, A.L.; Fowler, G.D. Synergistic benefits of recovered carbon black demineralisation for tyre recycling. *Resour. Conserv. Recycl.* **2023**, *198*, 107124. [CrossRef]
17. Silva, C.M.; Maganinho, C.; Mendes, A.; Rocha, J.; Portugal, I.; Silva, C.M. Recovered carbon black: A comprehensive review of activation, demineralization, and incorporation in rubber matrices. *Carbon Resour. Convers.* **2025**, 100334. [CrossRef]
18. Moulin, L.; Da Silva, S.; Bounaceur, A.; Herblot, M.; Soudais, Y. Assessment of Recovered Carbon Black Obtained by Waste Tires Steam Water Thermolysis: An Industrial Application. *Waste Biomass Valor.* **2017**, *8*, 2757. [CrossRef]
19. Hewitt, N. *Compounding Precipitated Silica in Elastomers*; William Andrew Publishing: Norwich, NY, USA, 2007.
20. Bridgestone & Michelin, Recovered Carbon Black Guidelines. 2023. Available online: https://business.michelinman.com/blog/articles/michelin-and-bridgestone-tackle-environmental-initiative (accessed on 26 August 2025).
21. Norris, C.J.; Hale, M.; Bennett, M. Pyrolytic carbon: Factors controlling in-rubber performance. *Plast. Rubber Compos.* **2014**, *43*, 245. [CrossRef]
22. *ASTM D1618-18*; Standard Test Method for Carbon Black Extractables—Transmittance of Toluene Extract. ASTM International: West Conshohocken, PA, USA, 2018.
23. *ASTM D8474-23*; Standard Test Method for Recovered Carbon Black (rCB)—Compositional Analysis by Thermogravimetry (TGA). ASTM International: West Conshohocken, PA, USA, 2023.
24. Darmstadt, H.; Roy, C.; Kaliaguine, S.; Sahouli, B.; Blacher, S.; Pirard, R.; Brouers, F. Fractal Analysis of Commercial and Pyrolytic Carbon Blacks Using Nitrogen Adsorption Data. *Rubber Chem. Technol.* **1995**, *68*, 330. [CrossRef]
25. Karthikeyan, S.; Sathiskumar, C.; Moorthy, R. Effect of process parameters on tire pyrolysis: A review. *J. Sci. Ind. Res. India* **2012**, *71*, 309.
26. Darmstadt, H.; Roy, C.; Kaliaguine, S. ESCA characterisation of commercial carbon blacks and of carbon blacks from vacuum pyrolysis of used tires. *Carbon* **1994**, *32*, 1399.
27. Yang, Y.; Wang, J.; Yan, L. Surface character of pyrolytic carbon black. *J. Chem. Ind. Eng.* **2005**, *56*, 720.
28. Pantea, D.; Darmstadt, H.; Kaliaguine, S.; Roy, C. Heat-treatment of carbon blacks obtained by pyrolysis of used tires. Effect on the surface chemistry, porosity and electrical conductivity. *J. Anal. Appl. Pyrol.* **2003**, *67*, 55. [CrossRef]
29. Darmstadt, H.; Roy, C.; Kaliaguine, S.; Cormier, H. Surface energy of commercial and pyrolytic carbon blacks by inverse gas chromatography. *Rubber Chem. Technol.* **1997**, *70*, 759. [CrossRef]
30. Chen, J.; Hu, M.; Li, Y.; Li, R.; Qing, L. Significant Influence of Bound Rubber Thickness on the Rubber Reinforcement Effect. *Polymers* **2023**, *15*, 2051. [CrossRef]
31. *ASTM D6556-21*; Standard Test Method for Carbon Black—Total and External Surface Area by Nitrogen Adsorption. ASTM International: West Conshohocken, PA, USA, 2021.
32. *ASTM WK87480*; New Test Method for Dry Powder rCB Particle Size Analysis via Laser Diffraction. ASTM International: West Conshohocken, PA, USA, 2023. Available online: https://www.astm.org/membership-participation/technical-committees/workitems/workitem-wk87480 (accessed on 26 August 2025).
33. *ASTM D5230-21*; Standard Test Method for Carbon Black—Automated Individual Pellet Hardness. ASTM International: West Conshohocken, PA, USA, 2021.
34. *ASTM D3849-22*; Standard Test Method for Carbon Black-Morphological Characterization of Carbon Black Using Electron Microscopy. ASTM International: West Conshohocken, PA, USA, 2022.
35. Grulke, E.A.; Rice, S.B.; Xiong, J.; Yamamoto, K.; Yoon, T.H.; Thomson, K.; Saffaripour, M.; Smallwood, G.J.; Lambert, J.W.; Stromberg, A.J.; et al. Size and Shape distributions of carbon lack aggregates by transmission electron microscopy. *Carbon* **2018**, *130*, 822. [CrossRef]
36. *ASTM D3191-10*; Standard Test Methods for Carbon Black in SBR (Styrene-Butadiene Rubber)—Recipe and Evaluation Procedures. ASTM International: West Conshohocken, PA, USA, 2010.
37. *ASTM D8491-23*; Standard Test Method for Recovered Carbon Black—Rheological Non-Linearity of a Rubber Compound by Fourier Transform Rheology. ASTM International: West Conshohocken, PA, USA, 2023.
38. *ASTM D5289-19a*; Standard Test Method for Rubber Property—Vulcanization Using Rotorless Cure Meters. ASTM International: West Conshohocken, PA, USA, 2019.
39. *ASTM D412-16*; Standard Test Methods for Vulcanized Rubber and Thermoplastic Elastomers—Tension. ASTM International: West Conshohocken, PA, USA, 2016.
40. *ASTM D2240-15*; Standard Test Method for Rubber Property—Durometer Hardness. ASTM International: West Conshohocken, PA, USA, 2015.
41. Hu, Y.; Yu, X.; Ren, J.; Zeng, Z.; Qian, Q. Waste tire valorization: Advanced technologies, process simulation, system optimization, and sustainability. *Sci. Total Environ.* **2024**, *942*, 173561. [CrossRef]

42. Czajczyńska, D.; Czajka, K.; Krzyżyńska, R.; Jouhara, H. Waste tyre pyrolysis—Impact of the process on its products on the environment. *TSEP* **2020**, *20*, 100690. [CrossRef]
43. Czajczyńska, D.; Krzyżyńska, R.; Ghazal, H.; Jouhara, H. Experimental investigation of waste tyres pyrolysis gas desulfurization through absorption in alkanolamines solutions. *Int. J. Hydrogen Energy* **2022**, *52*, 1006. [CrossRef]
44. Tricás, N.; Vidal-Escales, E.; Borrós, S.; Gerspacher, M. Influence of carbon black amorphous phase content on rubber filled compounds. *Compos. Sci. Technol.* **2003**, *63*, 1155. [CrossRef]
45. Medalia, A.I. Effective degree of immobilization of rubber occluded within carbon black aggregates. *Rubber Chem. Technol.* **1972**, *45*, 1171. [CrossRef]
46. Dannenberg, E.M. Bound rubber and carbon black reinforcement. *Rubber Chem. Technol.* **1986**, *59*, 512. [CrossRef]
47. Hallett, J. Dispersion kinetics of carbonaceous materials during elastomer mixing. In Proceedings of the Tire Tech, Hannover, Germany, 4–6 March 2025.
48. Payne, A.R. Dynamic mechanical properties of filler loaded vulcanisates. *Rubber Plast. Age* **1961**, *42*, 963.
49. Norris, C.J.; Lopez-Cerdan, A.; Murfitt, M. Ash. In Proceedings of the Recovered Carbon Black, Amsterdam, The Netherlands, 5–6 November 2024.
50. Costa, S.M.R.; Fowler, D.; Carreira, G.A.; Portugal, I.; Silva, C.M. Production and Upgrading of Recovered Carbon Black from the Pyrolysis of End-of-Life Tires. *Materials* **2022**, *15*, 2030. [CrossRef] [PubMed]
51. Zainal, N.; Halim, S. A review on demineralization, activation, and potential applications of the solid fraction obtained from the pyrolyzed waste tires. *Clean. Waste Syst.* **2025**, *11*, 100285. [CrossRef]
52. Jiang, G.; Pan, P.; Sun, Y. Recovery of high pure pyrolytic carbon black from waste tires by dual acid treatment. *J. Clean. Prod.* **2022**, *374*, 133893. [CrossRef]
53. *ASTM D1506-15*; Standard Test Methods for Carbon Black—Ash Content. ASTM International: West Conshohocken, PA, USA, 2015.

polymers

MDPI

Article

The Influence of Zinc Stearate Complexes on the Sulfur Vulcanization of Ethylene–Propylene–Diene Monomer

Krzysztof Kaczewiak [1,2,*], Piotr Głąb [2] and Magdalena Maciejewska [3]

[1] Interdisciplinary Doctoral School, Lodz University of Technology, 116 Żeromskiego Street, 90543 Lodz, Poland
[2] Hutchinson Poland Sp z o.o., 130 Kurczaki Street, 90543 Lodz, Poland
[3] Institute of Polymer and Dye Technology, Lodz University of Technology, 16 Stefanowskiego Street, 90543 Lodz, Poland
* Correspondence: krzysztof.kaczewiak@dokt.p.lodz.pl

Abstract

This article explores the influence of synthesized zinc stearate (ZnSt) complexes with different molar ratios of zinc oxide (ZnO) and stearic acid (StA) on the sulfur vulcanization and properties of the ethylene–propylene–diene monomer (EPDM). The aim of study was to reduce the amount of ZnO in elastomer composites without affecting their compression set. The research involves synthesizing zinc complexes, including the addition of sulfur, and using them as activators in EPDM compounds. The synthesized products were characterized using DSC and FTIR to identify their composition and thermal properties. The results of the compression set and equilibrium swelling tests indicated that ZnO was used in excess as an activator. Zinc complexes allowed for a significant reduction in zinc content compared to ZnO. The stoichiometric salt of ZnO and StA was the most effective in terms of vulcanization parameters and the compression set. Non-stoichiometric complexes were less effective, proportionally to their content. SEM images showed that the dispersion of components was relatively homogeneous in vulcanizates with active ZnO and commercial ZnSt. However, the blooming of ZnSt from vulcanizates was observed. Thus, using synthesized materials could reduce the zinc content in EPDM composites while maintaining good properties, but a further reduction is needed to avoid blooming.

Keywords: EPDM; cross-linking density; compression set; elastomers; carbon footprint

1. Introduction

Cross-linked rubber is a material with exceptional elastic properties, which plays a key role in many areas of our lives. Its ability to stretch and return to its original shape makes it irreplaceable in the production of tires, seals, medical gloves, and many other rubber products. Thanks to its unique properties, rubber is a material that has revolutionized many industries and continues to play a key role in the modern world.

The production of rubber composites is a complex process that requires precision and advanced technology to obtain products of high quality and durability. Rubber composites consist of both rubber and a number of other functional additives, e.g., fillers, plasticizers, activators, accelerators, or antioxidants, which improve their processing and facilitate properties of the vulcanizates. One of the substances widely used in the vulcanization process is zinc oxide (ZnO) [1,2]. It acts as an activator, speeding up the vulcanization reaction by activating the vulcanization accelerators [3]. When combined with stearic acid (StA), it increases the effectiveness of sulfur in the vulcanization process. Moreover, adding

ZnO to a rubber compound improves the tensile strength, abrasion resistance, and elasticity of vulcanizates. Due to the key role of ZnO in elastomer technology, it is estimated that over 50% of ZnO production is consumed by the rubber industry [4,5]. Other industries consuming ZnO include agriculture, ceramics, and concrete. ZnO is also used on a smaller scale in the electronics industry and cosmetics production. ZnO used in the rubber industry is most often obtained in a metallurgical process by roasting zinc ore in the presence of air [6,7]. Alternatively, ZnO can be obtained by using a number of chemical methods, not always applicable to the industrial-scale production of ZnO due to the low efficiency of synthesis and economics [8]. ZnO production also generates carbon dioxide (CO_2) and other greenhouse gas emissions, mainly due to the energy processes involved in roasting ores or drying and roasting the products of chemical synthesis methods. Depending on the method used, the carbon footprint of ZnO production can vary [9,10]. Metallurgical processes are usually more energy-intensive and generate larger CO_2 emissions. On the other hand, chemical methods can be less energy-intensive, but require the use of other reagents, which also has an impact on the environment. The production of ZnO, regardless of the method, is therefore a harmful process for the natural environment; hence, it is justified to look for possibilities of reducing its consumption in various industries, especially in the case of the rubber industry, which is the main consumer of this material.

Regarding the rubber industry, ZnO is considered as the best activator for sulfur cross-linking due to its higher reaction kinetics and promotion of short sulfur cross-links that increase the overall cross-linking density of vulcanized rubber [11,12]. It also acts as a filler and scavenger of harmful reaction products, a cure agent for halogenated or carboxylated rubbers, and even provides protection from molded product shrinkage or mold fouling. In addition, ZnO has a significant effect on some of the physical properties of vulcanizates. Owing to its poor dispersibility in the rubber matrix, ZnO demands a high dosage to ensure efficient vulcanization. From an ecological point of view, a high amount of ZnO raises a concern about its release due to the exploitation of rubber products and its toxicity for the environment [1]. Generally, ZnO is considered as a substance safe for humans, but based on the international standard, i.e., Globally Harmonized System of Classification and Labelling of Chemicals (GHS), it is classified as H400: very toxic to aquatic life. Hence, for the sake of the environment, it is recommended to reduce the amount of ZnO in rubber products. It should be noticed that, when ZnO is used in vulcanization in the form of microsized ZnO crystal particles, only a reduced portion is able to react with the curing compounds, leading to a residual amount of unreacted ZnO in the rubber matrix. This unreacted ZnO can penetrate into groundwater while rubber products are stored in landfills, or in the form of dust, which is generated as a result of rubbing tires on the road surface. In the case of tires, a consequence of the wear of tire treads is zinc leaching, which may generate an excess of zinc concentration in the environment, potentially increasing in the future due to the widespread and expanding use of ZnO. This makes the topic of ZnO reduction very important for the rubber industry, as one of the largest users of ZnO.

The efficiency of ZnO in vulcanization and its influence on the properties of rubber composites strongly depend on the dispersion degree of ZnO particles in the elastomer matrix. Obtaining a good dispersion of ZnO in the elastomer matrix, and consequently an availability of ZnO particles for reaction with other components of the cross-linking system, can significantly improve its activity in the cure process and the final mechanical properties of the vulcanizates. Sreethu and Naskar [11] compared the activation effectiveness and impact on mechanical properties and the cure characteristics of different types of ZnO, i.e., conventional, active, and nanopowder, in the vulcanization of natural rubber filled with carbon black. Their investigation showed that a more homogeneous dispersion and higher surface area of ZnO can help to reduce its content without decreasing the

mechanical properties of the rubber composites. The addition of fatty acids, such as StA, also plays a significant role in vulcanization [1,13]. They improve the dispersion of ZnO particles in the rubber matrix by boosting the contact surface of zinc ions with vulcanization accelerators. ZnO reacts with StA, forming zinc stearate (ZnSt), which is assumed as an essential cure activator. Junkong et al. [14] performed in situ research to study the activity of different fatty acids in comparison with StA and ZnSt in the vulcanization of isoprene rubber. It was shown that ZnO creates 2:2 bidentate zinc/stearate complexes, with StA also having some hydroxyl groups. These complexes act as catalysts to accelerate the sulfur cross-linking reactions in the rubber matrix. Heideman et al. [15] studied various metal oxides and a clay loaded with Zn^{2+} ions as a solution that can help reduce the zinc content in rubber composites. Hence, zinc stearate, zinc 2-ethylhexanoate, and zinc m-glycerolate were employed instead of ZnO to activate the sulfur vulcanization of the ethylene–propylene–diene monomer (EPDM) and styrene–butadiene (SBR) rubber. Zinc m-glycerolate, with the highest amount of zinc per 1 g, showed the highest activity in the vulcanization. However, no reduction in the zinc amount was provided compared to rubber compounds cured with ZnO, since the authors of the publication used zinc complexes in an amount equivalent to the content of zinc ions in the amount of ZnO used. Therefore, the possibility of reducing the amount of zinc in rubber products was not investigated, but only the possibility of replacing ZnO with other zinc compounds. Przybyszewska et al. [16] reported that the use of organic zinc activators in the form of zinc salts or zinc complexes with 1,3-diketones, depending on their structure, allowed for a reduction in the amount of zinc in rubber compounds by 70–90 wt.% compared to those containing ZnO and stearic acid. However, vulcanizates with a lower cross-link density compared to those containing ZnO were obtained, which can have a significant impact on their mechanical properties, e.g., the compression set, which is crucial for rubber seals. Thus, the results reported in the literature are quite optimistic, but they need to be investigated further due to a lack of clear knowledge of all variables that affect the vulcanization process.

Considering the vulcanization, there is a lot of information in the literature about ZnO and StA complex formation. Scotti [12] prepared an extensive review, which indicated that stoichiometric ZnSt is not an efficient activator of sulfur vulcanization. However, Junkong et al. [14] observed that non-stoichiometric salts of ZnO and fatty acids can effectively activate vulcanization. It was found that, at high temperatures, a dominant structure of the product formed in the ZnO and StA reaction was a bridging bidentate zinc/stearate complex with a molar ratio of 2:2. It involved two zinc ions bridged by two stearate (StA) ligands, where each stearate molecule coordinated to both zinc ions with its carboxylate group. This structure was represented as $(Zn_2(\mu\text{-}O_2CC_{17}H_{35})_2)^{2+}(OH–)_2{\cdot}R_1R_2$, where R_1 and R_2 can be water molecules or rubber segments, respectively. The most likely structure of the binuclear type bridging bidentate zinc/stearate complex is presented in Figure 1 [17].

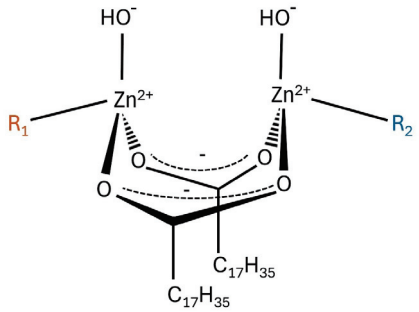

Figure 1. Binuclear type bridging bidentate zinc/stearate complex, where R_1 and R_2 are water and/or a rubber segment, based on [17].

A good example of a non-stoichiometric complex of ZnO and StA was also described by Setianto et al. [18]. The aim of this study was to produce ZnSt; however, ZnO and StA were mixed in non-stoichiometric proportions. Instead of 2 moles of StA per 1 mole of ZnO, the synthesis involved 3 moles of ZnO per 1 mole of StA, which resulted in a 6-fold excess of ZnO. Surprisingly, the tensile strength and hardness of the vulcanizates obtained by replacing ZnO and StA with a synthesis product showed significant improvement. This suggests that the non-stoichiometric complex of ZnO with StA can be potentially as active as the high amount of active ZnO, which is typically used in rubber compounds in the amount of 3 phr. Hence, the use of non-stoichiometric zinc complexes with StA can potentially contribute to the reduction in the amount of zinc in elastomer composites compared to those containing active ZnO, or even to the elimination of active ZnO. On the other hand, there is no information in the literature about sulfur-ZnO complex formation during the vulcanization of rubber compounds. The past research showed that there is a reaction between ZnO and sulfur, with the creation of zinc sulfide (ZnS), which is deposited on the surface of the vulcanization molds [19]. This proves that, during the vulcanization of rubber, like EPDM, some amount of ZnO is transformed into ZnS, which can influence the rubber cross-linking density and consequently the vulcanizate properties [3]. Thus, in this work, we synthesized zinc complexes using different molar ratios of ZnO:StA, while additionally introducing sulfur into some of these complexes. Standard zinc stearate (ZnSt) contains two moles of monovalent StA anions for one mole of divalent cation of zinc. Taking into consideration that, in the literature, there are plenty of studies confirming the formation of non-stoichiometric complexes between stearic acid and ZnO, we decided to check how they affect the curing characteristics of rubber composites and properties of the vulcanizates. During previously conducted research, we have also observed that heating sulfur with ZnO in a masterbatch before adding an accelerator pack improved the functional parameters of vulcanizates, i.e., the compression set, despite the cross-linking density reduction [20]. Therefore, in this research, samples with sulfur were also prepared. Moreover, syntheses in the presence of sulfur were performed to verify the potential formation of complexes between carboxylic acid, sulfur, and ZnO. Then, we used the obtained synthesis products as activators of sulfur vulcanization as an alternative to systems containing ZnO, StA, and sulfur separately. We believed that the use of these complexes would reduce the amount of ZnO in elastomer composites, and thus the harmfulness of ZnO to the environment and the carbon footprint associated with its application.

2. Materials and Methods

2.1. Materials

The masterbatch of the ethylene-propylene-diene monomer compound with the hardness of 74 Shore A (74ShA EPDM) used for the study was a serial product used on extrusion. This compound was vulcanized with a sulfur cure system. Its composition is not revealed due to the Hutchinson confidentiality policy. In case of cure system adjustments, the 74ShA compound was mixed in the form of a masterbatch that did not contain any components of the curing system, i.e., sulfur, ZnO, or StA. The accelerators were commercially available predispersions purchased from Konimpex Chemicals Sp. Z o.o. (Konin, Poland), with the following concentration of active ingredient: caprolactam disulfide (CLD)—80%, 2,2′-benzothiazyl disulfide (MBTS)—70%, N-cyclohexyl-2-benzothiazole sulfenamide (CBS)—80%, and zinc dialkyldithiophosphate (ZDTP)—50%. Zinc oxide with a specific surface area of 10 m^2/g (Huta Będzin, Będzin, Poland) and active zinc oxide with a specific surface area of 45 m^2/g (Silox India, Vadodara, India), together with stearic acid (Uniqema, Goole, UK), were used to synthesize zinc complexes. Zinc stearate with a purity > 98.5%

was purchased from Warchem (Trakt Brzeski, Poland), while sulfur was manufactured by Siarkopol (Tarnobrzeg, Poland).

2.2. Synthesis of Zinc Complexes and Salts

The sets of synthesis products were prepared in a flask heated with methyl silicone oil to 160 °C. Mixing was ensured by a magnetic stirrer. The synthesis station is presented in Supplementary Materials (Figure S1). The mixtures were prepared according to the recipes expressed in moles in Table 1.

Table 1. Composition of the mixtures of ZnO with StA and/or S in moles of each ingredient.

No.	Sample Symbol	Stearic Acid (mole)	Zinc Oxide [1] (mole)	Sulfur [2] (mole)
1	StZn_s_1	2	1	-
2	StZn_s_2	2	2	-
3	StZnS_s_1	2	1	8
4	StZnS_s_2	2	2	8
5	StZn_a_1	2	1 A	-
6	StZn_a_2	2	2 A	-
7	StZnS_a_1_7	2	1 A	8
8	StZnS_a_2_8	2	2 A	8
9	StZnS_a_1_9	2	1 A	8
10	StZnS_a_2_10	2	2 A	8

[1] The ZnO used for the synthesis was in two variants: standard ZnO and active ZnO with increased specific surface area, marked with the letter A in the table. [2] Sulfur in samples No. 3, 4, 7, and 8 was added after reaction between ZnO and StA. Sulfur in samples No. 9 and 10 was added to StA before ZnO.

For samples 1 to 8 given in Table 1, ZnO was added to the melted technical StA and stirred at 160 °C. After a turbulent synthesis reaction with the release of water vapor, sulfur was added according to the recipes presented in Table 1, and all samples were further heated and stirred for 45 min. Samples 9 and 10 were prepared according to the same recipe as samples 7 and 8 but differed in the order of dosing the individual components. Sulfur was added to the melted stearic acid, and, after it had melted, active ZnO was added. After the synthesis reaction had taken place, the mixture was stirred and heated for 45 min at 160 °C.

Stearic acid used for the synthesis was a standard material used in rubber industry, containing 57% of stearic acid ($C_{17}H_{35}COOH$), 35% of palmitic acid ($C_{15}H_{31}COOH$), and other fatty acids from C14 to C20. To calculate the amount of ZnO to technical StA in complex preparations, the assumption was made as for StA of 100% purity. Considering the difference in molecular weight between palmitic and stearic acid, a 3% excess of carboxylic acid vs. calculated molar ratio for 100% purity of StA should be expected. However, we decided to accept the possible slight excess of carboxylic acids in stoichiometric reactions.

The TD-GC-MS chromatogram presented in Figure 2 confirmed the compliance of the material with the manufacturer's declaration. The first peak (~21 min) corresponds to palmitic acids and the second (~23 min) to stearic acid. There are visible traces of shorter and longer carboxylic acids on the chromatogram as well.

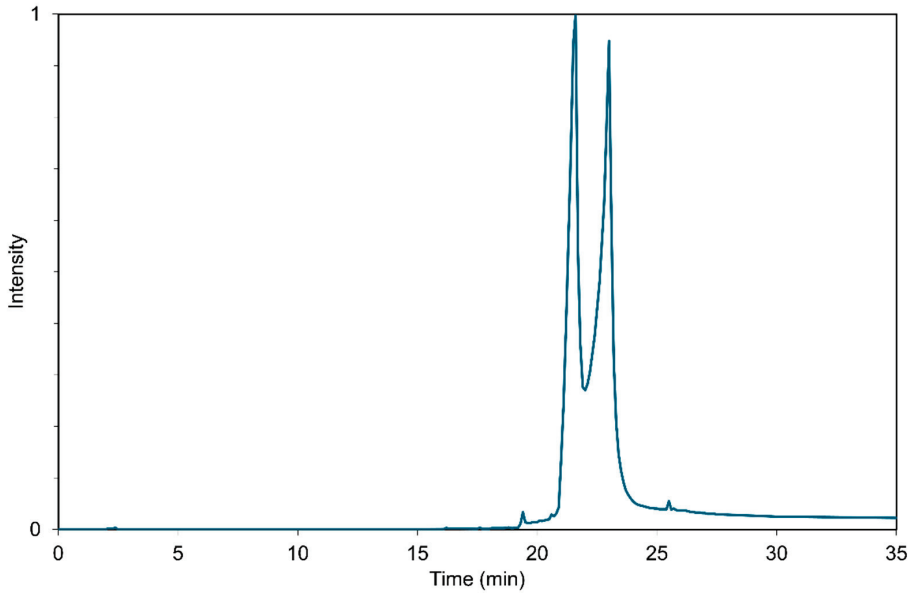

Figure 2. TD-GC-MS chromatogram of technical stearic acid used for synthesis reactions.

2.3. Preparation of Rubber Compounds

Three series of rubber compounds, with compositions given in Tables 2 and 3, were prepared and studied.

Table 2. Compositions of rubber compounds containing synthesized products described in Table 1.

Rubber Compound	Description	ZnO phr Equivalent	StA/Zn [mole/mole]
Ref0	Reference compound with standard ZnO.	3	0.15
Ref1	Reference compound with active ZnO.	3	0.15
Ref2	Reference compound with active ZnO and sulfur thermally transformed (200 °C/5 min) in masterbatch before adding accelerator set—experiment following the previous study [13].	3	0.15
Test1	Rubber compound with StZn_a_1. Targeted to stoichiometric ZnSt. Amount of StZn_a_1 equivalent to StA concentration in reference. A total of 13.6 times less Zn than the reference.	0.22	2
Test2	Rubber compound with StZn_a_1. Targeted to stoichiometric ZnSt. Amount of StZn_a_1 to obtain Zn equivalent 3 times less than the reference.	1	2
Test3	Rubber compound with StZn_a_2. Targeted to ZnSt complex. Amount of StZn_a_2 equivalent to stearic acid concentration in reference. A total of 6.7 times less Zn than the reference.	0.44	1
Test4	Rubber compound with StZn_a_2. Targeted to ZnSt complex. Amount of StZn_a_2 to obtain Zn equivalent 3 times less than the reference.	1	1
Test5	Rubber compound with StZn_s_1. Targeted to stoichiometric ZnSt. Amount of StZn_s_1 equivalent to StA concentration in reference. A total of 13.6 times less Zn than the reference.	0.22	2

Table 2. *Cont.*

Rubber Compound	Description	ZnO phr Equivalent	StA/Zn [mole/mole]
Test6	Rubber compound with StZn_s_1. Targeted to stoichiometric ZnSt. Amount of StZn_s_1 to obtain Zn equivalent 3 times less than the reference.	1	2
Test7	Rubber compound with StZn_s_2. Targeted to ZnSt complex. Amount of StZn_s_2 equivalent to StA concentration in reference. A total of 6.7 times less Zn than the reference.	0.44	1
Test8	Rubber compound with StZn_s_2. Targeted to ZnSt complex. Amount of StZn_s_2 to obtain Zn equivalent 3 times less than in reference.	1	1
Test9	Rubber compound with StZnS_a_1_7. Targeted to ZnSt/sulfur complex. Sulfur in amount equivalent to S_8 per one Zn, added at the end. Amount of StZnS_a_1_7 equivalent to StA concentration in reference. A total of 13.6 times less Zn than the reference. [1]	0.22	2
Test10	Rubber compound with StZnS_a_1_9. Targeted to ZnSt/sulfur complex. Sulfur in amount equivalent to S_8 per one Zn, added before ZnO. Amount of StZnS_a_1_9 equivalent to StA concentration in reference. A total of 13.6 times less Zn than the reference. [1]	0.22	2
Test11	Rubber compound with StZnS_a_1_7. Targeted to ZnSt/sulfur complex. Sulfur in amount equivalent to S_8 per one Zn, added at the end. Amount of StZnS_a_1_7 equivalent to double StA concentration in reference. A total of 6.7 times less Zn than the reference. [1]	0.44	2
Test12	Rubber compound with StZnS_a_2_8. Targeted to ZnSt/sulfur complex. Sulfur in amount equivalent to S_8 per one Zn, added at the end. Amount of StZnS_a_2_8 equivalent to StA concentration in reference. A total of 6.7 times less Zn than the reference. [1]	0.44	1
Test13	Rubber compound with StZnS_a_2_10. Targeted to ZnSt/sulfur complex. Sulfur in amount equivalent to S_8 per one Zn, added before ZnO. Amount of StZnS_a_2_10 equivalent to StA concentration in reference. A total of 6.7 times less Zn than the reference. [1]	0.44	1
Test14	Rubber compound with StZnS_s_1. Targeted to ZnSt/sulfur complex. Sulfur in amount equivalent to S_8 per one Zn, added at the end. Amount of StZnS_s_1 equivalent to StA concentration in reference. A total of 13.6 times less Zn than the reference. [1]	0.22	2
Test15	Rubber compound with StZnS_s_2. Targeted to ZnSt/sulfur complex. Sulfur in amount equivalent to S_8 per one Zn, added at the end. Amount of StZnS_s_2 equivalent to stearic acid concentration in reference. A total of 6.7 times less Zn than the reference. [1]	0.44	1

[1] NOTE: sulfur did not completely react with ZnSt during mixing in the reactive flask—the fraction of sulfur in the complex was lower than assumed; that is why a regular amount of sulfur was added. This can generate some excess of sulfur in the rubber compound.

Table 3. Composition of rubber compounds containing commercial ZnSt and synthesized products described in Table 1.

Rubber Compound	Description	ZnO phr Equivalent	StA/Zn [mole/mole]
Ref3	Reference compound with commercial ZnSt and 1 phr of StA. Amount of ZnSt to obtain Zn equivalent 3 times less than Ref1 (Table 2).	1	2.28
Test16	Rubber compound with commercial ZnSt and 1 phr of StA premixed in Brabender with masterbatch. Amount of ZnSt to obtain Zn equivalent like in Ref3.	1	2.28
Test17	Rubber compound with sulfur, ZnSt, and 1 phr of StA premixed in Brabender with masterbatch. Amount of ZnSt to obtain Zn equivalent like in Ref3.	1	2.28
Test18	Rubber compound with StZn_a_1. Targeted to stoichiometric ZnSt. Amount of StZn_a_1 to obtain Zn equivalent 3 times less than the reference. Composition like Test2 (Table 2) but added 0.5 phr of stearic acid. Similar StA/Zn ratio like in Ref3.	1	2.13
Test19	Rubber compound with StZn_a_2. Targeted to ZnSt complex. Amount of StZn_a_2 to obtain Zn equivalent 3 times less than the reference. Composition like Test4 (Table 2) but added 1 phr of stearic acid. Reduced StA/Zn ratio like in Ref3.	1	1.29

The first series, which consisted of the reference rubber compounds (Ref0, Ref1, and Ref2, respectively), was manufactured in a standard way using a two-roll mill (David Bridge & Co., Rochdale, UK). The reference rubber compounds contained standard ZnO or active ZnO and other components of the cross-linking system, i.e., sulfur, accelerators, and StA, added separately. During the preparation of the reference rubber compounds, the masterbatch was first plasticized for 3 min, and then ZnO, StA, and sulfur were added successively and mixed using the two-roll mill. The total time for preparing the rubber compound was 10 min. The mixing process was carried out at temperatures up to 50 °C, since in such conditions no chemical reaction between ZnO and stearic acid was expected before vulcanization.

The other two series of rubber compounds, which contained the previously prepared synthesis products obtained in the reaction of stearic acid, zinc oxide, and sulfur (S_8), were prepared using a Brabender mixer. These materials contained synthesis products together with a rubber masterbatch without the ingredients used to prepare the synthesis products and accelerators included in the cross-linking system. The aim of this task was to homogeneously mix the melted ingredients together with the masterbatch before mixing them with the rest of the masterbatch and vulcanization accelerators, which would not be possible at the later stage without starting the vulcanization process. Initial Brabender chamber temperature was set at 115 °C, with a mixing speed of 45 revolutions per minute (rpm). After masterbatch dosing, the speed was kept at 45 rpm for 1 min before other ingredients were dosed. After performing complete dosing, the speed was changed to 70 rpm for 5 min and then to 90 rpm. The discharge of premixing was when the temperature of mixing rose to a minimum of 130 °C. After introducing the synthesis products into the masterbatch in the molten state using a Brabender mixer, vulcanization accelerators and sulfur were added successively using a two-roll mill. and the sheets of rubber compounds were prepared after 10 min of mixing.

To check the differences between synthesized materials and commercial ZnSt, additional rubber compounds described in Table 3 were prepared. Two additional rubber composites (Test18 and Test19, respectively) were also manufactured to check if a higher amount of StA is necessary for accelerators and can have some positive impact on vulcanizate properties.

All rubber compounds and test conceptions are summarized in Figure 3 below.

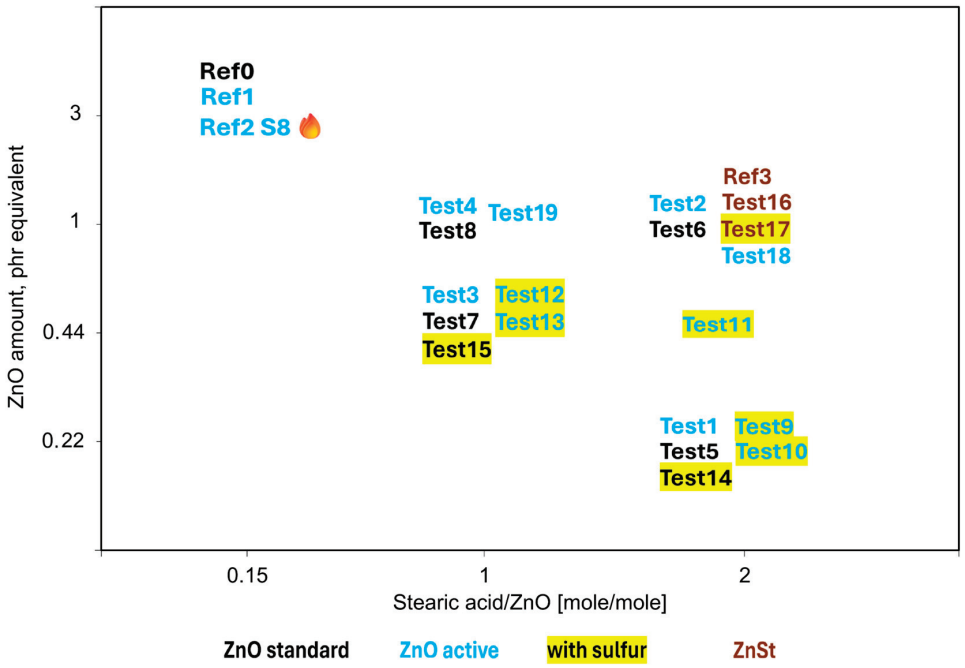

Figure 3. Drawing of the test concept for rubber compounds described in Tables 2 and 3.

2.4. Research Methods

Rheometric tests for rubber compounds were performed using Production Moving Die Rheometer MDR-P (Alpha Technologies, Hudson, OH, USA). The cure characteristics of EPDM compounds were studied at a temperature of 180 °C for the test time of 7 min.

Viscosity tests for rubber compounds were made using the MV 2000 Mooney viscometer (Alpha Technologies, Hudson, OH, USA) at a temperature of 125 °C according to the scorch test.

Samples of vulcanizates for compression set (CS) measurements and swelling tests were prepared using the Argenta AW 03 vulcanization press (Argenta, Kielce, Poland) with bottom and top heating plates and a temperature control system. Plates of vulcanizates with a thickness of approximately 2 mm were obtained at 180 °C and time of 10 min. There were five samples for each test prepared to minimize faults of measurements.

The equilibrium swelling tests were conducted for EPDM vulcanizates. Samples of rubber cut from 2 mm plates of vulcanizates were weighed on a laboratory scale and put in steel cans with xylene (mixture of isomers, purity 98%, Avantor Performance Materials S.A., Gliwice, Poland) for 48 h at a room temperature of approximately 23 °C. Then, the swollen samples were dried using a paper towel and secondly weighed. The equilibrium swelling (Q_w) of the vulcanizates was calculated using Equation (1):

$$Q_w = \frac{m_1 - m_0}{m_0} \cdot 100\%, \quad (1)$$

where

Q_w—equilibrium swelling (%),

m_1—weight of the swollen sample (mg),

m_0—weight of the sample before swelling (mg).

Compression set tests were performed using the standard procedure described in ISO 815-1:2019 method B [21]. The samples with a thickness of 6 mm were prepared from three layers of 2 mm plates. The height of the samples was measured, and then they were compressed by 25% for 22 h at 70 °C. After 2 h of conditioning at room temperature in a compressed state and 30 min of relaxation after removing the external stress, the height of the samples was secondly measured, and *CS* was calculated using Equation (2):

$$CS = \frac{h_0 - h_2}{h_1}, \quad (2)$$

where

h_0—initial thickness of the sample before test (mm),

h_1—height of compression (mm),

h_2—final thickness of the sample after test (mm).

The mechanical properties of vulcanizates were explored using the Zwick Roell 1435 (ZwickRoell, Ulm, Germany) universal testing machine. Tensile tests were carried out for four paddle-shaped samples with a thickness of approximately 1 mm and the width of the measuring section of 4 mm. All the samples were cut on press from vulcanizates cured at the temperature of 180 °C for 10 min. The crosshead speed during tensile tests was 500 mm/min.

Differential Scanning Calorimetry (DSC) tests were performed for the synthesized products employing the DSC1 analyzer (Mettler Toledo, Greifensee, Switzerland). Measurements were carried out at a temperature range from 25 °C to 200 °C, with a heating rate of 10 °C/min. The flow rate of nitrogen during the measurement was 80 mL/min. Based on DSC data, the expected heat of zinc stearate fusion was determined for synthesized products using Equations (3)–(8):

$$mStA = \frac{m_s \cdot LStAs}{LStA}, \quad (3)$$

where

mStA—mass of stearic acid in DSC sample (mg),

m_s—mass of DSC sample (mg),

LStAs—DSC measured sample heat of melting about StA phase transition temperature (J/g),

LStA—DSC measured heat of melting for pure StA (J/g).

$$m_0StA = \frac{m_s \cdot 2 \cdot MStA}{2 \cdot MStA + a \cdot MZnO}, \quad (4)$$

where

m_0StA—initial mass of stearic acid in sample (mg),

MStA—molar mass of StA (g/mol),

MZnO—molar mass of ZnO (g/mol),

a—molar proportion of ZnO in recipe (Table 1).

$$mRStA = m_0StA - mStA, \quad (5)$$

where

mRStA—reacted stearic acid during synthesis (mg).

$$m_yZnSt = \frac{mRStA \cdot MZnSt}{2 \cdot MStA}, \quad (6)$$

where

m_yZnSt—zinc stearate yielded (mg),
MZnSt—molar mass of ZnSt (g/mol).

$$LeZnSt = \frac{m_yZnSt \cdot LZnSt}{m_s}, \quad (7)$$

where

LeZnSt—expected heat of melting of zinc stearate yielded (J/g),
LZnSt—expected heat of melting of commercial zinc stearate (J/g).

$$\%y = \frac{mRStA}{m_0StA} \cdot 100\% \quad (8)$$

where

$\%y$—relative effectiveness of stearic acid conversion to carboxylic acid salt for stoichiometry products (%).

Fourier Transform Infrared Spectroscopy (FTIR) measurements for synthesized products were carried out using a ThermoScientific Nicolet 6700 FT-IR spectrometer (Thermo Fisher Scientific, Waltham, MA, USA) equipped with OMNIC 3.2 software. The attenuated total reflectance (ATR) technique with a single diamond ATR crystal was used for the tests. FTIR absorbance spectra were recorded in the wavenumber range of 4000–400 cm^{-1} using 128 scans.

Scanning Electron Microscopy (SEM) was used to investigate the distribution of solid particles in the rubber matrix. SEM images of the vulcanizates were taken using an SEM LEO 1450 microscope (Carl Zeiss AG, Oberkochen, Germany). Before measurement, the vulcanizates were fractured after cooling in liquid nitrogen, and their surfaces were covered with a thick layer of carbon. SEM with Energy-Dispersive X-ray Spectroscopy (EDS) was used to study the composition of agglomerates. SEM/EDS studies were performed using a HITACHI S-4700 (Hitachi, Mannheim, Germany) SEM microscope.

Thermal Desorption–Gas Chromatography–Mass Spectrometry (TD-GC-MS) was used for stearic acid composition verification. The apparatus used for analysis was from Perkin-Elmer (Shelton, CT, USA). Tests were performed by desorption at 200 °C on TurboMatrix 650. The column used for chromatography was Clarus 680, with He gas flow 2 mL/min. For identification of materials, mass spectroscopy on Clarus 600 C was used in EI+ ionization mode.

3. Results and Discussion

3.1. Characterization of the Zinc Salts and Complexes

While heating the components of the mixtures presented in Table 1, the synthesis reaction of ZnSt was observed, along with the release of water. In the case of active ZnO, this process was much more turbulent than for standard ZnO. In the case of samples with added sulfur, it was observed that the mixture delaminated due to the separation of melted sulfur in the lower part of the reaction flask. The prepared synthesis products were poured into aluminum containers and left to cool. The obtained products are presented in Figure 4.

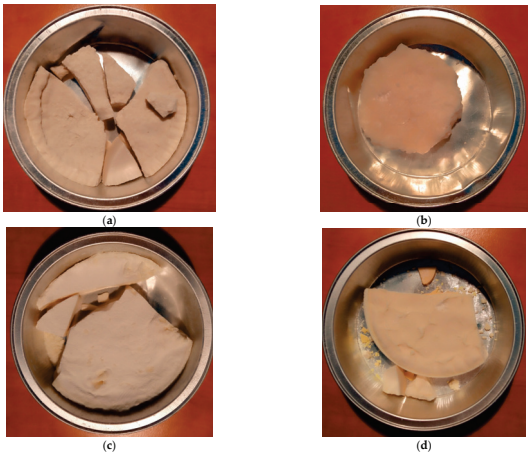

Figure 4. Images of synthesized products: (**a**) StZn_s_1; (**b**) StZn_a_1; (**c**) StZn_a_2; (**d**) StZnS_a_1_7.

The obtained synthesis products were subjected to DSC analysis in order to observe the differences in thermal transitions occurring during their heating and identify the synthesis products, as well as the presence of unreacted substrates. DSC curves for the synthesis products are presented in Figure 5a,b. Additionally, DSC measurements were conducted for technical stearic acid and pure sulfur (S8) (Figure 5c).

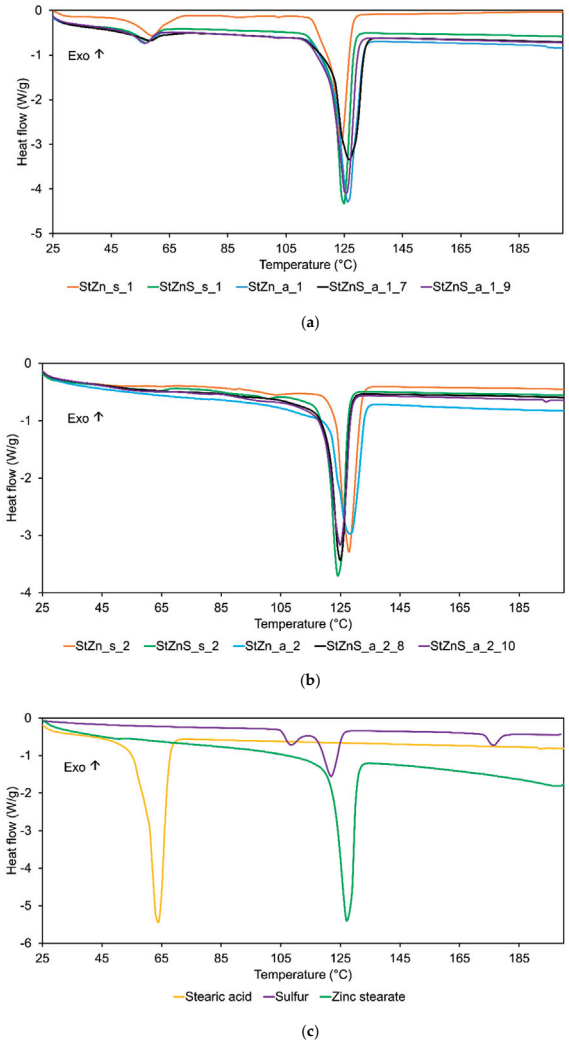

Figure 5. DSC results for synthesis products described in Table 1: (**a**) stoichiometric; (**b**) non-stoichiometric; (**c**) raw materials, i.e., commercial StA, S, and ZnSt.

Analyzing the DSC curves presented in Figure 5a, it was observed that the products obtained from the mixture containing 2 moles of StA per 1 mole of ZnO showed a melting of residual carboxylic acid in the temperature range of 50–70 °C. The residual carboxylic acid content resulted from the composition of technical stearic acid, which was a blend of palmitic and stearic acid. As mentioned earlier, the average molecular weight of acid blends is lower than that of the pure stearic acid, which resulted in the excess of carboxylic acid in the prepared mixture. The second intensive endothermic peak on the DSC curve in the temperature range of 110–130 °C was attributed to the melting of the products resulting from the reaction between StA and ZnO. However, for non-stoichiometric products, no melting peak for the residual carboxylic acid was observed, but only the sharp endothermic peak for melting of the synthesis products (Figure 5b).

On the other hand, for stoichiometric products, the DSC curves did not change significantly regardless of whether a standard or active ZnO was used. The addition of sulfur had no significant effect on the melting peak of the main synthesis product. Some residual endothermic peaks were observed on DSC curves at a temperature of 105 °C for synthesis products containing sulfur, which resulted from the allotropic transformation of sulfur.

From DSC measurements, the heat of the melting and peak temperatures for synthesized products and raw materials were determined and summarized in Table 4.

Table 4. Heat of melting and peak temperatures of synthesized products and raw materials determined by DSC.

Sample	Phase Change 1		Phase Change 2	
	Heat of Melting [J/g]	Peak [°C]	Heat of Melting [J/g]	Peak [°C]
StZn_s_1	−25.0	57.8	−102.6	121
StZn_s_2	-	-	−95.9	126
StZnS_s_1	−12.7	57.8	−134.2	123
StZnS_s_2	-	-	−108.5	122
StZn_a_1	−11.5	56.1	−162.4	124
StZn_a_2	-	-	−121.9	127
StZnS_a_1_7	−6.3	57.7	−142.3	125
StZnS_a_2_8	-	-	−104.9	123
StZnS_a_1_9	−8.9	56.6	−149.6	123
StZnS_a_2_10	-	-	−104.9	123
StA	−194.5	61.5	-	-
S	−9.1	108.0	−33.5	121
ZnSt	-	-	−153.3	126

The heat of melting determined for the zinc stearate sample was 153.3 J/g, lower than reported in the literature. Konkoly-Thege et al. [22] reported it as 103 kJ/mol, which gives 162.9 J/g. These researchers also determined the heat of melting for zinc palmitate as 93 kJ/mol, which gives 161.4 J/g. The melting temperatures were reported as 130 °C for zinc stearate and 134 °C for zinc palmitate, also a bit higher than the peak temperatures determined from DSC data in our study. The significantly higher heat of melting for residual carboxylic acid in the case of standard ZnO (sample StZn_s_1) compared to active ZnO (sample StZn_a_1) revealed that the standard ZnO was not fully converted during the reaction. It is also visible that the heat of melting of the carboxylic acid salt for the standard ZnO (sample StZn_s_1) was significantly lower than that for the active ZnO (sample StZn_a_1). A similar dependence was observed in the case of ZnO excess; the heat of melting for zinc salt produced from standard ZnO (sample StZn_s_2) was significantly lower than that for active ZnO (sample StZn_a_2).

Based on the DSC data, the expected heat of zinc stearate fusion was determined for synthesized products without sulfur and listed in Table 5. Mixtures with sulfur were excluded from estimations because part of the sulfur from those mixtures was not incorporated into the synthesized products and stayed on the bottom of the aluminum containers. On the other hand, the part of sulfur which was incorporated into the synthesis product had a similar melting point to ZnSt.

Table 5. Expected heat of melting calculated from DSC results for selected synthesis products described in Table 1.

Sample	Mass of DSC Sample [mg]	Mass of StA in DSC Sample [mg]	Initial Mass of StA in Sample [mg]	StA Reacted [mg]	ZnSt Yielded [mg]	Expected Heat of Melting [J/g]	Reacted StA [%]
StZn_s_1	11.8	1.52	10.3	8.8	9.8	−127.6	85
StZn_s_2	16.5	0.00	12.8	12.8	14.3	−132.9	100
StZn_a_1	13.6	0.80	11.9	11.1	12.3	−139.4	93
StZn_a_2	14.3	0.00	11.1	11.1	12.4	−132.9	100

The relative effectiveness of stearic acid conversion to carboxylic acid salt for stoichiometry products was 85% for standard ZnO and 93% for active ZnO (excess of acid), respectively. The higher effectiveness of the reaction for excess of ZnO (samples StZn_s_2 and StZn_a_2, respectively) can suggest that the reaction efficiency was linked to the size of the ZnO particles. The presence of a carboxylic acid melting peak suggests that there is no formation of non-stoichiometric ZnSt containing more carboxylic acid. However, this observation does not eliminate the possibility that a non-stoichiometric complex with an excess of Zn has been created. The heat of the melting of StA is higher than would be expected from a 3% excess of StA, which means that not all the ZnO has reacted. ZnO was dissolved by the carboxylic acid gradually. Thus, there is a residue of both carboxylic acid and ZnO or its impurities in the preparation. Based on the calculated results of reacted StA from DSC measurements and its 3% excess, non-reacted or complexed ZnO is about 12% for StZn_s_1 (standard ZnO) and 4% for StZn_a_1 (active ZnO).

The heats of melting for synthesized products differed from those determined theoretically based on DSC-measured stearic acid remains. For standard ZnO, they were lower than expected, but for active ZnO the results were opposite. The heats of melting determined through DSC for products from non-stoichiometric mixtures were significantly lower than for the stoichiometric one. On the other hand, the counted expected heats of melting were quite similar. All those differences could result from some non-stoichiometric zinc stearate particles formed as a binuclear bidentate or crystal structure of products yielded during synthesis. Zinc stearate can exhibit different crystal structures depending on the synthesis conditions, with two main types of geometry observed in zinc soaps, i.e., a highly symmetrical packing for long-chain saturated soaps and an alternating packing for zinc soaps with shorter, unsaturated, or dicarboxylic chains [23]. The method used to synthesize ZnSt can influence its crystal structure. For example, precipitation and fusion processes can yield ZnSt with slightly different melting points and crystal morphologies. The phase transition in ZnSt is not just a simple melting of the alkyl chains [24]. It also involves changes in the coordination of the stearate ions to the zinc ions, potentially forming ionic clusters in the liquid phase. In ZnSt, each zinc ion is coordinated to two stearate anions. This bidentate coordination is believed to contribute to the relatively high melting point and enthalpy of fusion compared to simple alkanes. At the temperature of the industrial vulcanization process, i.e., around 180 °C, the crystal structure of the yielded ZnSt should not have an impact on the vulcanization course and efficiency because those products should be in a liquid state.

The transitions of substrates into zinc salts in the reactive mixtures were checked using FTIR Spectroscopy. The FTIR spectra of StA used for the synthesis and commercial ZnSt were collected to compare them with those obtained for the reaction products prepared in stoichiometric (StZn_s_1) and non-stoichiometric (StZn_s_2) conditions (Figure 6). Regarding the FTIR spectrum for StA, the absorption peaks at about 2915 and 2849 cm^{-1} in the high-frequency region were attributed to $-CH_2-$ asymmetric and symmetric stretching vibrations, respectively. They were accompanied by stretching vibrations of the $-CH_2-$ band at a wave number of approximately 1472 cm^{-1} [25]. Furthermore, the strong and sharp peak at approximately 1700–1710 cm^{-1}, characteristic of the C=O stretching vibrations in the carboxylic acid group, and peaks at 1300–1420 cm^{-1}, characteristic of the O-H bending vibrations of the hydroxyl group in carboxylic acids, were observed. In addition, peaks corresponding to −C–O stretching vibrations in −COOH were identified in the wave number range of 930–1100 cm^{-1} [26]. It should be noticed that, in both spectra for synthesized products, the band at a wave number of approximately 1700 cm^{-1} characteristic for the double bond between carbon and oxygen in carboxylic acids, i.e., C=O band, changed to a sharp peak at approximately 1535 cm^{-1}, which is typical for asymmetric stretching vibrations of $-COO^-$ in carboxylate salts, accompanied by sharp peaks corresponding to symmetric stretching vibrations of $-COO^-$ at approximately 1400–1450 cm^{-1} [26]. This confirmed that a reaction took place between ZnO and stearic acid, and a carboxylic acid salt was formed. On the spectrum of StZn_s_1, it is also visible that a part of StA remained unreacted, since the small peak at approximately 1700–1710 cm^{-1}, characteristic of the C=O stretching vibrations in the carboxylic acid group, is still present. On the other hand, in the FTIR spectrum of StZn_s_2, the presence of non-reacted ZnO can be concluded, since the intensity of the peak at a wave number of approximately 400–600 cm^{-1}, which is typical for Zn–O stretching vibrations [27], is higher compared to the FTIR spectrum of the product synthesized in stoichiometric conditions, i.e., StZn_s_1 or pure ZnSt. The intensity of the bands in this wave number range is higher than for the product synthesized in stoichiometric conditions, even though this is already the limit of the measuring range of the device. Due to fact that, in this range of wave numbers, the absorbance is imposed with a ZnSt answer, i.e., Zn-O stretching, which confirms metal–oxygen bonding, it is difficult to determine the presence of unreacted ZnO for ZnSt_s_1. There is no difference in the spectra of ZnSt_s_1 and ZnSt_s_2 other than the lack of bands at 1700 cm^{-1} (typical for C=O group in carboxylic acids) and approximately 420 cm^{-1} (typical for Zn-O vibrations) in the spectrum of ZnSt_s_2. This observation supports the findings concluded based on DSC results that only carboxylic acids salts were formed without non-stoichiometric complexes.

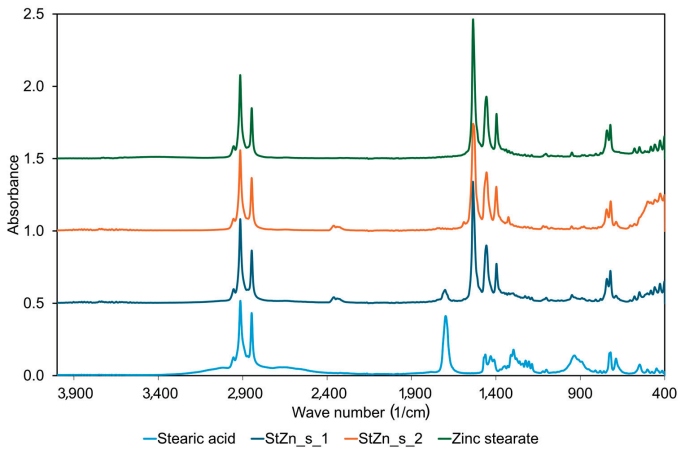

Figure 6. FTIR spectra for commercial StA, commercial ZnSt, and product of synthesis, i.e., StZn_s_1 and StZn_s_2, respectively.

3.2. Characterization of the EPDM Composites Containing the Synthesized Zinc Salts and Complexes

Having characterized the products of the performed synthesis, we used them to prepare rubber compounds. Then, the effects of standard ZnO, active ZnO, and the synthesized zinc salts and complexes on the rheometric properties of EPDM compounds were explored. The results are presented in Table 6.

Table 6. MDR and Mooney test results for compounds described in Tables 2 and 3 (MDR results: ML—minimum torque; MH—maximum torque; t_{s2}—time to 2% rise in torque; MH–ML—torque increment; t_{90}—time to 90% rise in torque; Mooney results: ML—minimum viscosity; t_5—time to increase the viscosity by 5 Mooney units (MU) from the ML value).

Compound	MDR Results					Mooney Results	
	ML [dNm]	MH [dNm]	MH–ML [dNm]	t_{s2} [min]	t_{90} [min]	ML [MU]	t_5 [min]
Ref0	1.54	7.79	6.25	0.97	1.79	32.8	14.0
Ref1	0.96	9.05	8.09	0.93	1.94	26.1	12.4
Ref2	1.05	9.53	8.48	0.93	2.01	28.3	11.8
Test1	1.17	8.15	6.98	1.00	1.78	31.8	12.7
Test2	1.05	9.21	8.16	1.21	2.88	26.1	18.6
Test3	1.23	8.82	7.59	0.95	1.78	32.0	12.0
Test4	1.10	8.95	7.85	1.10	2.26	28.4	17.2
Test5	1.06	8.02	6.96	0.98	1.74	27.9	12.1
Test6	0.93	8.11	7.18	1.13	2.52	23.4	17.9
Test7	1.18	8.43	7.25	0.96	1.70	29.0	13.0
Test8	1.06	7.47	6.41	1.10	1.88	26.4	16.7
Test9	1.05	8.07	7.02	0.93	1.93	27.8	12.6
Test10	0.99	7.99	7.00	0.88	1.62	27.0	11.4
Test11	1.03	8.32	7.29	0.95	2.27	25.0	16.3
Test12	1.11	8.43	7.32	0.90	1.73	27.9	13.4
Test13	1.04	8.65	7.61	0.86	1.88	27.6	12.8
Test14	1.08	8.11	7.03	0.95	1.80	28.3	12.5
Test15	1.10	8.45	7.35	0.91	1.66	28.8	12.3
Ref3	0.82	6.90	6.08	1.22	3.46	20.9	25.1
Test16	0.98	7.60	6.62	1.32	2.66	22.9	24.1
Test17	1.01	8.24	7.23	1.34	2.87	23.7	24.1
Test18	0.83	6.71	5.88	0.89	2.20	21.9	14.7
Test19	0.94	6.59	5.65	0.75	1.90	24.8	11.6

Analysis of the measurement results performed using the MDR and Mooney viscometer (Table 6) showed that, for the reference rubber compounds, the application of active ZnO (Ref1) increased the torque increment during the rheometric test (MH-ML), which is an indirect measure of the cross-linking degree of the rubber compound, whereas a slightly longer optimal vulcanization time t_{90} (time to reach 90% of maximum torque during rheometric test) compared to standard ZnO (Ref0) was achieved. This confirmed the higher activity of active ZnO compared to standard ZnO, which was due to the larger

specific surface area of active ZnO, resulting in a larger contact area between the components of the cross-linking system during vulcanization. Applying materials synthesized using active ZnO (Test1 to 4) allowed us to achieve the same trend compared with the materials obtained based on standard ZnO (Test5 to 8), but the differences were not so significant as in the case of the rubber compounds containing raw zinc oxides. Rubber compounds with a 3-times reduced quantity of ZnO showed both a higher MH–ML and longer t_{90} for active ZnO vs. standard ZnO (Test2 vs. 6 and Test4 vs. 8, respectively), which additionally confirmed the greater activity in vulcanization of both active ZnO and the synthesis product obtained using it. For rubber compounds containing a zinc amount equivalent to stearic acid in the reference rubber compound, the differences in MDR and Mooney test results compared to the standard and active ZnO were not so significant (Test1 vs. 5 and Test3 vs. 7). The rubber compounds containing materials synthesized with sulfur exhibited MDR and Mooney values similar to rubber compounds containing the synthesis products obtained using only StA and ZnO with the same ZnO equivalent (Test1, 9, 10 vs. 3, 12, 13). Adding sulfur before ZnO during the synthesis resulted in the decrease in t_{90} only for rubber compounds containing materials obtained in stoichiometric conditions (Test9 and 10, respectively). This indicated the lack of formation of sulfur complexes with ZnO and StA during the reaction—only sulfur melting and changes in its crystalline form took place during the mixing of the ingredients in the reaction flask. Applying commercial laboratory grade ZnSt (Ref3, Test16 and 17) resulted in torque values on similar levels as rubber compounds containing materials synthesized from standard ZnO, but with a significantly longer t_{90}. The differences in the rheometric data obtained for Ref3 and premixed in the Brabender mixer rubber compounds (Test16 and Test17) revealed that mixing in the molted state, aiming to obtain a perfect dispersion of the curatives, improved the torque increment MH-ML and decreased the cure time, thus having a beneficial effect on the effectiveness of vulcanization. Additional amounts of stearic acid, which can influence the activity of accelerators, significantly reduced the torque increment MH-ML, deteriorating the cross-linking degree of the elastomer and slightly decreasing the t_{90}, thus improving the rate of vulcanization (Test2 vs. 18 and Test4 vs. 19).

Having investigated the influence of standard and active ZnO, as well as their salts or complexes, with stearic acid on the vulcanization parameters, we then examined their impact on the functional properties of the EPDM vulcanizates, i.e., the compression set (CS), which is crucial for sealing applications. The results are presented in Table 7.

Table 7. Equilibrium swelling and compression set test results for rubber compounds described in Tables 2 and 3.

Compound	Compression Set [%]			Equilibrium Swelling [%]		
Ref0	72.5	+/−	1.7	96.1	+/−	2.0
Ref1	60.9	+/−	2.3	85.6	+/−	0.4
Ref2	57.9	+/−	1.4	82.6	+/−	1.1
Test1	73.7	+/−	1.1	103.9	+/−	1.9
Test2	52.9	+/−	2.1	74.7	+/−	0.4
Test3	66.8	+/−	1.7	95.2	+/−	0.5
Test4	56.5	+/−	0.9	81.6	+/−	0.5
Test5	74.9	+/−	1.6	105.9	+/−	1.4

Table 7. *Cont.*

Compound	Compression Set [%]			Equilibrium Swelling [%]		
Test6	56.3	+/−	1.2	81.3	+/−	1.1
Test7	69.3	+/−	1.1	100.2	+/−	2.0
Test8	61.9	+/−	1.5	93.9	+/−	1.2
Test9	70.4	+/−	0.8	102.1	+/−	2.5
Test10	71.4	+/−	1.6	103.7	+/−	1.4
Test11	68.4	+/−	0.8	92.0	+/−	1.1
Test12	69.2	+/−	1.5	98.9	+/−	1.3
Test13	69.2	+/−	0.2	97.8	+/−	1.3
Test14	70.3	+/−	1.7	102.3	+/−	1.4
Test15	67.9	+/−	1.6	97.1	+/−	0.5
Ref3	44.5	+/−	0.7	82.6	+/−	1.7
Test16	42.5	+/−	2.3	78.3	+/−	1.6
Test17	41.5	+/−	0.8	77.3	+/−	1.4
Test18	51.1	+/−	1.5	85.1	+/−	1.2
Test19	52.7	+/−	0.8	97.1	+/−	1.6

As it is widely known, the kind of ZnO and its quantity have a significant impact on vulcanizate properties. Analyzing the data collected in Table 7, rubber composites with active ZnO exhibited better properties, i.e., a lower CS and equilibrium swelling, compared to standard ZnO. However, when the synthesized materials based on these types of ZnO were applied, the differences between the obtained results were not so significant as in the case of reference composites with both types of ZnO. The CS and equilibrium swelling values decreased for EPDM vulcanizates with active ZnO (Ref1 and Ref2) compared to standard ZnO (Ref0). The lower equilibrium swelling allowed us to conclude that the active ZnO ensured that the vulcanizates had a higher cross-linking density compared to the standard ZnO. This correlates well with the results of rheometric tests. Ref3 with zinc stearate exhibited the best functional properties, i.e., the lowest CS, among all references, despite the fact that its zinc equivalent was three times lower than for other reference rubber compounds. A better dispersion of zinc and sulfur for rubber compounds premixed in the Brabender probably led to an improvement in the vulcanizate properties despite the zinc content reduction. This trend was observed for both kinds of ZnO and for zinc stearate.

The addition of stoichiometric zinc salt in an amount that was 3 times lower than in the reference (Test2) resulted in a significant improvement in CS (52.9% vs. 60.9%) obtained for Ref1, with a reduction in equilibrium swelling (74.7% vs. 85.6%, respectively), and, consequently, an increase in the cross-linking density of the vulcanizate. A further decrease in the zinc salt amount to a 13.6-times (Test1) lower equivalent of ZnO resulted in a CS on a level similar to vulcanization with standard ZnO, i.e., 73.7% vs. 72.5% (Ref0), whereas the equilibrium swelling increased significantly to 103.9% due to the decrease in the cross-linking density of the vulcanizate. Stoichiometric zinc salts produced from standard ZnO resulted in only a slightly higher CS of vulcanizates compared to zinc salts produced from active ZnO (Test5 vs. Test1 and Test6 vs. Test2, respectively), which was also in line with the increase in equilibrium swelling. Slight differences (on the level of measurement uncertainty) between the results obtained for vulcanizates containing zinc

salts synthesized from active ZnO and standard ZnO suggest that only the salt amount is important for the properties of vulcanizates, not the kind of ZnO used for the synthesis.

Non-stoichiometric products of synthesis, which contained almost half of the unreacted ZnO and half of the ZnSt, resulted in a slightly lower CS of vulcanizates compared to stoichiometric ZnSt only for Test3 vs. Test1, but for Test4 vs. Test2 the relationship was opposite. Those changes are in line with the equilibrium swelling results (lower equilibrium swelling and consequently higher cross-linking density accompanied by lower CS of vulcanizates). Hence, in order to obtain the proper CS of vulcanizates, the more important factor is not the type of vulcanization activator, but the cross-linking density of the vulcanizate, which can be obtained by using this particular activator. For vulcanizates containing the products synthesized from standard ZnO, the effects of additional amounts of ZnO on the CS and equilibrium swelling of vulcanizates have the same trend. Applying the mixtures containing ZnO, StA, and sulfur resulted in vulcanizates with CS and swelling results slightly lower for a very low ZnO equivalent (Test9 and 10 vs. Test5, 13.6-times lower zinc amount than in Ref1) and slightly higher for a low ZnO equivalent (Test12 and 13 vs. Test3, 6.7-times lower zinc amount than in Ref1). This suggests that sulfur did not form any complex with ZnO and StA during mixing; the obtained differences in CS of vulcanizates can be only due to the impact of ZnSt and sulfur content. A comparison of the CS and swelling results of vulcanizates for Test13 and 12, which contained the products obtained when sulfur was added before or after ZnO addition during the synthesis, showed no significant differences considering the measurement uncertainty. This supports the earlier statement that there was no formation of sulfur complex during the reaction of sulfur, ZnO, and StA. A comparison of the results obtained for vulcanizates containing synthesized products using standard ZnO vs. active ZnO for stoichiometric salts allowed us to observe that there were no significant differences between CS and swelling values for Test14 (standard ZnO) and Test9 (active ZnO). CS values for both vulcanizates were approximately 70.4%, and the equilibrium swelling of these vulcanizates was also similar, which indicates a similar cross-linking density. This further confirmed that only the amount of salt is important. A similar relationship was observed for Test15 vs. 12, i.e., zinc salts obtained from standard ZnO vs. active ZnO in non-stoichiometric conditions. An analysis of the obtained results allowed us to conclude that the excess of StA combined with ZnSt had a very important effect on the CS of the vulcanizates. For vulcanizates with ZnSt, i.e., Ref3, Test16, and Test17, CS was reduced to 41.5–44.5% from approximately 60.9% (Ref1—with active ZnO). This is an even better result than for Test2 (stoichiometric synthesis product, 1 phr of active ZnO), which exhibited a CS of approximately 52.9%. It proved that raw ZnSt ensured better curing conditions than a mix of other zinc salts, with ZnSt received in the product synthesized from commercial StA. The equilibrium swelling also decreased significantly, indicating a marked increase in the cross-linking density of the vulcanizates, which probably contributed to the decrease in CS. This confirmed that a better mixing of ZnSt can improve the availability of zinc ions during cross-linking reactions. A comparison of the results obtained for Test18 (1 phr of stoichiometric ZnSt from active ZnO) vs. Test2 (with addition of StA) showed no improvement in the CS; however, the equilibrium swelling increased, indicating a deterioration of the cross-linking density of the vulcanizate. This suggests that a small excess of StA can be beneficial for the activation of accelerators. On the contrary, a comparison of the results for Test19 (1 phr of non-stoichiometric ZnSt from active ZnO) vs. Test4 (with addition of StA) revealed an improvement in the CS, while Test4 did not contain any excess of StA. Thus, it was concluded that StA acted not only as a ZnSt precursor, but also as an activator of accelerators.

Most importantly, the performed studies proved that adding materials synthesized in the reaction of ZnO, StA, and sulfur could help to reduce the content of zinc in rubber

composites, while keeping a good level of both important manufacturing parameters, like the viscosity and cure time of rubber compounds, and also functional properties, i.e., the CS or cross-linking density, of the vulcanizates.

In the next step of the study, the tensile properties of the vulcanizates were examined. The results are presented in Table 8.

Table 8. Tensile test results of the vulcanizates described in Tables 2 and 3 (SE_{100}—stress at relative elongation of 100%, TS—tensile strength, E_b—elongation at break).

Compound	SE_{100} [MPa]			TS [MPa]			E_b [%]		
Ref0	2.6	+/−	0.2	3.0	+/−	0.6	123	+/−	17
Ref1	2.1	+/−	0.1	6.3	+/−	0.3	499	+/−	40
Test2	2.2	+/−	0.1	7.9	+/−	0.7	421	+/−	55
Test4	2.2	+/−	0.1	8.7	+/−	0.1	412	+/−	10
Test6	2.6	+/−	0.1	9.0	+/−	0.1	415	+/−	12
Test8	3.5	+/−	0.2	10.6	+/−	0.4	335	+/−	15
Test9	2.4	+/−	0.2	7.6	+/−	0.1	445	+/−	69
Test14	2.3	+/−	0.1	7.7	+/−	0.1	506	+/−	25
Ref3	2.3	+/−	0.1	8.5	+/−	0.2	435	+/−	8
Test16	2.7	+/−	0.1	8.5	+/−	0.2	352	+/−	23

The reference vulcanizate Ref0 with standard ZnO exhibited the lowest tensile strength (TS) and elongation at break (E_b). It should be noted that the E_b of this vulcanizate was approximately 120%, while for most other vulcanizates the E_b was above 400%. This indicates a very low elasticity of this vulcanizate compared to the others, which may be caused by its significantly higher degree of cross-linking. The vulcanizate with active ZnO (Ref1) showed twice the TS compared to that with standard ZnO, and a significantly better elasticity (E_b of approximately 500%). The vulcanizate with ZnSt (Ref3) also showed better tensile parameters, i.e., TS and E_b, compared to that with standard ZnO, despite having a 3-fold lower zinc equivalent. Most importantly, vulcanizates containing the synthesized zinc complexes exhibited a significantly higher TS and E_b than vulcanizates with standard (Ref0) or active ZnO (Ref1). Surprisingly, vulcanizates with a 13.6-times lower zinc amount (Test9 and 14) compared to the reference samples showed much better tensile properties despite a significantly higher equilibrium swelling and, consequently, lower cross-linking degree. This allowed us to assume that the ZnO-containing vulcanizates were slightly over-cross-linked compared to those containing synthesis products, which caused a deterioration of their TS and an increase in their brittleness. On the other hand, a high amount of StA in rubber compounds creates a huge issue to solve, i.e., the whitening of vulcanizates (blooming) [28]. With time, additives like the zinc salts of fatty acids migrate on the surface of vulcanizates, causing visual aspects and influencing the adhesion [29]. A higher content of StA in the recipe of rubber compounds results in a higher amount of ZnSt in the vulcanizates. In Figure 7 the problem is presented for the vulcanizates containing active ZnO with the standard amount of StA (Ref1), the reference with ZnSt (Ref3), Test16 with an StA equivalent about 5-times higher than in Ref1, Test2 with StA equivalent 6.7-times higher than in Ref1, and Test11 with an StA equivalent 2-times higher than in Ref1. Vulcanizates with a 2-times higher content of StA compared to Ref1, i.e., Test11, did not show any visual blooming aspects. The amount of created ZnSt in the reaction of StA with ZnO during the preparation of the rubber compound and the curing process should also be twice as high accordingly. The increasing of the ZnSt amount in the vulcanizate by a higher

amount of StA led to an unacceptable migration on the vulcanizate surface (Ref3, Test2, and Test16). For rubber composites containing synthesized materials, the reduction of zinc in the amount that did not impact their functional properties was not enough. In turn, a further reduction in the zinc amount to keep the equivalent StA as in the standard rubber compound (Ref1) or not creating blooming issues (Test11) did not guarantee keeping the demanded properties of the vulcanizates.

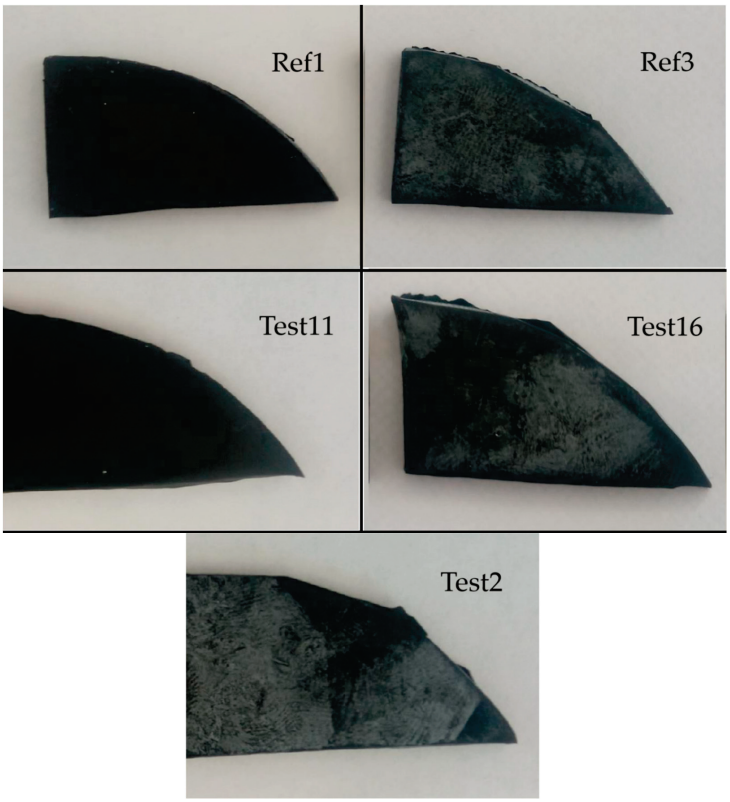

Figure 7. Blooming of vulcanizates described in Tables 2 and 3.

Parts of vulcanizates were examined using SEM to check whether their composition or the method of introducing the crucial cross-linking components (ZnO, StA, sulfur, ZnSt) separately or as products of the reaction influences their dispersion in the elastomer matrix. SEM images of the vulcanizate fractures are presented in Figure 8.

In the case of the reference vulcanizate with active ZnO, the overall dispersion of the components was relatively homogeneous (Figure 8a), although some agglomerates with a complex morphology and a size of several micrometers, representing clusters of primary particles less than 1 micrometer in size, also occurred (Figure 8b). These agglomerates were quite well wetted by the elastomer; most of the agglomerate visible in the photo was surrounded by an elastomer film. In the case of the vulcanizate containing stoichiometric ZnSt synthesized from active ZnO, the SEM image (Figure 8c) shows areas of both uniform particle dispersion and micrometric agglomerates. These agglomerates resulted from the agglomeration of particles smaller than 1 micrometer and demonstrated a better wettability by the elastomer compared to the agglomerates present in the SEM image of the vulcanizate containing active ZnO (Figure 8d). The elastomer film is clearly visible, penetrating between the agglomerate particles and surrounding them on all sides. The use of the product obtained by adding sulfur in the synthesis process of zinc salts/complexes did not have a significant effect on the overall dispersion of the mixture components (Figure 8e), although it seems that the wettability of the agglomerate visible in the SEM image (Figure 8f) is slightly worse in relation to the vulcanizate containing the synthesis

product without sulfur. In the case of the vulcanizate containing commercial ZnSt, the dispersion of the components can be considered the most homogeneous (Figure 8g). The wettability of the particles and their aggregates by the elastomer is very good, as all of them are coated with an elastomer film and embedded in it (Figure 8h). Overall, this vulcanizate exhibited one of the lowest CSs and highest cross-linking densities. In the case of the vulcanizate containing stoichiometric ZnSt synthesized from active ZnO with an additional amount of StA, the overall dispersion of the components in the elastomer matrix is quite good (Figure 8i), but several micrometer-sized agglomerates of varying morphology are also visible, representing clusters of relatively large primary particles with a fairly regular platelet or block shape (Figure 8j). These agglomerates demonstrate a low wettability by the elastomer.

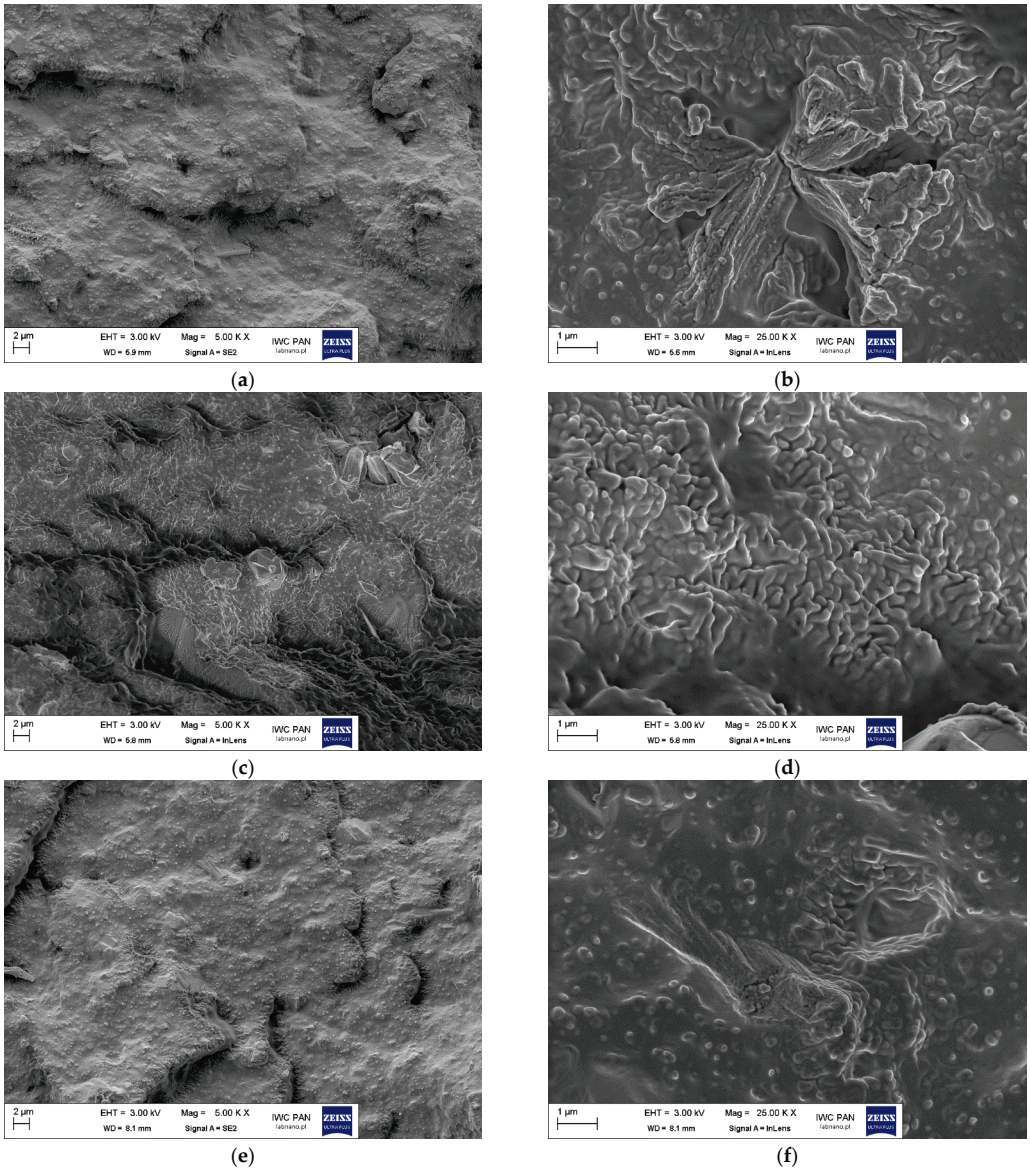

Figure 8. *Cont.*

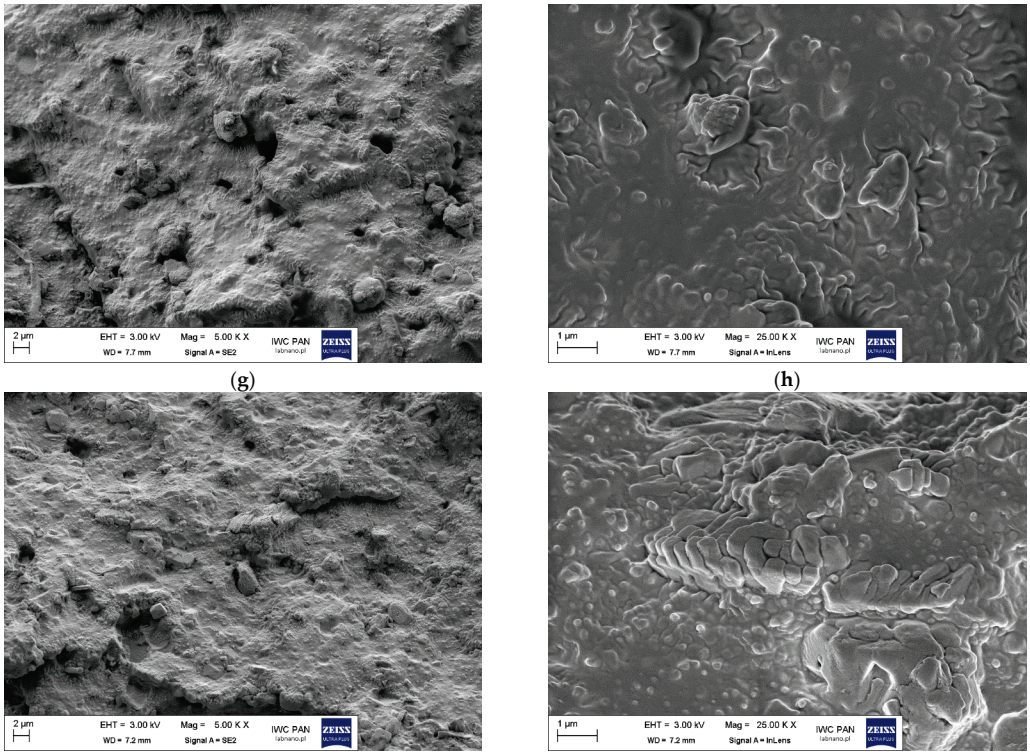

Figure 8. SEM images of vulcanizate fractures: (**a**,**b**) Ref1; (**c**,**d**) Test2; (**e**,**f**) Test11; (**g**,**h**) Test16; (**i**,**j**) Test18.

To identify the composition of the agglomerates visible in the above SEM images (Figure 8), SEM with EDS analysis was employed. The results in the form of EDS maps are presented in Figure 9.

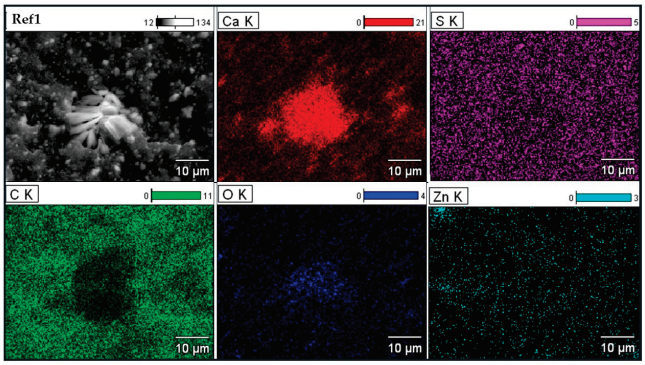

(**a**)

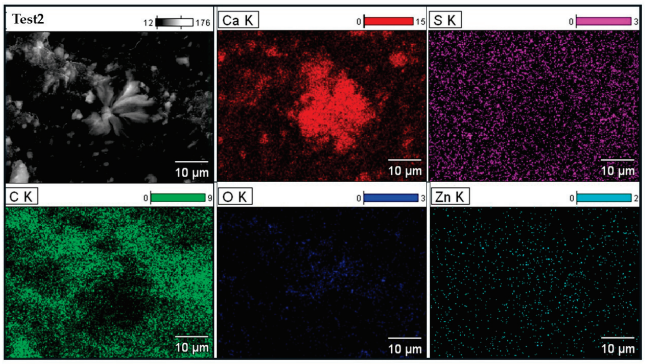

(**b**)

Figure 9. *Cont.*

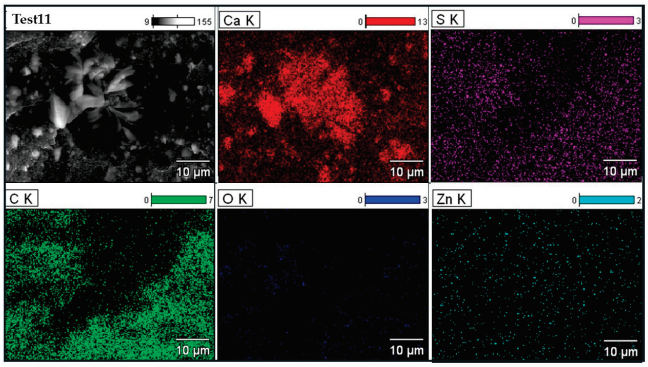

(**c**)

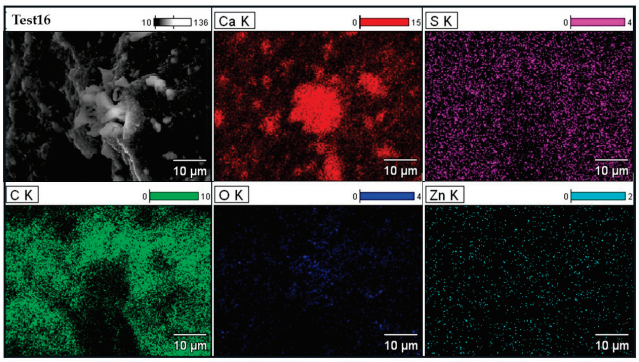

(**d**)

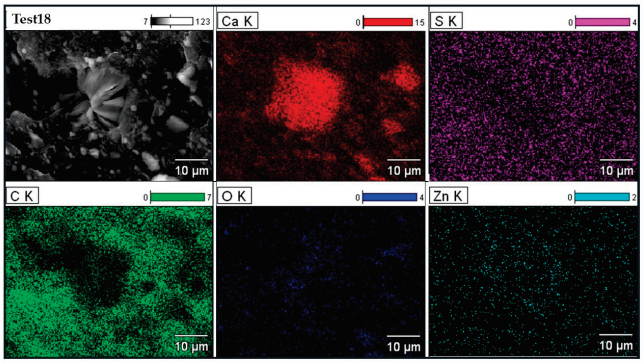

(**e**)

Figure 9. SEM images of vulcanizate fractures with EDS mapping for Ca, S, C, O, and Zn elements: (**a**) Ref1; (**b**) Test2; (**c**) Test11; (**d**) Test16; (**e**) Test18. Analysis of ESD mapping revealed that the agglomerates present in SEM images of the vulcanizates resulted from the agglomeration of calcium compounds present in the masterbatch composition, e.g., $CaCO_3$. On the other hand, EDS analysis showed that components of the curing system, i.e., sulfur and zinc compounds, were homogeneously dispersed in the elastomer matrix, regardless of whether ZnO or the synthesized products obtained in the reaction of ZnO and StA under stoichiometric or non-stoichiometric conditions were used as the vulcanization activator. Hence, it can be concluded that the composition of the elastomer composite, i.e., the type and amount of the activator, did not significantly influence the general dispersion of the rubber composite components.

4. Conclusions

In this research, zinc complexes with different molar ratios of ZnO and StA with or without the presence of sulfur were synthesized and studied as potential vulcanization activators for EPDM compounds. The vulcanization parameters and properties of the rubber composites containing synthesized materials were compared with those containing commercial ZnSt to verify the hypothesis on the key role in sulfur vulcanization played by non-stoichiometric zinc complexes.

DSC results confirmed that the reaction between ZnO and StA resulted in the formation of ZnSt. Complexes with different molar ratios of ZnO and StA contained the amount of ZnSt proportional to amount of StA used in the synthesis. In addition, an FTIR study of reaction products did not reveal any absorption bands different from those characteristic for StA and ZnSt. Active ZnO exhibited a higher reactivity in the formation of ZnSt than the standard ZnO, due to the higher specific surface area and lower size of particles that are consumed during the reaction. The heats of melting determined through DSC for the products from non-stoichiometric mixtures were significantly lower than for the stoichiometric ones. These differences could result from the difference in the crystallization process depending on the reaction conditions, since ZnSt particles can form binuclear bidentate or a crystal structure that differs in the heat of melting.

The stoichiometric salt of ZnO and StA was the most effective in terms of vulcanization parameters and the compression set of rubber composites. Non-stoichiometric complexes were less effective, proportionally to their content. However, they can also be a potential alternative to traditional ZnO and StA systems in the vulcanization of EPDM composites. The comparison with stoichiometric ZnSt revealed that the effect on the vulcanization state and compression set of rubber composites is mostly driven by stoichiometric salt. In case of non-stoichiometric complexes, the influence on the vulcanization parameters, cross-linking density, and compression set was proportional to the content of stoichiometric salt. Moreover, the amount of salt was more important than the type of ZnO used during the synthesis. Th excess of StA can improve the availability of zinc during cross-linking reactions, leading to improved properties of the vulcanizates. The addition of sulfur to zinc complexes did not significantly affect the vulcanization and properties of the EPDM composites, which disproved the hypothesis that sulfur formed complexes with StA and ZnO.

Supplementary Materials: The following supporting information can be downloaded at https://www.mdpi.com/article/10.3390/polym17212875/s1. Figure S1: Research station used for the synthesis of StA with ZnO and/or S reaction products.

Author Contributions: Conceptualization, K.K. and P.G.; methodology, K.K. and P.G.; validation, P.G. and M.M.; formal analysis, K.K.; investigation, K.K.; resources, K.K.; data curation, K.K., P.G. and M.M.; writing—original draft preparation, K.K.; writing—review and editing, P.G. and M.M.; visualization, K.K.; supervision, P.G.; project administration, K.K.; funding acquisition, M.M. All authors have read and agreed to the published version of the manuscript.

Funding: This work was supported by Ministerstwo Edukacji i Nauki (DWD/6/0559/2022).

Institutional Review Board Statement: Not applicable.

Data Availability Statement: The data presented in this study are available on request from the corresponding author due to the confidentiality policy of Hutchinson.

Acknowledgments: This work was completed while Krzysztof Kaczewiak was the Implementation Doctoral Candidate in the Interdisciplinary Doctoral School at the Lodz University of Technology, Poland.

Conflicts of Interest: Authors Krzysztof Kaczewiak and Piotr Głąb are employed by Hutchinson Poland Sp z o.o. company. The remaining authors declare that the research was conducted in the absence of any commercial or financial relationships that could be construed as a potential conflict of interest.

Abbreviations

The following abbreviations are used in this manuscript:

ZnSt	Zinc stearate
EPDM	Ethylene–propylene–diene monomer
ZnO	Zinc oxide
StA	Stearic acid
LCA	Life Cycle Analysis
GHS	Globally Harmonized System of Classification and Labelling of Chemicals
CLD	Caprolactam disulfide
MBTS	2,2′-benzothiazyl disulfide
CBS	N-cyclohexyl-2-benzothiazole sulfenamide
ZDTP	Zinc dialkyldithiophosphate
MDR	Moving Dye Rheometer
CS	Compression set
FTIR	Fourier Transform Infrared Spectroscopy
DSC	Differential Scanning Calorimetry
SEM	Scanning Electron Microscopy
TD-GC-MS	Thermal Desorption–Gas Chromatography–Mass Spectrometry
EDS	Energy-Dispersive X-ray Spectroscopy

References

1. Moezzi, A.; McDonagh, A.M.; Cortie, M.B. Zinc Oxide Particles: Synthesis, Properties and Applications. *Chem. Eng. J.* **2012**, *185–186*, 1–22. [CrossRef]
2. Yan, M.F. Zinc Oxide. In *Concise Encyclopedia of Advanced Ceramic Materials*; Elsevier: Amsterdam, The Netherlands, 1991; pp. 523–525. [CrossRef]
3. Heideman, G.; Datta, R.N.; Noordermeer, J.W.M.; van Baarle, B. Influence of Zinc Oxide during Different Stages of Sulfur Vulcanization. Elucidated by Model Compound Studies. *J. Appl. Polym. Sci.* **2005**, *95*, 1388–1404. [CrossRef]
4. Borysiewicz, M.A. ZnO as a Functional Material, a Review. *Crystals* **2019**, *9*, 505. [CrossRef]
5. Wilaiwong, W.; Smitthipong, W. Study of Non-Negligible Chemical Reduction of ZnO in the Rubber Industry. *IOP Conf. Ser. Mater. Sci. Eng.* **2022**, *1234*, 012014. [CrossRef]
6. Kołodziejczak-Radzimska, A.; Jesionowski, T. Zinc Oxide—From Synthesis to Application: A Review. *Materials* **2014**, *7*, 2833–2881. [CrossRef]
7. Macarrão, I.M.; Dutra, J.C. Sustainable Development Assessment of Zinc Oxide Production Focused on Agribusiness. *J. Eng. Exact. Sci.* **2020**, *6*, 577–584. [CrossRef]
8. Wojnarowicz, J.; Chudoba, T.; Lojkowski, W. A Review of Microwave Synthesis of Zinc Oxide Nanomaterials: Reactants, Process Parameters and Morphologies. *Nanomaterials* **2020**, *10*, 1086. [CrossRef]
9. Grund, S.C.; van Genderen, E. Life Cycle Assessment and Product Carbon Footprint for SHG Zinc Production. *J. Phys. Conf. Ser.* **2024**, *2738*, 012038. [CrossRef]
10. Buendia, E.; Tanabe, K.; Kranjc, A.; Jamsranjav, B.; Fukuda, M.; Ngarize, S.; Osako, A.; Pyrozhenko, Y.; Shermanau, P.; Federici, S. *2019 Refinement to the 2006 IPCC Guidelines for National Greenhouse Gas Inventories*; IPCC: Geneva, Switzerland, 2019.
11. Sreethu, T.K.; Naskar, K. Zinc Oxide with Various Surface Characteristics and Its Role on Mechanical Properties, Cure-Characteristics, and Morphological Analysis of Natural Rubber/Carbon Black Composites. *J. Polym. Res.* **2021**, *28*, 183. [CrossRef]
12. Mostoni, S.; Milana, P.; Di Credico, B.; D'Arienzo, M.; Scotti, R. Zinc-Based Curing Activators: New Trends for Reducing Zinc Content in Rubber Vulcanization Process. *Catalysts* **2019**, *9*, 664. [CrossRef]
13. Heideman, G.; Datta, R.N.; Noordermeer, J.W.M.; van Baarle, B. Activators in Accelerated Sulfur Vulcanization. *Rubber Chem. Technol.* **2004**, *77*, 512–541. [CrossRef]
14. Junkong, P.; Morimoto, R.; Miyaji, K.; Tohsan, A.; Sakaki, Y.; Ikeda, Y. Effect of Fatty Acids on the Accelerated Sulfur Vulcanization of Rubber by Active Zinc/Carboxylate Complexes. *RSC Adv.* **2020**, *10*, 4772–4785. [CrossRef]
15. Heideman, G.; Noordermeer, J.W.M.; Datta, R.N.; Van Baarle, B. Various Ways to Reduce Zinc Oxide Levels in S-SBR Rubber Compounds. *Macromol. Symp.* **2006**, *245*, 657–667. [CrossRef]
16. Przybyszewska, M.; Zaborski, M.; Jakubowski, B.; Zawadiak, J. Zinc Chelates as New Activators for Sulphur Vulcanization of Acrylonitrile-Butadiene Elastomer. *Express Polym. Lett.* **2009**, *3*, 256–266. [CrossRef]

17. Ikeda, Y.; Yasuda, Y.; Ohashi, T.; Yokohama, H.; Minoda, S.; Kobayashi, H.; Honma, T. Dinuclear Bridging Bidentate Zinc/Stearate Complex in Sulfur Cross-Linking of Rubber. *Macromolecules* **2015**, *48*, 462–475. [CrossRef]
18. Setianto, W.B.; Yohanes, H.; Astuti; Maisaroh; Atmaji, G. Synthesis of Palm Oil-Base Zinc Stearate and Its Application on Manufacture of Rubber Component. *IOP Conf. Ser. Earth Environ. Sci.* **2022**, *963*, 012028. [CrossRef]
19. Bukhina, M.F.; Morozov, Y.L.; Ven, P.M.; Noordermeer, J.W.M. Mold Fouling of EPDM Rubber Compounds. *Kautsch. Und Gummi Kunststoffe* **2003**, *56*, 172–183.
20. Kaczewiak, K.; Głąb, P.; Maciejewska, M. Vulcanization Temperature Impact on Cross-Linking Density and Compression Set of Sulfur-Cured Ethylene–Propylene–Diene Monomer. *J. Appl. Polym. Sci.* **2025**, *142*, e57188. [CrossRef]
21. *ISO 815-1:2019*; Rubber, Vulcanized or Thermoplastic—Determination of Compression set, Part 1: At Ambient or Elevated Temperatures. International Organization for Standardization: Geneva, Switzerland, 2019.
22. Konkoly-Thege, I.; Ruff, I.; Adeosun, S.O.; Sime, S.J. Properties of Molten Carboxylates Part 6. A Quantiative Differential Thermal Analysis Study of Phase Transitions in Some Zinc and Cadmium Carboxylates. *Thermochim. Acta* **1978**, *24*, 89–96. [CrossRef]
23. Zhang, X.; Wei, F.; Wang, Z.; Li, G.; Yang, S.; Feng, J. Comparative Investigation of the Structural Evolution of Zinc Stearate and Calcium Stearate in a Polypropylene Random Copolymer upon Heating and Cooling. *Polymer* **2023**, *267*, 125646. [CrossRef]
24. Ishioka, T.; Maeda, K.; Watanabe, I.; Kawauchi, S.; Harada, M. Infrared and XAFS Study on Structure and Transition Behavior of Zinc Stearate. *Spectrochim. Acta A Mol. Biomol. Spectrosc.* **2000**, *56*, 1731–1737. [CrossRef]
25. Zhu, J.; Liu, B.; Li, L.; Zeng, Z.; Zhao, W.; Wang, G.; Guan, X. Simple and Green Fabrication of Super-Hydrophobic Surface by One-Step Immersion for Continuous Oil/Water Separation. *J. Phys. Chem. A* **2016**, *120*, 5617–5623. [CrossRef]
26. Larkin, P.J.; Jackson, A. Interpretation of the Infrared Spectra of Metal-Stearate Salts. *Appl. Spectrosc. Pract.* **2024**, *2*, 27551857241253834. [CrossRef]
27. Albarakaty, F.M.; Alzaban, M.I.; Alharbi, N.K.; Bagrwan, F.S.; Abd El-Aziz, A.R.M.; Mahmoud, M.A. Zinc oxide Nanoparticles, Biosynthesis, Characterization and Their Potent Photocatalytic Degradation, and Antioxidant Activities. *J. King Saud. Univ. Sci.* **2023**, *35*, 102434. [CrossRef]
28. Choi, S.; Chung, H.; Joo, Y.; Yang, K.; Lee, S. Analysis of Whitening Phenomenon of EPDM Article by Humid Aging. *J. Appl. Polym. Sci.* **2012**, *123*, 2451–2457. [CrossRef]
29. Dimopoulos, M.; Roy Choudhury, N.; Ginic-Markovic, M.; Matisons, J.; Williams, D.R.G. Surface Studies on the Additive Migration and Diffusion in the Windowseal Rubber Component Influencing Adhesion to Coating. *J. Adhes. Sci. Technol.* **1998**, *12*, 1377–1390. [CrossRef]

polymers

MDPI

Article

Sustainable Rubber Solutions: A Study on Bio-Based Oil and Resin Blends

Frances van Elburg [1,*], Fabian Grunert [1], Claudia Aurisicchio [2], Micol di Consiglio [2], Auke Talma [1], Pilar Bernal-Ortega [1] and Anke Blume [1,*]

[1] Elastomer Technology & Engineering, Department of Mechanics of Solids, Surfaces & Systems (MS3), Faculty of Engineering Technology, University of Twente, Drienerlolaan 5, 7522 NB Enschede, The Netherlands; f.grunert@utwente.nl (F.G.); a.g.talma-1@utwente.nl (A.T.); m.d.p.bernalortega@utwente.nl (P.B.-O.)

[2] Bridgestone EU NV/SA, Italian Branch–Technical Center, Via del Fosso del Salceto 13/15, 00128 Rome, Italy

* Correspondence: f.a.vanelburg@utwente.nl (F.v.E.); a.blume@utwente.nl (A.B.)

Abstract

One of the most important challenges the tire industry faces is becoming carbon-neutral and using 100% sustainable materials by 2050. Utilizing materials from renewable sources and recycled substances is a key aspect of achieving this goal. Petroleum-based oils, such as Treated Distillate Aromatic Extract (TDAE), are frequently used in rubber compounds, and a promising strategy to enhance sustainability is to use bio-based plasticizer alternatives. However, research has shown that the replacement of TDAE oil with bio-based oils or resins can significantly alter the glass transition temperature (T_g) of the final compound, influencing the tire properties. In this study, the theory was proposed that using a plasticizer blend, comprising oil and resin, in a rubber compound would result in similar T_g values as the reference compound containing TDAE. To test this, the cycloaliphatic di-ester oil Hexamoll DINCH, which can be made out of bio-based feedstock by the BioMass Balance approach, was selected and blended with the cycloaliphatic hydrocarbon resin Escorez 5300. Various oil-to-resin ratios were investigated, and a linear increase in the T_g of the vulcanizate was obtained when increasing the resin content and decreasing the oil content. Additionally, a 50/50 blend, consisting of 18.75 phr Hexamoll DINCH and 18.75 phr Escorez 5300, resulted in the same T_g of −19 °C as a compound containing 37.5 phr TDAE. Furthermore, this blend resulted in similar curing characteristics and cured Payne effect as the reference with TDAE. Moreover, a similar rolling resistance indicator (tan δ at 60 °C = 0.115), a slight deterioration in wear resistance (ARI = 83%), but an improvement in the stress–strain behavior (M300 = 9.18 ± 0.20 MPa and Ts = 16.3 ± 0.6 MPa) and wet grip indicator (tan δ at 0 °C = 0.427) were observed. The results in this work show the potential of finding a balance between optimal performance and sustainability by using plasticizer blends.

Keywords: plasticizers; oils; resins; tire tread; sustainability

1. Introduction

Tire manufacturers aim to reduce their carbon footprint and even become carbon-neutral by 2050 [1]. One of the approaches to achieve this is the transition to using 100% sustainably produced raw materials. These sustainable materials are obtained from renewable sources or recycled substances, which reduces the CO_2 footprint compared to fossil-based materials [2,3]. Due to the increasing interest in using sustainable materials in

tire applications, the availability of scientific papers about the influence of these ingredients in rubber materials is also progressively increasing. Various review articles have been published in the last decade, which together provide an overview of the many sustainable polymers, fillers, plasticizers, and other additives investigated in rubber compounds [4–10].

One of the ingredient groups under investigation is the plasticizer. Together with the rubber polymer and reinforcing filler, plasticizers take up a large part of the rubber compound. In conventional rubber formulations, petroleum-based plasticizers are added to improve processing and increase the flexibility of the rubber compound [11]. The petroleum-based oil Treated Distillate Aromatic Extract (TDAE) is commonly used in tire tread compounds [12]. A previous study [13] showed that replacing TDAE with various vegetable oils shows potential, but certain material properties exhibit degradation. An important factor contributing to this deterioration in properties is the decrease of the glass transition temperature (T_g) to lower temperatures. This decrease in T_g was widely described in the literature when plant-based oils were used in rubber compounds [8].

Another material that has gained increasing interest in the tire industry is resin [14]. A resin is a low molecular weight (800–4000 g/mol) polymeric material, either in liquid or solid state at room temperature, depending on the softening point [15]. Various resins are available, with differences in chemical structure, molecular weight, and softening point. Resins can be derived from fossil feedstock (e.g., coumarone-indene and hydrocarbon resins) or natural sources (e.g., rosin and polyterpene resins) [15]. These materials act not only as tackifiers but also as softeners and plasticizers. Bernal-Ortega et al. investigated the use of hydrocarbon resins [16] and bio-based resins [17] as replacements for TDAE in simplified tire tread compounds. Based on these studies, it can be concluded that resins with a high softening point and glass transition temperature of the pure resin elevate the T_g of the rubber compound, in contrast to most vegetable oils that shift the T_g to lower temperatures. This phenomenon occurs when the resin and polymer used are compatible [15].

To achieve optimum performance in the rubber compound, a sustainable alternative to the commonly used petroleum-based plasticizer that results in a similar glass transition temperature is needed. A possible solution for this might be using oil and resin plasticizer blends. The practice of blending oils with resins has been addressed in the literature. Lopitaux [18] described a rubber compound containing 1,2-cyclohexane dicarboxylate diester and a resin. Although similar in-rubber properties were observed, the glass transition temperatures of the vulcanized materials were not analyzed. In another patent, the combination of vegetable oil with resin in rubber is claimed [19]. The experimental example of this patent shows silica-filled SBR/BR compounds with various combinations of petroleum-based oil, soybean oil, and traction resin. Compared to the compound with only petroleum-based oils, the plasticizer blends result in improved wet traction, a similar or worse abrasion resistance, and a slight deterioration in rolling resistance, but a clear improvement in tear strength. However, the T_g values of the various compounds were not reported as well.

In this study, the use of plasticizer blends comprising a di-ester oil and a cycloaliphatic hydrocarbon resin as alternatives to TDAE is proposed. It is hypothesized that blending the bio-based oil with resin will shift the glass transition temperature to values more comparable to compounds with TDAE, thereby positively influencing the final material properties of the vulcanized compound. In the first section, the cycloaliphatic di-ester oil Hexamoll DINCH is blended with the Escorez 5300 resin in various ratios to identify the optimal oil-to-resin blend ratio. A detailed evaluation of various plasticizer blend ratios is expected to reveal new trends and correlations in rubber performance properties. The second section explores the use of different di-ester oils (Hexamoll DINCH, Palatinol 10P,

and Plastomoll DOA) combined with Escorez 5300 in 50/50 blends, to assess the effects of various chemical structures present in the oils. High concentrations (80 phr) of the plasticizer blends are evaluated to gain a deeper understanding of the effects of replacing TDAE with plasticizer blends on various properties. Because the three selected di-ester oils can be created with the BioMass Balance approach, making these oils up to 100% bio-based [20–22] and reducing the CO_2 footprint by approx. 60% [23]. Therefore, replacement of the petroleum-based TDAE with one of these di-ester oils will improve the sustainability of the final rubber compound.

2. Materials and Methods

2.1. Materials

The polymers used in this study were Styrene Butadiene Rubber (S-SBR) (SPRINTAN® SLR 4601, styrene content 21%, molecular weight = 450 kg/mol) (Synthos Schkopau GMBH, Schkopau, Germany) and Butadiene Rubber (BR) (Buna® CB24, cis-1,4 content > 96%, molecular weight = 620 kg/mol) (Arlanxeo, Dormagen, Germany). ULTRASIL® 7000 GR (specific surface area (CTAB) 160 m2/g) and bis(triethoxysilylpropyl) disulfide (TESPD) were supplied by Evonik Industries (Wesseling, Germany), and used as highly reinforcing filler and coupling agent, respectively. The curing package consisted of the curing activators zinc oxide (ZnO) (Umicore Zinc Chemicals, Angleur, Belgium) and stearic acid (Emery Oleochemicals GmbH, Düsseldorf, Germany), sulfur (Zolfindustria, Trecate, Italy), the primary accelerator N-tert-butyl-benzothiazole sulfonamide (TBBS) (General Química S.A., Lantarón, Spain) and the secondary accelerator N,N′-diphenylguanidine (DPG) (MLPC International (Arkema Group), Rion-des-Landes, France).

Treated Distillate Aromatic Extract (TDAE) (Hansen & Rosenthal, Hamburg, Germany) was used as a plasticizer in the reference compound. Additionally, the di-ester oils Hexamoll® DINCH, Palatinol® 10P, and Plastomoll® DOA (BASF, Ludwigshafen am Rhein, Germany) were evaluated, as well as the resin Escorez™ 5300 (ExxonMobil, Houston, TX, USA). The di-ester oils were selected based on their availability, potential of being fully sustainable, and saturated nature. Because these oils contain no double bonds in their tail structures, less interference with other rubber ingredients is expected [13]. The Escorez 5300 resin was evaluated in a previous study [16] and showed promising results on the tire performance. Moreover, this resin is widely available and is expected to be compatible with the selected di-ester oils and the used polymers, due to the similarities in Hansen Solubility Parameter (HSP). The HSP values, as well as the molecular weight (Mw), density (ρ), glass transition temperature (T_g) and chemical structure of the plasticizers are summarized in Table 1. The rubber formulations of the various rubber compounds are shown in the introductions of the separate chapters.

Table 1. Main characteristics according to the technical data sheets of the studied plasticizers.

Ingredient	Mw in g/mol	ρ in g/cm^3	T_g * in °C	HSP ** in MPa$^{1/2}$	Chemical Structure
TDAE	x	0.95	−52	δ_D = 15.2 δ_P = 11.2 δ_H = 1.0 δ_{tot} = 18.9	Carbon distribution [12]: $C_{aromatic}$ = 25 wt% $C_{napthene}$ = 30 wt% $C_{paraffin}$ = 45 wt%
Hexamoll® DINCH	425	0.95	−90	δ_D = 16.1 δ_P = 1.9 δ_H = 2.6 δ_{tot} = 16.4	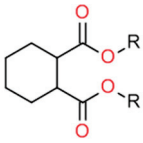 where R = C_9H_{19}

Table 1. *Cont.*

Ingredient	Mw in g/mol	ρ in g/cm^3	T_g * in °C	HSP ** in MPa$^{1/2}$	Chemical Structure
Palatinol® 10P	447	0.96	−79	δ_D = 16.8 δ_P = 4.2 δ_H = 2.3 δ_{tot} = 17.4	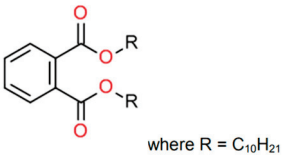
Plastomoll® DOA	371	0.92	−106	δ_D = 16.2 δ_P = 2.7 δ_H = 3.4 δ_{tot} = 16.7	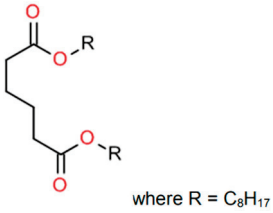
Escorez™ 5300	670	1.01	45	δ_D = 17.9 δ_P = 0.1 δ_H = 0.1 δ_{tot} = 17.9	Cycloaliphatic hydrocarbon resin

* Obtained with Differential Scanning Calorimetry measurements using the DSC 214 Polyma with a heat rate of 10 °C/min. ** Calculated with the Hansen Solubility Parameter in Practice (HSPiP) software (5th edition, version 5.4.04), except for the values of TDAE, which were obtained from [24]. In addition, the HSP values for the S-SBR/BR blend were calculated (δ_D = 18.5 MPa$^{1/2}$, δ_P = 0.9 MPa$^{1/2}$, δ_H = 1.7 MPa$^{1/2}$, δ_{tot} = 18.9 MPa$^{1/2}$).

2.2. Mixing Procedure

The Brabender Plasticorder 350S (Duisburg, Germany), an internal mixer with a chamber volume of 390 cm^3, was used to mix the rubber compounds, according to the mixing procedure displayed in Table 2. After each mixing stage, the compounds were sheeted out on a Polymix 80 T two-roll mill (Schwabenthan, Berlin, Germany).

Table 2. Mixing procedure.

Time	Action
m:s	**Stage 1:** *pre-heating 80 °C, 70 rpm, fill factor 72%*
0:00	Addition of rubber
1:00	Addition of 2/3 silica, 2/3 silane
2:30	Addition of 1/3 silica, 1/3 silane, ZnO, Stearic acid, and plasticizer
4:00	15-s ramp sweep
4:15	Increase of torque (increase temperature to 130 °C)
7:00	Stop mixing (reaching 140 °C)
m:s	**Stage 2:** *pre-heating 80 °C, 80 rpm, fill factor 69%*
0:00	Addition of elastomer masterbatch
0:50	Addition of DPG
1:00	Increase of torque (increase temperature to 130 °C)
5:00	Stop mixing (reaching 140 °C)
m:s	**Stage 3:** *pre-heating 50 °C, 50 rpm, fill factor 66%*
0:00	Addition of elastomer masterbatch, curatives (sulfur, and TBBS)
3:00	Stop mixing

2.3. Analytical Testing

2.3.1. Vulcanization

To determine the optimal vulcanization time, the Rubber Process Analyzer TA Elite (TA Instruments, New Castle, DE, USA) was employed. A frequency of 1.667 Hz and a deformation of 6.98% were applied, with the temperature maintained at 160 °C. The

curing behavior was monitored for one hour. The time to achieve 90% conversion (t90) was subsequently utilized to cure 2 mm thick test samples for stress–strain and dynamic mechanical analysis measurements. For the 6 mm thick abrasion, and the 12 mm thick hardness specimens, the samples were cured for an additional 3 and 5 min respectively, to ensure that the compounds were cured entirely. The rubber samples were vulcanized at 160 °C under a pressure of 100 bar using a Wickert WLP 1600 hydraulic press (Wickert, Landau in der Pfalz, Germany).

2.3.2. Cured Payne Effect

The Rubber Process Analyzer TA Elite (TA Instruments, New Castle, DE, USA) was utilized to determine the cured Payne effect. Samples were initially cured at 160 °C within the device, according to their t90 values. Immediately following this curing process, the storage modulus (G') was measured at 100 °C. Strain sweeps ranging from 0.1% to 100% were applied to the cured samples at a frequency of 1.667 Hz. The difference between 0.56% and 100% strain was calculated and used as the cured Payne effect.

2.3.3. Hardness

The hardness of the compounds was evaluated using a Zwick 3150 hardness tester (Zwick, Ulm, Germany) according to ISO 48-4 [25]. Measurements were performed on the Shore A scale.

2.3.4. Stress–Strain Behavior

The stress–strain behavior of the compounds was measured using the Universal Mechanical Tester Zwick Z01 (Zwick, Ulm, Germany) in accordance with ISO 37 [26] (die type 2). A crosshead speed of 500 mm/min was employed, and the tensile tests were conducted at room temperature. Five samples of each compound were tested, and the average values of these measurements were analyzed. Additionally, the median values for each compound are presented in stress–strain graphs.

2.3.5. Dynamical Properties

Dynamic mechanical analysis was conducted using the Gabo-Netzsch Eplexor tester (Netzsch, Germany). Rectangular samples with a thickness of 2 mm and a width of 5.5 mm were measured in tension mode. The analysis utilized a static strain of 0.3% and a dynamic strain of 0.1%. The test was performed over a temperature range from −80 to 80 °C with a heating rate of 2 °C/min and a dynamic load frequency of 10 Hz.

2.3.6. DIN Abrasion

The DIN abrader Montech ABR 3000 Rubber Abrasion Tester (MonTech USA GmbH, Columbia, IN, USA) was selected to analyze the abrasion resistance of the vulcanized in accordance with ISO 4649 [27] method A (non-rotating test piece configuration). The test specimens were cylindrical, with a diameter of 16 mm and a height of 6 mm. The percentage ratio of the volume loss of the test rubber to that of a standard rubber was calculated to obtain the abrasion resistance index (ARI, %). Three samples were tested for each compound, and the average volume loss from these samples was used to determine the ARI.

3. Results and Discussion

3.1. Various Oil and Resin Ratios

Compounds with different ratios between the oil and resin were evaluated to investigate how the oil and resin influence the properties of the material. As a reference, a compound with 37.5 phr TDAE oil was evaluated. The selected oil and resin were Hexam-

oll DINCH and Escorez 5300. Due to the cycloaliphatic nature of both substances, it was expected that they would be compatible with each other, enhancing the influence on the final properties of the rubber compound. Additional characteristics of the two substances are displayed in Table 1. Three different ratios between the Hexamoll DINCH and Escorez 5300 were evaluated, namely 20:80, 50:50, and 80:20. Table 3 shows the rubber formulations of these compounds.

Table 3. Rubber formulations for compounds with various ratios between oil and resin.

Compounds	S-SBR in phr	BR in phr	Silica in phr	TDAE in phr	Hexamoll DINCH in phr	Escorez 5300 in phr
TDAE	80	20	80	37.5	X	X
E20HE80	80	20	80	X	30	7.5
E50HE50	80	20	80	X	18.75	18.75
E80HE20	80	20	80	X	7.5	30

Furthermore, the compounds consisted of the same quantities of the remaining ingredients: 6.2 phr TESPD, 2.5 phr stearic acid, 2.5 phr zinc oxide, 1.4 phr sulfur, 2.0 phr TBBS, and 1.5 phr DPG.

In addition to the plasticizer blends, a compound with 37.5 phr of Hexamoll DINCH (H100) and a compound with 37.5 phr Escorez 5300 (E100) were mixed and evaluated. These results are shown and discussed in the evaluation of the DMA measurements.

3.1.1. Rheometer Curves and Payne Effect

Figure 1 depicts the rheometer curves of the compounds with various oil and resin ratios, and Table 4 contains additional curing characteristics like the scorch time (ts2), the optimum cure time (t90), maximum torque (MH), minimum torque (ML), and difference in torque (MH-ML).

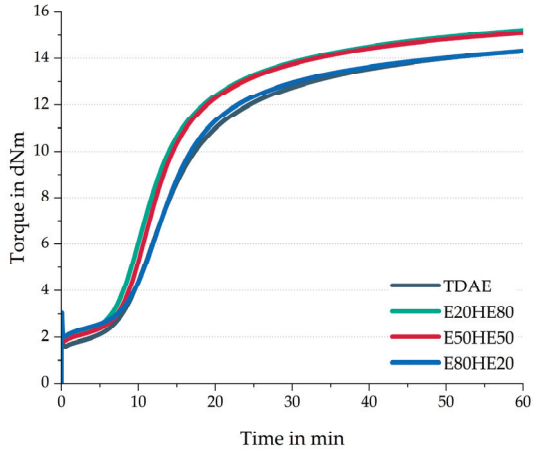

Figure 1. Rheometer curves of the compounds with various ratios between oil and resin.

Table 4. Curing characteristics and Payne effect data of the compounds with various ratios between oil and resin.

Compounds	ts2 in min	t90 in min	MH in dNm	ML in dNm	MH-ML in dNm	$G'_{0.56–100\%}$ in kPa	$G'_{100\%}$ in kPa
TDAE	8.9	33.1	14.3	1.6	12.7	719	525
E20HE80	7.9	30.6	15.2	1.9	13.3	724	566
E50HE50	8.6	30.3	15.1	1.9	13.2	738	564
E80HE20	9.5	31.5	14.3	2.0	12.3	640	610

Figure 1 and Table 4 reveal that the ML value is lowest for TDAE, while it is slightly higher for E20HE80 and E50HE50, and the highest value is obtained for E80HE20. The ML is related to the viscosity of the compound, where a higher ML indicates a higher compound viscosity [28]. Plasticizers are added to the compound to lower the viscosity of the compound and improve processing and dispersion [11]. Therefore, the high value obtained for the E80HE20 compound can be explained by the relatively high resin content, which has a higher molecular weight compared to the used oil (Table 1). In general, an increase in molecular weight is related to an increase in viscosity. Although the resin will change from a solid to a low viscous liquid at processing and curing temperatures [11], the viscosity is likely higher than the used di-ester oil at these temperatures.

A clear trend is visible between the oil and resin ratio and the scorch time. A higher concentration of oil, and a lower concentration of resin, results in a shorter scorch time. This can be explained by the concentration of ester-based oil in the compound. The ester groups might interact with the silica surface [29]. Due to these interactions, the silica surface is unable to absorb curing activators and accelerators, which become available for the vulcanization process. This could explain the faster scorch time, but also the higher maximum torque values for E20HE80 and E50HE50 because these are the two compounds with the highest concentration of ester-based oil. Usually, the maximum torque in the cure curve is correlated to polymer–polymer, polymer–filler, and filler–filler interactions [28]. As a result of more available curatives for the actual curing reaction in these compounds, more polymer–polymer interactions can be formed, causing an increase in the maximum torque.

Figure 2 shows the storage modulus of the cured samples over a range of low to high strain values. The difference between the storage modulus at low and high strains is the Payne effect, in this study indicated with $G'_{0.56–100\%}$. The Payne effect is associated with the breakdown of filler–filler interactions and a lower Payne effect is usually related to an improved micro-dispersion of the filler in the compound [30]. The $G'_{0.56–100\%}$ and the storage modulus at 100% strain ($G'_{100\%}$) are displayed in Table 4.

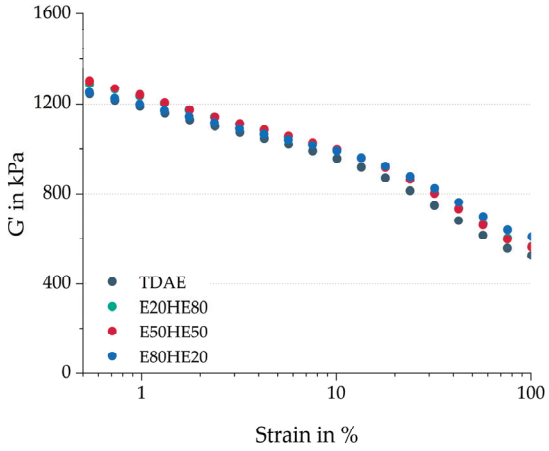

Figure 2. Cured Payne curves of the compounds with various ratios between oil and resin.

Although the figure shows similar Payne effect curves for all four compounds, when considering the values in the table, slight differences are visible. Especially E80HE20 results in different values, with a lower cured Payne effect, but a higher storage modulus at 100% strain. The lower cured Payne effect can be caused by the higher molecular weight of the resin, leading to higher shear forces during mixing, improving the silica dispersion. A similar effect was observed by Bernal-Ortega et al. [16], who used the Escorez 5300 resin in combination with TDAE oil in a silica-filled S-SBR/BR compound. The slightly higher Payne effect values for E20HE80 and E50HE50 indicate slightly more filler–filler

interactions, which might also contribute to the higher maximum torque values obtained for these two compounds in the cure curves (Figure 1) [28]. However, the differences are small, and therefore it is more likely that the higher maximum torque is caused by an increase in crosslink density. Equilibrium swelling is commonly used to evaluate the crosslink density of rubber samples. The widely used procedure, as described by Bernal-Ortega et al. [31], proved unsuitable for this study. It was observed that the resin did not dissolve during the initial extraction step using acetone, while the oil was effectively removed. As a result, the measurements were significantly affected by the presence of the undissolved resin, leading to invalid outcomes. Additional trials without the extraction step were performed, but these trials also resulted in non-reproducible and invalid values.

The storage modulus at 100% strain is influenced by the polymer network, the hydrodynamic effects, and in-rubber structures [30]. In this study, the higher $G'_{100\%}$ is most likely influenced by an increase in in-rubber structures, for example, due to more polymer–filler interactions. Bernal-Ortega et al. [17] studied the use of bio-based resins in silica-filled S-SBR/BR compounds and concluded that the pure resins could act as "glue" between the fillers, making the filler–filler interactions stronger. A similar phenomenon could occur when using the E80HE20 blend. This plasticizer blend might act as "glue" between the polymer and the filler, making these interactions stronger, and increasing the $G'_{100\%}$ slightly. This effect is less pronounced for the other plasticizer blends, due to the higher oil content.

Based on all characteristics obtained from the cure curves and the cured Payne measurements (Table 4), it can be concluded that the values of the E20HE80 and E50HE50 compounds are similar to each other, while the E80HE20 blend shows deviating behavior. This could indicate that the influence of the oil is more dominant when a similar or higher amount of oil is used compared to the resin. Because Hexamoll DINCH is more polar than Escorez 5300, as can be concluded from the δ_p values in Table 1, more interactions between the oil and the other rubber ingredients are expected. When the concentration of resin becomes higher, and the concentration of oil lower, the influence of the polar oil on the material properties becomes less substantial. Nonetheless, the three plasticizer blends lead to relatively similar curing behavior and cured Payne effect as the reference compound with TDAE.

3.1.2. Stress–Strain Behavior and Tire Performance

Figure 3 shows the stress–strain behavior of the compounds. In Table 5 the stress–strain properties like the modulus at 100% strain (M100) and 300% strain (M300), the tensile strength (Ts), and the elongation at break (E_{ab}) are presented. This table also contains the hardness values of the compounds.

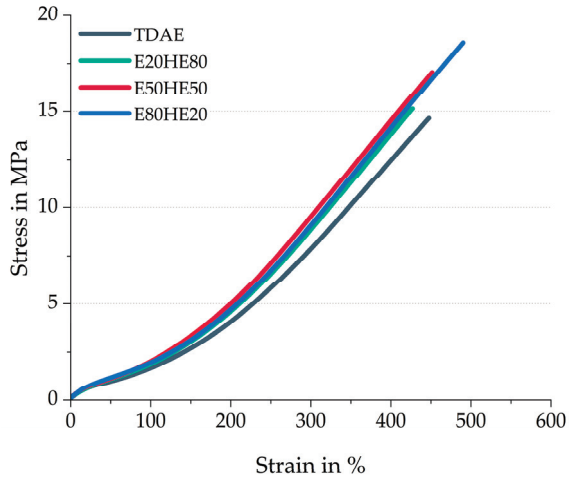

Figure 3. Stress–strain behavior of the compounds with various ratios between oil and resin.

Table 5. Stress–strain data and hardness values of the compounds with various ratios between oil and resin.

Compounds	Hardness in Shore A	M100 in MPa	M300 in MPa	E_{ab} in %	Ts in MPa
TDAE	52 ± 0	1.71 ± 0.04	7.95 ± 0.15	460 ± 30	15.2 ± 1.4
E20HE80	51 ± 0	1.82 ± 0.09	8.52 ± 0.27	440 ± 20	15.0 ± 1.0
E50HE50	54 ± 0	1.94 ± 0.05	9.18 ± 0.20	450 ± 10	16.3 ± 0.6
E80HE20	54 ± 0	1.94 ± 0.05	8.82 ± 0.18	490 ± 30	17.9 ± 1.5

An increasing value of tensile strength and elongation at break is obtained when increasing the resin content and decreasing the oil content in the compound, as shown in Figure 3. The stress–strain behavior was measured at room temperature. When mixing the pure Escorez 5300 in various ratios with the pure Hexamoll DINCH above the softening point of the resin, and cooling it down to room temperature, the mixture stays in a liquid form and no phase separation was observed. However, the ratio between oil and resin did influence the viscosity of the mixture, where a higher resin content resulted in a more viscous liquid than the mixture with a higher oil content. The higher viscosity of the E80HE20 plasticizer blend likely results in higher shear forces during mixing, enhancing the filler dispersion. Because of this, more filler–polymer interactions might be formed, increasing the strength of the compound.

All three plasticizer blends result in higher M100 and M300 values, compared to the reference compound with TDAE oil. This is presumably caused by the increased polymer–polymer and polymer–filler interactions in these three plasticizer blend compounds, which is in line with the higher $G'_{100\%}$ observed in the cured Payne effect measurements.

The hardness of the compounds as displayed in Table 5 is similar for all compounds, because the values lie within the measurement error of the device (±2 Shore A). Therefore, it is not possible to conclude that there is a significant hardness increase when using more resin in the plasticizer blend.

Based on the stress–strain behavior and hardness, the E50HE50 and E80HE20 show more similar values to each other, compared to the E20HE80 blend. This is in contrast with the cure characteristics and cured Payne effect, where the E50HE50 blend showed more similarities with E20HE80. A possible explanation is that at temperatures significantly higher than the glass transition temperature of the plasticizers, both plasticizers are liquid and behave similarly. This is evident in measurements of the cure characteristics at 160 °C and the Payne effect at 100 °C. At these high temperatures, the chemical differences between the plasticizers, such as the polarity of the di-ester oil, play a larger role than the physical state. At room temperature, the oil is still above the T_g, while the resin is below the T_g (Table 1). Therefore, the physical state of the resin differs and has a dominant influence on the final properties of the rubber compound.

Table 6 shows the normalized ARI values of the three plasticizer blends, compared to the reference with TDAE. All three plasticizer blends result in a lower resistance against wear, which has a negative influence on the durability of the tread compound. No clear trend between the oil and resin ratio and the wear resistance can be observed.

Table 6. Normalized abrasion resistance index values of the compounds with various ratios between oil and resin.

Compounds	ARI in %
TDAE	100
E20HE80	92
E50HE50	83
E80HE20	86

However, an inverse linear correlation between the ARI and the M300 is obtained for the compounds evaluated in this study, as shown in Figure 4. Although typically an increase in stiffness leads to improved wear resistance, excessive stiffness can lead to the opposite effect [32]. The material might be slightly more brittle, which makes it more prone to the formation of cracks.

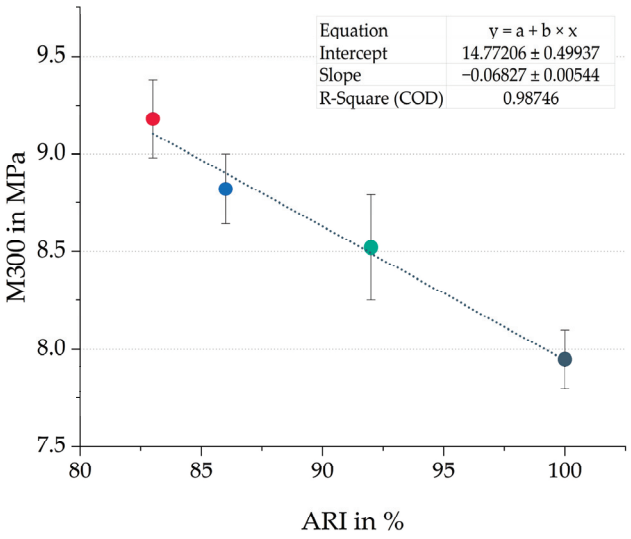

Figure 4. Correlation between wear resistance (ARI) and modulus at 300% strain (M300) of all four compounds. The colors correspond to the evaluated compounds (gray = TDAE, green = E20HE80, red = E50HE50 and blue = E80HE20).

Figure 5 depicts the tan δ curves of the compounds with various plasticizer blends. The peak position can be related to the glass transition temperature of the compound [33]. To understand the influence of the T_g of the pure oil and resin on the compound, the compounds with 37.5 phr of Hexamoll DINCH (H100), and the compound with 37.5 phr of Escorez 5300 (E100) are also included in Figure 5. Moreover, the tire tread indicators like the wet grip (tan δ at 0 °C) and rolling resistance (tan δ at 60 °C), as well as the glass transition temperature (T_g), are displayed in Table 7.

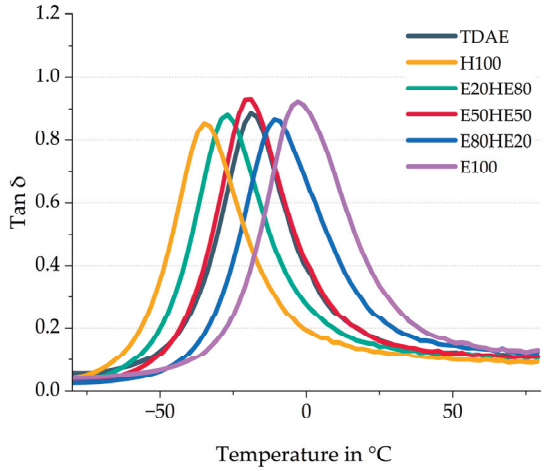

Figure 5. Tan δ curves of the compounds with various ratios between oil and resin.

Table 7. Tire properties of the compounds with various ratios between oil and resin.

Compounds	T_g in °C	tan δ at 60 °C	tan δ at 0 °C
TDAE	−19	0.117	0.406
E20HE80	−27	0.114	0.287
E50HE50	−19	0.115	0.427
E80HE20	−11	0.136	0.692

A higher content of oil results in a lower T_g value, while a higher resin concentration leads to a higher T_g. These shifts in T_g are even more pronounced for the H100 and E100 compounds. Table 1 displays the T_g of the pure plasticizers, and it can be observed that the T_g of the di-ester oil is much lower than that of the resin. Because a relatively large part of the compound consists of a plasticizer, the T_g of the pure plasticizer strongly influences the T_g of the final compound. This explains why the T_g of the compound with a high oil content is much lower than the T_g of the compounds with high resin content. Figure 6 shows the correlation graph of the T_g obtained with DMA measurements against the Escorez 5300 content.

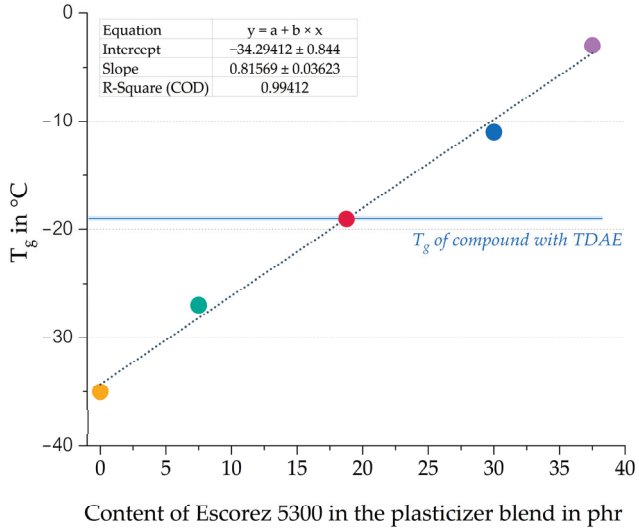

Figure 6. Glass transition temperature obtained with DMA plotted against the Escorez 5300 content. All compounds contain 37.5 phr of plasticizer (Escorez 5300 and Hexamoll DINCH) as shown in Table 3. The colors of the data points correspond to the evaluated compounds and match those used in Figure 5.

Based on Figure 6, it becomes clear that there is a linear correlation between the T_g of the compounds and the plasticizer blend ratios. Using various oil and resin blends makes it possible to modify the T_g of the vulcanizate, which is an efficient approach for tailoring the glass transition temperature according to specific customer requirements and the desired properties of the final product. Furthermore, the 50/50 blend of Hexamoll DINCH and Escorez 5300 results in a similar tan δ peak position as the reference compound with TDAE.

The wet grip and rolling resistance indicators can be obtained from the tan δ curves: the tan δ at low temperatures (0 to 20 °C) indicates the wet grip, and the tan δ at higher temperatures (40 to 80 °C) indicates the rolling resistance [34]. In this study, the tan δ at 0 °C and 60 °C are used as wet grip and rolling resistance indicators, respectively, and displayed in Table 7. A high tan δ at 0 °C and low tan δ at 60 °C are preferred. It needs to be considered that the wet grip indicator is less reliable than the rolling resistance indicator. The wet grip evaluated with Dynamic Mechanical Analysis (DMA) measurements does not always correlate with the wet grip obtained during actual breaking tests, especially

when resins are introduced [35]. Due to the influence of the resin on the T_g, shifting it to temperatures closer to 0 °C, the wet grip rises as well. Because the rolling resistance indicator is measured at temperatures further away from the T_g, this indicator is observed to be less influenced by the shift in T_g and is therefore more reliable. Additional measurements are needed to get better insight into the tire properties of the compounds. However, in this study, the DMA indicators are shown to give a first indication. Of the three plasticizer blends, the E80HE20 results in the highest wet grip indicator, due to the high resin content. However, this compound also results in the highest rolling resistance indicator. The best balance in tire performance properties obtained from the tan δ curves is obtained for the E50HE50 compound.

To summarize the most important tire properties, the magic triangle of tire performance is displayed in Figure 7. In this figure, the values are normalized, and the results obtained for the reference compound with TDAE are set to 100. For all three properties, a higher value is preferred.

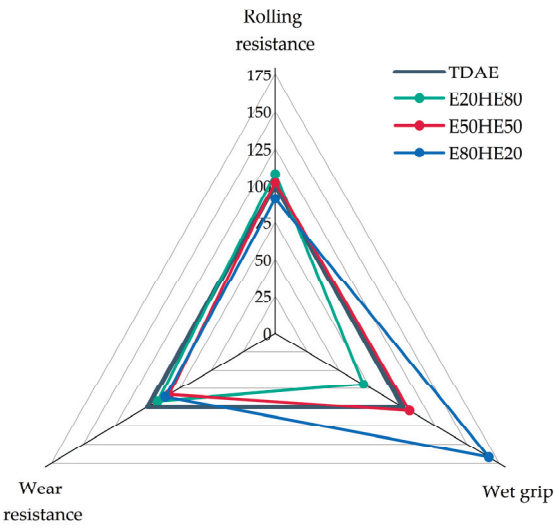

Figure 7. Magic triangle of the compounds with various oil and resin ratios.

Based on the results in Figure 7 it can be concluded that the various oil and resin blend ratios influence the wet grip to the greatest extent. Using a blend with a higher resin content, in this case 80%, results in a severe increase in the wet grip indicator. However, decreased values for the rolling resistance and wear resistance are obtained for this blend. The best balance can be observed for the 50/50 blend, which results in a slightly higher wet grip, a similar rolling resistance, and only slightly decreased wear resistance, compared to the reference compound. The blend ratio with only 20% of resin shows relatively good results for the wear resistance and rolling resistance, but a much lower value for the wet grip indicator. Based on these results and the T_g values, it can be concluded that the replacement of TDAE with 18.75 phr of Hexamoll DINCH and 18.75 phr of Escorez 5300 is the most feasible.

3.2. Plasticizer Blends with Resin and Different Di-Ester Oils

To further evaluate the plasticizer blends, three different di-ester oils were selected to blend with Escorez 5300. All oils are di-ester oils, with different chemical structures between the two ester groups. These structures and additional characteristics are displayed in Table 1. The oils were blended with the resin in a 50:50 ratio, because this was the most successful plasticizer blend ratio based on the tire properties, and this ratio resulted in a similar glass transition temperature as the reference compound with TDAE. In addition to the more conventional concentration of 37.5 phr plasticizer, the compounds were mixed

with high plasticizer concentrations of 80 phr (40 phr of oil, and 40 phr of resin). This way, the influence of the used plasticizer blends on the compound properties was assumed to become more visible. The rubber formulations of both the conventional concentration plasticizer and the high concentration are presented in Table 8. In the figures and tables presented in this chapter, the high-plasticizer compounds (80 phr) are indicated with an (H).

Table 8. Rubber formulations of the compounds with resin and different di-ester oils.

Compounds	S-SBR in phr	BR in phr	Silica in phr	TDAE in phr	Hexamoll DINCH in phr	Palatinol 10P in phr	Plastomoll DOA in phr	Escorez 5300 in phr
TDAE	80	20	80	37.5	X	X	X	X
E50HE50	80	20	80	X	18.75	X	X	18.75
E50PA50	80	20	80	X	X	18.75	X	18.75
E50PL50	80	20	80	X	X	X	18.75	18.75
TDAE (H)	80	20	80	80	X	X	X	X
E50HE50 (H)	80	20	80	X	40	X	X	40
E50PA50 (H)	80	20	80	X	X	40	X	40
E50PL50 (H)	80	20	80	X	X	X	40	40

Furthermore, the compounds consisted of the same quantities of the remaining ingredients: 6.2 phr TESPD, 2.5 phr stearic acid, 2.5 phr zinc oxide, 1.4 phr sulfur, 2.0 phr TBBS, and 1.5 phr DPG.

For the high-concentration plasticizer compounds, the resin was added in three separate portions to the compound. The portions were added in the first stage after 1 min, 2.5 min, and 4 min of mixing. Furthermore, the mixing procedure was kept the same as shown in Table 2.

3.2.1. Rheometer Curves and Payne Effect

In Figure 8 the rheometer curves of the compounds are shown. The solid lines indicate the conventional plasticizer concentrations, while the high-concentration plasticizer compounds are indicated with the dotted lines. Table 9 displays the additional curing characteristics.

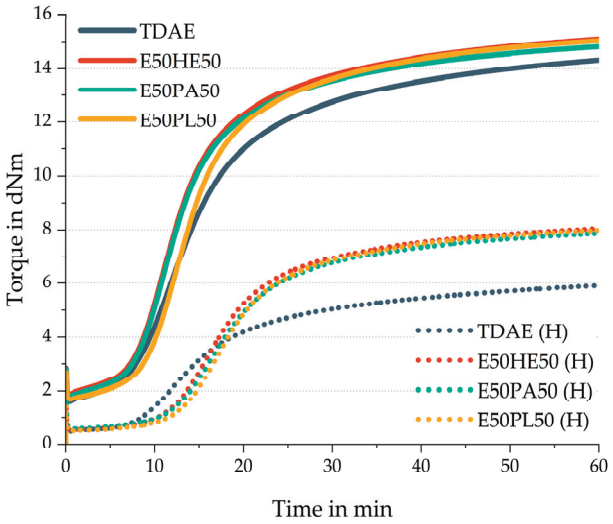

Figure 8. Rheometer curves of the compounds with resin and different di-ester oils. Compounds with high concentrations of plasticizer are indicated with (H).

Table 9. Curing characteristics and Payne effect data of the compounds with resins and different di-ester oils. Compounds with high concentrations of plasticizer are indicated with (H).

Compounds	ts2 in min	t90 in min	MH in dNm	ML in dNm	MH-ML in dNm	$G'_{0.56–100\%}$ in kPa	$G'_{100\%}$ in kPa
TDAE	8.9	33.1	14.3	1.6	12.7	719	525
E50HE50	8.6	30.3	15.1	1.9	13.2	738	564
E50PA50	8.6	29.6	14.8	1.8	13.0	723	579
E50PL50	9.7	30.8	15.0	1.7	13.4	766	567
TDAE (H)	13.0	37.6	5.9	0.5	5.4	440	201
E50HE50 (H)	14.7	35.1	8.1	0.5	7.5	526	306
E50PA50 (H)	15.2	35.6	7.9	0.6	7.3	522	282
E50PL50 (H)	15.7	35.2	8.0	0.5	7.5	489	280

All plasticizer blends show similar cure curves and curing characteristics compared to each other. When focusing on the compounds with 37.5 phr, the scorch time of TDAE is similar to the scorch times observed for the compounds with plasticizer blends. When comparing this characteristic in the high-concentration plasticizer compounds, a shorter scorch time is obtained for TDAE (H) than for the blends. According to the characteristics of TDAE as described by Rathi [12], this oil contains a small content of 0.8 wt% of sulfur. At lower concentrations, this sulfur in TDAE does not have a significant effect on the curing reaction. However, when higher concentrations of TDAE oil are used, relatively more sulfur is added to the compound, increasing the scorch time slightly.

Compared to the reference compound with TDAE, the plasticizer blends all show higher maximum torque values. This could be related to a higher crosslink density for these compounds. When evaluating the 80 phr plasticizer compounds, the difference between the maximum torque of the 50/50 blends and the reference is even more severe. This could be due to two influences. On the one hand, it might be that the plasticizer blends enhance the curing reaction. The ester groups in the plasticizer blends could interact with the silica surface, shielding this filler, which might result in more curing ingredients available in the compound. However, it would be expected that this would also result in a shorter scorch time, which is not observed for the high-concentration plasticizer blend compounds. On the other hand, TDAE could interfere with the curing process, for example by reacting with the sulfur and therefore hindering the vulcanization process. A reason for this can be that TDAE might contain some unsaturation, which can interact with the sulfur, leading to a lower crosslink density [13].

In general, much lower torque values are obtained for the high plasticizer compounds than for the compound with 37.5 phr plasticizer. When increasing the plasticizer concentration without changing the quantities of the other ingredients there are relatively fewer polymer, filler, and curing chemicals available in the compound. This influences the rubber network structure of the material, for example, fewer crosslinks can be formed.

The cured Payne effect curves are depicted in Figure 9. In this figure, the darker-colored dots are related to the compounds with conventional concentrations of plasticizer. The hollow hexagon-shaped markings indicate the results of the high-plasticizer compounds. The cured Payne effect values and storage moduli at 100% strain can be seen in Table 9.

The cured Payne effect of the compounds with 37.5 phr of plasticizers are all similar. A slight shift to higher G' values compared to TDAE can be observed which is likely due to a slightly higher crosslink density. These results are in agreement with the maximum torque values obtained from the rheometer curves (Figure 8).

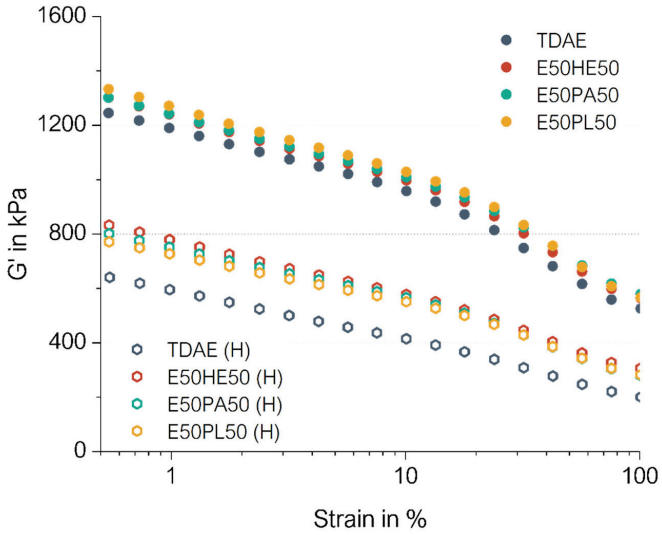

Figure 9. Cured Payne curves of the compounds with resin and different di-ester oils. Compounds with high concentrations of plasticizer are indicated with (H).

Comparing the cured Payne effect of the 37.5 phr plasticizer compounds with the 80 phr plasticizer compound, it becomes clear that much lower values are obtained for the high-concentration plasticizer compounds. This can be explained by the fact that the compounds contain relatively much more plasticizer, and therefore less filler and polymer. This results in less filler–filler, filler–polymer, and polymer–polymer interactions, resulting in lower storage modulus values, as well as lower cured Payne effect.

The compounds with a high content of plasticizer blends show a clear shift in the G' throughout the measurement, compared to TDAE (H). As explained previously, TDAE likely interferes with the curing reaction by interacting with the curing ingredients. Therefore, a lower crosslink density is obtained, leading to lower G' values during the applied strain sweep. This effect is more pronounced when high concentrations of the TDAE are used.

3.2.2. Stress–Strain Behavior and Tire Performance

The stress–strain behavior of the compounds is shown in Figure 10. The solid lines indicate the compounds with 37.5 phr of plasticizer, while the dotted lines indicate the high-plasticizer compounds. Table 10 contains additional stress–strain properties and the hardness of the compounds.

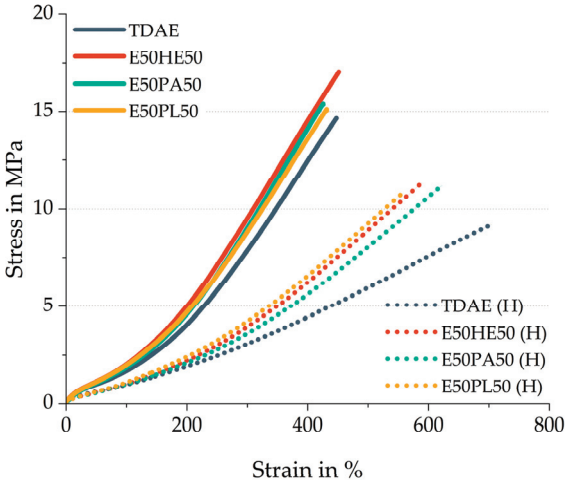

Figure 10. Stress–strain behavior of the compounds with resin and different di-ester oils. Compounds with high concentrations of plasticizer are indicated with (H).

Table 10. Stress–strain data and hardness values of the compounds with resin and different di-ester oils Compounds with high concentrations of plasticizer are indicated with (H).

Compounds	Hardness in Shore A	M100 in MPa	M300 in MPa	E_{ab} in %	Ts in MPa
TDAE	52 ± 0	1.71 ± 0.04	7.95 ± 0.15	460 ± 30	15.2 ± 1.4
E50HE50	54 ± 0	1.94 ± 0.05	9.18 ± 0.20	450 ± 10	16.3 ± 0.6
E50PA50	54 ± 0	1.94 ± 0.07	9.20 ± 0.09	430 ± 20	15.4 ± 0.9
E50PL50	54 ± 0	1.93 ± 0.05	8.85 ± 0.22	430 ± 10	14.9 ± 0.5
TDAE (H)	33 ± 0	0.93 ± 0.05	3.00 ± 0.12	700 ± 20	9.0 ± 0.3
E50HE50 (H)	39 ± 1	1.04 ± 0.05	4.05 ± 0.10	580 ± 20	11.1 ± 0.4
E50PA50 (H)	40 ± 0	1.03 ± 0.05	3.75 ± 0.19	620 ± 30	10.9 ± 0.7
E50PL50 (H)	39 ± 0	1.05 ± 0.04	4.15 ± 0.09	550 ± 30	10.6 ± 0.7

The 37.5 phr plasticizer compounds with 50/50 oil and resin blends show all three slightly higher modulus values compared to the reference compound with TDAE oil. These results are caused by the possible higher crosslink density and higher polymer–filler interactions, which is consistent with the observed findings from the curing behavior and cured Payne effect.

The E50HE50 shows the most distinct behavior compared to the two other blends, with a higher tensile strength and elongation at break. Because the results of the rheometer curves and the cured Payne effect are similar, it is not likely that the E50HE50 results in significant differences in network structure. The higher tensile strength and elongation at break might be due to an improved compatibility between the oil and the resin. Comparing the Hansen Solubility Parameter values in Table 1 of the resin with the three di-ester oils, it can be concluded that the Hexamoll DINCH results in a more similar δd and δh in comparison to Escorez 5300.

Comparing the M100 and M300 values of the high-concentration plasticizer compounds, the difference between the plasticizer blends and TDAE becomes more pronounced. This further illustrates that the plasticizer blends enhance the reinforcement of the vulcanizates. As previously mentioned, this can be explained by the possible higher crosslink density and the higher polymer–filler interactions.

The low tensile strength and high elongation at break obtained for TDAE (H) can be explained by the lower crosslink density of this sample, as explained in the previous subchapter. These stress–strain results are in line with the rheometer curves and cured Payne effect obtained for this compound.

Figure 11 shows the tan δ curves of the analyzed 50/50 blends, compared to the reference with TDAE. The dotted lines show the high-concentration plasticizer compounds. The values of the tire performance properties as well as the T_g are shown in Table 11.

Table 11. Tire properties of the compounds with resin and different di-ester oils. Compounds with high concentrations of plasticizer are indicated with (H).

Compounds	T_g in °C	tan δ at 60 °C	tan δ at 0 °C
TDAE	−19	0.117	0.406
E50HE50	−19	0.115	0.427
E50PA50	−19	0.120	0.453
E50PL50	−25	0.111	0.309
TDAE (H)	−21	0.151	0.377
E50HE50 (H)	−21	0.138	0.463
E50PA50 (H)	−19	0.139	0.571
E50PL50 (H)	−31	0.130	0.285

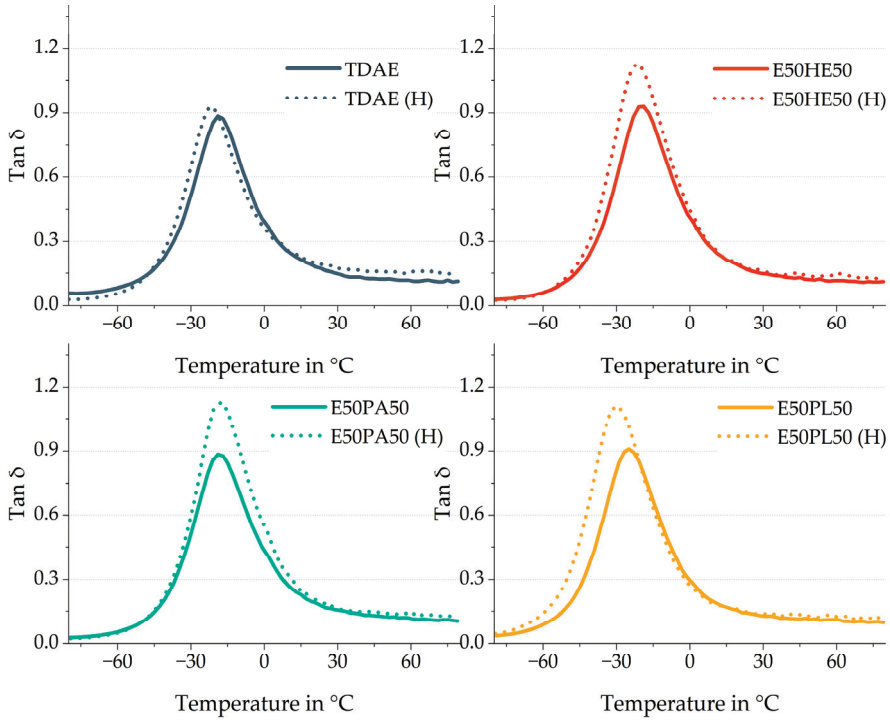

Figure 11. Tan δ curves of the compounds with resin and different di-ester oils. Compounds with high concentrations of plasticizer are indicated with (H).

One of the main differences that can be observed in Figure 11 is the height of the tan δ. For the high-concentration plasticizer blends, the peak is higher with values of approximately 1.1, compared to the compounds with the conventional amount of plasticizer which show tan δ values of approx. 0.9. The tan δ is the ratio between the loss modulus E″ and the storage modulus E′. A higher tan δ often indicates higher dissipation behavior, while a lower tan δ is related to a higher elastic behavior [33]. Increasing the plasticizer results in a larger viscous and dissipating part, increasing the loss modulus.

The T_g is also influenced by the higher concentration of plasticizer in the compounds with the E50PA50 and E50PL50 blends. This effect is most pronounced for E50PL50, which can be explained by the lower T_g of the pure Plastomoll DOA di-ester oil (Table 1). Because this oil inhibits a lower T_g, and the amount of oil is increased, the influence of the oil on the compound T_g becomes larger. For the E50PA50 a similar effect is obtained. However, the higher T_g of the pure Palationol 10P results in a slightly higher T_g of the compound compared to the TDAE (H) compound. E50HE50 shows the same T_g as TDAE when using 37.5 phr of plasticizer and when using 80 phr. This indicates that the combination of 50% Hexamoll DINCH and 50% Escorez 5300 results in the most similar T_g as TDAE.

Table 12 includes the normalized ARI values of the compounds with 37.5 phr of plasticizer. Based on these results, it becomes clear that the best wear resistance is obtained for the compound with the blend between Escorez 5300 and Plastomoll DOA. Veith [36] observed a linear correlation between the glass transition temperature and the wear resistance of SBR/BR rubber blends. A lower T_g of the compound resulted in better wear resistance. Therefore, it is assumed that the improved wear resistance of the E50PL50 compound compared to the other two plasticizer blends is due to the lower T_g of this rubber material. The plasticizer blends with a more similar T_g to the reference compound, namely the E50HE50 and E50PA50, show worse wear resistance. Full replacement of the TDAE oil with Escorez 5300 resin in the study of Bernal-Ortega et al. [16] showed an improved abrasion resistance index. This is explained by the possible better filler dispersion due to the higher shear forces obtained when mixing with resin. In this study, the cured Payne effect of all

50/50 plasticizer blends is slightly higher, which might indicate a slight deterioration in the filler dispersion compared to TDAE. The worse filler dispersion could be a reason for the lower wear resistance. Moreover, the 50/50 plasticizer blends show higher moduli in the stress–strain curves and higher hardness values compared to TDAE. This slight increase in stiffness and hardness could be another cause for the decrease in wear resistance.

Table 12. Normalized abrasion resistance index of the compounds with resin and different di-ester oils.

Compounds	ARI in %
TDAE	100
E50HE50	83
E50PA50	83
E50PL50	95

The magic triangle of tire performance is displayed in Figure 12. The rolling resistance, wet grip, and wear resistance are normalized based on the reference compound with TDAE. In the figure, a higher value indicates an improved performance. Only the compounds with 37.5 phr of plasticizer are displayed in this figure because the high-concentration plasticizer compounds are not feasible for tire tread applications due to their poor mechanical properties.

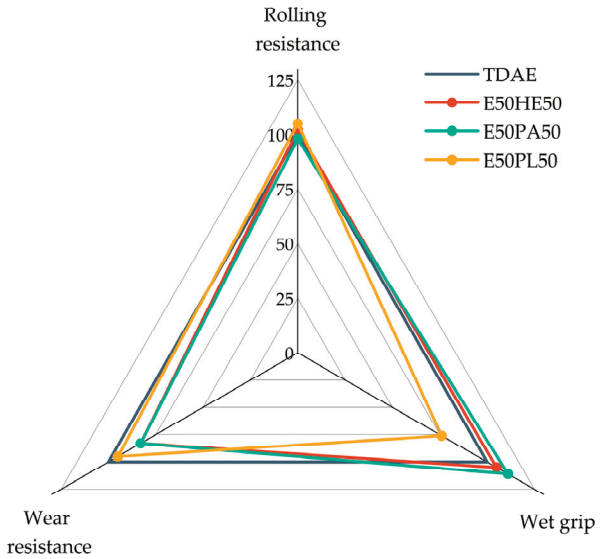

Figure 12. Magic triangle of compounds with resin and different di-ester oils.

Based on the magic triangle, it can be concluded that the E50PL50 compound shows the best rolling resistance and wear resistance, but the worst wet grip. The other two blends (E50HE50 and E50PA50) result in similar rolling resistance values as TDAE, slightly increased wet grip indicators, but lower wear resistance values. However, the differences are relatively small, and in general, the 50/50 blends result in similar values as the reference with TDAE, which is promising.

The differences between the chemical structures in the selected di-ester oils do not result in a severe influence on the final properties of the rubber compounds. It is more likely that the physical characteristics of the oils, like molecular weight and glass transition temperature, influence the slight differences obtained in this study. High-concentration plasticizer compounds show that the plasticizer blends possibly enhance the crosslink formation of the compounds, and result in improved reinforcement, compared to the compound with TDAE.

4. Conclusions

When using bio-based oils in rubber compounds, e.g., vegetable oils, the glass transition temperature is observed to shift towards lower temperatures. The opposite occurs when using resins. These shifts in T_g can influence the performance of the final rubber vulcanizate, which is not always advantageous. To find a plasticizer that is more sustainable, and results in a similar T_g to a compound with commonly used petroleum-based plasticizers, it was proposed to use an oil and resin plasticizer blend.

In the first part of this study, three different oil and resin blend ratios were used in a silica-filled S-SBR/BR compound, and compared to a reference compound with TDAE. The di-ester oil Hexamoll DINCH and resin Escorez 5300 were selected due to their cycloaliphatic nature. Various properties were evaluated, among which the curing characteristics, cured Payne effect, stress–strain behavior, hardness, viscoelastic behavior, and wear resistance. Most measurements showed relatively similar results for the compounds with plasticizer blends based on Hexamoll DINCH and Escorez 5300 compared to the compound with TDAE. However, a clear influence of the oil and resin blend ratio on the viscoelastic behavior of the material was observed. A correlation plot between the T_g of the compound and the Escorez 5300 concentration revealed a linear correlation. This suggests that the T_g of the compound can be easily modified using various plasticizer blend ratios, without influencing the curing behavior or strength of the material. This approach can be used to tailor the T_g of the rubber compound based on the application of the material. However, the various plasticizer blends do influence the laboratory predictors for the wet grip and rolling resistance. The best balance in properties was obtained for the 50/50 blend.

In the second part of this work, various di-ester oils were selected and used in 50/50 plasticizer blends with Escorez 5300. Compounds with more conventional concentrations of plasticizer (37.5 phr) as well as compounds with high plasticizer content (80 phr) were mixed. All three plasticizer blends showed similar results, except for some slight differences in the E50PL50 compounds. This could be explained by the lower molecular weight and lower T_g of the pure di-ester oil. The differences between the plasticizer blends and TDAE in the high-concentration plasticizer compounds were more severe. These compounds showed even more clearly that all three blends enhance the crosslinking formation and result in an improved reinforcement compared to the compound with TDAE. Among the three blends, the E50HE50 blend showed the most similar T_g in both plasticizer concentrations.

Because Hexamoll DINCH can be created via the BioMass Balance approach, the E50HE50 blend is 50% bio-based. This study demonstrates that using the E50HE50 blend as a replacement for TDAE results in similar performance while increasing the sustainability of the compound.

This study primarily focused on evaluating the performance characteristics of the final rubber compound. However, it is recognized that replacement of the plasticizer might influence the processability of the compound. Therefore, it is recommended that future research contains a more detailed analysis of processing properties, for example, the Mooney viscosity.

Author Contributions: Conceptualization, F.v.E., F.G., C.A., M.d.C., A.T. and A.B.; Methodology, F.v.E., F.G., C.A., M.d.C., A.T. and A.B.; Validation, F.v.E.; Formal analysis, F.v.E.; Investigation, F.v.E.; Resources, F.v.E., F.G., C.A., M.d.C. and A.B.; Data curation, F.v.E., F.G. and A.B.; Writing—original draft, F.v.E.; Writing—review & editing, F.G., C.A., M.d.C. and P.B.-O.; Visualization, F.v.E.; Supervision, F.G., C.A., M.d.C., A.T. and A.B.; Project administration, F.v.E., F.G. and A.B. All authors have read and agreed to the published version of the manuscript.

Funding: This research received no external funding.

Institutional Review Board Statement: Not applicable.

Data Availability Statement: The raw data supporting the conclusions of this article will be made available by the authors on request.

Acknowledgments: The authors express their gratitude to Bridgestone EU NV/SA for both scientific and financial support. They also thank BASF SE for supplying the di-ester oils and ExxonMobil Petroleum & Chemical BV for providing the resin used in this study.

Conflicts of Interest: Authors Claudia Aurisicchio and Micol di Consiglio were employed by the company Bridgestone EU NV/SA. The remaining authors declare that the research was conducted in the absence of any commercial or financial relationships that could be construed as a potential conflict of interest.

References

1. Top 10 Companies in Sustainable Tire Market in 2024 Shaping Global Industry Trends. Available online: https://www.emergenresearch.com/blog/top-10-companies-in-sustainable-tire-market?srsltid=AfmBOoqLPuRRTjrjbIVCTvBHVXWQfEaw6UA07K39yMqVMwRElQj3ztL_ (accessed on 25 June 2025).
2. Bavkar, V. Sustainable Tire Materials Market: Opportunities, Trends, and Industry Growth. Available online: https://www.marketsandmarkets.com/blog/CM/Sustainable-Tire-Materials-Market-Opportunities-Trends-Industry-Growth (accessed on 5 June 2025).
3. Dhamija, D. The Road to Sustainability: Exploring the Green Tires Market. Available online: https://blog.bccresearch.com/the-road-to-sustainability-exploring-the-green-tires-market (accessed on 5 June 2025).
4. Sarkar, P.; Bhowmick, A.K. Sustainable Rubbers and Rubber Additives. *J. Appl. Polym. Sci.* **2018**, *135*, 45701. [CrossRef]
5. Bardha, A.; Prasher, S.; Dumont, M.J. Waste Biomass-Derived Rubber Composite Additives: Review of Current Research and Future Investigations Into Biowaste Tire Formulation. *Biomass Bioenergy* **2024**, *183*, 107149. [CrossRef]
6. Chang, B.P.; Gupta, A.; Muthuraj, R.; Mekonnen, T.H. Bioresourced Fillers for Rubber Composite Sustainability: Current Development and Future Opportunities. *Green Chem.* **2021**, *23*, 5337–5378. [CrossRef]
7. Boonmahitthisud, A.; Boonkerd, K. Sustainable Development of Natural Rubber and Its Environmentally Friendly Composites. *Curr. Opin. Green Sustain.* **2021**, *28*, 100446. [CrossRef]
8. Mohamed, N.R.; Othman, N.; Shuib, R.K.; Hayeemasae, N. Perspective on Opportunities of Bio-Based Processing Oil to Rubber Industry: A Short Review. *Iran. Polym. J.* **2023**, *32*, 1455–1475. [CrossRef]
9. Tang, S.; Li, J.; Wang, R.; Zhang, J.; Lu, Y.; Hu, G.; Wang, Z.; Zhang, L. Current Trends in Bio-Based Elastomer Materials. *SusMat* **2022**, *2*, 2–33. [CrossRef]
10. Dadkhah, M.; Messori, M. A Comprehensive Overview of Conventional and Bio-Based Fillers for Rubber Formulations Sustainability. *Mater. Today Sustain.* **2024**, *27*, 100886. [CrossRef]
11. Moneypenny, H.G.; Menting, K.-H.; Gragg, F.M. General Compounding. In *Rubber Compounding: Chemistry and Applications*; Rogers, B., Ed.; CRC Press: Boca Raton, FL, USA, 2016; pp. 333–378, ISBN 9781482235500.
12. Rathi, A. Investigating Safe Mineral-Based and Bio-Based Process Oils for Tire Tread Application. Ph.D. Thesis, University of Twente, Enschede, The Netherlands, 2019.
13. van Elburg, F.; Grunert, F.; Aurisicchio, C.; di Consiglio, M.; di Ronza, R.; Talma, A.; Bernal-Ortega, P.; Blume, A. Exploring the Impact of Bio-Based Plasticizers on the Curing Behavior and Material Properties of a Simplified Tire-Tread Compound. *Polymers* **2024**, *16*, 1880. [CrossRef] [PubMed]
14. IndustryARC. Plasticizers & Tackifiers in Tyres Market by Type 2027. Available online: https://www.industryarc.com/Report/19142/plasticizers-tackifiers-in-tyres-market (accessed on 4 September 2024).
15. Duddey, J.E. Resins. In *Rubber Compounding: Chemistry and Applications*; Rodgers, B., Ed.; CRC Press: Boca Raton, FL, USA, 2016; pp. 379–418, ISBN 9781482235500.
16. Bernal-Ortega, P.; Gaillard, E.; van Elburg, F.; Blume, A. Use of Hydrocarbon Resins as an Alternative to TDAE Oil in Tire Tread Compounds. *Polym. Test.* **2023**, *126*, 108168. [CrossRef]
17. Bernal-Ortega, P.; van Elburg, F.; Araujo-Morera, J.; Gojzewski, H.; Blume, A. Heading Towards a Fully Sustainable Tire Tread Compound: Use of Bio-Based Resins. *Polym. Test.* **2024**, *133*, 108406. [CrossRef]
18. Lopitaux, G. Rubber Tyre Composition Containing Diester Plasticizer. U.S. Patent US8637597 B2, 28 January 2014.
19. Sandstrom, P.H.; Rodewald, S.; Ramanathan, A. Tire with Rubber Tread Containing Combination of Resin and Vegetable Oil, Particularly Soybean Oil. U.S. Patent US2014/0135437 A1, 15 May 2014.
20. BASF. Plastomoll® DOA BMB. Available online: https://products.basf.com/global/en/cp/plastomoll-doa-bmb (accessed on 19 September 2024).

21. BASF. Palatinol® 10P BMB. Available online: https://products.basf.com/global/en/cp/palatinol-10-p-bmb (accessed on 19 September 2024).
22. BASF. Hexamoll® DINCH BMB. Available online: https://products.basf.com/global/en/cp/hexamoll-dinch-bmb (accessed on 19 September 2024).
23. BASF's New Plastic Additives Reduces CO_2 Emissions by 60%. Available online: https://carboncredits.com/basfs-new-plastic-additives-reduces-co2-footprint-by-60/ (accessed on 17 March 2025).
24. Farshchi, N.; Abbasian, A. Inverse Gas Chromatography Study of Hansen Solubility Parameters of Rubber Process Oils (DAE, TDAE, MES, and NAP). *Rubber Chem. Technol.* **2020**, *93*, 297. [CrossRef]
25. *ISO 48-4:2018*; Rubber, Vulcanized or Thermoplastic—Determination of Hardness. ISO: Geneva, Switzerland, 2018.
26. *ISO 37:2017*; Rubber, Vulcanized or Thermoplastic—Determination of Tensile Stress-Strain Properties. ISO: Geneva, Switzerland, 2017.
27. *ISO 4649:2024*; Rubber, Vulcanized or Thermoplastic—Determination of Abrasion Resistance Using a Rotating Cylindrical Drum Device. ISO: Geneva, Switzerland, 2024.
28. Aggarwal, A.; Grunert, F.; Ilisch, S.; Stratton, T.; Blume, A. Investigation of Different Ingredients Contributing to the Cure Torque in Silica-Filled SSBR Compounds. In Proceedings of the IRC RubberCon, Edinburgh, UK, 9 May 2023.
29. Siwarote, B.; Sae-Oui, P.; Wirasate, S.; Suchiva, K. Effects of Bio-Based Oils on Processing Properties and Cure Characteristics of Silica-Filled Natural Rubber Compounds. *J. Rubber Res.* **2017**, *20*, 1–19. [CrossRef]
30. Fröhlich, J.; Niedermeier, W.; Luginsland, H.D. The Effect of Filler-Filler and Filler-Elastomer Interaction on Rubber Reinforcement. *Compos. Part A Appl. Sci. Manuf.* **2005**, *36*, 449. [CrossRef]
31. Bernal-Ortega, P.; Anyszka, R.; Morishita, Y.; di Ronza, R.; Blume, A. Determination of the Crosslink Density of Silica-Filled Styrene Butadiene Rubber Compounds by Different Analytical Methods. *Polym. Bull.* **2024**, *81*, 995–1018. [CrossRef]
32. MonTech USA. Key Factors That Affect DIN Abrasion Testing. Available online: https://www.montechusa.com/key-factors-din-abrasion (accessed on 28 October 2024).
33. Whitcomb, K. Measurement of Glass Transition Temperatures by Dynamic Mechanical Analysis and Rheology. Available online: https://www.tainstruments.com/pdf/literature/RH100.pdf (accessed on 17 March 2025).
34. Colvin, H. General-Purpose Elastomers. In *Rubber Compounding: Chemistry and Applications*; Rodgers, B., Ed.; CRC Press: Boca Raton, FL, USA, 2016; pp. 34–76, ISBN 9781482235500.
35. Babazadeh, K.; Blume, A.; Zeeman, R.; Bandzierz, K. Optimized Laboratory Prediction of Wet Grip Performance of Tires. In Proceedings of the Tire Technology Expo, Hannover, Germany, 23 March 2023.
36. Veith, A.G. Tire Treadwear: The Joint Influence of Tg, Tread Composition and Environmental Factors. A Proposed "Two-Mechanism" Theory of Treadwear. *Polym. Test.* **1987**, *7*, 177. [CrossRef]

polymers

MDPI

Article

Bouncy Idea or Solid Practice? Exploring Industry Barriers in the Incorporation of Devulcanized Rubber into Compounds for Rubber Products

Eric Roetman [1,2,*], Jelle Joustra [1], Geert Heideman [2] and Ruud Balkenende [1]

[1] Faculty of Industrial Design Engineering, Delft University of Technology, 2628 CE Delft, The Netherlands; j.j.joustra@tudelft.nl (J.J.); a.r.balkenende@tudelft.nl (R.B.)
[2] Polymer Engineering, University of Applied Sciences Windesheim, 8017 CA Zwolle, The Netherlands; g.heideman@windesheim.nl
* Correspondence: e.c.roetman@tudelft.nl

Abstract

Devulcanization has the potential to help meet circular economy goals by recovering end-of-life rubber. However, the adoption of devulcanized rubber by manufacturers remains low at the industry level. Devulcanization value chains are complex and involve multiple stakeholders, including waste collectors, sorters, recyclers, compounders, manufacturers and regulatory bodies. This study investigated the barriers compounders and manufacturers face when incorporating devulcanized rubber into new compounds and identified primary underlying causes. The research was conducted through in-depth interviews with compounders and manufacturers of tires and general rubber goods, focusing on the technical, market, institutional, and cultural factors related to incorporating recycled materials, specifically devulcanized rubber. From the results, we identified a number of barriers faced by the industry. A key barrier was the heterogeneity of devulcanized rubber, which made it more difficult to add to new rubber compounds with consistent quality. Other barriers included a lack of standardization and coordination, along with misaligned regulations that hamper the market adoption of devulcanized rubber. This implies that increasing the uptake of devulcanized rubber at the industry level will not be achieved through technological advancements alone or isolated market interventions; instead, it requires comprehensive, systemic solutions.

Keywords: circular economy; rubber; recycling; devulcanization; barriers

1. Introduction

Although devulcanization techniques for rubber have been claimed for decades [1], recent years have seen significant technological advancements, making it increasingly suitable for rubber recycling and raising the potential to meet the goals of the circular economy [2,3]. Despite these technological advancements and considerable investments, the market uptake of devulcanized rubber remains low compared to other rubber recycling routes [2,4].

Devulcanization is an interesting technology that can be used to meet circular economy goals. During rubber goods production, rubber is made firm, elastic, and durable by vulcanization. In that process, sulphur cross-links are created on a molecular level between the rubber polymer main chains. Vulcanization enhances rubber's durability and heat resistance but creates significant recycling challenges. Devulcanization is a group of

recycling technologies with the objective to reverse vulcanization by selectively breaking the sulphur cross-links. Devulcanization processes aim to recycle rubber while retaining most of its original properties [3,5,6]. Devulcanized rubber can be added to new rubber during the compounding stage when raw rubbers are compounded with various additives and fillers to achieve specific properties [6–8]. A rough estimation of the total current European production capacity for devulcanized rubber is 100 kton/year (In Roetman et al. [4], 17 companies were identified in Europe that devulcanized rubber. The interviewed companies had an average capacity of 1.45 ton/h. The assumption is that these companies can run 4000 h on a yearly basis, leading to a total annual capacity of 100 kton of devulcanized rubber) [4].

Devulcanization is a unique approach to rubber recycling because it specifically aims to preserve the original properties of the recycled rubber [2,9]. For comparison, an overview of the main recycling methods is presented in Appendix A. Devulcanization is unique because of its aim to preserve the material properties, as opposed to other methods that often lead to degradation or deterioration of the rubber. Devulcanization is important because of the significance of rubber for the circular economy. Synthetic rubber is primarily made from fossil fuels through energy-intensive methods [10,11]. Natural rubber is a critical and potentially scarce raw material and its regeneration presents challenges [12]. Thus, devulcanization contributes to a circular economy by offering a solution by preserving both material groups. Further, it fits the circular economy goal of maintaining performance and value as much as possible [13].

Even though devulcanized rubber can be used to replace primary, virgin rubber, its composition is different. Devulcanized rubber contains raw, natural or synthetic rubber as well as the additives of the original compounds [2]. These additives include processing aids, vulcanization agents and reinforcing fillers [14,15]. Additionally, the performance and quality of devulcanized rubber depends on the devulcanization technology, as well as the properties, quality, and consistency of the rubber waste collected [5,6,16].

Despite its potential to at least partially replace virgin rubber compounds and thus reduce the carbon footprint [2], there is a low uptake of this material by manufacturers and compounders who could potentially add devulcanized rubber to their compounds. Their perspective is important to investigate, as a study on companies that devulcanize rubber in Europe identified the low uptake of devulcanized rubber as a significant barrier for their business case [4].

Rubber compounders and manufacturers perform a crucial role in the rubber value chain by developing formulations and blending rubbers with additives to meet specific requirements [15]. Rubber compounders are specialized companies that develop rubber formulations and blend rubbers with additives to achieve the desired properties. While some rubber manufacturers have their own compounding divisions, their primary goal is production of goods containing rubber. We distinguish two types of manufacturers: tire manufacturers and manufacturers of rubber goods. Tire manufacturers consume the majority of the global rubber supply. Table 1 shows the consumption of different types of rubber on a global level and Table 2 compares the consumption of general rubber goods and tire production in Europe. Table 3 presents import and export data for rubber products within Europe, highlighting the significance of rubber production in the region.

General rubber goods manufacturers produce finished or semi-finished rubber products, such as conveyor belts, shoe soles, waterproof materials, electrical insulation, adhesives, O-rings, seals, hoses and belts, and industrial gloves for various industries [15,17]. In these goods general-purpose rubbers, such as SBR and natural rubber, as well as specialty rubbers are used that meet specific industry requirements (e.g., fluorocarbon (FPM), which

is resistant chemical and solvents) [18]. The rubber compounders and manufacturers are in the position to add devulcanized rubber to a wide range of compounds.

Table 1. Global rubber consumption in 2020 [19,20].

	Natural Rubber		Synthetic Rubber	
Region	**%**	**Million Metric Tons**	**%**	**Million Metric Tons**
Europe	8%	1.02	14%	1.99
China	43%	5.46	31%	4.40
India	8%	1.02	4%	0.57
Japan	5%	0.64	5%	0.71
USA	6%	0.76	11%	1.56
Rest of the world	30%	3.81	35%	4.97
Total	100%	12.7	100%	14.2

Table 2. Rubber consumption by industry in the EU and UK in 2020 [19,20].

	Natural Rubber		Synthetic Rubber	
	%	**Million Metric Tons**	**%**	**Million Metric Tons**
General rubber goods	27%	0.25	55%	1.09
Tires	73%	0.77	45%	0.90
Total	100%	1.02	100%	1.99

Table 3. Economic value of rubber products imported and exported from the EU in 2020 (excl. UK) [21].

	Imported	Exported
	€ Billion	**€ Billion**
General rubber goods	5.6	5.2
Tires	5.8	5.6
Total	11.4	10.8

In the academic literature, the main barriers identified for manufacturing to come to a circular economy are high startup costs, complex supply chains, challenging collaboration amongst companies, compromises on quality, and the high costs of disassembling products [22]. However, the specific reasons for the low uptake of devulcanized rubber have not been extensively investigated. Therefore, the main research question that will be addressed in this article is: What barriers do compounders and manufacturers encounter when incorporating devulcanized rubber into new rubber compounds, and what are the major underlying factors that contribute to these barriers? The studied factors include technical, market, institutional, and cultural factors, which are recognized in the academic literature as key to the circular economy transition [23].

The methods section outlines the selection of respondents, the type of interviews, and interpretation of these interviews. The results section presents key findings from the interviews. This section addresses the main subjects for the technical, economic, institutional, and cultural factors, while the discussion section interprets these findings by reflecting on potential interventions. Finally, the conclusion section summarizes the overall insights regarding the opportunities and barriers for devulcanization as a means to transition to a circular economy for the rubber industry.

2. Methods

For this study, a qualitative research method was used to identify the barriers for the uptake of devulcanized rubber and their underlying factors. We identified these barriers by interviewing representatives of compounding and manufacturing industries, the potential users of devulcanized rubber. We used purposive sampling [24], deliberately selecting organizations rather than randomly choosing them, and conducted in-depth interviews to identify key topics and gain an understanding of the underlying complexity [25,26].

Representatives for the interviews were selected from companies with in-depth knowledge and ample experience related to the addition of recycled materials to new compounds. The interviews were conducted in-person or via video conferencing, recorded, and transcribed for an accurate representation. The interviews were then coded and interpreted according to the coding scheme in Appendix C.

2.1. Selecting Respondents

This study focused on both compounders and manufacturers with experience of incorporating devulcanized rubber. We identified and approached potential participants through organizations with extensive networks in the rubber industry and through national sector specific associations for the rubber and tire industry in Europe. Companies based in Europe or with European subsidiaries were prioritized, although many were part of international corporations or holding companies. This generated an international view on the topic with an emphasis on Europe. We approached both tire manufacturers as well as general rubber goods manufacturers. Amongst the tire manufacturers, respondents were specifically selected from the 15 companies with the highest global turnover in 2023 [27].

Eight respondents were interviewed. Seven of these respondents had experience working with reclaimed and/or devulcanized rubber. Three of these respondents did not add devulcanized rubber to compounds for commercial products at the time of the interview but continued to do tests with new types of devulcanized rubber. One respondent, a compounder, had stopped adding devulcanized material because it could not be used as a drop-in, a direct replacement of virgin rubber. One respondent did not have any experience of working with devulcanized rubber but did have experience of working with non-vulcanized production waste. This allowed him to draw comparisons between the two materials, providing valuable insights and context for positioning devulcanized rubber in the analysis.

All interviewed companies were operating internationally, and they provided information not only about the European context but frequently also compared this context to the situation in other continents. Table 4 provides general information about the respondents and their companies.

Table 4. Information about the respondents.

#	Type of Company	Role Within Company	Reference Code
1	Tire manufacturer	Research and Development Manager	T1
2	Tire manufacturer	Research and Development Manager	T2
3	Tire manufacturer	Corporate Affairs Manager	T3
4	Compounder	Director	C1
5	Compounder	Research and Development Manager	C2
6	Compounder	Research and Development Manager	C3
7	Producer of general rubber goods	Director	G1
8	Producer of general rubber goods	Production Manager	G2

2.2. Interview Topics and Coding Scheme

The interviews lasted about one hour. Prior to the interview, the respondents received an opening statement, including the interview topics (Appendix B). The interview topics were derived from the literature on barriers to the circular economy transition. A common approach in these research papers is grouping the identified topics into sets of factors: technological, market, institutional, and cultural. This emphasizes the need for a multidisciplinary framework to identify the barriers [23,28–30]. This framework was also applied to plastics recycling in supply chains in other studies [31–33]. Table 5 provides an overview of the factors and research themes identified from the literature.

Table 5. Interview topics.

Technical factors are the material-related aspects and the industrial activities to incorporate recycled ingredients into compounds for new rubber.		
Identified research themes	**Sources**	**Key words**
Overall quality of supplied recycled materials.	[31,33–36]	Quality
Required changes in compound formulations and product designs to use recycled materials.	[31,36,37]	Compound formulation, product design
Consistency in both the quality and quantity of the supply of recycled materials.	[33,38]	Consistency, quality, supply
Market Factors are the aspects related to the cost, pricing and market acceptance.		
Identified research themes:	Sources	
Investment costs for compounding with recycled materials.	[31,33]	Investments, costs
Costs and pricing of recycled materials versus virgin materials.	[31–33,35]	Cost, pricing, recycled, virgin
Market dynamics for products with recycled materials.	[32,33,39]	Market dynamics
Cultural factors are related to how a culture is collaborative and focused on engaging in the circular economy, as well as aligning value to facilitate the use of recycled materials.		
Identified research themes:	Sources	
Position of sustainability in company culture.	[31,33,39]	Sustainability, company/organisation, culture
Coordinated efforts to align and increase the use of recycled materials in new products.	[33,35,40]	Coordination, alignment
End user appreciation of increasing the uptake of recycled materials.	[32,33]	End user, customer, appreciation
Institutional factors are the policies, rules, regulations, taxes and infrastructure that directly or indirectly influence the decision-making of companies.		
Identified research themes:	Sources	
Efforts towards industry alignment and standardization to increase the uptake of recycled materials.	[31,33]	Alignment, standards
Accountability mechanisms of manufacturers and compounders that impact the use of recycled materials.	[33,35,39]	Accountability/ responsibility, mechanisms
Alignment of regulations across sectors and geographical regions that impact the use of recycled materials.	[31,35]	Alignment, regulations, sectors, regions

2.3. Data Analysis

The interviews were coded using structural coding, an approach for analysing large segments of qualitative data along broad categories. This creates an overall framework that can be applied for in-depth analysis of these topics [41]. After the interviews, coding was done using QDA Minor. Supplemental codes were added to capture additional topics that emerged during the interviews. The interviews were interpreted and described along these codes. The coding scheme was adapted after analysing the interviews, leading to the grouping of some codes and the addition of others. The final coding scheme was based on the topics in Table 5 and can be found in Appendix C.

2.4. Comparison of Interview Data with the Literature

The literature on the use of devulcanized rubber by the industry is limited. Therefore, two recycled materials were selected from the academic literature for comparison, to gain a more in-depth understanding of the identified barriers and the extent to which these barriers are uniquely related to this type of recycling. This approach was used to determine if the identified barriers are found more often and to identify interventions that could facilitate the uptake of devulcanized rubber. Two materials were selected: recovered carbon black and mechanically recycled plastic.

Recovered carbon black was chosen as it is a recycled material with the potential to be added to rubber compounds in large quantities. It is retrieved from end-of-life rubber through pyrolysis and can be blended into new rubber compounds as a replacement for carbon black [42]. However, recovered carbon black has lower quality than the original material. One of the reasons is that its surface is often contaminated [43,44]. In a consultancy report, 12 companies were listed that in total recovered 20 kton/year of recovered carbon black in Europe, mainly in pilot factories. These companies announced plans to increase their production to 232 kton/year in the coming years [45]. Although the production capacity is currently relatively small, similar to devulcanization, it is expected to grow significantly in the coming years.

The second material selected was recycled granulate from the mechanical recycling of end-of-life thermoplastic waste [46]. This represents the bulk source of recycled polymer, accounting for more than 400 million metric tons in 2023 worldwide [47]. It is produced from a mixed range of input materials and is downgraded compared to the virgin raw materials.

By entering combinations of the main keywords of the identified research themes of Table 5 into Google Scholar and ScienceDirect and using terms such as ‘recovered carbon black’, the literature on these two groups of materials was identified. Only articles published after 2020 were included to obtain recent research findings on encountered barriers and interventions. The first 40 results were reviewed for each combination of keywords. If no academic literature was identified about recovered carbon black or thermoplastic recyclate, information was sought from white papers and consultancy reports. If information from such non-academic sources was used, this is explicitly stated in the text.

3. Results

The findings are presented according to the four categories outlined in the methods section: technical, market, institutional, and cultural factors. In each of these categories, the factors are described along with the specific results that emerged in the interviews. The results are provided in Tables 6–9, which also show which respondents referred to particular topics by differentiating between compounders (C), manufacturers of general rubber goods (G), and tire manufacturers (T). In the next column, the identified references to comparable barriers found in the literature on recycled carbon black (rCB) and thermoplastic recycled granulate (TRG) are listed.

3.1. Technical Factors

Table 6 lists the barriers that were found related to the technical factors. The introduction of a devulcanized rubber as a new ingredient impacts the overall composition of rubber compounds. All six respondents that used devulcanized rubber first did additional research and development and then reformulated their rubber compounds. If the quality of devulcanized rubber was not fully consistent, even more research was needed.

Table 6. Barriers related to the technical factors.

Barriers identified in interviews with compounders (C), general rubber goods (G), and tire manufacturers (T)	***Respondents***			*Similar barriers identified in the literature about recovered carbon black (rCB) and thermoplastic recycled granulate (TRG)*
	C	*G*	*T*	
Research theme: overall quality of supplied recycled ingredients.				
Not a drop-in replacement: devulcanized rubber is not considered to be a drop-in replacement for virgin rubber, as the properties are not similar to virgin materials.	*2*	*2*	*2*	**rCB:** the scientific literature only mentions different properties for rCB [44,48]. A white paper: [49]. **TRG:** [31,50–52].
Research theme: consistency in both the quality and quantity of the supply of recycled materials.				
Heterogeneity: respondents developed their own, exclusive compounds for unique products, which causes heterogeneous waste streams.	*2*	*2*	*2*	Causes of heterogeneity: **rCB:** [43,53]. **TRG:** [54].
Reduced material properties: devulcanized rubber was derived from mixed sources, which resulted in a heterogeneous mixture with inconsistent quality.	*3*	*1*	*1*	**rCB:** [44,55]. **TRG:** [32,34,46,51,56,57].
Unintended side effects: the addition of recycled material could lead to unexpected side effects during processing or use.	*2*	*1*	*1*	**rCB:** [44,58]. **TRG:** [57,59,60].
Research theme: Required changes in compound formulations and product designs to use recycled ingredients.				
Need to reformulate compounds: compounds needed to be reformulated to compensate for the composition of devulcanized rubber.	*2*	*1*	*2*	**rCB:** [44,58]. **TRG:** [61,62].
Numerous formulation variations: general rubber goods manufacturers and compounders often had dozens of different compound formulations for specific products, all of which needed to be adapted.	*3*	*1*	-	**rCB:** No literature identified. However, the literature does mention the limitations of rCB for specific purposes [44,48] **TRG:** No literature identified but limitations of TR were mentioned for specific purposes, such as applications in the automotive industry [56,63].

In recent years, more types of devulcanized rubber have entered the market, mainly sourced from different types of vulcanized production waste and rubber recovered from end-of-life tires. Respondents who tested these new types of devulcanized rubber mentioned that the technical properties were better than those of materials previously available. Despite these improvements, the devulcanized rubber was only added in small quantities for critical applications; respondent T2 mentioned that only 1–2 percent was added to the most critical compounds. Adding a larger amount to these compounds was deemed too risky.

The barriers, as experienced by the respondents, primarily arose from issues related to the inconsistent quality of devulcanized rubber, which was partially caused by the variability in feedstock from rubber waste streams. The negative effect of heterogeneously sourced material was also a challenge for recovered carbon black [44,48] and recycled granulate from thermoplastic waste [31,50,51]. Until recently, recovered carbon black was rarely used in the rubber industry due to inconsistent properties [64]. Recent studies have shown improved quality consistency by reducing the ash content [42,43,65]. As these

methods are still under development, the recovered carbon black industry also focusses on negating any negative effects [66], as is currently the case for devulcanized rubber.

In the case of the mechanical recycling of thermoplastic waste, the composition was made more homogeneous by automated separation and sorting [67] and with detection of the types of plastics by applying state-of-the-art vision technologies [68,69]. However, the quality was still inconsistent due to, e.g., layered or non-separable plastics and contaminations on the plastic [34,46,51,56]. An underlying reason was the municipal systems of plastic waste collection and separation before recycling, leading to additional contamination and mixing of materials [70]. This mirrors the challenges associated with car tires as a source of devulcanized rubber, as they consist of multiple layers of different rubber compounds and are gathered through diverse collection systems across Europe, each with its own processes and efficiencies [4].

3.2. Market Factors

Table 7 lists the barriers observed related to the market factors. Although devulcanized rubber had a lower purchasing price than virgin rubber, respondents did have to incur additional costs. These costs primarily arose from the effect of this new ingredient. Respondents noted that they had additional costs to compensate for the lower consistency in the quality of the material. More research and development were also needed to make the devulcanized rubber compatible with the rubber compound. Respondents C2 and G2 also included costs for troubleshooting for recycled materials in their calculations if unexpected effects occurred during processing or to address possible customer complaints. To account for these costs, respondent C2 mentioned that when new compounds needed to be developed for a customer, they required the customer to share in the associated development costs.

Table 7. Barriers related to the market factors.

Barriers identified in interviews with compounders (C), general rubber goods (G), and tire manufacturers (T).	***Devulcanization respondents***			*Similar barriers identified in the literature about recovered carbon black (rCB) and thermoplastic recycled granulate (TRG).*
	C	*G*	*T*	
Research theme: investment costs for compounding with recycled ingredients.				
Additional expenditures: additional expenditures to compensate for a less consistent quality of the material.	*2*	*2*	*2*	**rCB:** no literature identified. **TRG:** [31,33,35,51,56].
Research theme: costs of recycled ingredients versus virgin ingredients.				
Low purchasing cost: devulcanized rubber was cheaper than virgin rubber and less valuable on the market.	*1*	*1*	*2*	**rCB:** [71,72]. **TRG:** [31,73].
Research theme: market dynamics for products with recycled ingredients.				
More customer requests, greater diversity of supply: in business-to-business sales, more customers were requesting rubber compounds that included biobased or recycled materials, and an increasing number of suppliers were offering recycled materials.	*2*	*2*	*2*	**rCB:** [72]. In additional to this source, the topic was raised by tire manufacturers in their white paper [74]. **TRG:** the literature describes an imbalance between supply and demand in terms of availability, quality, and pricing [31,75].
Increased obligations: more requirements for recycled materials than for virgin materials; companies had to undergo additional audits and environmental impact assessment from their customers.	*3*	*1*	*3*	**rCB:** no literature identified. **TRG:** [29,33,76].

The market dynamics were also different from virgin materials. A reason was that respondents had to engage with new potential suppliers of recycled materials. For devulcanization, many of these suppliers were startups that needed launching customers.

Another reason was that respondents T2, T3, C1, C2, and C3 noted more requests for rubber products that contained recycled or biobased materials. The sustainability goals set by the automotive industry were an important driver. Respondent T2 cited an example of a car manufacturer that requested a tire that contained at least 40% sustainable materials.

Respondents C2, C3, and G1 explicitly mentioned that when they supplied products with recycled materials to such customers, they were expected to collaborate on the sustainability reporting of their customers. They needed to provide additional data to their customers related to the customer sustainability goals, such as a reduced CO_2 footprint. This included information about the recycled materials and environmental assessments.

According to the literature, market demand of recycled materials is vulnerable to fluctuations in the prices of the virgin materials, which is described for carbon black [71,77], plastics [31,73], and rubber [78]. In Europe, plastic recyclers went out of business due to the low prices of virgin plastics in 2024 [79]. In contrast, the business case for recovered carbon black through tire pyrolysis is not only dependent on carbon black but also on pyrolysis oil (naphtha), which can be blended into marine fuel and allows shipping operators to meet their obligations under the FuelEU Maritime Regulation [80]. Thus, although the market dynamics for these recycled materials differ, their prices are still influenced by factors such as supply and demand, production costs, and the prices of competing virgin materials.

3.3. Cultural Factors

Table 8 lists the barriers observed related to cultural factors. Respondents highlighted many of their efforts to increase the use of recycled materials in rubber compounds. However, respondents T1, T2, T3, C1, C2, C3, and G2 emphasized that product quality and overall costs were not allowed to be compromised. In contrast, G1 actively sought markets that accepted products made with recycled materials.

Table 8. Barriers related to the cultural factors.

Barriers identified in interviews with compounders (C), general rubber goods (G), and tire manufacturers (T)	*Devulcanization respondents*			*Similar barriers identified in the literature about recovered carbon black (rCB) and thermoplastic recycled granulate (TRG)*
	C	*G*	*T*	
Research theme: position of sustainability in company culture.				
Limited room for compromises on quality and costs: companies set clear sustainability goals, but have no willingness to compromise on either cost or quality.	*2*	*2*	*1*	**rCB:** no literature identified. **TRG:** [31,51,56,81].
Research theme: collaborative efforts to align and increase the use of recycled materials in new products.				
No coordination: coordinated industry wide efforts were identified to increase recovered carbon black but not devulcanized rubber.	-	-	*3*	**rCB:** no academic literature identified but other sources mention that tire manufacturers collaborated with rCB suppliers and other stakeholders [74]. **TRG:** Although no academic literature was identified, several inter-company collaborations were recognized: [82,83].
Research theme: end user appreciation for increasing the uptake of recycled ingredients.				
Low consumer demand for recycled materials: no demand was identified for tires made from sustainable materials.	*2*	-	*2*	**rCB:** no literature identified. **TRG:** [31,33,84].

The demand for more recycled materials in rubber came from customers from the industry, not from consumers. According to respondents T2 and T3 the demand from end users was low and they did not spot any willingness among consumers to pay a premium for rubber products containing recycled material, such as tires. Respondent T2 mentioned

that his company wanted to contribute to a campaign aimed at raising awareness among consumers to increase the acceptance of recycled and biobased materials in tires.

No industry-wide collaboration or coordination was mentioned by any of the respondents for an industry-wide commitment to the uptake of devulcanization. In contrast, respondents did mention such collaboration for recovered carbon black, which was also mentioned in consultancy reports and a white paper by the rubber industry [45,74]. For recycling of thermoplastic waste, several industry wide collaborations were identified that aimed to develop more recyclable products, coordinate waste collection systems and innovate recycling techniques [82,83,85].

3.4. Institutional Factors

Table 9 lists the barriers observed related to the institutional factors. Respondents T1, T2, and T3 considered quality standards to be important for the uptake of recycled materials. However, they identified such standards for recovered carbon black but not for devulcanized rubber. This is in line with the literature, in which standards were identified for recovered carbon black [55,86] and thermoplastic recycled granulate [87–89] but not for devulcanized rubber [3,4].

Table 9. Institutional factors.

Barriers identified in interviews with compounders (C), general rubber goods (G), and tire manufacturers (T).	*Devulcanization respondents*			*Similar barriers identified in the literature about recovered carbon black (rCB) and thermoplastic recycled granulate (TRG).*
	C	*G*	*T*	
Research theme: coordinated efforts for alignment and standardization to increase the uptake of recycled materials.				
No specific standards: respondents mentioned standards for other recycled materials but were not aware of such standards for devulcanization.	-	-	*3*	**rCB:** a specific ASTM standard, including a test method were developed for rCB [90,91].
				TRG: Standards were developed by industries for thermoplastic recyclate [76].
Research theme: accountability mechanisms of manufacturers that impact the use of recycled ingredients.				
Liability concerns: Companies were accountable for their products, including liability for any damages caused by those products or their components. This made the companies more risk-averse and reluctant to increase the amount of recycled materials.	*2*	*1*	*1*	**rCB:** no literature identified.
				TRG: no literature identified.
Research theme: alignment of regulations across sectors and geographical regions that impact the use of recycled ingredients.				
National regulatory differences: differences in interpretations of EU waste laws made it increasingly difficult to ship rubber across borders.	1	1	1	**rCB:** no literature identified.
				TP: [28,35].
Regulations from other domains: a key concern was meeting multiple regulations concerning environmental and safety goals.	1	1	3	**rCB:** no literature was identified
				TRG: [28,31,35,92,93].
Need for alignment of regulations: respondents indicated a need for better governmental alignment of regulations that directly or indirectly impact the adoption of recycled materials.	-	1	3	**rCB:** no literature was identified.
				TRG: [28,31,35,92].

Respondents T1, T2, and T3 noted that legislation could lead to an increase in the uptake of recycled materials in rubber but T1, T2, T3, C2, and G1 also expressed concerns about the implementation of upcoming legislation, such as a blending obligation of non-fossil ingredients in rubber. This was considered to have negative side effects by respondents T3, C1, and G1. The reasons were: effect on product quality, increased regulatory pressure, and its impact on pricing compared to international competition.

The current legislative framework in Europe was identified as a barrier to increase the uptake of recycled materials. A specific concern expressed by respondents T1, T2,

and T3 was that they already had to meet multiple environmental and safety regulations. These could conflict with the aim to increase recycling rates. Respondents T1, T2, T3, and G3 also mentioned uncertainties related to the effect of upcoming and future considered regulations that could make it more difficult to rely on recycled materials. For this reason, respondent T1 mentioned that they not only conducted a technical check but also a legal check to guarantee that such materials could be used in the coming 10 years. A first example mentioned by T2, T3 and G1 was the EU Deforestation Regulations [94], which could imply that the origin of recycled natural rubber had to be demonstrated, which is challenging in an open-loop recycling system. A second example mentioned by respondents T2, T3, and G1 was that recycled rubber is now considered exempt from Registration, Evaluation, Authorisation, and Restriction of Chemicals (REACH) because the material has already been registered during the initial production. However, the European Chemicals Agency is considering that recycled materials, such as rubber, need to be demonstrably free of substances of concern [95]. This uncertainty of such upcoming regulation is also described in the literature about thermoplastic recycling [92,96].

Respondents T3 and G2 noted that European member states are allowed their own interpretation and implementation of EU legislation for waste and trade, which made it more difficult for their companies to work and ship across borders [97,98], directly leading to higher costs. For this reason, respondents T1, T2, T3, C2, C3, and G1 considered better alignment and more coherent implementation of regulations an important condition to increase recycling rates. As became evident from both the interviews and the literature in Table 9, the regulatory issues are a widely shared concern within the plastics and rubber industry.

4. Discussion

This study identified barriers across the technical, market, institutional, and cultural factors faced by compounders and manufacturers when incorporating devulcanized rubber into new rubber compounds, along with their underlying causes. Respondents from tire manufacturers, general rubber goods manufacturers, and compounders were interviewed as experts on processing recycled materials, with a specific focus on devulcanized rubber. The respondents reflected on their experiences with the addition of devulcanized rubber and other types of recycled materials to their compounds. In this discussion we reflect on these observations by focusing on how devulcanized rubber can potentially be incorporated in larger quantities into new compounds and identifying system interventions to achieve this goal.

A recurring topic among the technical factors is that devulcanized rubber has a heterogeneous composition, which is a clear barrier for the uptake of rubber. This heterogeneity is partially inherent to devulcanization, as a devulcanized rubber contains both the original rubber polymers as well as the additives that were used to create the new rubber compound [6]. This also arises from the heterogeneity of rubber waste sources. If such a large variation in rubber products enters waste systems, the devulcanization material becomes inconsistent, thus reducing quality [6,16]. Therefore certain companies devulcanize rubber from specific sources, such as truck tire tread rubber, to obtain devulcanized rubber with a more consistent quality [4,5,16]. This is an example of a closed-loop/closed-source system, implying that end-of-life materials from a well-controlled source are recycled at relatively high quality and value [99]. Other research showed that the closed-loop/closed-source concept is based on the premise that the original equipment manufacturers take responsibility for collection to arrive at a relatively homogeneous input stream from selected sources [100].

An important barrier among the market factors is that recycled materials are valued lower by compounders and manufacturers than new, virgin rubber. A reason is the required additional research and development costs, as well as potential risks related to product liability. An underlying reason is a lack of standardization for devulcanization, which could be improved by setting standards, as were identified for recovered carbon black [90] and thermoplastic recycled granulate [76]. Additionally, compounders could specialize in blending devulcanized rubber with virgin rubber compounds to create materials with devulcanized content and a more consistent quality for manufacturers. Companies that specialize in this type of blending were identified for recovered carbon black, such as [66], and thermoplastic recycled granulate, such as [101]. Thus, by standardizing and consolidating the devulcanization value chain, opportunities could arise to enhance quality and potentially increase the value of devulcanized rubber.

A key barrier among the cultural factors is the lack of industry-wide engagement in preserving the value and usability of rubber. Devulcanization research and development strongly focuses on technology development, hardly addressing other factors that limit implementation [4]. In addition to technological solutions for improved sorting and separating, companies could be creating distinct material recycling loops within their respective value chains, as identified in plastics recycling [102]. This requires an involvement from compounders, manufacturers, distributors, and recyclers and necessitates infrastructure and appropriate regulations to facilitate these closed-loop recycling systems [99]. Given the diverse range of rubber products and markets, multiple recycling chains can be established to create effective closed-loop/closed-source systems, each tailored to specific material streams where applicable.

A recurring institutional barrier is the absence of appropriate regulations. When looking at improvements, it is important to also take plans by the European Union into consideration. In the Circular Economy Action Plan for 2030 [103] a European blending obligation was announced, which mandates the inclusion of non-fossil ingredients (either biobased or recycled) in plastics and rubber. This obligation could boost the uptake of recycled materials in general, but the results of this study showed that compounders and manufacturers have a strong preference for materials that can be blended into compounds without having to make any modifications to their recipes. However, modifications are needed in compounds to compensate for the additives in devulcanized rubber [6]. For this reason, such an obligation may increase the uptake of other types of biobased and recycled materials, but not necessarily devulcanized rubber.

Another potential legislative intervention is extended producer responsibility (EPR), which can be effective for collecting waste and creating a secondary raw material market [104,105]. These systems are a collective responsibility of manufacturers but also importers, organized by producer responsibility organizations. Such organizations exist in several European countries and are aimed at the collecting of end-of-life tires [106]. This has not yet resulted in the most optimal material reprocessing from a circular economy perspective [106,107]. Due to the collective responsibility of all manufacturers and importers, ERP systems are geared towards open-loop recycling. This poses a particular obstacle for devulcanization, as a closed-loop recycling system is desirable to reduce the heterogeneity of devulcanized rubber. Thus, an ERP system, in which manufacturers carry a collective responsibility does not provide the incentive needed to stimulate rubber recycling by devulcanization.

The drawbacks associated with the blending obligations for non-fossil ingredients and EPR systems highlight the need for a more comprehensive approach to address the complexities, as outlined in this study. A system would be needed that focusses on creating both the infrastructure as well as industry collaboration to achieve the highest

possible closed-loop recycling. To achieve this, policymakers should reconsider which stakeholders need to be involved to achieve the most optimal use and recycling of rubber. It is recommended as a topic for future research to study how an integrated approach could increase the circular economy for the rubber industry, specifically for devulcanization. This study demonstrates that achieving this goal requires more than just technological advancements; to reach higher quality standards on an industrial scale, collaboration across the supply chain is essential to enable closed-loop recycling via devulcanization.

The analytical framework depends on choices made during the analysis, which could restrict the scope of interpretations. Since most respondents were from Europe, the geographical validity of the results may be limited.

5. Conclusions

This study focused on identifying the barriers compounders and manufacturers face when using devulcanized rubber in new rubber compounds and finding the underlying causes to these barriers. It is demonstrated that significant changes are needed to increase the uptake of devulcanized rubber in the transition to a circular economy. It provides greater insight into the barriers, interconnections, and underlying causes, while also identifying opportunities for improved policy and collaboration, ultimately supporting the transition to the circular economy.

Most academic research on the topic of devulcanization has focused strongly on the technical aspects [2,3,108,109], but this study explored other factors influencing the uptake of devulcanized rubber that are essential to progress devulcanization beyond its niche in the industry. We investigated the technical, economic, institutional, and cultural factors that affect the uptake of devulcanized rubber as an ingredient in new rubber compounds.

Reflecting on the current situation, respondents identified barriers stemming from a variety of interrelated factors. Similar challenges have also been documented for recovered carbon black and thermoplastic recycled granulate, such as the lower homogeneity of recycled materials compared to new, virgin materials, leading to inconsistencies in quality. Barriers that were more specific to devulcanized rubber include limited industry collaboration and the need for greater standardization, both of which are important to improve efficiency and ensure consistency across the industry.

To produce high-quality devulcanized rubber, multiple interconnected barriers must be addressed. Overcoming these challenges on the industry level calls for systemic changes and effective collaboration among key stakeholders. Several approaches developed for other recycled materials could be worthwhile to increase the uptake of devulcanized rubber: industry standards, harmonized regulations, and closed-loop/closed-source recycling strategies.

Author Contributions: Conceptualization, E.R., J.J., G.H. and R.B.; formal analysis, E.R.; funding acquisition, G.H. and E.R.; investigation, E.R.; methodology, E.R., J.J. and R.B.; supervision, J.J. and R.B.; visualization, E.R.; data curation, E.R.; writing—original draft, E.R.; and writing—review and editing, J.J., G.H. and R.B. All authors have read and agreed to the published version of the manuscript.

Funding: This research was conducted as a part of the 'Hoogwaardige recycling door devulkanisatie' project (high-quality recycling by devulcanization). This research was funded by Regieorgaan SIA, which is a part of the NWO (Nederlandse Organistatie voor Wetenschappelijk Onderzoek). This research was part of the RAAK PRO subsidy framework, grant number RAAK.PRO04.027.

Institutional Review Board Statement: The study was conducted in accordance with the Declaration of Helsinki, and the protocol was approved by the Human Research Ethics Committee of the Delft University of Technology of 4351 on 7 July 2024.

Data Availability Statement: The data utilized in this study cannot be made publicly available as it contains proprietary company-specific information.

Acknowledgments: We would like to thank the respondents for the interviews and for sharing their knowledge and insights regarding the topic of devulcanization.

Conflicts of Interest: The authors declare no conflicts of interest. The funders had no role in the design of the study; in the collection, analyses, or interpretation of data; in the writing of the manuscript; or in the decision to publish the results.

Appendix A. End-of-Life Methods for Rubber

The following methods were identified in the literature [2,110].

	Feedstock	Working Principle	Applications
Devulcanization	Rubber crumbs or powder	Devulcanized rubber compounds are aimed at a higher quality than reclaimed rubber. Devulcanization is a process that aims to selectively break the cross-links while keeping the rubber polymers intact. This is achieved through various methods, such as exposing the rubber to heat, chemicals, and shear strength. The result is a rubber compound that can be re-vulcanized [3,9,110].	Devulcanized rubber can be used to replace virgin rubber and additives. In most cases, this material is blended into new rubber compounds to compromise for any loss of quality [5,6]. Additionally, devulcanized rubber is added to bitumen to partially replace the plasticizer SBS [4,111].
Reclaimed rubber	Rubber crumbs or powder	On the molecular scale, in a reclaim process, both the rubber polymers and cross-links and are randomly broken. The input of an industrial reclaim process consists of rubber crumbs or powder, which are converted into a rubber compound that can be re-vulcanized [3,9].	Reclaimed rubber is mostly added to rubber compounds and then re-vulcanized. It is mostly used for less critical applications or added in small quantities to new rubber compounds [9].
Binder systems	Rubber crumbs or powder	For certain applications, the granulated rubber is bound with a polyurethane or a thermoplast [112,113]. Additionally, the surface of the rubber powder can be treated for better bonding in a rubber compound [114].	This material can be used for various products, such as rubber tiles and mats and underlayment for floors [113].
Pyrolysis	Rubber crumbs or powder	Pyrolysis is a thermal process in which rubber compounds are decomposed by heat (400–800 degrees Celsius) in the absence of oxygen into smaller molecules, which leads to oil, carbon black, and gas [110].	Pyrolysis oil can be used as a fuel and in theory for producing new monomers to create new plastics and rubber [115]. The carbon black can replace certain grades of virgin carbon black [116]. Lastly, the gas can be a source for energy [117].

	Feedstock	Working Principle	Applications
Retreading	Passenger car tires, tuck tires, airplane tires, and off-the-road tires	In retreading the tread of a worn-out tire is removed. A new rubber tread compound is vulcanized onto the tire. Retreading is different from the recycling process, because the carcass of a tire can be reused [118]. The removed rubber from the tread can be recycled by another method, such as devulcanization [4]	Retreading is primarily used for tires from planes, truck, agricultural tires and sometimes passenger car tires [119].
Mechanical grinding	Different types of tires and rubber products, such as conveyor belts	Rubber is sorted from steel, canvas and other contaminants and is then mechanically processed into crumbs or powder of various sizes [113]. An alternative to mechanical processing is cryogenic shattering [120].	Rubber crumb or powder is used as a feedstock for various recycling methods, such as reclaim and devulcanization [9]. Additionally, rubber crumbs can be utilized as artificial turf on sports fields or recreational surfaces [120]. Rubber powder is also used as a simple filler material that can be added in small quantities to new rubber compounds [114]. Rubber crumbs are used as an additive for tarmac/asphalt [113].
Incineration	Tires and other end-of-life rubber products	Tires are disposed of by incineration, but this process produces toxic emissions [110]. Rubber is incinerated in cement plants [2] as an alternative source of heat, which produces less toxic emissions than coal [121]	Incineration can be used to recover 32.6 MJ/kg of embedded energy in tires [110].
Landfill	Tires and other end-of-life rubber products	Globally, 55 percent of all tires are dumped in landfills [122]	Large quantities of landfilled tires are known to pose a significant fire hazard. Additionally, they are toxic to soils and groundwater, and when burned, they cause air pollution [123]

Appendix B. Opening Statement and Topic List Used for Interviews

Appendix B.1. Opening Statement

My name is Eric Roetman, and I am a researcher at Windesheim University of Applied Sciences and a PhD candidate at TU Delft. I am conducting interviews with representatives from European companies that have devulcanized tires. I would like to interview you as a representative of one of these companies. During the interview, I aim to gather information about the key opportunities and barriers of adding recycled rubber to new rubber compounds.

During the interview, I will ask a set of questions on this topic. By posing these questions to you and representatives of other companies, we hope to gain an overview of the opportunities and barriers. The information will be recorded using a voice recorder and then transcribed. You will receive a copy of the main conclusions and have the opportunity to respond, suggest changes, or address any misinterpretations. If we wish to use non-anonymized quotes, or quotes traceable back to you, from the interview, we will contact you and only proceed with your explicit approval.

The aim of these interviews is to collect data for publication in an academic article and a PhD thesis. The information collected will be handled with great care, and the outcomes will be published in a manner that prevents identification of you or your company. Information traceable back to you will not be shared beyond the research team. The information from the interviews will be stored in a data repository by Hogeschool Windesheim (University of Applied Sciences).

Your answers in this study will be kept confidential to the best of our ability. Your participation in this study is entirely voluntary, and you can withdraw at any time.

If you have any questions or concerns about the interview or handling of the data, you can contact me directly by sending an email to e.c.roetman@tudelft.nl or calling me at [phone number].

Appendix B.2. Interview Topics

General

1. Why did you start to incorporate recycled materials in rubber products/compounds?
2. What type of recycled materials?
3. Since when do you incorporate recycled rubber into your products/compounds? Why at that moment?
4. Have you applied recycled material to a new type of product or to existing products?
5. What new skills, facilities and resources did you need in your company to add recycled materials to rubber?
6. Up to what degree do you experience an advantages or disadvantages of being one of the first companies that incorporates recycled material in rubber?

Technical factors

1. What types of recycled source material (devulcanized, reclaimed, micronized rubber material, etc.) are most and least suitable for you to add to your rubber compounds? How does devulcanization fit in this list?
2. What product categories are most suitable products to incorporate such recycled materials?
3. How do you experience the performance and processability of recycled source material compared to virgin rubber material?
4. To what degree do the properties of your recycled source material pose challenges, and how can you mitigate these challenges?
5. How would you rate the availability of the recycled source materials for production?
6. How do you assess the quality of the supplied rubber material, specifically regarding contamination such as the presence of PAHs?
7. Did you have to change your production process to process recycled rubber, and why?
8. Up to what extent did you have to change your research and development process for processing recycled rubber?

Market factors

1. How would you evaluate the overall reliability of suppliers of recycled source material?
2. Up to what extent is it an added value for your customers that you include recycled content in products, or do they have reservations?
3. Up to what extent did encounter additional costs when incorporating recycled materials into your products? Includes upfront costs?

Institutional factors

1. Did upcoming regulations positively or negatively influence your decision to incorporate recycled rubber into your products?

2. Up to what extent have you benefitted from financial incentives (e.g., subsidies) that encouraged you to use recycled materials in manufacturing processes?
3. (How) did industry standards positively or negatively influence your decision to incorporate recycled rubber into your products?

Cultural factors

1. Up to what degree do you perceive a willingness amongst customers to add recycled materials?
2. Up to what extent is your engagement with your suppliers of recycled material different from suppliers of virgin materials?
3. How does the addition of recycled material to products affect your relationship with your compounder(s)?

Closing the interview

1. Is there any topic that is not addressed during this interview and you would like to address?

Appendix C. Interview Coding

Technical factors are the material-related aspects and the industrial activities to process recycled ingredients into compounds for new rubber.
Identified research themes
Overall quality of supplied recycled materials • Performance devulcanized material • Performances (other) recycled materials • Technical challenges recycled materials • Suitability recycled materials for rubber products
Required changes in compound formulations and product designs to use recycled materials • Required changes to rubber compounds • Additional research and development • Required changes to production processes
Consistency in both the quality and quantity of the supply of recycled materials • Availability of recycled materials • Quality of recycled materials
Market factors are the aspects related to the cost, pricing, and market acceptance.
Identified research themes:
Investment costs for compounding with recycled materials • Required skills, facilities, resources • Additional costs to include recycled materials
Costs and benefits of recycled materials versus virgin materials • Additional costs of adding recycled materials • Financial benefits to include recycled materials
Market dynamics for products with recycled materials • Availability suppliers and supplies • Reliability of suppliers • Effect of adding recycled materials on trade

Cultural factors are related to the extent to which a culture is collaborative and focused on engaging in the circular economy, as well as aligning value to facilitate the use of recycled materials.
Identified research themes:
Position of sustainability in company culture • Willingness to include sustainability standards • Communication of sustainability goals
Coordinated efforts to align and increase the use of recycled materials in new products • Industry-wide collaborations • Engagement of suppliers • Engagement of business-to-business customers
Consumer appreciation and involvement aimed at increasing the uptake of recycled materials • Engagement of consumers
Institutional factors are the policies, rules, regulations, taxes, and infrastructure that directly or indirectly influence the decision-making of companies
Identified research themes:
Efforts for alignment and standardization to increase the uptake of recycled materials • Industry standards for devulcanization • Industry standards (general)
Accountability mechanisms of manufacturers that impact the use of recycled materials • Identified accountability mechanisms • Identified collaborations in industry
Alignment of regulations across sectors and regions that impact the use of recycled materials • Regulations (general) • Regulations across sectors • Regulations across national borders

References

1. Winkeman, H.A.; Busenburg, E.B. Effect of Stearic Acid on Reclaimed Rubber. *Ind. Eng. Chem. Ind. Ed.* **1929**, *21*, 730–732. [CrossRef]
2. Markl, E.; Lackner, M. Devulcanization technologies for recycling of tire-derived rubber: A review. *Materials* **2020**, *13*, 1246. [CrossRef] [PubMed]
3. Wiśniewska, P.; Wang, S.; Formela, K. Waste tire rubber devulcanization technologies: State-of-the-art, limitations and future perspectives. *Waste Manag.* **2022**, *150*, 174–184. [CrossRef] [PubMed]
4. Roetman, E.; Joustra, J.; Heideman, G.; Balkenende, R. Does the Rubber Meet the Road? Assessing the Potential of Devulcanization Technologies for the Innovation of Tire Rubber Recycling. *Sustainability* **2024**, *16*, 2900. [CrossRef]
5. Ghosh, R. *Transforming Silica-Silane Reinforced Rubber into a High Quality Devulcanizate*; University of Twente: Enschede, The Netherlands, 2024. [CrossRef]
6. van Hoek, H. Closing the Loop. Reuse of Devulcanized Rubber in New Tires. Ph.D. Thesis, University of Twente, Enschede, The Netherlands, 2022.
7. Bandyopadhyay, S. Chapter 1 Fundamentals of rubber compounding. In *Rubber Products*; Bireswar, B., Ed.; De Gruyter: Berlin, Germany; Boston, MA, USA, 2024; pp. 1–52.
8. De, S.K.; White, J.R. *Rubber Technologist's Handbook*; iSmithers Rapra Publishing: Shawbury, UK, 2001; Volume 1.
9. Saiwari, S.; Dierkes, W. 7—Regeneration and devulcanization. In *Tire Waste and Recycling*; Letcher, T.M., Shulman, V.L., Amirkhanian, S., Eds.; Academic Press: Cambridge, MA, USA, 2021; pp. 97–144.
10. Shanbag, A.; Manjare, S. Life cycle assessment of tyre manufacturing process. *J. Sustain. Dev. Energy Water Environ. Syst.* **2020**, *8*, 22–34. [CrossRef]
11. Wiśniewska, P.; Haponiuk, J.T.; Colom, X.; Saeb, M.R. Green Approaches in Rubber Recycling Technologies: Present Status and Future Perspective. *ACS Sustain. Chem. Eng.* **2023**, *11*, 8706–8726. [CrossRef]

12. European Commission. *Study on the Critical Raw Materials for the EU 2023—Final Report*; Publications Office of the European Union: Luxembourg, 2023.
13. Ellen MacArtur Foundation. What Is a Circular Economy? Available online: https://www.ellenmacarthurfoundation.org/topics/circular-economy-introduction/overview (accessed on 10 March 2025).
14. Rodgers, B.; Waddell, W. Chapter 9—The Science of Rubber Compounding. In *The Science and Technology of Rubber*, 4th ed.; Mark, J.E., Erman, B., Roland, C.M., Eds.; Academic Press: Boston, MA, USA, 2013; pp. 417–471.
15. Sisanth, K.S.; Thomas, M.G.; Abraham, J.; Thomas, S. 1—General introduction to rubber compounding. In *Progress in Rubber Nanocomposites*; Thomas, S., Maria, H.J., Eds.; Woodhead Publishing: Cambridge, UK, 2017; pp. 1–39.
16. Lacroix, F.; Seghar, S. *In-Product-Sorting End-of-Life Tires for Effective Recycling by Devulcanization*; Academic Press: Cambridge, MA, USA, 2021.
17. Boon, Z.H.; Teo, Y.Y.; Ang, D.T.-C. Recent development of biodegradable synthetic rubbers and bio-based rubbers using sustainable materials from biological sources. *RSC Adv.* **2022**, *12*, 34028–34052. [CrossRef]
18. Samsuri, A. Degradation of Natural Rubber and Synthetic Elastomers. *Shreir's Corros.* **2010**, *3*, 2407–2438.
19. Malaysian Rubber Board. Consumption of Natural and Synthetic Rubber Worldwide from 1990 to H1 2024 (in Million Metric Tons) [Graph]. In Statista. 2024. Available online: https://www.statista.com/statistics/275399/world-consumption-of-natural-and-synthetic-caoutchouc/ (accessed on 18 November 2024).
20. ETRMA. The ETRMA Statistics Report. Available online: https://www.etrma.org/wp-content/uploads/2021/12/20211030-Statistics-booklet-2021VF.pdf (accessed on 1 May 2025).
21. ETRMA. *European Tyre & Rubber Industry Statistics Report*; ETRMA: Brussels, Belgium, 2011.
22. Jaeger, B.; Upadhyay, A. Understanding barriers to circular economy: Cases from the manufacturing industry. *J. Enterp. Inf. Manag.* **2020**, *33*, 729–745. [CrossRef]
23. Kirchherr, J.; Piscicelli, L.; Bour, R.; Kostense-Smit, E.; Muller, J.; Huibrechtse-Truijens, A.; Hekkert, M. Barriers to the Circular Economy: Evidence From the European Union (EU). *Ecol. Econ.* **2018**, *150*, 264–272. [CrossRef]
24. Campbell, S.; Greenwood, M.; Prior, S.; Shearer, T.; Walkem, K.; Young, S.; Bywaters, D.; Walker, K. Purposive sampling: Complex or simple? Research case examples. *J. Res. Nurs.* **2020**, *25*, 652–661. [CrossRef] [PubMed]
25. Chaminade, C.; Edquist, C. From theory to practice: The use of the systems of innovation approach in innovation policy. In *Innovation, Science, and Institutional Change: A Research Handbook*; Oxford University Press: Oxford, MS, USA, 2006; pp. 141–163. Available online: https://www.sciencedirect.com/book/9780128206850/tire-waste-and-recycling (accessed on 11 March 2025).
26. Knott, E.; Rao, A.H.; Summers, K.; Teeger, C. Interviews in the social sciences. *Nat. Rev. Methods Primers* **2022**, *2*, 73. [CrossRef]
27. Tyrepress. The World's Leading Tyre Makers of 2023. Available online: https://www.tyrepress.com/wp-content/uploads/2023/06/Leading-Companies-2023.pdf (accessed on 18 October 2024).
28. Grafström, J.; Aasma, S. Breaking circular economy barriers. *J. Clean. Prod.* **2021**, *292*, 126002. [CrossRef]
29. Paletta, A.; Leal Filho, W.; Balogun, A.-L.; Foschi, E.; Bonoli, A. Barriers and challenges to plastics valorisation in the context of a circular economy: Case studies from Italy. *J. Clean. Prod.* **2019**, *241*, 118149. [CrossRef]
30. de Jesus, A.; Mendonça, S. Lost in Transition? Drivers and Barriers in the Eco-innovation Road to the Circular Economy. *Ecol. Econ.* **2018**, *145*, 75–89. [CrossRef]
31. van der Vegt, M.; Velzing, E.-J.; Rietbergen, M.; Hunt, R. Understanding Business Requirements for Increasing the Uptake of Recycled Plastic: A Value Chain Perspective. *Recycling* **2022**, *7*, 42. [CrossRef]
32. Baldassarre, B.; Maury, T.; Mathieux, F.; Garbarino, E.; Antonopoulos, I.; Sala, S. Drivers and Barriers to the Circular Economy Transition: The Case of Recycled Plastics in the Automotive Sector in the European Union. *Procedia CIRP* **2022**, *105*, 37–42. [CrossRef]
33. Pinheiro, M.F.; Ferreira, L.M.D.F.; Azevedo, S.G.; Magalhães, V.S.M. Barriers to the Circular Economy in the Plastics Industry: A Systematic Literature Review. In Proceedings of the Flexible Automation and Intelligent Manufacturing: Establishing Bridges for More Sustainable Manufacturing Systems, Porto, Portugal, 18–22 June 2023; Springer: Cham, Switzerland, 2024; pp. 850–858.
34. Shen, L.; Worrell, E. Chapter 31—Plastic recycling. In *Handbook of Recycling*, 2nd ed.; Meskers, C., Worrell, E., Reuter, M.A., Eds.; Elsevier: Amsterdam, The Netherlands, 2024; pp. 497–510.
35. Bening, C.R.; Pruess, J.T.; Blum, N.U. Towards a circular plastics economy: Interacting barriers and contested solutions for flexible packaging recycling. *J. Clean. Prod.* **2021**, *302*, 126966. [CrossRef]
36. Alassali, A.; Picuno, C.; Chong, Z.K.; Guo, J.; Maletz, R.; Kuchta, K. Towards Higher Quality of Recycled Plastics: Limitations from the Material's Perspective. *Sustainability* **2021**, *13*, 13266. [CrossRef]
37. Milios, L.; Holm Christensen, L.; McKinnon, D.; Christensen, C.; Rasch, M.K.; Hallstrøm Eriksen, M. Plastic recycling in the Nordics: A value chain market analysis. *Waste Manag.* **2018**, *76*, 180–189. [CrossRef]
38. McKinnon, D.; Bakas, I.; Herczeg, M.; Vea, E.B.; Busch, N.; Christensen, L.H.; Christensen, C.; Damgaard, C.K.; Milios, L.; Punkkinen, H. *Plastic Waste Markets: Overcoming Barriers to Better Resource Utilisation*; Nordic Council of Ministers: Copenhagen, Denmark, 2018.

39. Agarwal, S.; Tyagi, M.; Garg, R.K. Conception of circular economy obstacles in context of supply chain: A case of rubber industry. *Int. J. Product. Perform. Manag.* **2023**, *72*, 1111–1153. [CrossRef]
40. Schultz, F.C.; Valentinov, V.; Kirchherr, J.; Reinhardt, R.J.; Pies, I. Stakeholder governance to facilitate collaboration for a systemic circular economy transition: A qualitative study in the European chemicals and plastics industry. *Bus. Strategy Environ.* **2024**, *33*, 2173–2192. [CrossRef]
41. Saldana, J. *The Coding Manual for Qualitative Researchers*; SAGE Publications: Thousand Oaks, CA, USA, 2015.
42. Cardona-Uribe, N.; Betancur, M.; Martínez, J.D. Towards the chemical upgrading of the recovered carbon black derived from pyrolysis of end-of-life tires. *Sustain. Mater. Technol.* **2021**, *28*, e00287. [CrossRef]
43. Bowles, A.J.; Fowler, G.D. Assessing the impacts of feedstock and process control on pyrolysis outputs for tyre recycling. *Resour. Conserv. Recycl.* **2022**, *182*, 106277. [CrossRef]
44. Costa, S.M.R.; Fowler, D.; Carreira, G.A.; Portugal, I.; Silva, C.M. Production and Upgrading of Recovered Carbon Black from the Pyrolysis of End-of-Life Tires. *Materials* **2022**, *15*, 2030. [CrossRef]
45. Simon, P.; Plessis, S.; Ghanimi, A. Evaluating the Path to a Sustainable Tire Industry: Unlocking the Potential of Recovered Carbon Black. 2024. Available online: https://www.emerton.co/news/evaluating-the-path-to-a-sustainable-tire-industry-unlocking-the-potential-of-recovered-carbon-black (accessed on 24 November 2024).
46. Schyns, Z.O.G.; Shaver, M.P. Mechanical Recycling of Packaging Plastics: A Review. *Macromol. Rapid Commun.* **2021**, *42*, 2000415. [CrossRef]
47. Plastics Europe. Annual Production of Plastics Worldwide from 1950 to 2022 (in Million Metric Tons) [Graph] in Statista. Available online: https://www.statista.com/statistics/282732/global-production-of-plastics-since-1950/ (accessed on 18 November 2024).
48. Dwivedi, C.; Manjare, S.; Rajan, S.K. Recycling of waste tire by pyrolysis to recover carbon black: Alternative & environment-friendly reinforcing filler for natural rubber compounds. *Compos. Part B Eng.* **2020**, *200*, 108346. [CrossRef]
49. Semperit. *Sustainability Report 2023*; Semperit: Vienna, Austria, 2024.
50. Demets, R.; Van Kets, K.; Huysveld, S.; Dewulf, J.; De Meester, S.; Ragaert, K. Addressing the complex challenge of understanding and quantifying substitutability for recycled plastics. *Resour. Conserv. Recycl.* **2021**, *174*, 105826. [CrossRef]
51. Auer, M.; Schmidt, J.; Diemert, J.; Gerhardt, G.; Renz, M.; Galler, V.; Woidasky, J. Quality Aspects in the Compounding of Plastic Recyclate. *Recycling* **2023**, *8*, 18. [CrossRef]
52. Jager, R.; Vlugter, J.; Gort, I. *Gevolgen National Norm Circulaire Plastics. Verkenning naar de gevolgen van de Verplichting Voor een Minimumaandeel Recyclaat en/of Biogebaseerd Kunststof en Rubber Voor Nederlandse Converters*; Research was Commissioned by Rijksdienst voor Ondernemend Nederland; Rijksoverheid: The Hague, The Nederlands, 2023.
53. Kratina, O.; Stoček, R.; Voldánová, J. How the rubber compounds of different tire's components heat up? In *Constitutive Models for Rubber XII*; CRC Press: Boca Raton, FL, USA, 2022; pp. 199–204.
54. Wiesinger, H.; Wang, Z.; Hellweg, S. Deep Dive into Plastic Monomers, Additives, and Processing Aids. *Environ. Sci. Technol.* **2021**, *55*, 9339–9351. [CrossRef]
55. Anjum, A. Recovered Carbon Black from Waste Tire Pyrolysis: Characteristics, Performance, and Valorisation. University of Twente: Enschede, The Netherlands, 2021.
56. Gall, M.; Freudenthaler, P.J.; Fischer, J.; Lang, R.W. Characterization of Composition and Structure–Property Relationships of Commercial Post-Consumer Polyethylene and Polypropylene Recyclates. *Polymers* **2021**, *13*, 1574. [CrossRef] [PubMed]
57. Hahladakis, J.N.; Velis, C.A.; Weber, R.; Iacovidou, E.; Purnell, P. An overview of chemical additives present in plastics: Migration, release, fate and environmental impact during their use, disposal and recycling. *J. Hazard. Mater.* **2018**, *344*, 179–199. [CrossRef] [PubMed]
58. Norris, C.J.; Cerdán, A.L.; ter Haar, P. Understanding Recovered Carbon Black. *Rubber Chem. Technol.* **2023**, *96*, 196–213. [CrossRef]
59. Schlossnikl, J.; Pinter, E.; Jones, M.P.; Koch, T.; Archodoulaki, V.-M. Unexpected obstacles in mechanical recycling of polypropylene labels: Are ambitious recycling targets achievable? *Resour. Conserv. Recycl.* **2024**, *200*, 107299. [CrossRef]
60. Chea, J.D.; Yenkie, K.M.; Stanzione, J.F.; Ruiz-Mercado, G.J. A generic scenario analysis of end-of-life plastic management: Chemical additives. *J. Hazard. Mater.* **2023**, *441*, 129902. [CrossRef]
61. Ghosh, A. Performance modifying techniques for recycled thermoplastics. *Resour. Conserv. Recycl.* **2021**, *175*, 105887. [CrossRef]
62. Dorigato, A. Recycling of polymer blends. *Adv. Ind. Eng. Polym. Res.* **2021**, *4*, 53–69. [CrossRef]
63. Orzan, E.; Janewithayapun, R.; Gutkin, R.; Lo Re, G.; Kallio, K. Thermo-mechanical variability of post-industrial and post-consumer recyclate PC-ABS. *Polym. Test.* **2021**, *99*, 107216. [CrossRef]
64. Moulin, L.; Da Silva, S.; Bounaceur, A.; Herblot, M.; Soudais, Y. Assessment of recovered carbon black obtained by waste tires steam water thermolysis: An industrial application. *Waste Biomass Valorization* **2017**, *8*, 2757–2770. [CrossRef]
65. Kong, D.; Wang, S.; Shan, R.; Gu, J.; Yuan, H.; Chen, Y. Characteristics and chemical treatment of carbon black from waste tires pyrolysis. *J. Anal. Appl. Pyrolysis* **2024**, *178*, 106419. [CrossRef]
66. Cabot Corporation. *Industry User Guide: Reclaimed Carbon Blending Process*; Cabot Corporation: Boston, MA, USA, 2024.

67. Lubongo, C.; Bin Daej, M.A.A.; Alexandridis, P. Recent Developments in Technology for Sorting Plastic for Recycling: The Emergence of Artificial Intelligence and the Rise of the Robots. *Recycling* **2024**, *9*, 59. [CrossRef]
68. Yang, J.; Xu, Y.-P.; Chen, P.; Li, J.-Y.; Liu, D.; Chu, X.-L. Combining spectroscopy and machine learning for rapid identification of plastic waste: Recent developments and future prospects. *J. Clean. Prod.* **2023**, *431*, 139771. [CrossRef]
69. Neo, E.R.K.; Yeo, Z.; Low, J.S.C.; Goodship, V.; Debattista, K. A review on chemometric techniques with infrared, Raman and laser-induced breakdown spectroscopy for sorting plastic waste in the recycling industry. *Resour. Conserv. Recycl.* **2022**, *180*, 106217. [CrossRef]
70. Nyuk Khui, P.L.; Rahman, M.R.; Matin, M.M.; Bin Bakri, M.K. 7—Recycled rubber waste plastic and its composites. In *Recycled Plastic Biocomposites*; Rahman, M.R., Bin Bakri, M.K., Eds.; Woodhead Publishing: Cambridge, UK, 2022; pp. 147–163.
71. Okoye, C.O.; Jones, I.; Zhu, M.; Zhang, Z.; Zhang, D. Manufacturing of carbon black from spent tyre pyrolysis oil—A literature review. *J. Clean. Prod.* **2021**, *279*, 123336. [CrossRef]
72. Martınez, J.D.; Gisele Jung, C.; Bouysset, J.P. Recovered carbon black: Potential markets. *Tire Waste Recycl.* **2021**, 165–224. [CrossRef]
73. Faraca, G.; Martinez-Sanchez, V.; Astrup, T.F. Environmental life cycle cost assessment: Recycling of hard plastic waste collected at Danish recycling centres. *Resour. Conserv. Recycl.* **2019**, *143*, 299–309. [CrossRef]
74. Bridgestone, Michelin. Whitepaper Recovered Carbon Black Guidelines. 2023. Available online: https://cxf-prod.azureedge.net/b2b-experience-production/attachments/clp2vx72q0l6y01odzd738y3d-rcb-white-paper.pdf (accessed on 19 November 2024).
75. Kahlert, S.; Bening, C.R. Why pledges alone will not get plastics recycled: Comparing recyclate production and anticipated demand. *Resour. Conserv. Recycl.* **2022**, *181*, 106279. [CrossRef]
76. Calzolari, T.; Genovese, A.; Brint, A. The adoption of circular economy practices in supply chains—An assessment of European Multi-National Enterprises. *J. Clean. Prod.* **2021**, *312*, 127616. [CrossRef]
77. Donnet, J.-B. *Carbon Black: Science and Technology*; Routledge: London, UK, 2018.
78. Kumar, A.; Pinto, P.; Hawaldar, I.T.; Spulbar, C.M.; Birau, F.R. Crude oil futures to manage the price risk of natural rubber: Empirical evidence from India. *Agric. Econ.* **2021**, *67*, 423–434.
79. Taylor, B. BIR Autumn 2024: A Year of Setbacks. Profits Have Been Hard to Come by for Plastics Recyclers and Reprocessors in 2024, with Europe's Dismal Landscape a Particular Disappointment. Available online: https://www.recyclingtoday.com/news/plastic-bir-recycling-meeting-challenges-pricing-mandates-unep-singapore-2024/ (accessed on 19 November 2024).
80. European Union. *Regulation (EU) 2023/1805 of the European Parliament and of the Council of 13 September 2023 on the Use of Renewable and Low-Carbon Fuels in Maritime Transport, and Amending Directive 2009/16/EC*; European Union: Brussels, Belgium, 2023.
81. Chapman, A.; Sen, K.K.; Mochida, T.; Yoshimoto, Y.; Kishimoto, K. Overcoming barriers to proactive plastic recycling toward a sustainable future. *Environ. Chall.* **2024**, *17*, 101040. [CrossRef]
82. European Plastics Converters. Sustainability/Circular Economy. Available online: https://www.plasticsconverters.eu/ (accessed on 19 November 2024).
83. Plastics Europe. Sustainability. Available online: https://plasticseurope.org/sustainability/ (accessed on 19 November 2024).
84. Tan, J.; Tan, F.J.; Ramakrishna, S. Transitioning to a circular economy: A systematic review of its drivers and barriers. *Sustainability* **2022**, *14*, 1757. [CrossRef]
85. Alliance to End All Plastic Waste. Advancing a Circular Economy for Plastic. Available online: https://www.endplasticwaste.org/ (accessed on 5 March 2025).
86. Fan, Y.; Fowler, G.D.; Zhao, M. The past, present and future of carbon black as a rubber reinforcing filler—A review. *J. Clean. Prod.* **2020**, *247*, 119115. [CrossRef]
87. Cecon, V.S.; Da Silva, P.F.; Curtzwiler, G.W.; Vorst, K.L. The challenges in recycling post-consumer polyolefins for food contact applications: A review. *Resour. Conserv. Recycl.* **2021**, *167*, 105422. [CrossRef]
88. Vilaplana, F.; Karlsson, S. Quality Concepts for the Improved Use of Recycled Polymeric Materials: A Review. *Macromol. Mater. Eng.* **2008**, *293*, 274–297. [CrossRef]
89. Pfaendner, R. Restabilization—30 years of research for quality improvement of recycled plastics review. *Polym. Degrad. Stab.* **2022**, *203*, 110082. [CrossRef]
90. Marcinowski, M. Committee D36 on Recovered Carbon Black (rCB). Available online: https://www.astm.org/membership-participation/technical-committees/committee-d36 (accessed on 18 November 2024).
91. ASTM. *Resolve 2023 Annual Report*; ASTM: West Conshohocken, PA, USA, 2024.
92. De Tandt, E.; Demuytere, C.; Van Asbroeck, E.; Moerman, H.; Mys, N.; Vyncke, G.; Delva, L.; Vermeulen, A.; Ragaert, P.; De Meester, S.; et al. A recycler's perspective on the implications of REACH and food contact material (FCM) regulations for the mechanical recycling of FCM plastics. *Waste Manag.* **2021**, *119*, 315–329. [CrossRef]
93. Waszczyłko-Miłkowska, B.; Bernat, K.; Szczepański, K. Assessment of the Quantities of Non-Targeted Materials (Impurities) in Recycled Plastic Packaging Waste to Comply with EU Regulations and Sustainable Waste Management. *Sustainability* **2024**, *16*, 6226. [CrossRef]

94. European Union. *Commission Notice. Guidance Document for Regulation (EU) 2023/1115 on Deforestation-Free Products (C/2024/6789)*; European Union: Brussels, Belgium, 2023.
95. Manžuch, Z.; Akelytė, R.; Camboni, M.; Carlander, D. Chemical Recycling of Polymeric Materials from Waste in the Circular Economy. 2021. Available online: https://www.actu-environnement.com/media/pdf/news-38548-rapport-echa-recyclage-chimique.pdf (accessed on 18 November 2024).
96. de Römph, T.J.; Van Calster, G. REACH in a circular economy: The obstacles for plastics recyclers and regulators. *Rev. Eur. Comp. Int. Environ. Law* **2018**, *27*, 267–277. [CrossRef]
97. European Union. *Regulation (EU) 2024/1157 of the European Parliament and of the Council of 11 April 2024 on Shipments of Waste, Amending Regulations (EU) No 1257/2013 and (EU) 2020/1056 and Repealing Regulation (EC) No 1013/2006*; European Union: Brussels, Belgium, 2024.
98. European Commission. Guidance on the Interpretation of Key Provisions of Directive 2008/98/EC on Waste. Available online: https://ec.europa.eu/environment/pdf/waste/framework/guidance_doc.pdf (accessed on 18 November 2024).
99. Kara, S.; Hauschild, M.; Sutherland, J.; McAloone, T. Closed-loop systems to circular economy: A pathway to environmental sustainability? *CIRP Ann.* **2022**, *71*, 505–528. [CrossRef]
100. Bakker, C.; Balkenende, R.; Poppelaars, F. Design for product integrity in a circular economy. In *Designing for the Circular Economy*; Routledge: London, UK, 2018; pp. 148–156.
101. PureCycle. Multiple Compounds Successfully Created Using PureCycle Resin. Available online: https://www.purecycle.com/blog/multiple-compounds-successfully-created-using-purecycle-resin?utm_source=chatgpt.com (accessed on 14 February 2025).
102. Uekert, T.; Singh, A.; DesVeaux, J.S.; Ghosh, T.; Bhatt, A.; Yadav, G.; Afzal, S.; Walzberg, J.; Knauer, K.M.; Nicholson, S.R.; et al. Technical, Economic, and Environmental Comparison of Closed-Loop Recycling Technologies for Common Plastics. *ACS Sustain. Chem. Eng.* **2023**, *11*, 965–978. [CrossRef]
103. European Commission. *A New Circular Economy Action Plan for a Cleaner and More Competitive Europe*; European Commission: Brussels, Belgium, 2020.
104. Maitre-Ekern, E. Re-thinking producer responsibility for a sustainable circular economy from extended producer responsibility to pre-market producer responsibility. *J. Clean. Prod.* **2021**, *286*, 125454. [CrossRef]
105. Tumu, K.; Vorst, K.; Curtzwiler, G. Global plastic waste recycling and extended producer responsibility laws. *J. Environ. Manag.* **2023**, *348*, 119242. [CrossRef] [PubMed]
106. Winternitz, K.; Heggie, M.; Baird, J. Extended producer responsibility for waste tyres in the EU: Lessons learnt from three case studies—Belgium, Italy and the Netherlands. *Waste Manag.* **2019**, *89*, 386–396. [CrossRef] [PubMed]
107. Campbell-Johnston, K.; Calisto Friant, M.; Thapa, K.; Lakerveld, D.; Vermeulen, W.J.V. How circular is your tyre: Experiences with extended producer responsibility from a circular economy perspective. *J. Clean. Prod.* **2020**, *270*, 122042. [CrossRef]
108. Joseph, A.M.; George, B.; Madhusoodanan, K.; Alex, R. The current status of sulphur vulcanization and devulcanization chemistry: Devulcanization. *Rubber Sci.* **2016**, *29*, 62–100.
109. Bockstal, L.; Berchem, T.; Schmetz, Q.; Richel, A. Devulcanisation and reclaiming of tires and rubber by physical and chemical processes: A review. *J. Clean. Prod.* **2019**, *236*, 117574. [CrossRef]
110. Saputra, R.; Walvekar, R.; Khalid, M.; Mubarak, N.M.; Sillanpää, M. Current progress in waste tire rubber devulcanization. *Chemosphere* **2021**, *265*, 129033. [CrossRef]
111. Zhang, L.; Wang, H.; Zhang, C.; Wang, S. Laboratory testing and field application of devulcanized rubber/SBS composite modified asphalt. *Case Stud. Constr. Mater.* **2023**, *19*, e02285. [CrossRef]
112. Akhtar, A.Y.; Tsang, H.-H. Dynamic leaching assessment of recycled polyurethane-coated tire rubber for sustainable engineering applications. *Chem. Eng. J.* **2024**, *495*, 153351. [CrossRef]
113. Lapkovskis, V.; Mironovs, V.; Kasperovich, A.; Myadelets, V.; Goljandin, D. Crumb Rubber as a Secondary Raw Material from Waste Rubber: A Short Review of End-Of-Life Mechanical Processing Methods. *Recycling* **2020**, *5*, 32. [CrossRef]
114. Lazorenko, G.; Kasprzhitskii, A.; Mischinenko, V. Rubberized geopolymer composites: Effect of filler surface treatment. *J. Environ. Chem. Eng.* **2021**, *9*, 105601. [CrossRef]
115. Faussone, G.C.; Cecchi, T. Chemical Recycling of Plastic Marine Litter: First Analytical Characterization of The Pyrolysis Oil and of Its Fractions and Comparison with a Commercial Marine Gasoil. *Sustainability* **2022**, *14*, 1235. [CrossRef]
116. Zaino, M.M.; Mustaffa, N.; Hassan, A.H.; Mustapa, A.N.; Mamat, M.H.; Syed-Hassan, S.S.A.; Rahman, S.N.F.S.A.; Azli, A.A.M.; Hamdan, K. A Mini Review on Carbon Black Production as Rubber Reinforcement in Tyre Application. *Chem. Eng. Trans.* **2024**, *113*, 235–240.
117. Czajczyńska, D.; Krzyżyńska, R.; Jouhara, H.; Spencer, N. Use of pyrolytic gas from waste tire as a fuel: A review. *Energy* **2017**, *134*, 1121–1131. [CrossRef]
118. Gaidhane, J.; Ullah, I.; Khalatkar, A. Tyre remanufacturing: A brief review. *Mater. Today Proc.* **2022**, *60*, 2257–2261. [CrossRef]
119. Dabić-Ostojić, S.; Miljuš, M.; Bojović, N.; Glišović, N.; Milenković, M. Applying a mathematical approach to improve the tire retreading process. *Resour. Conserv. Recycl.* **2014**, *86*, 107–117. [CrossRef]

120. Myhre, M.; MacKillop, D.A. Rubber recycling. *Rubber Chem. Technol.* **2002**, *75*, 429–474. [CrossRef]
121. Vasiliu, L.; Gencel, O.; Damian, I.; Harja, M. Capitalization of tires waste as derived fuel for sustainable cement production. *Sustain. Energy Technol. Assess.* **2023**, *56*, 103104. [CrossRef]
122. Ferdous, W.; Manalo, A.; Siddique, R.; Mendis, P.; Zhuge, Y.; Wong, H.S.; Lokuge, W.; Aravinthan, T.; Schubel, P. Recycling of landfill wastes (tyres, plastics and glass) in construction—A review on global waste generation, performance, application and future opportunities. *Resour. Conserv. Recycl.* **2021**, *173*, 105745. [CrossRef]
123. Dabrowska, D.; Rykala, W.; Nourani, V. Causes, types and consequences of municipal waste landfill fires—Literature review. *Sustainability* **2023**, *15*, 5713. [CrossRef]

polymers

MDPI

Article

A Study on the Aging Mechanism and Anti-Aging Properties of Nitrile Butadiene Rubber: Experimental Characterization and Molecular Simulation

Min Zhu [1], Hanyuan Huang [1], Haiyan Li [1,*], Gui Huang [1,*], Jingjing Lan [1], Jing Fu [1], Juqin Fan [1], Yujun Liu [1], Zhiwu Ke [2], Xiaojie Guo [2], Hongkuan Zhou [2] and Yan Li [1]

[1] Naval University of Engineering, Wuhan 430033, China; min0zhu@163.com (M.Z.); h20209999@163.com (H.H.); tangerine1@163.com (J.L.); fujing_2005@sina.com (J.F.); 15172515814@163.com (J.F.); lyj2424@163.com (Y.L.); yacareft@163.com (Y.L.)

[2] China State Shipbuilding Corporation, Limited (CSSC) 719th Research Institute, Wuhan 430205, China; keylab_rndl@163.com (Z.K.); lucky_gxj_0372@163.com (X.G.); hongkuanzhou@hust.edu.cn (H.Z.)

* Correspondence: haiyanli1818@163.com (H.L.); julianxiaoban@163.com (G.H.)

Abstract

To tackle the degradation of sealing performance in nitrile butadiene rubber (NBR) seals due to material aging during long-term service, this study integrates experimental and molecular simulation methods to elucidate the aging mechanism. Experimental results reveal that the contents of C=C and C=O functional groups significantly decrease during aging, accompanied by enhanced hydrophobicity and increased crosslink density of NBR, indicating that crosslinking reactions dominate the aging process with the participation of C=C and C=O groups. Quantum mechanics (QM) and molecular dynamics (MD) simulations further demonstrate that α-H, C=C, and C≡N groups are preferentially oxidized due to their low bond energies. The oxidation of NBR generates unstable epoxy intermediates, which undergo chain scission to form ketones, aldehydes, and ultimately crosslinked structures. Using a multi-dimensional evaluation system based on bond dissociation energy (BDE), solubility parameter (Δδ), and migration coefficient (MSD), four antioxidants (4010NA, 4010, MC, and BHT) were screened. BHT emerges as the optimal choice, exhibiting superior free radical scavenging ability (BDE = 346.3 kJ/mol), good matrix compatibility (Δδ = 2.95), and anti-migration properties. The MD-based screening method established herein provides a theoretical basis for designing antioxidant systems in high-performance rubber materials, facilitating the development of advanced rubber products.

Keywords: rubber seal; aging; molecular model

1. Introduction

Nitrile butadiene rubber is widely used as a sealing ring in mechanical equipment due to its excellent wear resistance, airtightness, and waterproof performance. During long-term operation under humid, high-temperature, and compressive conditions, seals experience stress relaxation and compression set, leading to reduced contact stress with clamping rings and gradual loss of sealing efficiency. Therefore, investigating the aging mechanism of NBR seals is critical for ensuring equipment safety.

Analyzing failure mechanisms serves as the foundation for describing and confirming material degradation. Current research has established a multi-scale characterization sys-

tem to dissect this process: aging-induced mechanical property degradation is accelerated under humid–heat conditions, with compression set rates significantly higher than those in dry environments [1]. NBR aging damage is severe and non-uniform, with the most pronounced degradation occurring at edge regions. Crosslinking dominates the aging process [2,3], during which tensile strength initially increases with crosslink density but declines after reaching a peak [3]. FTIR and X-ray photoelectron spectroscopy (XPS) reveal the hydrolysis of nitrile groups during aging, accompanied by the formation of hydroxyl and carbonyl groups [4–6]. FTIR results also indicate plasticizer migration to the rubber surface during thermo-oxidative aging, with a competitive interplay between plasticizer volatilization and medium diffusion in oil environments—an effect more pronounced than in hot air [7].

While experimental studies have significantly advanced aging mechanism exploration, challenges remain: aging tests are time-consuming, and complex degradation pathways are difficult to characterize [8]. With breakthroughs in computational chemistry, multi-scale simulation techniques have emerged as a new paradigm for unraveling rubber aging mechanisms. At the microscale, quantum mechanics (QM) simulations are widely used to quantitatively analyze reaction energetics, such as transition state barriers and reaction free energies, and to derive thermodynamic parameters for hydrogen bonding interactions [9,10].

To enhance the antioxidant capacity of rubber composites, antioxidants are typically incorporated. Selection criteria involve analyzing their interactions with rubber matrices, with priority given to matrix compatibility—a parameter directly impacting composite mechanical properties—and key factors such as radical scavenging activity and migration resistance [11]. Traditional antioxidant screening for rubber composites requires extensive experimental work, whereas molecular dynamics (MD) simulations enable rapid prescreening by calculating solubility parameters (δ) to assess additive-matrix compatibility [12] and evaluating migration resistance through metrics like Mean square displacement (MSD) and free volume fraction [13].

In this study, we comprehensively evaluated the antioxidant capabilities and compatibility with nitrile–butadiene rubber (NBR) of four commercially available antioxidants, amine-type antioxidants 4010NA (N-isopropyl-N′-phenyl-p-phenylenediamine) and 4010 (N-cyclohexyl-N′-phenyl-p-phenylenediamine), phenolic antioxidant BHT (2,6-di-tert-butyl-p-cresol), and reactive antioxidant MC (N-(4-anilinophenyl)maleimide), whose molecular structures are presented in Figure 1. The amine-type antioxidants demonstrated strong free-radical scavenging abilities, making them particularly suitable for high-temperature environments; however, their discoloration and contamination tendencies limit their application mainly to dark-colored or black rubber and plastic products [14]. In contrast, the phenolic antioxidant BHT relied on its phenolic hydroxyl group to provide effective antioxidant protection at medium and low temperatures but suffered from limitations such as relatively low polarity matching degree, limited compatibility, and insufficient high-temperature stability [15]. Notably, the reactive antioxidant MC exhibited a unique dual functionality by covalently bonding to the rubber matrix or filler surface through chemical grafting of its double bond and aniline group, thereby achieving both “permanent” antioxidant properties and improved filler–rubber compatibility, which significantly inhibited antioxidant migration and enhanced interfacial bonding strength [16]. These works collectively provide valuable insights and guidance for the development of high-performance nitrile–butadiene rubber formulations.

In this study, we simulated the service environment of NBR and conducted thermo-mechanical accelerated aging tests to investigate surface property and crosslink density changes using FTIR, crosslink density analysis, and contact angle measurements. MD

simulations were employed to analyze bond energies in NBR's typical chemical structures, identify degradation-prone sites during aging, and elucidate the underlying aging mechanisms. Four antioxidants—4010NA, 4010, MC, and BHT—were systematically evaluated for their compatibility, antioxidant efficiency, and migration resistance in NBR matrices. This work provides theoretical guidance for developing polymer composites with optimized anti-aging and mechanical properties through multi-scale analysis of antioxidant-NBR interactions.

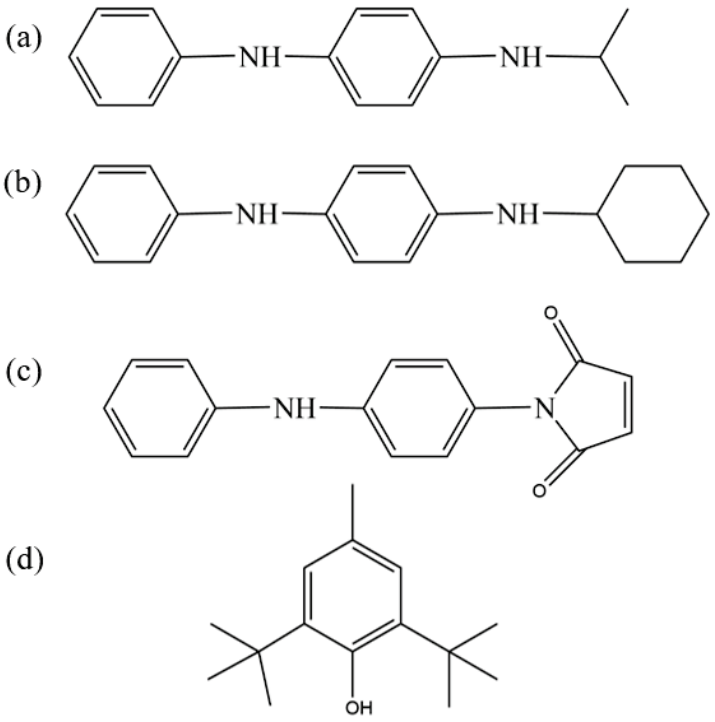

Figure 1. Chemical structures of antioxidants: (**a**) 4010NA; (**b**) 4010; (**c**) MC; and (**d**) BHT.

2. Methods

2.1. Aging of the Sample

The NBR used in this study was provided by Qingdao Yike Rubber & Plastics Co., Ltd. in Qingdao, China (specific formulation details were withheld by the company for commercial confidentiality). Test specimens were prepared according to GB/T 1683 standards [17] by cutting the NBR into small cylinders with dimensions of φ 10 mm × 10 mm (±0.2 mm height). Accelerated aging tests were conducted under a 30% compression ratio to simulate the actual service conditions of NBR seals. The aging procedure was conducted in a blast drying oven (HW-490 high-temperature aging chamber, manufactured by Aerospace Reliance Corporation in Tianjing, China). The aging temperature was set at 80 °C, which, based on our prior experimental results, exhibits a failure mechanism consistent with that at ambient temperature while enabling a moderate aging rate [18]. Specimens were extracted for characterization after aging at 80 °C under a 30% compression ratio for durations of 19 h, 76 h, 152 h, and 228 h, respectively.

2.2. Performance Test

Attenuated Total Reflection–Fourier Transform Infrared Spectroscopy (ATR-FTIR): Surface functional group changes during NBR aging were monitored via ATR-FTIR. A Nicolet 80 spectrometer (Thermo Fisher Scientific, Waltham, MA, USA) was used with a wavenumber range of 4000–500 cm^{-1}, a resolution of 4 cm^{-1}, and 32 co-added scans to reduce noise.

The sessile drop method using an SL200 contact angle analyzer (KINO, New York, NY, USA) was executed under controlled conditions maintained by HVAC systems: droplet volume = 2.0 ± 0.1 μL (0.5 mm needle), T = 25 ± 0.5 °C, and RH = 50–60%. Three independent measurements were taken at distinct regions (edge, center, and transition zone) per sample, with outliers excluded prior to mean calculation.

Crosslink Density Test: Crosslink density evolution during aging was measured using a modified equilibrium swelling method. Sulfured rubber samples (0.12–0.13 g, m_0) were swollen in a solution of 20 mL toluene and 5 mL ammonia (28 wt%) for 48 h at room temperature. Here, the role of ammonia water is to break the hydrogen bond interaction between the macromolecular chains and the fillers, ensuring that the obtained crosslinking density is derived more from the chemical crosslinking of the molecular chains. Swollen samples were dried to constant mass (m_2) in a vacuum oven at 70 °C. Crosslink density was calculated using the Flory–Rehner equation [19,20]. Three replicates per condition were averaged.

$$v_e = -\frac{\ln(1 - v_f) + v_f + \chi v_f^2}{V_S(v_f^{1/3} - v_f/2)} \quad (1)$$

where V_S represents the molar volume of toluene (106.5 mL/mol), χ denotes the Flory–Huggins interaction parameter between the polymer and toluene (0.435) [16], and v_f is the volume fraction of the polymer at equilibrium swelling, which is calculated using Equation (2):

$$v_f = \frac{m_2/\rho_p}{m_2/\rho_p + (m_1 - m_2)/\rho_s} \quad (2)$$

where ρ_p is the density of the NBR (1.02 g/cm^3) and ρ_s is the density of toluene (0.86 g/cm^3).

2.3. Molecular Dynamics Simulation

Bond Dissociation Energy (BDE) Calculation: The Materials Studio (MS) 2020 software (20.1 X64) was used to construct NBR models, and bond dissociation energies of NBR's typical chemical structures were calculated using the Dmol^3 module. The BDE calculation formula is as follows:

$$\Delta G = E(A\bullet) + E(B\bullet) - E(AB) \quad (3)$$

where $E(A)$, $E(B)$, and $E(AB)$ denote the energies of cleavage products A, B, and the reactant molecule AB, respectively.

MD simulations were performed using MS to construct unit cells for pure NBR, 4010NA, 4010, MC, and BHT. Solubility parameters of these systems were analyzed, followed by the creation of NBR/4010NA, NBR/4010, NBR/MC, and NBR/BHT composite cells to evaluate the MSD of antioxidants (denoted as AO) in NBR matrices. Each NBR molecular chain contained 100 repeating units with an acrylonitrile-to-butadiene ratio of 1:4. The pure NBR unit cell consisted of 4 NBR chains, while AO cells contained 30 antioxidant molecules. Composite NBR/AO cells included 4 NBR chains and 10 AO molecules.

The QM simulations in this study were implemented using the DMol^3 module of Materials Studio 2020. The specific settings are as follows: The electronic structure calculation is based on the Perdew–Burke–Ernzerhof (PBE) functional of generalized gradient approximation (GGA), combined with the dual-numerical polarization basis set (DNP+) to describe the system wave function. The characteristic of this basis set is that it contains the polarization p functions of all hydrogen atoms and has high accuracy. The Semi-core Pseudopotentials method was selected for external processing. The spin multiplicity is set according to the electronic characteristics of the system: For a system containing single-electron free radicals, the spin multiplicity = the number of lone pairs of electrons +1. To improve the convergence of SCF, the Fermi–Amaldi hybrid algorithm (with an initial

hybrid coefficient of 0.2) was adopted, and the Fermi level smoothing parameter (smearing width = 0.005 eV) was set. The convergence criteria for geometric optimization were set as energy change <1 × 10^{-5} Hartree and maximum atomic displacement <0.001 A, and the structure was optimized through the BFGS algorithm. The frequency analysis was carried out using the Vibrational Analysis command in the Tools tool to ensure that only one virtual frequency occurs in the transition state structure and the vibration mode is correct.

For MD simulations, the COMPASSII all-atom force field [21], validated for polymer systems, was employed with 50 annealing cycles (200 K → 500 K) to eliminate initial conformation bias. The equilibration protocol consisted of two phases: 200 ps pre-equilibration under the NVT ensemble (298 K, Nosé-Hoover thermostat, 1 ps relaxation time), followed by 500 ps equilibration under the NPT ensemble (298 K, 0.1 MPa, Berendsen barostat, compressibility 4.5 × 10^{-5} bar^{-1}) to achieve energy convergence (fluctuation < 0.5 kcal/mol/atom). The final 480 ps trajectory from the production phase was used to calculate solubility parameters via the Hildebrand equation and to analyze molecular mobility through mean squared displacement (MSD) [9,13,16,22,23].

3. Results and Discussion

3.1. FTIR Analysis

FTIR is a powerful analytical tool that can be used to evaluate the changes in the chemical structure of NBR during the aging process. By comparing the FTIR spectra at different aging stages, characteristic changes related to oxidative aging can be identified. Figure 2 shows the Fourier–transform infrared spectra of NBR before and after thermo-oxidative aging. In Figure 2, the peak at 3365 cm^{-1} corresponds to O-H stretching vibration, while those at 2916 cm^{-1}, 2850 cm^{-1}, and 1418 cm^{-1} are caused by the asymmetric stretching vibrations, symmetric stretching, and bending vibration of C–H in -CH_2 [24,25]. The peaks at 1731 cm^{-1}, 1540 cm^{-1}, and 1162 cm^{-1} arise from C=O stretching and C-O-C stretching vibrations [24,26], and those at 958 cm^{-1} and 903 cm^{-1} are assigned to the vibrations of C-H adjacent to unsaturated bonds in trans-1,4-polybutadiene and vinyl-1,2-polybutadiene units [26–28].

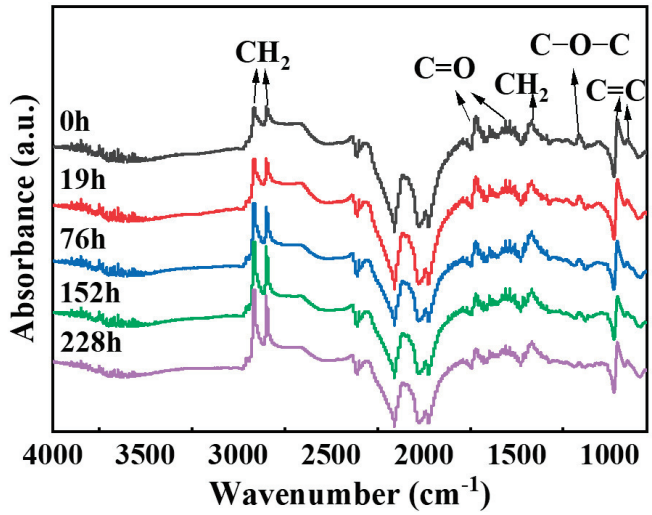

Figure 2. Infrared spectrum changes of nitrile butadiene rubber during aging.

Analysis of the intensity changes of each functional group was conducted by examining the peak areas of their respective vibration bands: -CH_2 (2945–2805 cm^{-1}), -C=O (1745–1675 cm^{-1}), C=C (976–847 cm^{-1}), and C-O-C (1190–1130 cm^{-1}). The peak areas are listed in Table 1. There are a large number of methylene groups (-CH_2) in NBR. Theoret-

ically, the change of methylene groups during the aging process is relatively small [29]. However, due to the crosslinking and degradation of NBR caused by aging, which leads to changes in the surface chemical environment, the relative intensity of the -CH_2 absorption peak is enhanced. In this paper, taking the intensity of the -CH_2 absorption peak as a standard, the changes in the intensities of each absorption peak relative to that of the -CH_2 absorption peak are shown in Table 2. The results show that the intensities of the absorption peaks of C=C, -C=O, and C-O-C all decrease during the aging process [3,30]. This is because during the aging process of NBR materials, the C=C and C=O groups participate in crosslinking reactions, leading to a reduction in their associated infrared absorption peaks as the degree of aging increases [26].

Table 1. Changes in characteristic peaks during the aging process of nitrile butadiene rubber.

Aging Time	CH_2	C=O (1731)	C=C (958)	C-O-C (1162)
0 h	3.41	2.40	7.19	0.82
19 h	3.95	2.20	7.46	0.77
76 h	4.81	1.63	5.59	0.61
152 h	5.50	1.25	5.30	0.50
228 h	5.52	1.37	6.03	0.27

Table 2. Change in characteristic peak strength relative to methylene peak during the aging of NBR.

Aging Time	CH_2	C=O	C=C	C-O-C
0 h	1.00	0.70	2.11	0.24
19 h	1.00	0.56	1.89	0.19
76 h	1.00	0.34	1.16	0.13
152 h	1.00	0.23	0.96	0.09
228 h	1.00	0.25	1.09	0.05

3.2. Crosslinking Density Change

The crosslinking density of nitrile rubber during the aging process was measured using the equilibrium swelling method. The evolution of NBR's crosslink density during aging is shown in Figure 3. As observed from the figure, crosslinking dominates the aging process, with crosslink density increasing progressively with aging time—a trend consistent with the previous literature [2,3].

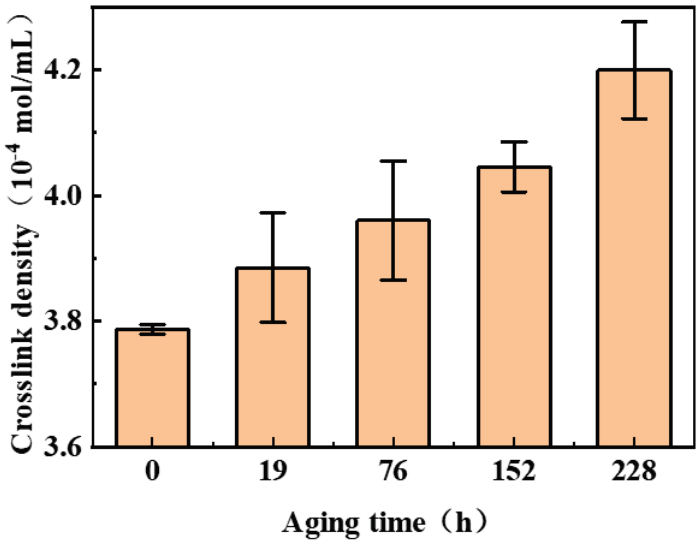

Figure 3. Variation in NBR crosslinking density with aging time.

3.3. Contact Angle Analysis

Contact angle variations reflect changes in NBR's surface polarity: more polar functional groups correspond to smaller water contact angles, while fewer polar groups result in larger angles. In NBR, -CH_2 groups exhibit strong hydrophobicity, whereas oxygen-containing groups like -C=O and C-O-C are highly polar.

The contact angle evolution of NBR during aging is shown in Figure 4. The results show that the contact angle of NBR first increases and then decreases with the extension of time. Moreover, the increase in the contact angle (enhanced hydrophobicity) was significantly correlated with the decrease in the relative content of C=O, indicating that the change in surface chemical composition dominated the wettability evolution.

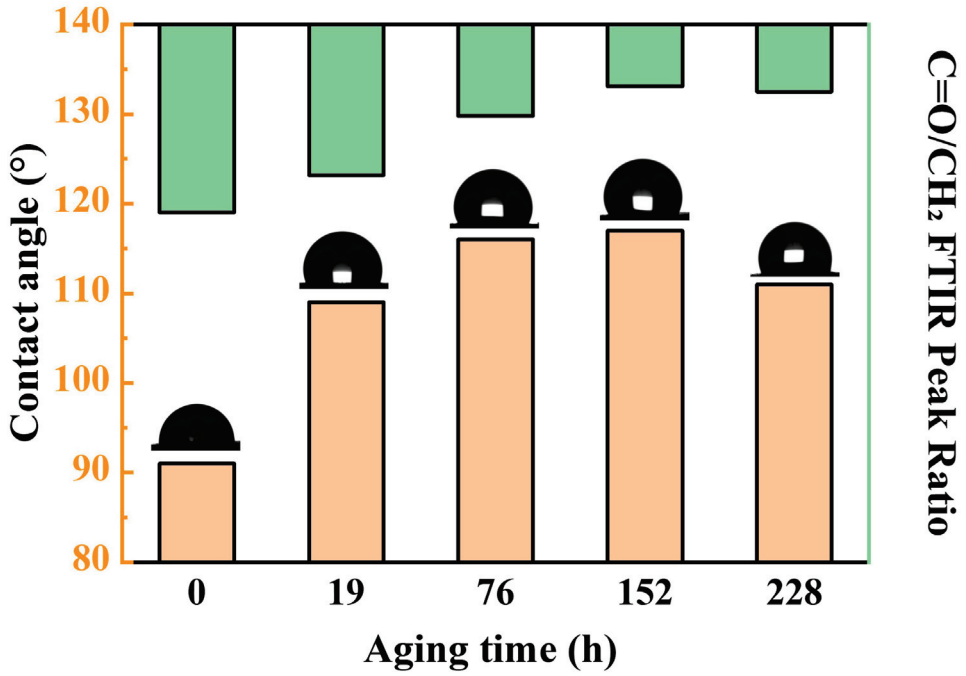

Figure 4. Change in the surface contact angle of NBR during the aging process.

3.4. Molecular Dynamics Analysis of the Aging Mechanism

In previous studies, changes in surface chemical groups and polarity of NBR during aging were characterized using FTIR and contact angle measurements. This section investigates the underlying mechanisms of these chemical changes through MD simulations, which reveal reaction sites and pathways in NBR molecular chains during thermo-oxidative aging.

NBR is synthesized from butadiene and acrylonitrile monomers with added fillers and antioxidants. This analysis focuses solely on the NBR matrix, excluding additive effects on aging. First, a typical structural unit of NBR was constructed using Materials Studio. QM simulations were then performed to calculate the BDE of NBR's representative molecular structures, followed by transition state barrier analysis for further decomposition and crosslinking of oxidation products. These computations provide mechanistic insights into NBR aging processes.

3.4.1. Bond Dissociation Energy

The typical structures of butadiene and acrylonitrile monomers in NBR were analyzed, and the BDE of these typical structures was calculated. The positions of the bonds for which the dissociation energies were calculated are shown in Figure 5, and the calculated dissociation energies are summarized in Table 3.

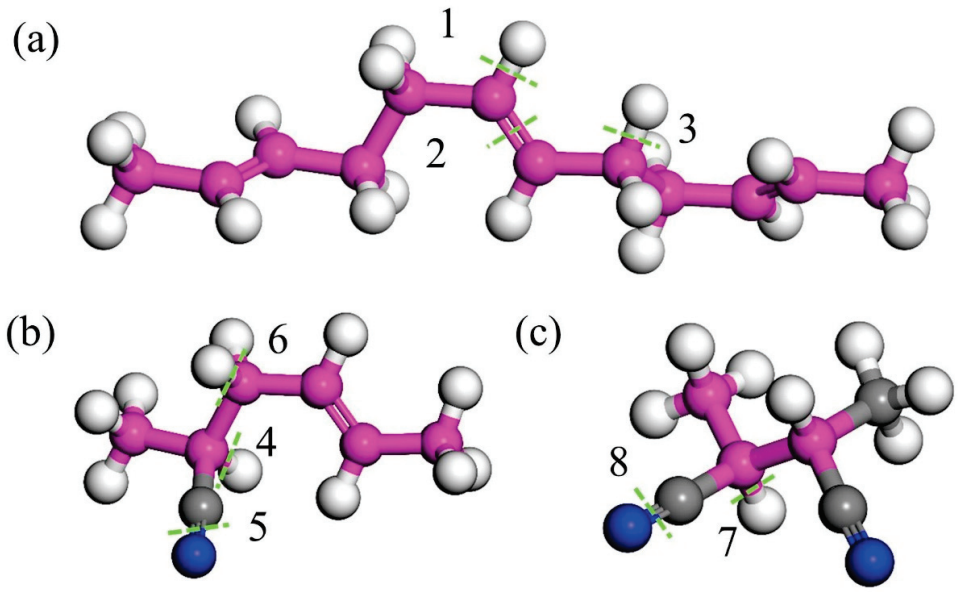

Figure 5. The solution of the typical structure of butylenitrile rubber: (**a**) the butadiene representative unit, (**b**) the acrylonitrile representative unit, and (**c**) acrylonitrile representative unit 2. Where pink beads represent carbon atoms on the carbon skeleton, gray beads represent carbon atoms on the branches, white beads represent hydrogen atoms, and blue beads represent nitrogen atoms. The green dashed line represents the location of key breakage, and its key energy corresponds one-to-one with positions 1–8 in Table 3.

Table 3. Energy and corresponding bond dissociation energies for different structures.

Structural Units	Dissociation Energy (kJ/mol)
H·	-
Butadiene Representative Unit	-
Acrylonitrile Representative Unit	-
Acrylonitrile Representative Unit 2	-
Position 1	467.1
Position 2	269.2
Position 3	371.4
Position 4	377.1
Position 5 (generates C≡N)	266.6
Position 5-2 (generates C−N)	438.9
Position 6	370.4
Position 7	390.7
Position 8 (generates C≡N)	314.0
Position 8-2 (generates C−N)	276.7
Position 9/9′	353.2/380.7
Position 10	351.4
Position 11	372.6
Position 12	377.3
Position 13	346.3

From the table, it can be seen that the C=C double bond (Structure 2 in Figure 5) and C≡N triple bonds (Structures 5 and 8 in Figure 5) exhibit low bond dissociation energies (BDEs). Additionally, the C≡N and C=N bonds in Structure 4c also have low cleavage energies, indicating that these structures are preferentially attacked by O_2 during aging—a finding consistent with the reduced peak intensities of C=C and C≡N bonds observed in FTIR spectra. We also observed that α-hydrogens adjacent to functional groups (Structures 3, 4, and 6) possess low BDEs. During aging, allylic structures like Structure 3 retain high

stability and persist for extended durations [31], making α-hydrogens highly reactive and prone to oxidation. As shown in Figure 6, during oxidation, α-hydrogens or C=C double bonds are activated by environmental factors to form radicals, which react with oxygen to generate new radicals and eventually epoxy structures [9,23].

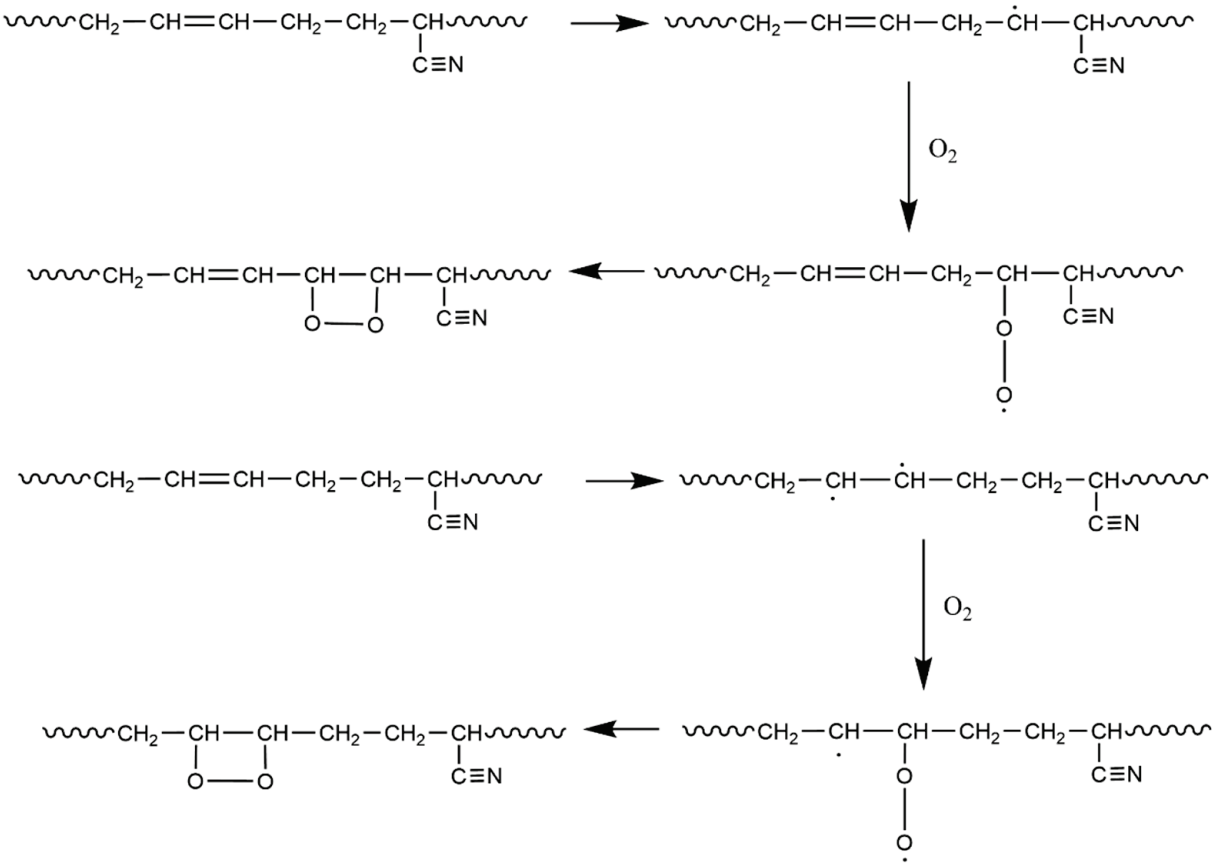

Figure 6. Reaction mechanism of α-H and double bonds with O_2.

3.4.2. Reaction Energy Barriers

The epoxy species formed during NBR oxidation are unstable and further react to generate C=O or -OH groups. This section reports transition state barrier calculations for epoxy decomposition into C=O and -OH via reaction pathway searches.

In physical chemistry, the occurrence of chemical reactions should not only consider thermodynamics but also dynamics. The reaction energy barrier reflects the reaction rate. Generally speaking, the lower the reaction energy barrier, the faster the chemical reaction rate. In order to further analyze the oxidation process of NBR, we simulated the $E_{barrier}$ of the NBR reaction with oxygen by QM. In the calculation process, we use the structure in Figure 5b as the representative unit, which contains both C≡N, C=C, and α-H, and the corresponding bond energy is low, which can affect the reaction process of NBR and oxygen.

Reaction pathways for epoxy decomposition into C=O and -OH (Figure 6) were analyzed. The calculation results (Figure 7a,b) reveal that epoxy groups do not directly form -OH but proceed through a C=O intermediate. The formation of C=O is accompanied by main chain scission, reducing crosslink density. This conclusion is consistent with the degradation pathway of the anti-degradation agent 6PPD reported by Rossomme, where an epoxy intermediate converts into aromatic compounds (aniline and catechol) and carbonyl products (aldehydes and ketones) [23]. Zheng et al. [32] and Ozonation et al. [33] also reported similar behavior, wherein the O-O bond in the epoxy intermediate state is

unstable under thermodynamic or ultraviolet conditions, breaks and decomposes into carbonyl products, and leads to chain opening. These findings support the plausibility of our proposed reaction pathway.

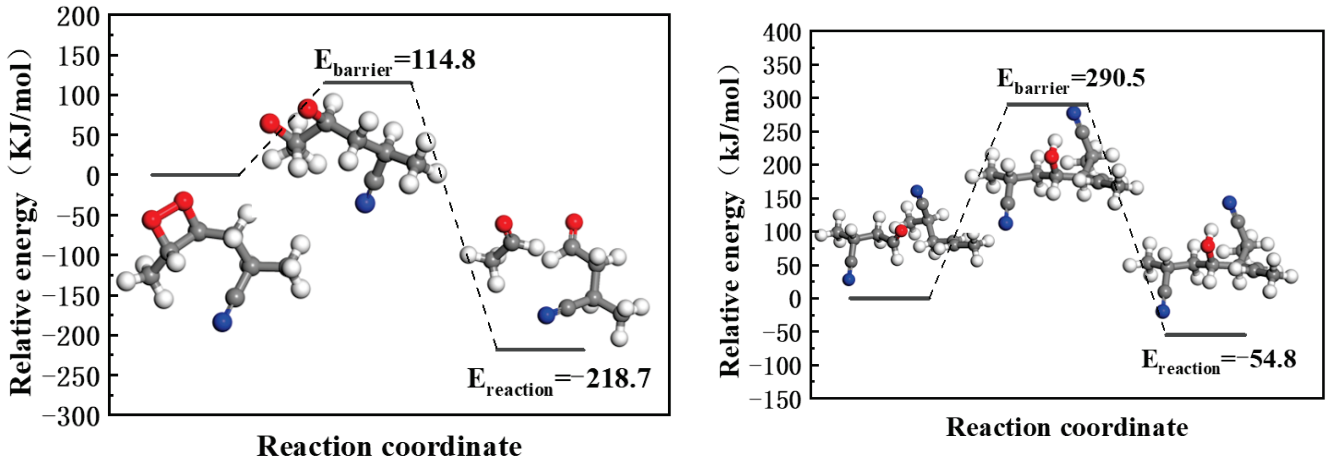

(**a**) Decomposition of epoxy structure into C=O analysis (**b**) Analysis of C=O Decomposition Path

Figure 7. Relationship between energy and chemical structure.

Our calculations also show (Figure 7b) that the oxidized C=O group can react with the unstable hydrogen on the NBR chain to form -OH, triggering crosslinking and spreading aging (with an activation energy of −54.8 kJ/mol). The crosslinking reaction pathway of C=O was confirmed by our experimental evidence and relevant literature. Our infrared spectroscopy results show a significant decrease in the C=O peak intensity during aging (Figure 2), accompanied by an increase in contact angle (Figure 4), indicating reduced surface polarity. This trend corroborates Luo et al.'s [26] conclusion that C=O groups participate in crosslinking reactions during aging. Together, these experimental observations and theoretical calculations provide multi-faceted support for our conclusions.

3.5. Antioxidant Screening

This section evaluates the BDEs, solubility characteristics, and migration/diffusion behaviors of four common AOs—4010NA, 4010, MC, and BHT—using MD simulations. Specifically, BDEs serve as critical indicators of radical-trapping efficiency, directly influencing antioxidant performance; solubility parameters reflect the uniformity of AO dispersion in rubber matrices; and diffusion coefficients correlate with AO durability and extraction resistance.

3.5.1. The Free Energy of Dissociation

As analyzed in Section 3.4, isolated double bonds, nitrile groups, and α-H in rubber macromolecules exhibit low bond dissociation energies (BDEs), making them prone to radical generation under thermo-oxidative conditions. Antioxidants (AOs) suppress oxidation by scavenging radicals, thereby delaying aging. The BDE of labile hydrogens in AOs is a critical metric for evaluating antioxidant efficacy. MD calculations of the labile hydrogen BDEs in Figure 8 (summarized in Table 3) show that all AO BDEs exceed those of double bonds and nitrile groups, indicating that AOs cannot protect these structures. AO BDEs (346.3–377.3 kJ/mol) closely match α-H BDE (371.4 kJ/mol), enabling partial protection against α-H decomposition. Among the tested AOs, BHT has the lowest BDE (346.3 kJ/mol) and the best protective effect.

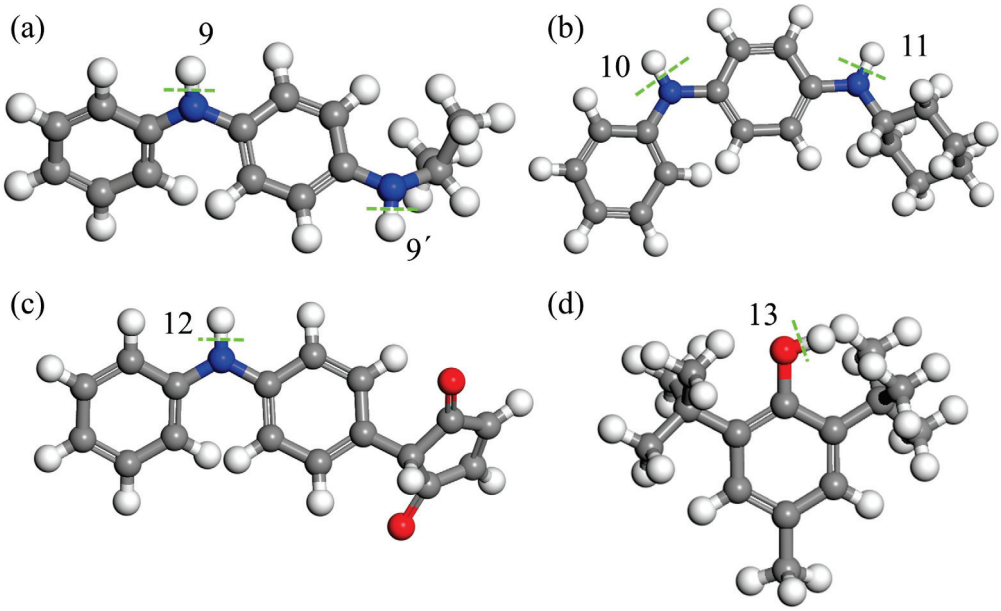

Figure 8. Bond dissociation energies of labile hydrogens: (**a**) 4010NA, (**b**) 4010, (**c**) MC, and (**d**) BHT molecular structure diagram, in which the underlined part is the active hydrogen site. Where red beads represent carbon atoms on the carbon skeleton, gray beads represent carbon atoms on the branches, white beads represent hydrogen atoms, and blue beads represent nitrogen atoms. The green dashed line represents the location of key breakage, and its key energy corresponds one-to-one with positions 9–13 in Table 3.

3.5.2. Solubility Parameters

The solubility parameters of each structure were obtained by statistically analyzing the equilibrium structure according to the MD calculation process in Section 2.3 (taking the average of the three segments). Solubility parameters of AOs and their solubility differences (Δδ) with NBR are listed in Table 4. Solubility parameters evaluate the compatibility of blended materials. According to semi-empirical methods, materials are fully miscible when $\Delta\delta < 2.05$ $MPa^{1}/^{2}$ and partially miscible when Δδ ranges from 2.05 $MPa^{1}/^{2}$ to 10.02 $MPa^{1}/^{2}$ [9]. In Table 4, the solubility order of AOs in NBR is as follows: BHT > 4010 > 4010 Na > MC. However, all AOs can partially dissolve in NBR and serve as antioxidants for NBR.

Table 4. Solubility parameters of AOs and their solubility differences (Δδ) with NBR.

Structure	NBR	4010NA	4010	MC	BHT
Solubility parameter δ	31.60 ± 0.07	38.03 ± 0.12	35.01 ± 0.13	39.09 ± 0.10	28.65 ± 0.11
△δ	-	6.43	3.41	7.49	2.95

3.5.3. Mean Square Displacement

Based on the AOs/NBR composite cell model constructed in Section 2.3, the composite cells were annealed and pre-balanced according to MD, and the balanced cells were statistically analyzed. And the MSD and diffusion coefficient are used to characterize the anti-extraction property of AO in the rubber matrix, which is expressed as follows [26,34]:

$$MSD(t) = \frac{1}{N}\sum_{i=1}^{N}\left\langle |r_i(t+t_0) - r_i(t_0)|^2 \right\rangle \quad (4)$$

$$D = \frac{1}{6N}\lim_{x\to\infty}\frac{d}{dt}\sum_{i=1}^{N}\left\langle |r_i(t+t_0) - r_i(t_0)|^2 \right\rangle = \frac{1}{6}\lim_{x\to\infty}\frac{d}{dt}MSD(t) \quad (5)$$

where N is the number of molecules, D is the diffusion coefficient, $r_i(t_0)$ is the displacement at t_0, and $r_i(t + t_0)$ is the displacement at $t + t_0$. The value of the diffusion coefficient in the text is equal to 1/6 of the slope of the *MSD* linear region.

The MSD curves and diffusion coefficients of four antioxidants in NBR are shown in Figure 9. Analysis shows that MC has the lowest migration rate in NBR, followed by BHT, and 4010 and 4010NA have poor anti-migration ability in NBR.

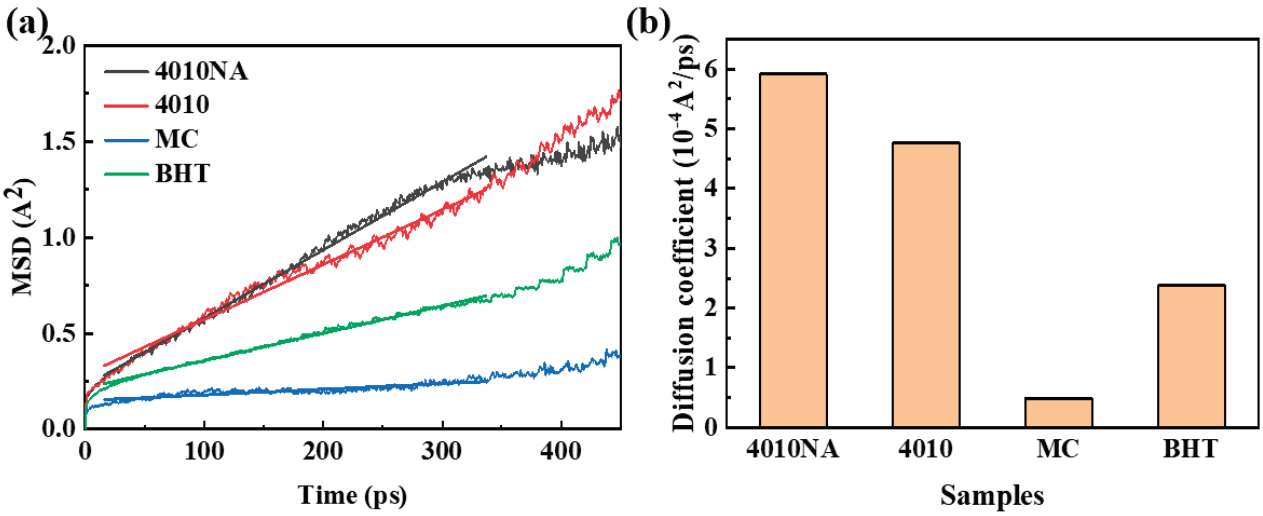

Figure 9. (**a**) MSD curves and (**b**) diffusion coefficient of 4 selected antioxidants in the NBR matrix.

3.5.4. Summary

Table 5 comprehensively summarizes the performance evaluations of four antioxidants, namely 4010NA, 4010, MC, and BHT, in terms of free radical scavenging ability, solubility, and diffusion coefficient within nitrile–butadiene rubber (NBR). The results indicate that MC exhibits outstanding anti-migration properties, maintaining a relatively stable distribution within the NBR matrix. However, it shows poor free radical scavenging efficiency and limited compatibility with NBR, potentially compromising its antioxidant effectiveness in practical applications. Due to their similar molecular structures, 4010NA and 4010 demonstrate comparable performance in free radical scavenging, solubility, and diffusion coefficient in NBR. Notably, 4010 outperforms 4010NA across all indicators, presenting a more balanced and efficient antioxidant profile. Among these antioxidants, BHT stands out with its superior free radical scavenging ability, excellent solubility, and good anti-migration properties. Its comprehensive performance makes it the most optimal antioxidant choice for NBR systems.

Table 5. Summary of free radical trapping ability, compatibility, and migration of four AOs in nitrile rubber.

Structure	4010NA	4010	MC	BHT
Free radical scavenging capacity	3 (353.2)	2 (351.4)	4 (377.3)	1 (346.3)
△δ	3 (6.43)	2 (3.41)	4 (7.49)	1 (2.95)
Diffusion capacity	4	3	1	2

4. Conclusions

This study systematically reveals the thermo-oxidative aging mechanism of NBR under thermo-mechanical coupling environments through a multi-scale research approach

combining experimental characterization and MD simulations. A multi-dimensional evaluation framework for antioxidants was established, providing an important theoretical basis for the development of high-performance rubber materials.

Our results showed that absorption peaks of C=C and C=O groups decreased during aging, corroborated by quantum mechanics (QM) simulations confirming preferential oxidation of α-H, C=C, and C≡N groups in NBR. Crosslink density measurements revealed increased crosslinking after aging, indicating dominant chain reorganization during oxidation.

Multidimensional evaluation results from molecular dynamics simulations of antioxidants demonstrate that BHT exhibits the most outstanding comprehensive performance among the four candidate antioxidants. In terms of free radical scavenging ability, BHT has an extremely low OH bond dissociation energy (BDE) of 346.3 kJ/mol, indicating that it can efficiently quench free radicals by releasing hydrogen atoms with minimal energy consumption. Regarding compatibility with the nitrile–butadiene rubber (NBR) matrix, BHT shows a solubility parameter difference (Δδ) of only 2.95 with NBR, significantly lower than that of other antioxidants. This suggests strong intermolecular forces between BHT and NBR, enabling uniform dispersion within the rubber matrix. Additionally, the simulation results confirm that BHT has a moderate diffusion rate within NBR, endowing it with excellent anti-migration properties and effectively preventing performance degradation caused by antioxidant loss due to migration. Through quantitative analysis of free radical scavenging efficiency, compatibility, and anti-migration characteristics, BHT is identified as the optimal choice among the four antioxidants, providing an ideal solution for enhancing the antioxidant performance of NBR materials.

This research provides a multi-faceted analysis of NBR's thermo-mechanical aging mechanism, deepening understanding of rubber degradation under coupled environments. Additionally, it establishes a multi-dimensional evaluation method for antioxidants in NBR, offering theoretical guidance for preparing high-performance antioxidant NBR materials.

Author Contributions: Conceptualization, M.Z.; Methodology, M.Z. and Y.L. (Yan Li); Software, H.H., G.H., J.F. (Jing Fu) and J.F. (Juqin Fan); Validation, H.L., G.H., Y.L. (Yujun Liu), Z.K. and H.Z.; Formal analysis, J.L. and J.F. (Jing Fu); Investigation, H.H. and H.L.; Resources, M.Z., J.F. (Jing Fu), Z.K. and X.G.; Data curation, J.L. and J.F. (Juqin Fan); Writing—original draft, H.L.; Writing—review & editing, G.H. and J.F. (Juqin Fan); Visualization, Y.L. (Yujun Liu); Supervision, Y.L. (Yujun Liu), Z.K., X.G. and H.Z.; Project administration, J.L., Z.K., X.G. and H.Z.; Funding acquisition, Y.L. (Yan Li). All authors have read and agreed to the published version of the manuscript.

Funding: This research received no external funding.

Institutional Review Board Statement: Not applicable.

Data Availability Statement: The original contributions presented in this study are included in the article. Further inquiries can be directed to the corresponding authors.

Conflicts of Interest: The authors declare that they have no conflicts of interest.

References

1. Gao, W.; Du, G.; Fan, W.N.; Wang, Y.; Wang, X.L.; Jia, Z.D. Hygrothermal aging characteristics and mechanism of nitrile rubber for transformer sealing. *High Volt. Eng.* **2023**, *49*, 608–617. (In Chinese)
2. Kömmling, A.; Jaunich, M.; Wolff, D. Effects of heterogeneous aging in compressed HNBR and EPDM O-ring seals. *Polym. Degrad. Stab.* **2016**, *134*, 133–141. [CrossRef]
3. Liu, J.; Li, X.; Xu, L.; Zhang, P. Investigation of aging behavior and mechanism of nitrile-butadiene rubber (NBR) in the accelerated thermal aging environment. *Polym. Test.* **2016**, *54*, 59–66. [CrossRef]
4. Wei, X.Q.; Wu, H.L.; Zhang, L.W.; Zhang, S.Y.; Xiao, Y.; Luo, T.Y. Failure Analysis of Nitrile Rubber O-Rings Static Sealing for Packaging Barrel. *J. Fail. Anal. Prev.* **2018**, *18*, 628–634. [CrossRef]

5. Lou, W.; Zhang, W.; Jin, T.; Liu, X.; Wang, H. Stress–thermal oxidative aging behavior of hydrogenated nitrile rubber seals. *J. Appl. Polym. Sci.* **2018**, *136*, 47156. [CrossRef]
6. Zheng, J.; Xiang, K.W.; Huang, G.S. Infrared spectroscopy study on aging mechanism and life prediction of butyl rubber. *Aerosp. Mater. Technol.* **2013**, *43*, 89–92. (In Chinese)
7. Li, G.; Zhuo, W.Y.; Yang, G.; Niu, Y.H.; Li, G.X. Aging behavior and mechanism of nitrile rubber under multi-factor coupling. *Acta Polym. Sin.* **2021**, *52*, 762–774. (In Chinese)
8. Zhang, F.; Yang, R.; Lu, D. Investigation of polymer aging mechanisms using molecular simulations: A review. *Polymers* **2023**, *15*, 1928. [CrossRef]
9. Lu, L.; Luo, K.; Yang, W.; Zhang, S.; Wang, W.; Xu, H.; Wu, S. Insight into the anti-aging mechanisms of natural phenolic antioxidants in natural rubber composites using a screening strategy based on molecular simulation. *RSC Adv.* **2020**, *10*, 21318–21327. [CrossRef]
10. Wang, X.; Huang, C.; Wang, X.; Luo, Y.; Wang, X. Multiscale simulation study on radiation aging of EPDM and preparation of radiation-resistant materials. *Compos. Sci. Technol.* **2024**, *252*, 110595. [CrossRef]
11. Zhu, M.; Shao, Z.Q.; Zhu, C.H.; Yang, Y. Research progress on additives for radiation-resistant rubber aging. *J. Nav. Univ. Eng.* **2024**, *36*, 57–63. (In Chinese)
12. Zhou, J.; Ranjith, P.G. Insights into interfacial behaviours of surfactant and polymer: A molecular dynamics simulation. *J. Mol. Liq.* **2022**, *346*, 117865. [CrossRef]
13. Yang, J.; Lou, W. Molecule dynamics simulation of the effect of oxidative aging on properties of nitrile rubber. *Polymers* **2022**, *14*, 226. [CrossRef] [PubMed]
14. Puskarova, I.; Breza, M. DFT studies of the effectiveness of p-phenylenediamine antioxidants through their Cu(II) coordination ability. *Polym. Degrad. Stab.* **2016**, *128*, 15–21. [CrossRef]
15. Zhao, W.; He, J.; Yu, P.; Jiang, X.; Zhang, L. Recent progress in the rubber antioxidants: A review. *Polym. Degrad. Stab.* **2023**, *207*, 110223. [CrossRef]
16. Song, M.; Yue, X.; Chang, C.; Cao, F.; Yu, G.; Wang, X. Investigation of the compatibility and damping performance of graphene oxide grafted antioxidant/nitrile-butadiene rubber composite: Insights from experiment and molecular simulation. *Polymers* **2022**, *14*, 736. [CrossRef]
17. *GB/T 1683-2018*; National Technical Committee for Standardization of Rubber and Rubber Products (SAC/TC 35). Determination Method for Constant Compression Permanent Deformation of Vulcanized Rubber. China Standard Press: Beijing, China, 2018.
18. Zhu, M.; Ma, D.; Zhou, Y.; Huang, H.; Shao, Z.; Wu, F.; Li, B. The change of sealing property in the aging process of NBR sealing equipment based on finite element analysis. *Coatings* **2024**, *14*, 1178. [CrossRef]
19. Sun, Y.; Cheng, Z.; Zhang, L.; Jiang, H.; Li, C. Promoting the dispersibility of silica and interfacial strength of rubber/silica composites prepared by latex compounding. *J. Appl. Polym. Sci.* **2020**, *137*, 49526. [CrossRef]
20. Liu, Q.; Huang, W.; Liu, B.; Wang, P.C.; Chen, H.B. Gamma radiation chemistry of polydimethylsiloxane foam in radiation-thermal environments: Experiments and simulations. *ACS Appl. Mater. Interfaces* **2021**, *13*, 41287–41302. [CrossRef]
21. Wan, S.; Li, T.; Chen, S.; Huang, X.; Cai, S.; He, X. Effect of multi-modified layered double hydroxide on aging resistance of nitrile-butadiene rubber. *Compos. Sci. Technol.* **2020**, *195*, 108193. [CrossRef]
22. Yang, B.; Li, Y.; Wang, S.; Nie, R.; Wang, Q. Aminosilane modified graphene oxide for reinforcing nitrile butadiene rubber: Experiments and molecular dynamic simulations. *Compos. Sci. Technol.* **2023**, *235*, 109956. [CrossRef]
23. Rossomme, E.; Hart-Cooper, W.M.; Orts, W.J.; McMahan, C.M.; Head-Gordon, M. Computational studies of rubber ozonation explain the effectiveness of 6PPD as an antidegradant and the mechanism of its quinone formation. *Environ. Sci. Technol.* **2023**, *57*, 5216–5230. [CrossRef]
24. Lou, W.; Zhang, W.; Liu, X.; Dai, W.; Xu, D. Degradation of hydrogenated nitrile rubber (HNBR) O-rings exposed to simulated servo system conditions. *Polym. Degrad. Stab.* **2017**, *140*, 199–208. [CrossRef]
25. Wang, H.; Liu, S.; Liu, G. Investigation on the Thermo—Oxidative Aging Resistance of Nitrile—Butadiene Rubber/Polyamide Elastomer Blend and the Swelling Behaviors in Fuels Predicted via Hansen Solubility Parameter Method. *Polym. Degrad. Stab.* **2023**, *217*, 110512. [CrossRef]
26. Luo, R.; Kang, D.; Huang, C.; Yan, T.; Li, P.; Ren, H.; Zhang, Z. Mechanical Properties, Radiation Resistance Performances, and Mechanism Insights of Nitrile Butadiene Rubber Irradiated with High—Dose Gamma Rays. *Polymers* **2023**, *15*, 3723. [CrossRef]
27. Redon, A.; Le Cam, J.-B.; Robin, E.; Miroir, M.; Fralin, J.-C. Aging Characterization of Different Nitrile Butadiene Rubbers for Sealing in a Pneumatic System: Linking the Change of the Physicochemical State to the Mechanical Properties. *J. Appl. Polym. Sci.* **2023**, *140*, e54068. [CrossRef]
28. Nguyen, D.M.; Tran, D.T.; Nguyen, T.T.; Grillet, A.C.; Kim, N.H.; Lee, J.H. Enhanced Mechanical and Thermal Properties of Recycled ABS/Nitrile Rubber/Nanofil N15 Nanocomposites. *Compos. B Eng.* **2016**, *93*, 280–288.
29. Ammineni, S.P.; Nagaraju, C.; Raju, D.L. Modal performance degradation of naturally aged NBR. *Polym. Test.* **2022**, *114*, 107683. [CrossRef]

30. Li, B.; Li, S.X.; Shen, M.X.; Xiao, Y.L.; Zhang, J.; Xiong, G.Y.; Zhang, Z.N. Tribological behaviour of acrylonitrile-butadiene rubber under thermal oxidation ageing. *Polym. Test.* **2021**, *93*, 106954. [CrossRef]
31. Martínez-Morlanes, M.J.; Castell, P.; Alonso, P.J.; Martinez, M.T.; Puértolas, J.A. Multi-walled carbon nanotubes acting as free radical scavengers in gamma-irradiated ultrahigh molecular weight polyethylene composites. *Carbon* **2012**, *50*, 2442–2452. [CrossRef]
32. Zheng, T.; Zheng, X.; Zhan, S.; Zhou, J.; Liao, S. Study on the ozone aging mechanism of Natural Rubber. *Polym. Degrad. Stab.* **2021**, *186*, 109514. [CrossRef]
33. Ozonation of anilines: Kinetics, stoichiometry, product identification and elucidation of pathways. *Water Res.* **2016**, *98*, 147–159. [CrossRef] [PubMed]
34. Zhou, M.; Liu, J.; Hou, G.; Yang, H.; Zhang, L. Study on structures, dynamics and mechanical properties of styrene butadiene rubber (SBR)/silica interfaces: A fully atomistic molecular dynamics. *Polymer* **2021**, *218*, 123523. [CrossRef]

polymers

MDPI

Article

Improved Rubber Performance Through Phenolic Resin-Modified Silica: A Novel Coupling Mechanism for Enhanced Recyclability

Pilar Bernal-Ortega [1,*], Rafal Anyszka [1], Raffaele di Ronza [2], Claudia Aurisicchio [2] and Anke Blume [1]

[1] Department of Mechanics of Solids, Surfaces & Systems (MS3), Faculty of Engineering Technology, University of Twente, 7522 NB Enschede, The Netherlands; r.p.anyszka@utwente.nl (R.A.); a.blume@utwente.nl (A.B.)
[2] Bridgestone EU NV/SA, Italian Branch—Technical Center, Via del Fosso del Salceto, 00128 Rome, Italy; claudia.aurisicchio@bridgestone.eu (C.A.)
* Correspondence: m.d.p.bernalortega@utwente.nl

Abstract

Passenger car tires (PCTs) usually consist of a silica/silane-filled Butadiene Rubber (BR) or Solution Styrene Butadiene (SSBR) tread compound. This system is widely used due to improvements observed in rolling resistance (RR) as well as wet grip compared to carbon black-filled compounds. However, the covalent bond that couples silica via silane with the rubber increases the challenge of recycling these products. Furthermore, this strong covalent bond is unable to reform once it is broken, leading to a deterioration in tire properties. This work aims to improve these negative aspects of silica-filled compounds by developing a novel coupling system based on non-covalent interactions, which exhibit a reversible feature. The formation of this new coupling was accomplished by reacting silica with silane and a phenolic resin in order to obtain simultaneous π–π interactions and hydrogen bonding. The reaction was performed using two different silanes (amino and epoxy silane) and an alkyl phenol–formaldehyde resin. The implementation of the new coupling resulted in improved crosslink density, better mechanical performance, superior fatigue behavior, and a similar rolling resistance indicator.

Keywords: silica; tires; silane; sustainability; coupling; recyclability; phenolic resin

1. Introduction

One of the main challenges to achieve sustainability in the rubber industry is reducing waste generation and improving the existing recycling methods. Managing and treating rubber waste, particularly from End-of-Life Tires (ELTs), is a major challenge [1–3]. Tires have a complex composition and structure. For example, the tread of a Passenger Car Tire (PCT) consists of a mixture of natural and synthetic rubbers, silica, silane, carbon black, oils and chemical additives. Additionally, the chemical crosslinks between the polymer chain as well as between silica and the polymer via silane, which are formed during the vulcanization process, make rubber recycling even more difficult [2,4,5].

Nowadays, a large number of tires is recycled, especially in Europe [2]. The main methodologies used for recycling of tires are mechanical recycling, pyrolysis, and devulcanization [3,6–8]. The ground rubber obtained after the mechanical recycling process can be used in low-value applications such as asphalt or playground surfaces [2]. In the case of pyrolysis, useful products like recovered carbon black or oil are obtained that can be used again in the production of tires. However, the pyrolysis process consumes high amounts of energy and the recovered carbon blacks obtained have a low reinforcing

potential [9]. Lastly, the devulcanization of rubber aims to break down the chemical sulfur crosslinks formed during the vulcanization process and go back to the original state of the material to be able to use it again in the production of new tires [6,10]. Still, devulcanization is a complex process, in which only di- and polysulfidic bonds can be broken. The obtained materials show a high deterioration of the in-rubber properties compared to the virgin rubber, which limits its application.

Today, modern passenger car tire tread compounds consist of a silica–SBR-reinforced system. This system is widely used due to the improvements observed in the rolling resistance compared to carbon black-filled compounds [11–13]. Nevertheless, the polar silica particles do not have a good interaction with the non-polar rubber. To improve the compatibility of silica with rubber, silane coupling agents are needed. Silanes are bi-functional structures that act as "bridges" between the silica surface and the rubber [14–16]. They create a chemical bond with the filler and the elastomer, enhancing in this way the in-rubber properties of silica-filled compounds. However, the presence of these covalent bonds is an additional challenge when recycling tire waste. Another drawback of the silica–rubber coupling is that it is short and stiff, and once it is broken under strain, it is not able to re-connect [17,18]. An additional disadvantage in the devulcanization of silica-filled systems is the nature of the silica−silane−polymer bonds. These systems are primarily composed of C−S−C monosulfidic bonds, which are highly stable and resistant to cleavage. As a result, selective breaking the polymer−sulfur−polymer bonds becomes nearly impossible. Consequently, the devulcanization process yields low-quality outcomes.

In recent years, one of the more studied approaches is the implementation of reversible bonds on rubber materials instead of strong covalent bonds to facilitate the devulcanization process [18–24]. In this regard, non-covalent interactions have been widely studied. Reversible non-covalent interactions are weaker than covalent bonds, but they show the ability to be (re-)formed and broken under certain conditions or stimuli, such as pressure, temperature, or the application of a magnetic or electric field [21,25]. This characteristic makes these bonds extremely attractive for polymeric materials in order to achieve products with higher durability or self-healing properties. Some examples of the most studied non-covalent interactions in rubber compounds are hydrogen bonding, π–π stacking, or cation–π interactions [19,20,26–28].

This study presents the development of a novel silica–rubber coupling based on non-covalent interactions with the aim of providing self-healing properties and facilitate the recycling of silica-filled compounds. This new coupling, based on π–π stacking interactions, was achieved through the use of a phenolic resin and silane. Phenolic resins are synthetic polymers derived from the reaction between phenol and formaldehyde [29–31]. They are known for their high thermal stability, mechanical strength, and chemical resistance [29,30,32]. In rubber compounds, they are mainly used as reinforcing, tackifying, or bonding agents. The addition of phenolic resins in rubber compounds leads to improvement in properties such as heat resistance, mechanical strength, and adhesion with other materials [33–36]. The aromatic rings present in the chemical structure of the phenolic resin might interact with the styrene units of the styrene–butadiene rubber through π–π stacking. Furthermore, if the resin has good compatibility with the SBR, physical interactions between the resin and the rubber might occur.

In this work, the formation of this new coupling was accomplished by the reaction of silica with silane and afterwards with a phenolic resin in order to obtain simultaneous π–π interactions and hydrogen bonding. The reaction was performed using two different silanes, 3-Aminopropyltriethoxysilane and 3-Glycidyloxypropyltrimethoxysilane. Additionally, an alkyl phenol–formaldehyde resin was used. The in-rubber results obtained for this

novel coupling were compared with a traditional silica–silane-rubber coupling using bis(triethoxysilylpropyl) disulfide as the coupling agent.

2. Materials and Methods

2.1. Materials

The rubber compounds analyzed in this work were prepared using Solution Styrene Butadiene Rubber (SSBR) and Butadiene Rubber (BR) as the polymers and silica as the filler. The polymers used in this work were Sprintan 4601 (SSBR, Synthos, Schkopau, Germany) and Buna CB24 (BR, Arlanxeo, Dormagen, Germany). Silica employed is a highly dispersible and reinforcing precipitated silica, ULTRASIL 7000 GR (Evonik Industries, Wesseling, Germany) with a specific BET surface area of approximately 175 m^2/g. For the preparation of the reference samples, Bis(triethoxysilylpropyl) disulfide silane (TESPD) (Evonik Industries, Wesseling, Germany) was used as a coupling agent. For the in situ modification of silica, 3-Aminopropyltriethoxysilane (Sigma Aldrich, Zwijndrecht, The Netherlands) and 3-Glycidyloxypropyltrimethoxysilane (Sigma Aldrich, Zwijndrecht, The Netherlands) were used as silanes and an alkyl phenol–formaldehyde resin (DUREZ 19900, Sumitomo Bakelite Europe, Ghent, Belgium) as the resin. The rest of ingredients used in the rubber formulations were as follows: zinc oxide (ZnO) and stearic acid were used as activators (Millipore Sigma, Hamburg, Germany); sulfur and N-tert-butyl-benzothiazole sulfenamide (TBBS) (Caldic B.V., Rotterdam, The Netherlands) as curatives, and Treated Distillate Aromatic Extracted (TDAE) (Hansen and Rosenthal, Hamburg, Germany) as oil.

2.2. Compounding and Mixing

The samples studied in this work were prepared according to the formulation shown in Table 1. The compounds studied were as follows:

- Reference: SSBR/silica compound using TESPD as a silane coupling agent;
- AMR5: SSBR/silica compound using 3-Aminopropyltriethoxysilane as silane and 5% of the phenolic resin;
- AMR10: SSBR/silica compound using 3-Aminopropyltriethoxysilane as silane and 10% of the phenolic resin;
- EPR5: SSBR/silica compound using 3-Glycidyloxypropyltrimethoxysilane as silane and 5% of the phenolic resin;
- EPR10: SSBR/silica compound using 3-Glycidyloxypropyltrimethoxysilane as silane and 10% of the phenolic resin.

Table 1. Formulation of the rubber compounds.

Compounds	SBR (phr)	BR (phr)	Silica (phr)	TESPD (phr)	Amino Silane (phr)	Epoxy Silane (phr)	Resin (phr)
Reference	80	20	80	6.2	-	-	-
AMR5	80	20	80	-	5.78	-	4
AMR10	80	20	80	-	5.78	-	8
EPR5	80	20	80	-	-	6.2	4
EPR10	80	20	80	-	-	6.2	8

The amount of resin added to the samples was 5% or 10% of the amount of silica in the compounds. The amount of silane was adjusted equimolarly for each compound based on the amount of TESPD in the reference sample.

The quantities of used ingredients were the same for all compounds: TDAE—37.5 phr, ZnO—2.5 phr, stearic acid—2.5 phr, sulfur—1.4 phr, and TBBS—2 phr.

The rubber compounds were mixed in an internal mixer (Brabender Plasticorder 350S, Duisburg, Germany) with a fill factor of 0.7, an initial temperature of 100 °C for steps 1 and

2, and an initial temperature of 50 °C for step 3, at an initial rotor speed of 50 rpm. The complete mixing procedure is shown in Table 2.

Table 2. Mixing procedure of rubber compounds.

Time (min)	Action
Stage 1. Pre-heating 100 °C—rotor speed 50 rpm	
0.00	Addition of rubber
1.20	Addition of 1/3 filler, 1/2 silane
2.40	Addition of 1/3 filler, 1/2 silane, TDAE
4.00	Addition of 1/3 filler and resin
5.00	Increase in temperature
10.00	End of mixing (reaching 140 °C)
Stage 2. Pre-heating 100 °C—rotor speed 50 rpm	
0.00	Addition of batch from stage 1
1.00	Addition of ZnO and Stearic Acid
1.20	Increase in temperature
5.00	End of mixing (reaching 140 °C)
Stage 3. Pre-heating 50 °C—rotor speed 50 rpm	
0.00	Addition of batch from stage 2
1.30	Addition of curatives (Sulfur, TBBS)
3.00	End of mixing

2.3. In-Rubber Tests

The following in-rubber characterizations were performed for all rubber compounds.

2.3.1. Cure Behavior

The vulcanization properties of rubber compounds were analyzed by using a Rubber Process Analyzer, RPA elite from TA instruments (New Castle, DE, USA), at 160 °C, by applying a deformation of 6.98% at a frequency of 1.667 Hz. The t_{90}, the time to reach 90% conversion of each compound was used as a molding time for vulcanizing the rubber samples in a hydraulic press (Wickert Maschinenbau GmbH, Landau, Germany).

2.3.2. Payne Effect

The micro-dispersion of the filler and the degree of filler–rubber interactions were analyzed by the study of the Payne effect. The Payne effect test was performed on a Rubber Process Analyzer, RPA elite from TA instruments (New Castle, DE, USA), with strain sweeps from 0.1% to 100% for cured samples at a frequency of 1.6 Hz and a temperature of 60 °C. The cured samples were vulcanized beforehand inside the equipment chamber according to the vulcanization conditions. The Payne effect is the difference between the storage moduli at 0.56% and 100% of strain.

2.3.3. Macro-Dispersion of the Filler

The macro-distribution of the silica particles in the rubber compounds was studied by the analysis of the macro-dispersion of the filler. The macro-dispersion was studied by means of a Dispergrader, Dispersion Tester Alpha View (Alpha Technologies, Hudson, OH, USA). The macro-dispersion of a filler describes the degree of a filler distribution at a scale of 2 μm up to 100 μm. The rubber samples were investigated by optical light microscopy with a 30° irradiation angle and at 100× magnification.

2.3.4. Crosslink Density

The crosslink density (CLD) of the compounds was studied using two different methods: equilibrium swelling experiments and stress–strain experiments using the Mooney–Rivlin approach.

- The crosslink density by equilibrium swelling experiments was obtained using the Flory Rehner equation [37]. Five vulcanized samples (~0.25 g) of each compound were swollen in toluene at room temperature for a period of 7 days. The samples were extracted before with acetone for 24 h in order to remove the oil and unreacted curing agents.
- The determination of the crosslink density by the Mooney–Rivlin approach was carried out by stress–strain assays performed in a universal testing machine Zwick Z010 (Zwick, Ulm, Germany). Test specimens were 2 mm thick, with a test length of 20 ± 0.5 mm and a width of the narrow portion of 4 ± 0.1 mm, according to the ISO 37 (dye type 2) standard [38]. The stress–strain assays consisted of two different steps:
  (i) In the first step, the samples were pre-cycled 10 times until 200% strain at a crosshead speed of 500 mm/min. This first step was performed in order to destroy the filler–filler network.
  (ii) In the second step, the specimens were stretched until a strain of 200% at a crosshead speed of 10 mm/min.

2.3.5. Stress–Strain Behavior

The mechanical properties of the compounds at room temperature were measured by a universal testing machine Zwick Z05 (Zwick, Ulm, Germany) operating with a crosshead speed of 500 mm/min according to the ASTM D412 standard [39]. For each compound, five samples were tested, and the average result of these samples was determined.

2.3.6. Dynamical Properties

Dynamic mechanical measurements of the vulcanized samples were carried out on a Gabo-Netzsch Eplexor tester (Netzsch, Selb, Germany). The measurements were performed with a frequency of 10 Hz, with a dynamic strain of 1% below 0 °C and 3% above 0 °C. The change in the strain was chosen because the rubber becomes softer at higher temperatures, which can generate noise in the measurements. The temperature range of the test was from −80 to 80 °C. The loss factor (tan δ) of each compound was evaluated at low (0 °C) and at high temperatures (60 °C).

2.3.7. Re-Connectivity of Bonds

After the study of how the new coupling systems affect the in-rubber properties, the best compound was selected and compared with the reference. These two compounds were tested to quantify the degree of the re-connectivity of the non-covalent interactions.

The re-connectivity of the new bonds created with the silica modification was analyzed by:

- The study of the mechanical response of the compounds at high temperatures

The mechanical properties of the compounds were measured by a universal testing machine Zwick Z010 (Zwick, Ulm, Germany) operating with a crosshead speed of 500 mm/min and with a limit strain of 330%, which is the thermal chamber limit. The tests were performed in a temperature chamber at 100 °C.

- Analysis of the changes in the dynamical properties after submitting the compounds to cycling (fatigue) test

The dynamic mechanical properties of the samples were compared before and after the cyclic strain at 100 °C. The measurements of the dynamic properties of the vulcanized

compounds before and after tensile cycling were performed in the same way as the dynamic mechanical measurements explained above. The tensile cycling of the samples was performed in a universal testing machine Zwick Z010 (Zwick, Ulm, Germany) operating with a crosshead speed of 500 mm/min. All the samples were cyclically strained from 0% to 100% five times at 100 °C. Immediately after performing the cycling, the dynamical mechanical properties were tested.

- Creep experiments

The creep experiments were measured by a universal testing machine Zwick Z010 (Zwick, Ulm, Germany). A force of 15 N was applied to the samples. This force was maintained for 1 h. After this time, the force was released and the changes in the strain of the samples were measured for another hour. The temperature of the experiments was 100 °C.

- Recycling test

The recyclability of the materials was tested by the study of the re-use of ground material in new compounds. The samples were cryo-ground, added to new compounds, and characterized. The samples were cryogenically ground in a grinder from Fritsch GmbH, Idar-Oberstein, Germany. The granules were frozen with liquid nitrogen and ground with a 0.6 mm sieve. This step was performed in order to facilitate the incorporation into the rubber. The properties of the compounds containing ground materials were compared to the ones of the original samples. For the preparation of the new compounds, the formulation shown in Table 1 was used, substituting 15 phr of the filler with the ground material. The ground material obtained from the selected best-performing sample was introduced to the same virgin compound, and the ground material from the reference was added to the virgin reference compound.

3. Results

The samples with the new coupling were characterized by different methodologies and compared to a reference compound with a traditional silica/silane coupling using TESPD as the coupling agent. The in situ modification of silica was performed in all cases during the mixing process. The new coupling system was developed by reacting silica with silane, followed by the reaction with a phenolic resin, to establish π–π interactions between the resin and the styrene–butadiene rubber. Two different silanes were studied, 3-Aminopropyltriethoxysilane and 3-Glycidyloxypropyltrimethoxysilane. A schematic representation of the possible reactions that can occur in the system is shown in Figure 1. In Figure 1a, the reaction using 3-Aminopropyltriethoxysilane is shown. First, the amino silane reacts covalently with the hydroxyl groups of the silica surface, and subsequently, the amino group (-NH_2) of silane can form hydrogen bonds with the hydroxyl groups of the phenolic resin. However, in extreme conditions (e.g., extremely high temperatures, catalysis), covalent bonding may also occur; however, under the conditions used in this study, hydrogen bonding is assumed to be the dominant interaction in this system. 3-Glycidyloxypropyltrimethoxysilane (Figure 1b), as amino silane, first reacts covalently with the silica surface. Afterwards, silane can form a covalent bond with the phenolic resin via the epoxide ring-opening reaction caused by the hydroxyl groups of the resin. In addition to covalent bonding, hydrogen bonding could occur between the hydroxyl groups on the phenolic resin and the newly formed secondary hydroxyl groups on the silane after the opening of the epoxide ring (Figure 1c). During the mixing process, an additional side reaction could occur. While mixing, silane coupling agents are exposed to atmospheric moisture, leading to their hydrolysis and subsequent condensation to form siloxane networks within the rubber matrix. This reaction pathway is particularly relevant in the presence of amino silanes, which can catalyze these processes. Under such conditions,

mechanisms similar to the Stöber process [40]—originally described for the controlled synthesis of monodisperse silica particles from alkoxysilanes in alcoholic media—may occur. In the compounding process, the presence of moisture and amine groups can enhance the in situ formation of silica-like domains via hydrolysis and polycondensation of silanes. This phenomenon could influence the filler dispersion and therefore the mechanical and dynamic properties of the final compound.

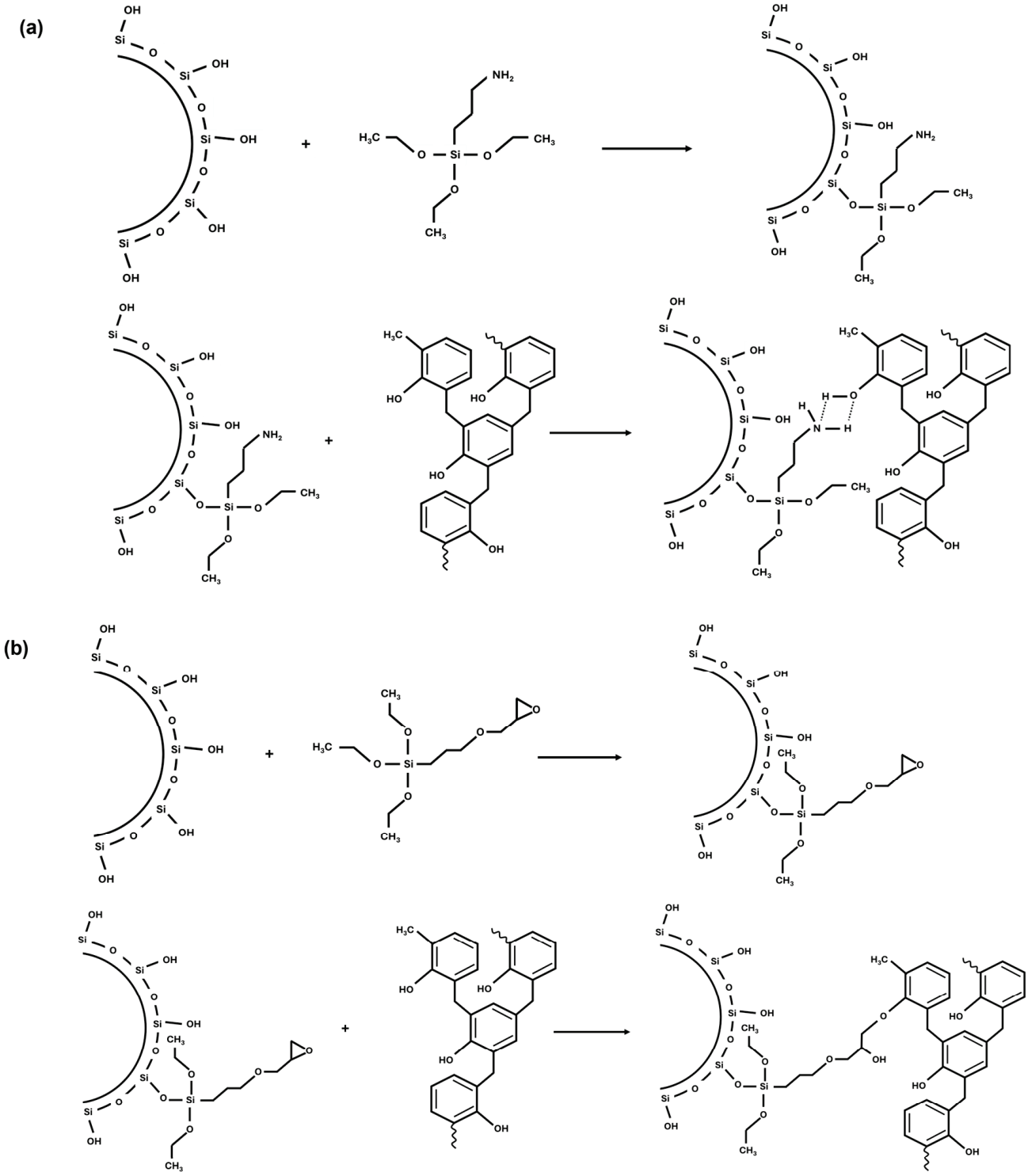

Figure 1. *Cont*.

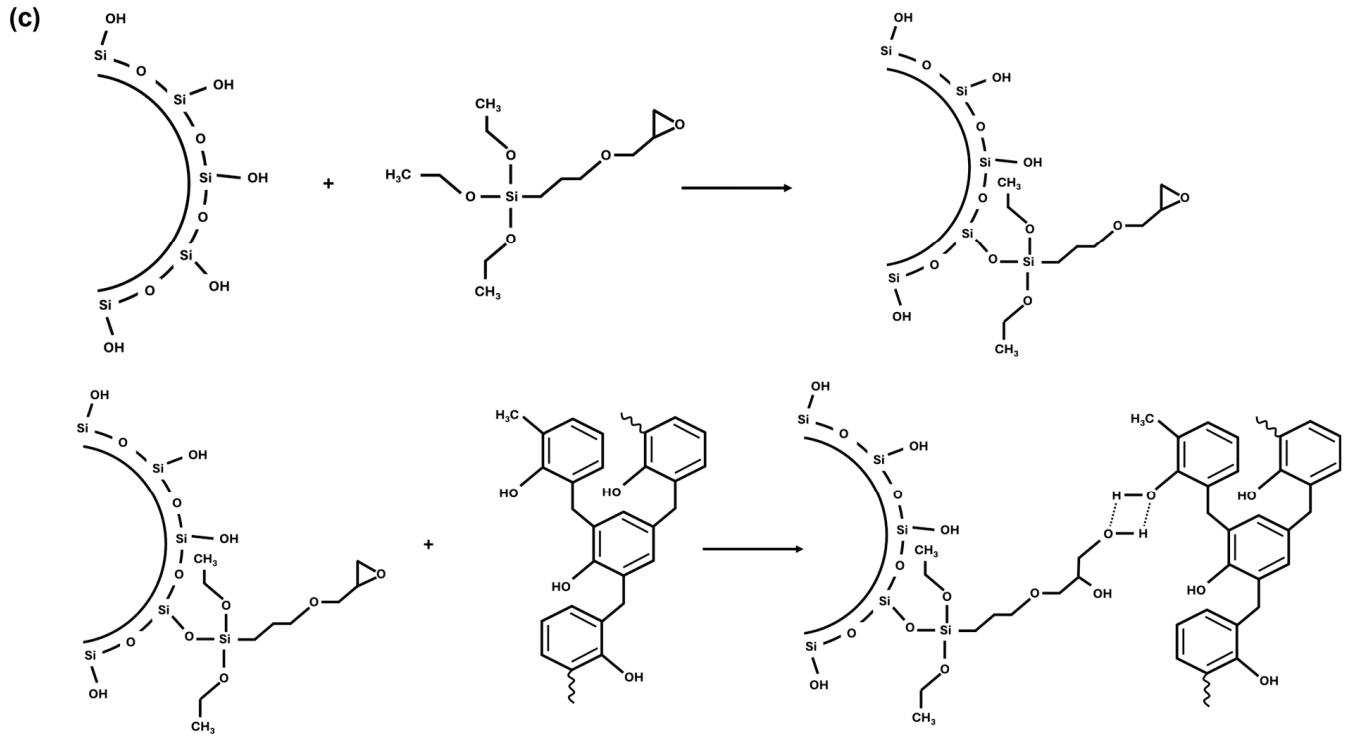

Figure 1. Schematic representation of the silica surface modification mechanism with the phenol resin using (**a**) amino silane, (**b**), and (**c**) epoxy silane.

3.1. Vulcanization

Figure 2 shows the cure behavior of the studied samples. In the graph, it can be observed that samples containing amino silane (AMR5 and AMR10) show a faster vulcanization compared to the samples with epoxy silane and the reference. This is caused by the presence of the amino group (-NH_2). It has been demonstrated that the amino group accelerates vulcanization because it is a base and promotes the opening of the sulfur ring and its conversion to more reactive forms [41,42]. The slow curing behavior of the reference compound is caused by the presence of only one accelerator in this sample. The compound was designed in this way to reduce the complexity of the system to avoid interference with the newly developed coupling systems. Comparing AMR5 and AMR10, the compound with only 5% resin has a faster vulcanization rate. This might be caused by a dilution effect—the higher the content of the resin, the lower the amount of elastomer per volume. Additionally, the phenolic resin can interact with the accelerator, deactivating it for the vulcanization process. The same occurs in the compounds with epoxy silane, where EPR5 undergoes faster vulcanization than EPR10. In the samples with amino silane, two opposite reactions occur in the system: the fastening of the crosslinking reaction due to the presence of the amino group and the deceleration of it due to the phenolic resin. In sample AM5, the effect of the amino silane is more predominant, but in sample AM10, with the increase in the phenolic resin content, the second reaction becomes more significant.

Figure 2 also shows that the samples with 5% of resin (AMR5 and EPR5), independently of silane, show the higher values of the maximum torque (M_H), with AMR5 reaching the highest value in all samples. The addition of 10% of resin in both systems leads to lower M_H. Compared to the reference, all samples with the new couplings show higher values of M_H. Commonly a higher value of maximum torque is an indication of higher crosslink density (CLD). Therefore, these results might suggest that the samples containing resins show a higher CLD than the reference. However, a higher maximum torque can also be caused by other factors. It can also be associated with higher filler–filler inter-

actions and thus worse dispersion in these compounds. This increase in the filler–filler interactions might be a consequence of the presence of many different interactions in these systems: filler–filler interactions (e.g., via silica–resin–silica) or polymer–filler interactions (via silica–resin–polymer).

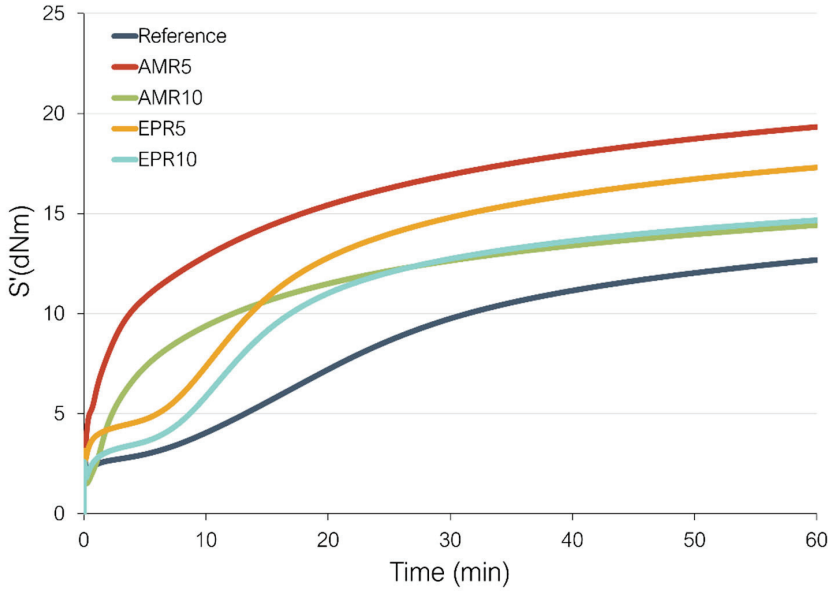

Figure 2. Vulcanization curves of the studied compounds.

3.2. Payne Effect

Figure 3 shows the reduction in the storage modulus (G′) with an increasing strain. This phenomenon is associated with the filler network breakdown, described in the literature as the Payne effect [43–45]. The Payne effect is an indirect method of analyzing the micro-dispersion of the filler in the rubber matrix [43–45]. A higher Payne effect, calculated as the difference between G′ at high and low strains, generally suggests a worse micro-dispersion. The Payne effect also contributes to the energy dissipation in rubber compounds, which is a key parameter in the performance of tires (wet grip and rolling resistance).

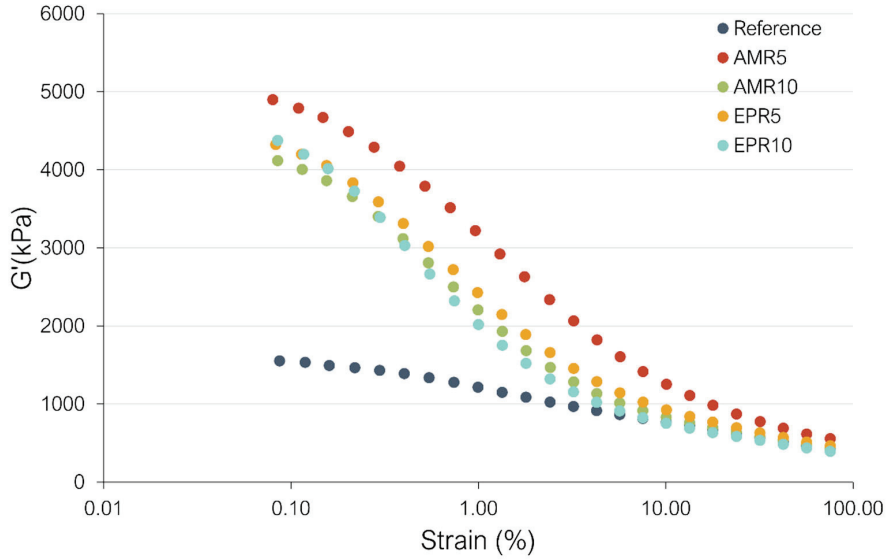

Figure 3. Payne effect curves of the studied compounds.

Figure 3 and Table 3 display that the reference sample has the lowest Payne effect of all samples. The compounds with the grafted resin, either with amino or epoxy silane, present significantly higher values. The sample AMR5 shows the highest Payne effect of all compounds. These results are in agreement with the higher maximum torques observed for these samples in the analysis of the cure behavior. Indicating that the higher torques observed are most likely to be caused by higher filler–filler interactions in these compounds instead of a higher CLD. Figure 3 also shows that in the case of the samples containing resin, the decay of G′ occurs faster than in the reference compound. Due to the increased polarity of the system in the compounds with the new coupling, the interaction possibilities between silica particles have significantly increased. It is possible that silanes (both amino and epoxy silane) can connect different silica particles. Both silanes can chemically couple to silica via the ethoxy group but can also form a hydrogen bond to another Si-OH from another silica particle. The distance between these silica particles might be bigger and more flexible than the one of a direct particle–particle interaction. A schematic representation of these interactions is shown in Figure 4.

Table 3. Payne effect (ΔG′) and G′ at 100% strain of the studied compounds.

Compound	ΔG′ (kPa)	G′ at 100% Strain (kPa)
Reference	1150	400
AMR5	4340	530
AMR10	3700	420
EPR5	3880	440
EPR10	4010	370

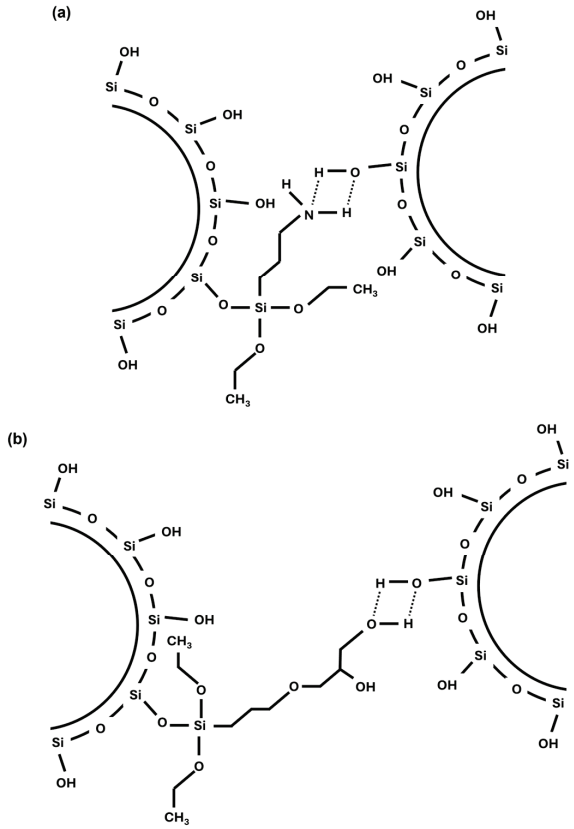

Figure 4. Schematic representation of the interactions between silica particles connected by (**a**) amino and (**b**) epoxy silane.

Another possible explanation for the higher Payne effect in the samples with the new coupling is that not only filler–filler interactions are breaking with the applied strain. It is possible that the non-covalent interactions present in these systems, such as hydrogen bonding or π–π stacking break when strain is applied due to its weaker nature compared to covalent bonding. Therefore, in these cases, the measurement of the Payne effect is the combination of two different effects, the filler–filler and the filler–rubber interactions [18]. This effect is also known from previous studies of functionalized polymers [46], where the interaction of the functionalization is based on hydrogen bonding and the Payne effect curves show similar behavior. At low strains, the non-covalent links remain intact, contributing to a higher value of G′ as can be seen in Figure 3. As the strain increases, these weaker interactions start to break down, causing a sharp drop in G′.

Comparing the effect of the different silanes (amino and epoxy silane) it is observed that with 5% of resin, the sample with amino silane shows a substantially higher Payne effect than the one with epoxy silane. In the case of the epoxy silane, it has more direct reactivity towards the phenolic resin through the ring opening. This reaction can lead to the formation of some covalent bonds, stronger and more stable. The amino silane primarily interacts with the resin via hydrogen bonding, and therefore the interactions are weaker and more prone to be broken when deformed.

As can be seen in Table 3 and Figure 3, all samples show similar values of G′ at high strains. This parameter is associated with higher rubber–filler interactions. Therefore, this result indicates that the new compounds present similar polymer–filler interactions than the reference that could result in a comparable mechanical performance. This also indicates that not all non-covalent interactions are broken down when the strain increases. It also could be an indication that some of the non-covalent interactions are reformed.

3.3. Macro-Dispersion of the Filler

The macro-dispersion of the filler in the analyzed compounds was evaluated using the optical Dispergrader (Alpha Technologies, Hudson, OH, USA) device. The resulting images are presented in Figure 5. All samples, except for AMR5, show a similar macro-dispersion of the filler. Sample AMR5 presents slightly poorer macro-dispersion, with the presence of larger clusters being noticeable. The implementation of the new coupling system and all the new possible interactions in the system (Figure 4) does not seem to have a significant effect on the macro-dispersion of the silica particles, contrary to what was observed in the Payne effect study which delivers hints on the micro-dispersion. However, both measurements refer to two different length scales and are two independent processes [43–45].

3.4. Crosslink Density

The crosslink density of the studied compounds is shown In Figure 6. The results obtained with equilibrium swelling correspond to the solid color bars and the ones obtained with the Mooney–Rivlin approach to the bars with stripes.

As can be seen in Figure 6, the results of both techniques show some differences. This might be caused by the differences between the two methods such as the use of a solvent in the equilibrium swelling experiments or the pre-treatment to destroy the filler network of the samples in the Mooney–Rivlin tests: In Figure 6, it is shown that the samples containing 5% resin, with both silanes, have a higher CLD than the reference compound. This is more evident in the equilibrium swelling results. In samples containing amino and epoxy silanes, the crosslinks are formed through the vulcanization process via the sulfur addition, but all the additional interactions facilitated by the new coupling system (hydrogen bonds, π–π stacking, or covalent bonding) are also present. These new interactions could contribute to the calculated CLD by swelling, enhancing the overall network structure.

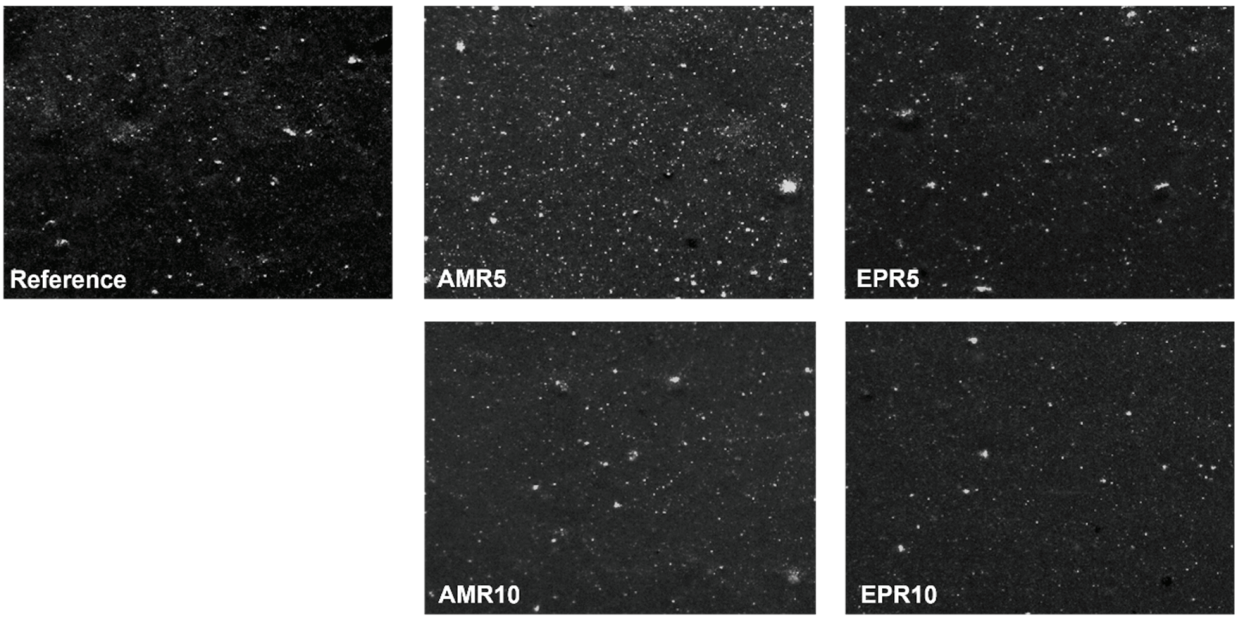

Figure 5. Dispergrader images of the analyzed rubber compounds (150 × 250 μm area).

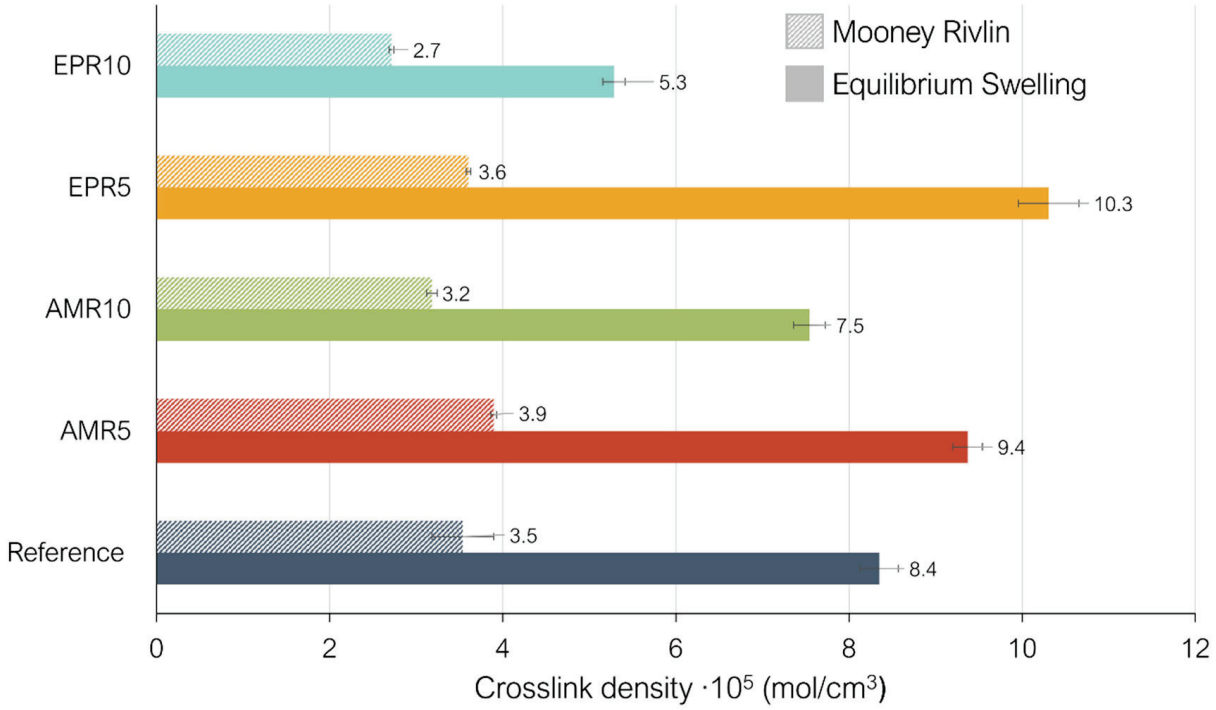

Figure 6. Crosslink density measured by equilibrium swelling and the Mooney–Rivlin approach applied to the studied compounds.

Furthermore, if the resin has good compatibility with the SBR, some physical interactions can be formed. The resin can be entangled in between the polymer chains of the SBR. All these additional interactions can contribute to a higher value of CLD measured by swelling in these compounds compared to the reference sample with TESPD. However, in the case of the CLD results obtained using the Mooney–Rivlin method, samples containing 5% resin exhibit a CLD comparable to that of the reference compound. This discrepancy with the swelling test results may arise from the fact that the Mooney–Rivlin method distinguishes between chemical crosslinks and physical entanglements. As such, the weaker additional interactions in the modified compounds are more likely to contribute

to entanglement density rather than to measurable crosslink density. This is supported by the results in Figure 7, where all modified samples show higher entanglement densities than the reference, with AMR5 displaying the highest value.

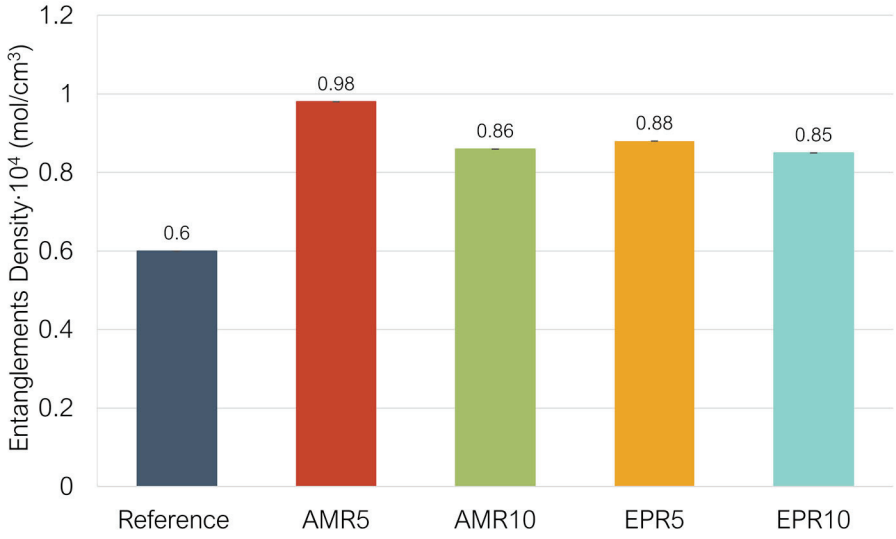

Figure 7. Entanglements density measured by the Mooney–Rivlin method applied to the studied compounds.

When 10% of the resin is added, a slight decrease in the CLD is observed for the compounds containing both silanes. As mentioned in the vulcanization analysis, it could be that 5% of resin is an optimum amount of the material, and 10% is an excessive quantity. The increasing resin content can elevate the possibility that the phenolic resin interacts with the accelerator, deactivating it during the vulcanization process and leading to lower values of CLD. These results, combined with the ones obtained for the Payne effect, seem to indicate that the higher values of the Payne effect and the maximum torques observed in the curing curves are a combination of the CLD, filler–filler, and polymer–filler interactions.

3.5. Stress–Strain Behavior

The mechanical properties of the compounds studied in this work are shown in Figure 8 and Table 4. As can be seen, all samples including resin have a higher tensile strength (T_s) and elongation at break (ϵ_b) than the reference. The notable increase in elongation at break compared to the reference can be attributed to the slippage of entangled polymer chains connected to silica, facilitated by the additional interactions in the new system among silica, silanes, resin, and elastomer [18]. These increased interactions in the newly developed systems contribute to the higher tensile strength observed in these samples.

Table 4. Mechanical properties of rubber compounds at RT.

Compound	Reinforcement Index ($M_{300\%}/M_{100\%}$)	T_s (MPa)	ε_b (%)
Reference	3.6 ± 0.01	10.7 ± 1.8	470 ± 60
AMR5	3.6 ± 0.1	17.5 ± 0.7	600 ± 80
AMR10	3.9 ± 0.1	19.0 ± 1.2	680 ± 70
EPR5	2.8 ± 0.5	15.7 ± 1.9	780 ± 90
EPR10	3.0 ± 0.2	16.6 ± 1.1	880 ± 70

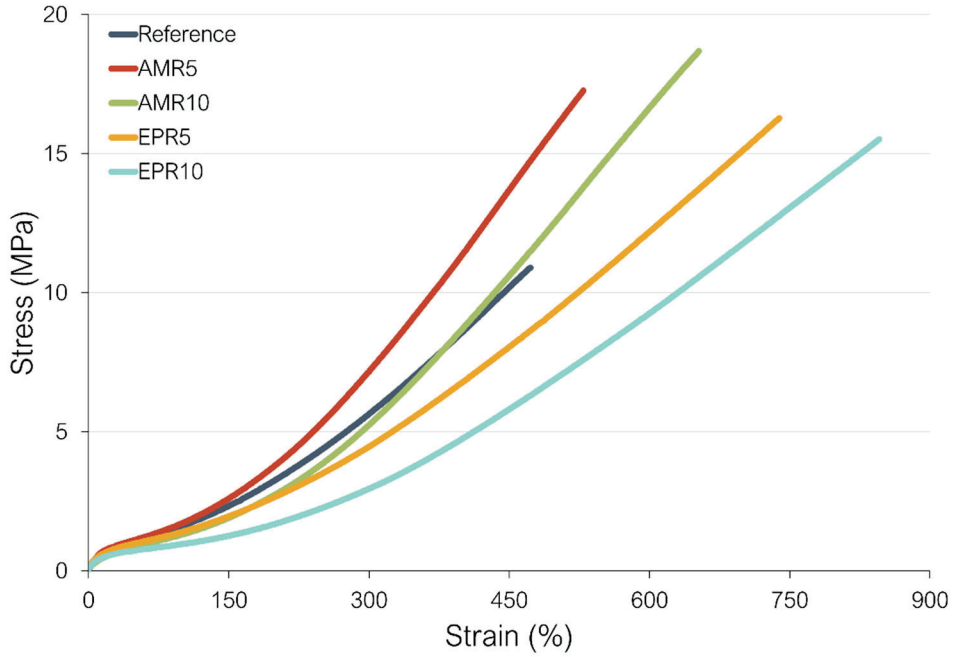

Figure 8. Stress–strain curves at RT of the rubber compounds.

The samples containing amino silane also present a higher reinforcement index (ratio between the modulus at 300% strain and the modulus at 100% strain). Both samples with amino silane exhibit an improved mechanical performance compared to the sample with TESPD and to the samples with epoxy silane. The sample with amino silane and 5% of resin (AMR5) shows the best performance of all compounds. These results are in agreement with the ones obtained for the Payne effect, in which this sample had the highest G′ at high strains, indicating higher filler–rubber interactions in this compound. As observed already in the cure behavior, the Payne effect, and CLD, an increase in the amount of resin to 10% seems to have a negative effect on some in-rubber properties. Independently of silane used (amino or epoxy silane), the addition of 10% of resin caused a deterioration of the moduli compared to the samples with 5%. This result is another hint that 10% of resin is above the optimum amount that should be added into the rubber compounds. As previously mentioned, at this higher material concentration, the resin appears to deactivate the accelerator, resulting in a significantly lower CLD compared to the reference as well as the compounds containing 5% resin.

3.6. Dynamic Properties

The impact of the implementation of the new coupling on the dynamic properties of the rubber compounds was studied through the analysis of the loss factor (tan δ) as a function of temperature. The loss factor is defined as the ratio between the loss and the storage moduli, and it is employed as an indicator of tire performance. Usually, the values of tan δ at low (0 °C) and high temperatures (60 °C) are used as indicators of the wet grip (WG) and the rolling resistance (RR), respectively [47]. These two properties are key in tire performance and form—together with the abrasion resistance—the Magic Triangle of tires. However, the prediction for the RR is more accurate than the one of the WG. The reason for this is that the wet grip is a complex phenomenon that takes place within a high-frequency range of 10^4 to 10^7 Hz, and these frequencies are too high to be measured using DMA [47].

The variation in the loss factor as a function of temperature is shown in Figure 9.

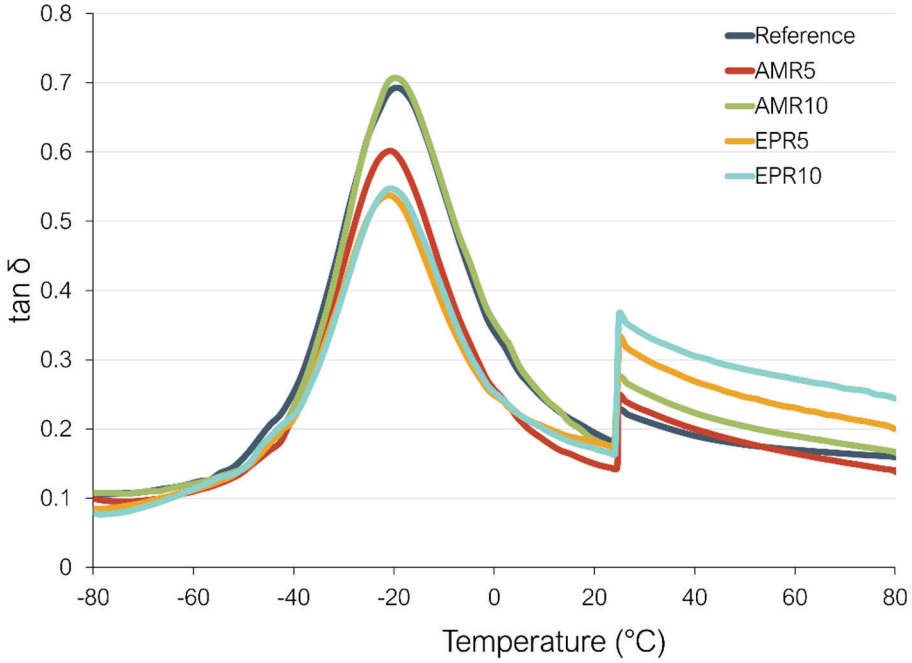

Figure 9. Variation in the loss factor (tan δ) as a function of temperature of the studied compounds (the sharp drop in the lost factor at 25 °C is caused by the increase in applied strain).

As can be seen in Figure 9, the application of the new coupling system has a significant impact on the dynamical properties of the compounds. Substantial differences can be observed at both low and high temperatures. Observing the values of the loss factor at 0 degrees, commonly used as the wet grip indicator, it is shown that samples AMR5, EPR5 and EPR10, present a lower value than the reference. While sample AMR10, shows a slightly higher loss factor at 0 degrees. The lower loss factor for the samples AMR5, EPR5, and EPR10 could be caused by a stronger network in these compounds. As discussed before, it is assumed that these samples contain more interactions in the system than the reference, leading to a more elastic material and therefore to lower hysteresis. These samples contain not only the crosslinks formed during the vulcanization but also additional non-covalent interactions between silica, the resin, and silanes. Regarding the sample AMR10, with 10% resin, it could be, as previously discussed, that the optimum amount of resin is exceeded and that the resin is also acting as a plasticizer, showing a result more similar to the reference. This behavior is not observed in the case of the sample with 10% of resin and epoxy silane, because as discussed beforehand, the epoxy silane has a higher reactivity towards the resin due to the ring opening. This could lead to the presence of stronger (covalent) interactions compared to the sample with amino silane. However, it is known [48] that the prediction of the wet grip using this method is not as reliable as for the rolling resistance when two different systems are compared. Therefore, only a real tire test can show the real grip performance.

Regarding the rolling resistance indicator (tan δ) at 60 °C, some differences to the reference compound are observed. In this case, the behavior of the new coupling is extremely influenced by the type of silane used. The samples AMR5 and AMR10 with amino silane show a significantly lower RR indicator than the samples with epoxy silane. Samples containing amino silane exhibit a behavior which is more similar to the reference, with AMR5 displaying the lowest RR indicator among all compounds. This sample shows a CLD similar to the reference and exhibits stronger rubber–filler interactions, as evidenced by the highest G′ value at high strains in the Payne effect measurement. These interactions contribute to greater elasticity and, consequently, reduced energy dissipation. In the case of

samples with epoxy silane, it could be that the higher energy dissipation at higher energy is caused by the bonding and debonding of the different interactions present in the system. This result could be a hint that the amount of these non-covalent interactions is higher in the compounds with epoxy silane.

Figure 9 also shows that the resin has good compatibility with the rubber matrix. When a non-compatible resin is used, a second peak in the tan δ curve is typically observed [49–52]. Therefore, in this case, without having such a second peak, the resin presents a good compatibility with the SBR.

3.7. Re-Connectivity of Bonds

After the analysis of the effects of the new coupling system on the in-rubber properties, the best-performing compound was selected for further analysis of its reversible nature and a recyclability study. The chosen compound was AMR5, in which 3-Aminopropyltriethoxysilane was used as silane together with 5% resin. The selection of this compound was performed because it showed the best overall in-rubber performance from all the newly designed compounds tested.

- Study of the mechanical response of the compounds at high temperatures

The behavior of the new coupling at high temperatures was analyzed by testing the mechanical response of the compounds at 100 °C. The mechanical properties of the reference and the sample AMR5 are shown in Figure 10.

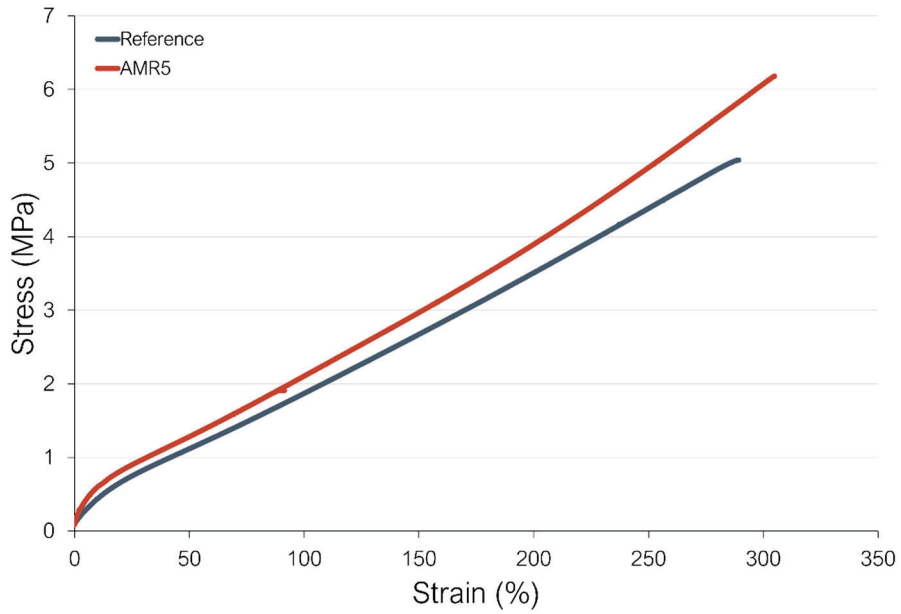

Figure 10. Stress–strain curves at 100 °C of the reference and AMR5.

As observed in Figure 10, the sample AMR5 shows higher moduli at 100 and 300% strain, tensile strength, and elongation at break at 100 °C than the reference. This improved mechanical performance at elevated temperatures could be caused by the reversible nature of the non-covalent interactions present in this system. When a connection is broken in the compound AMR5 due to the applied strain, it is possible to re-connect. This leads to observed higher resistance to applied strain at elevated temperatures than in the reference compound with TESPD.

- Creep experiments

In Figure 11, the results of the creep experiment at 100 °C are depicted.

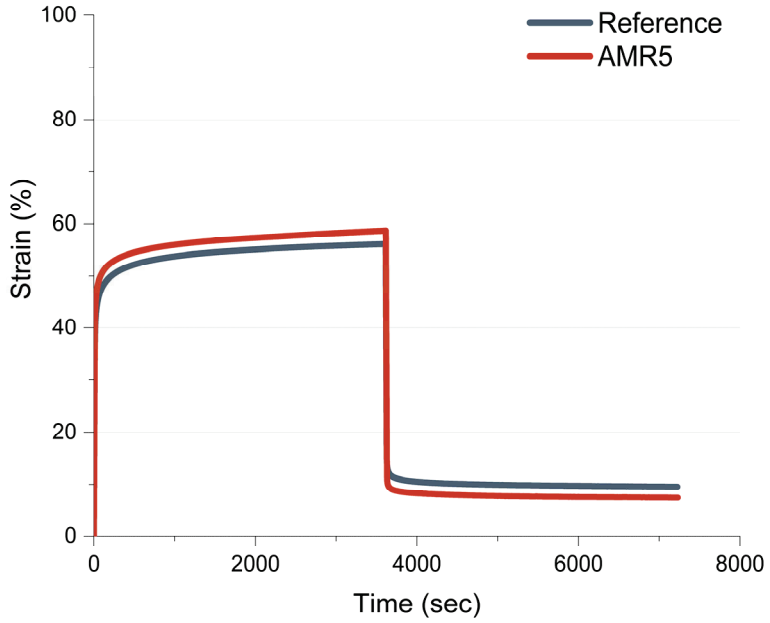

Figure 11. Variation in the strain during the creep experiments for the reference and AMR5.

When the initial force of 15 N is applied, the sample AMR5 reaches a slightly higher initial strain than the reference compound, approximately 50% for AMR5 and 47% for the reference. The stress is then maintained for one hour, in which the strain increases slowly until the stress is released. At this point, the sample AMR5 reaches a maximum strain of ~59% and the reference ~55%. Subsequently, when the stress is released, the compounds go back to their original shape. Both compounds almost regained their previous form. However, it can be observed that sample AMR5 shows a slightly higher recovery than the reference. This could indicate that the non-covalent interactions present in the new system provide the compound with a slightly higher thermo-mechanical fatigue resistance.

- Analysis of the changes in the dynamical properties after subjecting the vulcanizates to a cycling (fatigue) test

The dynamic properties of the selected compounds were analyzed before and after a fatigue test. Compound AMR5 and the reference were subjected to five tensile cycles, each stretched to 100% strain at 100 °C. Following this procedure, the dynamic properties were measured and compared with the values recorded before the cycling test. Figure 12 shows the evolution of the loss factor with temperature. Table 5 depicts the values of tan δ at 0 and 60 degrees.

Table 5. Values of tan δ at 60 °C and 0 °C of the studied compounds before and after the thermo-mechanical treatment.

Compound	tan δ at 60 °C	tan δ at 60 °C After Cycling 5 Times at 100 °C	tan δ at 0 °C	tan δ at 0 °C After Cycling 5 Times at 100 °C
Reference	0.169	0.203	0.352	0.244
AMR5	0.164	0.192	0.266	0.299

As depicted in Figure 12, the variations between the curves before and after fatigue testing are less pronounced for the AMR5 sample compared to the reference compound. For the reference compound, the rolling resistance (RR) indicator rose by approximately 20%, while the wet grip (WG) indicator dropped by around 30%. In comparison, the AMR5 sample

showed a 17% increase in the RR indicator and a 12% rise in the WG indicator. The compound with the new coupling shows better wet grip and rolling resistance indicators after the cycling test than the reference with TESPD. This suggests that the new coupling offers better resistance to higher temperatures and fatigue than the conventional silica/silane coupling.

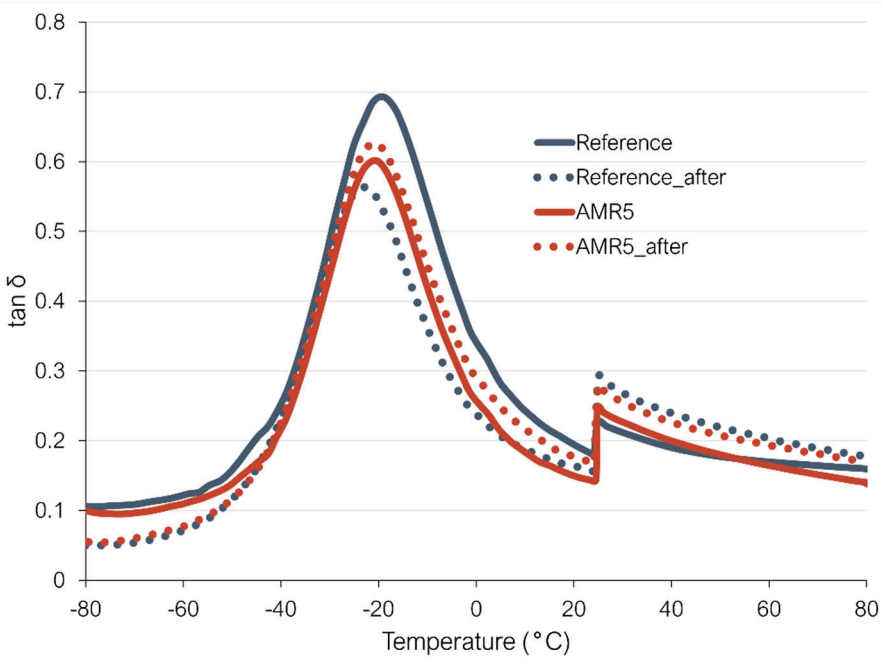

Figure 12. Variation in the loss factor as a function of temperature before and after the thermo-mechanical treatment (the sharp drop in the loss factor at 25 °C is caused by the increase in applied strain).

3.8. Recycling Study

One of the main goals of the development of a new coupling based on non-covalent interactions is to facilitate the recyclability of silica-filled rubber compounds. In order to explore the advantages of the new coupling regarding recyclability, a recycling study was conducted with samples AMR5 and the reference. The primary objective of this test is to determine whether the introduction of a reversible coupling positively influences the recyclability of the rubber compounds. The samples were subjected to a mechanical treatment in which they were ground to smooth its incorporation into virgin rubber compounds as explained in the experimental section of this manuscript. Figure 13 depicts the curing behavior, the Payne effect, stress/strain curves, and the loss factor as a function of temperature of the compounds containing ground rubber material in comparison with the original compounds. In both cases, the ground particles are included in a compound of the same composition as the ground rubber, e.g., AMR5 ground particles were included in the virgin AMR5 compound. As can be seen, all the compounds containing ground rubber show a deterioration in the in-rubber properties. Such behavior was reported in previous studies [6,7,10].

Figure 13a presents the cure curves for the compounds. AMR5_ground exhibits a higher maximum torque than AMR5, while the opposite is true for the reference compound, where the compound with ground rubber shows a decrease in this parameter. As discussed before, the maximum torque can be related to the CLD, filler–filler and polymer–filler interactions. In the case of AMR5_ground, the increase in M_H could be caused by a combination of both, a higher CLD and an increase in all the interactions present in this system. For the reference compound, most likely the decrease in the maximum torque is caused by a decrease in the CLD. In a previous study [52], it was reported that the

presence of ground rubber particles causes diffusion of sulfur towards these ground rubber particles. This phenomenon leads to an inhomogeneous distribution of the sulfur in the rubber samples and therefore an inhomogeneous CLD. This behavior could be less pronounced in the samples with the new coupling because the penetration of the sulfur is more difficult than in the reference compound. This can be explained by a higher overall network (crosslinks, filler–filler, and polymer filler interactions) in these samples, due to the possible reformation of the non-covalent interactions after breaking them during the grinding process.

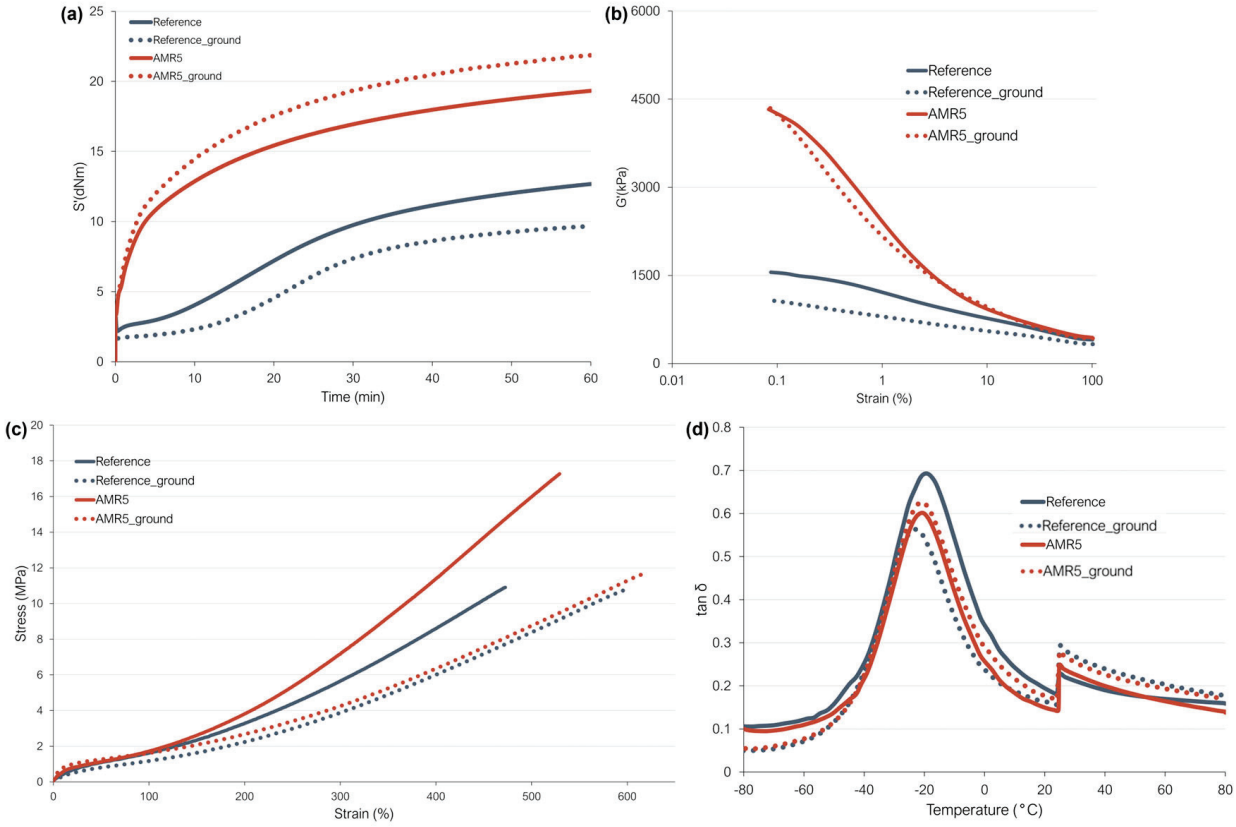

Figure 13. (**a**) Vulcanization curves, (**b**) Payne effect plots, (**c**) stress–strain curves and (**d**) variation in the loss factor as a function of temperature of the compounds analyzed in the recyclability study.

In Figure 13b, the Payne effect curves are depicted. Sample AMR5 with ground material shows a similar Payne effect compared to its original counterpart. However, as previously considered, it is also possible that the Payne effect in these samples is a combination of both the breakdown of the filler network and the break of the non-covalent bonds present in the system. It might be possible that in sample AMR5_ground also the non-covalent interactions present are breaking with the applied strain. In the case of the reference, a significant decrease in the Payne effect is observed. This phenomenon can be attributed to the reduced quantity of fillers in these compounds. In the sample containing ground material, 15 phr of the silica filler was replaced by ground rubber. Since this material consists of rubber, fillers, curatives, and other components, the overall filler content in the compounds that include ground rubber is lower than in the original compound. This reduction results in decreased particle–particle interactions, which in turn leads to a reduced Payne effect.

The mechanical performance of the samples is shown in Figure 13c and Table 6. It can be seen that the compounds with ground material show a significant worsening of the mechanical properties. As explained before, this can also be caused by the inhomogeneity in

CLD caused by the sulfur diffusion to the ground particles [53]. This behavior occurs in both the reference and the sample with the new coupling system. However, the deterioration of the mechanical performance is more pronounced in the sample with the new coupling system. The higher degree of deterioration of the properties for the sample AMR5_ground could be explained in addition by a worse micro-dispersion in this sample as observed by the Payne effect results.

Table 6. Mechanical properties of the compounds analyzed in the devulcanization study.

Compound	Reinforcement Index ($M_{300\%}/M_{100\%}$)	T_s (MPa)	ε_b (%)
Reference	3.6 ± 0.12	11.6 ± 1.8	470 ± 60
Reference_ground	3.2 ± 0.12	10.7 ± 1.0	630 ±30
AMR5	3.6 ± 0.1	17.5 ± 0.7	600 ± 80
AMR5_ground	3.1 ± 0.2	9.5 ± 0.3	620 ± 40

Lastly, the dynamical mechanical properties of the compounds were analyzed. The loss factor as a function of temperature of the studied samples is shown in Figure 13d. As with the other properties, significant changes can be observed in the samples with ground material. However, in the case of the sample AMR5, the changes in the tan δ curve are smaller than in the reference compound. As mentioned before, the changes in the dynamical properties can be explained by the diffusion of sulfur to the ground particles [53] that is less prominent for the samples with the new coupling.

4. Conclusions

This study explores the development of a new silica/rubber coupling mechanism based on non-covalent interactions. The silica surface was modified with phenolic resin, which was grafted onto silica by reacting with silane that had previously interacted with the silica surface. Two different silanes were analyzed, 3-Aminopropyltriethoxysilane and 3-Glycidyloxypropyltrimethoxysilane. The modification of silica was performed during the mixing of the rubber compounds. The in-rubber results of the compounds containing the new coupling were compared to a conventional silica/silane system with TESPD.

This work revealed that the implementation of this novel coupling based on non-covalent interactions using amino silane and 5% of resin (sample AMR5) leads to an improvement in crosslink density, mechanical performance, and rolling resistance indicator. Tensile test results showed that the samples containing amino silane exhibit superior modulus, tensile strength, and elongation at break compared to the reference, indicating more efficient stress transfer between the filler and rubber matrix, likely due to enhanced filler dispersion and stronger interfacial interactions. Furthermore, these samples also show a promising dynamic behavior, with similar energy dissipation at 60 degrees (rolling resistance indicator) than the reference. However, the use of the new coupling has a negative effect on the Payne effect. Nevertheless, it is possible that the breaking and re-connection of the non-covalent interactions present in these systems is contributing to the higher values of the Payne effect. The improvement in the properties of the new compounds can be explained by the presence of a high number of additional interactions and a good compatibility of the phenolic resin with the rubber matrix. The new coupling also exhibits a reversible nature, which results in better performance when tested at high temperatures and after being subjected to mechanical fatigue. The creep testing supported this theory, showing thar under prolonged loading the new compound had reduced permanent deformation. Furthermore, the new coupling also shows encouraging results

in the recyclability study, with a smaller deterioration of the properties compared to the virgin material.

This work shows the capability of the use of non-covalent interactions to develop a new silica/rubber coupling. This system has the potential to be optimized to obtain a higher improvement in rubber performance and recyclability.

Author Contributions: Conceptualization, P.B.-O., R.A. and A.B.; Methodology, P.B.-O., R.A., R.d.R., C.A. and A.B.; Validation, R.A. and A.B.; Formal analysis, P.B.-O.; Investigation, P.B.-O., R.A., R.d.R., C.A. and A.B.; Resources, R.d.R. and A.B.; Data curation, P.B.-O.; Writing—original draft, P.B.-O.; Writing—review & editing, R.A., C.A. and A.B.; Visualization, P.B.-O. and A.B.; Supervision, R.A., R.d.R., C.A. and A.B.; Project administration, R.d.R., C.A. and A.B.; Funding acquisition, R.d.R. and A.B. All authors have read and agreed to the published version of the manuscript.

Funding: This research was funded by Bridgestone EU NV/SA, Italian Branch—Technical Center.

Institutional Review Board Statement: Not applicable.

Data Availability Statement: Data are contained within the article.

Conflicts of Interest: Author Claudia Aurisicchio was employed by the company Bridgestone EU NV/SA. The remaining authors declare that the research was conducted in the absence of any commercial or financial relationships that could be construed as a potential conflict of interest.

References

1. Ramarad, S.; Khalid, M.; Ratnam, C.T.; Chuah, A.L.; Rashmi, W. Waste Tire Rubber in Polymer Blends: A Review on the Evolution, Properties and Future. *Prog. Mater. Sci.* **2015**, *72*, 100–140. [CrossRef]
2. Araujo-Morera, J.; Verdejo, R.; López-Manchado, M.A.; Hernández Santana, M. Sustainable Mobility: The Route of Tires through the Circular Economy Model. *Waste Manag.* **2021**, *126*, 309–322. [CrossRef] [PubMed]
3. Grammelis, P.; Margaritis, N.; Dallas, P.; Rakopoulos, D.; Mavrias, G. A Review on Management of End of Life Tires (Elts) and Alternative Uses of Textile Fibers. *Energies* **2021**, *14*, 571. [CrossRef]
4. Shulman, V.L. Tire Recycling. In *Waste*; Elsevier: Amsterdam, The Netherlands, 2019; pp. 489–515.
5. De, S.K.; Isayev, A.I.; Khait, K. Rubber Recycling. *Choice Rev. Online* **2006**, *43*, 43–2826. [CrossRef]
6. Kumar, A.; Dhanorkar, R.J.; Mohanty, S.; Gupta, V.K. Advances in Recycling of Waste Vulcanized Rubber Products via Different Sustainable Approaches. *Mater. Adv.* **2024**, *5*, 7584–7600. [CrossRef]
7. van Hoek, H. *Closing the Loop: Reuse of Devulcanized Rubber in New Tires*; University of Twente: Enschede, The Netherlands, 2022.
8. Bockstal, L.; Berchem, T.; Schmetz, Q.; Richel, A. Devulcanisation and Reclaiming of Tires and Rubber by Physical and Chemical Processes: A Review. *J. Clean. Prod.* **2019**, *236*, 117574. [CrossRef]
9. Anjum, A.; Ramani, B.; Bramer, E.; Brem, G.; Dierkes, W.; Blume, A. Role of Recovered Carbon Black Ash Content Composition on In-Rubber Performance. In Proceedings of the International Rubber Conference, IRC 2019, London, UK, 3–5 September 2019.
10. Wiśniewska, P.; Haponiuk, J.T.; Colom, X.; Saeb, M.R. Green Approaches in Rubber Recycling Technologies: Present Status and Future Perspective. *ACS Sustain. Chem. Eng.* **2023**, *11*, 8706–8726. [CrossRef]
11. Dannenberg, E.M. The Effects of Surface Chemical Interactions on the Properties of Filler-Reinforced Rubbers. *Rubber Chem. Technol.* **1975**, *48*, 410–444. [CrossRef]
12. Collins, J.M.; Jackson, W.L.; Oubridge, P.S. Relevance of Elastic and Loss Moduli of Tire Components to Tire Energy Losses. *Rubber Chem. Technol.* **1965**, *38*, 400–414. [CrossRef]
13. Waddell, W.H.; Evans, L.R. Use of Nonblack Fillers in Tire Compounds. *Rubber Chem. Technol.* **1996**, *69*, 377–423. [CrossRef]
14. Mittal, K.L. *Silanes and Other Coupling Agents*; Brill Academic Pub: Leiden, The Netherlands, 2007; Volume 4, ISBN 9789047414025.
15. Goerl, U.; Hunsche, A.; Mueller, A.; Koban, H.G. Investigations into the Silica/Silane Reaction System. *Rubber Chem. Technol.* **1997**, *70*, 608–623. [CrossRef]
16. Blume, A. Kinetics of the Silica-Silane Reaction. *KGK Kautsch. Gummi Kunststoffe* **2011**, *64*, 38–43.
17. Anyszka, R.; Beton, K.; Szczechowicz, M.; Bielinski, D.M.; Blume, A. Velcro-Inspired Supramolecular System for Silica-Rubber Coupling. *Rubber Chem. Technol.* **2020**, *93*, 672–682. [CrossRef]
18. Bernal-Ortega, P.; Anyszka, R.; Gojzewski, H.; di Ronza, R.; Aurisicchio, C.; L Valentín, J.; M Salamanca, F.; Blume, A. New Silica/Polymer Coupling by the Use of Cation-π Interactions. *Ind. Eng. Chem. Res.* **2024**, *63*, 3525–3538. [CrossRef]
19. Li, L.; Kim, J.K. Thermoreversible Cross-Linking Maleic Anhydride Grafted Chlorobutyl Rubber with Hydrogen Bonds (Combined with Ionic Interactions). *Rubber Chem. Technol.* **2014**, *87*, 459–470. [CrossRef]

20. Jiang, Z.; Bhaskaran, A.; Aitken, H.M.; Shackleford, I.C.G.; Connal, L.A. Using Synergistic Multiple Dynamic Bonds to Construct Polymers with Engineered Properties. *Macromol. Rapid Commun.* **2019**, *40*, e1900038. [CrossRef]
21. Wojtecki, R.J.; Meador, M.A.; Rowan, S.J. Using the Dynamic Bond to Access Macroscopically Responsive Structurally Dynamic Polymers. *Nat. Mater.* **2011**, *10*, 14–27. [CrossRef]
22. Wang, D.; Zhang, H.; Cheng, B.; Qian, Z.; Liu, W.; Zhao, N.; Xu, J. Dynamic Cross-Links to Facilitate Recyclable Polybutadiene Elastomer with Excellent Toughness and Stretchability. *J. Polym. Sci. A Polym. Chem.* **2016**, *54*, 1357–1366. [CrossRef]
23. Wemyss, A.M.; Bowen, C.; Plesse, C.; Vancaeyzeele, C.; Nguyen, G.T.M.; Vidal, F.; Wan, C. Dynamic Crosslinked Rubbers for a Green Future: A Material Perspective. *Mater. Sci. Eng. R Rep.* **2020**, *141*, 100561. [CrossRef]
24. Bernal-Ortega, P.; Anyszka, R.; di Ronza, R.; Aurisicchio, C.; Blume, A. Dynamic Imine Bonds in Tire Tread Compounds: A Pathway to a Circular Economy and Reduced Waste. *ACS Sustain. Chem. Eng.* **2025**, *13*, 3209–3221. [CrossRef]
25. Zou, W.; Dong, J.; Luo, Y.; Zhao, Q.; Xie, T. Dynamic Covalent Polymer Networks: From Old Chemistry to Modern Day Innovations. *Adv. Mater.* **2017**, *29*, 1606100. [CrossRef]
26. Sattar, M.A.; Gangadharan, S.; Patnaik, A. Design of Dual Hybrid Network Natural Rubber-SiO2 Elastomers with Tailored Mechanical and Self-Healing Properties. *ACS Omega* **2019**, *4*, 10939–10949. [CrossRef]
27. Deng, Y.; Zhang, Q.; Feringa, B.L. Dynamic Chemistry Toolbox for Advanced Sustainable Materials. *Adv. Sci.* **2024**, *11*, e2308666. [CrossRef]
28. Berki, P.; Khang, D.Q.; Minh, D.Q.; Hai, L.N.; Tung, N.T.; Karger-Kocsis, J. Interphase Tailoring via π-Cation Interaction in Graphene and Graphene Oxide Containing NR Nanocomposites Prepared by Latex Compounding. *Polym. Test.* **2018**, *67*, 46–54. [CrossRef]
29. Ibeh, C.C. Phenol-Formaldehyde Resins. *Handb. Thermoset Plast.* **1998**, *2*, 23–71.
30. Santos, C.; Santos, T.; Fonseca, R.; Melo, K.; Aquino, M. Phenolic Resin and Its Derivatives. In *Phenolic Polymers Based Composite Materials*; Jawaid, M., Asim, M., Eds.; Springer: Singapore, 2021; pp. 1–11. ISBN 978-981-15-8932-4.
31. Gardziella, A.; Pilato, L.A.; Knop, A. *Phenolic Resins: Chemistry, Applications, Standardization, Safety and Ecology*; Springer Science & Business Media: Cham, Switzerland, 2013; ISBN 3662041014.
32. Pilato, L. *Phenolic Resins: A Century of Progress*; SpringerLink: Springer e-Books; Springer: Berlin/Heidelberg, Germany, 2010; ISBN 9783642047145.
33. Shojaei, A.; Faghihi, M. Physico-Mechanical Properties and Thermal Stability of Thermoset Nanocomposites Based on Styrene-Butadiene Rubber/Phenolic Resin Blend. *Mater. Sci. Eng. A* **2010**, *527*, 917–926. [CrossRef]
34. Kaynak, C.; Cagatay, O. Rubber Toughening of Phenolic Resin by Using Nitrile Rubber and Amino Silane. *Polym. Test.* **2006**, *25*, 296–305. [CrossRef]
35. Guo, Y.; Hu, L.; Jia, P.; Zhang, B.; Zhou, Y. Enhancement of Thermal Stability and Chemical Reactivity of Phenolic Resin Ameliorated by NanoSiO2. *Korean J. Chem. Eng.* **2017**, *35*, 298–302. [CrossRef]
36. Ming, L.Y.; Feng, C.P.; Siddig, E.A.A. Effect of Phenolic Resin on the Performance of the Styrene-Butadiene Rubber Modified Asphalt. *Constr. Build. Mater.* **2018**, *181*, 465–473. [CrossRef]
37. Flory, P.J.; Rehner, J. Statistical Mechanics of Cross-Linked Polymer Networks II. Swelling. *J. Chem. Phys.* **1943**, *11*, 521–526. [CrossRef]
38. *ISO 37:2024*; Rubber, Vulcanized or Thermoplastic—Determination of Tensile Stress-Strain Properties. ISO: Geneva, Switzerland, 2024.
39. *ASTM D412-16(2021)*; Standard Test Methods for Vulcanized Rubber and Thermoplastic Elastomers—Tension. ASTM: West Conshohocken, PA, USA, 2021.
40. Sivolapov, P.; Myronyuk, O.; Baklan, D. Synthesis of Stober silica nanoparticles in solvent environments with different Hansen solubility parameters. *Inorg. Chem. Commun.* **2022**, *143*, 109769. [CrossRef]
41. Hayichelaeh, C.; Reuvekamp, L.A.E.M.; Dierkes, W.K.; Blume, A.; Noordermeer, J.W.M.; Sahakaro, K. Reinforcementof Natural Rubber by Silica/Silane in Dependence of Different Amine Types. *Rubber Chem. Technol.* **2017**, *90*, 651–666. [CrossRef]
42. Krebs, H. The Mechanism of Accelerator Action. *Rubber Chem. Technol.* **1957**, *30*, 962–971. [CrossRef]
43. Grunert, F. *Analytical Method Development to Predict the In-Rubber Dispersibility of Silica*; University of Twente: Enschede, The Netherlands, 2018; ISBN 9789036546553.
44. Jin, J.; Kaewsakul, W.; Noordermeer, J.W.M.; Dierkes, W.K.; Blume, A. The Relation between Macro- and Micro-Dispersion of Silica Filler in Rubber Matrix. In Proceedings of the International Rubber Conference, London, UK, 3–5 September 2019; IRC: London, UK, 2019; pp. 1–8.
45. Jin, J.; Kaewsakul, W.; Noordermeer, J.W.M.; Dierkes, W.K.; Blume, A. Macro- and Micro-Dispersion of Silica in Tire Tread Compounds: Are They Related? *Rubber Chem. Technol.* **2021**, *94*, 355–375. [CrossRef]
46. Yamada, C. *Influence of Functionalized S–SBR on Silica–Filled Rubber Compound Properties*; University of Twente: Enschede, The Netherlands, 2023.
47. Conant, F.S. Tire Temperatures. *Rubber Chem. Technol.* **1971**, *44*, 397–439. [CrossRef]

48. Heinz, M. Customer Seminar—Dynamic Testing of Rubber—An Introduction. 2018.
49. Indriasari; Noordermeer, J.; Dierkes, W. Incorporation of Oligomeric Hydrocarbon Resins for Improving the Properties of Aircraft Tire Retreads. *Appl. Sci.* **2021**, *11*, 9834. [CrossRef]
50. Vleugels, N.; Pille-Wolf, W.; Dierkes, W.K.; Noordermeer, J.W.M. Understanding the Influence of Oligomeric Resins on Traction and Rolling Resistance of Silica-Reinforced Tire Treads. *Rubber Chem. Technol.* **2015**, *88*, 65–79. [CrossRef]
51. Bernal-Ortega, P.; van Elburg, F.; Araujo-Morera, J.; Gojzewski, H.; Blume, A. Heading towards a Fully Sustainable Tire Tread Compound: Use of Bio-Based Resins. *Polym. Test.* **2024**, *133*, 108406. [CrossRef]
52. Bernal-Ortega, P.; Gaillard, E.; van Elburg, F.; Blume, A. Use of Hydrocarbon Resins as an Alternative to TDAE Oil in Tire Tread Compounds. *Polym. Test.* **2023**, *126*, 108168. [CrossRef]
53. Frosch, S.; Herrmann, V.; Grunert, F.; Blume, A. Quantification of Sulfur Distribution on Rubber Surfaces by Means of μ-X-Ray Fluorescence Analysis. *Polym. Test.* **2023**, *128*, 108237. [CrossRef]

polymers

MDPI

Article

Effect of Proteins on the Network Formation and Degradation of Peroxide Cross-Linked Natural Rubber Elucidated by Time-Domain NMR

Adun Nimpaiboon [1,2], Antonio González-Jiménez [3,4], Roberto Pérez-Aparicio [5], Fernando Martín-Salamanca [5], Zenen Zepeda-Rodríguez [5], Juan López-Valentín [5,*] and Jitladda Sakdapipanich [6,*]

[1] Rubber Technology Research Centre (RTEC), Faculty of Science, Mahidol University, Nakhon Pathom 73170, Thailand; adun.nim@mahidol.ac.th
[2] Department of Chemistry and Center of Excellence for Innovation in Chemistry, Faculty of Science, Mahidol University, Bangkok 10400, Thailand
[3] Plastic Research Center (AIMPLAS), València Parc Tecnològic, C/Gustave Eiffel 4, 46980 Paterna, Spain; angonzalez@aimplas.es
[4] Escuela Superior de Ingeniería y Tecnología (ESIT), Universidad Internacional de La Rioja (UNIR), Av. de la Paz 137, 26006 Logroño, Spain
[5] Institute of Polymer Science and Technology (CSIC), C/Juan de la Cierva 3, 2800 Madrid, Spain; rperezaparicio@gmail.com (R.P.-A.); fms@ictp.csic.es (F.M.-S.); zenen@ictp.csic.es (Z.Z.-R.)
[6] Department of Chemistry and Center of Excellence for Innovation in Chemistry, Faculty of Science, Mahidol University, Nakhon Pathom 73170, Thailand
* Correspondence: jlvalentin@ictp.csic.es (J.L.-V.); jitladda.sak@mahidol.ac.th (J.S.)

Abstract

The importance of sustainable polymers has increased greatly in the last years since most polymers are derived from non-renewable sources. Sustainable polymers (i.e., biopolymers) such as natural rubber (NR) are proposed as a solution for this concern. A comparative study between NR and deproteinized NR (DPNR) was carried out to elucidate the role of proteins on the network formation and degradation of peroxide cross-linked NR using time-domain NMR experiments. The ^{1}H multiple-quantum (MQ) NMR experiments provided information on the cross-link density and its spatial distribution, while the actual fraction of non-coupled network defects was obtained by exploiting the Hahn echo approach measured on swollen samples. The results showed that proteins influenced the network formation during the vulcanization process of NR, leading to a higher number of non-elastic network defects and promoting the creation of additional cross-links with a broader spatial distribution. The formation of network heterogeneities in different length scales deeply influences the mechanical properties of NR samples. On the other hand, the proteins showed a pro-oxidant activity on the degradation behavior by accelerating the degradation process of peroxide cross-linked NR.

Keywords: biopolymers; natural rubber; proteins; sustainability; multiple-quantum NMR

1. Introduction

Sustainable rubbers are natural materials or materials derived from renewable, recycled, and waste carbon resources and their combinations, which at the end of life can be recycled, biodegraded, or composted [1–3]. Sustainable rubbers also exhibit a reduced environmental impact throughout their life cycle. Biopolymers can be derived from renewable resources, or they can be partially made from renewables and synthesized like

traditional polymers, as in the case of bio-based polymers [4]. Rubber from *Hevea brasiliensis*, known as natural rubber (NR), has been recognized as the most important biopolymer in the rubber industry, although more than 2000 species of plants and fungi have also been found to produce rubber hydrocarbon. NR is a very high-molecular-weight and long-chain branched biopolymer, composed primarily of *cis*-1,4-polyisoprene containing about 6% of non-rubber constituents such as proteins, lipids, carbohydrates, and other ingredients [5]. NR is a unique material for many industrial as well as medical applications, such as aircraft and truck tires, surgical gloves, and condoms, owing to its superior crack growth resistance and excellent tensile properties in comparison with other naturally occurring and synthetic polyisoprenes. The structural characterization of NR using high-resolution ^{13}C and ^{1}H NMR revealed that the fundamental structure of NR is long-chain isoprene units with end-groups, i.e., with initiating ω-terminal groups and terminating α-terminal groups. The ω-terminal group is not revealed yet but has been presumed to interact with proteins [6,7]. The α-terminal group is proposed as mono- or di-phosphate linked with phospholipids [8,9]. These findings suggest that the interaction of proteins and lipids at the molecular chain ends of NR possibly forms a three-dimensional pseudo-end-linked network, contributing to the numerous characteristics of un-vulcanized NR, such as gel formation [7,10] or strain-induced crystallization [11]. Therefore, proteins are one of the essential components believed to bring about these marvelous properties of NR. However, some proteins exuding from NR products are found to be associated with the severe allergic reactions termed a *Type I* allergy, which is potentially serious or even life-threatening. The U. S. Food and Drug Administration (FDA) issued a medical alert to rubber device producers in 1991 after a number of patients died of this protein allergy [12]. Proteins in latex can usually be removed by the enzymatic decomposition of proteins in the presence of surfactant, followed by centrifugation [11,13,14].

The cross-linking process of rubber is generally known as vulcanization, where three-dimensional networks are formed by chemical or physical methods [15,16]. The most useful vulcanizing systems in rubber technology are sulfur/accelerator systems and organic peroxides [17–21]. The role of proteins on cross-linked NR was studied based on accelerated sulfur systems. It was proven that the proteins and nitrogenous compounds in NR act as natural accelerators for sulfur vulcanization [22], as evidenced by the deproteinized NR (DPNR) that demonstrates a slower cure as well as a lower cross-link density compared to raw NR. In addition, the proteins play a strong role in the network structure and distribution of the three types of sulfidic cross-linking [22]. Peroxide vulcanization is preferred in some applications due to the good heat resistance, low compression set, and high transparency of NR products. Moreover, the absence of some additives offers a solution for solving the nitrosamine contamination as a carcinogen and *Type IV* allergy (allergic contact dermatitis) caused by the amine-based accelerators in sulfur vulcanization [23]. As the peroxide vulcanization process takes place via a radical mechanism, the proteins in NR that might associate with radicals need to be clarified.

Several techniques such as inverse gas chromatography [24], osmometry [25], mechanical analysis [26], equilibrium swelling experiments [27], dielectric measurements [28], high-resolution solid-state NMR [29,30], or scattering techniques [31,32] have been used to partially elucidate the network structure of elastomers. Recently, time-domain solid-state NMR has been shown to be a robust and versatile technique to obtain direct and local evidence about the different parameters that define the polymer network structure [33–39]. This is based on the direct measurement of residual dipolar couplings that persist because of the presence of cross-links and other topological constraints, such as entanglements, that restrict the number of accessible segmental conformations, which leads to local chain ordering caused by the non-isotropic fast segmental motions. Many NMR experiments,

e.g., ^{1}H transverse relaxation [40], two-dimensional (2D) magnetization exchange spectroscopy [41], and Hahn, together with solid echoes [42], were used to determine various parameters controlled by residual dipolar couplings. Nevertheless, it is already well known that ^{1}H double-quantum (DQ) (or more generally multiple-quantum, MQ) NMR can be considered the most quantitative and reliable method for the measurement of weak residual dipolar couplings [37,43]. By suitable data analysis, the coherent dipolar effect, related to the number of constraints and their spatial distribution (inhomogeneities), could be independently separated from the temperature-dependent segmental dynamics for rubber networks [37].

The aim of this work is to study the role of proteins in the network formation and degradation process of NR vulcanized with an organic peroxide system by means of different time-domain NMR experiments performed in low-field spectrometers. In this sense, the ^{1}H MQ-NMR experiment was used to evaluate the evolution of cross-link density and the spatial distribution of cross-links for NR and DPNR samples during the peroxide vulcanization as well as during the degradation process. Additionally, the actual fraction of non-coupled network defects, e.g., free chain ends, dangling chain ends, or loops, was obtained by applying Hahn echo experiments on swollen samples with deuterated solvent. The contributions of those proteins to the network structure and its influence on the network formation in NR is crucial to determine quantitative knowledge about the most important biopolymer in the rubber industry.

2. Experimentation

2.1. Sample Preparation

NR was prepared by diluting fresh NR (FNR) latex to 30% dry rubber content (DRC) and adding 1% (*w*/*v*) formic acid to coagulate the latex. The coagulum was rinsed with water several times and then dried in an oven at 70 °C for 24 h.

DPNR was carried out by incubating 30% DRC of the FNR latex with 0.04% (*w*/*v*) proteolytic enzyme (KP-3939, Kao Co., Tokyo, Japan) and 1% (*w*/*v*) sodium dodecyl sulfate (SDS) at 37 °C for 12 h, followed by centrifugation twice. The cream phase was cast on a glass plate and dried under the same method as the NR.

The NR and DPNR were compounded with 1 part per hundred rubber (phr) of dicumyl peroxide (DCP) in an open two-roll mill using the standard procedure and then vulcanized by compression molding at 160 °C by varying times.

2.2. Characterization

The protein content was measured using nitrogen analysis using a LECO Nitrogen Analyzer (model FP 528) (LECO, St. Joseph, MO, USA) and generally calculated using a universal conversion factor of 6.25.

The content of the long-chain fatty acid ester group was determined by FTIR measurements based upon a calibration using a series of mixtures of methyl stearate and synthetic *cis*-1,4-polyisoprene (Kuraprene IR10). The quantity of fatty acid ester groups per weight of rubber was determined by the intensity ratio of the bands at 1739 cm^{-1} (C=O) to 1664 cm^{-1} (C=C).

The quantitative analysis of the metal content was determined by inductively coupled plasma atomic emission spectroscopy (ICP-AES).

The cure behavior and the optimum cure time (t_{95}) were monitored by the Rubber Process Analyzer (RPA) (Alpha Technologies® RPA 2000™, Heilbronn, Germany), where t_{95} is the time required for the torque of the rheometer to increase up to 95% of the total torque at 160 °C.

The time-domain proton NMR experiments were performed on a Bruker minispec mq20 spectrometer (Bruker, Billerica, MA, USA) operating at a resonance frequency of 20 MHz, with a 90° pulse length of 3 μs and a dead time of 12 μs. The sample temperature was controlled with an air-operated BVT3000 heater (Bruker, Billerica, MA, USA).

The tensile tests were performed on type 2 dumbbell specimens according to ISO 37 in an Instron model 3365 dynamometer (Instron, Norwood, AR, USA) equipped with a video camera to measure deformations at a strain rate of 500 mm/min.

2.2.1. ^{1}H DQ-NMR Experiment

Time-domain ^{1}H DQ-NMR spectroscopy is based on the measurement of the residual dipolar couplings (NMR observable) between protons originating from the orientational anisotropy due to constraints, such as cross-links and entanglements. Such local anisotropy can be described by a non-zero dynamical orientation of the polymer backbone $\langle P_2(\cos\theta)\rangle$ (second-order Legendre polynomial). The NMR experiments are in the timescale related to the length R and orientation α of the end-to-end vector. Assuming a freely jointed rigid rod chain model, the average segment orientation is as follows:

$$\langle P_2(\cos\theta)\rangle \approx \frac{3}{5}\frac{R^2}{N^2b^2}\frac{3\cos^2\alpha - 1}{2} \approx S_b\frac{3\cos^2\alpha - 1}{2} \quad (1)$$

where N is the number of statistical segments between constraints and b is the statistical segment length. The overall NMR signal is the contribution of the individual monomer or segment signals, which are at least partially time-averaged over the distribution of the end-to-end vectors between constraints. From this, an average value of the local backbone orientation, S_b, with respect to the end-to-end vector, arises (Equation (1)). For ideal chains $R^2 \approx Nb^2$, it may be written as follows:

$$S_b \approx \frac{3}{5}\frac{R^2}{N^2b^2} \propto \frac{1}{N} \approx v \quad (2)$$

being proportional to the constraint density v. Since the proton dipolar coupling depends on molecular orientation, S_b is detected in NMR because it gives a non-zero residual dipolar coupling and, then, is calculated from the experimental average residual dipolar coupling constant D_{res}, by comparison with its static counterpart, D_{stat}, as follows (k is a correction factor <1 accounting for the spin arrangement and motions within a statistical segment):

$$S_b = k\frac{D_{res}}{D_{stat}} \quad (3)$$

According to Equations (2) and (3), D_{res} is inversely proportional to the average molecular weight of the rubber chains between constraints M_x. There are different models [44] that describe the contribution of cross-links (M_c) and entanglements (M_e) to the NMR observable (D_{res}) and the measured order parameter (S_b). Assuming the additivity of entanglement and cross-link constraints [45,46], we may write $D_{res} \propto 1/M_c + 1/M_e$.

The ^{1}H DQ-NMR experiment technique is based on enhanced Baum–Pines pulse sequences [37,47]. The raw experimental data from such experiments need to be normalized in such a way that the temperature-independent network structure effect (at temperatures far above the T_g) can be separated from the temperature-dependent segmental dynamics without invoking any specific model, as was widely explained elsewhere [37,43,47]. A proper analysis of the NMR signals by means of a numerical inversion procedure based on the fast Tikhonov regularization analysis [48] provides the actual distribution of dipolar couplings that can be defined by the average apparent coupling constant D_{res}, and

the standard deviation, σ, characterizing the distribution width of the residual dipolar couplings.

From published spin dynamic simulations and assuming a reasonable model for the intra-segmental motions, the relationship between the experimental residual dipolar coupling constant, D_{res}, and the molecular weight between constraints, M_x, was obtained in the NR samples as the following equation [37]:

$$M_x^{(NR)} = \frac{617\ \text{Hz}}{D_{res}/2\pi}[\text{kg/mol}] \quad (4)$$

assuming a constant entanglement density (then, $M_x^{(NR)} \propto M_c^{(NR)}$), tetra-functional cross-links, and a phantom network model (to take into account the non-affinity of real systems at the scale of the cross-links) [49], the cross-link density, v_{NMR}, can be determined by $v_{NMR} = 1/M_c$.

2.2.2. Hahn Echo Experiments Measured on Swollen Samples

The fraction of non-coupled network defects has been investigated by ^{1}H DQ-NMR and Hahn echo experiments [37,49]. In the dry state, the fraction of non-coupled defects depends on temperature, and it is always underestimated because chain packing or topological constraints promote some restrictions in the fast-segmental motions of dangling chain segments and loops [43]. Thus, some fractions of network defects are, in fact, observed as dipolar coupled and elastically active segments because the slow arm retraction process is not able to relax the dangling chains in the experimental NMR timescale [50,51]. The topological restrictions are released, and the chain dynamics are speeded up by swelling the rubber networks with a suitable solvent, leading to fast isotropic motions. Consequently, the NMR experiments on the swollen samples provide a reliable measure of the actual fraction of non-coupled and elastically inactive network defects [49]. In the present work, the rubber samples were swollen in deuterated toluene at room temperature for 24 h in sealed dark vials in order to prevent them from degradation [27].

The complex thermodynamics and heterogeneous nature of the swelling process [27,52] hide substantial structural information from the stretched network, making nonsensical the use of complex DQ-NMR experiments to perform a deeper analysis of a direct signal that codifies the dipolar coupling information. For that reason, simpler Hahn echo experiments (which also have a dipolar origin for the transverse relaxation) were performed to identify and quantify the actual fraction of non-coupled polymer segments in the swollen samples.

3. Results and Discussion

3.1. Characterization of Rubber Samples

The characteristics of the rubber samples are given in Table 1. The NR samples contained 2.62% (w/w) of proteins that could be selectively removed by deproteinization, as evidenced by the very low protein content of DPNR. The ester content of the NR and DPNR, which represented the lipid part, showed similar values. The metal content (Cu^{2+}, Fe^{2+}, Mn^{2+}) of both the NR and DPNR, which strongly influences the radical mechanism [53], was negligible.

Table 1. The characteristics of the rubber samples.

Samples	Protein Content (% *w*/*w*)	Ester Content (mmol/kg-Rubber)	Metal Content (% *w*/*w*)		
			Cu^{2+}	Fe^{2+}	Mn^{2+}
NR	2.62	14.28	ND	0.0016	ND
DPNR	0.06	14.23	ND	0.0014	ND

3.2. Pseudo-End-Linked Network

Although the main goal of this work is to investigate the network structure formed by peroxide vulcanization, un-vulcanized NR also contains a pseudo-end-linked network that has been believed to bring about superior elastic properties rather than synthetic polyisoprene (IR) [54]. The cross-linking point of the end-linked network is classified into two types, i.e., (i) the intermolecular interaction of the proteins via hydrogen bonding at the initiating ω-terminal group [6,7] and (ii) the micelle formation or association of the polar head-groups of phospholipid molecules at the terminating α-terminal group [8,9]. Thus, the deproteinization process decomposes the network formed by the proteins in the DPNR, wherein the network derived from the phospholipids still remains. Additional trans-esterification treatment (explained in the Supplementary Information) removes the phospholipids and avoids the formation of the end-linked network. The proposed pseudo-end-linked network structure of NR, including the structural change after deproteinization and trans-esterification, can be seen in the Supplementary Information, Figure S1 [10].

In the un-vulcanized NR samples, the existence of the pseudo-end-linked network has been proved to cause an apparent increment in molecular weight and the related development of entanglements and their dependent properties [55]. In this sense, it is well known that D_{res} is sensitive and directly proportional to any constraints (independently of its nature) that restrict the segmental motion of polymer chains [56–58]. Therefore, ^{1}H DQ-NMR experiments have been successfully used to analyze the segmental autocorrelation function of un-vulcanized (linear melt) samples [59,60], which is dominated by the restrictions imposed by entanglements and topological constraints (caused by the polymer molecular weight and chain architecture). Note that D_{res} for a linear melt is an apparent quantity that depends on temperature and time. According to these statements, the variation in the average D_{res} for the different un-vulcanized samples studied in this work (see Figure 1) must be related to changes in the topological constraints and chain mobility.

Figure 1 shows the temperature dependence of the squared local backbone orientation parameter, S_b^2, which corresponds to the orientation autocorrelation function at the timescale of the DQ-NMR experiments for the un-vulcanized samples: u-NR, u-DPNR, trans esterified DPNR (u-TE-DPNR), and synthetic polyisoprene (u-IR). S_b^2 decreases in the chosen temperature range and the actual NMR experimental time window is related to changes in segmental conformations inside the constrained space caused by faster dynamics in the reputation regime [61], where the dimensions of the apparent tube are determined by the real molecular weight between entanglements, M_e, for each sample. In the case of u-NR and u-DPNR, they present higher S_b^2 values than the trans-esterified counterpart (u-TE-DPNR) at any temperature, which might reflect the presence of the pseudo-end-linked network that can promote higher anisotropy in the rubber motions. In this sense, the importance of phospholipids (absent in the u-TE-DPNR sample) on the formation of thermo-sensitive cross-link points should be more evident in comparison with the almost negligible effect that the proteins (u-DPNR) imposed on the chain motions of the u-NR sample. A synthetic u-IR sample was also investigated in order to compare it with the u-TE-DPNR sample. The differences between u-IR and u-TE-DPNR should be related to changes in the molecular weight. These results are completely aligned with the

elastic properties of these samples: u-NR and u-DPNR showed almost the same properties, while u-TE-DPNR was quite similar to u-IR [54]. It can be confirmed that the topological constraints in NR should be dominated by the entanglements and the pseudo-end-linked network derived from phospholipids (with an almost negligible contribution from proteins). In this sense, the actual molecular weight between junction points was not properly estimated in the un-vulcanized samples because (i) this pseudo-end-linked network was unstable at temperatures above 100 °C [62] and (ii) at temperatures below 100 °C, the segmental dynamics in NR and DPNR were not fast enough to average out all the available conformations according to the restrictions caused by them.

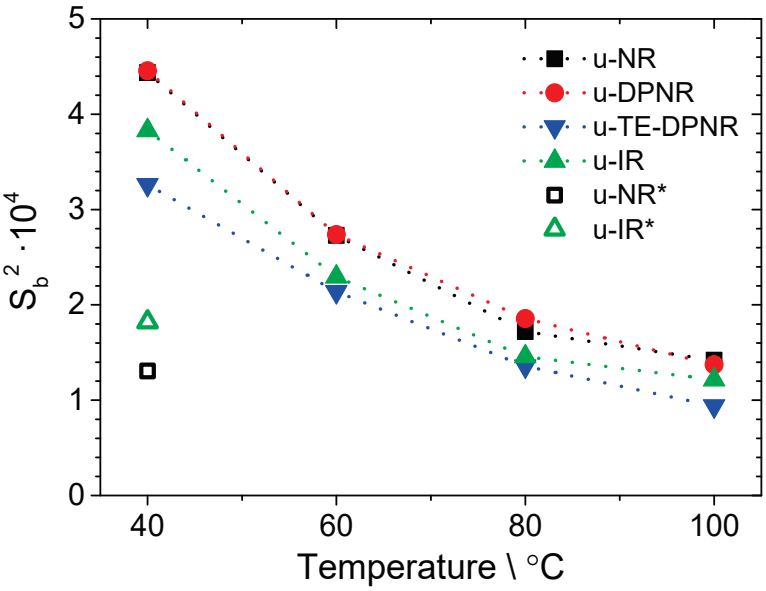

Figure 1. Temperature dependence of the squared local backbone orientation parameter (S_b^2) for un-vulcanized linear melt samples: natural rubber (u-NR), deproteinized natural rubber (u-DPNR), trans-esterified natural rubber DPNR (u-TE-DPNR), and synthetic polyisoprene (u-IR), respectively. On the other hand, u-NR* and u-IR* are samples subjected to mastication treatment on a two-roll mill for 15 min. The preparation details of the u-TE-DPNR and u-IR samples are explained in the Supplementary Information.

It is worth pointing out that those samples were not subjected to any mechanical treatment, unlike the vulcanized samples, which were masticated during their compounding. In order to consider these effects on the rubber samples, Figure 1 also shows the S_b^2 value for the natural rubber (u-NR*) and synthetic polyisoprene (u-IR*) samples (measured at 40 °C) after a mastication treatment on a two-roll mill for 15 min (equivalent to the compounding step on the vulcanized samples). The results indicate a stronger effect of the mechanical treatment on the rubber chain molecular weight and, hence, on the entanglement effect in the case of the u-NR* compared to the synthetic counterpart. These results could be related to the effect of mastication on the pseudo-end-linked network in natural rubber.

The temperature dependence of D_{res} for the un-vulcanized rubber samples (see Figure 1) was completely suppressed in the vulcanized samples (3 min at 160 °C) in the temperature range from 40 °C to 120 °C for both the NR and DPNR samples, as shown in Figure 2A. This means that the measuring temperature is far above the rubber T_g, and the segmental dynamics are fast enough to average out all the accessible conformations in the time window imposed by the NMR measurement [43]. Consequently, in those samples, D_{res} reflects the constraints that define the rubber network structure without any interference from the polymer dynamics (temperature-dependent effects).

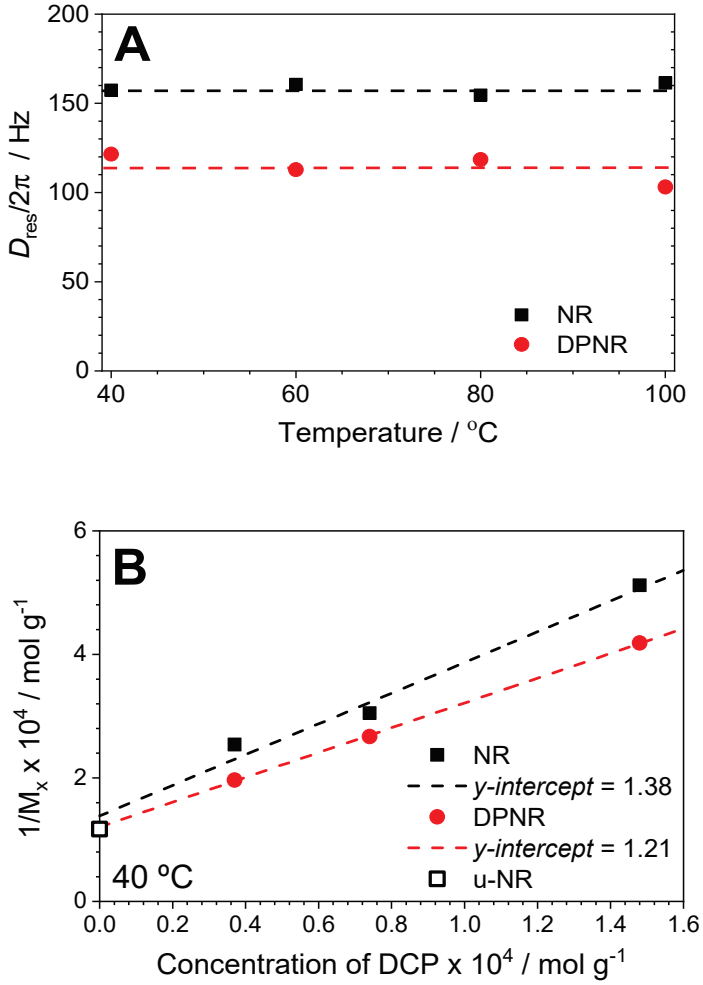

Figure 2. (**A**) Residual dipolar couplings, D_{res}, for vulcanized NR and DPNR with 1 phr of DCP (3 min at 160 °C) as a function of the NMR measuring temperature. (**B**) Relationship between the density of constraints (given as $1/M_x$ after 3 min of vulcanization time at 160 °C) and the concentration of DCP for the NR and DPNR samples measured at 40 °C. The y-intercept value represents the contribution of the entanglements ($1/M_e$) to the total amount of constraints assuming additive contributions ($1/M_c + 1/M_e$). The result shown in (B) for the un-vulcanized sample subjected to mastication treatment on a two-roll mill for 15 min (u-NR*) reflects the apparent (time and temperature-dependent) restrictions obtained from the measured D_{res} for that linear rubber melt (see also Figure 1).

In order to demonstrate the linear relationship between the cross-link density measured by NMR and the concentration of peroxide for the NR and DPNR samples (see Figure 2B), additional samples containing 1, 2, and 4 phr of DCP were prepared under the same conditions, and vulcanized at 160 °C for 3 min, as expected. According to the previous explanation, the molecular weight between constraints, M_x, measured by NMR, in fact, codifies the actual number of constraints imposed by (i) cross-links, (ii) entanglements (including those that are trapped), and (iii) the pseudo-end-linked network. Therefore, the extrapolated *y*-intercept value in Figure 2B represents the constraints in terms of $1/M_e$ for the NR and DPNR after the vulcanization process. The NR and DPNR show quite similar *y*-intercept values, which match with the D_{res} value obtained in the un-vulcanized NR (u-NR*) sample after the mastication process (see Figure 1). These results point out the strong effect of mastication and vulcanization dominating over the pseudo-end-linked network structure formed by the proteins and phospholipids. The latter governs the outstanding properties of un-vulcanized NR (in terms of green strength) but has a negligible effect in

the vulcanized samples, whose elastic properties mainly depends on the network structure formed by C-C cross-links (in the case of the peroxide-cured samples). Although the presence of proteins has a minimal effect on the topological constraints for the vulcanized samples (*y*-intercept), the slope in Figure 2B likely indicates a strong influence of these non-rubber substances on the vulcanization process, which undoubtedly enhanced the cross-linking efficiency in the NR, compared to the DPNR.

At this point, it is important to remark on some limitations by other experimental approaches to quantitatively analyze the effect of proteins on the actual network structure of NR in comparison with the ^{1}H DQ-NMR experiments. On the one hand, the widely used swelling experiments provide only partial and qualitative information about the cross-link density because of the uncertainties associated with the complex thermodynamics of the swelling process and the elastic model that defines the behavior of swollen networks [27]. On the other hand, the most complete information about the NR network structure obtained by the small-angle neutron scattering (SANS) technique was intensely disturbed by the strong scattering of the protein aggregates [63].

Because of these statements, the evolution of the main parameters that define the network structure, e.g., the cross-link density and its spatial distribution, as well as the non-coupled network defects, during the vulcanization process have been deeply studied in the following sections by using ^{1}H DQ-NMR experiments. These measurements were carried out at 40 °C because, at this temperature, the chain dynamics of the studied samples are fast enough to reach the plateau value of D_{res} (see Figure 2A). Additionally, this low temperature prevents the subsequent reactions of unreacted peroxides (especially at the initial steps of the vulcanization process) and NR degradation.

3.3. Evolution of Cross-Link Density During the Vulcanization Process

The formation of cross-links between polymer chains during the vulcanization process transforms rubber samples into an elastic material. It strongly influences their mechanical properties [64]. Figure 3 shows the evolution of cross-link formation for the NR and DPNR with the vulcanization time determined by NMR and rheometer measurements. A good correlation was clearly found between both techniques showing a characteristic curve for peroxide vulcanization. Peroxide vulcanization has a radical pathway that initiates the cross-linking reaction immediately after the homolytic scission of peroxide, as evidenced by the lack of scorch time in the vulcanization curve. The increased cross-link density (as measured by NMR) with the vulcanization time was reflected in the torque measured by the rheometer until a plateau was reached at the end of the process.

By comparing the NR and DPNR vulcanization curves, it is obvious that the proteins in NR increased the cross-link density without any influence on the vulcanization rate, since the optimum vulcanization time, defined as t_{95}, is quite similar for both samples. In that sense, the proteins might act as a coagent, improving the efficiency of peroxide as a cross-linking agent. An enhancement in the efficiency of vulcanization via radical reaction could be associated with different mechanisms, such as the suppression of the non-network forming the side reactions, i.e., chain scission and disproportionation [65,66], as well as the formation of bridges between polymer chains contributing to additional cross-links [67]. The coagent bridges which are covalently bonded to the polymer chains are possibly a grafting of coagents [67,68], an interpenetrating network of homo-polymerized coagents [69], and an aggregation of coagents like filler particles [70,71], depending on several factors, such as the readiness of the coagent to homo-polymerize, the concentration polarity, and the solubility of the coagent [17,68]. The role of the existing protein in NR as a coagent was supported by the presence of radicals on the molecules of protein extracted from the NR. The electron paramagnetic resonance (ESR) technique (see Supplementary

Information, Figure S2) can detect the presence of radicals on the proteins of NR, for which the *g* value at 2.004 corresponds to the carbon radicals on the backbone and the side chain of proteins similar to the results from the studies of amino acids and proteins examined elsewhere [72–74].

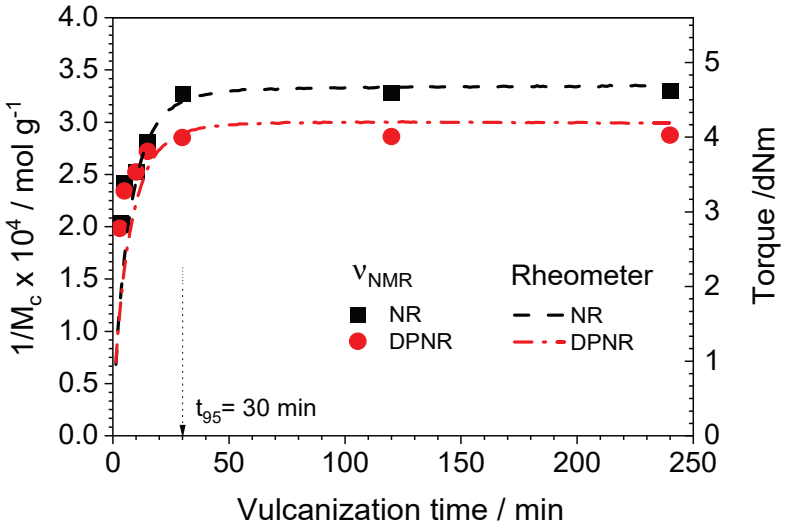

Figure 3. Evolution of cross-link formation for the NR and DPNR samples with 1 phr of DCP at 160 °C as a function of vulcanization time determined by NMR (symbols) and rheometer (dashed lines), respectively.

The proteins in NR are rather polar molecules, and therefore, their miscibility with the non-polar NR chains is quite poor. Such proteins tend to separate and then form aggregates of cross-linked proteins caused by the recombination of the protein radicals and homo-polymerized proteins at the unsaturated bond of the side chain, e.g., phenylalanine and tryptophan. The possible mechanism reaction of proteins as a coagent in peroxide cross-linked NR adapted from ref. [75] is given in Figure 4. When the radical is formed on the NR chain, the protein radical (a single protein molecule and/or an aggregate of cross-linked proteins) with more than one radical on that molecule is attached to the NR chain. Finally, the termination reaction can occur by the combination of radical intermediates, i.e., radicals on the NR and NR-proteins, leading to extra cross-links.

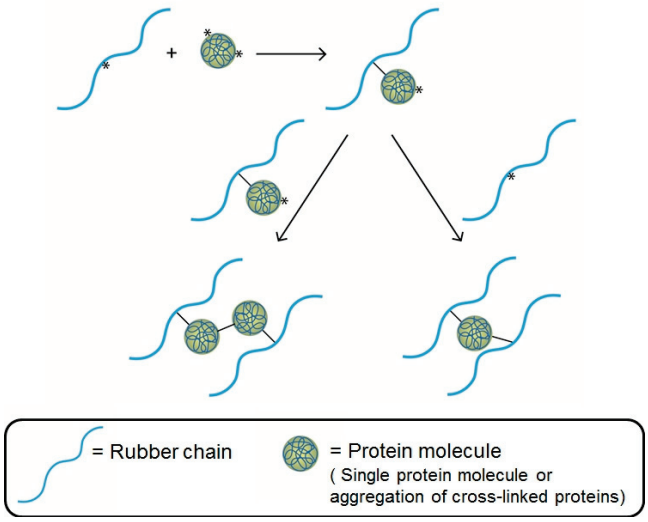

Figure 4. Schematic representation of the possible mechanism reaction of proteins as a coagent in peroxide cross-linked NR, where radicals have been represented by the symbol *. Adapted from ref. [75].

In addition, proteins can be oxidized by the presence of radicals and O_2 to generate protein hydroperoxides [76–79] (more details and evidence of protein degradation will be discussed in the following sections). Although the concentration of O_2 during the vulcanization process is quite low, some proteins might be oxidized by peroxide along with trace amounts of O_2 to generate additional radicals in the vulcanization process.

NR samples always show higher cross-link density than DPNR because of the presence of proteins independently of the involved mechanism, which seems to be related to the higher concentration of radicals during the vulcanization process.

3.4. Evolution of Non-Elastic Network Defects During the Vulcanization Process

Even though most of the literature in the rubber field supposes perfect networks obtained from the cross-linking reaction to explain the elastic properties of those materials, non-elastic network defects, mainly dangling chain ends and loops, have recently been reported as an important factor to consider when describing the structure of vulcanized rubber samples [43,49] and understanding their stress–relaxation processes [80–82].

The non-elastic network defects for the NR and DPNR samples during peroxide vulcanization are shown in Figure 5A. Similar tendencies on the evolution of non-elastic network defects for the NR and DPNR up to the optimum vulcanization time (t_{95}) were observed: the network defects decreased with the vulcanization time because of the formation of cross-links. At longer times, a slight increase in the fraction of network defects could be measured for the NR samples, whereas the DPNR seems to be a more stable sample with a constant number of defects above the optimum vulcanization times.

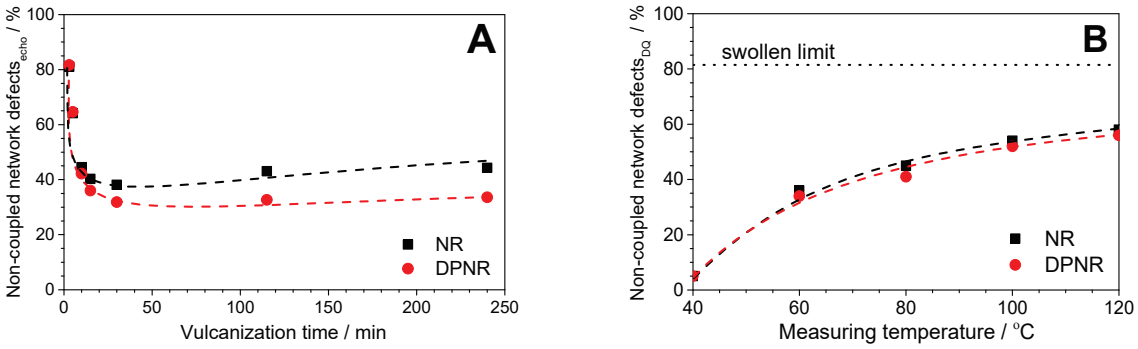

Figure 5. Evolution of non-coupled network defects for NR and DPNR as (**A**) a function of vulcanization time (measured at 40 °C in the swollen state by using Hahn echo experiments) and (**B**) as a function of the measuring temperature for samples vulcanized for 3 min (measured in the dry state by using DQ-NMR experiments). The swollen limit in (**B**) reflects the actual fraction of non-coupled defects for samples vulcanized for 3 min as measured by NMR in a swollen state at 40 °C from (**A**).

The first phenomenon is due to the progressive cross-linking reaction that reduces the fraction of un-cross-linked chains and shortens the molecular weight of the chain ends. Nevertheless, in any case, the actual fraction of non-coupled network defects for the optimum cross-linked NR samples reaches values of 30–40%. This means that peroxide vulcanization seems to be a quite ineffective process to form elastic cross-linked network structures in NR, whereas the side reactions that provide dangling chains (e.g., chain scission processes) seem to be favored in comparison with other elastomers [43].

Obviously, this scenario depends on temperature (see Figure 5B) and the observed timescale, minimizing the effect of network defects on the mechanical properties. The actual fraction of non-coupled defects (measurable only in a swollen state) is always underestimated when it is measured in dry samples (see Figure 5B) because chain packing or topological constraints promote some restrictions on the chain ends that provide some

anisotropy in the movement to those entangled segments. Therefore, the fraction of non-elastic network defects measured by NMR decreases drastically at lower temperatures. The clearest example is given by the samples vulcanized for 3 min, whose actual fraction of defects is around 80% (as measured in the swollen state), but only 5% of those polymer segments behave as non-elastic defects at 40 °C in the dry state in the NMR timescale.

These statements support the assumption that cross-linking and chain scission reactions are competing and sequential reactions during the vulcanization process of NR with peroxides [83]. Before the optimum vulcanization time, t_{95}, the overall process seems to be dominated by the cross-linking reaction: an increase in cross-link density and elastic torque and a decrease in the non-coupled network defects. However, the chain scission reaction seems to govern this process after achieving the network formation at t_{95} for the NR samples. It is important to remark that the increase in non-elastic network defects observed above the optimum vulcanization time for the NR sample (Figure 5A) has neither a visible effect on the average molecular weight between constraints nor on the elastic torque measured in the rheometer as demonstrated in Figure 3. This could be explained by the combined (and opposite) changes in the network structure caused by the presence of competing reactions, the cross-linking and the chain scission that modify the spatial distribution of cross-links, as will be discussed in the following sections.

By comparing the NR and DPNR samples, it is possible to establish that the proteins have a negative effect in this complex process since the NR showed a higher fraction of non-elastic network defects than the DPNR. In this sense, the higher concentration of radicals due to the presence of proteins increases the cross-link density. It enhances the chain scission reactions that occur during the NR vulcanization with peroxides, contributing to the higher fraction of defects of the NR. In addition, the proteins can form ineffective cross-links, i.e., proteins bound to a single rubber chain without forming any bridge with other chains that create dangling and pendant proteins grafted to NR chains. Proteins can raise the fraction of network defects in NR vulcanized with peroxides independently of the assumed mechanism involved in the process.

3.5. Evolution of Spatial Distribution of Cross-Links During the Vulcanization Process

The ^{1}H DQ-NMR experiments not only allow the calculation of an average cross-link density, but also provide information on the spatial distribution of cross-links. Previous works have demonstrated that NR samples vulcanized with peroxide exhibited a broader distribution of cross-links than sulfur-based networks [43,57], and, in some cases (according to the peroxide concentration, vulcanization temperature, and type of elastomer), they contained highly cross-linked areas (inhomogeneities) termed as clusters [84], which were formed by the subsequent radical addition mechanism (similar to a polymerization reaction) to the double bond on the chain backbone [85–87].

The ratio between the standard deviation and the average value of the dipolar coupling distribution measured by NMR [47] is a robust parameter to describe a variation in the spatial distribution of the cross-links with the vulcanization time (see Figure 6). The quite broad cross-link distribution in the initial steps of vulcanization for both the NR and DPNR progressively decreased with the vulcanization time up to the optimum vulcanization time when it reached the narrowest distribution. At longer times (above the optimum vulcanization time), the scenario turned, and the distribution became broader again. This trend can be explained by the coexistence of two competitive reactions, i.e., the formation of cross-links and the chain scission reactions during the vulcanization process.

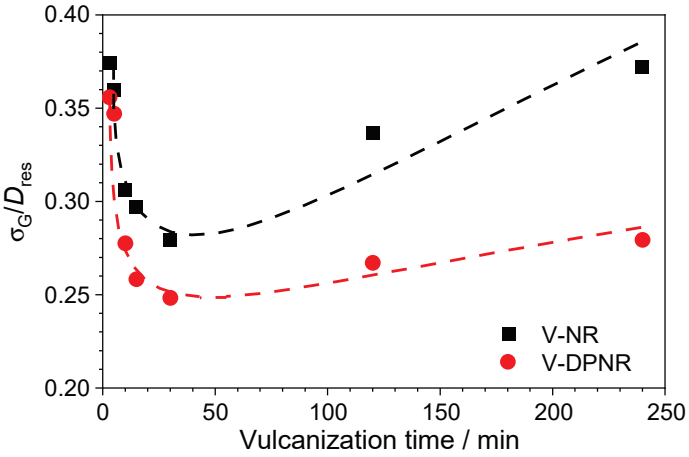

Figure 6. Variation in the relative width of the distribution of cross-link density as a function of vulcanization time for NR and DPNR, where σ represents the standard deviation and D_{res} the average value of the dipolar coupling distribution.

The spatial distribution of cross-links became narrower with the progress of vulcanization because the formation of additional cross-links randomly distributed (according to the radical pathway that governs the vulcanization based on peroxides) was dominant over other side reactions. Consequently, the cross-link density and spatial homogeneity of the formed network increased during this process.

To understand the network evolution over the optimum vulcanization time, it is mandatory to analyze in detail the actual spatial distribution of cross-links (see Figure 7). In the case of the NR, the distribution of cross-links became broader when the vulcanization time increased over t_{95} (at 120 and 240 min, respectively) because both extremes in the distribution shifted to lower and higher cross-link densities, respectively. This is molecular evidence about the opposite effects of the two main reactions during the vulcanization process: (i) chain scission reactions that increase the fraction of non-elastic network defects (see Figure 5A) and the molecular weight between cross-links (M_c), and (ii) the cross-linking reactions that promote the formation of areas with higher cross-link densities. Both opposite processes seem to compensate for their effects, and, consequently, the average cross-link density (measured as the average value of D_{res} distribution) and the elastic torque measured in the rheometer remain constant, as demonstrated in Figure 3.

The deproteinized sample, DPNR, did not show any effect derived from chain scission reactions over the optimum vulcanization time (completely aligned with the almost constant value in the non-coupled network defects, as shown in Figure 5A). In that case, the broadening of the spatial cross-link distribution was caused by the formation of additional cross-links thanks to the persistence of radicals in the sample.

Since the proteins in the NR increased the concentration of radicals in the system and enhanced both the cross-linking and the chain scission reactions, the NR sample showed a higher fraction of network defects, higher cross-link density, and broader spatial distribution of cross-links than the DPNR sample. Chain scission reactions were minimized, and their negative effect on the network structure was almost negligible. These effects were amplified at vulcanization times over t_{95}, where the proteins were active in this complex process.

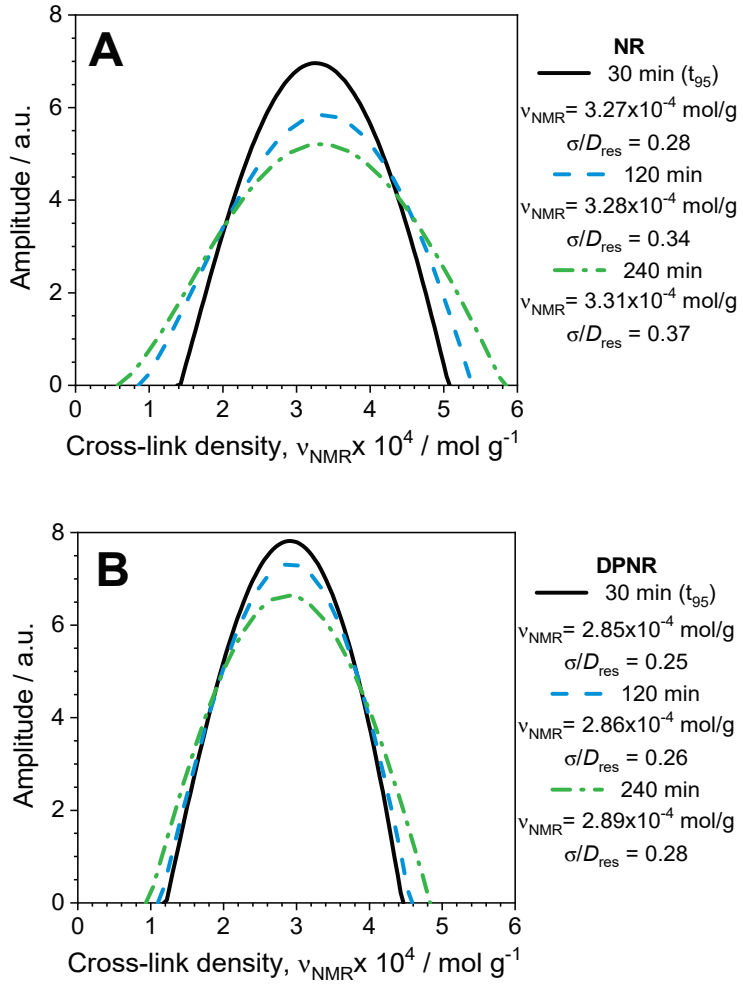

Figure 7. Spatial distribution of cross-links at various vulcanization times for (**A**) NR and (**B**) DPNR according to the regularization analysis of NMR data. Average cross-link density (υ_{NMR}) and the relative width of the distributions (σ / D_{res}) are indicated.

Nevertheless, it is important to point out that in both cases, the low concentration of added peroxide (only 1 phr) cannot allow for the formation of highly cross-linked areas or clusters as was previously demonstrated in NR for samples with higher concentrations of peroxide [43]. This type of local inhomogeneity in the network structure for peroxide vulcanized samples should not be confused with the larger length-scale inhomogeneities caused by protein aggregates in both the un-cross-linked [87] and peroxide cross-linked [63] NR samples as was observed by atomic force microscopy (AFM) and SANS techniques, respectively. The latter is a larger-scale inhomogeneity that is undetectable by the more local NMR technique, and it has no influence on the actual structural information analyzed from the NMR experiments.

Consequently, the protein aggregation in the peroxide cross-linked NR needed to be confirmed, and this could be clarified by AFM and nitrogen analysis. The protein aggregations in the peroxide cross-linked NR were found even after leaching with hot water, which is an effective method for removing proteins from sulfur cross-linked NR products [88–92]. Furthermore, the nitrogen content of the peroxide cross-linked NR insignificantly changed after the leaching process (see Supplementary Information, Figure S3). These results signify that protein aggregates can be covalently bonded to the rubber backbone during the vulcanization of NR with peroxide, unlike the sulfur cross-linked NR.

It should be noted that NMR experiments are sensitive to very local information on the length scale of 10 nm, whereas AFM is measured in the micrometer scale. These techniques

provide complementary information on different length scales, allowing us to conclude that the NR samples vulcanized with peroxide show inhomogeneities on different length scales caused by the consecutive addition reaction to the double bond (the formation of clusters of cross-links) and by the grafting of protein aggregates to the rubber chains.

Based on the cross-link density, the fraction of non-elastic network defects, and the spatial cross-link distribution results obtained by NMR measurements and the AFM results in this work, the proposed network structures derived from the presence of proteins in peroxide cross-linked NR are schematically illustrated in Figure 8, where some additional cross-links are derived from protein hydroperoxides, the bridge of proteins, and the aggregation of cross-linked proteins according to AFM results, while the dangling and pendant proteins grafted to the NR chain do not form any cross-links.

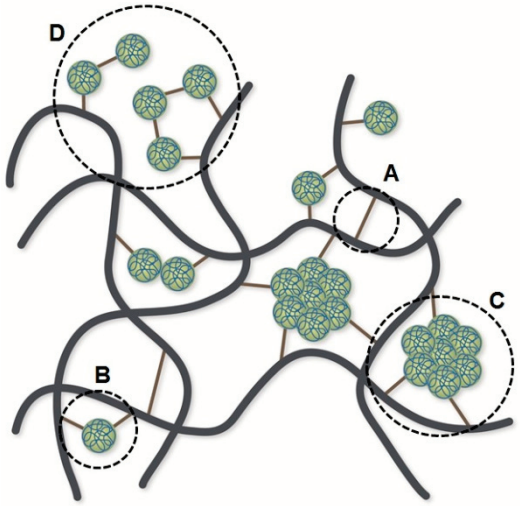

Figure 8. Schematic representation of the network structures associated with proteins in peroxide cross-linked NR. Cross-links are derived from (A) protein hydroperoxides, (B) the bridge of proteins, and (C) the aggregation of cross-linked proteins. No cross-link is derived from (D) dangling and pendant proteins grafted to the NR chain.

3.6. Effect of Network Heterogeneities on the Mechanical Properties

The mechanical properties of vulcanized rubber depend on the different local parameters that define the network structure: the fraction of dangling chain ends; the cross-link density; the nature, functionality, and spatial distribution of cross-links; the effect of entanglements; and the junction mobility [82,93–96]. Several of these structural parameters are drastically modified during the vulcanization process, making it quite difficult to study the influence of each individual factor on the mechanical properties of rubber, which is usually dominated by the effect of cross-link density. Nevertheless, above the optimum vulcanization time, the variation in the cross-link density is almost neglectable for both the NR and DPNR samples, which provides an opportunity to evaluate the effect of other structural parameters in the tensile properties of those networks.

Figure 9 shows that tensile strength decreases with the vulcanization time when the optimum time has been exceeded (t_{95} = 30 min) for the vulcanized NR and DPNR samples with 1 phr of DCP at 160 °C. The reported tensile strength values are the median of five test specimens, and the error bars represent their standard deviation. As discussed above, at those long vulcanization times, the coexistence of cross-linking reactions and chain scission processes in NR drives the formation of a higher fraction of non-elastic network defects and a broader spatial distribution of cross-links, but maintains the almost constant cross-link density in the sample. The absence of proteins reduces these negative reactions and the

subsequent effects on the network structure of DPNR, showing higher tensile performance with lower cross-link density compared with NR.

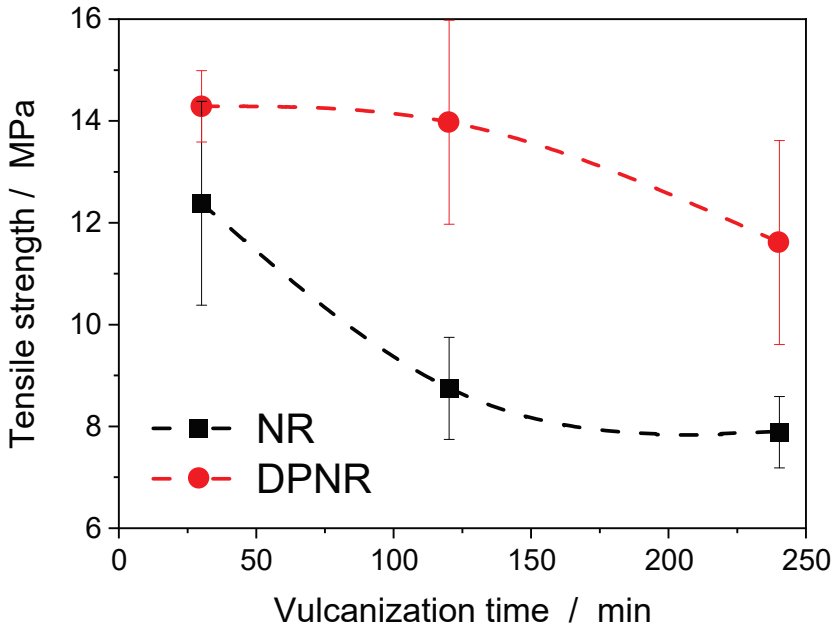

Figure 9. Variation in tensile strength with the vulcanization time for the NR and DPNR samples vulcanized with 1 phr of DCP at 160 °C.

On the one hand, Figure 10 shows a clear relationship between the decrease in the tensile strength and the relative width of the spatial distribution of cross-links, demonstrating that network inhomogeneities strongly influence the tensile strength of these rubber samples. On the other hand, the effect of non-elastic network defects on the tensile strength is difficult to evaluate. Although the presence of a high fraction of dangling chain ends (30–40%) was demonstrated in those samples, their elastic response depends on temperature and the observed timescale, minimizing the effect of these network defects on the mechanical properties.

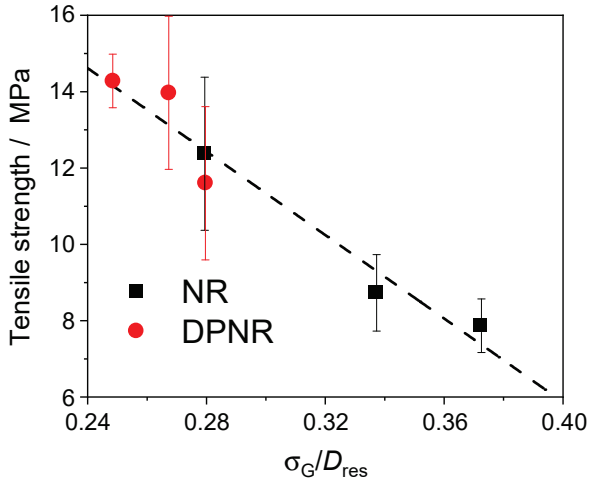

Figure 10. Relationship between tensile strength and the relative width of the spatial distribution of cross-links for the vulcanized rubber samples (NR and DPNR) with 1 phr of DCP at 160 °C.

These results suggest that rubber materials are not ideal networks because they contain non-elastic network defects (which should be considered) and a heterogeneous spatial

distribution of cross-links. The latter seems to be a critical structural factor in understanding the ultimate tensile properties of rubber samples.

3.7. Thermal–Oxidative Degradation of Peroxide Cross-Linked NR

The effects of some non-rubber constituents on the degradation behavior of NR have been reported. For example, tocotrienols exhibited antioxidant activity [97], whereas copper accelerated the degradation as a pro-oxidant [98]. The role of proteins has been also investigated on the degradation of NR, concluding that proteins showed either insignificant protection [99] or antioxidant activity [100] against thermal–oxidative aging. This might be due to a variety of testing conditions and analyzing techniques used for that purpose. To clarify this issue, the rubber samples were aged at 100 °C under air atmosphere for 6, 24, and 48 h in order to monitor the progressive degradation and evolution of the network structure by using NMR experiments. Figure 11 shows the changes in the cross-link density for NR and DPNR (vulcanized at their optimum vulcanization times, t_{95}) at various aging times.

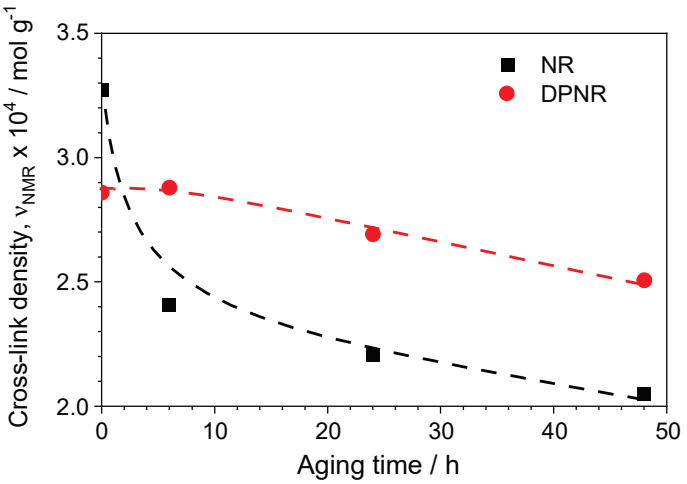

Figure 11. Evolution of cross-link density for the NR and DPNR samples (vulcanized at t_{95}) as a function of aging time. Lines are a guide for the eyes.

It was found that after 6 h of aging, the cross-link density for the NR remarkably decreased, while the DPNR sample showed no significant change with respect to the original structure. After that time, the cross-link density for both samples decreased with aging times up to 48 h in a similar way. These results evidence the active role of proteins in this process since they affect the degradation behavior of NR by increasing both the degradation rate and the final state of degradation. Nevertheless, it is important to remark that the effect of proteins seems to be limited to the initial stages of this thermo-oxidative process.

Additional details about how networks are degraded were provided by the analysis of the actual spatial distribution of cross-links at various aging times, as shown in Figure 12. The degradation behavior for the DPNR and NR samples is, in both cases, complex. However, it is different for each sample: the spatial distribution of cross-links for the aged NR was only shifted towards lower cross-link densities by the preferential effect of the chain scission reaction (see Figure 12A), whereas the distribution for the DPNR sample was widened by both extremes, at lower and higher cross-link densities, respectively, due to the coexistence of the chain scission and cross-linking reactions during the degradation process (see Figure 12B).

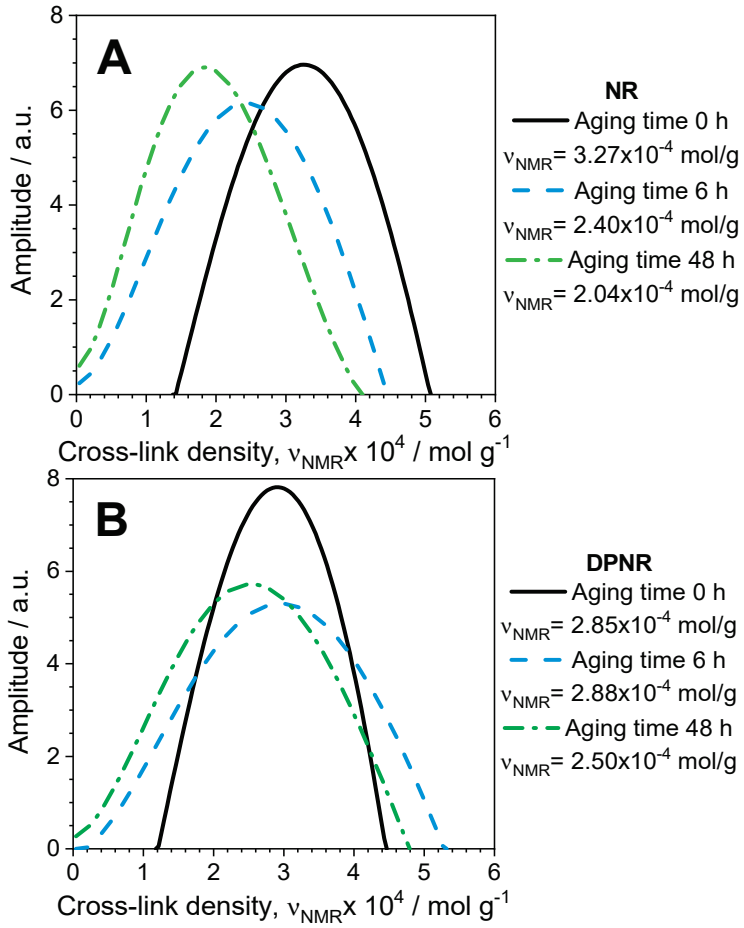

Figure 12. Spatial distribution of cross-link density at various aging times for (**A**) NR and (**B**) DPNR according to the regularization analysis.

Reactive oxygen species damage proteins at the protein backbones and the 20 common amino acid side chains, contributing to numerous protein degradation products such as carbonyl compounds, alcohols, and protein hydroperoxides [76–79]. The protein hydroperoxides can generate secondary radicals that induce damage to other proteins and other molecules as a chain reaction [78,101,102]. This is consistent with the assumption that proteins raise the rate and state of degradation in NR.

The analysis of the protein hydroperoxides of NR was carried out using extracted proteins as the model compound to confirm the formation of hydroperoxides caused by protein degradation (see Supplementary Information, Figure S4).

This confirmatory evidence indicates that the proteins in NR create hydroperoxides during the aging process, accelerating the degradation of other protein aggregates (further hydroperoxides can be generated as a chain reaction) and rubber chains. Consequently, the proteins in NR can prove to be pro-oxidant molecules that actively affect the degradation behavior of peroxide cross-linked NR and minimize the cross-linking reactions via radical mechanisms in the presence of oxygen.

4. Conclusions

Biopolymers are materials that can be derived from renewable resources or synthesized using a combination of renewable feedstocks and traditional polymerization methods, as observed in bio-based polymers. These biopolymers and bio-based polymers present a sustainable alternative to conventional petroleum-based polymers, being sourced from diverse feedstocks such as agricultural products (e.g., corn or soybeans) and non-traditional

sources like algae or food waste. Additionally, these polymers are engineered with properties including biodegradability and composability.

The role of proteins on the pseudo-end-linked network, which characterizes the un-vulcanized NR, and their effects on the network formation and degradation of peroxide cross-linked NR was elucidated by time-domain ^{1}H-NMR experiments. This experimental procedure has proven to be a successful approach to obtain quantitative and complete local information about the actual fraction of non-elastic network defects, the cross-link density, and its spatial distribution in NR without any interference from proteins and their aggregates. This is a superior advantage shown by NMR approaches with respect to qualitative swelling experiments and the small-angle neutron scattering (SANS) technique that is intensely disturbed by the strong scattering phenomenon of protein aggregates.

In un-vulcanized NR samples, the accessible conformational space for chain segments is always restricted with respect to the synthetic polyisoprene (IR) counterpart because of the presence of a pseudo-end-linked network as was demonstrated by ^{1}H DQ-NMR experiments. The successive subtraction of proteins and phospholipids from the NR samples has demonstrated the main role of micelle formation or the association of the polar head-groups of phospholipid molecules at the α-terminal of the rubber chain as the cross-linking points of the naturally occurring networks, whereas the effect of proteins as cross-linkers at the NR chain ends seems to be minimal.

Although proteins have a negligible effect on the pseudo-end-linked network formed in un-vulcanized NR samples, they played an active role as coagents during the peroxide vulcanization of this material. It has been demonstrated that this type of vulcanization is a highly ineffective complex process for the NR matrix because at least two main competing reactions take place: cross-linking and chain scission phenomena. The existence of proteins in NR increases the concentration of radicals and provokes the effect on both opposite reactions. Consequently, the NR always showed a higher fraction of network defects, higher cross-link density, and broader (more heterogeneous) cross-link distribution than its deproteinized counterpart (DPNR). It is important to note that the extraction of proteins minimizes the importance of chain scission reactions, making their effects on the network structure negligible during the vulcanization process (in the absence of oxygen).

In addition to the local spatial inhomogeneities observed by NMR, NR samples vulcanized with peroxides also contain aggregates of proteins covalently grafted to the rubber backbone, as demonstrated by AFM. Those aggregates form larger length-scale inhomogeneities (in the range of microns) compared to the size of the highly cross-linked areas (in the range of tens of nm) in the rubber network structure. The latter has a deep impact on the tensile strength properties of these rubber samples.

Finally, proteins have a detrimental effect on the thermo-oxidative degradation of peroxide cross-linked NR because they act as pro-oxidant agents generating hydroperoxides that accelerate the degradation process. As a consequence, chain scission reactions are enlarged during this radical process to increase both the degradation rate and the final state of degradation. Contrary to this behavior, both opposite processes take place in deproteinized NR, and the spatial distribution of cross-links expands to both extremes, the higher and lower cross-link densities, although the chain scission reactions are predominant.

Supplementary Materials: The following supporting information can be downloaded at: https://www.mdpi.com/article/10.3390/polym17081063/s1, Figure S1. Scheme of a proposed pseudo-end-linked network structure of NR (proteins at the ω-terminal and phospholipid molecules at the α-terminal). Figure S2. ESR spectrum and g value of the extracted proteins. Figure S3. AFM micrographs and nitrogen content for vulcanized NR, vulcanized DPNR and leached NR samples. The phase images were obtained by AFM tapping mode. Figure S4. Hydroperoxides content generated from extracted proteins at various aging times. Reference [103] is cited in the supplementary materials.

Author Contributions: A.N., J.L.-V. and J.S.: writing—original draft, investigation, data acquisition, formal analysis, methodology, and conceptualization; A.G.-J. and R.P.-A.: investigation and methodology.; F.M.-S. and Z.Z.-R.: supervision, writing—review and editing; J.L.-V. and J.S.: funding acquisition and project administration. All authors have read and agreed to the published version of the manuscript.

Funding: This research was partially funded by the Spanish Ministry of Science and Innovation (MINECO) grant number PID2020-119047RB-I00, PLEC2021-00779 and PID2023-147542OB-I00 and Mahidol University and the National Research Council of Thailand grant number NRCT5-TRG63009-09.

Institutional Review Board Statement: Not applicable.

Data Availability Statement: The original contributions presented in this study are included in the article/Supplementary Material. Further inquiries can be directed to the corresponding authors.

Acknowledgments: The authors would like to acknowledge the Faculty of Science, Mahidol University, the Center of Excellence for Innovation in Chemistry (PERCH-CIC), Ministry of Higher Education, Science, Research, and Innovation. Sincere appreciation is extended to the Thai Rubber Latex Corporation (Thailand) Public Co., Ltd., for supplying the NR samples. The authors also acknowledge the Spanish Ministry of Science and Innovation (MINECO) (PID2020-119047RB-I00, PLEC2021-00779 and PID2023-147542OB-I00) and the Mahidol University and the National Research Council of Thailand: (NRCT5-TRG63009-09) for the partial financial support of this work.

Conflicts of Interest: The authors declare no conflicts of interest.

References

1. Saleh, T.A. *Polymer Hybrid Materials and Nanocomposites: Fundamentals and Applications*; William Andrew: Jeddah, Saudi Arabia, 2021.
2. Blume, A.; van Elburg, F.; Grunert, F.; Talma, A. "Re-Think" Sulfur Curing. *Molecules* **2024**, *29*, 5198. [CrossRef] [PubMed]
3. Zhu, Y.; Romain, C.; Williams, C. Sustainable polymers from renewable resources. *Nature* **2016**, *540*, 354–362. [CrossRef]
4. Mohanty, A.K.; Wu, F.; Mincheva, R.; Hakkarainen, M.; Raquez, J.M.; Mielewski, D.F.; Narayan, R.; Netravali, A.N.; Misra, M. Sustainable polymers. *Nat. Rev. Methods Primers* **2022**, *2*, 46. [CrossRef]
5. Allen, P.W.; Bloomfield, G.F. Natural rubber hydrocarbon. In *Chemistry and Physics of Rubber-like Substance*; Bateman, L., Ed.; MacLaren and Sons: London, UK, 1963; Chapter 1, pp. 1–17.
6. Eng, A.H.; Tanaka, Y.; Gan, S.N. FTIR studies on amino groups in purified Hevea rubber. *J. Nat. Rubber Res.* **1992**, *7*, 152–155.
7. Tangpakdee, J.; Tanaka, Y. Characterization of sol and gel in Hevea natural rubber. *Rubber Chem. Technol.* **1997**, *70*, 707–713. [CrossRef]
8. Tarachiwin, L.; Sakdapipanich, J.T.; Ute, K.; Kitayama, T.; Bamba, T.; Fukusaki, E.; Kobayashi, A.; Tanaka, Y. Structural characterization of α-terminal group of natural rubber 1. Decomposition of branch-points by lipase and phosphatase treatments. *Biomacromolecules* **2005**, *6*, 1851–1857. [CrossRef] [PubMed]
9. Tarachiwin, L.; Sakdapipanich, J.T.; Ute k Kitayama, T.; Tanaka, Y. Structural characterization of α-terminal group of natural rubber 2. Decomposition of branch-points by phospholipase and chemical treatments. *Biomacromolecules* **2005**, *6*, 1858–1863. [CrossRef]
10. Tarachiwin, L.; Sakdapipanich, J.; Tanaka, Y. Structure and origin of long-chain branching and gel in natural rubber. *Kautsch. Gummi Kunstst.* **2005**, *58*, 115–122.
11. Amnuaypornsri, S.; Sakdapipanich, J.; Toki, S.; Hsiao, B.; Ichikawa, N.; Tanaka, Y. Strain-induced crystallization of natural rubber: Effect of proteins and phospholipids. *Rubber Chem. Technol.* **2008**, *81*, 753–766. [CrossRef]
12. Food and Drug Administration. *Allergic Reaction to Latex-Containing Medical Devices*; FDA Medical Alert 1991; Food and Drug Administration: Silver Spring, MD, USA, 1991; MDA91-1.
13. Ichikawa, N.; Aik-Hwee, E.; Tanaka, Y. Properties of deproteinised natural rubber. In *Natural Rubber: Current Development in Product Manufacture and Application, Proceedings of the International Rubber Technology Conference 1993, Kuala Lumpur, Malaysia, 14–16 June 1993*; Kadir, A.A.S.A., Ed.; Rubber Research Institute of Malaysia: Kuala Lumpur, Malaysia, 1993; pp. 101–110.
14. Nakade, S.; Kuga, A.; Hayashi, M.; Tanaka, Y. Highly purified natural rubber. IV. Preparation and characteristics of gloves and condoms. *J. Nat. Rubb. Res.* **1997**, *12*, 33–42.
15. Coran, A.Y. Vulcanization: Conventional and dynamic. *Rubber Chem. Technol.* **1995**, *68*, 351–375. [CrossRef]
16. Aprem, A.S.; Joseph, K.; Thomas, S. Recent developments in crosslinking of elastomers. *Rubber Chem. Technol.* **2005**, *78*, 458–488. [CrossRef]

17. Dluzneski, P.R. Peroxide vulcanization of elastomers. *Rubber Chem. Technol.* **2001**, *74*, 451–492. [CrossRef]
18. Coleman, M.M.; Shelton, J.R.; Koenig, J.L. Sulfur vulcanization of hydrocarbon diene elastomers. *Ind. Eng. Chem. Prod. Res. Dev.* **1974**, *13*, 154–165. [CrossRef]
19. Krejsa, M.R.; Koenig, J.L. A review of sulfur crosslinking fundamentals for accelerated and unaccelerated vulcanization. *Rubber Chem. Technol.* **1993**, *66*, 376–410. [CrossRef]
20. Akiba, M.; Hashim, A.S. Vulcanization and crosslinking in elastomers. *Prog. Polym. Sci.* **1997**, *22*, 475–521. [CrossRef]
21. Heideman, G.; Datta, R.N.; Noordermeer, J.W.M. Activators in accelerated sulfur vulcanization. *Rubber Chem. Technol.* **2004**, *77*, 512–541. [CrossRef]
22. Suchiva, K.; Kowitteerawut, T.; Srichantamit, L. Structure properties of purified natural rubber. *J. Appl. Polym. Sci.* **2000**, *78*, 1495–1504. [CrossRef]
23. Conde-Salazar, L.; del-Río, E.; Guimaraens, D.; González Domingo, A. Type IV allergy to rubber additives: A 10-year study of 686 cases. *J. Am. Acad. Dermatol.* **1993**, *29*, 176–180. [CrossRef]
24. Tan, Z.; Jaeger, R.; Vancso, G.J. Crosslinking studies of poly(dimethylsiloxane) networks: A comparison of inverse gas chromatography, swelling experiments and mechanical analysis. *Polymer* **1994**, *35*, 3230–3236. [CrossRef]
25. Arndt, K.F.; Schreck, J. Netzwerkcharakterisierung durch dampfdruckosmotische Messungen. *Acta Polym.* **1985**, *36*, 56–57. [CrossRef]
26. Patel, S.K.; Malone, S.; Cohen, C.; Gillmor, J.R.; Colby, R.H. Elastic modulus and equilibrium swelling of poly(dimethylsiloxane) networks. *Macromolecules* **1992**, *25*, 5241–5251. [CrossRef]
27. Valentín, J.L.; Carretero-González, J.; Mora-Barrantes, I.; Chassé, W.; Saalwächter, K. Uncertainties in the determination of cross-link density by equilibrium swelling experiments in natural rubber. *Macromolecules* **2008**, *41*, 4717–4729. [CrossRef]
28. Imanishi, Y.; Adachi, K.; Kotaka, T.J. Further investigation of the dielectric normal mode process in undiluted cis-polyisoprene with narrow distribution of molecular weight. *Chem. Phys.* **1988**, *89*, 7585–7592.
29. Zaper, A.M.; Koenig, J.L. Solid State Carbon-13 NMR Studies of Vulcanized Elastomers. II, Sulfur Vulcanization of Natural Rubber. *Rubber Chem. Technol.* **1987**, *60*, 252–277. [CrossRef]
30. Orza, R.A.; Magusin, P.C.M.M.; Litvinov, V.M.; van Duin, M.; Michels, M.A.J. Mechanism for peroxide cross-linking of EPDM rubber from MAS 13C NMR Spectroscopy. *Macromolecules* **2009**, *42*, 8914–8924. [CrossRef]
31. Pyckout-Hintzen, W.; Springer, T.; Forster, F.; Gronski, W. Small-angle neutron scattering investigation of a multilinked polybutadiene network crosslinked in solution. *Macromolecules* **1991**, *24*, 1269–1274. [CrossRef]
32. Ikeda, Y.; Higashitani, N.; Hijikata, K.; Kokubo, Y.; Morita, Y.; Shibayama, M.; Osaka, N.; Suzuki, T.; Endo, H.; Kohjiya, S. Vulcanization: New focus on a traditional technology by small-angle neutron scattering. *Macromolecules* **2009**, *42*, 2741–2748. [CrossRef]
33. Litvinov, V.M.; De, P.P. (Eds.) *Spectroscopy of Rubbers and Rubbery Materials*; Rapra Technology Ltd.: Shawbury, UK, 2002.
34. Cohen-Addad, J.P. Effect of the anisotropic chain motion in molten polymers: The solidlike contribution of the nonzero average dipolar coupling to NMR signals theoretical description. *J. Chem. Phys.* **1973**, *60*, 2440–2453. [CrossRef]
35. Brereton, M.G. NMR transverse relaxation function calculated for constrained polymer chains: Application to entanglements and networks. *Macromolecules* **1990**, *23*, 1119–1131. [CrossRef]
36. Graf, R.; Heuer, A.; Spiess, H.W. Chain-order effects in polymer melts probed by 1H double-quantum NMR spectrocopy. *Phys. Rev. Lett.* **1998**, *80*, 5738–5741. [CrossRef]
37. Saalwächter, K. Proton multiple-quantum NMR for the study of chain dynamics and structural constraints in polymeric soft materials. *Prog. Nucl. Magn. Reason. Spectrosc.* **2007**, *51*, 1–35. [CrossRef]
38. Vieyres, A.; Pérez-Aparicio, R.; Albouy, P.-A.; Sanseau, O.; Saalwächter, K.; Long, D.R.; Sotta, P. Sulfur-Cured Natural Rubber Elastomer Networks: Correlating Cross-Link Density, Chain Orientation, and Mechanical Response by Combined Techniques. *Macromolecules* **2013**, *46*, 889–899. [CrossRef]
39. Basterra-Beroiz, B.; Rommel, R.; Kayser, F.; Westermann, S.; Valentín, J.L.; Heinrich, G. New Insights into Rubber Network Structure by a Combination of Experimental Techniques. *Rubber Chem. Technol.* **2017**, *90*, 347–366. [CrossRef]
40. Litvinov, V.M. EPDM/PP thermoplastic vulcanizates as studied by proton NMR relaxation: Phase composition, molecular mobility, network structure in the rubbery phase, and network heterogeneity. *Macromolecules* **2006**, *39*, 8727–8741. [CrossRef]
41. Demco, D.E.; Hafner, S.; Fülber, C.; Graf, R.; Spiess, H.W. Two-dimensional proton magnetization-exchange NMR spectroscopy in cross-linked elastomers. *J. Chem. Phys.* **1996**, *105*, 11285–11296. [CrossRef]
42. Callaghan, P.T.; Samulski, E.T. Molecular ordering and the direct measurement of weak proton-proton dipolar interactions in a rubber network. *Macromolecules* **1997**, *30*, 113–122. [CrossRef]
43. Valentín, J.; Posadas, P.; Fernández-Torres, A.; Malmierca, M.A.; González, L.; Chassé, W.; Saalwächter, K. Inhomogeneities and chain dynamics in diene rubbers vulcanized with different cure systems. *Macromolecules* **2010**, *43*, 4210–4222. [CrossRef]

44. Basterra-Beroiz, B.; Rommel, R.; Kayser, F.; Valentín, J.L.; Westermann, S.; Heinrich, G. Revisiting Segmental Order: A Simplified Approach for Sulfur-Cured Rubbers Considering Junction Fluctuations and Entanglements. *Macromolecules* **2018**, *51*, 2076–2088. [CrossRef]
45. Saalwächter, K.; Herrero, B.; López-Manchado, M.A. Chain Order and Cross-Link Density of Elastomers As Investigated by Proton Multiple-Quantum NMR. *Macromolecules* **2005**, *38*, 9650–9660. [CrossRef]
46. Saleesung, T.; Reichert, D.; Saalwächter, K.; Sirisinha, C. Correlation of crosslink densities using solid state NMR and conventional techniques in peroxide-crosslinked EPDM rubber. *Polymer* **2015**, *56*, 309–317. [CrossRef]
47. Saalwächter, K.; Ziegler, P.; Spyckerelle, O.; Haidar, B.; Vidal, A.; Sommer, J.U. 1H multiple-quantum nuclear magnetic resonance investigations of molecular order distributions in poly(dimethylsiloxane) networks: Evidence for a linear mixing law in bimodal systems. *J. Chem. Phys.* **2003**, *119*, 3468–3482. [CrossRef]
48. Chassé, W.; Valentín, J.L.; Genesky, G.D.; Cohen, C.; Saalwächter, K. Precise dipolar coupling constant distribution analysis in proton multiple-quantum NMR of elastomers. *J. Chem. Phys.* **2011**, *134*, 044907. [CrossRef] [PubMed]
49. Chassé, W.; Lang, M.; Sommer, J.-U.; Saalwächter, K. Cross-link density estimation of PDMS networks with precise consideration of networks defects. *Macromolecules* **2012**, *45*, 899–912. [CrossRef]
50. Acosta, R.H.; Vega, D.A.; Villar, M.A.; Monti, G.A.; Vallés, E.M. Double quantum NMR applied to polymer networks with low concentration of pendant chains. *Macromolecules* **2006**, *39*, 4788–4792. [CrossRef]
51. Acosta, R.H.; Monti, G.A.; Villar, M.A.; Vallés, E.M.; Vega, D.A. Transiently trapped entanglements in model polymer networks. *Macromolecules* **2009**, *42*, 4674–4680. [CrossRef]
52. Sommer, J.-U.; Chassé, W.; Valentín, J.L.; Saalwächter, K. Effect of excluded volume on segmental orientation correlations in polymer chains. *Phys. Rev. E* **2008**, *78*, 051803. [CrossRef]
53. Iqbal, J.; Bhatia, B.; Nayyar, N.K. Transition metal-promoted free-radical reactions in organic synthesis: The formation of carbon-carbon bonds. *Chem. Rev.* **1994**, *94*, 519–564. [CrossRef]
54. Tanaka, Y. Structural characterization of natural polyisoprenes: Solve the mystery of natural rubber based on structural study. *Rubber Chem. Technol.* **2001**, *74*, 355–375. [CrossRef]
55. Toki, S.; Che, J.; Rong, L.; Hsiao, B.S.; Amnuaypornsri, S.; Nimpaiboon, A.; Sakdapipanich, J. Entanglements and networks to strain-induced crystallization and stress−strain relations in natural rubber and synthetic polyisoprene at various temperatures. *Macromolecules* **2013**, *46*, 5238–5248. [CrossRef]
56. Valentin, J.L.; Lopez, D.; Hernandez, R.; Mijangos, C.; Saalwachter, K. Structure of Poly(vinyl alcohol) Cryo-Hydrogels as Studied by Proton Low-Field NMR Spectroscopy. *Macromolecules* **2009**, *42*, 263–272. [CrossRef] [PubMed]
57. Che, J.; Toki, S.; Valentin, J.L.; Brasero, J.; Nimpaiboon, A.; Rong, L.; Hsiao, B.S. Chain Dynamics and Strain-Induced Crystallization of Pre- and Postvulcanized Natural Rubber Latex Using Proton Multiple Quantum NMR and Uniaxial Deformation by in Situ Synchrotron X-ray Diffraction. *Macromolecules* **2012**, *45*, 6491–6503. [CrossRef]
58. Malmierca, M.A.; Mora-Barrantes, I.; Posadas, P.; Rodríguez, A.; Ibarra, L.; Gonzalez-Jiménez, A.; Nogales, A.; Saalwachter, K.; Valentín, J.L. Characterization of Network Structure and Chain Dynamics of Elastomeric Ionomers by Means of 1H Low-Field NMR. *Macromolecules* **2014**, *47*, 5655–5667. [CrossRef]
59. Vaca Chávez, F.; Saalwächter, K. Time-domain NMR observation of entangled polymer dynamics: Analytical theory of signal functions. *Macromolecules* **2011**, *44*, 1560–1569. [CrossRef]
60. Vaca Chávez, F.; Saalwächter, K. Time-domain NMR observation of entangled polymer dynamics: Universal behavior of flexible homopolymers and applicability of the tube model. *Macromolecules* **2011**, *44*, 1549–1559. [CrossRef]
61. Doi, M.; Edwards, S.F. *The Theory of Polymer Dynamics*; Claredon Press: Oxford, UK, 1986.
62. Amnuaypornsri, S.; Sakdapipanich, J.; Tanaka, Y. Green strength of natural rubber: The origin of the stress–strain behavior of natural rubber. *J. Appl. Polym. Sci.* **2009**, *111*, 2127–2133. [CrossRef]
63. Suzuki, T.; Osaka, N.; Endo, H.; Shibayama, M.; Ikeda, Y.; Asai, H.; Higashitani, N.; Kokubo, Y.; Kohjiya, S. Nonuniformity in cross-linked natural rubber as revealed by contrast-variation small-angle neutron scattering. *Macromolecules* **2010**, *43*, 1556–1563. [CrossRef]
64. Whelan, A.; Lee, K.S. (Eds.) *Development in Rubber Technology*; Applied Science: London, UK, 1979; Volume 1.
65. García-Quesada, J.C.; Gilbert, M. Peroxide crosslinking of unplasticized poly(vinyl chloride). *J. Appl. Polym. Sci.* **2000**, *77*, 2657–2666. [CrossRef]
66. Busci, A.; Szocs, F. Kinetics of radical generation in PVC with dibenzoyl peroxide utilizing high-pressure technique. *Macromol. Chem. Phys.* **2000**, *201*, 435–438.
67. Keller, R.C. Peroxide curing of ethylene-propylene elastomers. *Rubber Chem. Technol.* **1988**, *61*, 238–254. [CrossRef]
68. Murgic, Z.H.; Jelencic, J.; Murgic, L. The mechanism of triallylcyanurate as a coagent in EPDM peroxide vulcanization. *Polym. Eng. Sci.* **1998**, *38*, 689–692. [CrossRef]
69. Class, J. A review of the fundamentals of crosslinking with peroxides. *Rubber World* **1999**, *220*, 35–39.

70. Oh, S.J.; Koenig, J.L. Studies of peroxide curing of cis-1,4-Polyisoprene/Diallyl phthalate blends by spectroscopic techniques. *Rubber Chem. Technol.* **1999**, *72*, 334–342. [CrossRef]
71. Oh, S.J.; Koenig, J.L. Studies of peroxide curing of polybutadiene/zinc diacrylate blends by fast FT-IR imaging. *Rubber Chem. Technol.* **2000**, *73*, 74–79. [CrossRef]
72. Schaich, K.M.; Karel, M. Free radical reactions of peroxidizing lipids with amino acids and proteins: An ESR study. *Lipids* **1976**, *11*, 392–400. [CrossRef]
73. Gardner, H.W. Lipid hydroperoxide reactivity with proteins and amino acids: A review. *J. Agric. Food Chem.* **1979**, *27*, 220–229. [CrossRef]
74. Saeed, S.; Fawthrop, S.A.; Howell, N.K. Electron spin resonance (ESR) study on free radical transfer in fish lipid–protein interaction. *J. Sci. Food Agric.* **1999**, *79*, 1809–1816. [CrossRef]
75. Endstra, W.C. Application of coagents for peroxide crosslinking. *Kautsch. Gummi Kunstst.* **1990**, *43*, 790–793.
76. Simpson, J.A.; Narita, S.; Gieseg, S.; Gebicki SGebick, J.M.; Dean, R.T. Long-lived reactive species on free-radical-damaged proteins. *Biochem. J.* **1992**, *282*, 621–624. [CrossRef]
77. Gebicki, S.; Gebicki, J.M. Formation of peroxides in amino acids and proteins exposed to oxygen free radicals. *Biochem. J.* **1993**, *289*, 743–749. [CrossRef]
78. Dean, R.T.; Fu, S.; Stocker, R.; Davies, M.J. Biochemistry and pathology of radical-mediated protein oxidation. *Biochem. J.* **1997**, *324*, 1–18. [CrossRef] [PubMed]
79. Hawkins, C.L.; Davies, M.J. Generation and propagation of radical reactions on proteins. *Biochim. Biophys. Acta* **2001**, *1504*, 196–219. [CrossRef]
80. Curro, J.G.; Pincus, P. A theoretical basis for viscoelastic relaxation of elastomers the long-time limit. *Macromolecules* **1983**, *16*, 559–562. [CrossRef]
81. Roth, L.E.; Vega, D.A.; Valles, E.M.; Villar, M.A. Viscoelastic properties of networks with low concentration of pendant chains. *Polymer* **2004**, *45*, 5923–5931. [CrossRef]
82. Batra, A.; Cohen, C.; Archer, L. Stress relaxation of end-linked Polydimethylsiloxane elastomers with long pendent chains. *Macromolecules* **2005**, *38*, 7174–7180. [CrossRef]
83. Moore, C.G.; Scanlan, J.J. Determination of degree of crosslinking in natural rubber vulcanizates. Part VI. Evidence for chain scission during the crosslinking of natural rubber with organic peroxides. *Polym. Sci.* **1960**, *43*, 23–33. [CrossRef]
84. Mark, H.F. Elastomers-Past, Present, and Future. *Rubber Chem. Technol.* **1988**, *61*, G73–G96. [CrossRef]
85. González, L.; Rodríguez, A.; Marcos, A.; Chamorro, C. Crosslink reaction mechanisms of diene rubber with dicumyl peroxide. *Rubber Chem. Technol.* **1996**, *69*, 203–214. [CrossRef]
86. Valentín, J.L.; Fernández-Torres, A.; Posadas, P.; Marcos-Fernandez, A.; Rodríguez, A.; González, L. Measurements of freezing-point depression to evaluate rubber network structure. Crosslinking of natural rubber with dicumyl peroxide. *J. Polym. Sci. Part B Polym. Phys.* **2007**, *45*, 544–556. [CrossRef]
87. Karino, T.; Ikeda, Y.; Yasuda, Y.; Kohjiya, S.; Shibayama, M. Nonuniformity in natural rubber as revealed by small-angle neutron scattering, small-angle x-ray scattering, and atomic force microscopy. *Biomacromolecules* **2007**, *8*, 693–699. [CrossRef]
88. Pailhories, G. Reducing proteins in latex gloves: The industrial approach. *Clin. Rev. Allergy* **1993**, *11*, 391–402. [CrossRef]
89. Ng, K.P.; Yip, E.; Mok, K.L. Production of natural rubber latex gloves with low extractable protein content: Some practical recommendations. *J. Nat. Rubber Res.* **1994**, *9*, 87–95.
90. Ghazaly, H.M. Factory production of examination gloves from low protein latex. *J. Nat. Rubber Res.* **1994**, *9*, 96–108.
91. Dalrymple, S.J.; Audley, B.G. Allergenic proteins in dipped products: Factors influencing extractable protein levels. *Rubber Dev.* **1992**, *45*, 51–60.
92. Leynadier, F.; Xuan, T.T.; Dry, J. Allergenicity suppression in natural latex surgical gloves. *Allergy* **1991**, *46*, 619–625. [CrossRef]
93. Klüppel, M.; Heinrich, G. Network Structure and Mechanical Properties of Sulfur Cured Rubbers. *Macromolecules* **1994**, *27*, 3595–3603. [CrossRef]
94. Wu, B.; Chassé, W.; Peters, R.; Brooijmans, T.; Dias, A.A.; Heise, A.; Duxbury, C.J.; Kentgens, A.P.M.; Brougham, D.F.; Litvinov, V.M. Network Structure in Acrylate Systems: Effect of Junction Topology on Cross-Link Density and Macroscopic Gel Properties. *Macromolecules* **2016**, *49*, 6531–6540. [CrossRef]
95. Lang, M. Relation between Cross-Link Fluctuations and Elasticity in Entangled Polymer Networks. *Macromolecules* **2017**, *50*, 2547–2555. [CrossRef]
96. Vilgis, T.A.; Heinrich, G. Statics and dynamics of heterogeneous polymer networks. *Macromol. Theory Simul.* **1971**, *3*, 271–293. [CrossRef]
97. Nadarajah, M.; Tirimanne, A.S.L.; Coomarasamy, A.; Kasinathan, S. Some naturally occurring antioxidants in Hevea brasiliensis latex. *J. Rubb. Res. Inst. Sri Lanka* **1971**, *48*, 202–211.
98. Tuampeomsab, S.; Sakdapipanich, J.; Tanaka, Y. Influence of some non-rubber components on aging behavior of purified natural rubber. *Rubber Chem. Technol.* **2007**, *80*, 159–169. [CrossRef]

99. Hasma, H. Role of some non-rubber constituents on thermal oxidative aging of natural rubber. *J. Nat. Rubb. Res.* **1990**, *5*, 1–18.
100. Tuampeomsab, S.; Sakdapipanich, J. Role of naturally occurring lipids and proteins on thermal aging behaviour of purified natural rubber. *Kautsch. Gummi Kunstst.* **2007**, *12*, 678–684.
101. Halliwell, B.; Gutteridge, J.M.C. *Free Radicals in Biology and Medicine*, 3rd ed.; Clarendon Press: Oxford, UK, 1999.
102. Gebicki, J.M. Protein hydroperoxides as new reactive oxygen species. *Redox Rep.* **1997**, *3*, 99–110. [CrossRef]
103. Tanaka, Y.; Tarachiwin, L. Recent advances in structural characterization of natural rubber. *Rubber Chem. Technol.* **2009**, *82*, 283–314. [CrossRef]

polymers

MDPI

Article

Sulfur and Peroxide Cross-Linking of Lignosulfonate-Filled Compounds Based on Acrylonitrile–Butadiene Rubber and Styrene–Butadiene Rubber

Ján Kruželák [1,*], Michaela Džuganová [1], Andrea Kvasničáková [1], Ján Hronkovič [2], Jozef Preťo [2], Ivan Chodák [3] and Ivan Hudec [1]

[1] Department of Plastics, Rubber and Fibres, Faculty of Chemical and Food Technology, Slovak University of Technology in Bratislava, Radlinského 9, 812 37 Bratislava, Slovakia; michaela.dzuganova@stuba.sk (M.D.); andrea.kvasnicakova@stuba.sk (A.K.); ivan.hudec@stuba.sk (I.H.)
[2] VIPO a.s., Gen. Svobodu 1069/4, 958 01 Partizánske, Slovakia; jan.hronkovic@vipo.sk (J.H.); jpreto@vipo.sk (J.P.)
[3] Slovak Academy of Sciences, Polymer Institute, Dúbravská Cesta 9, 845 41 Bratislava, Slovakia; ivan.chodak@savba.sk
* Correspondence: jan.kruzelak@stuba.sk

Abstract

Calcium lignosulfonate was incorporated into rubber compounds based on styrene–butadiene rubber (SBR) and acrylonitrile–butadiene rubber (NBR) in amounts ranging from 10 to 60 phr. A sulfur-based curing system and a peroxide curing system consisting of dicumyl peroxide in combination with methacrylic acid zinc salt were used for cross-linking of the compounds. The aim of the work was to investigate the influence of lignosulfonate and curing system composition of the cross-linking process, morphology, physical–mechanical and dynamic–mechanical characteristics of the composites. The achieved results showed that peroxide cured composites demonstrated higher cross-link density, which was found not to be influenced by the content of lignosulfonate. The cross-link density of sulfur-cured composites was lower and showed a decreasing tendency with increasing amounts of the biopolymer. A lower cross-linking degree was reflected in a higher elongation at break and higher increase in the elongation at break of the corresponding composites. On the other hand, peroxide-cured composites exhibited a higher modulus M100 and higher hardness. The microscopic analysis revealed that co-agent in peroxide vulcanization contributed to the improvement of adhesion between the biopolymer and the rubber resulting in higher tensile strength of the equivalent composites. The higher cross-link density of peroxide-cured composites caused higher restriction of the chain segments' mobility, due to which these composites exhibited a higher glass transition temperature.

Keywords: rubber; biopolymer; sulfur curing system; peroxide curing system; cross-linking; properties

1. Introduction

The depletion of sources, global warning, and negative effects on the environment have shifted the awareness towards bio-economy and green technologies. Lignocellulosic raw materials represent suitable alternatives to petroleum-based products, as they are highly available and sustainable and have a positive effect on global greenhouse gas reduction. Lignin is the second most widespread biopolymeric material in the world and thus bears a huge application potential. The annual production of technical lignin is about 50–70 million

tons, of which only 1–2% is used to produce the value-added goods. The rest is landfilled or burned to generate energy or to recover chemicals [1,2]. Lignin exhibits highly branched amorphous aromatic structure with diversity of functional groups as carboxyls, carbonyls, hydroxyls, or methoxy groups. Due to these groups, lignin exhibits attractive properties including antimicrobial, antioxidant, UV absorption, adhesive properties, hydrophobicity, etc. [3–7].

There are several types of lignin depending on the processing method and extraction procedures [7–11]. Sulfur and sulfur-free extraction processes are the most common procedures to obtain lignin from lignocellulosic parts of wood and plants. Sulfur-based lignins include Kraft lignin and lignosulfonates. Kraft lignin is derived by Kraft pulping using sodium sulfide and sodium hydroxide at pH between 13 and 14. The sulfite pulping process is acid-catalyzed and basic (pH between 1 and 2) using an aqueous sulfur dioxide and a sodium, calcium, ammonium, or magnesium salt-based acid. When compared to Kraft lignin, lignosulfonates contain less free carboxyl and phenolic hydroxyl groups and higher amount of sulfur, mainly in the form of sulfonate groups [12,13]. Due to the presence of sulfonate groups, they are water-soluble. Lignosulfonates have been widely used as dispersant agents, surfactants, binders, compatibilizers, additives to concretes, and composites [14–17]. In addition, due to their aromatic structure, high amount of carbon, good mechanical stability, and viscoelastic properties, they are suitable materials as additives and fillers in rubber-based compounds and composites [18–22]. To fabricate polymer composite materials with good applicable and utility properties, good adhesion and interactions between the filler and the rubber matrix on their interfacial region must be formed. Lignins and lignosulfonates are polar materials and thus their compatibility with non-polar matrices is usually poor, often resulting in weak physical–mechanical properties of the final composites. On the other hand, polar functional moieties provide space for surface modification and thus increasing interactions with rubber matrices. Good adhesion and formation of interactions between the filler and the rubber on the filler–rubber interface is the basic principle for rubber composites' reinforcement.

The final utility properties of rubber goods are achieved during the vulcanization or curing. Vulcanization is a physical–chemical process during which a plastic rubber compound is transformed into cross-linked highly elastic products—vulcanized by chemical reactions between functional groups of rubber and curing additives. The cross-linked network improves the dimensional stability of rubber materials; increases elasticity, mechanical, and dynamical properties; and reduces hysteresis or plasticity. A variety of curing systems have been applied for the cross-linking of rubber compounds, such as sulfur-based systems, organic peroxides, phenol–formaldehyde resins, quinones, metal oxides, amines, ureas, etc. Among them, sulfur curing systems are the most commonly used, accounting for about 90% or rubber-based articles, followed by organic peroxides.

Sulfur vulcanization is the oldest method used for cross-linking unsaturated rubbers. Sulfur is always used in combination with activators and accelerators. Sometimes, retarders of vulcanization or prevulcanization inhibitors can be part of sulfur curing systems, too. The mechanism and chemistry of sulfur vulcanization is very complex and still not comprehensibly elucidated. During the process, rubber chains segments are linked with sulfur-based cross-links having different lengths and amounts of sulfur in sulfur bridges (monosulfidic, disufidic, and polysulfidic cross-links) [23,24]. In general, sulfur-cured vulcanizates demonstrate good tensile behavior, good elastic and dynamic properties, good abrasion resistance, or good resistance to dynamic fatigue. On the other hand, due to the low bonding energy of sulfidic cross-links, their thermo-oxidative stability is usually weak [25–27].

Organic peroxides can be applied to vulcanize both saturated and unsaturated rubbers. By the application of organic peroxides, carbon–carbon bonds are formed between the chains [28]. C-C bonds have higher dissociation energy when compared to sulfidic cross-links, and thus the main feature of peroxide-cured rubbers is higher thermal resistance and higher resistance to degradation factors, like oxygen and heat [29,30]. On the other side, when compared to sulfur-cured vulcanizates, they usually have worse tear and tensile strength and weaker dynamic properties.

To boost the cross-linking process with organic peroxides, double bonds containing organic compounds, termed as co-agents, are often used [31,32]. The co-agents help to increase the efficiency of peroxide curing process by enhancing the cross-link density and by modifying the cross-links' structure. Couple of reaction mechanisms have been proposed for particular types of co-agents. In general, network enhancement through the homopolymerization and grafting of co-agents between the chain segments are the main co-agents' reaction mechanisms [33–36]. As a lot of co-agents are polar materials, they also increase the polarity of rubber compounds and enhance adhesion towards polar fillers and additives in the rubber compounding.

In this study, calcium lignosulfonate in various amounts was incorporated into NBR- and SBR-based formulations. A sulfur curing system and organic peroxide in combination with a co-agent were applied for cross-linking. The main aim was to compare the effect of vulcanization systems on the cross-linking process, physical–mechanical, and dynamic–mechanical properties of the composites.

2. Experimental

2.1. Materials

Styrene–butadiene rubber (SBR, Kralex 1502, styrene content—23.5 wt.%, Mooney viscosity ML 1 + 4 (100 °C)—52) prepared by cold emulsion polymerization was supplied from Synthos Kralupy, a.s., Kralupy nad Vltavou, Czech Republic. Acrylonitrile–butadiene rubber (NBR, SKN 3345, acrylonitrile content—31–35%, Mooney viscosity ML 1 + 4 (100 °C)—45) was supplied from Sibur International, Moscow, Russia. Calcium lignosulfonate having trade name Borrement CA120 was provided by Borregaard Deutschland GmbH, Karlsruhe, Germany. The molecular weight of lignosulfonate was 24,000 $g \cdot mol^{-1}$ and the specific surface area was 3.9 $m^2 \cdot g^{-1}$. In addition to carbon (46.63 wt.%), the biopolymer contained hydrogen (5.35 wt.%), nitrogen (0.14 wt.%), sulfur (5.62 wt.%), and hydroxyl groups (1.56 wt.%). Lignosulfonate was applied into rubber formulations in a concentration scale ranging from 10 to 60 phr. For the cross-linking of rubber compounds, sulfur and peroxide curing systems were used. The sulfur-based curing system consisted of zinc oxide (3 phr) and stearic acid (2 phr) as activators, accelerator *N*-cyclohexyl-2-benzothiazole sulfenamide CBS (1.5 phr), and sulfur as curing agent (1.5 phr). The additives of the sulfur curing system were supplied from Vegum a.s., Dolné Vestenice, Slovak Republic. The peroxide curing system consisted of dicumyl peroxide DCP as curing agent (1 phr) and methacrylic acid zinc salt ZDMA (10 phr) as co-agent. DCP and ZDMA were supplied from Sigma-Aldrich, St. Louis, MO, USA.

2.2. Methods

2.2.1. Fabrication and Curing

The fabrication of the composites was performed in a laboratory kneader Brabender (Brabender GmbH & Co. KG, Duisburg, Germany) at 90 °C and 55 rpm. The mixing process was carried out in two steps.

First, rubber was plasticated for 1 min, then the activators of the sulfur curing system were added. Calcium lignosulfonate was introduced after 2 min, and the rubber mixture was compounded for the next 4 min. After the first step of mixing, the rubber compounds

were additionally homogenized and sheeted by using a two-roll mill. Sulfur and the accelerator were introduced in the second step, and the mixing process continued in the kneader for 4 min at 90 °C with rotor speed set up to 55 rpm. Finally, the rubber compounds were sheeted in a two-roll mill.

The compounding procedure of rubber formulations with the peroxide curing system proceeded following the same conditions (90 °C, 55 rpm, overall time of mixing 10 min). The rubber and the filler were compounded in the first step, which took 6 min, and additives of curing systems were applied in the second step. Final homogenization and sheeting were accomplished in a two-roll mill.

The curing process was carried out using a Fontijne hydraulic press (Fontijne, Vlaardingen, The Netherlands) following the optimum cure time of each rubber compound. The temperature of curing was 170 °C and the press was 15 MPa. After curing, thin sheets with dimensions of 15 × 15 cm and a thickness of 2 mm were obtained.

2.2.2. Determination of Curing Characteristics

An MDR 2000 oscillatory rheometer (Alpha Technologies, Akron, OH, USA) was used to determine curing isotherms and curing characteristics.

The investigated curing parameters were as follows:

M_L (dN·m)—minimum torque;

M_H (dN·m)—maximum torque;

ΔM (dN·m)—torque difference, $\Delta M = M_H - M_L$;

t_{c90} (min)—optimum curing time;

t_{s1} (min)—scorch time.

2.2.3. Determination of Cross-Link Density

To calculate the cross-link density ν, dried and weighted samples were immersed in xylene, in which they swelled. The samples were taken out from the solvent every hour, wiped out of solvent, and weighted. When the weight of the samples was constant, equilibrium swelling was reached and used for the determination of cross-link density by the Krause-modified Flory–Rehner equation [37].

2.2.4. Investigation of Physical–Mechanical Characteristics

The tensile tests were performed according to valid technical standards using Zwick Roell/Z 2.5 tearing equipment (Zwick GmbH & Co. KG, Ulm, Germany). The cross-head speed was set up to 500 mm·min^{-1} with a gauge length of 25 mm. Dumbbell-shaped specimens (width 6.4 mm, length 80 mm) were cut with a special knife from a 2 mm thick cured rubber plate. The hardness in Shore A was measured by using a durometer.

2.2.5. Microscopic Analysis

The surface morphology was evaluated by a JEOL JSM-7500F scanning electron microscope (Jeol Ltd., Tokyo, Japan). The samples were first cooled down in liquid nitrogen under glass transition temperature and then fractured into small fragments with surface area of 3 × 2 mm. The fractured surface was covered with a thin layer of gold and put into the microscope. The source of electrons was a cold cathode UHV field emission gun, the accelerate voltage ranged from 0.1 kV to 30 kV, and the resolution was 1.0 nm at 15 kV and 1.4 nm at 1 kV. SEM images were captured by a CCD-Camera EDS (Oxford INCA X-ACT, Jeol Ltd., Tokyo, Japan).

3. Results and Discussion

3.1. Curing Process and Cross-Link Density

The corresponding vulcanization isotherms of rubber compounds cured with the sulfur and peroxide systems are illustrated in Figure 1. It becomes apparent from them that the course of curing isotherms was influenced by the type of rubber as well as by the curing system composition. From Figure 2, it becomes apparent that the minimum torque M_L of both SBR- as well as NBR-based compounds show an increasing trend with increasing content of the biopolymer. The minimum torque, to a certain extent, relates to the viscosity of the compounds before the curing process started, which suggests that the incorporation of the biopolymer resulted in an increase in viscosity. The highest minimum torque was exhibited by rubber compounds based on SBR cured with the peroxide system, followed by the equivalent compounds cured with the sulfur system. The compounds based on NBR cured with both vulcanization systems demonstrated a lower M_L. This points to the higher viscosity of SBR-based rubber formulations, as SBR exhibited higher Mooney viscosity. When comparing curing systems, higher minimum torque and thus higher viscosity were manifested by rubber compounds with the peroxide system applied. The maximum torque showed an increasing trend with increasing amounts of the biopolymer, too. As shown in Figure 1A,B, the M_H of the compounds based on SBR and NBR cured with the sulfur system was very similar. When comparing both types of rubber formulations cured with the peroxide system (Figure 1C,D), one can see that higher maximum torque was exhibited by those based on SBR.

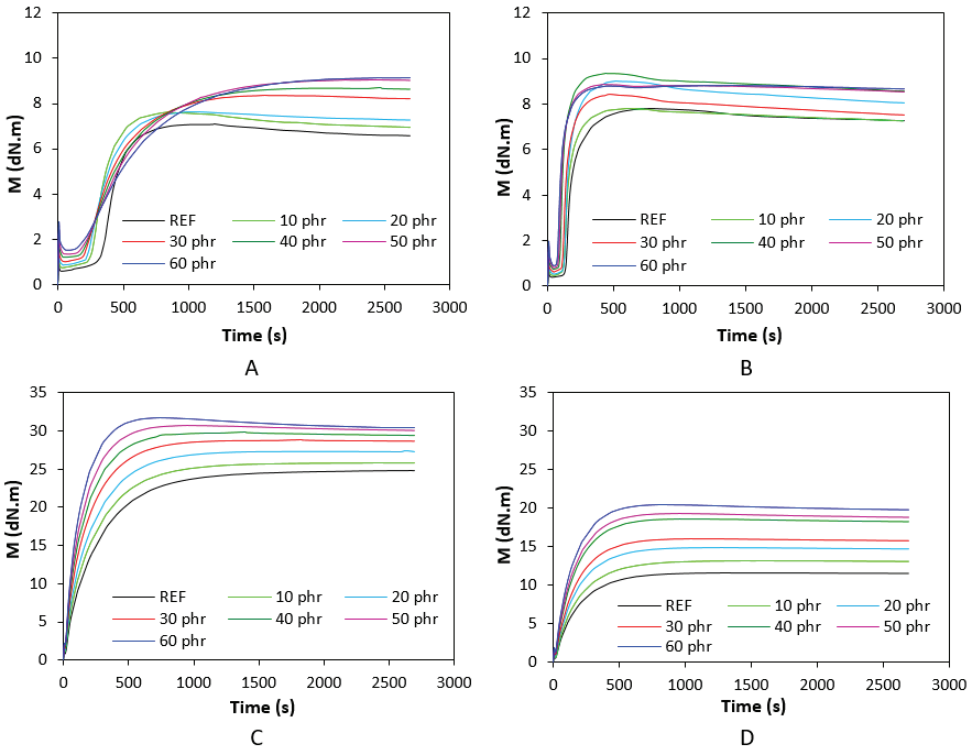

Figure 1. Curing isotherms of SBR-based composites cured with sulfur system (**A**). NBR-based composites cured with sulfur system (**B**). SBR-based composites cured with peroxide system (**C**). NBR-based composites cured with peroxide system (**D**).

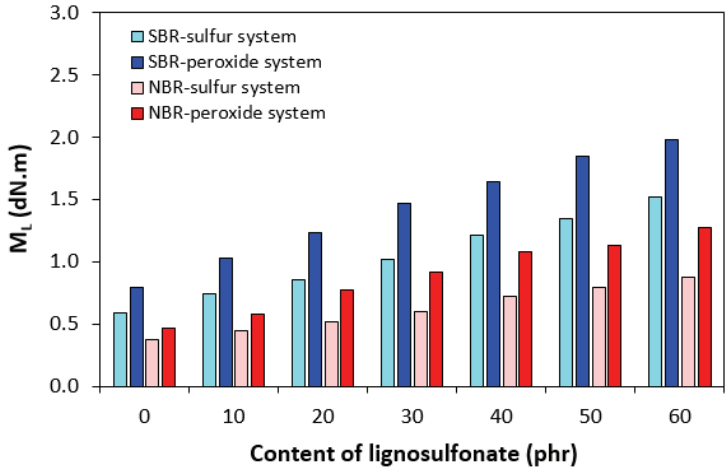

Figure 2. Influence of lignosulfonate content and curing system composition on minimum torque M_L of composites.

The highest difference between the maximum and minimum torque ΔM was demonstrated by SBR-based formulations cured with peroxide system, followed by the equivalent compounds based on NBR (Figure 3). The SBR- and NBR-based compounds cured with sulfur system exhibited lower ΔM. The difference between maximum and minimum torque ΔM is to a large extent proportional to the cross-link density, and when comparing Figures 3 and 4, one can see a very close correlation between both characteristics. The highest cross-link density was exhibited by peroxide-cured composites based on SBR having the highest ΔM. On the other hand, SBR-based composites cured with the sulfur system with the lowest torque difference demonstrated the lowest degree of cross-linking (Figure 4). The incorporation of lignosulfonate resulted in a slight decrease in cross-link density for both SBR- and NBR-based compounds cured with the sulfur system. On the other hand, almost no influence of the biopolymer on cross-link density was recorded for rubber formulations cured with the peroxide system. The corresponding swelling indexes are presented in Figure 5. The higher the degree of cross-linking, the shorter the chain segments between the cross-links and the lower the free volume in the matrix. With a lower free volume, a lower amount of solvent can diffuse into the compounds. As seen in Figure 5, the highest amount of xylene was diffused into the samples in the initial stages of swelling, up to 5–6 h. Equilibrium swelling was achieved after 24 h.

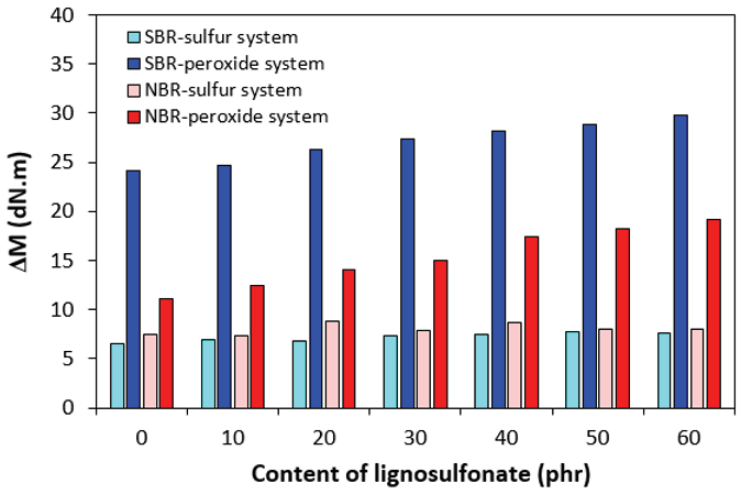

Figure 3. Influence of lignosulfonate content and curing system composition on torque difference ΔM of composites.

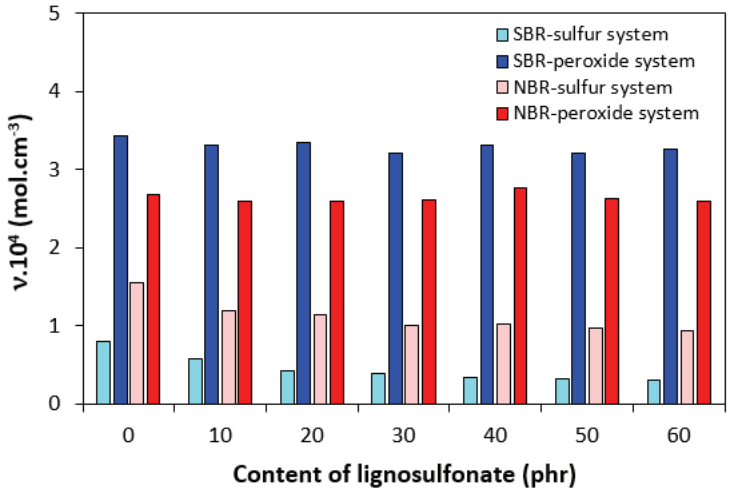

Figure 4. Influence of lignosulfonate content and curing system composition on cross-link density v of composites.

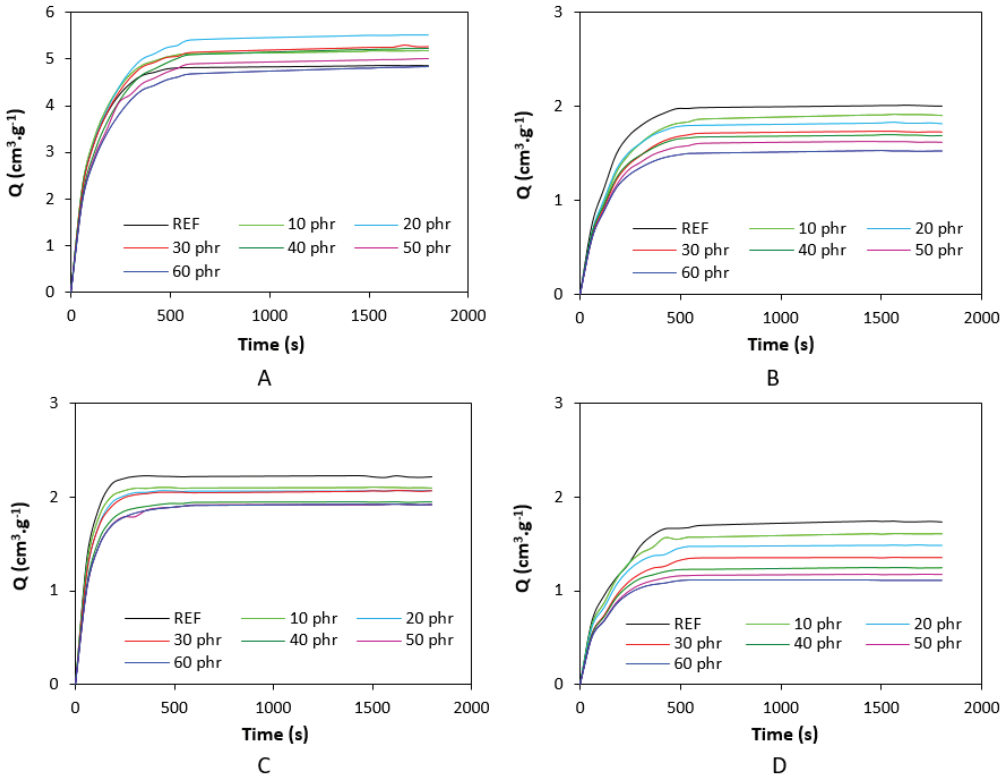

Figure 5. Swelling indexes of SBR-based composites cured with sulfur system (**A**). NBR-based composites cured with sulfur system (**B**). SBR-based composites cured with peroxide system (**C**). NBR-based composites cured with peroxide system (**D**).

The application of lignosulfonate caused a decrease in scorch time t_{s1} for rubber formulations cured with the sulfur system (Figure 6). The scorch time of the compounds cured with the peroxide system was much lower and was found to be independent on the content of the biopolymer. With the exception of the compounds based on SBR cured with the sulfur system, the optimum cure time t_{c90} showed a decreasing trend with increasing content of lignosulfonate (Figure 7). On the other hand, a significant prolongation of the optimum cure time was recorded for sulfur-cured SBR-based formulations with high biopolymer content.

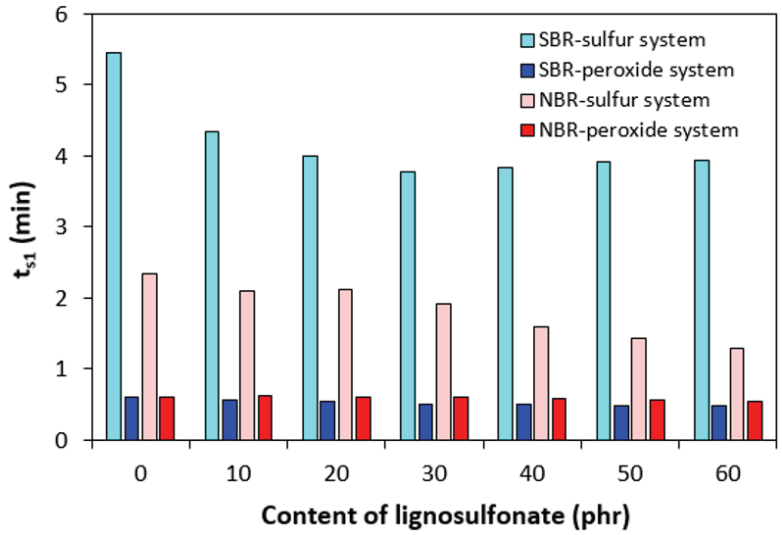

Figure 6. Influence of lignosulfonate content and curing system composition on scorch time t_{s1} of composites.

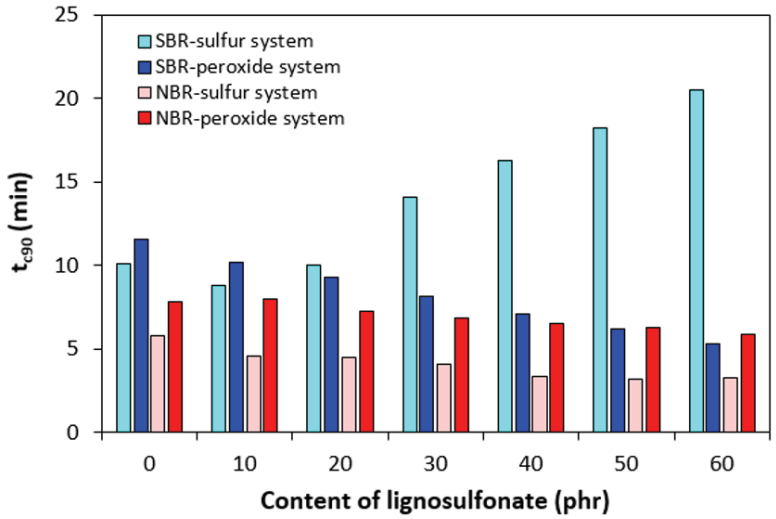

Figure 7. Influence of lignosulfonate content and curing system composition on optimum cure time t_{c90} of composites.

Peroxide vulcanization is a radical process, during which organic peroxide first undergoes homolytic cleavage via breaking labile oxygen–oxygen bonds at a curing temperature [38]. The formed radical species promptly react with rubber chain segments to form cross-links between them. To that corresponds a very low scorch time (Figure 6). The regulation of scorch time during peroxide vulcanization is very complicated as it is achieved only by the type of peroxide and its dissociation rate at a curing temperature [39–41]. It becomes apparent from Figure 6 that scorch time for both types of rubber formulations cured with the peroxide system was very similar and fluctuated by only around half a minute.

Both NBR- and SBR-based compounds cured with the peroxide system exhibited very similar curing kinetics, i.e., scorch time and optimum cure time, but differed in torque difference and cross-link density. Thus, the insight into the mechanism of vulcanization should be outlined. SBR and NBR are copolymers of styrene or acrylonitrile, respectively. Styrene and acrylonitrile structural units do not provide active sites for cross-linking. Cross-linking of both rubbers is performed exclusively via butadiene structural units [27,36,42–44]. The active radical species formed from peroxide decomposition can react with rubber chains in two ways. The first mechanism involves the abstraction of reactive allylic hydrogens from rubber

chains to form macromolecular radicals. During the second mechanism, the peroxide-derived radicals attack the double bonds in the rubber structure, again followed by the formation of macromolecular radicals. The formed macroradicals can either mutually recombine or participate in addition reactions with the free double bonds in rubber chains, mainly those situated in 1,2-butadiene structural units. Pendant vinyl units are very prone to radical addiction mechanisms. Moreover, they are less sterically hindered and thus more accessible for radical species when compared to double bonds in the main chains (cis/trans) [45–47]. The chain character of addition reactions results in high cross-linking effectiveness. The highest torque difference and cross-link density were exhibited by peroxide-cured composites based on SBR. The peroxide cross-linking efficiency of NBR is lower, as NBR contains lower amount of butadiene structural units. Also, electron-withdrawing acrylonitrile groups make double bonds in NBR less reactive, so addition reactions have been reported to be of lower importance than in the case of SBR [36,48]. Thus, the equivalent NBR-based composites exhibited lower torque difference and lower cross-link density. The co-agent used in combination with dicumyl peroxide contributed to the increase in the cross-link density of both composite types, too. The specific reaction mechanism of methacrylic acid zinc salt in peroxide vulcanization is discussed in following section.

On the other hand, sulfur vulcanization of rubber compounds is a very complex process. Although it is still not clearly understood, it has been proposed that it proceeds in three general stages. In the first stage, the accelerator reacts with the activators to form a transition complex, which then reacts with sulfur to generate an active sulfurating agent. This stage is called the induction period, and the length of induction period is dependent on the composition of the sulfur curing system, mainly on the type of accelerator. The used accelerator CBS is the class of delayed-action accelerators, which is characterized by a prolonged induction period [49,50]. To that corresponds the longer scorch time of sulfur-cured formulations when compared to those cured with the peroxide system (Figure 6). In the second stage, the active sulfurating agent substitutes the allylic hydrogens in rubber chains via a sulfur bridge, forming cross-link precursors. A primary vulcanizate network with a prevalence of polysulfidic cross-links is formed. In the third phase, the restructuration of the formed polysulfidic cross-links and modification of the rubber chains occur, and the final three-dimensional vulcanizate network is generated [27,51].

The experimental results showed that sulfur-cured rubber compounds based on NBR demonstrated a lower scorch time and lower optimum cure time when compared to corresponding compounds based on SBR. Simultaneously, both characteristics showed a decreasing trend with increasing content of the biopolymer, demonstrating its accelerating effect on the sulfur vulcanization of NBR-based formulations. However, the prolongation of the optimum cure time of SBR-based formulations with increasing content of lignosulfonate suggests that it has a retarding effect in the sulfur vulcanization of SBR.

Sulfur-cured SBR-based formulations demonstrated lower cross-link density, which seems to be a bit surprising as SBR contains a higher amount of butadiene structural units and thus a higher amount of active cross-linking sites. The higher cross-link density of composites based on NBR might be attributed to higher branching and entanglements of the rubber chains and polar structural units of NBR. Upon generation of chemical cross-links between adjacent entangled and branched rubber chains, the physical entanglements can also act as cross-linking points. Due to the presence of polar acrylonitrile units, stronger intermolecular interactions are formed between the chain segments, which could contribute to the higher cross-linking degree of NBR-based formulations, too. As also shown in Figure 4, the cross-link density of sulfur-cured composites based on NBR as well as SBR showed a slight decreasing trend with increasing content of calcium lignosulfonate. A possible explanation for this is that lignosulfonate could sterically hinder the formation of

the cross-links between the chain segments. On the other hand, no negative influence of the biopolymer on the cross-link density of peroxide-cured composites suggest that organic peroxide in combination with a co-agent could cause the cross-linking of lignosulfonate or contribute to the formation of linkages between the biopolymer and the rubber matrix.

3.2. Physical–Mechanical Properties and Morphology

The incorporation of lignosulfonate resulted in an increase of the composites' hardness, suggesting that the hardness of the biopolymer was higher than that of the rubbers (Figure 8). The dependence of hardness on the type of rubber matrix and curing system composition was directly proportional to cross-link density (Figure 4). The highest cross-link density of composites based on SBR cured with the peroxide system was responsible for the highest hardness. On the other hand, the equivalent composites cured with the sulfur system with the lowest cross-linking degree exhibited the lowest hardness. The hardness of composites based on NBR ranged between the sulfur- and peroxide-cured composites based on SBR and was higher for peroxide-cured counterparts, again following the trend of cross-link density.

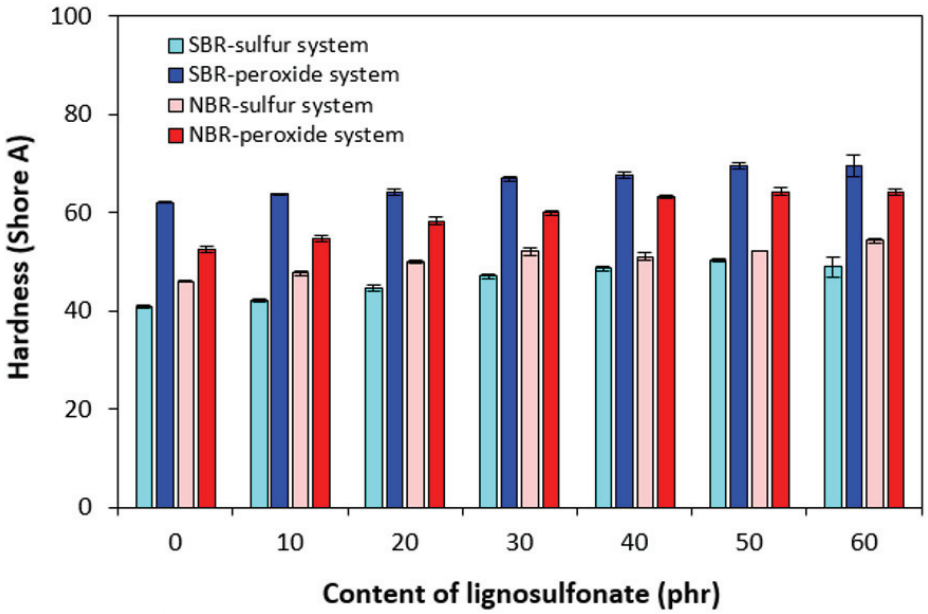

Figure 8. Influence of lignosulfonate content and curing system composition on hardness of composites.

The higher cross-linking degree of both composite types cured with peroxide system was reflected in the higher modulus M100 (Figure 9). The M100 of NBR-based composites cured with the peroxide system was found to increase with increasing content of calcium lignosulfonate. The M100 of the peroxide-cured reference based on SBR was not possible to detect as this sample ruptured before reaching 100% elongation. The composites cured with the sulfur system demonstrated almost the same modulus with no influence on the biopolymer content. As also shown, the M100 of sulfur-cured composites was much lower than that of peroxide-cured equivalents due to their much lower cross-link density.

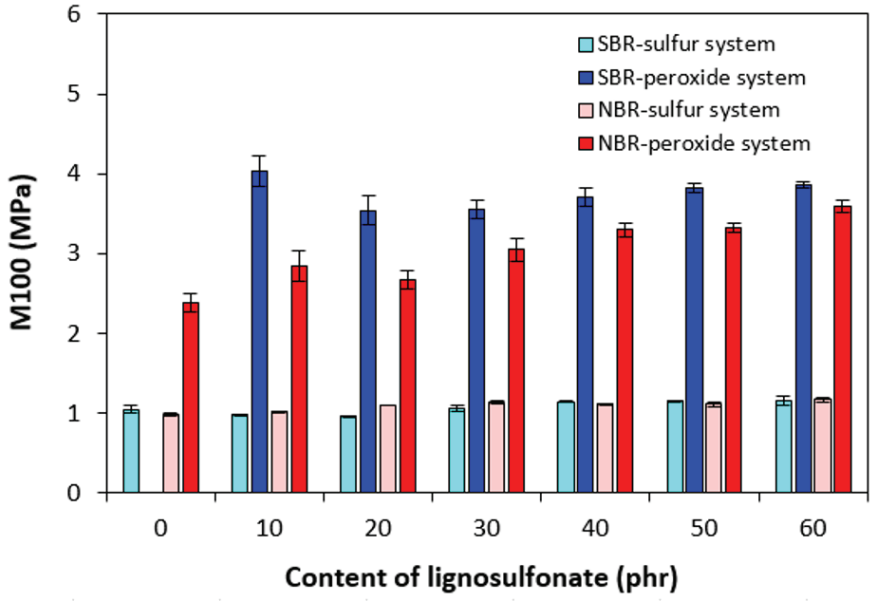

Figure 9. Influence of lignosulfonate content and curing system composition on modulus M100 of composites.

On the other hand, the lower cross-link density of composites cured with the sulfur system resulted in their higher elongation at break (Figure 10). The elongation at break of the sulfur-cured composites based on NBR and SBR was very similar and was significantly dependent on the amount of the biopolymer. At the maximum lignosulfonate content, the elongation at break increased by less than 500% for SBR-based composites (from about 340% for the reference up to 830% for the composite with 60 phr of the biopolymer). In the case of sulfur-cured NBR-based composites, the elongation at break increased from 460% up to 790% by an increase in biopolymer content from 0 up to its maximum content. The higher the cross-link density, the higher the restriction of rubber chain segments' elasticity and mobility, resulting in a decrease in elongation at break. The lowest elongation at break was exhibited by the SBR-based composites cured with the peroxide system with the highest cross-linking degree. As the cross-link density of peroxide-cured composites almost did not change with the change in lignosulfonate content, the elongation at break of the equivalent composites was much less dependent on lignosulfonate content. When compared to the references, the elongation at break increased by about 90% and 140% for the maximally filled composites based on NBR or SBR, respectively. Another factor contributing to the different elongation at break of sulfur- and peroxide-cured composites is the structure of the formed cross-links. Longer and more flexible sulfidic cross-links facilitate micro-Brownian motion of the chain segments between the cross-links, which results in better elastic properties in the sulfur cured rubber materials. Higher elasticity of the chain segments causes higher redistribution of the deformation strains within the rubber matrix, resulting in higher tensile characteristics, too. On the other hand, shorter and rigid carbon–carbon bonds restrict the orientation and mobility of the chain segments, which results in formation of local stress concentrations. To that correspond the worse dynamic and tensile behavior of peroxide-cured vulcanizates in general [27,29,52].

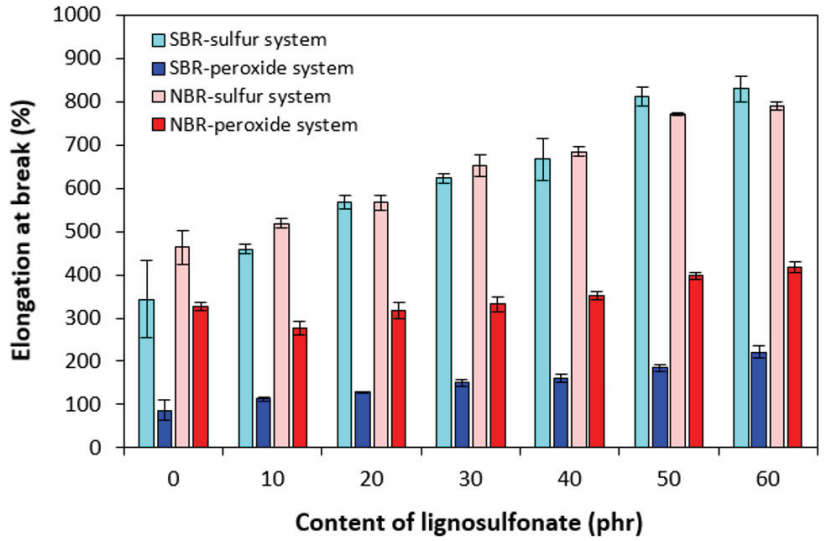

Figure 10. Influence of lignosulfonate content and curing system composition on elongation at break of composites.

From Figure 11, it becomes apparent that with the exception of the peroxide-cured reference sample based on NBR, the other reference samples exhibited roughly the same tensile strength. The tensile strength of sulfur-cured composites based on SBR was almost not influenced by the amount of the biopolymer, and it fluctuated only in a very low range of experimental values. The influence of lignosulfonate on the tensile strength of sulfur-cured NBR-based composites was also very low, though highly filled NBR-based composites exhibited slightly higher tensile strength when compared to equivalent sulfur-cured composites based on SBR. The application of the peroxide curing system resulted in the enhanced tensile behavior of composites, and the highest tensile strength was manifested by peroxide-cured composites based on NBR. By the incorporation of 10 phr of the biopolymer, an improvement in the tensile strength of both peroxide-cured composites was recorded when compared to the references. Then, no significant influence of lignosulfonate content on tensile strength was observed. The higher tensile characteristics of peroxide-cured vulcanizates can be attributed to the presence of a co-agent in peroxide vulcanization.

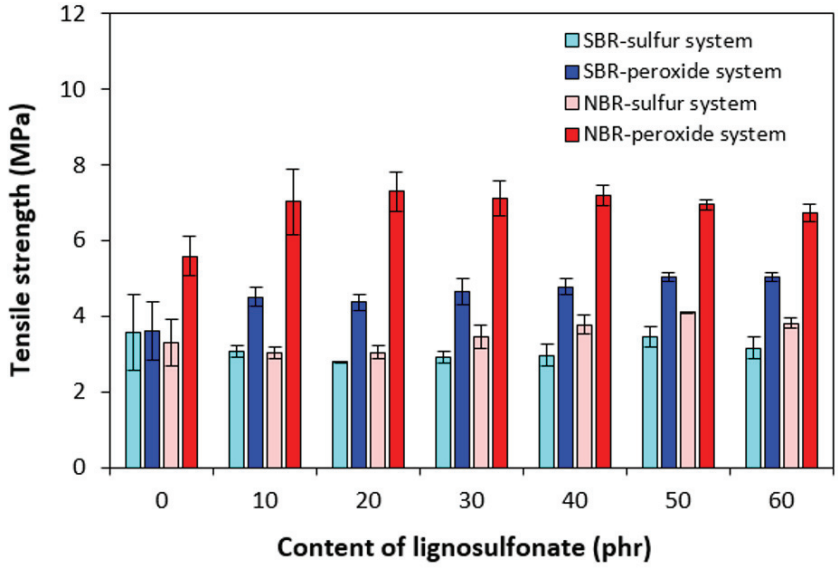

Figure 11. Influence of lignosulfonate content and curing system composition on tensile strength of composites.

It has been reported that methacrylic acid zinc in the presence of organic peroxide can undergo in situ polymerization within the rubber matrix. Polymerized molecules of ZDMA can be physically adsorbed or chemically grafted onto rubber chains [53–55]. Thus, they form physical and chemical linkages in the rubber matrix. In addition, having polar-character ZDMA exhibits strong adhesion to polar materials [56,57]. Due to the presence of zinc ions, ZDMA can form ionic cross-links or ionic clusters, which can interact with polar functional groups of lignosulfonate. This leads to improvement in the adhesion and compatibility between the rubber and the biopolymer on the filler–rubber interface. Subsequent improvement in tensile strength was achieved. It becomes apparent from Figure 11 that higher tensile strength was demonstrated by composites based on NBR. As NBR, calcium lignosulfonate, and ZDMA are polar materials, their adhesion, compatibility, and formation of physical interactions between the components is higher when compared to non-polar SBR.

The surface morphology of composites was studied by performing scanning electron microscopy (SEM). SEM images of the SBR-based composites cured with the sulfur system are presented in Figure 12 on the left side, while SEM images of the equivalent composites based on NBR are depicted in Figure 12 on the right side. Similarly, SEM images of peroxide-cured composites based on SBR and NBR are presented in Figure 13 on the left or right side, respectively. It is shown in Figure 12 that lignosulfonate tended to agglomerate in sulfur-cured composites. The agglomeration and worse dispersion of lignosulfonate within the rubber matrices cured with the sulfur system are the main reasons why lignosulfonate does not behave as a reinforcing filler. However, it should be remarked that although the application of lignosulfonate did not result in improvement in the tensile strength, no negative effect on the characteristic was recorded even at high lignosulfonate contents. Looking at Figure 13, one can see that the surface fractures of composites cured with peroxide system seem to be more compact, and better adhesion between the rubber and lignosulfonate on the interfacial region was achieved due to the presence of ZDMA. Some surface cracks visible on SEM images can be attributed to lignosulfonate, which was first melted during vulcanization at high temperatures. Then, the samples were frozen in liquid nitrogen, which might result in the brittleness of lignosulfonate. The cracks could then be caused by the fracturing of frozen samples for SEM analysis.

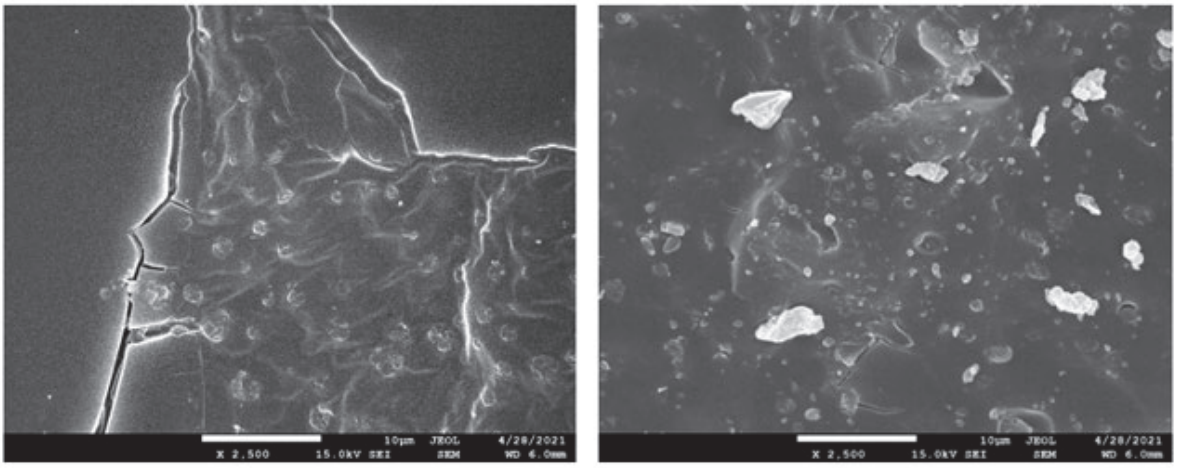

Figure 12. *Cont.*

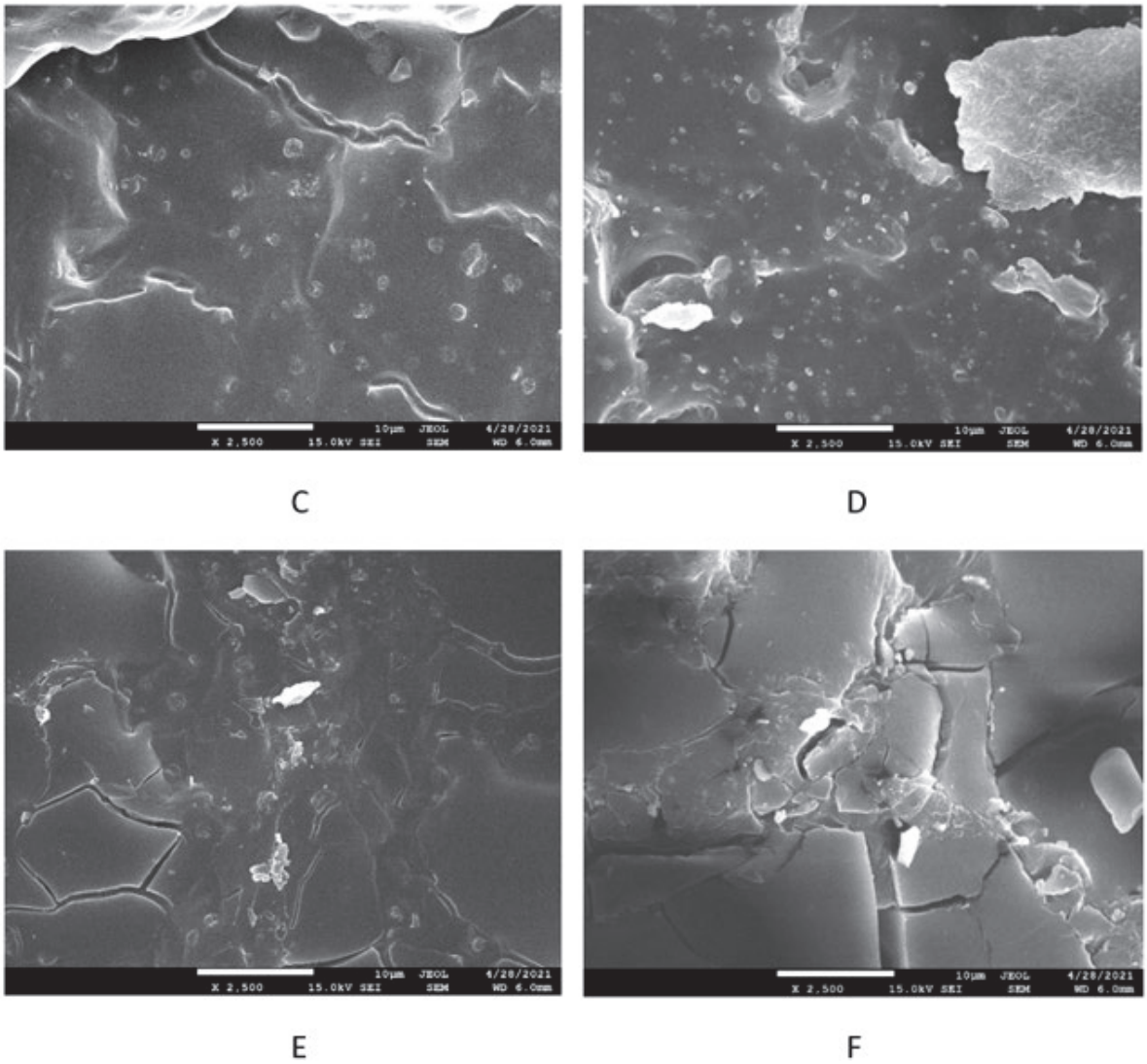

Figure 12. SEM images of sulfur-cured SBR-based composites filled with 10 phr of lignosulfonate (**A**), 30 phr of lignosulfnate (**C**), and 60 phr of lignosulfonate (**E**); sulfur-cured NBR-based composites filled with 10 phr of lignosulfnate (**B**), 30 phr of lignosulfnate (**D**), and 60 phr of lignosulfonate (**F**).

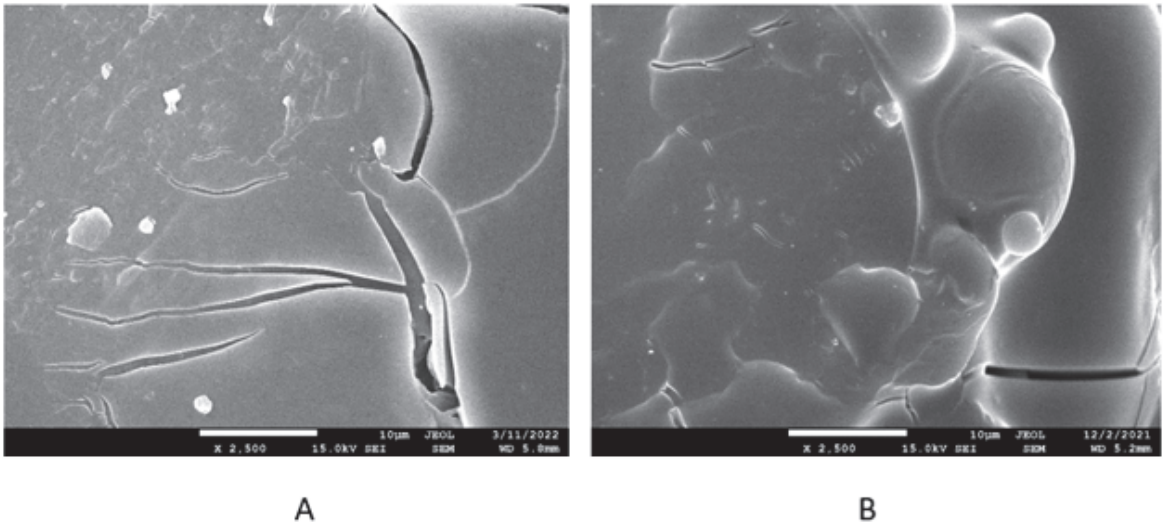

Figure 13. *Cont*.

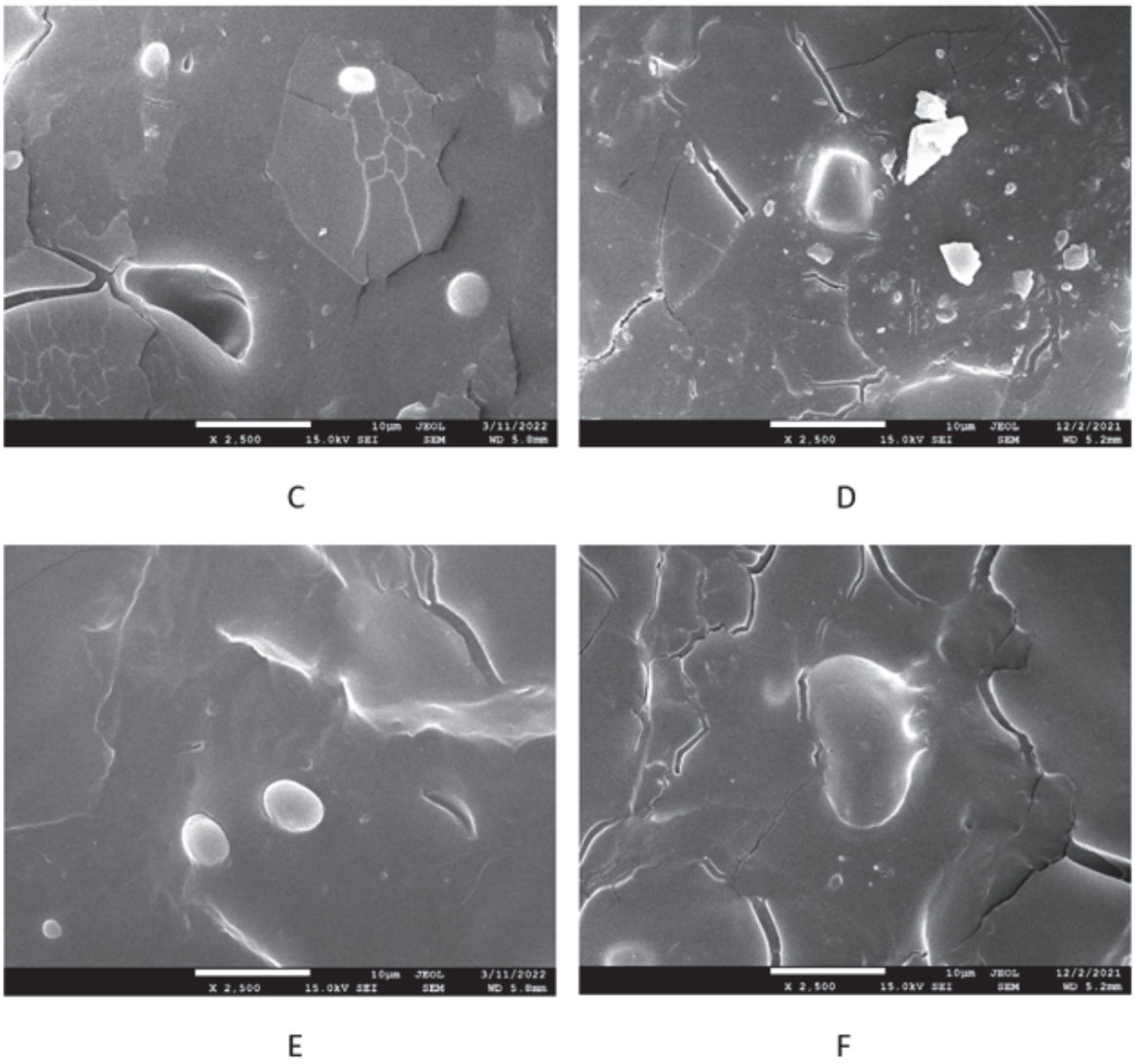

Figure 13. SEM images of peroxide-cured SBR-based composites filled with 10 phr of lignosulfonate (**A**), 30 phr of lignosulfnate (**C**), and 60 phr of lignosulfonate (**E**); peroxide cured NBR-based composites filled with 10 phr of lignosulfnate (**B**), 30 phr of lignosulfnate (**D**), and 60 phr of lignosulfonate (**F**).

3.3. Dynamic–Mechanical Analysis

The temperature dependences of loss factor tan δ for tested materials are illustrated in Figure 14, while the values of tan δ at chosen temperatures are summarized in Tables 1–4. Tan δ is a ratio of loss and storage modulus and corresponds to the energy lost to energy absorbed and returned by the system pre unit cycle. With the rise in temperature, tan δ reaches the maximum in the transition region, followed by a subsequent decrease in the rubbery region. The peak maximum corresponds to the glass transition temperature *Tg*. In glassy region below *Tg*, the damping is low, as the chain segments are immobilized and deformations are mostly elastic due to limited propensity of the chain segments to viscous flow. In the rubbery region, damping is low, because the rotational movement of the chain segments enables free movement with minimum resistance to flow. In the transition region, damping and energy dissipation is high due to the inception of micro-Brownian movement in the chains and chain stress relaxation, although not all the segments are able to participate in such relaxations together. As shown in Figure 14, the application of lignosulfonate resulted in the lowering of the tan δ peak and a reduction in area in the transition region, resulting in lower energy dissipation, which can be attributed to a higher

storage modulus in this region. In all cases, the lowest area in a transition region was demonstrated by composites filled with maximum lignosulfonate content.

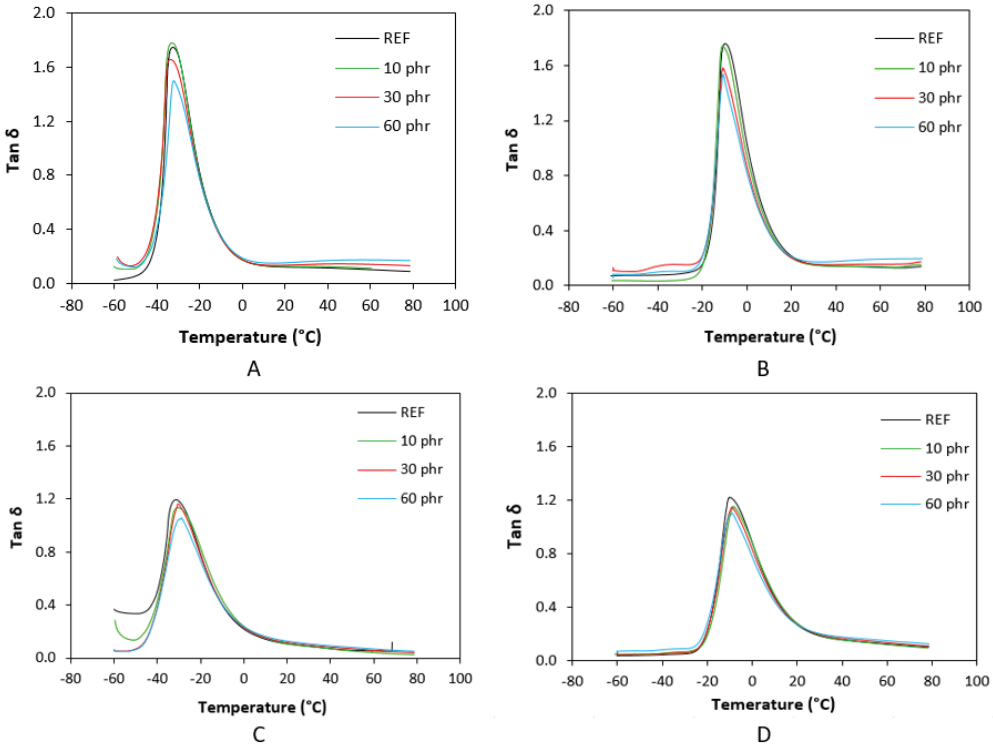

Figure 14. Temperature dependences of loss factor tan δ for SBR-based composites cured with sulfur system (**A**), NBR-based composites cured with sulfur system (**B**), SBR-based composites cured with peroxide system (**C**), and NBR-based composites cured with peroxide system (**D**).

Table 1. Glass transition temperature *Tg* and loss factor tan δ of SBR-based composites cured with sulfur system.

Lignosulfonate (phr)	*Tg* (°C)	tan δ at *Tg*	tan δ (−50 °C)	tan δ (−20 °C)	tan δ (0 °C)	tan δ (20 °C)	tan δ (50 °C)
0	−32.4	1.74	0.06	0.83	0.18	0.12	0.11
10	−33.0	1.77	0.11	0.81	0.17	0.13	0.12
30	−33.6	1.66	0.14	0.79	0.18	0.14	0.15
60	−32.4	1.50	0.12	0.77	0.18	0.15	0.17

Table 2. Glass transition temperature *Tg* and loss factor tan δ of SBR-based composites cured with peroxide system.

Lignosulfonate (phr)	*Tg* (°C)	tan δ at *Tg*	tan δ (−50 °C)	tan δ (−20 °C)	tan δ (0 °C)	tan δ (20 °C)	tan δ (50 °C)
0	−31.3	1.20	0.33	0.78	0.22	0.10	0.06
10	−30.7	1.13	0.14	0.82	0.24	0.11	0.05
30	−30.4	1.16	0.06	0.77	0.23	0.12	0.07
60	−28.9	1.05	0.06	0.73	0.23	0.13	0.08

Table 3. Glass transition temperature *Tg* and loss factor tan *δ* of NBR-based composites cured with sulfur system.

Lignosulfonate (phr)	*Tg* (°C)	tan *δ* at *Tg*	tan *δ* (−50 °C)	tan *δ* (−20 °C)	tan *δ* (0 °C)	tan *δ* (20 °C)	tan *δ* (50 °C)
0	−9.8	1.76	0.07	0.15	1.03	0.21	0.13
10	−10.9	1.74	0.04	0.14	0.96	0.20	0.14
30	−10.7	1.58	0.10	0.21	0.88	0.21	0.16
60	−10.7	1.53	0.08	0.21	0.82	0.21	0.19

Table 4. Glass transition temperature *Tg* and loss factor tan *δ* of NBR-based composites cured with peroxide system.

Lignosulfonate (phr)	*Tg* (°C)	tan *δ* at *Tg*	tan *δ* (−50 °C)	tan *δ* (−20 °C)	tan *δ* (0 °C)	tan *δ* (20 °C)	tan *δ* (50 °C)
0	−10.1	1.22	0.04	0.22	0.89	0.27	0.14
10	−8.2	1.15	0.05	0.18	0.88	0.28	0.14
30	−8.9	1.15	0.05	0.23	0.83	0.27	0.15
60	−8.9	1.10	0.07	0.28	0.77	0.27	0.16

From Figure 14 and Tables 1–4, it becomes apparent that sulfur- as well as peroxide-cured composites based on SBR exhibited a lower *Tg* when compared to the corresponding composites based on NBR. It is a logical reflection of the higher amount of rubbery butadiene units in SBR's structure. The *Tg* of sulfur-cured composites based on SBR moved around −33 °C, while the *Tg* of peroxide cured composites was slightly higher (around −31 °C). This can be attributed to the higher cross-linking degree of peroxide-cured composites, suggesting that increased cross-link density restricts the chain segments' elasticity and mobility, thus elevating *Tg*. The same can be applied to composites based on NBR. The higher cross-link density of peroxide cured composites resulted in an increase in *Tg* by about 2 °C (from about −11 °C for sulfur-cured composites to around −9 °C for peroxide-cured equivalents).

It can also be seen from Tables 1–4 that the *Tg* in some samples increases, while in others, it slightly decreases with increasing filler content. However, there was no recorded direct influence of the filler on *Tg* regarding the type of rubber matrix or curing system composition. It can also be stated that the values tan *δ* in the glassy and rubbery region were significantly influenced neither by the amount of lignosulfonate nor by the type of curing system applied. This may suggest a lack of strong filler–rubber interactions, implying no molecular-level changes.

4. Conclusions

Calcium lignosulfonate-filled formulations based on SBR and NBR were cured with sulfur as well as peroxide curing systems. The results revealed that peroxide-cured composites exhibited a lower scorch time, higher torque difference, and higher cross-link density. Higher cross-link density resulted in a higher hardness and modulus and a lower elongation at break in the corresponding composites. Peroxide-cured composites demonstrated higher tensile strength, which can be attributed to higher compatibility and adhesion and between the filler and the rubber on their interface due to the presence of methacrylic acid zinc salt in peroxide vulcanization. The highest tensile strength of composites based on NBR can be attributed to the polar nature of the rubber, the biopolymer, and the co-agent

resulting in the best adhesion and physical interactions between the components. The application of lignosulfonate in all rubber systems resulted in an increase in elongation at break and hardness, while a more significant influence on elongation at break was recorded for sulfur-cured counterparts. The presence of the biopolymer in the compounds did not significantly influence the *Tg* of the composites and tan δ in the glassy and rubbery region. The decrease in the tan δ peak and lowering of the area in the transition region with the increase in lignosulfonate content point to reduced damping in that region.

Author Contributions: Methodology, J.K. and J.H.; Validation, J.P.; Formal analysis, I.C.; Investigation, M.D. and A.K.; Writing—original draft, J.K.; Supervision, I.H. All authors have read and agreed to the published version of the manuscript.

Funding: This work was funded by the Slovak Research and Development Agency under the contract No. APVV-19-0091, APVV-22-0011 and by the Slovak Scientific Grant Agency VEGA under the contract No. 1/0056/24.

Institutional Review Board Statement: Not applicable.

Data Availability Statement: The original contributions presented in this study are included in the article. Further inquiries can be directed to the corresponding author.

Conflicts of Interest: Authors Ján Hronkovič and Jozef Preťo were employed by VIPO a.s. The remaining authors declare that the research was conducted in the absence of any commercial or financial relationships that could be construed as a potential conflict of interest.

References

1. Ruwoldt, J. A critical review of the physicochemical properties of lignosulfonates: Chemical structure and behavior in aqueous solution, at surfaces and interfaces. *Surfaces* **2020**, *3*, 622–648. [CrossRef]
2. Hemmilä, V.; Hosseinpourpia, R.; Adamopoulos, S.; Eceiza, A. Characterization of wood-based industrial biorefinery lignosulfonates and supercritical water hydrolysis lignin. *Waste Biomass Valori* **2020**, *11*, 5835–5845.
3. Lu, X.; Gu, X.; Shi, Y. A review on lignin antioxidants: Their sources, isolations, antioxidant activities and various applications. *Int. J. Biol. Macromol.* **2022**, *210*, 716–741. [PubMed]
4. Morena, A.G.; Bassegoda, A.; Natan, M.; Jacobi, G.; Banin, E.; Tzanov, T. Antibacterial properties and mechanisms of action of sonoenzymatically synthesized lignin-based nanoparticles. *ACS Appl. Mater. Interfaces* **2022**, *14*, 37270–37279.
5. Wang, H.; Qiu, X.; Liu, W.; Fu, F.; Yang, D. A novel lignin/ZnO hybrid nanocomposite with excellent UV absorption ability and its application in transparent polyurethane coating. *Ind. Eng. Chem. Res.* **2017**, *56*, 11133–11141.
6. Younesi-Kordkheili, H.; Pizzi, A. A comparison among lignin modification methods on the properties of lignin–phenol–formaldehyde resin as wood adhesive. *Polymers* **2021**, *13*, 3502. [CrossRef]
7. Lisý, A.; Ház, A.; Nadányi, R.; Jablonský, M.; Šurina, I. About hydrophobicity of lignin: A review of selected chemical methods for lignin valorisation in biopolymer production. *Energies* **2022**, *15*, 6213. [CrossRef]
8. Sugiarto, S.; Leow, Y.; Li Tan, C.; Wang, G.; Kai, D. How far is Lignin from being a biomedical material? *Bioact. Mater.* **2022**, *8*, 71–94.
9. Fabbri, F.; Bischof, S.; Mayr, S.; Gritsch, S.; Bartolome, M.J.; Schwaiger, N.; Guebitz, G.M.; Weiss, R. The biomodified lignin patform: A review. *Polymers* **2023**, *15*, 1694.
10. Saadan, R.; Alaoui, C.H.; Ihammi, A.; Chigr, M.; Fatimi, A. A brief overview of lignin extraction and isolation processes: From lignocellulosic biomass to added-value biomaterials. *Environ. Earth Sci. Proc.* **2024**, *31*, 3. [CrossRef]
11. Alam, M.M.; Greco, A.; Rajabimashhadi, Z.; Corcione, C.E. Efficient and environmentally friendly techniques for extracting lignin from lignocellulose biomass and subsequent uses: A review. *Clean. Mater.* **2024**, *13*, 100253. [CrossRef]
12. Shorey, R.; Salaghi, A.; Fatehi, P.; Mekonnen, T.H. Valorization of lignin for advanced material applications: A review. *RSC Sustain.* **2024**, *2*, 804. [CrossRef]
13. Gonçalves, S.; Ferra, J.; Paiva, N.; Martins, J.; Carvalho, L.H.; Magalhães, F.D. Lignosulphonates as an alternative to non-renewable binders in wood-based materials. *Polymers* **2021**, *13*, 4196. [CrossRef]
14. Madyaratri, E.W.; Ridho, M.R.; Aristri, M.A.; Lubis, M.A.R.; Iswanto, A.H.; Nawawi, D.S.; Antov, P.; Kristak, L.; Majlingová, A.; Fatriasari, W. Recent advances in the development of fire-resistant biocomposites—A review. *Polymers* **2022**, *14*, 362. [CrossRef]
15. Guterman, R.; Molinari, V.; Josef, E. Ionic liquid lignosulfonate: Dispersant and binder for preparation of biocomposite materials. *Angew. Chem. Int. Ed.* **2019**, *58*, 13044–13050. [CrossRef]

16. Breilly, D.; Fadlallah, S.; Froidevaux, V.; Colas, A.; Allais, F. Origin and industrial applications of lignosulfonates with a focus on their use as superplasticizers in concrete. *Constr. Build. Mater.* **2021**, *301*, 124065. [CrossRef]
17. Antov, P.; Mantanis, G.I.; Savov, V. Development of wood composites from recycled fibres bonded with magnesium lignosulfonate. *Forests* **2020**, *11*, 613. [CrossRef]
18. Mohamad Aini, N.A.; Othman, N.; Hussin, M.H.; Sahakaro, K.; Hayeemasae, N. Lignin as alternative reinforcing filler in the rubber industry: A review. *Front. Mater.* **2020**, *6*, 329. [CrossRef]
19. Thungphotrakul, N.; Dittanet, P.; Loykulnunt, S.; Tanpichai, S.; Parpainainar, P. Synthesis of sodium lignosulfonate from lignin extracted from oil palm empty fruit bunches by acid/ alkaline treatment for reinforcement in natural rubber composites. *IOP Conf. Ser. Mater. Sci. Eng.* **2019**, *526*, 012022. [CrossRef]
20. Kruželák, J.; Džuganová, M.; Kvasničáková, A.; Preťo, J.; Hronkovič, J.; Hudec, I. Influence of plasticizers on cross-linking process, morphology, and properties of lignosulfonate-filled rubber compounds. *Polymers* **2025**, *17*, 393. [CrossRef]
21. An, D.; Cheng, S.; Jiang, C.; Duan, X.; Yang, B.; Zhang, Z.; Li, J.; Liu, Y.; Wong, C.P. A novel environmentally friendly boron nitride/lignosulfonate/natural rubber composite with improved thermal conductivity. *J. Mater. Chem. C* **2020**, *8*, 4801–4809.
22. Džuganová, M.; Stoček, R.; Pöschl, M.; Kruželák, J.; Kvasničáková, A.; Hronkovič, J.; Preťo, J. Strategy for reducing rubber wear emissions: The prospect of using calcium lignosulfonate. *Express Polym. Lett.* **2024**, *18*, 1277–1290.
23. Nardelli, F.; Calucci, L.; Carignani, E.; Borsacchi, S.; Cettolin, M.; Arimondi, M.; Giannini, L.; Geppi, M.; Martini, F. Influence of sulfur-curing conditions on the dynamics and crosslinking of rubber networks: A time-domain NMR study. *Polymers* **2022**, *14*, 767. [CrossRef] [PubMed]
24. Kaur, A.; Fefar, M.M.; Griggs, T.; Akutagawa, K.; Chen, B.; Busfield, J.J.C. Recyclable sulfur cured natural rubber with controlled disulfide metathesis. *Commun. Mater.* **2024**, *5*, 212.
25. Naebpetch, W.; Junhasavasdikul, B.; Saetung, A.; Tulyapitak, T.; Nithi-Uthai, N. Influence of accelerator/sulphur and co-agent/peroxide ratios in mixed vulcanisation systems on cure characteristics, mechanical properties and heat aging resistance of vulcanised SBR. *Plast. Rubber Compos.* **2016**, *45*, 436–444.
26. Shahrampour, H.; Motavalizadehkakhky, A. The Effects of sulfur curing systems (insoluble-rhombic) on physical and thermal properties of the matrix polymeric of styrene butadiene rubber. *Pet. Chem.* **2017**, *57*, 700–704.
27. Kruželák, J.; Sýkora, R.; Hudec, I. Sulphur and peroxide vulcanisation of rubber compounds—Overview. *Chem. Pap.* **2016**, *70*, 1533–1555. [CrossRef]
28. Rodríguez Garraza, A.L.; Mansilla, M.A.; Depaoli, E.L.; Macchi, C.; Cerveny, S.; Marzocca, A.J.; Somoza, A. Comparative study of thermal, mechanical and structural properties of polybutadiene rubber isomers vulcanized using peroxide. *Polym. Test.* **2016**, *52*, 117–123.
29. Peidayesh, H.; Nógellová, Z.; Chodák, I. Effects of peroxide and sulfur curing systems on physical and mechanical properties of nitrile rubber composites: A comparative study. *Materials* **2024**, *17*, 71.
30. Wei, B.X.; Yi, X.T.; Xiong, Y.J.; Wei, X.J.; Wu, Y.D.; Huang, Y.D.; He, J.M.; Bai, Y.P. The preparation and characterization of a carbon fiber-reinforced epoxy resin and EPDM composite using the co-curing method. *RSC Adv.* **2020**, *10*, 20588.
31. Bhattacharya, A.B.; Gopalan, A.M.; Chatterjee, T.; Vennemann, N.; Naskar, K. Exploring the thermomechanical properties of peroxide/co-agent assisted thermoplastic vulcanizates through temperature scanning stress relaxation measurements. *Polym. Eng. Sci.* **2021**, *61*, 2466–2476.
32. Laing, B.; De Keyzer, J.; Seveno, D.; Van Bael, A. Effect of co-agents on adhesion between peroxide cured ethylene–propylene–diene monomer and thermoplastics in two-component injection molding. *J. Appl. Polym. Sci.* **2020**, *137*, 48414.
33. Hayichelaeh, C.; Boonkerd, K. Enhancement of the properties of carbon-black-filled natural rubber compounds containing soybean oil cured with peroxide through the addition of coagents. *Ind. Crop Prod.* **2022**, *187*, 115306.
34. Kruželák, J.; Kvasničáková, A.; Hložeková, K.; Hudec, I. Influence of dicumyl peroxide and Type I and II co-agents on cross-linking and physical–mechanical properties of rubber compounds based on NBR. *Plast. Rubber Compos.* **2020**, *49*, 307–320.
35. Zhao, X.; Cornish, K.; Vodovotz, Y. Synergistic mechanisms underlie the peroxide and coagent improvement of natural-rubber-toughened poly(3-hydroxybutyrate-co-3-hydroxyvalerate) mechanical performance. *Polymers* **2019**, *11*, 565. [CrossRef]
36. Kruželák, J.; Sýkora, R.; Hudec, I. Vulcanization of rubber compounds with peroxide curing systems. *Rubber Chem. Technol.* **2017**, *90*, 60–88.
37. Kraus, G. Swelling of filler-reinforced vulcanizates. *J. Appl. Polym. Sci.* **1963**, *7*, 861–871.
38. Hosseini, S.M.; Razzaghi-Kashani, M. On the role of nano-silica in the kinetics of peroxide vulcanization of ethylene propylene diene rubber. *Polymer* **2017**, *133*, 8–19.
39. Nikolova, S.; Mihaylov, M.; Dishovsky, N. Mixed peroxide/sulfur vulcanization of ethylene-propylene terpolymer based on composites. Curing characteristics, curing kinetics and mechanical properties. *J. Chem. Technol. Metall.* **2022**, *57*, 881–894.
40. Wang, H.; Zhuang, T.; Shi, X.; Van Duin, M.; Zhao, S. Peroxide cross-linking of EPDM using moving die rheometer measurements. II. Effects of the process oils. *Rubber Chem. Technol.* **2018**, *91*, 561–576.
41. George, B.; Alex, R. Stable free radical assisted scorch control in peroxide vulcanization of EPDM. *Rubber Sci.* **2013**, *27*, 135–145.

42. Choi, S.S.; Kim, J.C. Lifetime prediction and thermal aging behaviors of SBR and NBR composites using crosslink density changes. *J. Ind. Eng. Chem.* **2012**, *18*, 1166–1170. [CrossRef]
43. Valentín, J.L.; Posadas, P.; Fernández-Torres, A.; Malmierca, M.A.; González, L.; Chassé, W.; Saalwächter, K. Inhomogeneities and chain dynamics in diene rubbers vulcanized with different cure systems. *Macromolecules* **2010**, *43*, 4210–4222. [CrossRef]
44. González, L.; Rodríguez, A.; Marcos-Fernández, A.; Valentín, J.L.; Fernández-Torres, A. Effect of network heterogeneities on the physical properties of nitrile rubbers cured with dicumyl peroxide. *J. Appl. Polym. Sci.* **2007**, *103*, 3377–3382. [CrossRef]
45. Kruželák, J.; Kvasničáková, A.; Hudec, I. Peroxide curing systems applied for cross-linking of rubber compounds based on SBR. *Adv. Ind. Eng. Polym. Res.* **2020**, *3*, 120–128. [CrossRef]
46. Liu, X.; Zhou, T.; Liu, Y.; Zhang, A.; Yuan, C.; Zhang, W. Cross-linking process of cis-polybutadiene rubber with peroxides studied by two-dimensional infrared correlation spectroscopy: A detailed tracking. *RSC Adv.* **2015**, *5*, 10231–10242. [CrossRef]
47. González, L.; Rodríguez, A.; Del Campo, A.; Marcos-Fernández, A. Effect of heterogeneities on the physical properties of elastomers derived from butadiene cured with dicumyl peroxide. *Polym. Int.* **2004**, *53*, 1426–1430. [CrossRef]
48. Valentín, J.L.; Rodríguez, A.; Marcos-Fernández, A.; Gonzáles, L. Dicumyl peroxide cross-linking of nitrile rubbers with different content in acrylonitrile. *J. Appl. Polym. Sci.* **2005**, *96*, 1–5. [CrossRef]
49. Charoeythornkhajhornchai, P.; Samthong Ch Somwangthanaroj, A. Influence of sulfenamide accelerators on cure kinetics and properties of natural rubber foam. *J. Appl. Polym. Sci.* **2017**, *134*, 44822. [CrossRef]
50. Ghosh, J.; Ghorai, S.; Jalan, A.K.; Roy, M.; De, D. Manifestation of accelerator type and vulcanization system on the properties of silica-reinforced SBR/devulcanize SBR blend vulcanizates. *Adv. Polym. Technol.* **2018**, *37*, 2636–2650. [CrossRef]
51. Lian, Q.; Li, Y.; Li, K.; Cheng, J.; Zhang, J. Insights into the vulcanization mechanism through a simple and facile approach to the sulfur cleavage behavior. *Macromolecules* **2017**, *50*, 803–810. [CrossRef]
52. Sheng, C.; Hu, Z.; Martin, H.; Duan, Y.; Zhang, J. Effect of a small amount of sulfur on the physical and mechanical properties of peroxide-cured fully saturated HNBR compounds. *J. Appl. Polym. Sci.* **2015**, *132*, 41612. [CrossRef]
53. Strohmeier, L.; Balasooriya, W.; Schrittesser, B.; van Duin, M.; Schlögl, S. Hybrid in situ reinforcement of EPDM rubber compounds based on phenolic novolac resin and ionic coagent. *Appl. Sci.* **2022**, *12*, 2432. [CrossRef]
54. Siaw, C.; Baharulrazi, N.; Che Man, S.H.; Othman, N. Effect of zinc dimethacrylate concentrations on properties of emulsion styrene butadiene rubber/butadiene rubber blends. *Plast. Rubber Compos.* **2023**, *52*, 315–329. [CrossRef]
55. Li, C.; Yuan, Z.; Ye, L. Facile construction of enhanced multiple interfacial interactions in EPDM/zinc dimethacrylate (ZDMA) rubber composites: Highly reinforcing effect and improvement mechanism of sealing resilience. *Compos. A Appl. Sci.* **2019**, *126*, 105580. [CrossRef]
56. Cao, Y.; Gu, N.; Hu, S.; Jin, R.; Zhang, J. Preparation and properties of zinc-diacrylate-modified montmorillonite/rubber nanocomposite. *Appl. Mech. Mater.* **2012**, *182–183*, 47–51. [CrossRef]
57. Henning, S.K.; Costin, R. Fundamentals of curing elastomers with peroxides and coagents. *Rubber World* **2006**, *233*, 28–35.

polymers

MDPI

Article

Concentrated Pre-Vulcanized Natural Rubber Latex Without Additives for Fabricating High Mechanical Performance Rubber Specimens via Direct Ink Write 3D Printing

Lin Liu [1,2], Jizhen Zhang [2], Zirong Luo [2], Na Kong [2], Xu Zhao [2], Xu Ji [1], Jihua Li [3], Shenbo Huang [2], Pengfei Zhao [2], Shuang Li [2], Yanqiu Shao [1,*] and Jinlong Tao [2,3,*]

[1] Heilongjiang Key Laboratory of Photoelectric Functional Materials, College of Chemistry and Chemical Engineering, Mudanjiang Normal University, Mudanjiang 157011, China; liulin990705@163.com (L.L.); 18345260314@163.com (X.J.)

[2] Hainan Provincial Key Laboratory of Natural Rubber Processing, Agricultural Products Processing Research Institute, Chinese Academy of Tropical Agricultural Sciences, Zhanjiang 524001, China; quickly3000@126.com (J.Z.); luozirong3@163.com (Z.L.); kongna109101@126.com (N.K.); zx19960211@163.com (X.Z.); a641167221@163.com (S.H.); pengfeizhao85ac@163.com (P.Z.); shuangl163163@163.com (S.L.)

[3] Rubber Research Institute, Chinese Academy of Tropical Agricultural Sciences, Haikou 571101, China; foodpaper@126.com

* Correspondence: 1001002@mdjnu.edu.cn (Y.S.); j.l.tao@catas.cn (J.T.)

Abstract

Direct ink writing (DIW) is an economical, straightforward, and relatively energy-efficient 3D printing technique that has been used in various domains. However, the utilization of rubber latex for DIW remains limited due to its high fluidity and inadequate support, which makes it challenging to meet the required ink rheological characteristics for DIW. In this study, a concentrated pre-vulcanized natural rubber latex (CPNRL) ink with a high solid content of 73% without additives is developed for DIW 3D printing. The CPNRL ink is concentrated using superabsorbent polymer (SAP) beads, which demonstrates good colloidal stability, favorable rheological properties, and superior printability. The impact of printing angles on the mechanical properties of the rubber specimens based on the CPNRL-73 ink is explored in detail, wherein the tensile strength of the specimen printed at a 90° angle reaches an impressive 26 MPa and a strain of approximately 800%, which surpasses the majority of 3D-printed rubber latex specimens. Additionally, the CPNRL ink can be used to print a wide range of intricate shapes, demonstrating its advantages in excellent formability. The preparation of 3D printable ink using the absorption method will expand the application of elastomers in fields such as customized flexible sensing and personalized rubber products.

Keywords: concentrated pre-vulcanized natural rubber latex; superabsorbent polymer beads; additive-free; high mechanical performance; direct ink writing

1. Introduction

In contrast to conventional manufacturing processes, 3D printing enables swift and precise model creation [1–4] as well as facilitates a reduction in material waste, the optimization of shape, and an improvement in production efficiency [5–7]. The 3D printing of elastomers has garnered significant attention in recent years, particularly within the domains of bionic organs, soft robotics, and intelligent healthcare [8,9]. Natural rubber,

as a bio-based elastomer, exhibits exceptional elasticity, high tensile strength, and superior tensile recovery [10,11]. These properties render it indispensable across various domains [12]. The swift advancement of 3D printing technology paves a novel pathway for the development and advancement of natural rubber [13–20].

Currently, rubber is mainly printed by fused deposition modeling (FDM) [21–24], by vat photo-polymerization (VPP) [1,25–27] using photo-curable precursors, and by direct ink writing (DIW) [28–30]. They have been used to successfully fabricate various complicated elastic rubber structures. However, they also demonstrate some limitations. For example, the 3D printing of FDM needs a much higher temperature, preventing its wide application in rubber and restraining the use of additives that are not resistant to high temperatures. For the VPP technique, toxic photo-initiators are required. Regarding the DIW technique, it is only necessary to regulate the rheological properties of the ink, for instance, by introducing rheological modifiers to satisfy specific requirements. In comparison with the two aforementioned methods, DIW exhibits lower costs and simpler operational procedures [28]. In summary, compared to FDM and VPP, the DIW 3D printing of rubber elastomers is regarded as one of the most promising technologies. It eliminates the need for high temperatures and photosensitizers while enabling the incorporation of a wider range of additives in 3D printing inks. However, the addition of substances such as rheological regulators may result in increased costs and volume shrinkage of printed samples. Moreover, these additives may compromise the mechanical properties of the printed objects. Consequently, there is an urgent need for an additive-free and scalable method to manufacture rubber samples with superior mechanical properties through direct ink writing 3D printing.

In this paper, a new type of CPNRL ink with a high solid content and without the addition of any thickening agents was fabricated through the absorption concentration method based on SAP beads, which is specifically suitable for DIW 3D printing (Figure 1). The colloidal and rheological properties of the CPNRL ink were systematically analyzed. The optimal printing conditions were identified by evaluating a range of extrusion pressures and linear velocities, and the printing accuracy was also explored. Furthermore, the mechanical properties of the printed specimens can be adjusted by raster orientation, and the tensile strength reached an impressive 26.4 MPa when printed in the 90°direction, accompanied by an elongation at break close to 800%. Its mechanical properties surpass the film prepared using the casting method and the majority of 3D-printed specimens based on rubber latex. Additionally, the CPNRL ink can be used to print a wide variety of complex structures and shapes with high precision. The exceptional mechanical properties of natural rubber are fully retained, providing new insights into the processing of complex natural rubber structures with high mechanical performance.

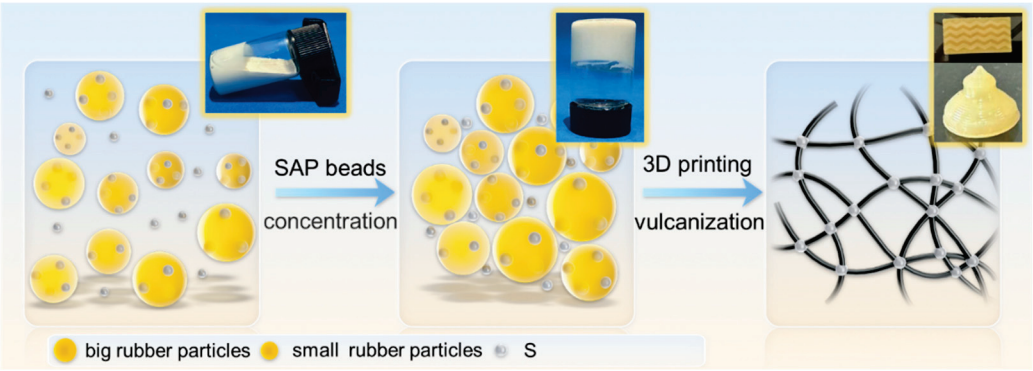

Figure 1. Schematic illustration of the preparation of CPNRL ink using SAP beads and a vulcanization diagram.

2. Materials and Methods

2.1. Materials

Concentrated natural rubber latex (60% in dry rubber content) was obtained from GuangKen Group Company in Guangdong (Yangjiang, China). Zinc oxide (ZnO), sulfur, zinc diethyl dithiocarbamat (ZDC), potassium oleate, sodium fluorosilicate, formaldehyde, antiaging agent-264, diffusible agent-N, casein, and 2-mercaptobenzene were purchased from Shanghai Aladdin Biochemical Technology Co., Ltd. (Shanghai, China). The commercial SAP beads were procured from Dinghao Corporation (Yiwu, China). The extrusion 3D bio-printer EFL-BP-6601 was purchased from Suzhou Yong qinquan Intelligent Equipment Co., Ltd. (Suzhou, China), and all the printed specimens in this article were completed by this equipment.

2.2. Preparation of PNRL and CPNRL

Pre-vulcanized natural rubber latex (PNRL) is usually fabricated using concentrated natural rubber latex and a curing system that includes sulfur, an accelerator, and an activator. According to the formulation in Table S1, the mixture was poured into a ball milling tank and milled at 40 rpm·min^{-1} for 72 h to obtain a 50% mass fraction of the vulcanized hybrid dispersion. It is important to note that the dispersion should be filtered through a sieve to remove any bulk material and foam before use. The stabilizer and vulcanizing dispersant were slowly added to the concentrated natural rubber latex while stirring, and the mixing ratios are shown in Table S2. After the addition, the mixed system was heated and stirred at 52~60 °C for 3 h. At the end of the reaction, the rubber temperature was cooled to room temperature, and PNRL with 58% solids was obtained.

Concentrated pre-vulcanized natural rubber latex (CPNRL) was prepared as follows: 3 wt% SAP beads were slowly added into PNRL with low-speed stirring at 180 rpm·min^{-1}. By regulating the duration of the concentration process, CPNRL with a solid content ranging from 62% to 73% can be achieved. CPNRL-62, CPNRL-65, CPNRL-69, CPNRL-71, and CPNRL-73 represent the solid contents of CPNRL of 62%, 65%, 69%, 71%, and 73%, respectively.

2.3. Scale Accuracy of 3D-Printed Rubber Specimens

All 3D-printed models were processed using Slic3r software (V1.2.3 (230313)). The design of the rectangular tracing model comprised a length of 20 cm and a width of 1 cm (Figure S3). The height of the gap between the tip of the nozzle and the substrate was set to 90% of the diameter of the nozzle, which was 21 G (inner diameter 0.51 mm). The linear speed was fixed at 1000 mm/min, and the pressure was controlled from 35 to 55 kPa. Additionally, the extrusion pressure was fixed at 45 kPa, and the linear speed was from 100 to 2000 mm/min.

For accuracy testing, the cuboid structures were 3D-printed using a $1 \times 2 \times 3$ cuboid model integrated into the Slic3r software (V1.2.3 (230313)). These structures were printed with a 21 G nozzle head at 100% infill density. Five cube samples were printed for testing accuracy, and the average values were used for analysis.

2.4. Preparation of the 3D-Printed Tensile Model and Film Using the Casting Method Based on CPNRL-73

The 3D-printed specimen based on CPNRL-73 for studying tensile properties was designed to be a standardized dog bone tensile model with 100% packing density. Afterward, the printed specimens were vulcanized at 90 °C in an oven for 4 h. For comparison, the CPNRL-73 film was prepared using the casting method. In accordance with the GB/T 18011-2008 (ISO 498:1992, IDT) standard [31,32], CPNRL-73, which initially had a solid

content of 73%, was diluted to achieve a solid content of 62% to prepare the casting film. It was filtered using a 200-mesh screen and then casted into the glass plate to keep static conditions for 48 h at normal temperature. Finally, it was heated in an oven at 35 °C for 48 h to complete the vulcanization.

2.5. Printing of Complex Rubber Structure Based on CPNRL-73 Ink

The models of letters, simplified tire treads, associated rotating components, and a hollow air rubber bag were created using Slic3r software. Subsequently, these models were fabricated via the CPNRL ink. Finally, the printed complex structures underwent a four-hour heat treatment at 90 °C to complete the vulcanization.

2.6. Characterization

The particle size and Zeta potential of PNRL and CPNRL were determined by using Malvern Zetasizer Nano ZS90 (Malvern Instruments Ltd., Worcestershire, UK). Scanning electron microscopy (HITACHI S4800, Tokyo, Japan) was used to study the morphology of the rubber particles present in PNRL and CPNRL and the surface and cross-section morphology of the 3D-printed specimens. TPNRL and CPNRL were diluted 50 times and stained with a 2 wt% osmium tetroxide aqueous solution before testing. The viscoelastic behavior of CPNRL with various solid contents was measured using a 20 mm plate device on a Rheometer (Thermo Scientific™ HAAKE™ MARS, Waltham, MA, USA) at room temperature. The steady-state mode was employed, with shear rates ranging from 0.01 to 1000 s^{-1}. The storage modulus and loss modulus were determined in the vibration mode at an angular frequency of 10 rad·s^{-1}. The range of shear stress applied was from 0 to 1000 Pa. The tensile tests of the casting rubber film and 3D-printed specimens were conducted utilizing an electronic universal testing machine (ETM103C). Each sample underwent five sets of parallel experiments, and the average values were used for analysis. According to GB/T 528-2009 [33], a dog-bone-shaped specimen was selected and tested at a speed of 500 mm/min to obtain the stress–strain curve.

The equilibrium swelling method was employed to determine the cross-linking density of the vulcanized sample. After precisely weighing 0.2 g of the vulcanized sample, we added 100 mL of toluene solution and stored it in darkness for 7 days. After removing the swollen sample's surface-attached toluene solution, its weight was measured. The Flory–Rehner Formula (1a)–(1c) was utilized to calculate the cross-link density of several groups of samples.

$$\Phi_r = \frac{m_1/\rho_p + m_2/\rho_s}{m_1/\rho_p} \tag{1a}$$

$$-\ln(1-\Phi_r) - \Phi_r - X_r\Phi_r^2 = nV_0\left(\Phi_r^{1/3} - \frac{1}{2}\Phi_r\right) \tag{1b}$$

$$M_c = \frac{\rho}{n} \tag{1c}$$

The formula includes the swelling ratio (Φ_r), density of natural rubber (ρ_p) (0.930 g/cm^3), density of toluene (ρ_s) (0.886 g/cm^3), molar volume of toluene (V_0 = 106.2 mL/mol), interaction parameter between natural rubber and toluene (X_r = 0.393), and average molecular mass between cross-linking points (M_c). The molar volume of toluene and the interaction parameters between natural rubber and toluene are considered constants, while the remaining values are experimentally determined.

3. Results and Discussion

3.1. Colloid Properties of PNRL and CPNRL

The initial solid content of pre-vulcanized natural rubber latex (PNRL) before concentration is 58%, which is insufficient for direct application in DIW 3D printing due to its high fluidity and inadequate support. This study employed the absorption concentration method based on SAP beads to increase the solid content of PNRL and regulate the rheological properties of CPNRL. CPNRL with various solid contents of 62%, 65%, 69%, 71%, and 73% can be prepared by precisely controlling the adsorption concentration time. As shown in Figure S1, CPNRL-62, CPNRL-65, and CPNRL-69 all exhibit excellent mobility. However, the mobility of CPNRL starts to reduce when the solid content reaches 71% and continues to reduce as the solid content reaches 73%, indicating that CPNRL-73 should be suitable for DIW 3D printing. The stability of PNRL, as assessed by the Zeta potential, was examined both before and after water removal using SAP (Figure 2a). The Zeta potential of PNRL was approximately −37.8 mV, while it increased to around −38.3 mV for CPNRL-73 after concentration by removing the water present in PNRL using SAP beads. The Zeta potential value serves as an indicator of the stability of PNRL [34,35]. The similar potential value of PNRL and CPNRL-73 demonstrates that concentration does not reduce the stability of CPNRL-73.

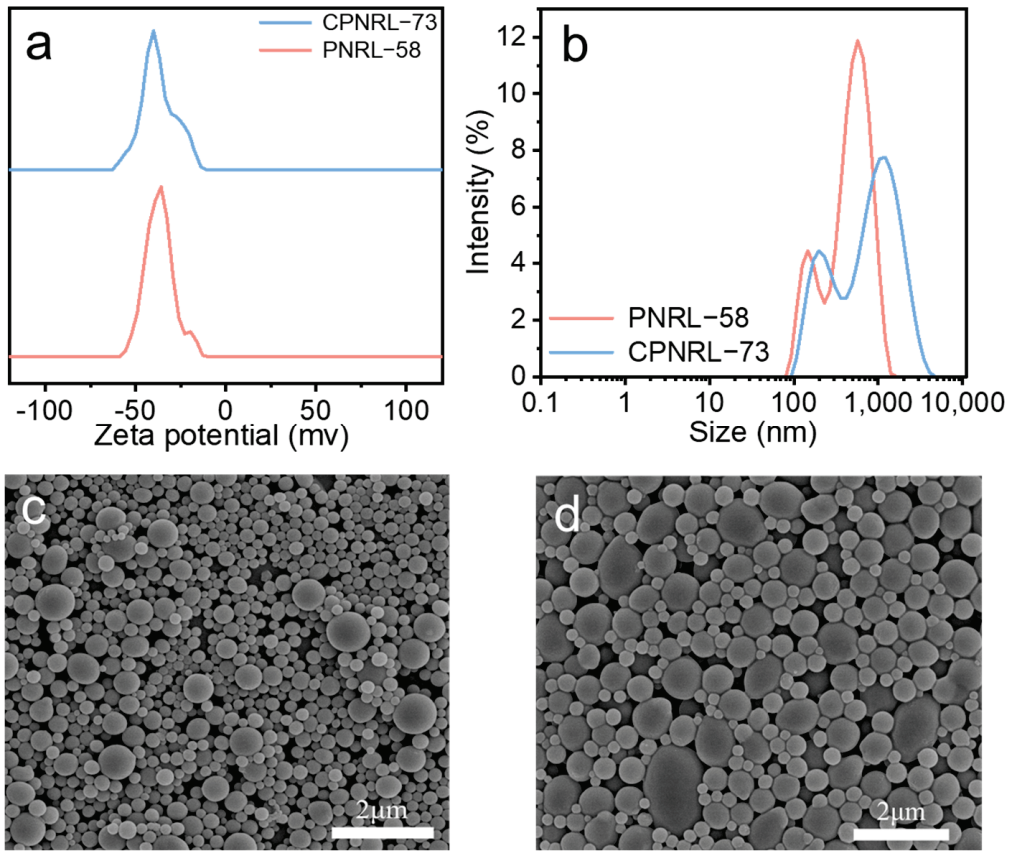

Figure 2. Characterization of the colloidal properties and morphology of PNRL-58% and CPNRL-73%: (**a**) Zeta potential, (**b**) particle size, (**c**,**d**) SEM images.

The particle size of CPNRL-73 exhibited a significant increase (Figure 2b), with the average diameter expanding from 354.6 nm to 505.3 nm. The figure illustrates that both smaller and larger rubber particles underwent an increase in size, likely attributed to the fusion and cross-linking of these particles as a result of water reduction during the concentration process. Furthermore, the SEM images revealed that the rubber particles were

predominantly spherical, with smaller particles being more abundant prior to concentration, interspersed with some larger particles (Figure 2c). However, following the concentration treatment, the number of smaller particles decreased, while pear-shaped and larger particles became more prevalent (Figure 2d).

3.2. Rheological Properties of CPNRL

Three-dimensional printed inks, which are typically utilized in DIW printing, should demonstrate suitable rheological properties, including apparent viscosity, yield stress under both shear and compressive forces, and viscoelastic characteristics (i.e., loss and elastic moduli) [36–38]. The results of the rheological test of CPNRL are presented in Figure 3a,b. As depicted in the figure, the viscosity of CPNRL is influenced by shear strain, indicating the significance of enhancing the rheological properties of printing ink for improved quality. High viscosity hinders the proper extrusion and shape retention of printed samples after extrusion from the nozzle under external stress. This phenomenon demonstrates the shear thinning behavior characteristic of non-Newtonian fluids, where fluid viscosity decreases with increasing shear stress [39]. Additionally, it is evident that when the solid content reaches 71%, the CPNRL ink exhibits excellent shear thinning ability, initially increasing and then declining. In the shear modulus diagram (Figure 3b), it can also be observed that $G' > G''$ for CPNRL with solid contents of 71% and 73% under low shear stress conditions. However, under higher shear forces, $G' < G''$ demonstrates remarkable performance in terms of shear thinning behavior. Consequently, we conclude that CPNRL ink with a solid content of 73% or higher possesses favorable characteristics for 3D printing applications, aligning well with the rheological properties of inks required by DIW 3D printing.

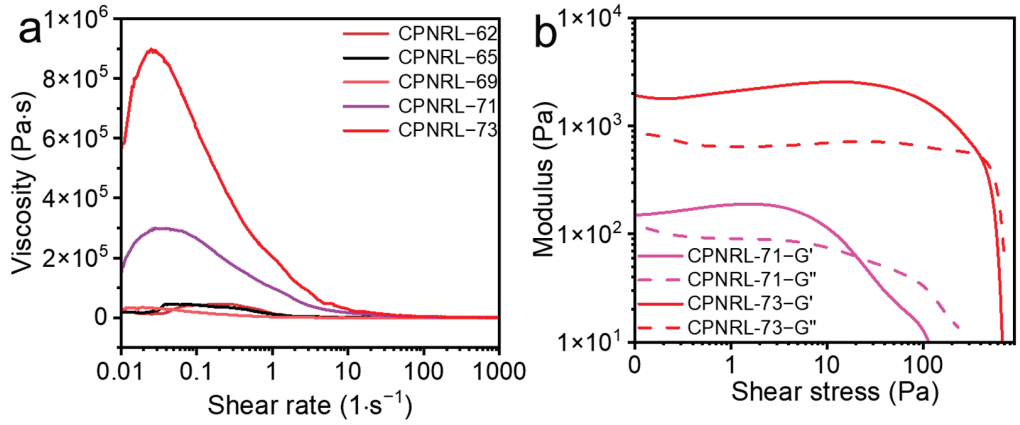

Figure 3. (**a**) Viscosity as a function of the shear rate of different CPNRL samples. (**b**) The correlation between modulus and shear stress of CPNRL suitable for 3D printing.

3.3. The Stability of Line Printing, the Stacking of CPNRL Ink, and the Analysis of Scale Accuracy

The fundamental principle of DIW 3D printing to create a self-supporting extrusion layer is directly dependent on the printability and shape fidelity of the ink [38,40]. Machine parameters, such as nozzle diameter and printing velocity, significantly influence the accuracy and resolution of the printed output [41]. Typically, a nozzle with a smaller diameter can enhance printing resolution. However, this necessitates higher extrusion pressure and extended printing time to prevent nozzle clogging. Likewise, reduced print speeds generally lead to improved shape tolerances and fidelity, although this also prolongs the printing process [38].

In order to determine optimal printing parameters, the CPNRL-73 ink was subjected to testing under different printing pressures and speeds. The printing results under various combinations of pressure and speed are shown in Figure 4a,b. To ascertain the

optimal printing parameters, the CPNRL-73 ink was evaluated across a range of extrusion pressures and printing velocities. Figure 4a illustrates the line width at varying speeds from 100 to 2000 mm·min^{-1}, with a constant extrusion pressure of 45 kPa. The average line width of the CPNRL-73 ink is approximately double the nozzle diameter at a speed of 100 mm·min^{-1}. The line width aligns closely with the nozzle diameter within the range of 500 to 1000 mm·min^{-1}. Figure 4b illustrates the line width of the ink within the pressure range of 35 to 55 kPa, with increments of 5 kPa and a constant speed of 1000 mm·min^{-1}. The CPNRL-73 ink can be smoothly extruded from the nozzle under a pressure of 35 kPa. In contrast, when the pressure reaches 50 kPa, the average printing line width exceeds twice the nozzle diameter. A slow line speed or excessive pressure results in excessive ink extrusion, which hinders the formation of a stable support structure, making it challenging to meet the requirements for multi-layer printing. At a printing speed of 1500 mm·min^{-1}, the lines exhibit excellent form, with their width being precisely three-quarters (75%) of the nozzle diameter. Consequently, after thorough consideration, we determined that a pressure range of 45 kPa, in conjunction with a constant linear velocity of 1500 mm·min^{-1}, constituted the optimal printing conditions.

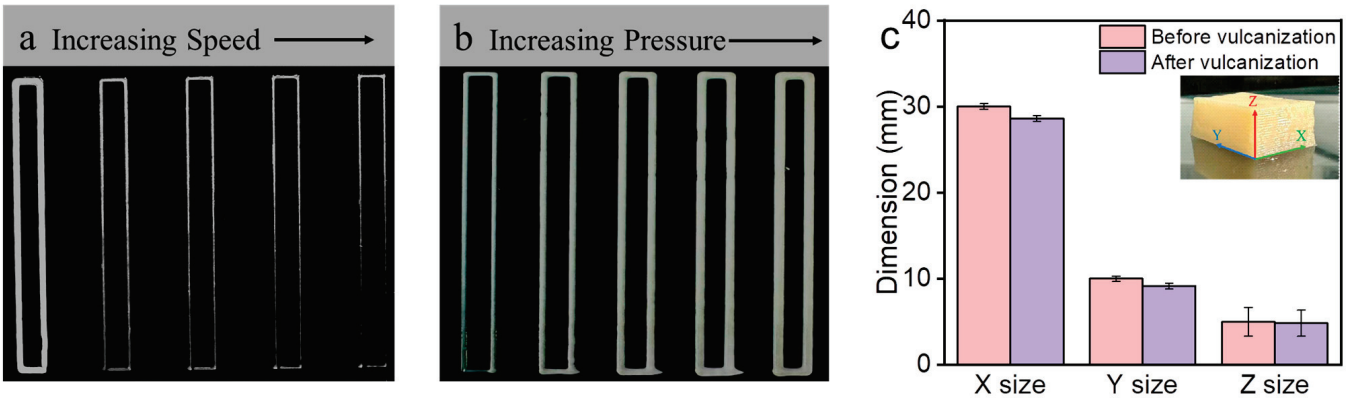

Figure 4. Characterization of the printing line drawings and accuracy of the CPNRL-73 ink. (**a**) At a constant pressure of 45 kPa across various speeds. (**b**) At a constant speed of 1000 mm/s under different pressures. (**c**) The dimension of the accuracy of the cubic sample in the XYZ direction after vulcanization.

The shrinkage of a specimen is inevitable when using hydrogel or rubber latex ink for 3D printing [28]. The shrinkage phenomenon of 3D-printed specimens based on the CPNRL-73 ink is also observed in this study. To evaluate the accuracy of the 3D-printed samples, we selected a solid rubber cube as a model. The inserted image in Figure 4c illustrates the XYZ orientation of the solid rubber cube after vulcanization. As depicted in Figure 4c, the dimensional fidelity of the vulcanized samples was 95.3%, 91.6%, and 96.6% in the XYZ direction, respectively. There was a decrease in volume for the printed rubber cube after vulcanization. Prior to vulcanization, the CPNRL-73 ink still contains some water, which evaporates during the vulcanization process due to heating. This results in the overall shrinkage of the structure and subsequently reduces the volume of the 3D-printed specimens.

3.4. Mechanical Properties

To compare the mechanical properties of the 3D-printed rubber specimens with different orientations and those prepared using the traditional casting method, a standardized dog bone tensile model was created through CAD modeling and printed by using CPNRL-73. The results indicate that different printing orientations have certain effects on the mechanical properties of the 3D-printed rubber specimens. For instance, when printed at

0°, only a strain of 720% and a stress of up to 22 MPa can be achieved. However, as the printing angle changes, there is a significant increase in stress for the samples printed at 45° and 90°. Simultaneously, the tensile strength at 90° and the elongation at break can achieve 26 MPa and approximately 800%, respectively. This phenomenon may be attributed to the anisotropic nature of the material. An increase in the angle relative to the direction of the applied force results in a reduction in the sample's strength, which is particularly evident in polymeric materials [29]. When printed at a 90° raster angle, the contact area between the lines is maximized, and the lines align with the direction of the applied force during stretching. Conversely, the mechanical properties at 0° and 45° grating angles tend to diminish due to the misalignment between the angle and the direction of the applied force [29]. Additionally, compared to traditional casting films, the 3D-printed models exhibit higher cross-linking density across different printing angles. This discrepancy may be attributed to the lower vulcanization temperature used in traditional casting methods, leading to a reduced cross-linking density post-vulcanization compared to 3D-printed models.

Owing to the excellent interfacial compatibility between the printing layers (as shown in Figure 5), the mechanical properties of the 3D-printed rubber specimens are markedly superior to those reported in other studies (Figure 6f) [1,24–28,42]. The surface and cross-sectional morphology of the 3D-printed rubber specimen were examined using SEM. Distinct linear structures are evident on the surface of the rubber specimen, suggesting it was printed and fabricated layer by layer. However, no distinct interlayer interface was observed in the cross-section of the rubber specimen, indicating that excellent cross-linking between layers was formed during the vulcanization process and demonstrating a high degree of uniformity and consistency. Furthermore, the mechanical properties of the 3D-printed rubber specimen at various angles were evaluated. The device printed at 90° exhibited the highest tensile strength at 26 MPa, whereas the device printed at 0° demonstrated a strength of 22 MPa, indicating only a slight reduction. This suggests that the cross-linking between layers remained high during the vulcanization process, preventing significant delamination and preserving the superior mechanical properties of the 3D-printed rubber specimen.

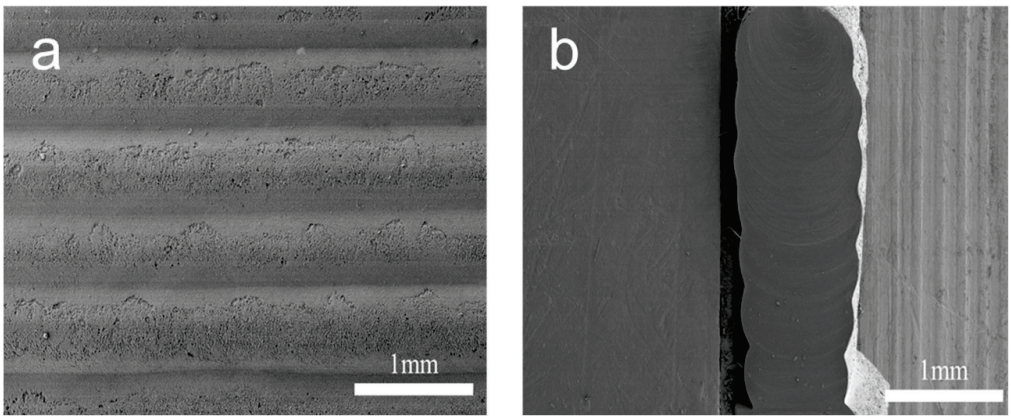

Figure 5. SEM images of the cross-section and surface of the 3D-printed rubber specimen. (**a**) Surface topography. (**b**) Cross-section morphology.

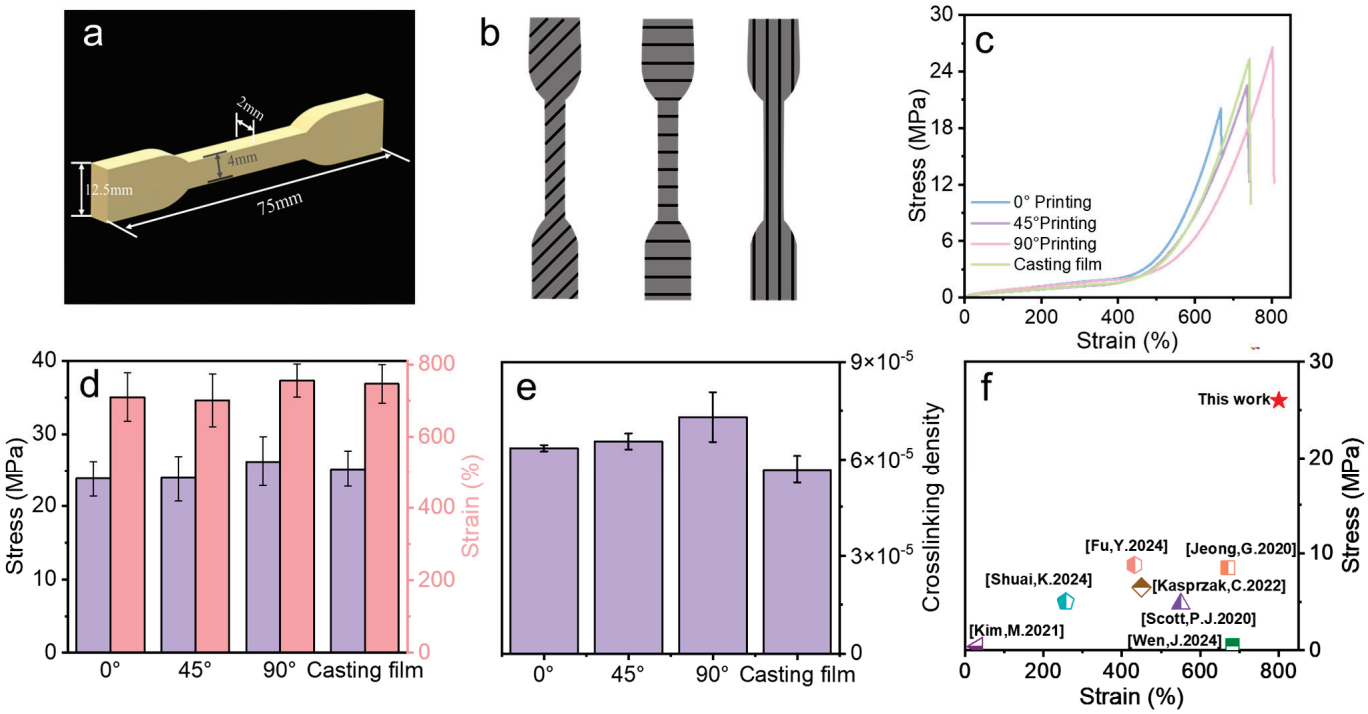

Figure 6. Mechanical testing and characterization. (**a**) Drawing and dimensions of CAD-generated dog bone. (**b**) Diagrams of the models for the tensile test prepared in various printing orientations. (**c**) Stress–strain curves for specimens printed in different directions. (**d**) Comparison diagram of stress–strain. (**e**) Cross-linking density of specimens printed in different directions and prepared using the casting method. (**f**) A comparative analysis of the mechanical properties of various 3D-printed elastomers [1,24–28,42].

3.5. The 3D Structures Fabricated Using CPNRL-73 Ink

Four distinct structural models were designed using CAD software and printed with the CPNRL-73 ink: a letter model, a tire tread model, rotary-shaped components, and an air rubber bag. In Figure 7, the computer-generated model, the un-vulcanized rubber specimens, and the vulcanized rubber specimens are displayed from left to right. The un-vulcanized printed specimens appear white in color because of the presence of water in the CPNRL-73 ink, and they become light yellow after vulcanization and drying by heating. The surface of the 3D-printed tire tread model was printed according to a 100% infill density, indicating that the ink was smoothly squeezed out during accumulation without any residual ink around the nozzle. The remaining 3D-printed models were stacked by rubber lines, and no collapse or inclination was observed, proving that the CPNRL-73 ink has good support and stability. Following vulcanization, the product exhibits enhanced precision with a reduced rate of shrinkage and deformation. The printed rubber product retains a shape nearly identical to the original design model.

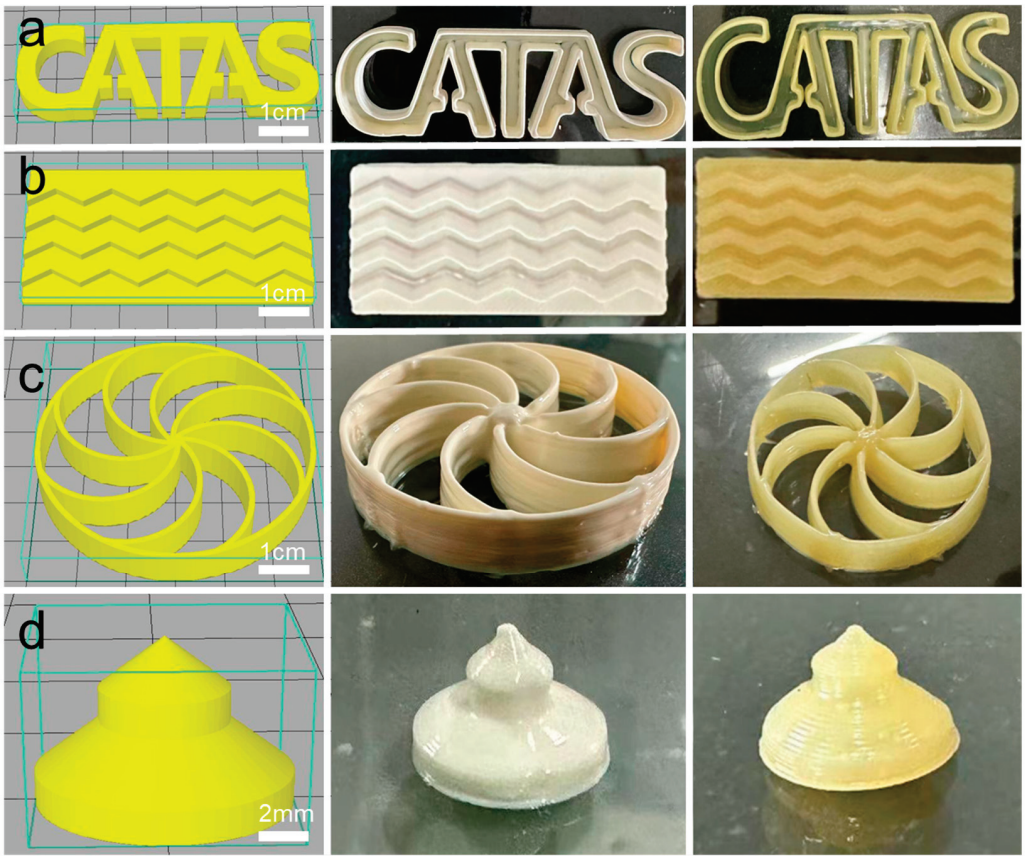

Figure 7. Demonstration of different 3D-printed shapes before and after vulcanization. (**a**) Alphabetic model. (**b**) Tread model. (**c**) Special-shaped part model. (**d**) Air rubber bag.

4. Conclusions

In this study, we developed a new type of PNRL ink using the absorption concentration method based on SPA beads for DIW 3D printing without using additives. The total solid content of the CPNRL ink is up to 73%, and the resulting ink demonstrates good colloidal stability and 3D printability, proving that the absorption concentration method is an effective approach to fabricating rubber latex ink for DIW 3D printing. The optimal extrusion pressure was found to be approximately 45 kPa, while the optimal extrusion speed was determined to be 1500 mm/min. Furthermore, the tensile strength of the printed specimen reached an impressive 26.4 MPa when printed in the 90°direction, accompanied by a strain exceeding approximately 800%, which surpasses the majority of rubber latex specimens produced by 3D printing. The superior mechanical properties may be derived from excellent interface compatibility between the printing layers. Additionally, a wide variety of complex elastic structures with high precision can be 3D-printed by using CPNRL ink, demonstrating excellent printing adaptability and support. This study not only develops a scalable method to fabricate rubber latex ink for DIW 3D printing but also offers fresh insights into processing and structural design possibilities for complex and multifunctional rubber latex products.

Supplementary Materials: The following supporting information can be downloaded at https://www.mdpi.com/article/10.3390/polym17030351/s1: Table S1: The vulcanization system formula of pre-vulcanized natural rubber latex; Table S2: The formula of pre-vulcanized natural rubber latex; Table S3: Comparative analysis of the mechanical properties of various 3D-printed elastomers. Figure S1. Photographs of CPNRL with different solid contents. Figure S2. Scale precision model of 3D-printed rubber sample.

Author Contributions: L.L.: Writing—original draft, review, and editing, visualization, software, formal analysis, and data curation. J.Z.: Writing—review and editing, resources, methodology, funding acquisition, conceptualization, and investigation. Z.L.: Writing—review and editing and supervision. N.K.: Software, methodology, supervision, and investigation. X.Z.: Methodology. X.J.: Formal analysis. J.L.: Methodology. S.H.: Methodology. P.Z.: Methodology. S.L.: Methodology. Y.S.: Formal analysis. J.T.: Writing—review and editing, project administration, and funding acquisition. All authors have read and agreed to the published version of the manuscript.

Funding: This work was supported by the Foundation of National Key R&D Program of China (No. 2024YFD2300904), the Science and Technology Program of Hainan Province (ZDYF2020230, ZDYF2022GXJS226), the Hainan Provincial Natural Science Foundation of China (521QN0931), the Guangdong Basic and Applied Basic Research Foundation (2024A1515011788), the Central Public-interest Scientific Institution Basal Research Fund for Chinese Academy of Tropical Agricultural Sciences (1630122022007), and the Chinese Academy of Tropical Agricultural Sciences for Science and Technology Innovation Team of National Tropical Agricultural Science Center (CATASCXTD202306).

Data Availability Statement: The original contributions presented in this study are included in the article/Supplementary Materials. Further inquiries can be directed to the corresponding author.

Conflicts of Interest: The authors declare that they have no known competing financial interests or personal relationships that could have appeared to influence the work reported in this paper.

References

1. Jeong, G.; Park, C.H.; Kim, B.-Y.; Kim, J.; Park, S.-D.; Yang, H.; Lee, W.S. Photocurable Elastomer Composites with SiO_2-Mediated Cross-Links for Mechanically Durable 3D Printing Materials. *ACS Appl. Polym. Mater.* **2020**, *2*, 5228–5237. [CrossRef]
2. Ligon, S.C.; Liska, R.; Stampfl, J.; Gurr, M.; Mülhaupt, R. Polymers for 3D printing and customized additive manufacturing. *Chem. Rev.* **2017**, *117*, 10212–10290. [CrossRef] [PubMed]
3. Nadgorny, M.; Ameli, A. Functional polymers and nanocomposites for 3D printing of smart structures and devices. *ACS Appl. Mater. Interfaces* **2018**, *10*, 17489–17507. [CrossRef]
4. Farahani, R.D.; Chizari, K.; Therriault, D. Three-dimensional printing of freeform helical microstructures: A review. *Nanoscale* **2014**, *6*, 10470–10485. [CrossRef]
5. Bean, R.H.; Rau, D.A.; Williams, C.B.; Long, T.E. Rheology guiding the design and printability of aqueous colloidal composites for additive manufacturing. *J. Vinyl Addit. Technol.* **2023**, *29*, 607–616. [CrossRef]
6. Chaturvedi, I.; Jandyal, A.; Wazir, I.; Raina, A.; Ul Haq, M.I. Biomimetics and 3D printing—Opportunities for design applications. *Sens. Int.* **2022**, *3*, 100191. [CrossRef]
7. Hisham, M.; Dileep, D.; Jacob, L.; Butt, H. Additive manufacturing of carbon nanocomposites for structural applications. *J. Mater. Res. Technol.* **2024**, *28*, 4674–4693. [CrossRef]
8. Wallin, T.J.; Pikul, J.; Shepherd, R.F. 3D printing of soft robotic systems. *Nat. Rev. Mater.* **2018**, *3*, 84–100. [CrossRef]
9. Zhou, L.-Y.; Fu, J.; He, Y. A Review of 3D Printing Technologies for Soft Polymer Materials. *Adv. Funct. Mater.* **2020**, *30*, 2000187. [CrossRef]
10. Dasgupta, A.; Dutta, P. Printability of elastomer as a 3D printing material for additive manufacturing. *J. Rubber Res.* **2024**, *27*, 137–157. [CrossRef]
11. Li Na, S.; Abdul Kariem, A. Elastomers and Their Potential as Matrices in Polymer Electrolytes. In *Elastomers*; Nevin, C., Ed.; IntechOpen: Rijeka, Croatia, 2017.
12. Whba, R.; Su'ait, M.S.; Whba, F.; Sahinbay, S.; Altin, S.; Ahmad, A. Intrinsic challenges and strategic approaches for enhancing the potential of natural rubber and its derivatives: A review. *Int. J. Biol. Macromol.* **2024**, *276*, 133796. [CrossRef]
13. Alkadi, F.; Lee, J.; Yeo, J.-S.; Hwang, S.-H.; Choi, J.-W. 3D Printing of Ground Tire Rubber Composites. *Int. J. Precis. Eng. Manuf. Green Technol.* **2019**, *6*, 211–222. [CrossRef]
14. Alkadi, F.; Lee, K.-C.; Bashiri, A.H.; Choi, J.-W. Conformal additive manufacturing using a direct-print process. *Addit. Manuf.* **2020**, *32*, 100975. [CrossRef]
15. Adhikari, B.; De, D.; Maiti, S. Reclamation and recycling of waste rubber. *Prog. Polym. Sci.* **2000**, *25*, 909–948. [CrossRef]
16. Fang, Y.; Zhan, M.; Wang, Y. The status of recycling of waste rubber. *Mater. Des.* **2001**, *22*, 123–128. [CrossRef]
17. De, D.; Das, A.; De, D.; Dey, B.; Debnath, S.C.; Roy, B.C. Reclaiming of ground rubber tire (GRT) by a novel reclaiming agent. *Eur. Polym. J.* **2006**, *42*, 917–927. [CrossRef]
18. Wu, B.; Zhou, M.H. Recycling of waste tyre rubber into oil absorbent. *Waste Manag.* **2009**, *29*, 355–359. [CrossRef] [PubMed]

19. Sunthonpagasit, N.; Duffey, M.R. Scrap tires to crumb rubber: Feasibility analysis for processing facilities. *Resour. Conserv. Recycl.* **2004**, *40*, 281–299. [CrossRef]
20. Fiksel, J.; Bakshi, B.R.; Baral, A.; Guerra, E.; DeQuervain, B. Comparative life cycle assessment of beneficial applications for scrap tires. *Clean Technol. Environ. Policy* **2011**, *13*, 19–35. [CrossRef]
21. Gao, Y.; Li, Y.; Hu, X.; Wu, W.; Wang, Z.; Wang, R.; Zhang, L. Preparation and Properties of Novel Thermoplastic Vulcanizate Based on Bio-Based Polyester/Polylactic Acid, and Its Application in 3D Printing. *Polymers* **2017**, *9*, 694. [CrossRef]
22. Hu, X.; Kang, H.; Li, Y.; Geng, Y.; Wang, R.; Zhang, L. Preparation, morphology and superior performances of biobased thermoplastic elastomer by in situ dynamical vulcanization for 3D-printed materials. *Polymer* **2017**, *108*, 11–20. [CrossRef]
23. Wissamitanan, T.; Dechwayukul, C.; Kalkornsurapranee, E.; Thongruang, W. Proper Blends of Biodegradable Polycaprolactone and Natural Rubber for 3D Printing. *Polymers* **2020**, *12*, 2416. [CrossRef]
24. Fu, Y.; Shi, Z.; Feller, K.D.; Schulz, M.D.; Long, T.E.; Williams, C.B. Vat photopolymerization of silica reinforced styrene-butadiene rubber elastomeric nanocomposites. *Appl. Mater. Today* **2024**, *40*, 102370. [CrossRef]
25. Wen, J.; Bean, R.H.; Nayyar, G.; Feller, K.; Scott, P.J.; Williams, C.B.; Long, T.E. Vat Photopolymerization of Synthetic Isoprene Rubber Latexes. *ACS Appl. Polym. Mater.* **2024**, *6*, 2169–2176. [CrossRef]
26. Scott, P.J.; Meenakshisundaram, V.; Hegde, M.; Kasprzak, C.R.; Winkler, C.R.; Feller, K.D.; Williams, C.B.; Long, T.E. 3D Printing Latex: A Route to Complex Geometries of High Molecular Weight Polymers. *ACS Appl. Mater. Interfaces* **2020**, *12*, 10918–10928. [CrossRef]
27. Kasprzak, C.; Brown, J.R.; Feller, K.; Scott, P.J.; Meenakshisundaram, V.; Williams, C.; Long, T. Vat Photopolymerization of Reinforced Styrene–Butadiene Elastomers: A Degradable Scaffold Approach. *ACS Appl. Mater. Interfaces* **2022**, *14*, 18965–18973. [CrossRef] [PubMed]
28. Kim, M.; Choi, J.-W. Rubber ink formulations with high solid content for direct-ink write process. *Addit. Manuf.* **2021**, *44*, 102023. [CrossRef]
29. Chansoda, K.; Suvanjumrat, C.; Wiroonpochit, P.; Kaewprakob, T.; Chookaew, W. Support medium development for 3D printing natural rubber latex via direct ink writing in the support bath technique. *Clean. Mater.* **2024**, *13*, 100257. [CrossRef]
30. Banks, J.D.; Emami, A. Influence of filler concentration and type on rheological and mechanical properties of liquid isoprene rubber for high-strength parts via material extrusion. *Addit. Manuf.* **2023**, *78*, 103851. [CrossRef]
31. *GB/T 18011-2008*; Natural Rubber Latex Concentrate—Preparation of Dry Films. China Standards Press: Beijing, China, 2008.
32. *ISO 498:1992*; Natural Rubber Latex Concentrate—Preparation of Dry Films. ISO: Geneva, Switzerland, 1992.
33. *GB/T 528-2009*; Rubber, Vulcanized or Thermoplastic—Determination of Tensile Stress—Strain Properties. China Standards Press: Beijing, China, 2009.
34. Yusof, N.H.; Singh, M.; Mohd Rasdi, F.R.; Tan, K.S. Properties of concentrated skim rubber latex using membrane separation process and its comparison with other natural rubber latexes. *J. Rubber Res.* **2023**, *26*, 169–177. [CrossRef]
35. Huang, S.; Luo, Z.; Zhang, J.; Kong, N.; Li, J.; Zhao, P.; Wu, J.; Tan, S.; Tao, J. An eco-friendly, high-yield and scalable method for processing concentrated natural rubber latex with superabsorbent polymer beads. *Chem. Eng. J.* **2024**, *502*, 158013. [CrossRef]
36. Neumann, T.V.; Dickey, M.D. Liquid Metal Direct Write and 3D Printing: A Review. *Adv. Mater. Technol.* **2020**, *5*, 2000070. [CrossRef]
37. Smay, J.E.; Cesarano, J.; Lewis, J.A. Colloidal Inks for Directed Assembly of 3-D Periodic Structures. *Langmuir* **2002**, *18*, 5429–5437. [CrossRef]
38. Saadi, M.A.S.R.; Maguire, A.; Pottackal, N.T.; Thakur, M.S.H.; Ikram, M.M.; Hart, A.J.; Ajayan, P.M.; Rahman, M.M. Direct Ink Writing: A 3D Printing Technology for Diverse Materials. *Adv. Mater.* **2022**, *34*, 2108855. [CrossRef] [PubMed]
39. Kavalli, T.; Wolf, R.; Lalevée, J. Ultrafast Epoxy-Anhydride Photopolyaddition Reaction. *Macromol. Chem. Phys.* **2020**, *221*, 2000236. [CrossRef]
40. M'Barki, A.; Bocquet, L.; Stevenson, A. Linking Rheology and Printability for Dense and Strong Ceramics by Direct Ink Writing. *Sci. Rep.* **2017**, *7*, 6017. [CrossRef]
41. Maguire, A.; Pottackal, N.; Saadi, M.A.S.R.; Rahman, M.M.; Ajayan, P.M. Additive manufacturing of polymer-based structures by extrusion technologies. *Oxf. Open Mater. Sci.* **2021**, *1*, itaa004. [CrossRef]
42. Shuai, K.; Zhang, K.; Yao, S.; Ni, Z.; Shi, D.; Miao, J.-T.; Chen, M. 3D Printing of Branched Polyurethane with Tough Mechanical Properties for Stretchable Sensors. *Adv. Eng. Mater.* **2024**, *26*, 2301103. [CrossRef]

polymers

MDPI

Article

Evaluating Oil Palm Trunk Biochar and Palm Oil as Environmentally Friendly Sustainable Additives in Green Natural Rubber Composites

Narong Chueangchayaphan, Manop Tarasin, Wimonwan Phonjon and Wannarat Chueangchayaphan *

Faculty of Science and Industrial Technology, Prince of Songkla University, Surat Thani Campus, Surat Thani 84000, Thailand; narong.c@psu.ac.th (N.C.); manop.ta@psu.ac.th (M.T.); phonjonwimonwan@gmail.com (W.P.)
* Correspondence: wannarat.p@psu.ac.th

Abstract

This research examines the possibility of palm oil and oil palm trunk biochar (OPTB) from pyrolysis effectively serving as alternative processing oils and fillers, substituting petroleum-based counterparts in natural rubber (NR) composites. Chemical, elemental, surface and morphological analyses were used to characterize both carbon black (CB) and OPTB, by using Fourier transform infrared spectroscopy (FTIR), X-ray diffraction (XRD), Brunauer–Emmett–Teller (BET) gas porosimetry, and scanning electron microscopy (SEM). The influences of OPTB contents from 0 to 100 parts per hundred rubber (phr) on thermal, dielectric, dynamic mechanical, and cure characteristics, and the key mechanical properties of particulate NR-composites were investigated. OPTB enhanced the characteristics of the composites, as demonstrated by a rise in dielectric constant, thermal stability, storage modulus, glass transition temperature (T_g), hardness and modulus at 300% elongation, along with a decrease in the loss tangent (tan δ). Tear strength exhibited an increase with OPTB content up to a specific threshold, whereas tensile strength and elongation at break declined. This implies a compromise between the various mechanical properties when incorporating OPTB as a filler. This work supports the potential application of OPTB as a renewable substitute for CB in the rubber industry, particularly in tire production and other industrial rubber applications, which would also bring environmental, sustainability, and economic benefits for the palm oil-related industry.

Keywords: oil palm trunk; biochar; palm oil; sustainable additive; natural rubber; green composites

1. Introduction

Biopolymers have gained a lot of attention in recent years due to their potential to lessen the need for fossil fuel resources and nonbiodegradable polymers, both of which contribute significantly to environmental pollution [1]. Natural rubber (NR), derived from the *Hevea brasiliensis* plant, is a naturally occurring polymer consisting of a combination of poly(*cis*-1,4-isoprene) and biological components. This unique composition imparts distinct characteristics to the material [2]. Thus, there has been a consistent rise in the significance of NR for human beings due to its inherent qualities of elasticity, low hysteresis, high strength, exceptional toughness, and versatile production capabilities [3]. However, it should be noted that raw NR possesses a soft texture and exhibits relatively low mechanical properties. Consequently, the incorporation of additives and the process of vulcanization

have become imperative in order to enhance its overall performance [4]. Processing oil is an additive needed in NR compounds because it acts as an internal lubricant to achieve acceptable processability, improves flex life at a low temperature, filler dispersion, end-use properties, and gives a cost benefit [5,6]. Vegetable oil has replaced petroleum-based oil for decades because of its broad availability, non-toxicity, affordability, environmental sustainability, and being a renewable resource [7]. Vegetable oils have been extensively studied as alternative processing aids in rubber compounds due to their environmental benefits and ability to replace petroleum-based oils. Castor oil has been investigated as a plasticizer in natural rubber (NR), showing improved processability and mechanical properties [8]. Similarly, the natural oils soybean, palm, and sunflower oil have been explored for their effectiveness as processing aids and activators in carbon black-filled NR [9]. Soybean oil and its modified forms have demonstrated potential in replacing petroleum oils across various elastomers, including NR, styrene-butadiene rubber (SBR), and ethylene-propylene-diene monomer rubber (EPDM), contributing to enhanced filler dispersion, processing characteristics, and mechanical performance [10–15]. Palm oil, a readily available and renewable resource, has also been shown to improve the processing and mechanical properties of EPDM and silica-filled NR composites [16,17]. In nitrile butadiene rubber (NBR), palm-based processing aids have optimized curing systems and physical properties [18]. These findings highlight the versatility and potential of vegetable oils to advance sustainable practices in rubber manufacturing. In this study, palm oil was selected as the processing oil for the fabrication of green composite natural rubber. This selection was based on a review of the relevant literature, highlighting its status as the most extensively manufactured vegetable oil globally, accounting for a substantial share of the vegetable oil industry and offering a reasonable price for large-scale industrial applications [19,20]. Palm oil is derived from renewable resources and contains key fatty acids, including palmitic, oleic, and linoleic acids [21], which contribute to its excellent lubricating properties, high heat resistance [9] and compatibility with rubber matrices. Additionally, its renewable and environmentally friendly nature aligns with the objectives of developing sustainable and eco-friendly rubber composites. These factors collectively support the suitability of palm oil as an effective alternative to petroleum-based processing oils in rubber compounding.

Filler is one of the compounding ingredients required to enhance the properties of rubber, and common ones are carbon black, clay, calcium carbonate, silica, etc. [22]. The type of filler most frequently utilized in the rubber industry as a reinforcing substance is carbon black (CB) [23]. Despite the advantageous physical, mechanical, thermal, and barrier qualities that CB imparts to rubber composites, it is not without its drawbacks. CB is produced from the incomplete combustion of heavy petroleum products. The incomplete combustion of petroleum products can result in the emission of poisonous fumes and the generation of hazardous waste [24]. As a result, the production and utilization of CB give rise to numerous risks of health complications and environmental damage. Thus, it is imperative that the rubber industry adopts alternative, renewable, and environmentally favorable filler materials in place of CB. Biochar is a solid carbon-rich substance like CB; it is obtained by subjecting biomass to elevated temperatures in a sealed chamber with varying degrees of oxygen lack. In this controlled environment, biomass undergoes a thermochemical transformation, producing biochar. Because of its affordability and environmentally friendly nature, biochar has garnered significant interest for diverse uses such as enhancing soil quality, managing waste, mitigating greenhouse gas emissions, and generating energy [25,26]. Biomass derived from oil palm plantations presents itself as a highly promising and viable option as fuel and feedstock of carbon black, serving as a commendable alternative to conventional renewable and sustainable resources.

Palm oil is the predominant oil produced on a global scale, playing a substantial role in the vegetable oil market [20]. The increasing worldwide need for palm oil has resulted in intensified production in the oil palm estates. This heightened cultivation has resulted in the significant production of substantial amounts of biomass from milling operations and plantations. Among the various categories of residual oil palm biomass are empty fruit bunches (EFBs), palm kernel shells (PKSs), mesocarp fiber (MF), oil palm fronds (OPFs), and oil palm trunks (OPTs). OPTs hold significant appeal due to their consistent year-round availability following the felling of oil palm trees [27,28]. The substantial volume of OPTs generated poses inevitable challenges in waste management. Instead of resorting to landfill disposal or open burning, which result in significant air pollution, there is an opportunity to transform this waste into value-added materials. To achieve a significant reduction in the organic compound content, OPT is subjected to pyrolysis to generate biochar. In contrast to unprocessed biomass, biochar is more advantageous owing to its superior qualities, which include reduced moisture content, elevated calorific value, decreased density for storage purposes, and long-lasting durability [29]. This approach can effectively address and mitigate waste disposal concerns. Other than its application, as previously mentioned, the biochar produced possesses the ability to serve as an additive in rubber composites. This would provide an alternative to carbon black, which is derived from petroleum. In the prior literature, there are reports on the utilization of biochar from oil palm biomass as bio-filler in rubber composites, for example the incorporation of palm kernel shell biochar (PKSB) in NR composites [22,30–32] and in carboxylated nitrile butadiene rubber (XNBR) [22]. The viability of using OPTB as a flame-retardant component has been examined in two varieties of specialty natural rubber (SpNR) latex foam, epoxidized and deproteinized, providing a limited study of the application of OPTB as a filler in vulcanized natural rubber [33].

The concept of a sustainable circular economy has gained significant attention for its economic, social, and environmental benefits. By utilizing green and renewable materials, it supports industrial applications that benefit both current and future generations [19]. This study is innovative in simultaneously utilizing two renewable materials—OPTB as a filler and palm oil as a processing oil—to replace carbon black- and petroleum-based processing oils in NR composites. To our knowledge, no previous research has combined these materials in a single formulation. The functional groups, chemical composition, and morphology of OPTB were characterized using FTIR, XRD, and SEM. The effects of OPTB content (0–100 phr) on the cure characteristics and thermal, dynamic mechanical, dielectric, and mechanical properties of NR composites were analyzed. Comparative samples with CB as a filler were prepared using the same methodology. This approach offers a significant advance in reducing fossil fuel consumption and developing eco-friendly additives by transforming agricultural waste into high-value materials, aligning with sustainability and circular economy principles.

2. Materials and Methods

2.1. Materials

Palm oil was obtained from Suksomboon Vegetable Oil Co., Ltd. (Chonburi, Thailand). Standard Thai Rubber (STR20) was used in the rubber formulation and the other chemicals were N-phenyl-p-phenylenediamine (6PPD), zinc oxide (ZnO), stearic acid (SA), diphenyl guanidine (DPG), 2-Mercaptobenzothiazyl disulfide (MBTS), carbon black (N550), and sulfur (S), supplied by Bossoftical Public Co., Ltd. (Songkhla, Thailand). All the chemicals were utilized as received, without further purification. OPTs were gathered from a nearby palm plantation located in Surat Thani, Thailand. OPTs used in this study were from the Surat Thani 2 cultivar, harvested from a 22-year-old plantation located in Mueang District, Surat Thani, Thailand. The palms had an average trunk height of 9.5 m. For the experiment,

the trunks were cut into 10 cross-sectional discs (thickness: 5 cm each) at intervals of 1 m along the length of the trunk to ensure a representative sampling of the material. These discs were pre-dried at 100 ± 5 °C in a controlled oven until their weights stabilized, which is essential for achieving efficient pyrolysis and minimizing energy consumption during the process. The pre-dried samples were then arranged evenly in the pyrolysis chamber to optimize heat distribution and ensure uniform carbonization. The OPTs were heated gradually from ambient temperature and held at 600 °C for 6 h. The resulting pyrolytic OPTB was allowed to cool for 24 h before being ground using a grinder. Following this, the ground material was sifted through a 250-mesh sieve and dried in an oven at 105 °C until no further changes in quality were observed.

2.2. Characterization of CB and OPTB Powder

FTIR spectra were obtained using a Vertex70 FTIR spectrometer (Thermo Scientific, Bruker, Ettlingen, Germany) with the KBr pellet technique. XRD analysis was conducted with Cu-Kα radiation, operating at 40 kV and 30 mA, scanning from 10° to 90° (2θ), and equipped with a 0.154 monochromator. Specific surface area was determined using Brunauer–Emmett–Teller (BET) gas porosimetry (ASAP2060, Micromeritics, Norcross, GA, USA) employing the BET N2 method. Particle size and morphology of CB and OPTB powders were analyzed using a particle size analyzer (Beckman Coulter LS 230, Vernon Hills, IL, USA) and SEM (QUANTA400, Thermo Fisher Scientific, Brno, Czech Republic), respectively. Prior to SEM imaging, a thin layer of gold was sputter-coated onto the surfaces of CB and OPTB powders under a vacuum.

2.3. Preparation and Characterizations of NR Composites

The compositions of the compounds, expressed in parts per hundred of rubber (phr), are detailed in Table 1.

Table 1. Formulations used for NR composites with, alternatively, OPTB or CB filler.

Component	Case of OPTB (phr)				
	OPTB0	**OPTB10**	**OPTB30**	**OPTB50**	**OPTB100**
STR20	100	100	100	100	100
ZnO	5	5	5	5	5
SA	1	1	1	1	1
6PPD	1	1	1	1	1
Palm oil	10	10	10	10	10
MBTS	1	1	1	1	1
DPG	0.5	0.5	0.5	0.5	0.5
C	2.5	2.5	2.5	2.5	2.5
OPTB or CB	0	10	30	50	100

NR composites were prepared by blending in a two-roll mill for 30 min. Following sheeting out, the compound was left to rest for 16–24 h before undergoing vulcanization at 160 °C utilizing an electrically heated plate press (Charoen Tut Co., LTD., Bangkok, Thailand) operating at a pressure of 1500 psi for the optimal curing time determined using a moving die rheometer (MDR) (Alpha-Technologies Co., Ltd., Hudson, OH, USA) in accordance with ASTM D5289 standards, resulting in 2 mm thick sheets.

2.4. Characterization of NR Composites

2.4.1. Rheological Property Measurement

The Mooney viscosity (ML(1 + 4), 100 °C) was determined at 100 °C using a large rotor for a duration of 4 min following 1 min of preheating. Results were recorded as ML(1 + 4)

and obtained using a MonTech Mooney viscometer (MV2020) in compliance with ASTM D1646 standards. The Payne effect assessment was conducted utilizing a rubber process analyzer (RPA2000, Alpha Technologies, Hudson, OH, USA) operating in the strain sweep mode. This involved evaluating the storage modulus of uncured NR composites at various strain amplitudes. Strain sweep tests were employed to measure the storage shear moduli (G_0) of samples across different shear strain amplitudes, ranging from 0.56 to 1000%, with a fixed oscillation frequency of 1 Hz at a temperature of 100 °C.

2.4.2. Thermal and Dynamic Mechanical Properties

Thermogravimetric analysis (TGA/DSC 3+ model, Mettler Toledo, Greifensee, Switzerland) was conducted using a simultaneous thermal analyzer, employing a heating rate of 10 °C/min within the temperature range from 25 to 1000 °C under a nitrogen atmosphere. Dynamic mechanical thermal analysis was performed using a PerkinElmer DMTA 8000. Samples were subjected to tension mode testing from −100 to 150 °C at a heating rate of 3 °C/min, with fixed frequency and strain set at 10 Hz and 0.1%, respectively.

2.4.3. Dielectric and Mechanical Properties

The dielectric constant (ε') was determined using an impedance analyzer across the frequency range of 10^3–10^6 Hz at an AC potential of 1 V. Durometer (Instron, Norwood, MA, USA) measurements were employed to assess the hardness of 6 mm thick samples in accordance with ASTM D2240 standards. Tear and tensile tests were conducted using a universal tensile testing machine (Tinius Olsen, model 10ST, Salfords, UK) on dumbbell-shaped test specimens prepared according to ASTM D624 and ASTM D412, respectively, at a crosshead speed of 500 mm/min. For each test, five duplicate samples were used to ensure the accuracy and reproducibility of the results.

3. Results and Discussion

3.1. Characterization of CB and OPTB

Pyrolytic chars are the most economically viable substitutes for carbon black in the rubber industry, used as carbon fillers. To assess feasibility, a pyrolytic OPTB was analyzed and compared to a commercial CB, N550. The FTIR analysis was performed in order to ascertain the chemical functional groups present in both CB and OPTB, as shown in Figure 1a. It is evident that the weaker peaks in both cases, located between 2800 and 2975 cm^{-1}, which are attributed to the stretching vibrations of -CH bonds [34], could be the consequence of pyrolysis-induced alkane breakdown resulting in the significantly reduced hydrogen content of the carbons [35]. In addition, the prominent absorption peak at approximately 3400 cm^{-1}, corresponding to the stretching vibrations of -OH of hydroxyl, indicates carboxylic and phenolic functional groups present in both the materials [36]. For the case of CB, the peak at around 1625 cm^{-1} was exclusively seen, and it is attributed to C=C stretching vibrations [37,38]. Meanwhile, Zang et al. (2023) ascribed the observed peaks to the stretching of C=O bonds, indicating the presence of carboxyl, ketenes, lactones [39], and pyrones [40]. In addition, the CH stretching of the aromatic molecule was shown by the weak intensity absorption at 1380 cm^{-1} [38]. The vinyl ether was detected at a wavenumber of 1023 cm^{-1}, corresponding to the stretching vibrations of the C-O bond. The spectrum for OPTB exhibited clearly visible bands at 1580 cm^{-1}, attributed to an aromatic skeleton vibration of the C–C bond [41]. This signifies the aromatic ring of lignin [42,43]. According to Zappielo et al. (2016), a noticeable peak around 1580 cm^{-1} indicates the presence of carbonyl or hydroxyl groups. The absorption bands at 1424 cm^{-1} represent C–H deformation by the bending of alkanes or alkyl groups, while 1258 cm^{-1} is for the C–O–C stretching of ester groups [37]. The peaks detected at 874, 814,

and 755 cm^{-1} likely originated from the bending of C–H bonds in aromatic rings [44,45]. The aforementioned results show that, while the FTIR peaks of the two raw materials, OPTB and CB, were slightly different, the chemical structures of CB and OPTB had certain identical functional groups, such as C=C stretching in aromatic and oxygen-containing groups, including carboxylic, hydroxyl, phenolic (hydroxyl), carbonyl, lactone, carboxylic acid anhydride, and cyclic peroxide groups, as reported by [46–48]. This was most likely caused by the varied sources and methods used to prepare OPTB and CB.

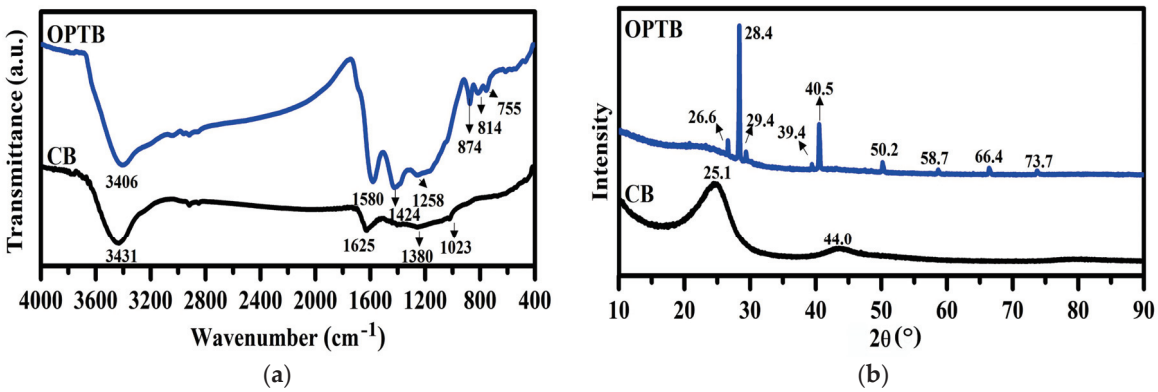

Figure 1. (**a**) FTIR spectra and (**b**) XRD analyses of CB and OPTB.

XRD was used to characterize the CB and OPTB fillers, as shown in Figure 1b. It was found that CB demonstrated typical amorphous carbon in the diffractograms. The carbons show no signs of prominent Bragg peaks caused by mineral impurities. Nevertheless, a broad diffraction peak at 2θ values ranging from 20 to 30° (002) and 40 to 50° (100) indicates the existence of graphitic carbon alongside amorphous carbon [34–36,49,50]. In contrast, the XRD patterns of OPTB exhibited several sharp diffraction peaks reflecting different mineralogical phases, indicating miscellaneous mineral crystals and other inorganic components. It was noted that several peaks overlapped and provided multiple-peak combinations. The major crystalline peaks of the OPTB were for potassium chloride (KCl), silicon oxide (SiO_2), and calcium carbonate ($CaCO_3$). These mineral elements (silicate, potassium salt, and calcium carbonate) made up the majority of the ash that was released as the cellulose and lignin components of OPT were progressively broken down [51].

The BET surface area of the CB that was determined in this investigation (37 m^2/g) was comparable to that which previous studies have found [40]. The BET specific surface area of OPTB was higher than that of CB, as shown in Table 2. Despite this, the CB particles demonstrated smaller diameters, not only in the mean value (D_{50}), but also for 10% and 90% thresholds in sample volume (D_{10} and D_{90}, respectively) when compared to OPTB. Apparently, the abundant inorganic materials and metal elements in OPTB (shown in XRD analysis) generated pores or catalytically accelerated the creation of pores in the carbonaceous material [36].

Table 2. Specific surface areas (from BET) and particle size distribution statistics for CB and OPTB.

Parameter	CB	OPTB
S_{BET} (m^2/g)	37.06	68.09
D_{10} (μm)	0.5	6.4
D_{50} (μm)	2.2	17.9
D_{90} (μm)	7.2	35.7

Figure 2 provides SEM images of CB and OPTB, demonstrating significant differences between the samples. It was found that CB showed different shapes of carbon black

aggregates, often spheroidal or ellipsoidal with a rough surface. OPTB had larger sized particles with pores on their surfaces. The images distinctly depict the porous structure of OPTB, with pores evident on the surface and displaying discernible sizes and shapes of both cylindrical and polygonal cross-sections. The formation of these porous channels resulted from the gradual breakdown of the lignocellulosic constituents, cellulose, hemicelluloses, and lignin. The residual non-volatile components were transformed into biochar [52]. It is the porosity of the larger particles in OPTB that explains its larger specific surface.

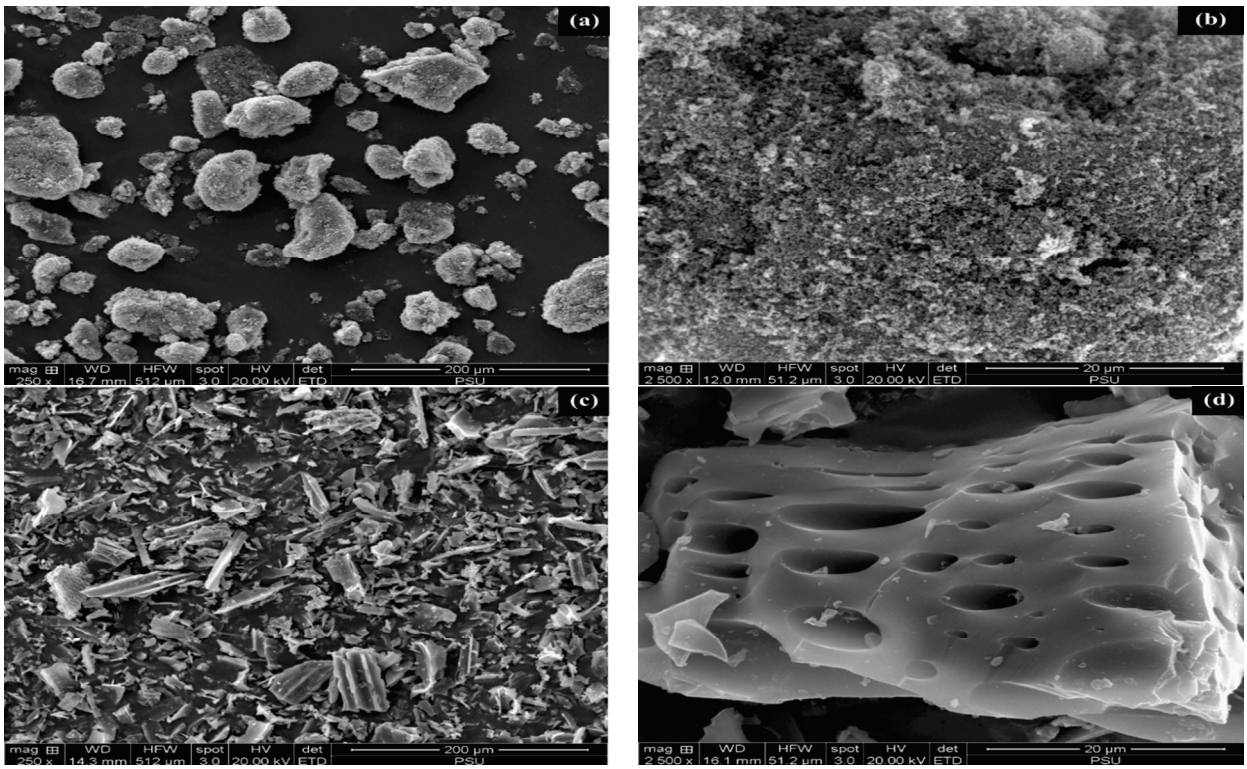

Figure 2. SEM images of CB and OPTB showing the morphologies of (**a**) CB at ×250 magnification, (**b**) CB at ×2500 magnification, (**c**) OPTB at ×250 magnification, and (**d**) OPTB at ×2500 magnification.

3.2. Thermal Stability Study

The influence of OPTB content on NR composites is shown in Figure 3. The thermal behavior of all specimens showed mutual resemblance, characterized by a primary decomposition peak. It can be noted that the TGA curves gradually declined until reaching a stage where the NR composites started to decompose. Thermal degradation of pure NR occurred between 195 and 430 °C, with T_{max} around 373 °C. It was also observed that the T_{max} slightly shifted to higher temperatures with increasing OPTB content, as listed in Table 3. This suggests that adding OPTB to NR composites increased their thermal stability. Pure NR produced the least final residue at 600 °C among the composites examined in the study. The ultimate residual amount rose with increasing OPTB content, attributable to the buildup of a greater amount of char capable of enduring high temperatures. Moreover, OPTB exhibits a slower decomposition rate in comparison to NR. Consequently, with the rise in OPTB concentration, a greater residual weight was noted [33].

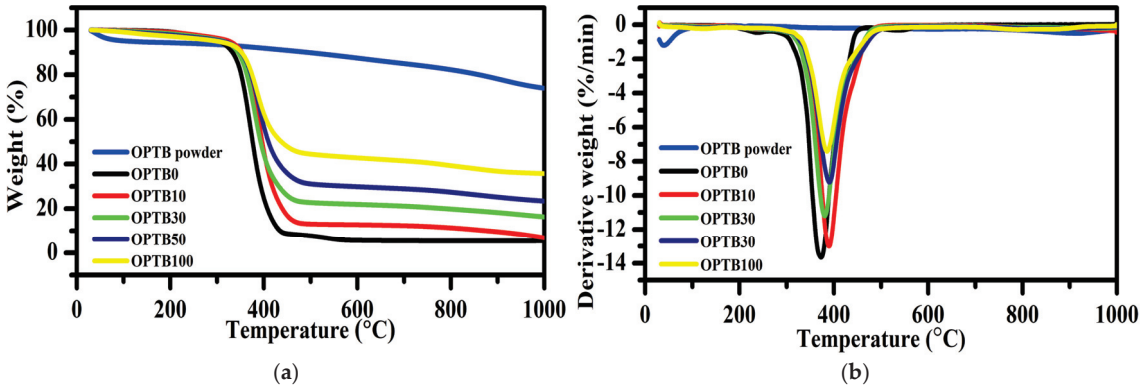

(**a**) (**b**)

Figure 3. Thermal properties of OPTB powder and NR composites: (**a**) TGA curves and (**b**) DTG curves.

Table 3. Thermal properties and dynamic mechanical properties of NR composites according to DMA and TGA.

Case	DMA			TGA	
	tan δ (at 0 °C)	tan δ (at 60 °C)	T_g (°C)	T_{max} (°C)	Residue (%)
OPTB0	0.047	0.000	−50.20	373	5.46
OPTB10	0.076	0.004	−47.15	390	6.85
OPTB30	0.074	0.013	−44.75	381	16.31
OPTB50	0.082	0.023	−44.30	391	23.41
OPTB100	0.108	0.049	−44.50	386	35.70

3.3. Dielectric Properties

Figure 4 depicts the relative dielectric constant for NR composites with variable OPTB contents, at various frequencies and environmental conditions. It can be noted that as frequency increased, the dielectric constant declined across all NR composites. This is because the polarization of the specimen is unable to synchronize with a high-frequency electric field [53], as well as a gradual reduction in dipole movement or alteration in orientation. Pure NR exhibited the lowest dielectric constant (1.50 at 1 kHz) due to its hydrophobic (nonpolar) structure. The addition of OPTB raised the dielectric constant of NR composites over the whole frequency range. For example, 100 phr OPTB-NR composite demonstrated the highest dielectric constant (3.80 at 1 kHz), for an increase by 153%, suggesting that OPTB is more prone to polarization by an electric field than NR. The increased dielectric constant can be due to the significant interfacial polarization in OPTB/NR composites. Interfacial polarization is generated by charge accumulation at the phase interfaces of the filler (here biochar) and rubber matrix [54]. In addition, the presence of carbonaceous elements within biochar could be pivotal in fostering significant polarization within the material. The FTIR results demonstrated π electrons found in carbon materials, which have the freedom to move across wide areas, presenting a particularly intriguing phenomenon [55]. Moreover, the dielectric constant increased with OPTB loading due to the mineral phases identified by XRD. As OPTB content rises, the mineral concentration in the matrix increases, resulting in more charge carriers for polarization and a higher dielectric constant.

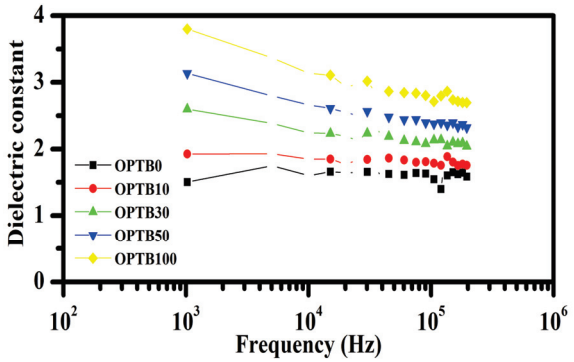

Figure 4. Dielectric constants of NR composites by frequency of excitation.

3.4. Dynamic Behaviors

It is commonly known that elastic modulus and stored energy are both quantified by the storage modulus. The temperature dependence of storage modulus is reported in Figure 5a. The results show that when temperature increased, the storage modulus generally decreased, because chain mobility increased and physical bonding and chain entanglements decreased [56]. The NR composite with 100 phr OPTB had the highest storage modulus in the glassy region. When OPTB was introduced to NR composites, the storage modulus rose in comparison to pure NR. This is because the NR chain motion is restricted by the high-stiffness OPTB filler.

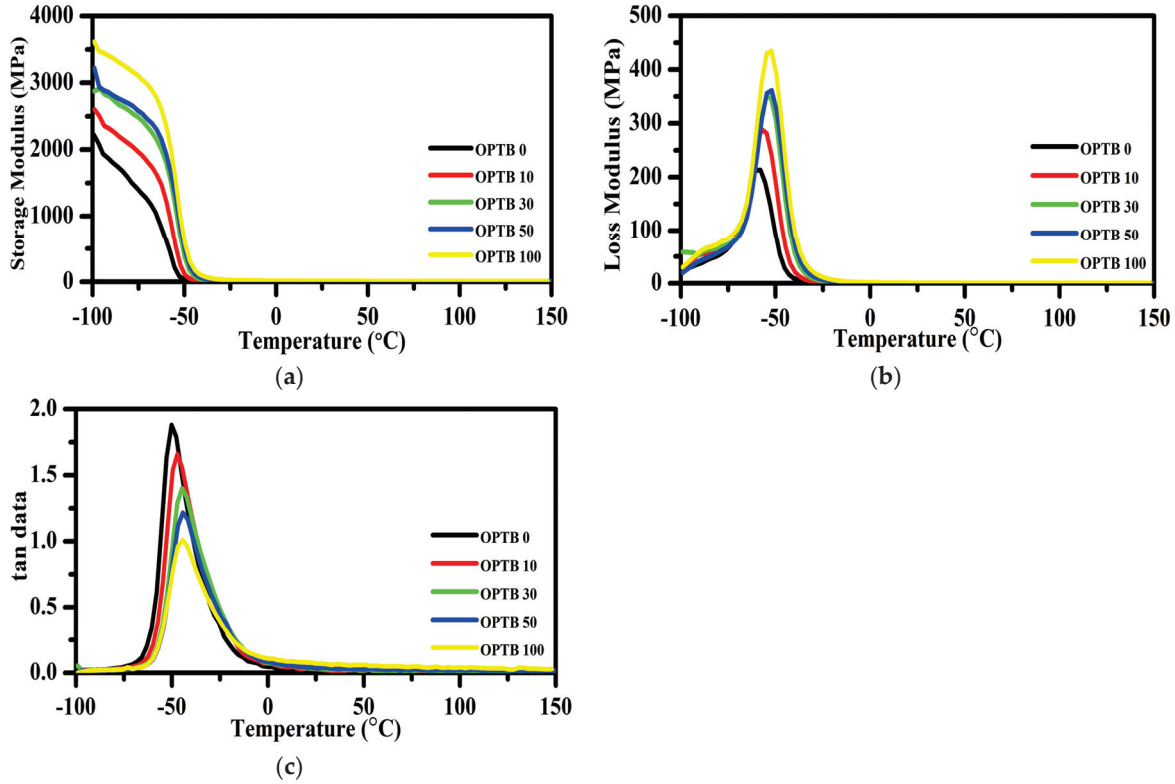

Figure 5. (**a**) Storage modulus, (**b**) loss modulus, and (**c**) tan δ for the experimental NR composites.

The loss modulus (E″) represents the viscous response and damping as a result of energy dissipation as heat. The addition of OPTB to the NR matrix broadened the loss modulus peak, as seen in Figure 5b. This could be explained by the fact that the addition of filler results in a larger number of chain segments inside the composites, which inhibits relaxation [57].

Figure 5c depicts the temperature-dependent evolution of the damping factor, also known as tan δ (loss to storage modulus ratio). The OPTB in NR composites resulted in a much lower height of the tan δ peak, indicating a lower lost-to-stored energy ratio in the T_g zone. The decrease in tan δ_{max} may be attributed to the dense and entangled OPTB filler network, which significantly hinders chain mobility during glass transition. It has been documented that natural rubber is among the polymer materials exhibiting the highest damping factor, attributed to the inherent movement of the polyisoprene backbone. The presence of additional materials in its matrix tends to limit damping capacity [56].

The transition to the maximum of a tan δ peak is closely related to the glass transition temperature T_g. The tan δ peak parameters are summarized in Table 3. The glass transition temperatures of NR composites were impacted by the addition of OPTB. When OPTB was added to NR composites, a shift in T_g to a higher temperature was noted. It resulted from filler–rubber interactions limiting the mobility of the rubber chains. The rolling resistance and wet traction properties of NR are extremely significant for car tire applications. It is common practice to use the dynamic mechanical loss angle tan δ at 60 °C of vulcanized compounds as a predictor of rolling resistance. As a result, a low tan δ at 60 °C is of importance, since it indicates that the vulcanized compound is performing better. When rolling resistance is reduced, less energy is needed to maintain the speed of the vehicle, which conserves fuel for the internal combustion engine and lowers the emissions. Results show that the rolling resistance of NR composites tended to decrease with OPTB content. The energy loss of the rubber vulcanizate, or tan δ at 0 °C, is used to assess the good wet-grip qualities. A high tan δ at 0 °C indicates good wet-grip. The highest tan δ at 0 °C was recorded for 100 phr OPTB filled NR composite, while tan δ at 0 °C was lower or the wet-grip characteristics were poorer for pure NR.

It is well known that the addition of fillers to a rubbery matrix significantly alters its viscoelastic behavior. The Payne effect characterizes alterations in the characteristics of an elastomeric component in relation to the applied strain. It can be explained in terms of a filler–filler network in the rubber matrix. The variation in storage modulus of NR filled with varying loadings of OPTB as a function of dynamic strain amplitude and a summary of findings are demonstrated in Figure 6 and Table 4. It was found that the storage modulus decreased with strain, which is attributed to the filler–filler network breaking down at larger dynamic strains. In addition, the Payne effect increased with OPTB content. The maximum storage modulus and Payne effect magnitude were observed for NR composite filled at 100 phr with OPTB, indicating the strongest effects of a filler–filler network in the elastomer matrix. This is, however, an excessive filler content causing a loss of key material properties.

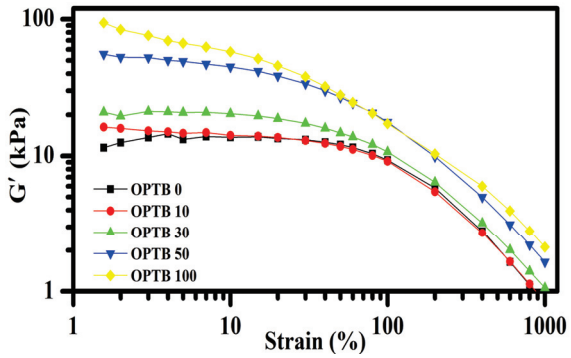

Figure 6. Storage modulus vs. strain for the NR composites.

Table 4. Payne effect for the NR composites.

Case	$G'_{1.56}$	G'_{100}	G'_{1000}	$\Delta G' = G'_{1.56} - G'_{100}$	$\Delta G' = G'_{1.56} - G'_{1000}$
OPTB0	11.49	9.31	0.79	2.18	10.7
OPTB10	16.27	9.13	0.83	7.14	15.44
OPTB30	20.94	10.71	1.06	10.23	19.88
OPTB50	55.51	17.65	1.64	37.86	53.87
OPTB100	94.32	17.25	2.11	77.07	92.21

3.5. Rheological Properties

The rheological responses of NR compounds, acquired at 160 °C using an MDR rheometer, are displayed in Figure 7, and the summarizing data for scorch time (t_{s1}), cure time (t_{c90}), cure rate index (CRI), minimum torque (M_L), maximum torque (M_H), and delta torque (M_H–M_L) are given in Table 5. t_{s1} for pure NR and NR composites were similar, with the exception of the 100 phr OPTB case, which had a 50% decrease in t_{s1} compared to pure NR. On the other hand, t_{c90} displayed a marginally rising trend with OPTB content. This may be because the surface activity of OPTB, which includes oxygen-containing compounds such as hydroxyl functional groups (see the previously discussed FTIR analysis of OPTB), retards t_{c90}. The M_L and M_H denote viscosity and rigidity, as well as the stiffness of the rubber compound, respectively. It was found that the characteristics for the vulcanization of all prepared rubber compounds had the same trend of increasing M_L and M_H with filler content, because the filler was limiting the molecular motions of NR chains. These results are supported by the Mooney viscosity of unvulcanized rubber, often influenced by the macrostructure and flow properties of the rubber composite. It revealed that a rise in Mooney viscosity in unvulcanized rubber composites was associated with an increase in OPTB content, attributed to the hydrodynamic impact of the filler within the rubber. The crosslink density from both chemical and physical crosslinks can be assessed from delta torque (M_H–M_L). Pure NR exhibited the least M_H–M_L, whereas OPTB-filled NR composites displayed a rising trend with OPTB loading. This could be attributed to crosslinking between filler and NR matrix phases.

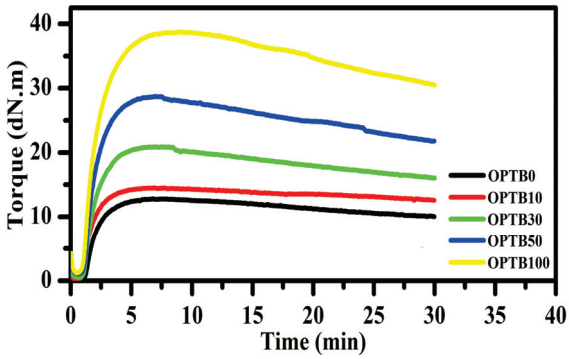

Figure 7. Time profiles of torque for the NR compounds.

Table 5. Cure characteristics and Mooney viscosities of the NR compounds.

Case	Mooney Viscosity (MU)	M_L (Ib/In)	M_H (Ib/In)	M_H–M_L (Ib-In)	t_{s1} (min)	t_{c90} (min)	CRI (min^{-1})
OPTB0	8.80	0.38	12.78	12.40	1.17	3.47	27.65
OPTB10	9.30	0.25	14.51	14.26	0.57	3.21	30.58
OPTB30	14.10	0.48	20.88	20.40	1.07	3.41	28.26
OPTB50	24.50	1.06	28.71	27.65	1.04	3.45	27.95
OPTB100	33.10	1.18	38.76	37.58	0.58	4.19	23.29

3.6. Mechanical Properties

The incorporation of OPTB resulted in increases in hardness (Figure 8a), modulus at 100% elongation (M100), and modulus at 300% elongation (M300) (Figure 8d) in the OPTB filled NR composites. This can be ascribed to the notably high hardness and modulus of OPTB, along with the strong interfacial adhesion between OPTB filler and NR matrix. Consequently, OPTB particles could proficiently resist the load, enhancing the indentation resistance of the composites [58]. The tear strength exhibited an increasing trend with OPTB loading up to 70 phr (Figure 8b). This enhancement can be attributed to improved interfacial adhesion between the OPTB filler and NR matrix. The adhesion mechanism involves hydrogen bonding between the carboxylic (-COOH) and phenolic (-OH) groups present on the OPTB surface and the proteins and phospholipids found in the non-rubber components of NR, as evidenced by the FTIR analysis discussed previously. However, the tear strength shows a significant decrease when OPTB loading exceeds 70 phr, reaching its lowest value at 100 phr. Obviously, the tensile strength decreased gradually with OPTB loading, from pure NR onwards (Figure 8e). Nevertheless, incorporating CB enhanced tensile strength, attributed to the interactions between CB filler and rubber matrix, alongside its heightened activity and smaller particle size compared to OPBT [4]. The sizable particles of OPTB induced localized stresses within the composites, which undermined the strength of the composite, in particular reducing the tensile strength [59]. Furthermore, the greater particle size of OPTB may prevent the strain-induced crystallization of NR, also reducing tensile strength. This is the opposite effect to that of adding biochar to synthetic rubber [4,22,60,61]. There are studies seeking to improve the tensile strength of biochar/polymer (or rubber) composites by reducing the particle size of biochar [62,63]. When OPTB was increased to 100 phr, there was a significant reduction in tensile strength and tear strength. This indicates an excessive filler content that caused the filler to aggregate, hindering appropriate filler–matrix interactions and forming stress-concentration points initiating fracture failures. A substantial incorporation of OPTB markedly reduced the elongation at break of the NR composites (Figure 8f), signifying diminished ductility and toughness. Typically, as filler content increases, ductility and toughness decrease due to the filler particles serving as hindrances, impeding the slippage and movement of rubber chains, and consequently reducing ductility [58].

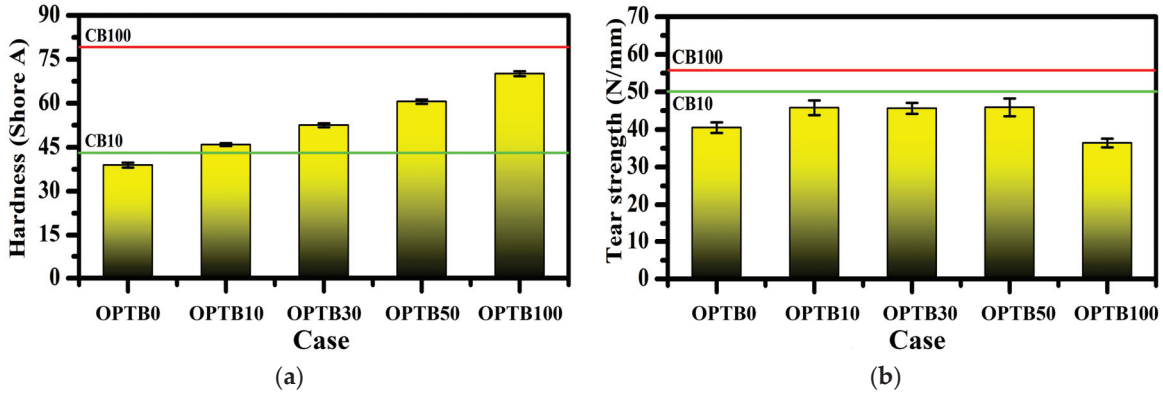

Figure 8. *Cont.*

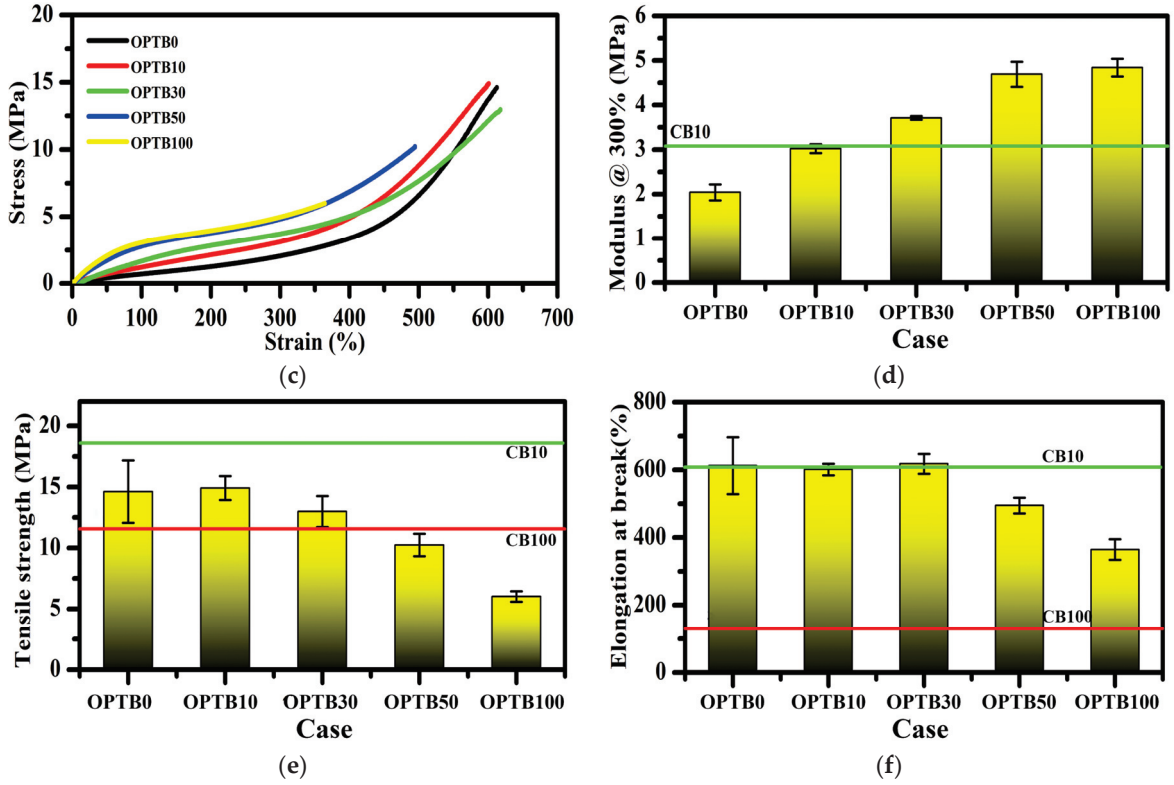

Figure 8. Physical and mechanical properties of NR composites: (**a**) hardness, (**b**) tear strength, (**c**) stress–strain curves, (**d**) modulus @300%, (**e**) tensile strength, and (**f**) elongation at break.

4. Conclusions

This study investigated the feasibility of using pyrolytic OPTB as a replacement for commercial CB in the rubber industry. FTIR analysis revealed the presence of similar functional groups in both CB and OPTB, including C=C and oxygen-containing groups. However, XRD analysis showed that CB possessed an amorphous structure, while OPTB contained various crystalline mineral phases. The addition of OPTB significantly enhanced key composite characteristics. The glass transition temperature (T_g) increased by approximately 5.7 °C, indicating reduced polymer chain mobility and greater rigidity due to the filler's reinforcing effect. Thermal stability improved by 13 °C, reflecting enhanced heat resistance, while the dielectric constant rose by about 153%, demonstrating improved electrical energy storage capabilities. However, the mechanical properties were not uniformly improved. Hardness, modulus, and tear strength increased with OPTB contents up to a certain point, while tensile strength and elongation at break decreased. This suggests a trade-off between the various mechanical properties when using OPTB as a filler. Overall, the results suggest that OPTB has the potential to partly replace CB in rubber composites. Nonetheless, challenges remain, including optimizing filler content and particle size to achieve a better balance of properties. Additionally, the large-scale adoption of OPTB faces hurdles such as feedstock variability, high production costs, and resistance from industries reliant on carbon black. Addressing these issues through precise process control and sustainable practices is essential for establishing OPTB as a competitive, eco-friendly filler.

Author Contributions: Conceptualization, N.C., M.T. and W.C.; methodology, N.C. and W.P.; validation, N.C., W.P. and W.C.; formal analysis, N.C.; investigation, W.P.; resources, M.T.; data curation, N.C. and W.C.; writing—original draft preparation, N.C. and W.C.; writing—review and editing, W.C.; visualization, W.P.; supervision, N.C.; project administration, N.C. and M.T.; funding acquisition, M.T. All authors have read and agreed to the published version of the manuscript.

Funding: This research was funded by the Research and Development Office (RDO), Prince of Songkla University, Grant No. SIT6601265S and Prince of Songkla University, Surat Thani Campus, 2024.

Institutional Review Board Statement: Not applicable.

Data Availability Statement: The original contributions presented in this study are included in the article. Further inquiries can be directed to the corresponding author.

Acknowledgments: We are grateful to Seppo Karrila for his assistance with manuscript preparation.

Conflicts of Interest: The authors declare no conflicts of interest.

References

1. Sintharm, P.; Phisalaphong, M. Green natural rubber composites reinforced with black/white rice husk ashes: Effects of reinforcing agent on film's mechanical and dielectric properties. *Polymers* **2021**, *13*, 882. [CrossRef] [PubMed]
2. Vaysse, L.; Bonfils, F.; Thaler, P.; Sainte-Beuve, J. Natural rubber. In *Sustainable Solutions for Modern Economies*; Höfer, R., Ed.; RSC Publishing: Cambridge, UK, 2009; pp. 339–367. [CrossRef]
3. Fan, Y.; Fowler, G.D.; Zhao, M. The past, present and future of carbon black as a rubber reinforcing fller—A review. *J. Clean. Prod.* **2020**, *247*, 119115. [CrossRef]
4. Lubura, J.; Kojić, P.; Ikonić, B.; Pavličević, J.; Govedarica, D.; Bera, O. Influence of biochar and carbon black on natural rubber mixture properties. *Polym. Int.* **2022**, *71*, 1347–1353. [CrossRef]
5. Pechurai, W.; Chiangta, W.; Tharuen, P. Effect of vegetable oils as processing aids in SBR compounds. *Macromol. Symp.* **2015**, *354*, 191–196. [CrossRef]
6. Hayichelaeh, C.; Nun-Anan, P.; Purbaya, M.; Boonkerd, K. Unfilled natural rubber compounds containing bio-oil cured with different curing systems: A comparative study. *Polymers* **2022**, *14*, 2479. [CrossRef]
7. Fu, Q.; Tan, J.; Wang, F.; Zhu, X. Study on the synthesis of castor oil-based plasticizer and the properties of plasticized nitrile rubber. *Polymers* **2020**, *12*, 2584. [CrossRef]
8. Raju, P.; Nandanan, V.; Kutty, S.K.N. A study on the use of castor oil as plasticizer in natural rubber compounds. *Prog. Rubber Plast. Recycl. Technol.* **2007**, *23*, 169–180. [CrossRef]
9. Jayewardhana, W.G.D.; Perera, G.M.; Edirisinghe, D.G.; Karunanayake, L. Study on natural oils as alternative processing aids and activators in carbon black filled natural rubber. *J. Natl. Sci. Found. Sri Lanka* **2009**, *37*, 187–193. [CrossRef]
10. Petrović, Z.S.; Ionescu, M.; Milić, J.; Halladay, J.R. Soybean oil plasticizers as replacement of petroleum oil in rubber. *Rubber Chem. Technol.* **2013**, *86*, 233–249. [CrossRef]
11. Wang, Z.; Han, Y.; Zhang, X.; Huang, Z.; Zhang, L. Plasticization effect of transgenic soybean oil. I. on ethylene propylene diene monomer (EPDM), as substitute for paraffin oil. *J. Appl. Polym. Sci.* **2013**, *130*, 4457–4463. [CrossRef]
12. Boontawee, H.; Nakason, C.; Kaesaman, A.; Thitithammawong, A.; Chewchanwuttiwong, S. Benzyl esters of vegetable oils as processing oil in carbon black-filled SBR compounding: Chemical modification, characterization, and performance. *Adv. Polym. Technol.* **2015**, *36*, 320–330. [CrossRef]
13. Li, J.; Isayev, A.I.; Ren, X.; Soucek, M.D. Toward replacement of petroleum oils by modified soybean oils in elastomers. *Rubber Chem. Technol.* **2016**, *89*, 608–630. [CrossRef]
14. Petrović, Z.S.; Milić, J.; Ionescu, M.; Halladay, J.R. EPDM rubber plasticized with polymeric soybean oil of different molecular weights. *Rubber Chem. Technol.* **2017**, *90*, 667–682. [CrossRef]
15. Siriwong, C.; Khansawai, P.; Boonchiangma, S.; Sirisinha, C.; Sae-Oui, P. The influence of modified soybean oil as processing aids in tire application. *Polym. Bull.* **2020**, *78*, 3589–3606. [CrossRef]
16. Wang, Z.; Peng, Y.; Zhang, L.; Zhao, Y.; Vyzhimov, R.; Tan, T.; Fong, H. Investigation of palm oil as green plasticizer on the processing and mechanical properties of ethylene propylene diene monomer rubber. *Ind. Eng. Chem. Res.* **2016**, *55*, 2784–2789. [CrossRef]
17. Siwarote, B.; Sae-oui, P.; Wirasate, S.; Suchiva, K. Effects of bio-based oils on processing properties and cure characteristics of silica-filled natural rubber compounds. *J. Rubber Res.* **2017**, *20*, 1–19. [CrossRef]
18. Hanif, H.M.; Yong, K.C.; Lee, S.Y. Effects of a newly developed palm-based processing aid and curing systems on the physical properties of nitrile rubber composites. *Sains Malays.* **2020**, *49*, 2187–2196. [CrossRef]
19. Roy, K.; Poompiew, N.; Pongwisuthiruchte, A.; Potiyaraj, P. Application of different vegetable oils as processing aids in industrial rubber composites: A sustainable approach. *ACS Omega* **2021**, *6*, 31384–31389. [CrossRef]
20. Aprianti, N.; Kismanto, A.; Supriatna, N.K.; Yarsono, S.; Nainggolan, L.M.T.; Purawiardi, R.I.; Fariza, O.; Ermada, F.J.; Zuldian, P.; Raksodewanto, A.A.; et al. Prospect and challenges of producing carbon black from oil palm biomass: A review. *Bioresour. Technol. Rep.* **2023**, *23*, 101587. [CrossRef]

21. Ribeiro, W.B.; Damo, T.; Zattera, A.J.; Brandalise, R.N. Green compounds of SBR with nanofibrilated cellulose and palm oil in replacement to traditionally compounds used. *J. Elastomers Plast.* **2022**, *54*, 635–655. [CrossRef]
22. Abidin, Z.Z.; Mamauod, S.N.L.; Romli, A.Z.; Sarkawi, S.S.; Zainal, N.H. Synergistic effect of partial replacement of carbon black by palm kernel shell biochar in carboxylated nitrile butadiene rubber composites. *Polymers* **2023**, *15*, 943. [CrossRef]
23. Farida, E.; Bukit, N.; Ginting, E.M.; Bukit, B.F. The effect of carbon black composition in natural rubber compound. *Case Stud. Therm. Eng.* **2019**, *16*, 100566. [CrossRef]
24. Dominic, M.; Joseph, R.; Begum, P.M.S.; Kanoth, B.P.; Chandra, J.; Thomas, S. Green tire technology: Effect of rice husk derived nanocellulose (RHNC) in replacing carbon black (CB) in natural rubber (NR) compounding. *Carbohydr. Polym.* **2020**, *230*, 115620. [CrossRef]
25. Panwar, N.L.; Pawar, A.; Salvi, B.L. Comprehensive review on production and utilization of biochar. *SN Appl. Sci.* **2019**, *1*, 168. [CrossRef]
26. Muda, N.A.; Yoshida, H.; Ishak, H.; Ismail, M.H.S.; Izhar, S. Production and properties of solid biochar from oil palm trunk waste using sub-critical water technology. *J. Oil Palm Res.* **2020**, *32*, 526–536. [CrossRef]
27. Razali, N.; Kamarulzaman, N.Z. Chemical characterizations of biochar from palm oil trunk for palm oil mill effluent (POME) treatment. *Mater. Today Proc.* **2020**, *31*, 191–197. [CrossRef]
28. Pulingam, T.; Lakshmanan, M.; Chuah, J.A.; Surendran, A.; Zainab-L, I.; Foroozandeh, P.; Uke, A.; Kosugi, A.; Sudesh, K. Oil palm trunk waste: Environmental impacts and management strategies. *Ind. Crops Prod.* **2022**, *189*, 115827. [CrossRef]
29. Nudri, N.A.; Ghani, W.A.W.A.K.; Bachmann, R.T.; Baharudin, B.T.H.T.; Ng, D.K.S.; Said, M.S.M. Co-combustion of oil palm trunk biocoal/sub-bituminous coal fuel blends. *Energy Conv. Manag X* **2021**, *10*, 100072. [CrossRef]
30. Abbas, K.; Ghazali, A.M.M.; Ong, S.K. The effect of particle size of palm kernel shell on the mechanical properties and physical properties of filled natural rubber vulcanizates. *Mater. Today Proc.* **2019**, *19*, 1599–1607. [CrossRef]
31. Malomo, D.; Olasupo, A.D.; Adesigbin, A.M.; Egharevba, O.; Adewuyi, S.O.; Odubunmi, J.O.; Idemudia, L.; Abimbade, S.F.; Ogunyemi, E.K. Comparative studies on the physico-mechanical properties of natural rubber filled with CB/CPKS and CB/APKS vulcanizates. *JCBPS* **2020**, *10*, 211–226. [CrossRef]
32. Arraudhoh, M.T.N.; Haziq, M.F.M.; Zafirah, Z.A.; Liyana, M.S.N.; Hayawin, Z.N. Comparative studies on cure characteristics and mechanical properties of oil palm biomass filled natural rubber composites. *J. Oil Palm Res.* **2022**, *36*, 128–139. [CrossRef]
33. Ramli, R.; Chai, A.B.; Kamaruddin, S.; Ho, J.H.; Rasdi, F.R.M.; De Focatiis, D.S.A.; Ong, S.K.; Bachmann, R.T. Effects of oil palm trunk biochar on the thermal stability and acoustic properties of specialty natural rubber latex foam. *J. Rubber. Res.* **2023**, *26*, 1–15. [CrossRef]
34. Paul, S.; Rahaman, M.; Ghosh, S.K.; Kateria, A.; Das, T.K.; Patel, S.; Das, N.C. Recycling of waste tire by pyrolysis to recover carbon black: An alternative reinforcing filler. *J. Mater. Cycles Waste Manag.* **2023**, *25*, 1470–1481. [CrossRef]
35. Borah, D.; Satokawa, S.; Kato, S.; Kojima, T. Characterization of chemically modified carbon black for sorption application. *Appl. Surf. Sci.* **2008**, *254*, 3049–3056. [CrossRef]
36. Wang, M.; Zhang, L.; Li, A.; Irfan, M.; Du, Y.; Di, W. Comparative pyrolysis behaviors of tire tread and side wall from waste tire and characterization of the resulting chars. J. *Environ. Manag.* **2019**, *232*, 364–371. [CrossRef]
37. Zappielo, C.D.; Nanicuacua, D.M.; dos Santos, W.N.L.; da Silva, D.L.F.; Dall'Antônia, L.H.; de Oliveira, F.M.; Clausen, D.N.; Tarley, C.R.T. Solid phase extraction to on-line preconcentrate trace cadmium using chemically modified nano-carbon black with 3-mercaptopropyltrimethoxysilane. *J. Braz. Chem. Soc.* **2016**, *27*, 1715–1726. [CrossRef]
38. Sugatri, R.I.; Wirasadewa, Y.C.; Saputro, K.E.; Muslih, E.Y.; Ikono, R.; Nasir, M. Recycled carbon black from waste of tire industry: Thermal study. *Microsyst. Technol.* **2018**, *24*, 749–755. [CrossRef]
39. Zang, G.; Jiang, Y.; Wang, S.; Zhang, Y. Influence of a novel coupling agent on the performance of recovered carbon black filled natural rubber. *Compos. B Eng.* **2023**, *255*, 110614. [CrossRef]
40. Yepes, W.U.; Uribe, N.C.; Isaza, C.A.V.; Martínez, J.D. Incorporating the recovered carbon black produced in an industrial-scale waste tire pyrolysis plant into a natural rubber formulation. *J. Environ. Manag.* **2021**, *287*, 112292. [CrossRef]
41. Nagalakshmi, T.V.; Emmanuel, K.A.; Babu, C.S.; Chakrapani, C.; Divakar, P.P. Preparation of mesoporous activated carbon from jackfruit PPI-1 waste and development of different surface functional groups. *Int. Lett. Chem. Phys. Astron.* **2015**, *54*, 189–200. [CrossRef]
42. Som, A.M.; Wang, Z.; Al-Tabbaa, A. Palm frond biochar production and characterization. *Earth Environ. Sci. Trans. R. Soc. Edinb.* **2012**, *103*, 39–50. [CrossRef]
43. Razali, N.; Kamarulzaman, N.Z. Chemical characterizations of biochar from oil palm frond for palm oil mill secondary effluent treatment. *Malays. J. Anal. Sci.* **2022**, *26*, 370–383.
44. Barhtiar, M.H.A.M.; Sari, N.B.A.; Yaacob, A.B.; Yunus, M.F.B.M.; Ismail, K.B. Characterization of oil palm empty fruit bunch (EFB) biochar activated with potassium hydroxide under different pyrolysis temperature. *JESTEC* **2019**, *14*, 2792–2807.
45. Hassan, N.; Abdullah, R.; Khadiran, T.; Elham, P.; Vejan, P. Biochar derived from oil palm trunk as a potential precursor in the production of high-performance activated carbon. *Biomass Convers. Biorefin.* **2023**, *13*, 15687–15703. [CrossRef]

46. Boehm, H.P. Some aspects of the surface chemistry of carbon blacks and other carbons. *Carbon* **1994**, *32*, 759–769. [CrossRef]
47. Leblanc, J.L. Rubber–filler interactions and rheological properties in filled compounds. *Prog. Polym. Sci.* **2002**, *27*, 627–687. [CrossRef]
48. Sajjadi, B.; Chen, W.Y.; Egiebor, N.O. A comprehensive review on physical activation of biochar for energy and environmental applications. *Rev. Chem. Eng.* **2019**, *35*, 735–776. [CrossRef]
49. Saleh, T.A.; Danmaliki, G.I. Adsorptive desulfurization of dibenzothiophene from fuels by rubber tyres-derived carbons: Kinetics and isotherms evaluation. *Process Saf. Environ. Prot.* **2016**, *102*, 9–19. [CrossRef]
50. Liang, Y.; Wang, Y.; Ding, N.; Liang, L.; Zhao, S.; Yin, D.; Cheng, Y.; Wang, C.; Wang, L. Preparation and hydrogen storage performance of poplar sawdust biochar with high specific surface area. *Ind. Crops Prod.* **2023**, *200*, 116788. [CrossRef]
51. Wang, T.; Liu, H.; Duan, C.; Xu, R.; Zhang, Z.; She, D.; Zheng, J. The eco-friendly biochar and valuable bio-oil from caragana korshinskii: Pyrolysis preparation, characterization, and adsorption applications. *Materials* **2020**, *13*, 3391. [CrossRef]
52. Sianipar, E.M.; Hutapea, S.; Panjaitan, E.; Mardiana, S. Applicability assessment of oil palm trunk biochar for use as soil amendment: Morphology, structure, and chemical properties. *Sci. Technol. Asia* **2024**, *29*, 256–270.
53. Ni, Y.; Yang, D.; Wei, Q.; Yu, L.; Ai, J.; Zhang, L. Plasticizer-induced enhanced electromechanical performance of natural rubber dielectric elastomer composites. *Compos. Sci. Technol.* **2020**, *195*, 10820. [CrossRef]
54. Qian, M.; Zou, B.; Shi, Y.; Zhang, Y.; Wang, X.; Huang, W.; Zhu, Y. Enhanced mechanical and dielectric properties of natural rubber using sustainable natural hybrid filler. *Appl. Surf. Sci. Adv.* **2021**, *6*, 10017. [CrossRef]
55. Salema, A.A.; Yeow, Y.K.; Ishaque, K.; Ani, F.N.; Afzal, M.T.; Hassan, A. Dielectric properties and microwave heating of oil palm biomass and biochar. *Ind. Crops Prod.* **2013**, *50*, 366–374. [CrossRef]
56. Oboh, J.O.; Okafor, J.O.; Kovo, A.S.; Abdulrahman, A.S. Dynamic mechanical properties of crosslinked natural rubber composites reinforced with cellulosic nanoparticles. *Niger. J. Technol.* **2018**, *37*, 668–673. [CrossRef]
57. Jyoti, J.; Arya, A.K. EMI shielding and dynamic mechanical analysis of graphene oxide-carbon nanotube-acrylonitrile butadiene styrene hybrid composites. *Polym. Test.* **2020**, *91*, 106839. [CrossRef]
58. Li, S.; Xu, Y.; Jing, X.; Yilmaz, G.; Li, D.; Turng, L.S. Effect of carbonization temperature on mechanical properties and biocompatibility of biochar/ultra-high molecular weight polyethylene composites. *Compos. B Eng.* **2020**, *196*, 10812. [CrossRef]
59. Peterson, S.C. Coppiced biochars as partial replacement of carbon black filler in polybutadiene/natural rubber composites. *J. Compos. Sci.* **2020**, *4*, 147. [CrossRef]
60. Jiang, C.; Bo, J.; Xiao, X.; Zhang, S.; Wang, Z.; Wang, Z.; Yan, G.; Wu, Y.; Wong, C.; He, H. Converting waste lignin into nano-biochar as a renewable substitute of carbon black for reinforcing styrene-butadiene rubber. *Waste Manag.* **2020**, *102*, 732–742. [CrossRef]
61. Silva, V.D.; Ferrari, M.D.; Brandalise, R.N.; Benvenutti, E.V.; Schrekker, H.S.; Amico, S.C. EPDM with biochar, carbon black, aramid pulp and ionic liquid-compatibilized aramid pulp. *Fibers Polym.* **2021**, *22*, 1180–1188. [CrossRef]
62. Richard, S.; Rajadurai, J.S.; Manikandan, V. Influence of particle size and particle loading on mechanical and dielectric properties of biochar particulate-reinforced polymer nanocomposites. *Int. J. Polym. Anal. Charact.* **2016**, *21*, 462–477. [CrossRef]
63. Peterson, S.; Kim, S. Reducing biochar particle size with nanosilica and its effect on rubber composite reinforcement. *J. Polym. Environ.* **2020**, *28*, 317–322. [CrossRef]

polymers

MDPI

Article

Enhancing Mechanical and Antibacterial Performance of Tire Waste/Epoxidized Natural Rubber Blends Using Modified Zinc Oxide–Silica

Napasorn Kingkohyao [1], Tanit Boonsiri [2], Jobish Johns [3], Raymond Lee Nip [4] and Yeampon Nakaramontri [1,*]

[1] Sustainable Polymer & Innovative Composite Materials Research Group, Department of Chemistry, Faculty of Science, King Mongkut's University of Technology Thonburi, Bangkok 10140, Thailand; napasorn.king@mail.kmutt.ac.th
[2] Department of Microbiology, Phramongkutklao College of Medicine, Bangkok 10140, Thailand; boonsiri-t@hotmail.com
[3] Department of Physics, Rajarajeswari College of Engineering, Bangalore 560074, India; jobish_johns@rediffmail.com
[4] Global Chemical Co., Ltd., Bangpoo Industrial Estate, Muang 10280, Samutprakarn, Thailand; rlnip@glochem.com
* Correspondence: yeampon.nak@kmutt.ac.th

Abstract

This study investigates the synergistic effects of incorporating modified zinc oxide–silica ($ZnO\text{-}SiO_2$) into tire waste (TW) and epoxidized natural rubber (ENR) blends, with a focus on crosslinking dynamics, mechanical reinforcement, and antibacterial activity. The addition of $ZnO\text{-}SiO_2$ significantly enhanced crosslink density, as evidenced by increased torque and accelerated cure rates. An optimal concentration of 10 phr was found to yield the highest performance. This optimal balance between chemical activation and mechanical reinforcement resulted in exceptional tensile properties, including notable improvements in Young's modulus, tensile strength, and strain-induced crystallization (SIC). These enhancements were attributed to the strong interactions between ENR molecular chains and SiO_2 surfaces. However, excessive $ZnO\text{-}SiO_2$ concentrations caused filler agglomeration, which reduced both mechanical and antibacterial performances. An antibacterial analysis revealed a remarkable 99.9% bacterial reduction at 10 phr $ZnO\text{-}SiO_2$, attributed to the Zn^{2+} ion release and reactive oxygen species (ROS) generation, with sustained activity even after thermal aging. This durability underscores the composites' potential for long-term applications. The findings establish $ZnO\text{-}SiO_2$ as a dual-functional filler that optimizes crosslinking, enhances mechanical properties, and provides durable antibacterial efficiency. These results highlight the potential of TW/ENR blends while offering critical insights into mitigating filler agglomeration to improve overall material performance.

Keywords: tire waste; zinc oxide; antibacterial efficiency; epoxidized natural rubber; silica

1. Introduction

The global demand for sustainable materials has intensified the focus on recycling and upcycling industrial waste, particularly tire waste (TW), which is a major contributor to environmental pollution. Each year, millions of tires are discarded, posing significant ecological and disposal challenges. However, TW, which is rich in rubber, carbon black, and other additives, holds immense potential as a resource for advanced composite materials [1,2]. When blended with polymers such as natural rubber (NR), synthetic rubbers, and

modified NR, specifically, epoxidized natural rubber (ENR) [3], TW can be transformed into value-added materials. These composites benefit from the synergistic effects of the active chemicals in TW and the addition of new ingredients, improving the rate of crosslinking, mechanical and dynamic mechanical properties, and thermal stability [4,5]. Due to the unknown ingredients in TW, particularly the mix of hydrophobic and hydrophilic fillers along with various rubber types, epoxidized natural rubber (ENR), derived from renewable NR, offers unique properties, such as enhanced polarity, oil resistance, and compatibility with polar fillers. Additionally, the hydrocarbon chains in ENR can interact physically with the non-polar regions of TW through induced dipole–induced dipole intermolecular forces [6,7]. These attributes make ENR an excellent matrix for enhancing the utility of TW in composite formulations. However, the limited reinforcing ability of residual fillers in TW, such as carbon black (CB), poses a significant challenge. These fillers often exhibit poor dispersion and weak interactions with fresh ENR molecular chains [8,9] due to the presence of embedded rubber molecules from tire preparation. This limitation underscores the need for innovative strategies to enhance filler performance and optimize the properties of TW-based composites.

Recent studies have highlighted the potential of hybrid fillers, such as modified zinc oxide combined with particulate fillers like calcium carbonate (ZnO-$CaCO_3$), titanium dioxide (ZnO-TiO_2), and silica (ZnO-SiO_2), in addressing these challenges. Previously, ZnO-$CaCO_3$ and ZnO-TiO_2 were used in NR latexes for film and foam applications [10–13]. These hybrids demonstrated the synergistic effects of ZnO, a vulcanization accelerator with the reinforcing and interfacial adhesion properties of $CaCO_3$ and TiO_2 [14,15], widely used fillers in rubber materials. Modified ZnO hybrids have been shown to enhance crosslink density, mechanical strength, and functional properties, including the antibacterial activity of NR films and foams. The dual functionality of ZnO-$CaCO_3$ and ZnO-TiO_2 also allows them to act as reactive fillers, improving the interactions between rubber chains and promoting the absorption of volatile organic compounds (VOCs) [16]. However, excessive filler concentrations can lead to agglomeration, which diminishes both mechanical performance and antibacterial efficacy. In addition to mechanical reinforcement, antibacterial functionality has become increasingly important for advanced composite materials, especially in healthcare and hygiene applications. ZnO is well documented for its antibacterial properties, primarily attributed to the release of zinc ions (Zn^{2+}) and the generation of reactive oxygen species (ROS) [17,18]. A key challenge lies in maintaining antibacterial efficiency during prolonged use and under thermal aging conditions, which is critical for ensuring the reliability of these composites in real-world applications. However, the incorporation of ZnO-$CaCO_3$ and ZnO-TiO_2 into rubber composites using melt blending technology has not been previously examined, particularly regarding the elucidation of the ZnO effect in relation to residual chemicals in TW, such as ZnO, fillers, accelerators, and curing agents. As discussed, the compatibilization of TW with rubbers—especially polar rubbers like ENR—is promising and warrants further investigation, particularly with the use of modified ZnO combined with polar fillers like SiO_2. The ability of SiO_2 to form hydrogen bonds with ENR molecular chains enhances the dispersion and distribution of ZnO within the bulk matrix, thereby improving the overall performance of the composite [19].

This study aims to bridge the gap in understanding the multifunctional role of ZnO-SiO_2 in TW/ENR composites. By systematically evaluating the effects of ZnO-SiO_2 loading on chemical crosslinking behavior, tensile performance, and antibacterial activity, the study identifies the optimal ZnO-SiO_2 concentration to achieve a balance between mechanical and bioactive properties. Heat-aging tests further assess the long-term durability of these blends, focusing on the retained activity of ZnO within the TW. The insights gained from this research not only advance the design of high-performance, sustainable materials, but also

address critical challenges in recycling TW for high-value applications. The findings hold broad implications for industries seeking to develop eco-friendly, multifunctional materials that combine superior mechanical properties with durable antibacterial functionality.

2. Materials and Methods

2.1. Materials

Epoxidized natural rubber containing 25 mol% epoxide (ENR25) was obtained from Muang Mai Guthrie Co., Ltd., located in Surat Thani, Thailand. Waste tire rubber (TW) was supplied by Thai Rubb Tech Co., Ltd., based in Bangkok, Thailand, specifically from truck tire waste. The TW was derived from the tire tread of a truck tire after undergoing reclamation processes, which involved the random cleavage of crosslinked rubber chains, both along the rubber main chains and at the -C-S- bonds. With a viscosity of ML (1+4@100 °C) of 52.17, TW may contain an unknown rubber matrix, along with activators such as ZnO and stearic acid, as well as fillers including carbon black (CB), silica (SiO_2), and/or calcium carbonate ($CaCO_3$). Silicon dioxide-modified zinc oxide nanoparticles (ZnO-SiO_2), with a ZnO:SiO_2 weight ratio of 90:10 through wet processes, were collaborated and received from Global Chemical Co., Ltd., located in Samut Prakan, Thailand. The ZnO-SiO_2 nanoparticles possess a surface area of approximately 100 m^2/g, with the aggregate sizes ranging from 100 to 300 nm and individual particle sizes below 10 nm. Stearic acid and sulfur were procured from Imperial Chemical Co., Ltd., in Pathum Thani, Thailand, while 2,2′-dithiobis(benzothiazole) (MBTS) was supplied by Flexsys Inc., located in Termoli, Italy.

2.2. Preparation of TW/ENR Blends Filled with Modified ZnO

The compounding process involved masticating the TW/ENR with modified ZnO in an internal mixer (MX500, Charoen Tut Co., Ltd., Samutprakarn, Thailand) using various ratios of ZnO-SiO_2 concentrations at 0–20 phr. The mixing conditions were standardized with a temperature of 80 °C, a fill factor of 75%, and a rotor speed of 60 rpm. Initially, the ENR was masticated until its viscosity matched that of TW, after which TW was introduced into the mixer. Subsequently, additional chemicals listed in Table 1, including the ZnO-SiO_2 with the different concentrations, were incorporated. The total mixing process lasted 8 min, followed by the rolling of the mixture through a two-roll mill (Charoen Tut Co., Ltd., Samutprakarn, Thailand) to enhance dispersion and distribution. Rheometer testing was conducted to determine the production time before the blends were shaped via compression molding at 160 °C. It is important to note that the present formulation was specifically designed to elucidate the synergistic effects between the residual ZnO in TW and the additional ZnO-SiO_2 in the blends. Consequently, only the key potential chemicals, namely, the co-activator, accelerator, and sulfur curing agent, were included in the formulation.

Table 1. Formulation compositions of TW/ENR blends filled with modified ZnO-SiO_2.

Ingredients	Content (phr *)
TW/ENR	50/50
Stearic acid	1
ZnO-SiO_2	0, 10, 15, and 20
MBTS	1
Sulfur	2.5

* phr refers to part per hundred rubber.

2.3. Cure Characterization

The crosslink propagation of the TW/ENR compounds, along with the details of their chemical crosslinking, was analyzed using a moving die rheometer (MDR3000M, Mon-Tech, Buchen, Germany) operated at 160 °C for 30 min, with a fixed oscillation frequency of 1.66 Hz and an amplitude of 0.5° arc. The key parameters, including scorch time (T_{s1}), cure time (T_{90}), minimum torque (M_L), maximum torque (M_H), and the torque difference (M_H–M_L), were measured to evaluate the compounds' curing characteristics and crosslinking efficiency.

2.4. Tensile Properties

The tensile properties of TW/ENR blends filled with different concentrations of ZnO-SiO_2 were evaluated by conducting tensile tests on specimens cut from crosslinked sheets. These sheets were prepared through compression molding into dumbbell-shaped specimens in accordance with ISO 37 Type 2 standards [ISO 37: Rubber, vulcanized or thermoplastic—Determination of tensile stress-strain properties]. The tests were performed using a universal testing machine (Zwick Z 1545, Zwick GmbH & Co. KG, Ulm, Germany) at a crosshead speed of 500 mm/min under room temperature conditions. The tensile strength, elongation at break, and moduli at 100% and 300% elongation were measured and analyzed to assess the mechanical performance of the blends.

2.5. Morphologies

The morphologies and elemental compositions of the fractured surfaces of TW/ENR blends were analyzed using scanning electron microscopy (SEM) coupled with energy-dispersive X-ray spectroscopy (EDS). High-resolution images were obtained with an FE-SEM (Nova NanoSEM 450, EDS X Flash 6 series, FEI, Australia) at an accelerating voltage of 10 kV. To prepare the cross-sectional surfaces for analysis, the specimens were cryogenically fractured in liquid nitrogen. The fractured surfaces were then coated with a thin layer of gold to prevent electrical charging during the measurements, ensuring accurate imaging and compositional analysis. In addition, in order to characterize the surface roughness of a wider area, the optical microscope (OM) (Carl Zeiss Microscope GmbH, Oberkochen, Germany) was applied. The blends were quickly cut with a razor blade to create a smooth surface before capturing microscopic photographs. Also, a transmission electron microscope (TEM) (Model JEOL, JEM-1400, Tokyo, Japan), operated at an accelerating voltage of 80 kV, was also used to provide a clearer visualization of the particles. The powder specimens were dispersed in ethanol and sonicated for 30 min, then deposited onto carbon-coated copper grids. The solvent was allowed to evaporate completely before analysis.

2.6. Antibacterial Efficiency

The antimicrobial efficiency of the tire waste (TW)/epoxidized natural rubber (ENR) blends was evaluated by quantitatively measuring their ability to inhibit the growth of *Staphylococcus aureus* (*S. aureus*, ATCC 25923) and *Escherichia coli* (*E. coli*, ATCC 25922). Bacterial suspensions were prepared in liquid culture media (Nutrient Broth, NB) with an initial concentration of approximately 10^6 colony-forming units per milliliter (CFU/mL). A volume of 0.4 mL of each bacterial suspension was placed onto sterilized 5 × 5 cm^2 samples of the TW/ENR blends, which were kept in a Petri dish. To maintain contact between the bacterial suspension and the surface of the samples while preventing drying, the droplet was covered with a sterilized 4 × 4 cm^2 polyethylene (PE) film. The samples were then incubated at 37 °C for 24 h. After incubation, both the sample and the PE film were washed with 10 mL of soybean-casein digest medium (SCDLP). Following the washing step, the bacterial suspensions underwent a 10-fold dilution and were plated onto a nutrient agar

(NA) medium. After incubation at 37 °C for 24 h, the number of viable bacteria was counted. The percentage reduction in bacterial count (%R) was calculated according to Equation (1):

$$\%R = [(A - B)/A] \times 100 \quad (1)$$

where A is the number of viable bacteria in the treated samples after incubation and B is the number of viable bacteria in the control samples after incubation.

3. Results and Discussion

3.1. Cure Characteristics

The cure characteristics of the compounds and vulcanizate composites after exposure to a constant temperature for various durations is illustrated in Figure 1, which depicts the changes in torque as a function of time. When considering the over-cure performance of the composites, reversion curves appear with the addition and increasing concentration of ZnO-SiO_2. However, the maximum torque tends to increase, which can be attributed to two factors: (i) The higher ZnO content enhances the crosslink density by increasing activator levels in the crosslinking system. (ii) The greater SiO_2 loading within the bulk TW/ENR matrix improves the reinforcement efficiency, particularly in the ENR phase. Nonetheless, as the degree of polysulfide crosslinking intensifies, thermo-oxidative degradation sets in, leading to a decline in torque after the optimal crosslinking levels are reached [20]. Examining the cure rate slope reveals that a ZnO-SiO_2 loading of 10 phr results in the steepest slope, indicating the fastest crosslinking rate due to a balanced chemical loading that fulfills multiple roles in activation and reinforcement. However, at concentrations exceeding 10 phr, SiO_2 agglomeration becomes evident, impacting the overall performance. In addition, the thermal stability of the blends filled with varying concentrations of ZnO-SiO_2 was evaluated by monitoring the torque as a function of time at a fixed temperature of 160 °C, revealing significant differences. It was observed that the pure TW exhibited a constant torque over time, presenting a characteristic plateau curve. However, when blended with ENR, reversion curves appeared, showing a delayed decrease in torque as the ZnO-SiO_2 concentration increased. This reversion in ENR is attributed to thermo-oxidative degradation, resulting from the high reactivity of ENR's epoxide groups with oxygen. Additionally, the increase in polysulfidic bonds leads to the decomposition of sulfur linkages between TW and ENR molecules. As shown in Figure 1, the initiation of reversion was slightly delayed with increasing ZnO-SiO_2 concentrations. This indicates that the enhanced crosslink density, driven by the higher ZnO-SiO_2 content, slows down the degradation of rubber chains.

Figure 1 also illustrates the crosslinking curves, while Table 2 summarizes the minimum torque (M_L), maximum torque (M_H), and the torque difference (M_H–M_L), which corresponds to the estimated crosslink density of the TW/ENR composites. The table additionally provides the scorch time (T_{s1}) and cure time (T_{90}) of the compounds, highlighting variations in the production time of the composites. The observed increase in M_H with rising ZnO-SiO_2 concentrations reflects a higher crosslink density, as crosslinking restricts chain mobility and forms chemical bonds between TW/ENR molecules, while also enables the absorption of rubber chains onto the surfaces of ZnO and SiO_2 particles [21]. Furthermore, Figure 2 shows the morphologies of ZnO-SiO_2 in comparison to the active ZnO and commercial ZnO white seal. Active ZnO particles are significantly smaller than commercial ZnO. For ZnO-SiO_2, the chemical absorption of ZnO onto SiO_2 surfaces results in improved ZnO dispersion due to controlled interparticle distances. The rough surface of SiO_2 enhances interactions with rubber molecular chains, particularly ENR, forming a bound rubber layer that contributes to reinforcement. However, at higher SiO_2 concentra-

tions within the bulk TW/ENR matrix, the polar functional groups on the SiO_2 surface promote filler–filler interactions, leading to agglomeration and a subsequent reduction in reinforcement efficiency [22].

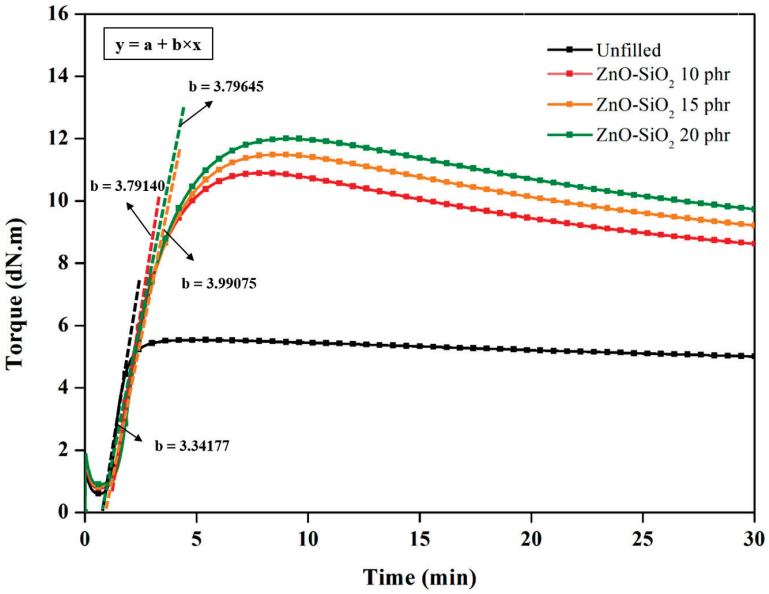

Figure 1. Cure characteristic curves of TW/ENR blend with different modified ZnO-SiO_2 loading. "Unfilled" refers to the TW:ENR ratio of 50:50 phr without ZnO-SiO_2.

Table 2. Crosslink properties of TW/ENR blends from compounds to vulcanizates with varying concentrations of the ZnO-SiO_2 activator.

Formulations	T_{s1} (min)	T_{90} (min)	M_L (d.Nm)	M_H (d.Nm)	M_H–M_L (d.Nm)
Unfilled	1.37	2.18	0.60	5.59	4.98
ZnO-SiO_2 10 phr	1.72	4.65	0.77	10.86	10.09
ZnO-SiO_2 15 phr	1.77	5.00	0.82	11.48	10.60
ZnO-SiO_2 20 phr	1.81	5.28	0.89	12.00	11.11

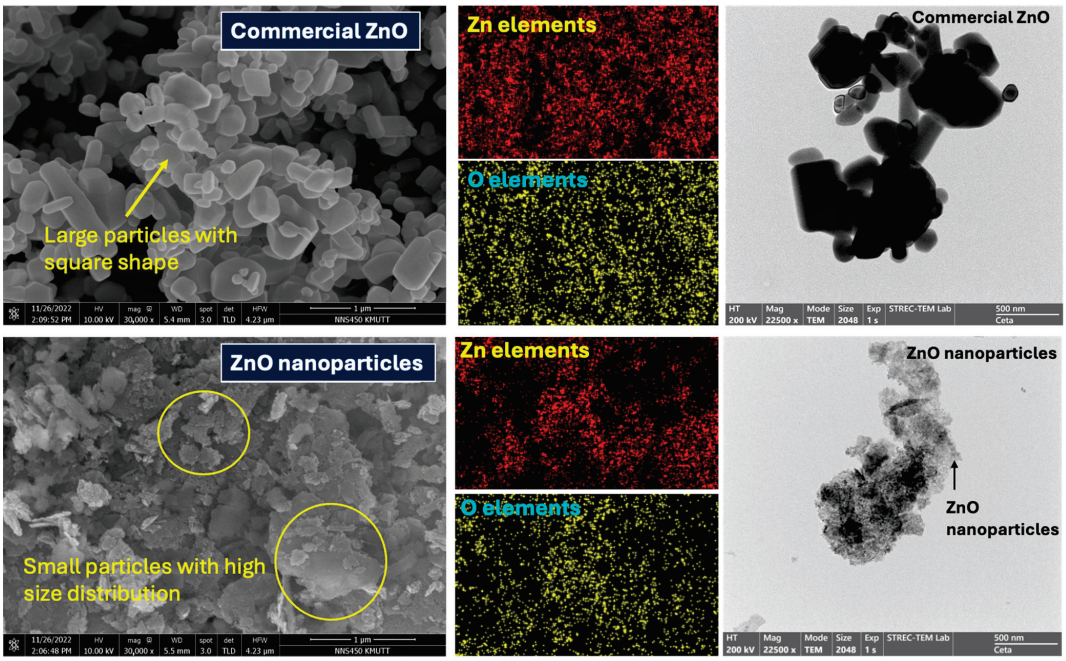

Figure 2. *Cont.*

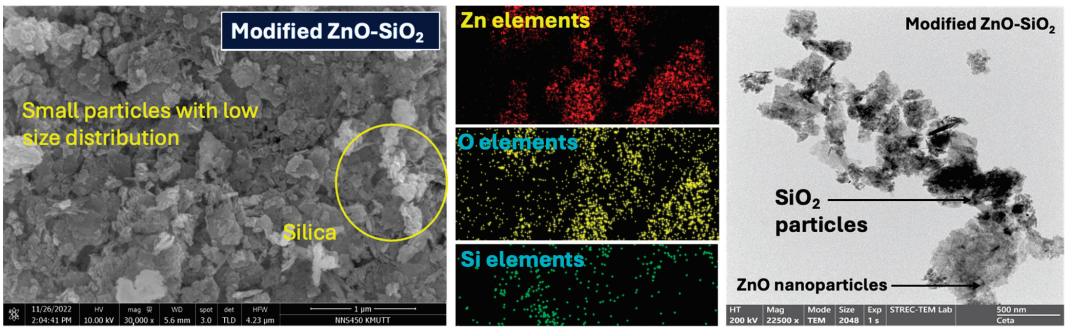

Figure 2. Morphologies of the solely ZnO-SiO_2, relative to the commercial ZnO.

3.2. Tensile Properties

Figure 3 shows the stress–strain plots, performed according to mechanical measurement standards. The formation of crosslinks that provide resistance to breakage, and three distinct regions of the tensile curves, are interpreted as follows:

(i) **Reinforcement region:** Without ZnO-SiO_2, the blends exhibit poor vulcanization, and their strength arises mainly from chain entanglement contributed by additional ENR. Young's modulus and the 100% modulus reflect these effects, with both increasing as ZnO-SiO_2 concentration rises. This behavior confirms an increase in chemical crosslink density, which enhances the blends' resistance to chain breakage. Notably, the modulus of blends without ZnO-SiO_2 is very low, indicating that the residual carbon black (CB) in TW does not provide significant reinforcement due to the insufficient diffusion of ENR molecules onto the particle surfaces. Conversely, the addition of ZnO-SiO_2 facilitates the activation of chemical crosslinking between the remaining TW and un-crosslinked ENR chains. The SiO_2 particles function as a reinforcing filler, interacting with rubber molecules to prevent blend breakage under applied mechanical deformation [23]. However, at concentrations exceeding 10 phr, no significant improvement is observed due to SiO_2 particle agglomeration.

(ii) **Rubber chain relaxation:** This region corresponds to the physical interactions between rubber chains and filler surfaces. An increased slope in this region indicates stronger rubber–rubber and rubber–filler interactions, resulting in greater friction among chains during extension. The slope of this region increases with ZnO-SiO_2 concentrations in the range of 10–20 phr, which can be attributed to the enhanced crosslink density and improved ENR-SiO_2 interactions.

(iii) **Strain-induced crystallization (SIC) and rubber failure:** SIC occurs as molecular chains align into a crystalline structure during elongation, typically noticeable at approximately 400% strain. Figure 3 shows that the increased crosslink density from ZnO activation enhances the degree of crystallization. Furthermore, hydrogen bonding between ENR molecules and SiO_2 particles accelerates the alignment of molecular chains along the direction of extension, as depicted in the proposed interaction mechanism in Figure 4 (Zone 3) [23,24]. However, differences in SIC improvement are reflected in the tensile strength and elongation-at-break data presented in Table 3. This difference highlights the need to consider the entire TW/ENR matrix, as shown in Figure 4 (Zones 1 and 2). In the TW proportion of the blends, filler particles with rubber molecular chain absorption are present. Without pyrolysis, rubber chains remain embedded on the filler surfaces as glassy or sticky bound rubber, with only the outer chains interacting with the SiO_2 surface and ENR molecules [25]. These interactions occur via induced dipole–dipole forces between the SiO_2 surface and polar groups on ENR molecules (Zone 2), as well as induced dipole–induced dipole interactions on the non-polar regions of ENR (Zone 1) [26]. However, at excessive

ZnO-SiO_2 concentrations, SiO_2 agglomeration inhibits interactions between the TW and ENR phases, leading to reduced tensile strength and limited elongation at break. It is important to note that ENR chains can also interact with ZnO particles due to the polarity of ZnO, particularly at higher concentrations. However, this interaction primarily occurs during the mixing and compounding stages. During vulcanization, the applied heat facilitates the release of Zn^{2+} ions and ROS from the ZnO surfaces, shifting ZnO's role to that of an activator for chemical crosslinking. Additionally, the residual ZnO in the rubber matrix continues to release ions, which predominantly contributes to properties such as antibacterial activity. This indicates that the reinforcement efficiency of the blends is primarily associated with the SiO_2 particles.

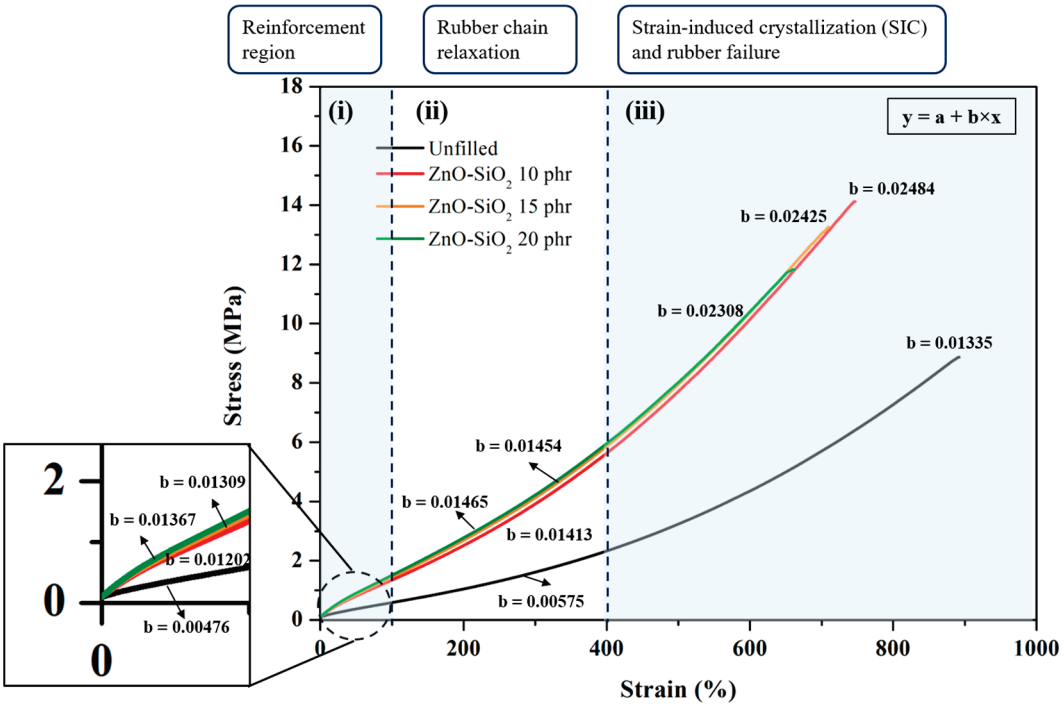

Figure 3. Stress–strain curves of TW/ENR filled with different concentrations of ZnO-SiO_2 to elucidate crosslinking behavior.

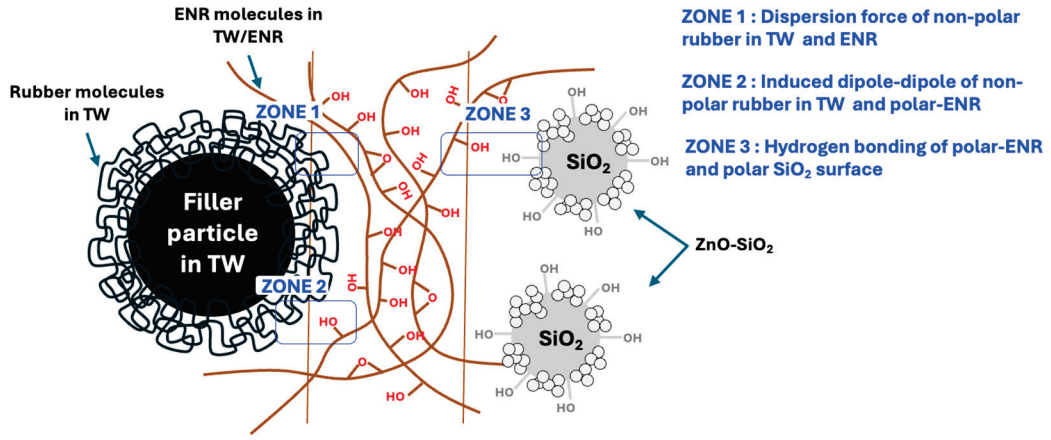

Figure 4. Proposed interaction of ENR with SiO_2 in ZnO-SiO_2, as well as the TW phases separation.

Table 3. Mechanical properties of TW/ENR blend with different modified ZnO-SiO_2 loading.

Formulations	100% Modulus (MPa)	300% Modulus (MPa)	Tensile Strength (MPa)	Elongation at Break (%)
Unfilled	0.60 ± 0.02	1.64 ± 0.04	8.79 ± 0.15	879.72 ± 22.09
ZnO-SiO_2 10 phr	1.35 ± 0.02	3.91 ± 0.05	14.24 ± 0.16	749.77 ± 22.86
ZnO-SiO_2 15 phr	1.45 ± 0.01	4.16 ± 0.03	13.59 ± 0.19	715.51 ± 25.22
ZnO-SiO_2 20 phr	1.50 ± 0.04	4.25 ± 0.03	12.34 ± 0.38	668.86 ± 37.80

3.3. Antibacterial Properties and Morphologies

The antibacterial efficiency of the TW/ENR blends is attributed to the release of zinc ions (Zn^{2+}) onto the blend surfaces, facilitated by the thickness of the bound rubber layer surrounding the ZnO embedded in TW and the additional ZnO-SiO_2 at varying concentrations. This occurs because the excess ZnO in both TW and ENR continues to release Zn^{2+} and reactive oxygen species (ROS) onto the rubber surfaces. The ROS react with bacterial cell walls, while Zn^{2+} penetrates the bacterial cells, interacting with their DNA and cytoplasm [27–29]. This mechanism, previously described in the literature, highlights the antibacterial activity of ZnO. Based on the crosslinking curves in Figure 1, it is evident that ZnO remains active even though the sulfur has been fully consumed during tire manufacturing. This demonstrates that the antibacterial properties of the blend arise from the positive synergy between residual ZnO in TW and the newly introduced ZnO-SiO_2.

To investigate the ability of Zn^{2+} and ROS to migrate through the rubber layer covering the ZnO surfaces, a swelling test was conducted to measure the total bound rubber (ß) and bound rubber layer thickness (δ') in the blends with increasing ZnO-SiO_2 concentrations. Blend compounds without accelerators or sulfur were pressed at 160 °C for 5 min, and approximately 2 g of the sample powders were placed in specific sieves and immersed in toluene at room temperature for 7 days. The weight of the blends was recorded, and the ß value was calculated using Equation (2), as provided below:

$$ß\ (\%) = (W_{fg} - W_f)/W_p \quad (2)$$

where W_f is the approximated weight of the filler in TW received from the remaining ash of the thermogravimetric analysis (TGA) and additional ZnO-SiO_2 concentrations. The factor W_p is the weight of the rubber, estimated from the TGA and ENR existing in the blends, and W_{fg} is the weight of the remaining filler with absorbed rubber after toluene extraction. Also, the δ' was evaluated through Equation (3) as follows:

$$\delta'\ (nm) = (m_2 - m_1(C_f))/\rho_r m_1(C_f)(S_f) \quad (3)$$

where m_1 is the mass of the rubber compound before extraction, and m_2 is the mass of the rubber–filler gel consisting of the non-dissolving bound rubber part and the filler. Parameters C_f and S_f are the mass concentration and the specific surface area of fillers in the blends regarding carbon black and SiO_2, respectively, whereas ρ_r refers to the density of solely ENR matrix.

The results of the ß and δ' values are summarized in Table 4. It was found that the TW/ENR blend exhibited approximately 20% bound rubber, correlating with the rubber absorption on the filler surfaces in TW and indicating a δ' value of 14.12%. This is attributed to the absence of pyrolysis reactions during the reclamation processes. On the other hand, the addition of ZnO-SiO_2 to the blends increased the ß value while reducing the δ' value. This behavior is due to the increase in SiO_2 filler content, which enhances rubber molecule absorption on the rough surface of the filler [30]. Consequently, the δ' value tends to decrease significantly. With an increasing ZnO-SiO_2 content, the highest ß value was

observed at 10 phr, accompanied by the lowest δ' value. This is likely due to the onset of ZnO-SiO_2 agglomeration within the TW/ENR matrix. This phenomenon highlights the enhanced opportunity for ion movement through the blend's surfaces, enabling further reactions with bacterial cell walls.

Table 4. Results of bound rubber and bound rubber layer thickness of the TW/ENR blends for elucidating the Zn^{2+} and ROS ions diffusion.

Formulations	β (%)	δ' (nm)
Unfilled	20.43 ± 0.13	14.12 ± 0.11
ZnO-SiO_2 10 phr	30.44 ± 1.05	2.99± 0.01
ZnO-SiO_2 15 phr	29.78 ± 1.12	4.34 ± 0.13
ZnO-SiO_2 20 phr	27.93 ± 1.78	4.95 ± 0.02

The antibacterial efficiency was initially evaluated using qualitative disk diffusion and quantitative cell counting methods under controlled conditions for 8 and 24 h. As shown in Figure 5, the qualitative test revealed no distinct inhibition zone. This suggests that the antibacterial activity, attributed to Zn^{2+} ions and reactive oxygen species (ROS), is likely confined to the surface of the blend, even at ZnO-SiO_2 concentrations of up to 20 phr, and does not extend to the surrounding areas. This behavior contrasts with the broader diffusion observed with silver (Ag) and copper (Cu) nanoparticles [31–33]. Thus, the use of ZnO-SiO_2 to release Zn^{2+} ions and ROS does not lead to the contamination of adjacent surfaces.

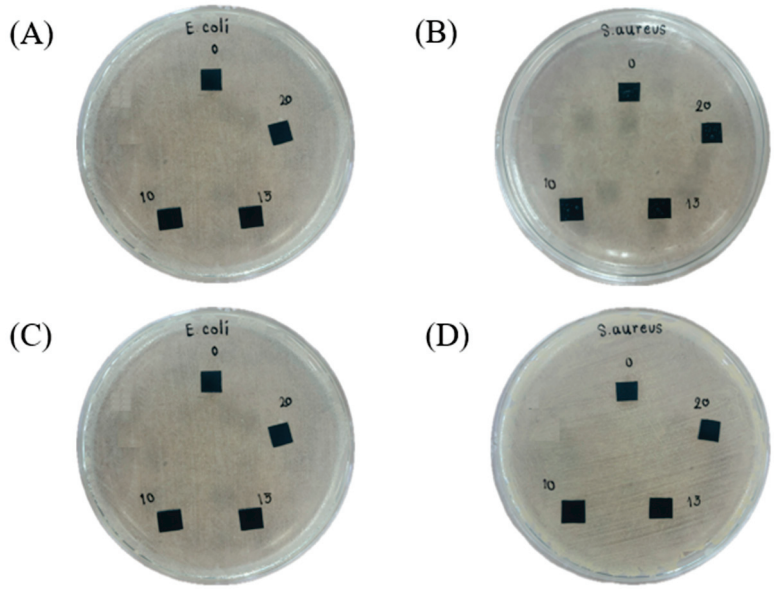

Figure 5. Disk diffusion qualitative measurement of TW/ENR filled with different concentrations of ZnO-SiO_2 against *Gram-negative E. coli* and *Gram-positive S. aureus* was performed at 8 h (**A**,**B**) and 24 h (**C**,**D**).

To evaluate the durability of the antibacterial performance after prolonged use, the blends were subjected to thermal aging at 70 °C for 72 h in a hot air oven, followed by quantitative antibacterial testing. As shown in Figure 6, the antibacterial efficiency remained largely unchanged, except for the TW/ENR blend without ZnO-SiO_2. This result indicates that the release of Zn^{2+} ions and ROS under photocatalytic conditions is limited in blends containing only ZnO. In contrast, blends with at least 10 phr of ZnO-SiO_2 maintained their antibacterial activity even under these harsh conditions. Figure 7 illustrates the surface morphologies and elemental composition analyzed using OM and SEM-EDX. As shown

in Figure 7A, the TW/ENR blend without ZnO-SiO_2 exhibits a smooth surface without agglomeration, as ZnO-SiO_2 is absent from the bulk matrix. However, in the TW/ENR matrix with ZnO alone, the ZnO particles were dispersed unevenly, potentially limiting the release of Zn^{2+} ions and ROS to the surface.

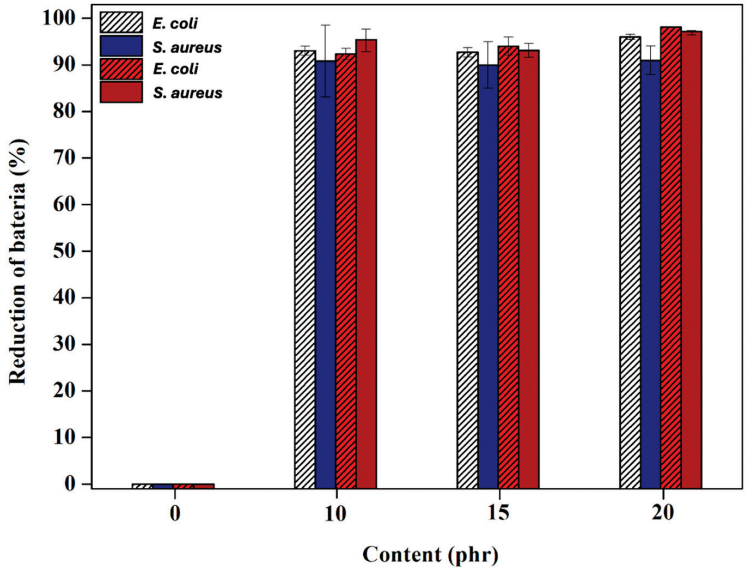

Figure 6. Antibacterial activities of the TW/ENR filled with different concentrations of ZnO-SiO_2 against *E. coli* and *S. aureus* within 8 h before and after aging at 70 °C for 72 h.

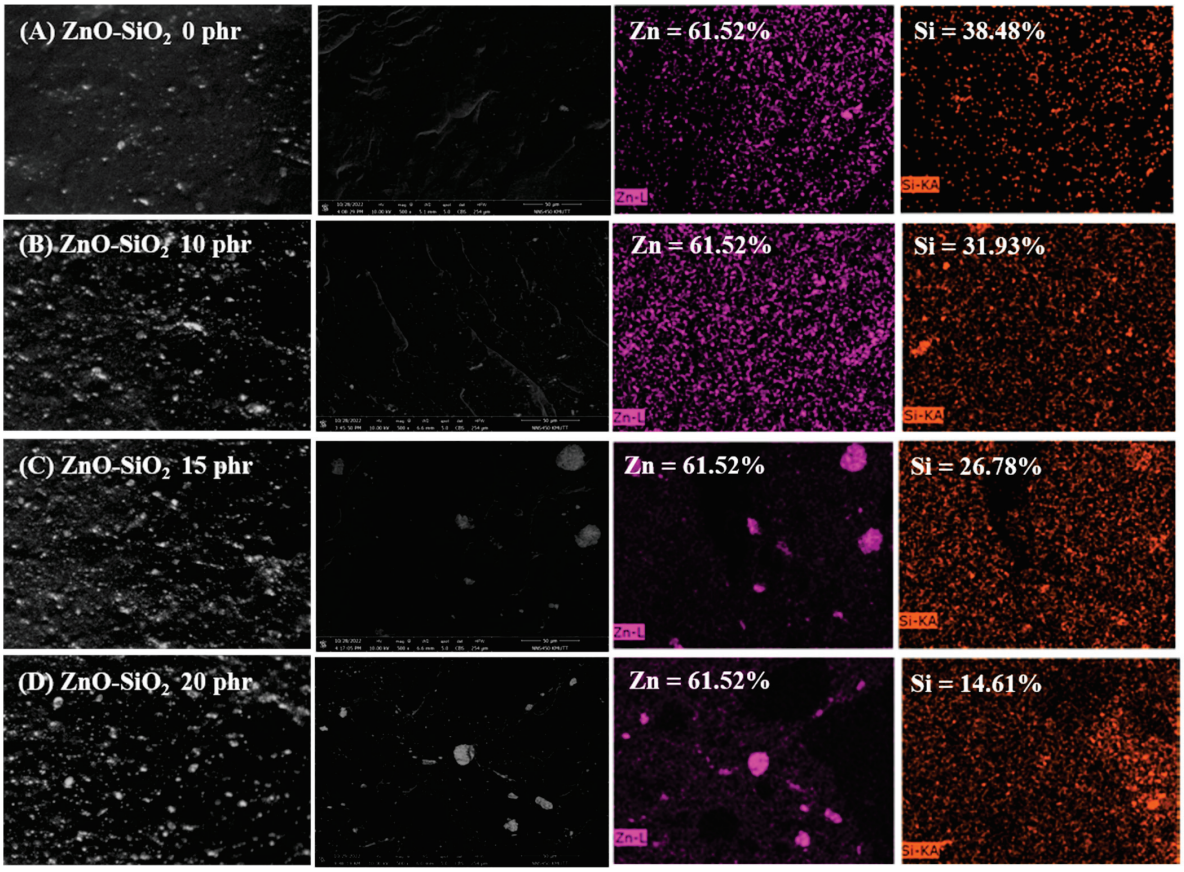

Figure 7. OM and SEM images, along with EDX elemental analysis, of TW/ENR blends filled with different concentrations of ZnO-SiO_2 after aging for 72 h at 70 °C: blend without ZnO-SiO_2 (**A**), blends with ZnO-SiO_2 at concentrations of 10 phr (**B**), 15 phr (**C**), and 20 phr (**D**) together with atom percentage % within TW/ENR matrix.

In blends containing 10 phr of ZnO-SiO_2, the optimal dispersion and distribution of ZnO throughout the TW/ENR matrix was achieved, as seen in Figure 7B. On the other hand, strong agglomeration was observed in blends with 15 or 20 phr of ZnO-SiO_2, indicating that the excessive SiO_2 content from ZnO modification led to particle clustering (Figure 7C,D) although a high concentration of Zn elements was found at the blend's surfaces. This agglomeration not only reduced antibacterial efficiency but also negatively affected the tensile properties, including tensile strength and elongation at break. Based on these findings, the optimal concentration of ZnO-SiO_2 was identified as 10 phr. At this concentration, ZnO acts effectively as an activator to enhance the antibacterial efficiency of the blends, while SiO_2 contributes to reinforcement. However, concentrations exceeding 10 phr result in pronounced agglomeration, compromising both mechanical and antibacterial properties.

4. Conclusions

The present study explored the effects of incorporating ZnO-SiO_2 into TW/ENR blends, at a ratio of 50:50 phr, on cure characteristics, mechanical properties, and antibacterial efficiency, with the key findings summarized below:

- The incorporation of ZnO-SiO_2 significantly enhanced the crosslink density, as indicated by the increased maximum torque and shorter cure times. At the optimal ZnO-SiO_2 loading of 10 phr, the composite exhibited the fastest crosslinking rate, attributed to the balanced effects of chemical activation and reinforcement. However, higher SiO_2 concentrations (>10 phr) resulted in filler agglomeration, which negatively impacted the crosslinking efficiency and mechanical properties.
- Tensile properties were enhanced at the optimal concentration of ZnO-SiO_2 at 10 phr. The enhancements in Young's modulus and tensile strength were attributed to the synergistic interactions between ENR molecules and SiO_2 surfaces, as well as strain-induced crystallization, which further reinforced the matrix during extension. However, at concentrations beyond 10 phr, particle agglomeration reduced the reinforcement efficiency, leading to reduced tensile strength and elongation at break.
- ZnO-SiO_2 contributed significantly to antibacterial activity, achieving up to 99.9% bacterial reduction at 10 phr. This efficiency was attributed to the release of Zn^{2+} ions and reactive oxygen species (ROS), which interact with bacterial cell walls and DNA. Notably, the antibacterial performance remained stable even after heat aging, confirming the durability of the ZnO-SiO_2-modified blends. However, higher ZnO-SiO_2 concentrations led to agglomeration, reducing the surface exposure and antibacterial effectiveness.
- The study identified 10 phr as the optimal ZnO-SiO_2 concentration, offering a balance between mechanical reinforcement, crosslinking efficiency, and antibacterial performance. While ZnO served as an activator and antibacterial agent, SiO_2 provided mechanical reinforcement through its rough surface interactions with ENR molecules.

These findings highlight the dual functionality of ZnO-SiO_2 in TW/ENR composites, showcasing its potential applications as a result of enhanced mechanical performance and antibacterial activity. This study lays the foundation for optimizing rubber-based materials for a wide range of applications, including healthcare and engineering. Further investigations into alternative filler designs and advanced processing methods could provide additional opportunities to enhance performance while minimizing agglomeration effects.

Author Contributions: N.K.: conceptualization, methodology, validation, formal analysis, writing—original draft preparation; T.B.: conceptualization, methodology, validation, formal analysis; J.J.: writing—review and editing; R.L.N.: writing—review and editing; Y.N.: visualization, supervision,

formal analysis, writing—review and editing, funding acquisition. All authors have read and agreed to the published version of the manuscript.

Funding: This research was funded by The Asahi Glass Foundation and King Mongkut's University of Technology Thonburi under the KIRIM ID: 27480, as well as the Petchra Pra Jom Klao Master's Degree Research Scholarship from King Mongkut's University of Technology Thonburi.

Data Availability Statement: All the data are available from the authors and can be provided on request.

Acknowledgments: This work was supported by King Mongkut's University of Technology Thonburi under the supported scholarships. Also, the Phramongkutklao College of Medicine is also acknowledged.

Conflicts of Interest: Author Raymond Lee Nip was employed by the company Global Chemical Co., Ltd. The remaining authors declare that the research was conducted in the absence of any commercial or financial relationships that could be construed as a potential conflict of interest.

References

1. Bhalla, G.; Kumar, A.; Bansal, A. Performance of scrap tire shreds as a potential leachate collection medium. *Geotech. Geol. Eng.* **2010**, *28*, 661–669. [CrossRef]
2. Martínez, J.D.; Cardona-Uribe, N.; Murillo, R.; García, T.; López, J.M. Carbon black recovery from waste tire pyrolysis by demineralization: Production and application in rubber compounding. *Waste Manag. Res.* **2019**, *85*, 574–584. [CrossRef] [PubMed]
3. Baker, C.S.L.; Gelling, I.R.; Newell, R. Epoxidized natural rubber. *Rubber Chem. Technol.* **1985**, *58*, 67–85. [CrossRef]
4. Darestani Farahani, T.; Bakhshandeh, G.R.; Abtahi, M. Mechanical and viscoelastic properties of natural rubber/reclaimed rubber blends. *Polym. Bull.* **2006**, *56*, 495–505. [CrossRef]
5. Li, S.; Lamminmäki, J.; Hanhi, K. Improvement of mechanical properties of rubber compounds using waste rubber/virgin rubber. *Polym. Sci. Eng.* **2005**, *45*, 1239–1246. [CrossRef]
6. Kroshefsky, R.D.; Price, J.L.; Mangaraj, D. Role of compatibilization in polymer nanocomposites. *Rubber Chem. Technol.* **2009**, *82*, 340–368. [CrossRef]
7. Olejnik, O.; Masek, A. Recent progress in bio-based elastomers with intrinsic self-healing mechanisms-part I: Natural rubber modifications. *J. Saudi Chem. Soc.* **2023**, *27*, 101676. [CrossRef]
8. Mensah, B.; Kang, S.I.; Wang, W.; Nah, C. Effect of graphene on polar and nonpolar rubber matrices. *Mech. Adv. Mater. Mod. Process.* **2018**, *4*, 1. [CrossRef]
9. Krainoi, A.; Boonkerd, K. Mechanical/electrical properties and strain sensibility of epoxidized natural rubber nanocomposite filled with carbon nanotube: Effect of sodium alginate as a surfactant on latex technology process. *Express Polym. Lett.* **2023**, *17*, 850–866. [CrossRef]
10. Krainoi, A.; Prasert, W.; Kesakomol, P.; Thongdee, P.; Nitchaphanit, S.; Sungsirin, N.; Boonsiri, T.; Watanaveeradej, V.; Ounjai, K.; Nakaramontri, Y. Effect of modified zinc oxide nanoparticles on enhancement of mechanical, thermal and antibacterial properties of disinfectant natural rubber latex foams. *Mater. Today Commun.* **2023**, *35*, 105601. [CrossRef]
11. Krainoi, A.; Poomputsa, K.; Kalkornsurapranee, E.; Johns, J.; Songtipya, L.; Nip, R.L.; Nakaramontri, Y. Disinfectant natural rubber films filled with modified zinc oxide nanoparticles: Synergetic effect of mechanical and antibacterial properties. *Express Polym. Lett.* **2021**, *15*, 1081–1100. [CrossRef]
12. Toh-ae, P.; Saramolee, P.; Chiarakorn, S.; Waraho-Zhmayev, D.; Kamthong, A. Enhanced photocatalysis of natural rubber foams filters boosted by modified-titanium oxide hybrid fillers: Gaseous benzene removal, antibacterial properties and air permeability. *Express Polym. Lett.* **2022**, *16*, 1229–1252. [CrossRef]
13. Laurentowska, A.; Ciesielczyk, F.; Siwińska-Stefańska, K.; Jesionowski, T. Precipitation of ZnO-SiO_2 oxide composites in the presence of natural rubber latex and selected non-ionic surfactants. *Pigm. Res. Technol.* **2022**, *41*, 199–209. [CrossRef]
14. Norazlina, H.; Fahmi, A.R.M.; Hafizuddin, W.M. $CaCO_3$ from seashells as a reinforcing filler for natural rubber. *J. Mech. Eng. Sci.* **2015**, *8*, 1481–1488. [CrossRef]
15. Meera, A.P.; Said, S.; Grohens, Y.; Luyt, A.S.; Thomas, S. Tensile stress relaxation studies of TiO_2 and nanosilica filled natural rubber composites. *Ind. Eng. Chem. Res.* **2009**, *48*, 3410–3416. [CrossRef]
16. Shayegan, Z.; Lee, C.S.; Haghighat, F. TiO_2 photocatalyst for removal of volatile organic compounds in gas phase—A review. *J. Chem. Eng.* **2018**, *334*, 2408–2439. [CrossRef]

17. Mendes, C.R.; Dilarri, G.; Forsan, C.F.; Sapata, V.D.M.R.; Lopes, P.R.M.; de Moraes, P.B.; Montagnolli, R.N.; Ferreira, H.; Bidoia, E.D. Antibacterial action and target mechanisms of zinc oxide nanoparticles against bacterial pathogens. *Sci. Rep.* **2022**, *12*, 2658. [CrossRef] [PubMed]
18. Zhang, L.; Jiang, Y.; Ding, Y.; Daskalakis, N.; Jeuken, L.; Povey, M.; O'neill, A.J.; York, D.W. Mechanistic investigation into antibacterial behaviour of suspensions of ZnO nanoparticles against *E. coli*. *J. Nanopart. Res.* **2010**, *12*, 1625–1636. [CrossRef]
19. Raksaksri, L.; Chuayjuljit, S.; Chaiwutthinan, P.; Boonmahitthisud, A. Use of TBzTD as noncarcinogenic accelerator for ENR/SiO_2 nanocomposites: Cured characteristics, mechanical properties, thermal behaviors, and oil resistance. *Int. J. Polym. Sci.* **2017**, *2017*, 9721934. [CrossRef]
20. Wang, M.; Wang, R.; Chen, X.; Kong, Y.; Huang, Y.; Lv, Y.; Li, G. Effect of non-rubber components on the crosslinking structure and thermo-oxidative degradation of natural rubber. *Polym. Degrad. Stab.* **2022**, *196*, 109845. [CrossRef]
21. Peng, Z.; Kong, L.X.; Li, S.D.; Chen, Y.; Huang, M.F. Self-assembled natural rubber/silica nanocomposites: Its preparation and characterization. *Compos. Sci. Technol.* **2007**, *67*, 3130–3139. [CrossRef]
22. Li, G.; Zhao, T.; Zhu, P.; He, Y.; Sun, R.; Lu, D.; Wong, C.P. Structure-property relationships between microscopic filler surface chemistry and macroscopic rheological, thermo-mechanical, and adhesive performance of SiO_2 filled nanocomposite underfills. *Compos.—A Appl. Sci.* **2019**, *118*, 223–234. [CrossRef]
23. Chen, Y.; Peng, Z.; Kong, L.X.; Huang, M.F.; Li, P.W. Natural rubber nanocomposite reinforced with nano silica. *Polym. Sci. Eng.* **2008**, *48*, 1674–1677. [CrossRef]
24. Wang, Y.; Liao, L.; Zhong, J.; He, D.; Xu, K.; Yang, C.; Luo, Y.; Peng, Z. The behavior of natural rubber–epoxidized natural rubber–silica composites based on wet masterbatch technique. *J. Appl. Polym. Sci.* **2016**, *133*, 43571–43580. [CrossRef]
25. Sengloyluan, K.; Sahakaro, K.; Dierkes, W.K.; Noordermeer, J.W.M. Silica-reinforced tire tread compounds compatibilized by using epoxidized natural rubber. *Euro. Polym. J.* **2014**, *51*, 69–79. [CrossRef]
26. Tang, X.; Chen, Z.; Liu, J.; Chen, Z.; Xie, W.; Evrendilek, F.; Buyukada, M. Dynamic pyrolysis behaviors, products, and mechanisms of waste rubber and polyurethane bicycle tires. *J. Hazard. Mater.* **2021**, *402*, 123516. [CrossRef]
27. Susteric, Z.; Kos, T. Elastomer-Clay nanocomposites: Effect of Elastomer Polarity. *Macromol. Symp.* **2010**, *296*, 311–315. [CrossRef]
28. Wang, L.; Hu, C.; Shao, L. The antimicrobial activity of nanoparticles: Present situation and prospects for the future. *Int. J. Nanomed.* **2017**, *12*, 1227–1249. [CrossRef] [PubMed]
29. Sirelkhatim, A.; Mahmud, S.; Seeni, A.; Kaus, N.H.M.; Ann, L.C.; Bakhori, S.K.M.; Hasan, H.; Mohamad, D. Review on zinc oxide nanoparticles: Antibacterial activity and toxicity mechanism. *Nanomicro Lett.* **2015**, *7*, 219–242. [CrossRef] [PubMed]
30. Nordin, R.; Yusof, R.; Nawawi, W.I.; Salihin, M.Z.; Ishak, Z.A.M. Effect of several commercial rubbers as substrates for zinc oxide in the photocatalytic degradation of methylene blue under visible irradiation. *Express Polym. Lett.* **2020**, *14*, 838–847. [CrossRef]
31. Choi, S.S.; Ko, E. Novel test method to estimate bound rubber formation of silica-filled solution styrene-butadiene rubber compounds. *Polym. Test.* **2014**, *40*, 170–177. [CrossRef]
32. Amany, A.; El-Rab, S.F.G.; Gad, F. Effect of reducing and protecting agents on size of silver nanoparticles and their antibacterial activity. *Pharm. Chem.* **2012**, *4*, 53–65.
33. Ruparelia, J.P.; Chatterjee, A.K.; Duttagupta, S.P.; Mukherji, S. Strain specificity in antimicrobial activity of silver and copper nanoparticles. *Acta Biomater.* **2008**, *4*, 707–716. [CrossRef]

MDPI AG
Grosspeteranlage 5
4052 Basel
Switzerland
Tel.: +41 61 683 77 34

Polymers Editorial Office
E-mail: polymers@mdpi.com
www.mdpi.com/journal/polymers

Academic Open
Access Publishing

mdpi.com

ISBN 978-3-7258-7574-0